Department of Exploration Geophysics

Hydrogeophysical investigation of water recharge into the Gnangara Mound

Elmar Strobach

This thesis is presented for the Degree of

Doctor of Philosophy

of

Curtin University

March 2013

To the best of my knowledge and belief this thesis contains no material previously published by any other person except where due acknowledgment has been made. This thesis contains no material which has been accepted for the award of any other degree or diploma in any university.

ABSTRACT

Increased demand for freshwater in combination with a drying climate has led to water table decline on the Gnangara Groundwater Mound north of Perth, Western Australia. For sustainable groundwater management, a regional-scale modelling system has been developed. Accurate groundwater modelling requires good estimates of aquifer recharge, which in the case of the Superficial Aquifer may be achieved by a Vertical Flux Model. Recharge studies provide this model with input parameters such as unsaturated hydraulic conductivity, soil moisture content and water retention potential. Another key component of sustainable water resource management is to understand the biophysical processes that are involved in surface- and groundwater and plant interaction in order to conserve the natural ecosystem.

Hydrogeophysical measurements have the potential to provide non-invasive, in-situ physical parameter estimation for the near-surface. As such it provides a tool to quantify and monitor unsaturated zone dynamics. From hydrogeophysical observations, hydrogeologic parameters can be deduced and then used as constraints for the numerical modelling. Geophysical monitoring further provides field evidence to corroborate or reject modelling results. Some subsurface physical properties are invariable over long time-scales (e.g. depositional features, porosity) and can be mapped with geophysical measurements. Other subsurface components are subject to temporal variations. They are determined by environmental factors, for example the water content changes during the hydrogeologic cycle. Capturing those seasonal variations requires time lapse investigation.

The groundwater recharge rates at the Gnangara Mound are dominated by winter rainfall in a Mediterranean climate setting. Rainwater infiltrates through a sandy soil profile that contains water retentive soil horizons. In this thesis, the physical properties of the soil and their temporal variations are explored using Ground-Penetrating Radar (GPR) and neutron logging to delineate the influence of water retentive soil horizons.

The spatial distribution of indurated, friably cemented sand layers varies spatially. To delineate these layers, large-scale surface 2D common offset GPR reflection profiles that span the entire groundwater mound are examined. It is found that these layers produce strong reflections in the radargrams that suggest a strong contrast in water content; indicating water retentiveness is present. An analysis scheme is developed that allows large-scale classification of water retention potential based on spatial reflector configuration and reflection strength. The results from spatial investigation indicate that the distribution of potentially water retentive layers is patchy. Where pronounced layers exist, they commonly show dip, which in combination with pipe structures (dissolution and root channels) is likely to result in preferential flow.

Laboratory dielectric experiments on samples with variable water saturation demon-

strate that retentive and non-retentive soil horizons have a similar dielectric permittivity versus water content relationship which corroborates that high reflectivity indicates elevated water content.

Six test sites were selected for time lapse investigation based on soil properties and hydrogeologic setting. A range of surveys were performed before, during and after the annual rainfall cycle in 2011 to capture the temporal variability of vertical water content distribution. Time-lapse crosswell- and surface-to-hole borehole radar datasets were acquired. To obtain high certainty moisture content profiles from those data, a new processing scheme is proposed based on a combined use of zero-offset profiling and vertical radar profiling. Sequential and baseline difference curves are calculated and reveal infiltration scenarios ranging from simple wetting and unsaturated flow regime, to delayed wetting and impeded flow. While some impact on infiltration can be attributed to retentive soil layers, it was found that vegetation appears to play a crucial role in determining soil moisture depletion between wetting cycles. The results from the time-lapse GPR were validated by analysis of long-term time-lapse neutron logging. Neutron logging reinforces the view that retention horizons are unlikely to store additional plant available water compared to the clean sand intervals.

Very near-surface water content measurements are a challenge with commercial common offset GPR systems. I develop a new analysis methodology that enables estimation of water content as part of the spatial and temporal characterization of shallow moisture distribution. Dispersion curves are derived from shallow diffracted wavefields that appear in common offset GPR due to a waveguide structure. Inversion based on modal wave propagation in a waveguide allows derivation of waveguide parameters. Dispersion curves are demonstrated to be sensitive to small changes in waveguide properties, which are strongly dependent upon water content. Field examples illustrate the full potential of this technique in lateral near-surface water content quantification.

The small- and large scale surveys presented in this thesis form the basis for examination and advancement of the radar methodology in a sandy environment as well as providing field evidence for hydrogeologic significance and distribution of water retentive soil horizons in the unsaturated zone of the Swan Coastal Plain, Western Australia.

Acknowledgements

Firstly, I would like to thank the German, Australian and US American people to largely finance the education I have received from elementary school through to university. Without the public funding for excellent education systems and research institutes in those countries, none of this work would have been possible. I hope that world-class academic education will continue to be free of charge in Germany, and that universities, departments and researchers can continue to perform publicly funded basic research.

Secondly, I am grateful for the education I received from my parents Elisabeth and Eckhard who raised me as a curious individual, who enjoys to discover the world we live in from a scientific perspective, but without having lost the naive sense for the beauty of our environment and the people that live in it. Financial support from my family that extends to my grandparents was always greatly appreciated and allowed me to survive as student and to participate in various field trips.

The last family member whose ongoing mental support helped me get through the hard times of BSc, MSc and PhD thesis completion is my partner Franka, without her, those challenging times would have often been unbearable.

I am grateful to my supervisors Anton, Brett, Christian and Michael for providing me with the research challenge and for ongoing support to perform field experiments, attend conferences and for editing my written word.

I would like to acknowledge the Department of Exploration Geophysics and Curtin University for financial support through a CIPRS scholarship; and the ASEG Research Foundation for providing a three year research grant to perform field experiments and to visit conferences.

Special thanks goes to Water Corporation and the Department of Water of Western Australia for supporting hydrogeophysical projects at our department, and for providing a wealth of spatial information (i.e. borehole logs, water table model, digital elevation model, soil and geologic maps, airphotography etc.). People I am grateful to in those institutions for their help are Michael Martin, Penny Wallace-Bell, Claire Robertson, Jon-Philippe Pigois, Peter Muirden, Rosemary Lerch, Chengchao Xu, Sandie McHugh and Sarah Bourke.

Ray Froend and Muriel Davies from Edith Cowan University provided me with soil information and direct moisture content measurements at Whiteman Park which

supported the neutron logging data. They also helped distributing neutron data which was measured by Kel Baldock from HydroSmart. I thank Kel Baldock for providing me with neutron data and for practical insights into the neutron measurements.

The dielectric lab measurements were performed on the equipment and with the help of Matthew Josh and Ben Clennell from CSIRO.

GroundProbe kindly provided me with the Mala borehole radar antennae which is greatly appreciated as it made the time-lapse investigations possible.

Gavan McGrath from University of Western Australia lend me the SuperSting resistivity meter.

My field work would have not been possible without the help of numerous people, namely Andrew Greenwood, Konstantin Tertyshnikov, Dominic Howman, Franka Menzel, David Euteneuer, Eva Caspari, Sinem Yavuz, Christian Dupuis, Brett Harris, Claire Robertson, Penny Wallace-Bell, Majed Almalki, Michaela Spiske and Marietta Garcia.

My final thanks goes to all of my colleagues and friends who catered for interesting and productive discussions, both, on a personal and professional level.

Preface

Liquid water is the essence of life on earth. While oceans provide a practically infinite reserve of water molecules, they are contaminated by dissolved salt. Terrestrial flora and fauna have largely adapted to survive on water with low salt concentrations and thus humans not only depend on freshwater resources for direct consumption, but also for agriculture and industrial applications. In dry environments where surface freshwater from lakes, rivers and ice are in short supply, groundwater is a valuable resource for human activity and groundwater dependent ecosystems.

Global climate change appears to affect arid regions the most, which leads to increased water stress in already dry environments (*Kundzewicz et al.*, 2007). Future scenarios that have to be considered as one of the big challenges of human-kind in the 21^{st} century are human migration away from these regions and conflicts where countries compete for freshwater resources.

In arid and semi-arid climates, the groundwater recharge is small and thus a good understanding of the groundwater system and recharge mechanisms is paramount. With a clear understanding of recharge and its spatial distribution, regional water resources can be managed in a sustainable way and predictions can help secure future water availability.

In Perth, Western Australia, the aquifers found on the Gnangara Groundwater Mound are the most important freshwater resource for a growing society. The major aim of groundwater resource management is conserving the natural environment in order to preserve the biodiversity of local flora and fauna, for example in wetlands. On the Swan Coastal Plain, the freshwater of the superficial aquifer supports life in these ecosystems, thus protecting them means to limit the influence of human activity on the shallow groundwater level, which in turn requires sustainable exploitation of the groundwater resource.

Perth has the Indian ocean at its doorstep, which enables a rich country like Western Australia to consider desalination as a feasible alternative to groundwater extraction. However, freshwater is a commodity which not only has a value, but also a price. The cost of groundwater extraction is lower than for desalination, which makes it attractive to exploit the natural subsurface freshwater resource. Under the constraint of conservation, economics provide a secondary motivation for this work.

I devoted my postgraduate research to hydrogeophysics because I believe that, just as oil replaced gold, water might replace oil as the most precious natural resource for generations to come. But not only the potential economic impact of water as a resource guided my decision to get involved into the science of water. Even more so did my great concern for the natural environment as we tend to become reckless and destructive in every respect once greed of gain grips us.

This work makes a small contribution to better understand the recharge mechanisms to ultimately support sustainable groundwater management of the Gnangara Groundwater Mound resource. The non-invasive hydrogeophysical techniques used in this dissertation enable monitoring of rainfall infiltration through the sandy sediments and investigate the influence of water retentive cementation horizon on the local flow. Along the way, I have critically reviewed and partially enhanced some of the measurement techniques that I applied during my measurement campaigns. The case-studies in this work provide examples that can be applied in other parts of the world where water supply is a key factor for survival.

Contents

Chapter 1

Introduction

The Preface addressed my motivation to undertake this research in a global context. In this short chapter, I would like to state the research objectives from a scientific and technical perspective.

1.1 Motivation for Research

To sustainably manage the Gnangara Mound groundwater system is a demand of the environmentally conscious Australian citizens, and the responsibility of the Department of Water (DoW), Western Australia. The DoW monitors groundwater levels of the Gnangara Mound aquifers and allocates water extraction permits. As climate, land-use and extraction rates have changed in recent decades, groundwater levels of the supericial aquifer have declined. This change has had a demonstrated impact on local ecosystems. In order to better understand and manage the groundwater resources, the DoW and the Water Corporation have developed a numeric modeling system called the Perth Regional Aquifer Modeling System (PRAMS). The Vertical Flux Model (VFM) is a recharge model that is built on top of PRAMS. This VFM attempts to quantify the net water flux to the water table. The algorithm used for flux calculation is called WAVES (Water, Atmosphere, Vegetation, Evapotranspiration and Soil). As a process-based biophysical numerical model, it requires a multitude of input parameters which have to be measured or derived from assumptions. More detail about the modeling systems will be given in Section 2.3.3. The deployment of an unsaturated flow modeling system for recharge estimation is rarely performed on that scale. However, large-scale

WAVES modeling is a reasonable approach under the climatic and lithologic conditions of the Swan Coastal Plain because parameterization can be simplified by introducing few representative recharge units (i.e. the number of realistic combinations of lithology, climate, etc. is manageable). Recharge on the Gnangara Mound is characterized by drainage from rainfall which occurs in strong rainfall events during the wet winter months. The summer is largely dry and hot and the soil profile is gradually depleted of water. The simple lithology (i.e. aeolian sands) in combination with climatic characteristics makes unsaturated flow calculation for this environment in principle less complex in comparison to more geologically diverse areas (e.g. floodplain deposits where clay lenses and sand/gravel are interbedded in the shallow subsurface).

Some parameters used for WAVES modeling, however, are still under-determined, such as the soil properties. Soils are currently classified based on the main geologic and landform units and associated, characteristic soil type (i.e. dune systems versus fluvial deposits). However, heterogeneities within the soils classified as dune sands are not yet included. A close inspection of the soil profiles reveals that indurated sand horizons occur throughout the Gnangara Mound. Those accumulation horizons are part of a Podosol soil and are locally called ”coffee rock”. They create an inhomogeneous complex soil profile which dominates large parts of the central Bassendean Sand formation. The VFM in its current form does not explicitly account for those complex duplex soils. This has lead to over-estimation of recharge in some cases where the accumulation horizons impede flux or store additional water which is then lost to evapotranspiration.

It is possible, however, that this storage of water can be desirable for the ecosystems as it may provide plant-available water usable by native vegetation during the dry summer period. This, in turn, may mean that the adverse effect of falling water table levels may be compensated by water retentive lithologies.

The main hydrogeologic objectives of this study are to better understand how layers influence infiltration, what the layer characteristics are (i.e. physical and spatial properties) and how they are distributed on a large scale.

In the same hydrogeologic context, the DoW and Water Corporation are investigating the connection between the most superficial water table and deeper water tables of the Superficial formations. Some clays are known to form locally perch water, which

means that the pumping of deeper aquifers may have less impact on the most superficial water level, thus the impact on ecosystems is reduced. Some of these submerged layers are discussed in this thesis, but the focus is on the unsaturated zone.

Ground-penetrating Radar (GPR) is the main geophysical remote sensing tool used in this thesis to detect potentially water retentive layers, and to investigate their influence on infiltration in a natural environment. This work is the first GPR study that addresses the beforementioned objectives to be published for the Gnangara Mound. Thus, parts of this work have an elementary and explorative character which lays the basis for future investigations.

Water retentive soil layers appear as strong reflections in the common offset (CO) GPR data. Thus, GPR images, also called radargrams, can provide valuable insight into the layers' spatial continuity, their topology and other features which might be indicative of their hydraulic properties and their influence on local flow. The large-scale shape of the water table reflection, which is evident in some GPR profiles, can provide valuable information about the hydraulic properties of the Superficial formations on a scale that is not captured by the sparsely distributed boreholes. Time-lapse borehole radar (BHR) has been applied to characterize infiltration on a test-site scale. The BHR technique allows to quantify water content in between two boreholes. When acquired in a time-lapse manner, unsaturated zone dynamics can be monitored and provide information on unsaturated flow (i.e. initial wetting) and vadose zone water balance (i.e. wetting - drying cycle). It also resolves the vertical complexity of the soil profile, and aids in interpreting the surface 2D GPR cross-sections.

In order to better understand the petrophysical properties of the soil materials, particularly with regard to differentiation of clean sand from accumulation horizons, I collected and investigated a range of different soil samples in the field. A coaxial transmission line laboratory setup enables to measure the electrical conductivity and dielectric permittivity as a function of soil water content. The outcomes of dielectric laboratory experiments provide valuable information also for the large-scale GPR data analysis. GPR wave propagation in the subsoil (i.e. velocity, reflectivity) is mainly determined by dielectric permittivity and contrasts in dielec. perm. (or water content and water distribution, respectively). The petrophysical relationship between permittivity and water content further provides the basis for interpretation of smaller scale test-site

studies, including 3D GPR and borehole radar (BHR).

In emerging sciences such as hydrogeophysics, the development and improvement of new and existing methods provides another objective for researchers. Although GPR has rapidly evolved and has been used extensively over the last two decades, the fields of application remain numerous, while the GPR community remains comparably small (i.e. compared to, for example, the seismic/seismologic community). Thus, case-studies in certain research areas are still rare (e.g. long term time-lapse, borehole radar) and standardized procedures are still under development. This work showcases several case-studies that should be of general interest and further our understanding of the use of GPR methods in sandy podosol environment. Data analysis procedures contain some new aspects that enhance processing procedures and information extraction from GPR records, and ultimately contribute to the practitioners' toolkit.

1.2 Thesis Outline

This thesis is composed of seven chapters. For the benefit of the reader, the organization of these chapters and their content are summarized in the following.

Following this introductory chapter, chapter 2 puts the geographic features of the Gnangara Mound area into the perspective of groundwater recharge. Climate, landforms, geology and hydrogeology are summarized. The chapter is concluded by a detailed inspection of the Podosol soil and the accumulation horizons present in the shallow subsurface.

Chapter 3 deals with the physical properties of the sands found throughout the Gnangara Mound area. The hydrophysical characteristics of the sand are outlined by examining existing data such as grain size distribution, hydraulic conductivity core tests, water retention curves and neutron logging data. The second part of this chapter is a synopsis of electric and dielectric laboratory measurements and analysis made on representative soil samples with varying water saturation (i.e. as a function of water content). The samples were collected in order to span a wide range of the most prominent soil constituents. The measured dielectric permittivity versus water content curves are compared with empirical relationship and two mixing models: the Lichtenecker-Rother and a recently published Hashin-Shtrikman average model, both

of which contain physically meaningful fitting parameters. The main outcome of this work is that the ”coffee rock” soil horizons have very similar dielectric properties to the clean sands, while the hydraulic properties are in contrast.

Chapter 4 is dedicated to 2D and 3D surface GPR used to delineate the spatial distribution and properties of reflectors within the soil. The general hydrogeologic setting is analysed based on two large-scale 2D GPR transects which span the Gnangara Mound in an East-West direction. I interpret the ground response and provide possible scenarios for the origin of reflectors, and soil layer development. In this context, a small-scale pseudo 3D survey reveals the 3D constellation of a distinct unsaturated zone reflector which confirms the undulating topology observed on the large-scale 2D transect. Based on a test-site scale 3D survey at Whiteman Park, I show that absolute reflected energy within the unsaturated zone shows good correlation with the bulk dielectric permittivity of that same interval if a reflector (i.e. water retentive horizon) is present. Those case studies lay the basis for large-scale semi-quantitative analysis of unsaturated zone reflectors in the last setion of this chapter. Subsections 4.2.2 and 4.2.3 contain concepts which have been presented at conferences in 2010 (*Strobach et al.*, 2010a,b) and 2011 (*Strobach et al.*, 2011), respectively. Due acknowledgement is made in the text.

The last technical chapter 5 is an extension of a paper accepted for publication in Journal of Geophysical Research (*Strobach et al.*, 2013). The research outcome of this work presents a new method to exploit the information content of dispersive diffractions observed in common offset GPR data. These shallow diffracted wavefields arise as a result of a waveguide geometry that forms due to near-surface stratification. This occurs for example when a wet layer develops over dry sand after rainfall. The original motivation for this work was to better understand the origin of unexpected shallow diffracted wave arrivals and to investigate their dispersive character. After a literature review revealed that these wavefields had not been closely studied yet, the main objective for this work became the novelty of the described methodology. However, the hydrogeologic outcomes from this research corroborate our understanding of groundwater infiltration characteristics. This chapter therefore integrates well into the main objectives of this dissertation.

Chapter 6 deals with borehole radar and neutron logging time-lapse datasets; from

acquisition to analysis and interpretation. Seasonal changes in soil moisture distribution are analyzed with respect to soil retention properties and unsaturated flow characteristics. This chapter has two major motivations: The first is of technical and methodological character where I propose a scheme to improve the precision and accuracy of crosswell zero-offset radar profiling by using vertical radar profiles. The second objective is from a hydrologic perspective where I try to improve our understanding of the mechanisms and impact that water retentive layers have as they impede unsaturated flow, and how water balance is affected.

Finally, chapter 7 summarizes the main outcomes from the studies presented in this thesis. Aspects that require further investigation are pointed out in order to direct future work.

Chapter 2

Geography of the Gnangara Mound area

The Gnangara Mound area is located on the Swan Coastal Plain north of Perth in Western Australia. It spans an area of roughly 2000 km^2 stretching approximately 70 km along the coastline and 30 km inland (see extent in Figure 2.1b and c). It derives its name from Lake Gnangara which is located at the suburb Gnangara north of the city center. The word Gnangara originates from the aboriginal Noongaar language and possibly means spring[1].

The current landscape of the Gnangara Mound area is predominantly formed by vegetated dune systems with wetlands dividing dune systems of different ages. The Gnangara Mound is considered a groundwater mound due to its hydrogeologic characteristics, which is discussed in section 2.3.1. Its hydrologic bounds are i) the Darling Fault in the east, ii) the Swan River in the south, iii) the Indian Ocean in the west and iv) the Moore River in the north (*Davidson*, 1995; *Davidson and Yu*, 2006). The aquifers that comprise the Gnangara Mound groundwater system are currently the main freshwater resources for the Perth region.

Several Perth suburbs are located on the Gnangara Mound area, especially at the southern margins close to Perth city center. Other land use includes agriculture especially in the east (i.e. pasture for cattle), pine tree plantations in the west, and natural banksia bushland in conservation areas and state forest on the central mound (see Figure 2.2). For this study, the natural banksia bushland on the central Bassendean Sand

[1] http://noongarculture.org.au/ncd/uploads/brendan/Perth suburbs aboriginal names.pdf

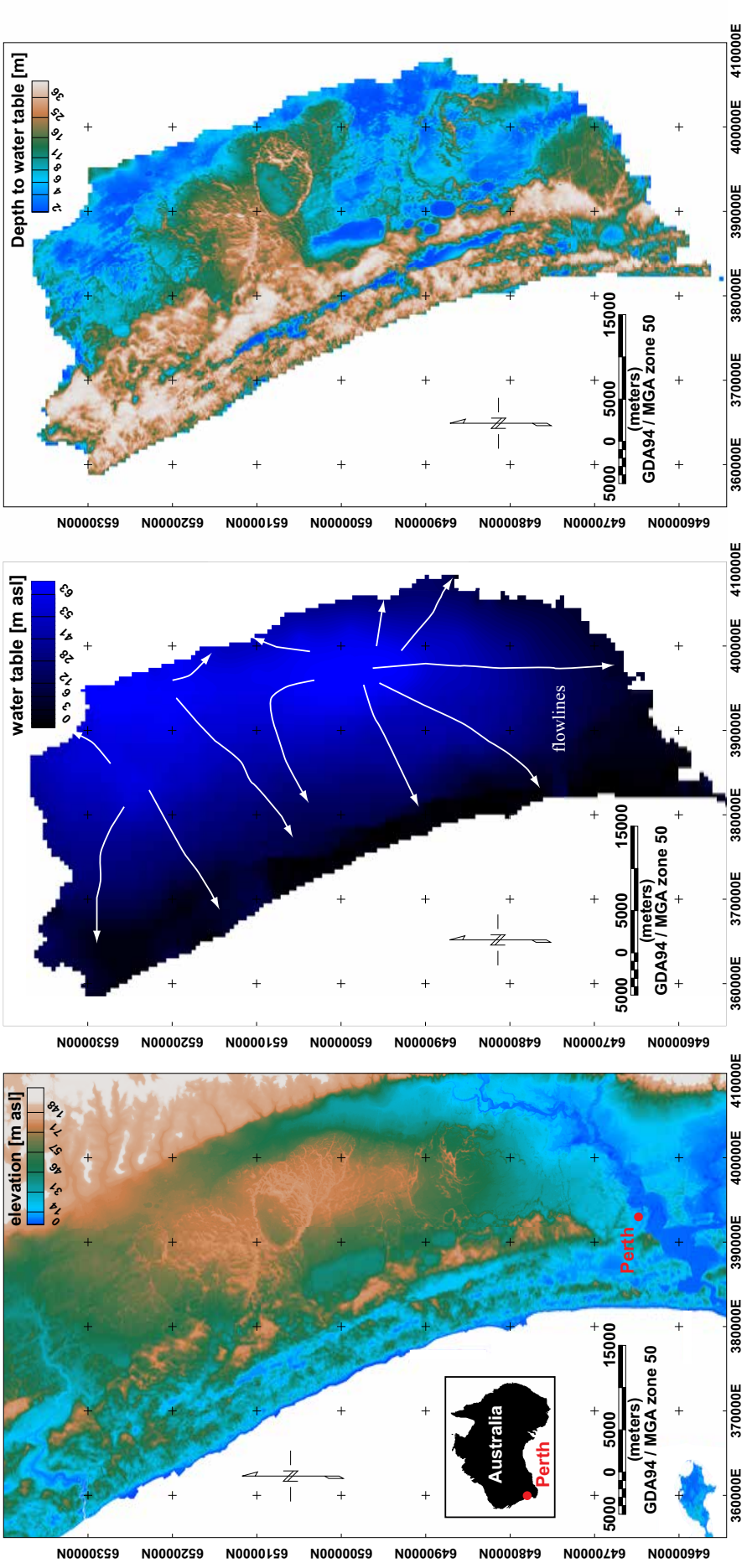

Figure 2.1: *Topography (left), regional superficial water-table (middle) and depth to water (right) for the Gnangara Mound, north of Perth, Western Australia. Data have been provided by Water corporation. Topography represents a Digital Elevation Model created from several datasets (Landsat, LiDAR). Water table elevation is the minimum value of 2005 created from a selection of observation boreholes for the PRAMS model.*

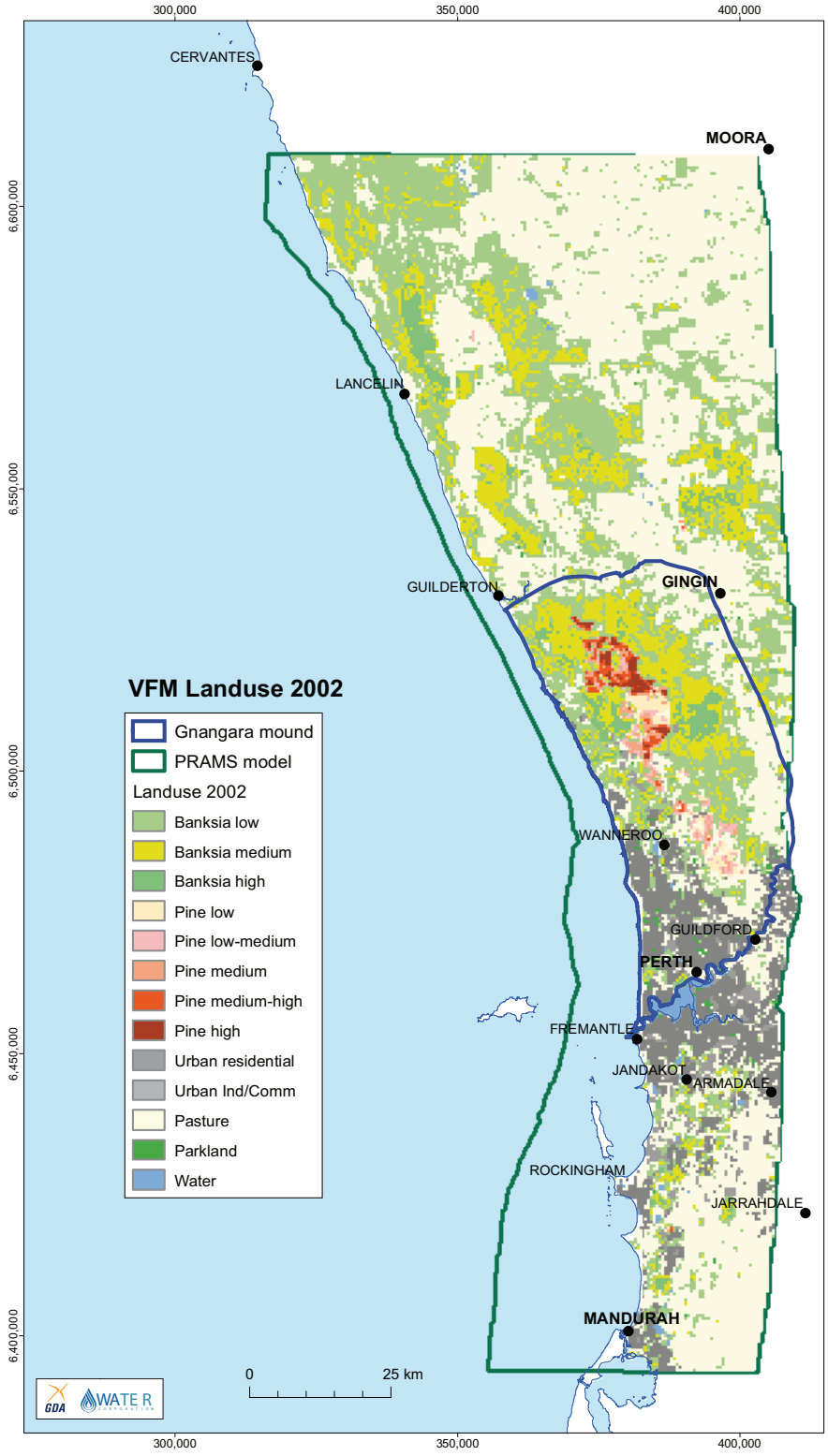

Figure 2.2: *Landuse 2002 for the Vertical Flux Model including the Gnangara Mound (north) and Jandakot Mound (south). Figure reproduced from Xu et al. (2008).*

formation is of main interest due to its recharge capacity, and the preserved banksia woodland.

The following sections will give a brief introduction into the hydrogeology and geology of sediments found throughout the study area. A separate section describes the podosol soil profile that has developed on the Bassendean Sand as this particular lithology may play a pivotal role in the recharge dynamics of the mound.

2.1 Climate

The climate in southwestern Western Australia is Mediterranean with dry, hot, long summers and humid winters. Summer temperatures exceed 40°C with mean maximum temperature above 30°C in January and February. Winter maximum temperatures are moderate at around 20°C, while night temperatures can drop below 5°C. Annual rainfall accumulates during the winter months from May/June to September/October (see Gingin example in Figure 2.3b) during distinct rainfall events. This distribution of rainfall has a great impact on how recharge works on the Gnangara Mound and will be of major importance in chapter 6.

The long term average annual rainfall is around 800 mm. However, during the last century, a drying trend is obvious as shown in Figure 2.4. This is correlated with an increase in evapotranspiration as shown in Figure 2.5 for years from 1970 onwards. Recent years have shown variable precipitation between 400 mm and 800 mm. The graph in Figure 2.3b reveals that daily rainfall can be extreme and may reach monthly averages. Rain typically precipitates in high rainfall events of around 10 - 30 mm. Continuous rain and cloud cover over several days is uncommon. Such rainfall patterns also lead to great spatial inhomogeneity of cumulative rainfall. Figure 2.6 shows the 2011 cumulative rainfall for various climate stations throughout the Gnangara Mound area. While some stations (Whiteman Park, Perth airport, Mariginiup) show annual rainfall of above 800 mm, other stations such as Pearce RAAF and Wanneroo recorded around 650 mm.

The potential evapotranspiration rates in southwestern Australia are high in summer and annual rates greatly exceed annual rainfall with pan evaporation values at around 1800 mm (Figure 2.5). Detailed daily rainfall data for recent years are dis-

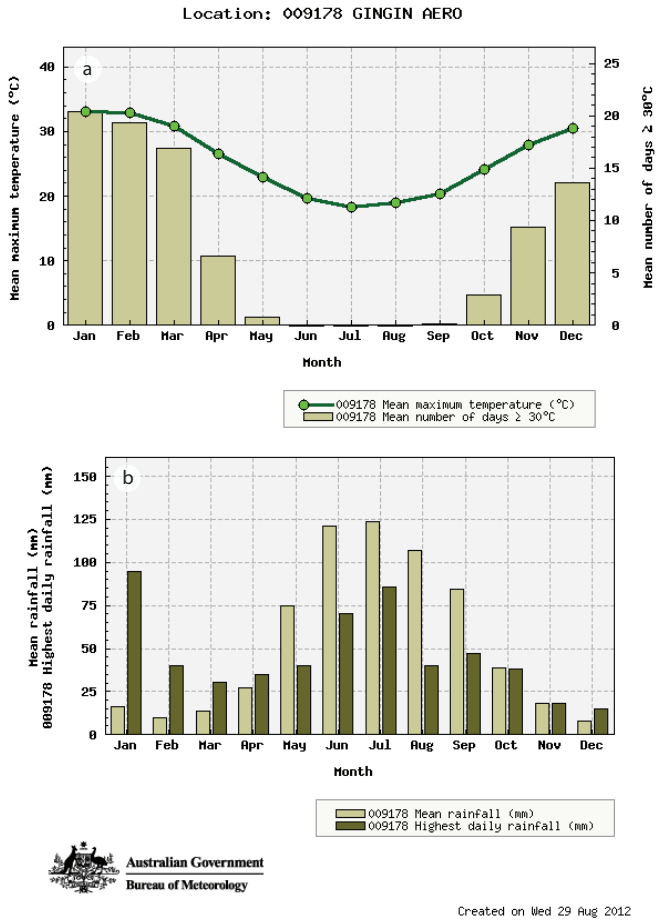

Figure 2.3: *(a) Variation in long-term mean maximum monthly temperature for the Perth area, (b) long-term mean monthly rainfall compared to highest daily rainfall on record showing that single events can make up or exceed average rainfall. Plots interactively produced on webpage of Australian Bureau of Meteorology (BoM, www.bom.gov.au/climate).*

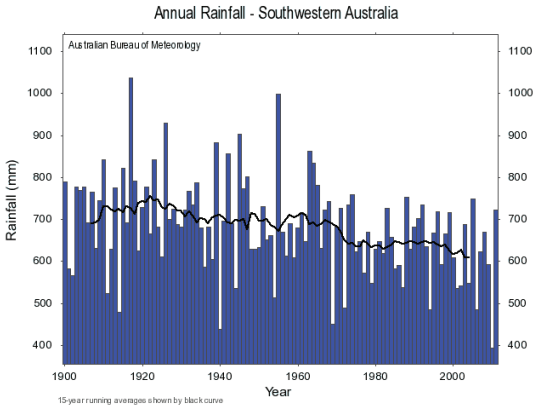

Figure 2.4: *Cumulative annual rainfall for southwestern Australia from 1900 to present. Black lines represents 15-year running average indicating a drying trend. Plots interactively produced on BoM webpage.*

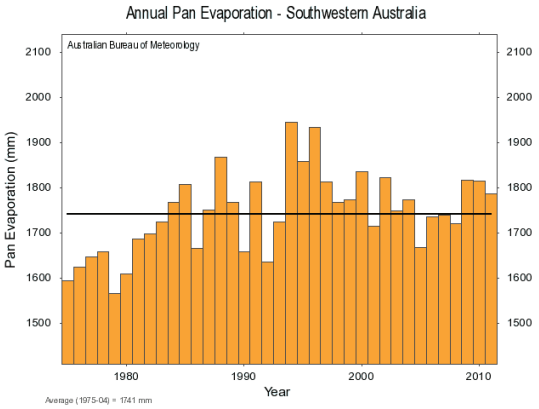

Figure 2.5: *Cumulative annual pan evapotranspiration for southwestern Australia from 1970 to present. Plots interactively produced on BoM webpage.*

played in chapter 6, Figures 6.9 and 6.10.

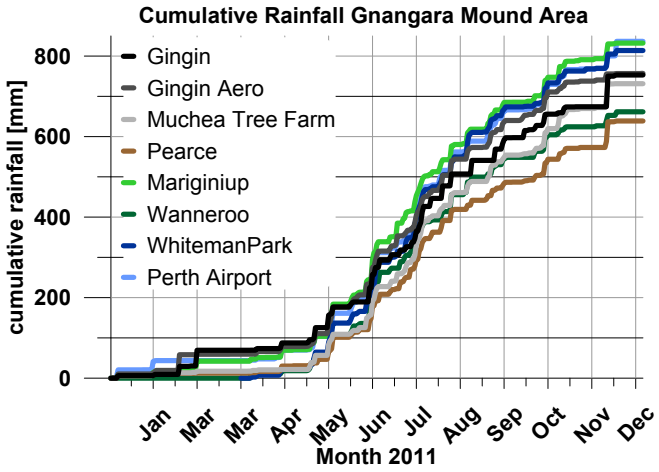

Figure 2.6: *2011 daily cumulative rainfall for eight stations on the Gnangara Mound showing spatial variability throughout the study area. Data from BoM climate archive.*

2.2 Geology

The aquifers of the Gnangara Mound groundwater system include Cenozoic sediments of the Superficial Formations that are underlain by Mesozoic deposits and Proterozoic crystalline bedrock at their base at around 12 km depth (*Davidson*, 1995). The depositional environment during the Mesozoic formed as a consequence of dip-slip faulting (normal faulting) initiated by crustal extension when the Australian plate broke apart, firstly from Gondwana in the Permian, and later from Antarctica during the Jurassic. The old Proterozoic Darling Fault was then reactivated as a normal fault which created a Graben system with downthrow to the west and the crystalline Yilgarn craton in the east. The Graben was then filled with sediments during subsidence which formed the formations of the Perth Basin.

For this study sediments of the youngest superficial formations are of interest as they are sampled by the shallow geophysical methods employed. For more information on deeper hydrostratigraphic units, I refer the reader to *Davidson* (1995) and reports published by the Department of Water of Western Australia in their hydrogeological record series (e.g. *Davidson and Yu* (2006)) and references therein.

Superficial Formations

Understanding the characteristics of the superficial sediments is key to ground-penetrating radar interpretation, as these are the formations that can be imaged by that technique.

Superficial Formations include from youngest to oldest: Safety Bay Sand, Becher Sand, Tamala Limestone, Bassendean Sand, Gnangara Sand, Guildford Clay, Yoganup Formation and Ascot Formation (see map in Figure 2.7). On the Gnangara Mound,

landforms and very shallow sediments are mainly from the Safety Bay Sand, Tamala Limestone, Bassendean Sand and Guildford Clay formations. The erosional base of the Pleistocene superficial formations is at topographic levels between approximately -25 m above sea level (asl) and 25 m asl (see Figure 2.8).

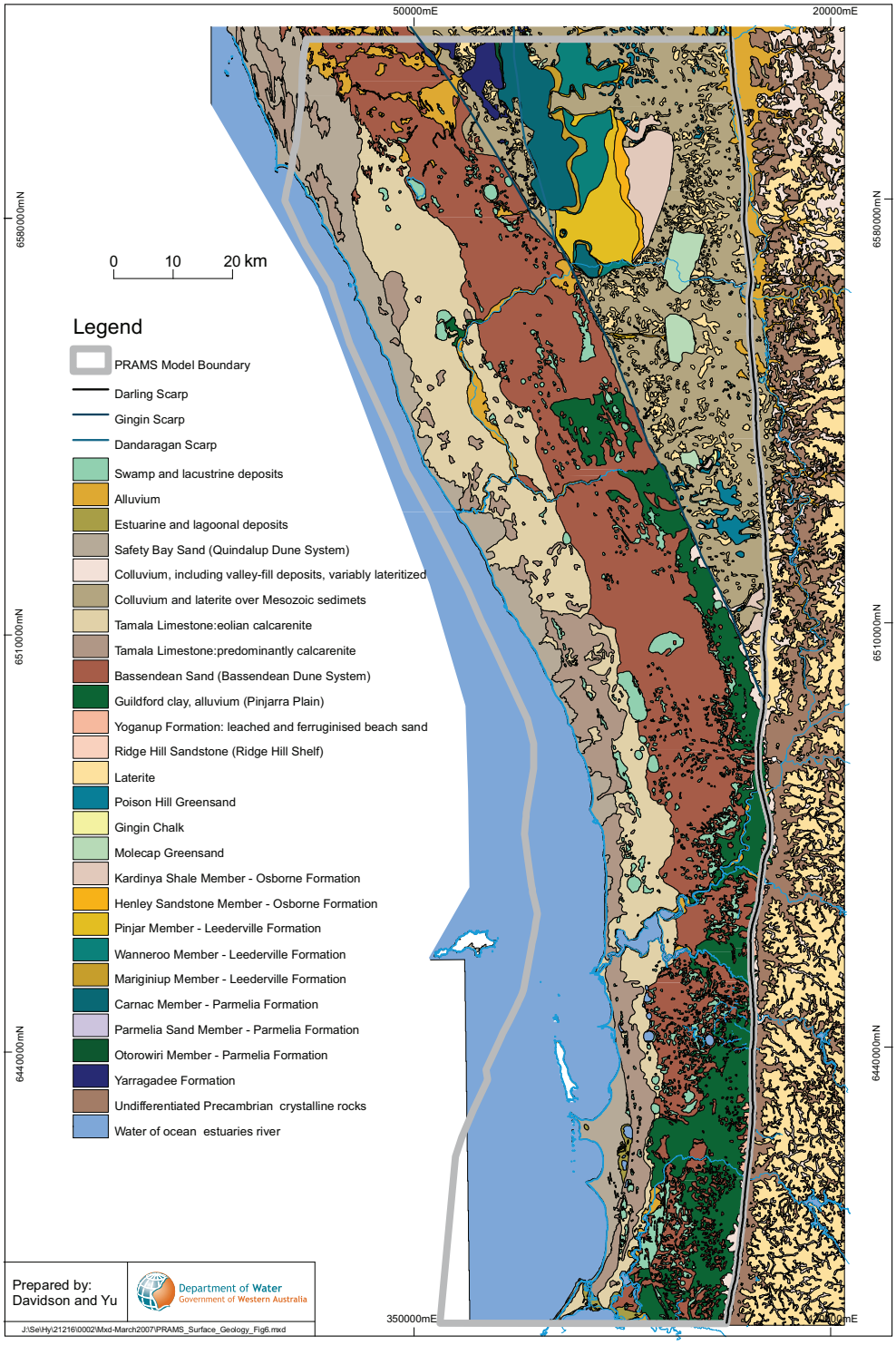

Figure 2.7: *Shallow geologic map of the Swan Coastal Plain around the Perth area. Age of shallow quaternary sediments increases from West to East (i.e. Holocene to Pleistocene deposits). Map reproduced from Davidson and Yu (2006).*

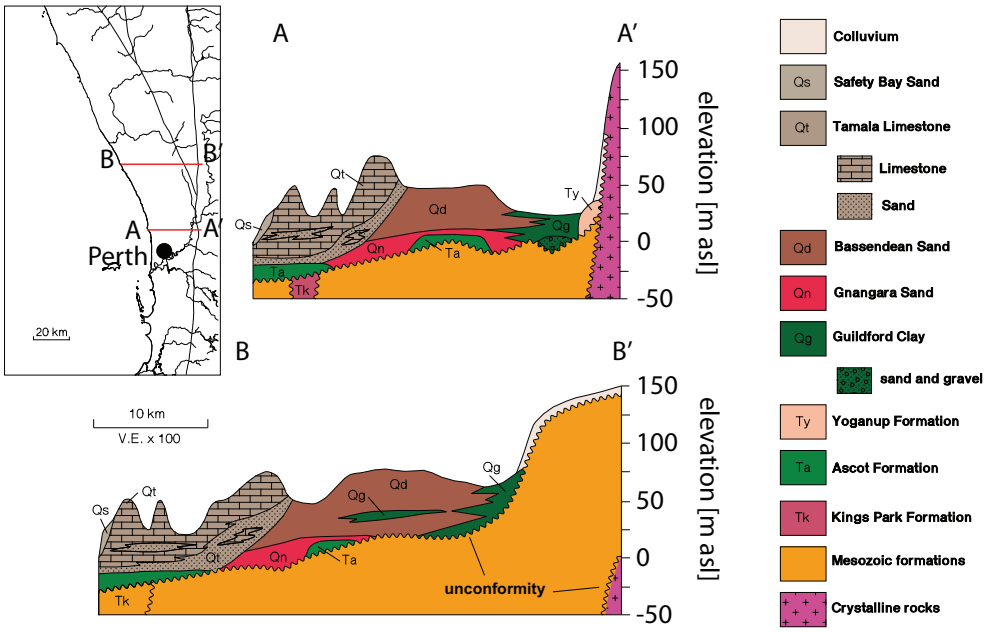

Figure 2.8: *Geologic cross-sections through quaternary sediments for southern and northern Gnangara Mound. Note the interfingering and interstratification of Guildford Clay into the Bassendean Sands. Figure modified from Davidson and Yu (2006).*

The surface topography is dominated by inactive and vegetated dune systems (Figure 2.9) that form topographic highs. Dune crests can reach heights of up to 110 masl. Figure 2.1a shows the surface topography based on a digital elevation model (DEM) measured by satellite and LiDAR (provided by Water Corporation). Landforms are dominated by three main dune systems which are in chronological order and from east to west as described by *McArthur and Bettenay* (1974): a) Bassendean Dunes at the central mound (Bassendean Sand), b) Spearwood Dunes (Tamala Limestone) and c) Quindalup Dunes (Safety Bay Sand) towards the ocean (see also Figure 2.7 and 2.9). To the east is the Guildford Formation (or Guildford Clay), which is of alluvial origin and doesn't form any major topographical features.

The Tamala Limestone Formation consists of aeolic calcareous sands with a leached upper soil horizon that forms the Spearwood Dune system. The sands below the leached horizon are typically yellow to orange in colour due to iron oxide staining, followed by limestone.

The Tamala Limestone unconformably overlies the Bassendean Sand towards the east, and the Spearwood Dunes overlap Bassendean Dunes near the contact between the two units. A detailed map of the Bassendean Sand substrata based on soil classification is shown in Figure 2.9 including Jandakot (Ja), Gavin (G) and Joel (J) soil

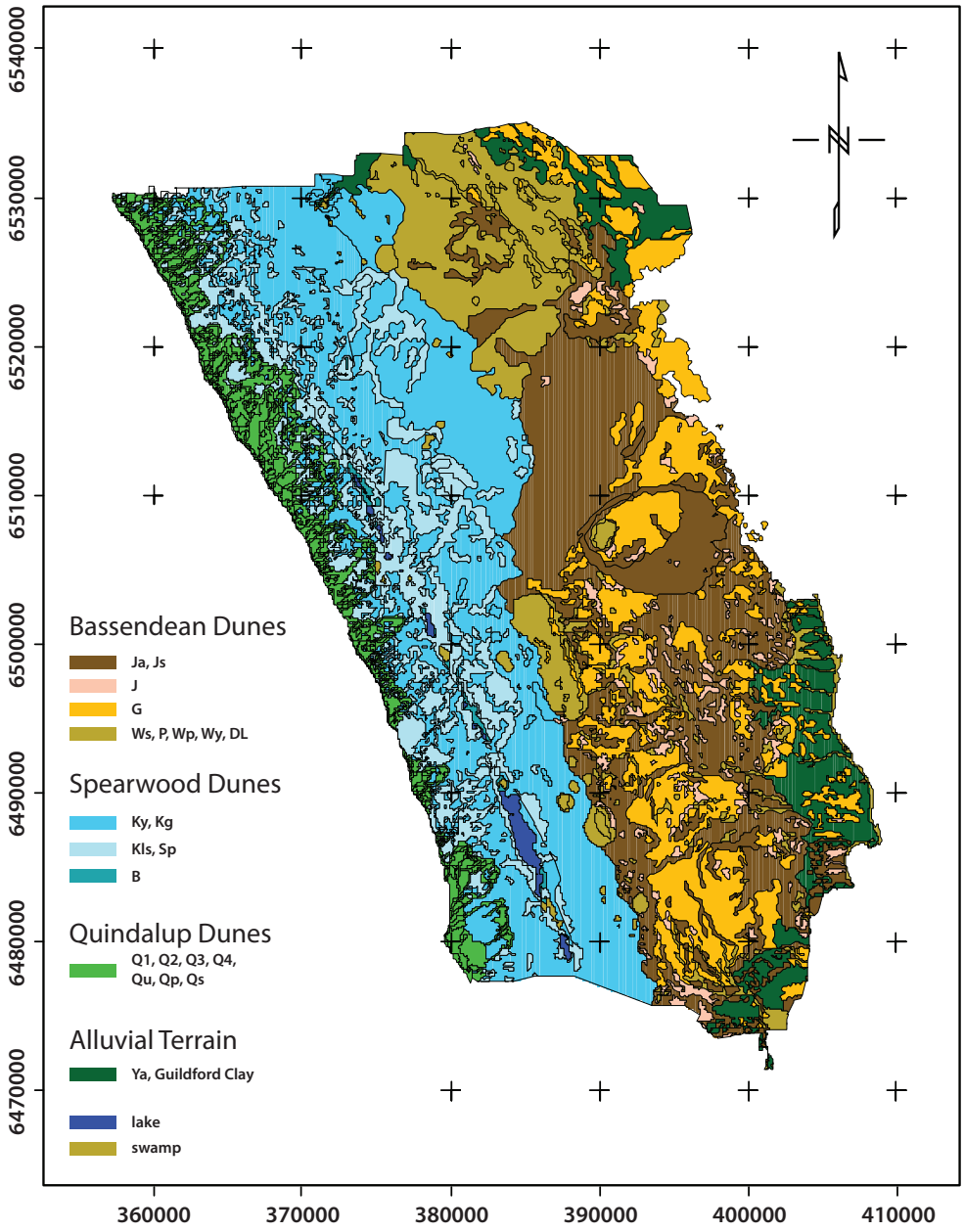

Figure 2.9: *Soil and landforms of the Gnangara Mound area. Dune systems are consistent with geologic formations. From west to east (youngest to oldest) landforms and formations are: Quindalup Dunes and Safety Bay Sand, Spearwood Dunes and Tamala Limestone, Bassendean Dunes and Bassendean Sand and alluvial Pinjarra Plain and Guildford Clay. Map modified from Salama et al. (2005).*

classes. Bassendean Sands mainly consist of leached white to grey quartz sand near the surface. Calcareous material has been dissolved due to intensive weathering during the last 800,000 years. A distinct feature of the Bassendean Sand is the podosolic soil profile which contains an accumulation horizon (B-horizon) usually within several meters of the water table. This horizon, also locally called ”coffee rock”, will be discussed in section 2.4. Soil horizons (as evidenced by charcoal) and old swamp or lake deposits (indicated by peaty sand or diatomaceous earth) are occasionally intersected

deeper in the profile.

Towards the east, the Bassendean Sand interfingers with the Guildford Clay sediments indicating a geologic history of a changing coastline. During the Pleistocene, transgression and regression of the ocean lead to alternating shallow marine, estuarine and fluvial depositional environments (*Davidson*, 1995). The schematic geologic cross-sections in Figure 2.8 (modified from *Davidson and Yu* (2006)) indicate sediments of the Guildford Formation interstratified into the central Bassendean Sand. The Guildford Clay consists of brown silty, sandy clay with lenses of conglomeratic, poorly sorted sand at its base.

2.3 Hydrogeology

2.3.1 Shallow Regional Groundwater

The regional superficial water table domes up in the central Gnangara Mound and inclines towards the hydrologic boundaries, hence the name groundwater mound. Figure 2.1b shows the minimum water table 2005, which is based on a selection of observation wells (provided by Water Corporation). Water table elevation peaks at around 65 masl in the central mound. This leads to a large depth to water table below the Spearwood dunes in the west and a shallower water table towards the centre. A depth to water table map calculated from the minimum water table and the DEM is shown in Figure 2.1c (i.e. c = a - b). The first order depth to water table on the central mound is around 5 - 15 meter below natural surface (mbNS) based on average topographic and water table elevation. Due to the Bassendean Dune system, which stretches in a north-south direction throughout the central mound, a second order depth to water table is controlled by the topography and can vary between 0 mbNS (wetland) and 45 mbNS (dunes).

The natural hydraulic level (i.e. water table elevation) is mainly controlled by recharge from rainfall, but can also be influenced by recharge from deeper aquifers and discharge to deeper aquifers. Due to human activity, groundwater levels are no longer only controlled by natural factors such as rainfall and vegetation. Land clearing for agriculture, pine tree plantations as well as groundwater extraction have led to local changes in groundwater levels (*Salama et al.*, 2002; *Davidson and Yu*, 2006;

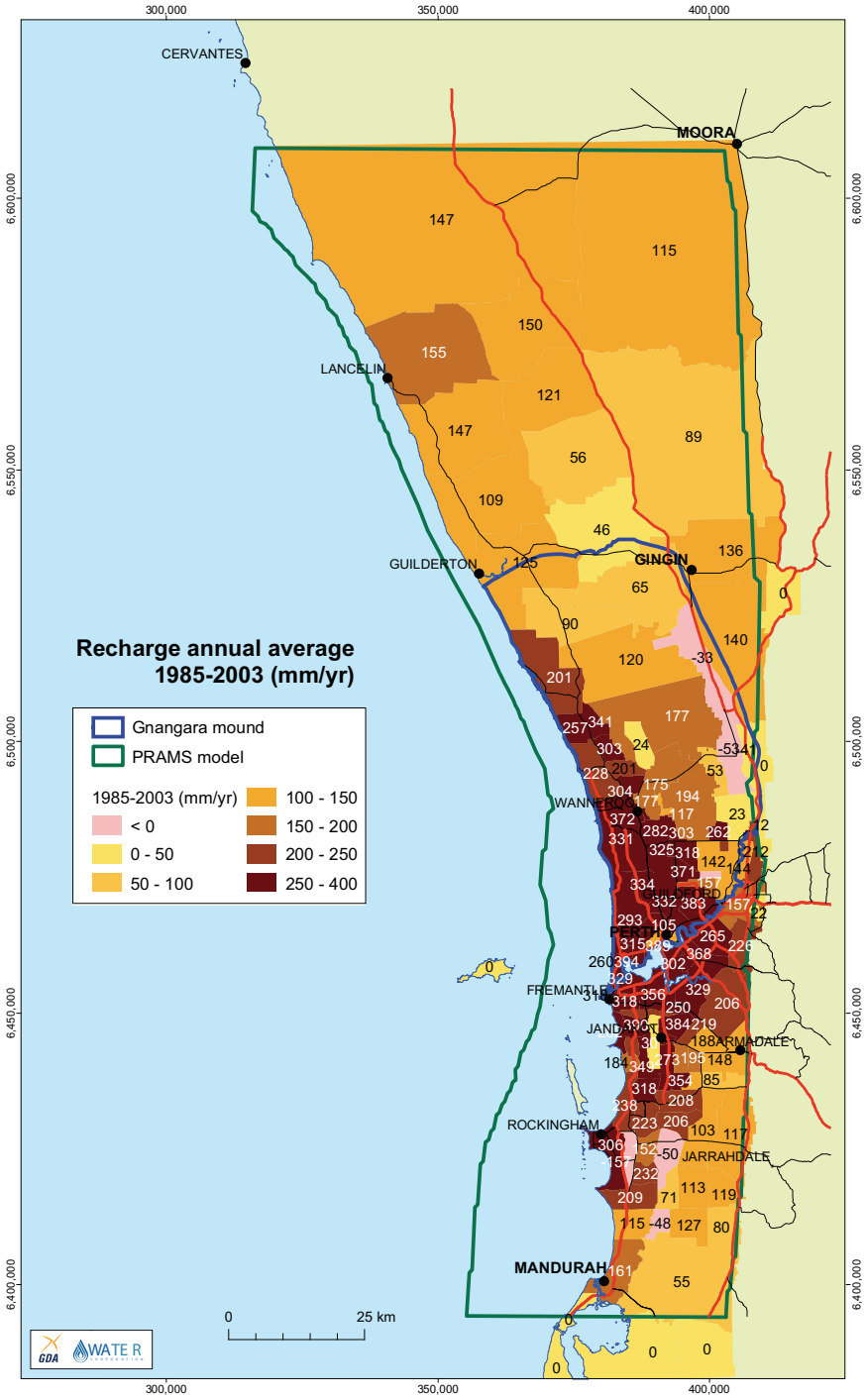

Figure 2.10: *Average annual recharge map predicted by Vertical Flux Model for years 1985 - 2003. Map reproduced from Xu et al. (2008).*

Yesertener, 2002). While pine tree plantations and water extraction lower the natural shallow groundwater levels, the replacement of natural banksia and eucalyptus woodland with pasture has led to increases in recharge resulting in water table rises that can create temporary water-logging (*Davidson and Yu*, 2006). Besides water sinks and sources, the hydraulic properties of the superficial formations influence how ground-

water levels will develop. The Bassendean Sands have generally high saturated hydraulic conductivities between 10 and 100 m/d and on average 15 m/d (*Davidson and Yu*, 2006). High hydraulic conductivities allow for rapid equalisation of hydraulic gradients and lead to a fairly flat water table. Where hydraulic conductivities are much lower such as for the Guildford Clay (between 0.1 and 10 m/d) and at hydrologic boundaries such as rivers, steeper hydraulic gradients occur. At the boundary between the Tamala Limestone and the Bassendean Sand, hydraulic gradients are large due to the high hydraulic conductivities of the cavernous limestone (100 - 1000 m/d) which drains the mound towards the ocean.

2.3.2 Wetlands

Wetlands in form of lakes and swamps have formed at topographic depressions mostly in between dune systems. Those can be recognised in the DEM (Figure 2.1a, large areas with identical elevation) and the depth to water table map (Figure 2.1c, depth to water table around 0), as well as the geologic maps in Figures 2.7 and 2.9. Although wetlands are mainly found in between adjacent dune systems, several wetlands are dispersed throughout the Bassendean Sands forming lacustrine deposits (Figure 2.7). Most of those lakes and swamps are temporarily water logged in the winter months and dry out during summer. Lakes within the Bassendean Dunes are created by either groundwater discharge or throughflow lakes (central mound), or perched lakes, especially in the northern Yeal and Gingin area (*Davidson and Yu*, 2006). Lake sediments are typically of biogenic origin and therefore rich in organic material. Sediments include peat, peaty sands, diatomaceous earth and calcareous clay.

2.3.3 Groundwater Recharge on the Gnangara Mound

Because groundwater recharge is the main hydrogeological theme of this thesis, I will briefly introduce the current understanding of groundwater recharge mechanisms on the Gnangara Mound and summarise efforts made to calculate recharge rates. More detail on particular methods and measurement campaigns is discussed in more detail in sections 6.1, 6.2 and 6.6 of my thesis.

Rainfall redistribution on the soil surface and infiltration into the subsurface is controlled by various factors such as surface and subsurface soil properties, vegetation

(canopy, litter) and climate. Recharge maps estimated from two different methods are published by *Davidson and Yu* (2006) (chloride mass balance) and *Xu et al.* (2008) (numerical modelling, results shown in Figure 2.10). Gross recharge estimates can be made based on the geography of the Gnangara Mound area. The main contribution to recharge is rainfall. However, for any given climate land use is the main factor controlling recharge as it controls surface soil properties (e.g. moist due to watering in agriculture, sealed surfaces in built-up areas) and vegetation (i.e. pasture vs pine tree vs banksia woodland). In the case of a hydraulically impermeable surface (e.g. Guildford Clay in the east), surface run-off and perching layers will inhibit vertical water infiltration. In built up areas, on the other hand, the controlled environment leads to high recharge rates when collected rain water is directly guided into the aquifer. Vegetation controls recharge by providing a large surface area for collecting water available for direct evaporation, for example, due to canopy and leaf litter. As part of their metabolism plants also actively transpire water which is lost from the groundwater system. Water uptake by plants can be so influential that groundwater recharge under pine tree plantations is negligible or negative (i.e. plants use more water than annual rainfall provides) (*Xu et al.*, 2008). Pasture on the other hand does not use much water, nor does it produce large surface areas for evaporation; hence, recharge under pasture on sand is very high (approx. 45 % of rainfall) (*Xu et al.*, 2008). The natural banksia woodland evapotranspiration varies and depends on plant density. Recharge rates are estimated between 10% and 40 % of annual rainfall (*Xu et al.*, 2008).

Groundwater recharge is directly and indirectly influenced by depth to water table. If the depth to water is very small, that is between 0 (lake) and 1 - 1.5 m (wetland, swamp), direct evaporation tends to occur. Also, the depth to water indirectly influences recharge due to different plant water uptake regimes. Intermediate water tables allow vegetation to directly draw water from the capillary fringe which increases transpiration (*Xu et al.*, 2008). Where water tables are deep, such as on dune crests, vegetation cannot rely on groundwater and adapts to water uptake from the unsaturated zone and minimises its transpiration.

Based on the key components influencing groundwater recharge, a vertical flux model (VFM) was constructed for the Gnangara Mound in a collaborative effort between CSIRO, Water Corporation and Dept. of Water (*Silberstein et al.*, 2009; *Xu*

et al., 2008). One of the main components of the VFM is a numerical forward modelling algorithm called WAVES[2] (water, atmosphere, vegetation, evapotranspiration and soil) (*Zhang and Dawes*, 1998). Water redistribution in the subsurface and net flux is modelled based on unsaturated flow and water balance equations. Input parameters are related to the key components: climate (rainfall, evaporation), vegetation (leaf area index, leaf litter) and soil (unsaturated hydraulic conductivity, van Genuchten parameters). The advantage of a numerical modelling system over observed recharge is the ability to test the influence of environmental changes on recharge rates. Scenario modelling can include changes in land use (e.g. deforestation of pine plantations, bushfires temporarily removing vegetation), impact of climate change (e.g. reduced/increased rainfall) and any combination of those. As the results of the VFM directly feed into the saturated flow model, the Perth Regional Aquifer Modelling System (PRAMS) (*Xu et al.*, 2008; *Silberstein et al.*, 2009; *Davidson and Yu*, 2006), it also assists in identifying conceptual or numerical inconsistencies in the formulation of recharge between areas.

As previously mentioned, the VFM in its current state does, for practical reasons, not account for any internal structure of the shallow soils, which might result in overestimation of local recharge. The following section describes the complexity of the soil profile and describes soil forming processes and elements of the resultant soil.

2.4 The Bassendean Soil Profile: A variable environment

An in-depth background knowledge of the origin and history of subsurface materials can aid the interpretation of geophysical measurements. The informed geophysical interpreter expects to recognise certain structural and geologic elements in the data. Without this awareness and anticipation, some features are easily left unidentified or misinterpreted. This section is therefore dedicated to geologic background knowledge I collected from relevant literature and should be kept in mind in following chapters.

Different soils have formed on the Bassendean Sands. The wetlands at topographic depressions have already been described in the previous section. Shallow swamp and

[2]http://www.clw.csiro.au/products/waves/

wetland soils are characterised by high organic content in form of peat, and fine materials such as diatomaceous earth and clays. They differ greatly from the soils found on dune slopes and crests. Those typically show a podsolic soil profile (podosols in Australian Soil classification. The podosol can be either aeric (i.e. above the water table, no perched water, see example profile in Figure 2.11), or aquic, that is around or below the saturated zone. A complete soil profile from dune crest to base can consist of aeric and aquic podosolic soil horizons. Other materials that may be interstratified into the Bassendean Sands are Guildford Clays as mentioned earlier, and heavy mineral accumulations in thin bands which are likely associated with shallow marine deposition (*Davidson and Yu*, 2006). Both of those interstratifications are not a result of soil forming processes, but constitute first-order sedimentological mechanisms. Publications that describe the distribution and spatial extent of both, Guildford Clays within Bassendean Sands, or heavy mineral accumulations on the Gnangara Mound area, in detail could not be found in my literature searches.

As the depositional environment experienced continuous changes during the last approximately 700,000 years, and soil forming processes overprinted the deposits, a high complexity within shallow strata has to be expected.

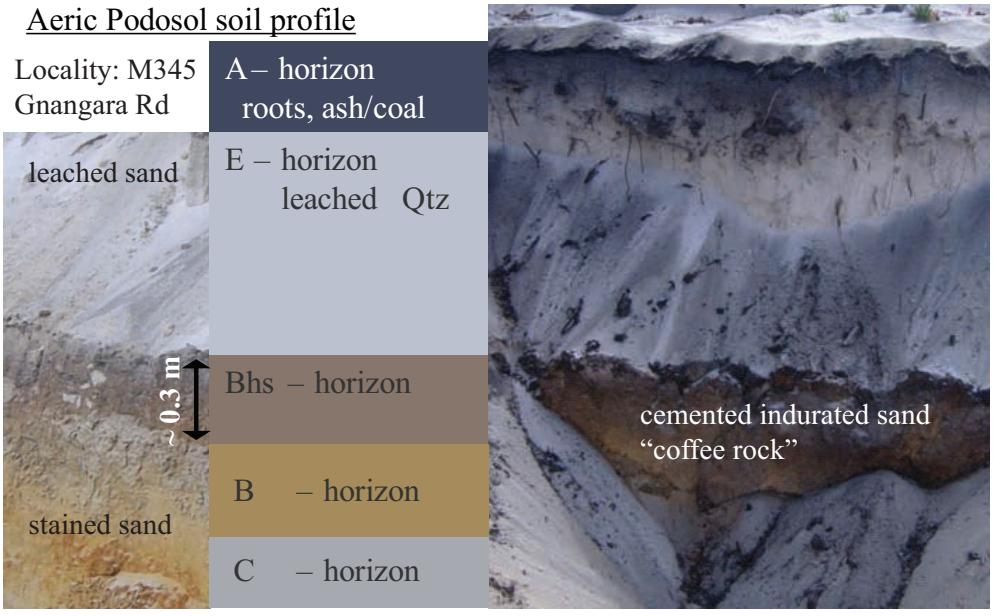

Figure 2.11: *Podosol profile at M345, Gnangara Road, showing typical sequence of soil horizons after podsolisation.*

2.4.1 Podosol

Understanding the processes that form, and possibly destroy, distinct soil horizons (e.g. podosol B-horizon) give an insight into the structures that might be expected in the subsurface and are important for geophysical interpretation radar cross-sections, as an example.

When the Bassendean dunes became inactive, vegetation settled and sands were exposed to weathering that was further facilitated by rainfall. Vegetation of the dunes produces an upper surface layer containing organic material in form of roots, carbon from bushfire and leaf litter (A-horizon). Mechanical separation and chemical processes lead to eluviation of the fine materials, mobilisation of minerals and dissolution of organic matter (humic substances). These processes produce a bleached uniform sand horizon, called the E-horizon below the A-horizon as shown in Figure 2.11. Below the eluviation horizon is an accumulation horizon, called B-horizon, where fine materials illuviate, and soluble organic matter and inorganic elements precipitate (*Prakongkep et al.*, 2009). Such soil profiles are shown in Figures 2.11 (M345), 2.12 (northeast M345, Rocla mine site) and 2.13 (Mandalay Beach, 250 km south of Perth). B-horizon characteristics appear to depend on topographic position (*Thompson*, 1981, 1992; *Singh and Wong*, 2010). *Singh and Wong* (2010) claim that the humus content is inversely related to topographic elevation on the Swan Coastal Plain. They state that dune crests show ”iron podsol” (i.e. podosol), dune mid-slopes ”iron-humus podsol” and topographic lows ”humus podsol” which they call ”coffee rock” (dark brown, strongly cemented). No specification is given where the mid-slope and crest podosol appears relative to the water-table, while the humus podosol is identified as an aquic podosol (i.e. accumulation horizon fully saturated). *Davidson and Yu* (2006) describes a ”friable, mostly weakly limonite-cemented sand, colloquially called ”coffee rock”, which is situated around the water-table throughout most of the Bassendean Sands. From both of their descriptions, it appears that they are not talking about the same material. The description by *Davidson and Yu* (2006) seems to relate to mid-slope or crest iron-mineral bearing indurated sands rather than aquic podosol. *Thompson* (1992) and *Cox et al.* (2002) describe apparently identical accumulation horizons found on sand dunes in coastal Queensland. *Cox et al.* (2002) points to the confusion created by different names given by different authors. They cite terms such as ”hardpan”, ”san-

drock", "beachrock", "humicrete" and "coffee rock" and conclude that it is most reasonable to call accumulation horizons in sand dunes "indurated" sands. Another term found for cemented horizons in podosols are laterites or lateritic podosols (*Verboom and Pate*, 2006). In case of cementation by iron hydroxides, terms such as ferricrete, or duricrust are also commonly used to describe similar soil horizons.

2.4.2 Formation And Development Of Podosol Profiles

The processes involved in podosol soil formation are complex and it appears that two slightly different approaches exist that explain the causes of leaching and accumulation. One viewpoint regards purely inorganic, physio-chemical mechanisms as the main cause of chemical dissolution and mechanic eluviation in the E-horizon, and accumulation due to redox-reactions and precipitation and illuviation in the B-horizon. An alternative explanation for those processes involves vegetation in symbiosis with microorganisms (fungi, bacteria) to play an active role in controlling a physiochemical environment that promotes podosol development. The organic involvement in podsolisation is a topic currently discussed in the literature for Australian and not necessarily resolved (*Verboom and Pate*, 2006, 2012). *Verboom and Pate* (2006) introduced a hypothesis in which Western Australian vegetation "bioengineers" soil profiles as part of evolutionary adaption. The theory is called the phytotarium concept where specialised vegetation such as banksias and Eucalyptus actively take part in forming an environment, the phytotarium, that benefits them and their seedlings while suppressing other vegetation in competition for water and nutrients. Acidic litter production can be one of those adaptations and has been previously proposed for conifer needles, which contain poisonous substances and are hard to decompose (and therefore suppress undergrowth). *Verboom and Pate* (2006) propose biogenic induced formation of hardpans, laterites, clay and accumulation horizons (bioengineered soil horizons) for duplex soils such as podosols. Layer characteristics can then depend on vegetation, horizons can be stacked (paleosols) and accumulation horizons can be continuously "repaired" by vegetation. In the case of vegetation change layers are subject to being overprinted by changed Flora, and in case of vegetation loss layers are weathered. These considerations suggest that podosol soil profiles might vary not only due to climatic or host material conditions, but also because of different and time-varying vegetation and the

sequence of vegetation establishment.

Thompson (1981) and *Thompson* (1992) follow a rather inorganic approach. They describe a "podsol" [podosol] chrono-sequence in coastal Queensland. After B-horizons develop, they migrate downwards and result in giant podsols whose A- and E-horizon (in their publication called A1 and A2) thicknesses can reach magnitudes of tens of meters. Interestingly, *Thompson* (1992) observes a good correlation between vegetation and depth to B(hs)-horizon. Young soils without or only poorly developed B-horizon show poor vegetation cover, while intermediate aged soil with A- and E-horizon thickness of around 2 - 4 m show maximum vegetation. Vegetation height and foliage cover decreases on older dunes with increasing depth to B-horizon.

Distinctive features of accumulation horizons under Proteacea are shown to include vertical pipes that develop around roots that promote preferential flow (*Verboom and Pate*, 2006; *Sawkins et al.*, 2011). I have observed those features at the Rocla mine site (Figure 2.12), but did not have an opportunity to record with a photograph. They have a similar character to the rhizolithes found in coastal outcrops of Tamala Limestone. *Thompson* (1992) also describes pipes of leached sand from E-horizon reaching up to 10 m into the B-horizon. Similar to the thickness development of A- and E-horizon with dune age, *Thompson* (1992) also observes a development in interface roughness between E- and B-horizon. Young soil profiles show boundary irregularities with a variation of several centimetres that increases to 10 - 15 cm for intermediate ages and finally the forementioned pipes appear. The diameter of those pipes can be as great as 1 m at the boundary and may decrease to 1 cm at depth (i.e. cone-shaped). This finding is somewhat confirmed by the outcrop at Rocla compared to the outcrop at M345 (Figures 2.12 and 2.11, respectively). The shallow "coffee rock" in Figure 2.11 appears to have a regular interface and the staining of the sand below reaches only 1 m. In contrast, at Rocla the indurated sand layers are deeper and have a much stronger interface roughness and deeper staining.

Stacked podosols, as for example shown in Figure 2.13 or in *Verboom and Pate* (2012), do not seem to show an increase in interface roughness with depth. This might be explained by dune development sequentially burying shallow podosol layers. Due to decreased infiltration, those layers are not weathered and remain intact by being continuously "fed" with water rich in organic and mineral solubles. The rate of water

infiltration might further be reduced due to healthy vegetation taking up water from the unsaturated zone.

It should be noted that the dating of soils in the study by *Thompson* (1992) is based on dune ages and chronology. B-horizons have not been explicitly dated, and the development observed might not be age dependent. Following the logic of *Verboom and Pate* (2006) one could argue that specialised vegetation is not a result, but a cause of different soil profiles. The reality probably lies somewhere in between these hypotheses.

As mentioned before, several sequences of E- and B-horizons can occur due to stacking of paleopodosols (*Verboom and Pate*, 2006; *Prakongkep et al.*, 2009; *Verboom and Pate*, 2012). Another characteristic is spatial discontinuity as observed by *Sawkins et al.* (2011), *Verboom and Pate* (2006) or Ray Froend (pers. comm.) and as shown in Figures 2.12 and 2.13. The degree of cementation reportedly varies laterally and can range from extremely cemented ironstones to friable cemented quartz grains. Saturated layers can also be cohesive and plastic. Lateral characteristics and continuity of soil horizons has not been studied on sub-regional scales to my knowledge, and analysis so far is limited to borehole information and exposed rock at outcrops or quarries.

Another soil property described by *Verboom and Pate* (2006) associated with plants is shallow non-wettability (hydrophobicity) of the A-horizon quartz grains. The spatial distribution of hydrophobic sand is inhomogeneous and creates areas of run-off and patchy infiltration hotspots.

Brooke et al. (2008) investigate the indurated sand layers in the unsaturated zone of coastal deposits. They find that indurated sand formation also depends of texture and depositional setting of the host material. The strongest cementation occurs where channel fill with high hydraulic conductivity (coarse material) promotes water flow and cements precipitate from the shallow groundwater. This might be the cause of the strong ferritic cementation shown in Figure 2.13c and d.

2.4.3 Aquic Podosol

The processes described in the previous section are mainly formulated for the unsaturated zone. A different scenario arises where accumulation horizons meet the water table. *Prakongkep et al.* (2009) investigate aquic podosols on the Swan Coastal Plain.

Their objective is to determine whether a soil, or soil horizon, has to be considered as acid sulphate soil. Groundwater acidification occurs when acid sulphate soil horizons are exposed to air and minerals, such as pyrite, oxidise to sulphuric acid. Hence they investigate material from accumulation B-horizons below the water table. The soil profile described by *Prakongkep et al.* (2009) differs to the aeric podosol in that they describe an additional uncemented brown illuviation horizon B1 with apparently high porosity. Below B1 is the cemented B2 horizon they call ”coffee rock”. This horizon has an apparent reduced porosity (not shown by them) due to precipitation of humic matter, iron oxyhydroxides and allophane. The cemented ”coffee rock” is described as very dark, reddish brown to black. Not many publications about the formation of those aquic podosols in Australian sand plains can be found in the literature. Some investigations took place in Queensland (*Thompson et al.*, 1996; *Cox et al.*, 2002), but don't provide a hypothesis of the mechanisms of formation except for the general accumulation and precipitation concept.

Thompson et al. (1996) observe perched water for several months over hardpans (note that the investigated hardpans are underlain by sandy clay loam and clay which might have promoted perching). They describe that one site has a sloping B-horizon and drains water within days, probably due to the dipping layer. It is concluded that those layers are of hydrogeologic significance for groundwater flow.

2.4.4 Mineralogy of indurated sand

Podosol B-horizons mainly contain inorganic and organic complexes of iron (Fe), aluminium (Al), silica (Si) and humic substances. Precipitates of sesquioxides (Fe and Al, Bs-horizon), newly formed clay minerals such as allophane or imogolite (alumino-silicates), and aluminium-organic complexes are commonly the cementing agents of accumulation horizons (*Thompson*, 1992; *Prakongkep et al.*, 2009). Other constituents can be iron hydroxides such as limonite and goethite, and in small amounts pyrite or marcasite. The aeric podosol B-horizon has not been analysed for its mineralogical composition by *Prakongkep et al.* (2009) and might be different to the aquic podosol spodic material. Considering the similarity between aquic podosols from the Gnangara Mound (*Prakongkep et al.*, 2009) and Queensland (*Thompson et al.*, 1996), the indurated sand horizons in the unsaturated zone at both locations are possibly also sim-

ilar. Chemical analyses by *Skjemstad et al.* (1992) reveal that the B-horizons described by *Thompson* (1992) also undergo a development with age. Firstly, aluminium accumulates and precipitates as Al-organic matter complexes in aeric Bh and Bhs-horizons, and as proto-imogolite allophane in Bhs and Bs horizons. Older podosols (pipey podosol) show iron accumulation as Fe-oxyhydroxides (mostly as goethite). Iron is then depleted in humus podosols within Queensland dunes which represents the final stage of podsolisation .

2.4.5 Summary

Podosol accumulation horizons can differ significantly as shown by direct field evidence based on studies found in the literature. Their properties depend on: topographic level, vegetation cover, age, climate and host soil. This results in a diverse range of layer characteristics such as layer composition (mineralogy), layer topology (flat vs dipping vs undulating) and distinguished layer features such as fissures, erosional surfaces or pipes. These characteristics determine the layers' appearance in the field, for example their colour or the interface properties (i.e. rough vs. smooth or gradual vs. distinct). Apart from a changing appearance, the layers' hydraulic properties are also expected to differ spatially. In combination with the variability of the previously described structural elements, the layers' influence on water infiltration, and consequently groundwater recharge, is likely variable throughout a large area such as the Gnangara Mound. The characteristics of indurated or cemented accumulation horizons described in this chapter provide a basis for expected layer properties. This will aid in interpreting geophysical measurements.

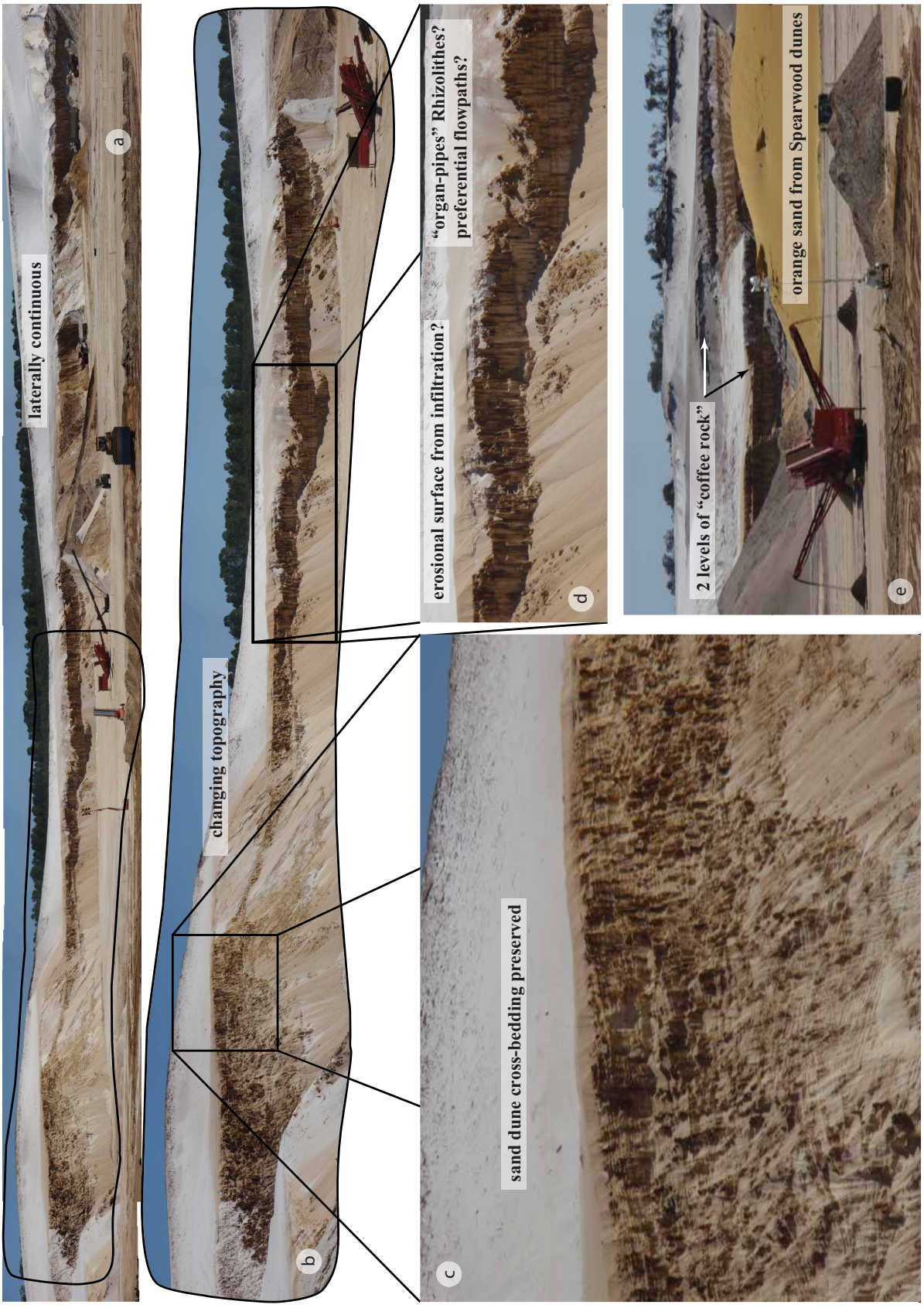

Figure 2.12: *Podosol B-horizon (indurated sand or "coffee Rock") at Rocla mine site. Several characteristics of B-horizon can be studied here, including varying topographic level, erosional surface, potential preferential flow paths and several levels (stacked paleosol). Approximate location in GDA94/MGA Zone 50 is 6487000N/400000E.*

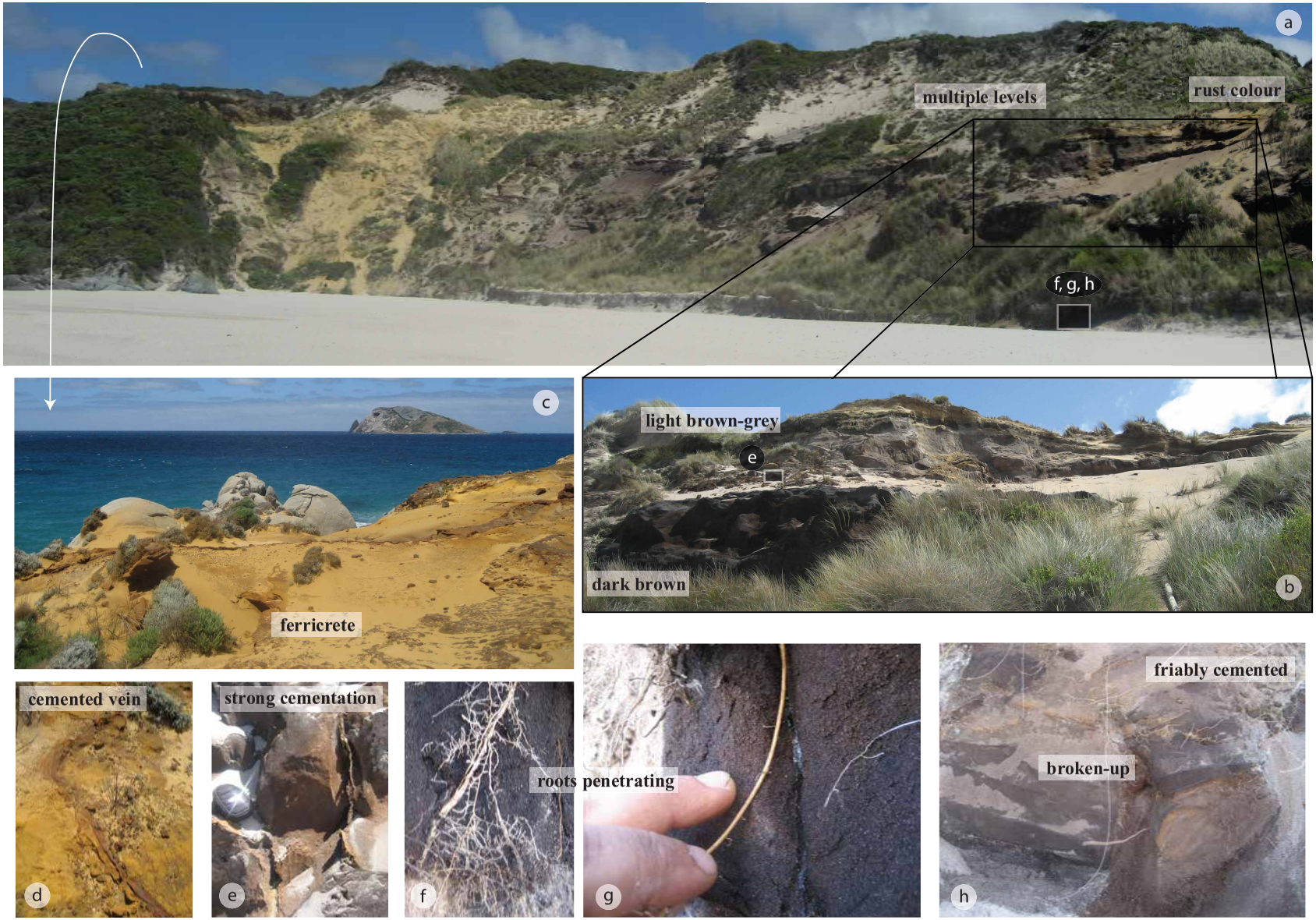

Figure 2.13: *Indurated sands at Mandalay Beach, southeast of Broke Inlet, d'Entrecasteaux national Park, Western Australia. A stacked paleosol profile further to the east (GDA94/MGA Zone 50 6126400N/457300E) shows several layers of indurated sand with varying degree of cementation and colouration ranging between dark reddish brown (f, g and h) to light grey and rust colour (h, e). To the west is a reddish rust coloured sand (6126400N/456560E, c and d) with variable degree of cementation (iron hydroxides) which overlies granite. Note the internal structure of indurated sand with roots penetrating the darker friably cemented horizons (f, g, h) and precipitation veins in the ferritic cemented horizons (d, e).*

Chapter 3

Petrophysical Analysis

In this chapter, many relevant physical properties of the soil horizons described in the previous chapter are investigated. Parameters such as grain size distribution and hydraulic conductivity are important to understand hydrologic processes, and to obtain a framework for plant physiology throughout the seasons. Dielectric and electric material properties may be directly related to geophysical measurements and indirectly to hydrogeological properties and processes. Results from dielectric lab measurements reveal differences and similarities in electric and dielectric properties throughout different soil types and soil horizons as a function of water content. The "coffee rock" and clean sand samples show similar dielectric and electric properties in relation to water content. Whereas some cemented materials show increased electrical conductivity, such as the ferricrete from Mandalay Beach, and a clayey layer below the water table found at the northeastern Gnangara Mound. Such physical properties are crucial for predicting, understanding and evaluating Ground-Penetrating Radar performance in this inhomogeneous environment.

3.1 Grain Size And Hydraulic Properties

Most of the laboratory data presented in the following section are provided by Water Corporation. The measurements were done in 2002 - 2004 (Pinjar area) and from 2006 onwards (Whiteman Park) to investigate unsaturated soil hydraulic properties from samples taken from shallow drill holes. Analyses included lithologic logs, grain size analysis, saturated hydraulic conductivity, water retention analysis and neutron log-

ging. Most of the data have not been previously published to my knowledge and only parts are reported in internal Water Corporation reports. Some of the raw results have been included in the PRAMS and VFM modelling (*Xu et al.*, 2008; *Silberstein et al.*, 2009). The lack of public access led me to include and present some of the most valuable and representative datasets into this dissertation. The raw data material provided by Water Corporation does not always state the investigator; thus, a specific reference may be missing for some data sets. Various persons and institutions that were definitely involved are: Keith Smettem and Assoc. and University of Western Australia (Pinjar PM, PV, P50; Lexia), Ray Froend and Muriel Davies from Edith Cowan University (Whiteman Park) and Kel Baldock from HydroSmart (Neutron logging). Additional information on lithology and neutron logging is provided by the Department of Water of Western Australia for a variety of wetland settings investigated under the "Perth Shallow Groundwater Sytems Investigation" (from 2008 onward). None of this data is reproduced in this chapter, but are used to support my work in chapter 6. An extensive selection of time-lapse neutron logging is presented in the appendix B.

3.1.1 Grain Size

I performed some grain size measurements on different sands from M345 (close Whiteman Park on Gnangara Road) and NG16 (North Gnangara Airfield Rd., Dept. of Water drill hole no. 16) by sieve analysis (Figure 3.1a, b). Samples were collected from an excavation site during development of M345 pumping wells (see outcrop in Figure 2.11, right), and during drilling of NG16 (sample from a bailer). An additional grain size dataset from the borehole S2 (Pinjar area) was provided by Water Corporation(Figure 3.1 c).

The sieve mesh sizes used for M345 and NG16 are (in μm) 150, 224, 300, 425, 600 and 850. Those sieves fractions allow reasonable characterisation of the medium sands (i.e. $200 - 630$ μm), but lack size fraction resolution in the fine (i.e. $6.3 - 200$ μm) and coarse sand fractions (i.e. $630 - 2000$ μm). A separation of clay, silt and fine sand was not possible and are summarised as fines. Sieving was done with dry material. The plots in Figure 3.1 represent the weight percentage of material that passed the sieve, cumulatively subtracted from 1 (or 100 %). The classification indicated in dashed black lines in Figure 3.1 is based on the ISO 14688-1 norm and categorises grain sizes below

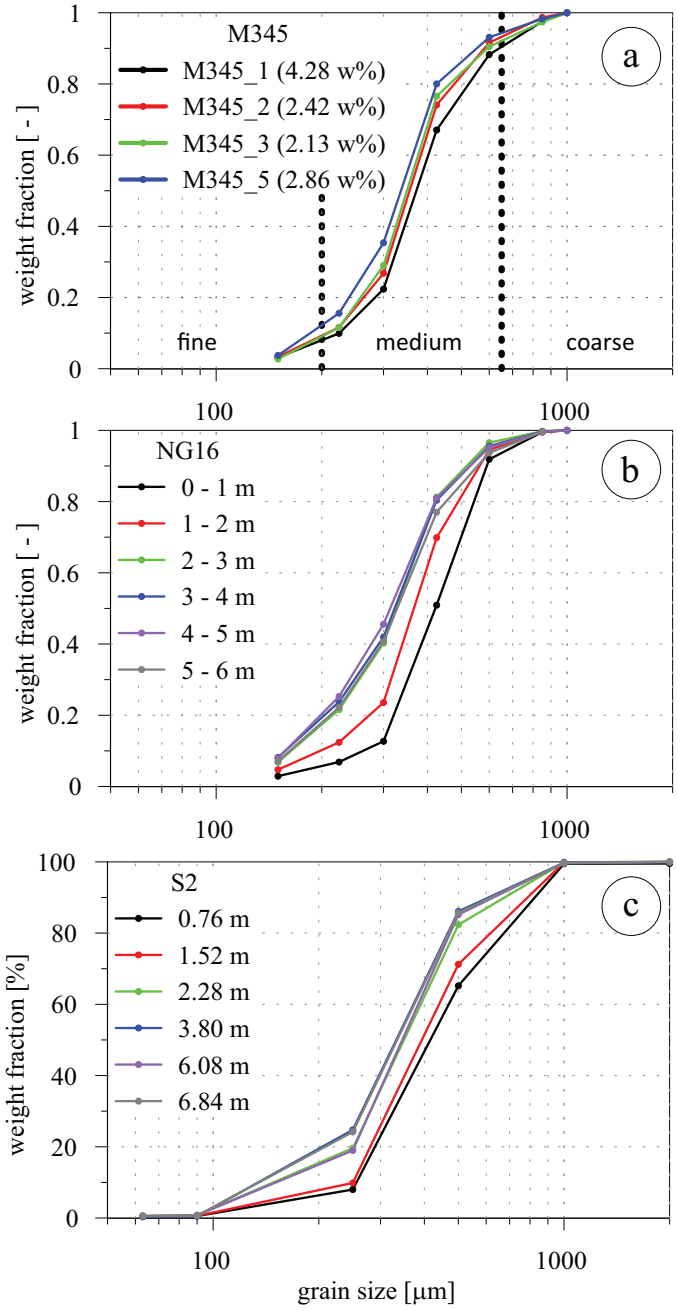

Figure 3.1: *Grain size distribution with depth for clean sand samples at (a) M345, (b) NG16, and (c) borehole S2 (Pinjar area). In Figure (a), values in brackets are gravimetric water contents as determined from the field samples collected in November.*

2 μm as clay, below 63 μm as silt, between 63 μm and 200 μm as fine sand, between 200 μm and 630 μm as medium sand and above 630 μm as coarse sand. All graphs show a fining downward sequence for the first few meters. The slope of the grain size curves are very steep for the shallowest sands (i.e. black curves) indicating good sorting in the medium sand fraction. They contain 80 % (M345, S2) or 90 % of material above 300 μm. The next deeper samples (i.e. red curves) display an increase in fine materials and a gradual flattening towards the finer fractions. The deeper sands (i.e. $>$ 6 m at NG16 or sample 5 at M345 below "coffee rock") contain higher contents of fine-to-medium fine components and are not as well sorted. Some additional grain size

data for the Pinjar area were provided by Water Corporation (measured by Smettem and Assoc.) which are displayed in Figures 3.2 and 3.3 for drill holes PM and PV, respectively. The categorisation of clay, silt and sand grain size limits in those figures

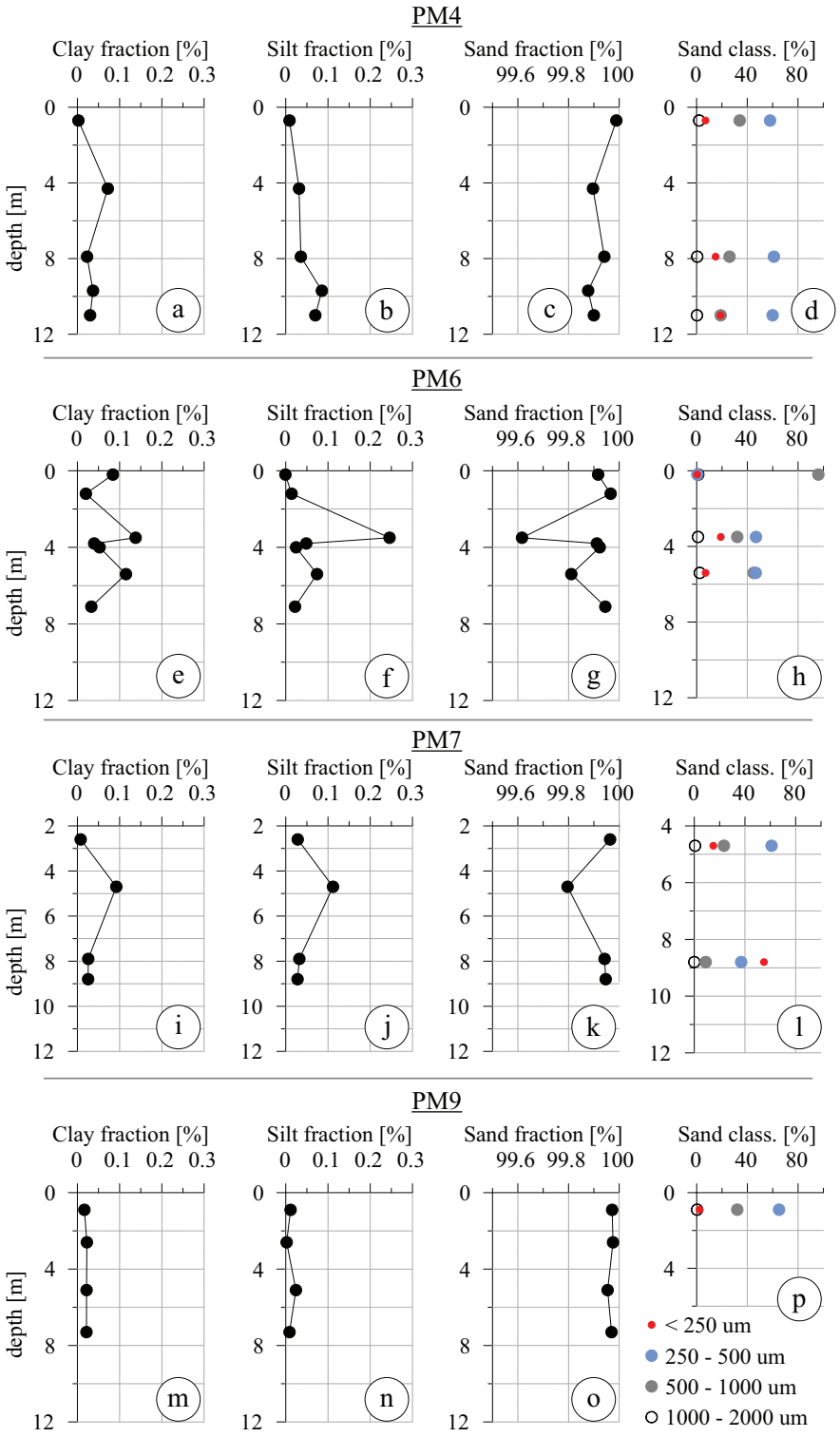

Figure 3.2: *Clay, silt and sand fractions for boreholes PM4, PM6, PM7 and PM9 (Pinjar area). Data provided by Water Corporation, measurements performed by Smettem and Assoc.*

is based on a classification where grain sizes smaller than 2 μm are clay, between

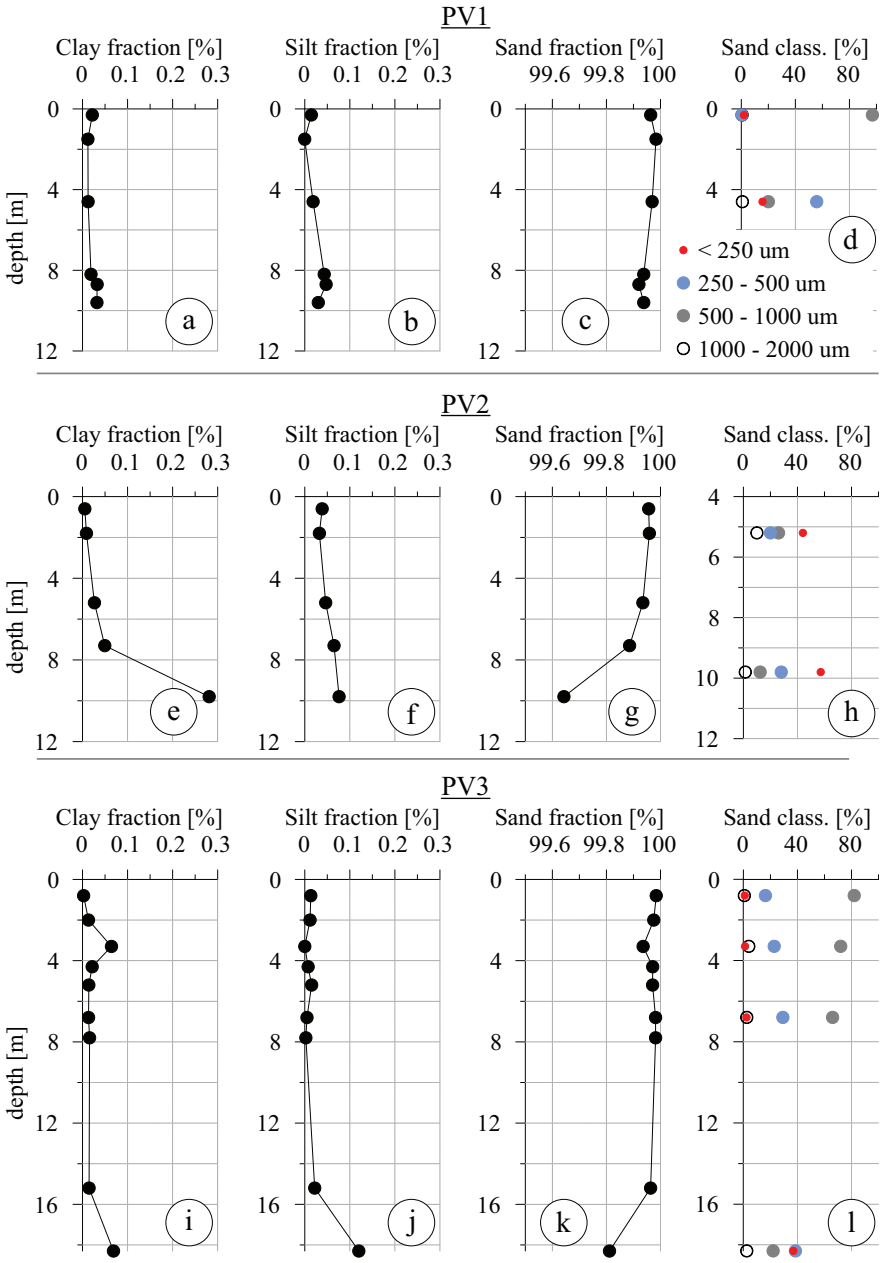

Figure 3.3: *Clay, silt and sand fractions for boreholes PV1, PV2 and PV3 (Pinjar area). Data provided by Water Corporation, measurements performed by Smettem and Assoc.*

2 μm and 20 μm are silt and above 20 μm sand. Note that this classification neither conforms with the ISO 14688-1, nor with the commonly used Wentworth scale where the silt fraction starts at particle sizes below 63 μm and silt particle sizes below 20 μm are considered medium and fine silt. We can note that all materials encountered in drill holes within the Bassendean Sands are well-sorted medium sands with variable fine sand fractions between 10 - 20 % . The fine fraction below 20 μm are typically below 1 % (see Figures 3.2 and 3.3). Figure 3.4 shows an example of PM6 which appears to be a stacked podosol soil profile with several water retentive layers at approx. 3.5,

5.2 and 7.5 mbNS. Although there seems to be a large difference between the layer at 3.5 m (originally marked as "chocolate layer" in the drill report, i.e. B(hs) horizon), the overall grain size distribution reveals that over 99 % of the material falls into the sand fraction. An exception is the fine sand fraction (which here includes coarse silt) in the 3.5 m layer is 20 % and therefore substantially higher than that of the surrounding cleaner sands that contain less than 10 % fine sand (Figure 3.2h).

The grain size distribution is an indicator for porosity and hydraulic properties because packing, pore geometry and pore size vary with the degree of sorting. Well sorted and fine grained soils are typically higher in porosity than poorly sorted coarse soils. Some bulk density measurements are reported by Smettem and Assoc. for boreholes P50 and Lexia (Figures 3.5c, d and 3.6b, c). Bulk density can be transformed into a porosity if grain density is known using equation 3.20 (see following section). The reported bulk density values range between 1.6 g/cm^3 and 1.75 g/cm^3 which corresponds to porosities of 39 % and 33 % , respectively (grain density 2.63 g/cm^3 for quartz). Some of the shallow soil that contains organic material (e.g. Lexia "wetland", Figure 3.6) shows a smaller bulk density of 1.2 g/cm^3. Note that I obtained similar bulk densities between 1.64 g/cm^3 and 1.72 g/cm^3 for measurements I performed in the dielectric cell (see section 3.2.3.2, Figure 3.17).

3.1.2 Saturated Hydraulic Properties

Saturated hydraulic conductivity (K_{sat}) was measured on soil core samples in the field for boreholes PM, PV, P50 and Lexia by Smettem and Assoc. in years 2002 - 2004. Results are plotted in Figures 3.4f, 3.5b, e, 3.6b, c and 3.7. Most samples show saturated hydraulic conductivity values between 10 and 150 meter per day (m/d). The "coffee rock" material produced lower K_{sat} values between 10 - 20 m/d at PM6 and PM7 which is likely due to elevated fine sand content (Figures 3.4f and 3.7e, f). At PM4, a similar layer produced a smaller effect and is indistinguishable of the surrounding clean sand. Some profiles such as PV2, PM4, P50 and Lexia show smaller K_{sat} values well below 100 m/d, whereas profiles PV3 and PM6 have large saturated conductivities around 130 and 170 m/d, respectively. In contrast, the hydraulic conductivity of the hydrophobic sand in the shallow P50 hole 3 is greatly reduced to 3 - 4 m/d (10 - 11 m/d in hole 2, Figure 3.5). For PV2 and PM6, some "dispersed clay" reduced K_{sat} to 0.2 m/d and

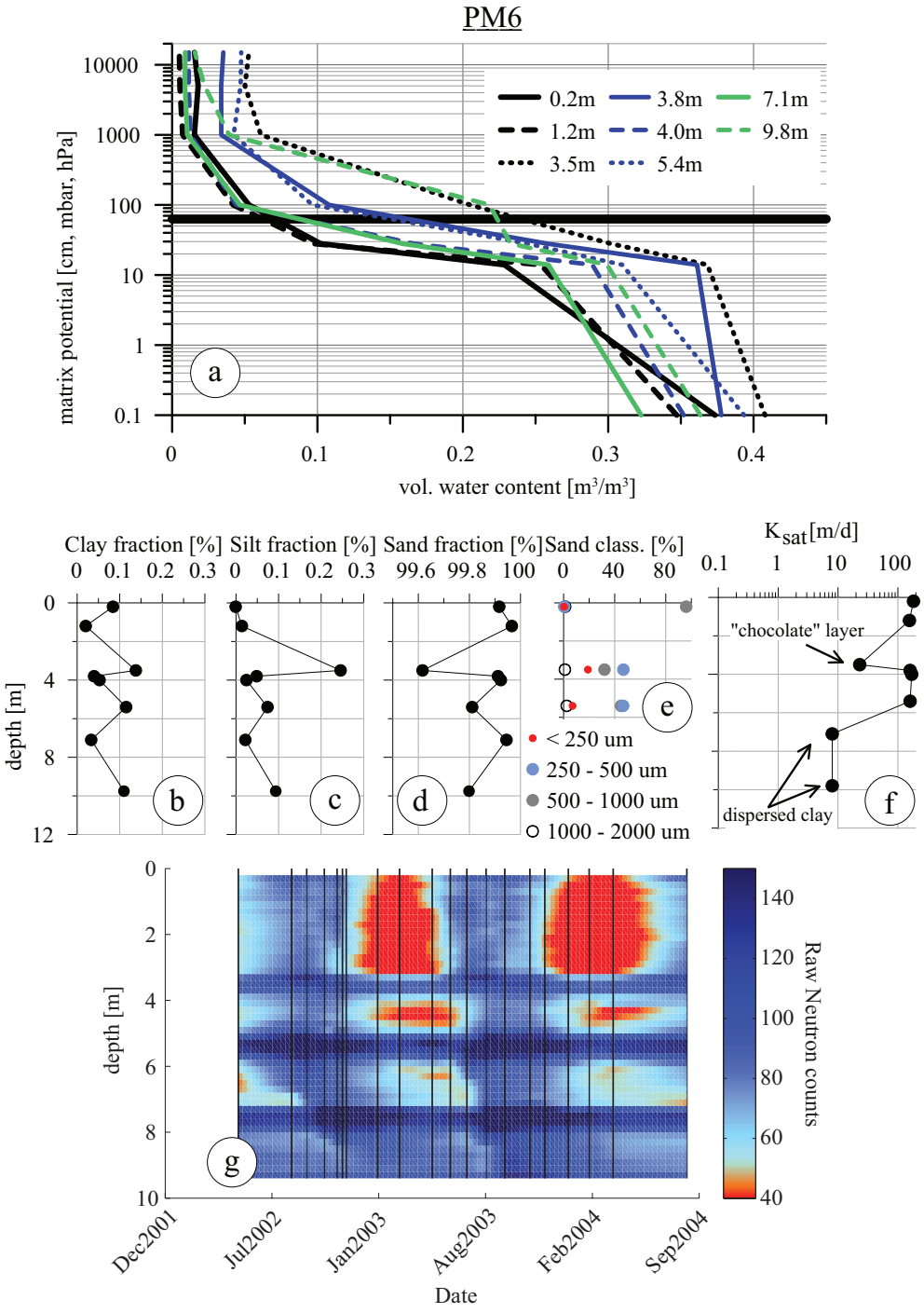

Figure 3.4: *Soil water retention (upper), grain size distribution (middle) and time-lapse Neutron logging (lower) for borehole PM6. Neutron logging reveals water retentive layers at three depth levels possibly indicating a stacked paleo-podosol. Those layers have higher soil water retention potential as shown in (a) for 3.5, 3.8, 5.4 and 9.8 m. Material from 3.8 m and 9.8 m shows elevated clay and silt content in (b),(c) and (e) and slightly reduced hyd. conductivity.*

8 m/d, respectively (Figure 3.7b, e). The driller reports a “tight sandy dry clay layer” at 9.7 mbNS in PM6 and “fine clay material in sand” at 9.8 mbNS at PV2. The laboratory hydraulic conductivity measurements by Smettem and Assoc., however, seem to have been made on a sand mixture, which seems to have only contained some of the clay of

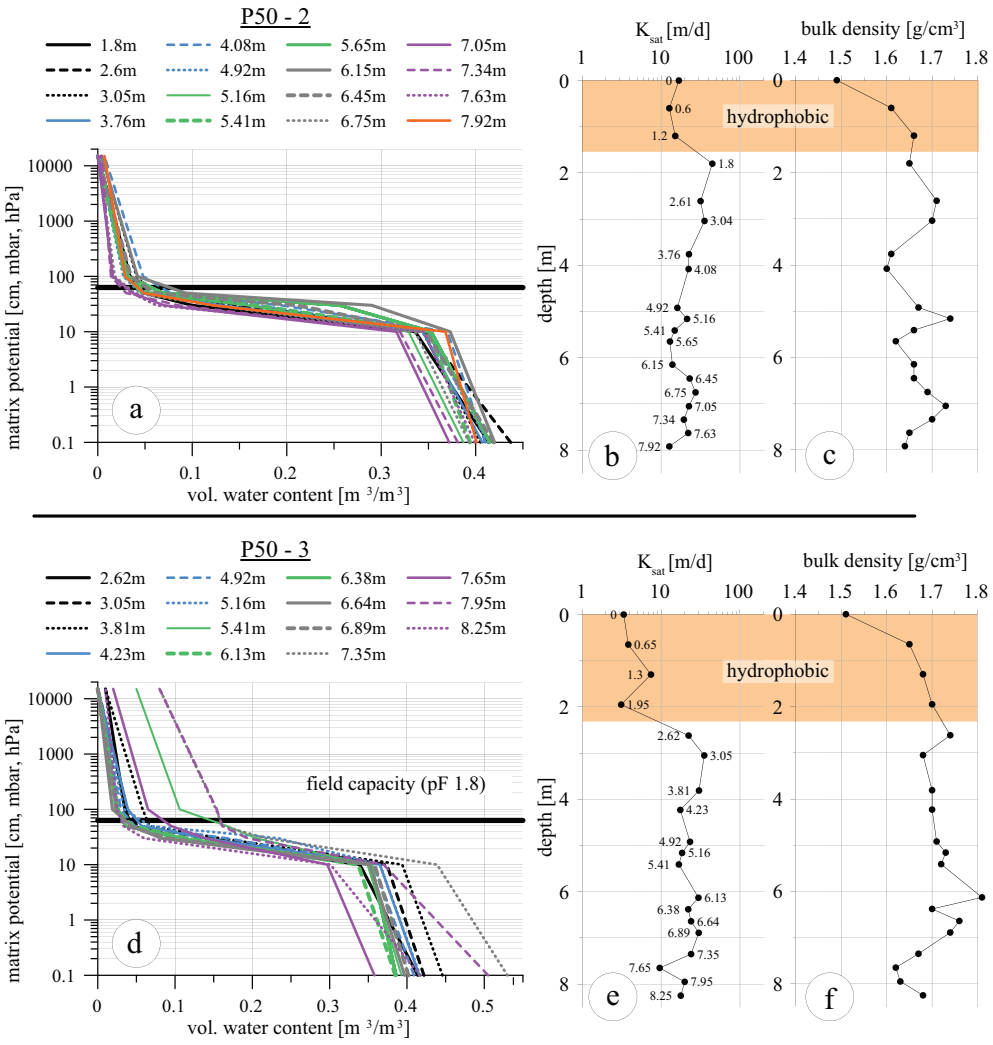

Figure 3.5: *Water retention, saturated hydraulic conductivity and bulk soil density as a function of depth for two boreholes at P50. Note the hydrophobic sand down to 2 mbNS and the low soil density for the very shallow soil, probably due to organic material.*

the main clay layer. The hydraulic conductivity of the clay layer itself could be orders of magnitude less; thus, unsaturated flow would then be controlled by the continuity and the topography of that clay horizon.

It is questionable whether laboratory measurements on loose sand samples are representative for in-situ soil conditions. If the main difference between ”coffee rock” and clean clean sand is cementation material at grain contacts (e.g. allophane clay mineral, iron hydroxides), then the break-up of the friable bond would mobilise the cementation material that otherwise would stay intact and immobile. The released fine material might accumulate in layers and possibly block flow during the hydraulic experiment. On the other hand, the forced flow in laboratory experiments might wash out preferential flow channels within the broken-up sample that do not occur in the

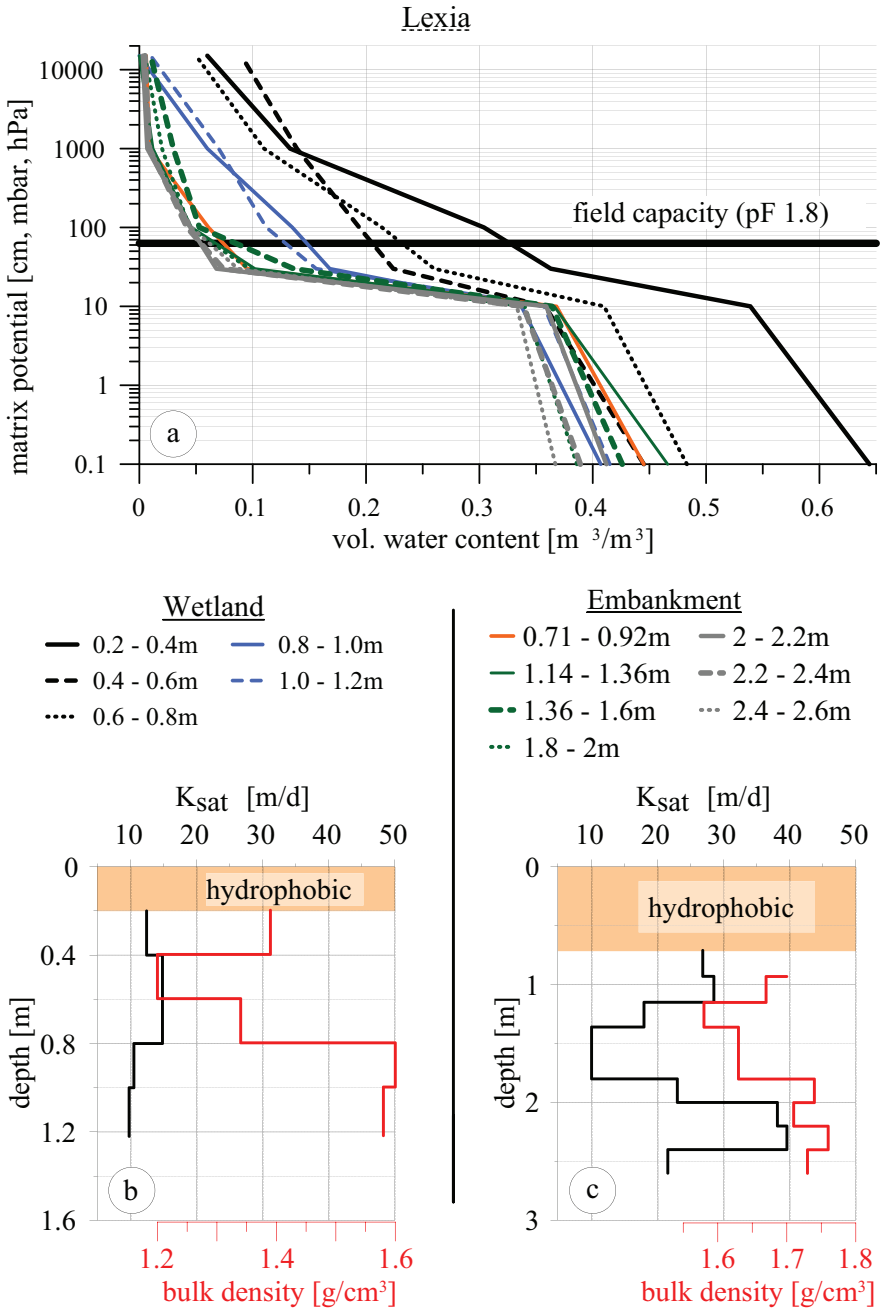

Figure 3.6: *Soil water retention, sat. hydraulic conductivity and soil density for wetland and embankment soil profile at Lexia. Note the increased water retention for the shallow wetland soil. The wetland soil shows a low density layer at 0.5 mbNS indicating high organic content.*

natural environment as the hydraulic gradients are small, flow is slow and cementation material stays in place. The apparent hydraulic conductivity would therefore be larger from lab measurements. Overall, it is difficult to judge whether laboratory hydraulic conductivity tests represent the large scale unsaturated flow regime for a real soil profile. Any borehole contains one dimensional information which, for inhomogeneous soil, leads to a layered earth model (i.e. layers in series). Hence it underestimates flow

as it does not account for preferential flow. Preferential flow may occur along macropores (e.g. roots and burrows) penetrating horizons with lower hydraulic conductivity, or pathways induced by a patchy hydrophobic sand distribution (*Hendrickx and Flury*, 2001). Also lateral guided flow, which can be initiated for example by capillary barrier effects and dipping interfaces, is typically not considered in laboratory experiments and has to be measured in the field (e.g. by tracer/dye experiments, *Kung* (1990)).

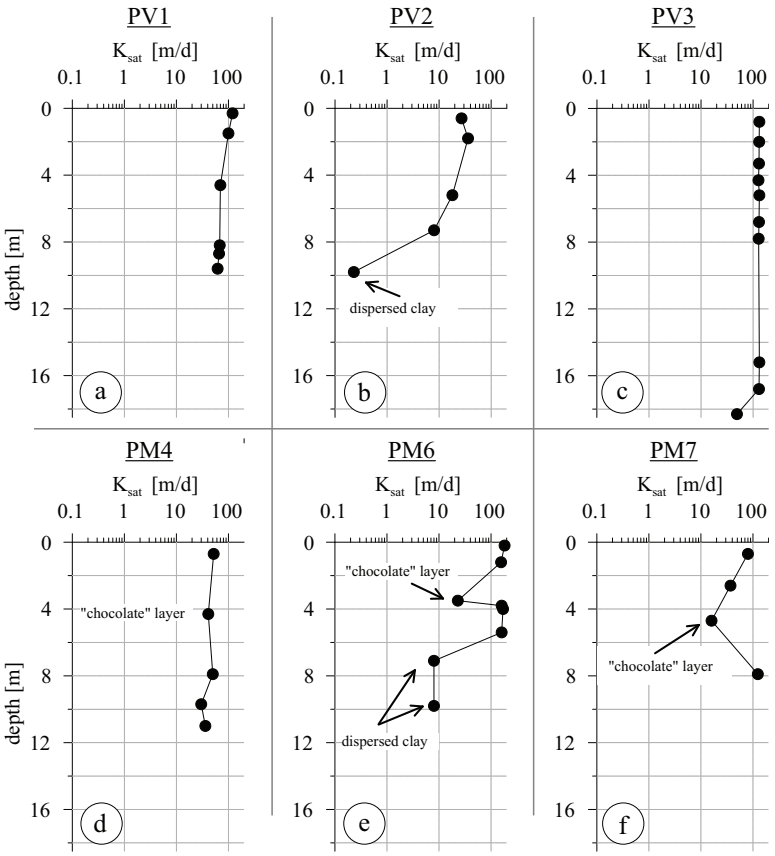

Figure 3.7: *Saturated hydraulic conductivities for Pinjar boreholes PV and PM. Note the reduced values for "coffee rock" layers.*

3.1.3 Unsaturated Hydraulic Properties

Unsaturated hydraulic conductivity was tested by two methods. Firstly, Smettem and Assoc. performed water retention analysis on core samples. I will present this data as it was obtained at various boreholes at depths analogous to the saturated hyd. conductivity. Secondly, Smettem and Assoc. performed field infiltration experiments with a borehole permeameter. These in-situ measurements, are limited to depths below 1 mbNS. Hence, they might be influenced by hydrophobic sand characteristics, and may not represent the indurated and cemented sand layers that are of most interest in

my studies; however, the water retention analysis, includes “coffee rock” samples that are important in my studies. For example, Figure 3.8b, shows the water retention curve for the “coffee rock” layer at 3.5 mbNS (black dotted line) and on the same figure, PM7 has two cemented horizons at 4.7 and 7.9 mbNS. The water retention characteristics in the aforementioned figures are quite different to the clean sand layers. The field capacity, that is the volumetric water content at which capillary forces can hold water against gravitational pull, is greater compared to the other retention curves and lies between 20 - 30 v%. Note that the black curve which indicates field capacity at a pF - value of 1.8 (i.e. potential of 63 hPa ($10^{1.8}$)) is a typical value and applies to various soils (e.g. used in the German soil science community). However, field capacity is unique for every soil and the potential which defines field capacity can therefore vary throughout different materials, especially fine versus coarse textured soils (i.e. loam versus sand, *Veihmeyer and Hendrickson* (1931, 1949)) . The permanent wilting point, which is often defined at a potential of 15.000 hPa (or pF 4.2) where typical plants cannot access pore water anymore, lies at approximately 5 % for the “coffee rock”, and between 1 - 2 % for the clean sands. Therefore, the span of total available water for plant usage (also called available water capacity), which is the difference between water content at field capacity and the wilting point, appears to be greater for the “coffee rock” than for the clean sands (i.e . 20 % vs. 10 %). That means that a “coffee rock” layer may effectively function like a sponge. It can soak up water and store it at shallow depth against gravitational pull. More importantly, it may be able to provide that water for plant usage with only a small amount of water not accessible to the plants. From a groundwater recharge perspective, that water could be lost to evapotranspiration. The time-lapse neutron logs that are part of chapter 6 and B discuss further the effect of field capacity, and provide field evidence that the plants might not use the extra water stored within ”coffee rock” layers at the investigated sites.

3.1.4 Summary

The physical properties of Bassendean Sand materials vary depending on their position within the Podosol profile. While the shallow sands are very well sorted and slightly coarser than deeper sands, they are hydrophobic and can contain organic material such as roots, ash and leaf litter. Despite their coarser grain size and good sorting, they show

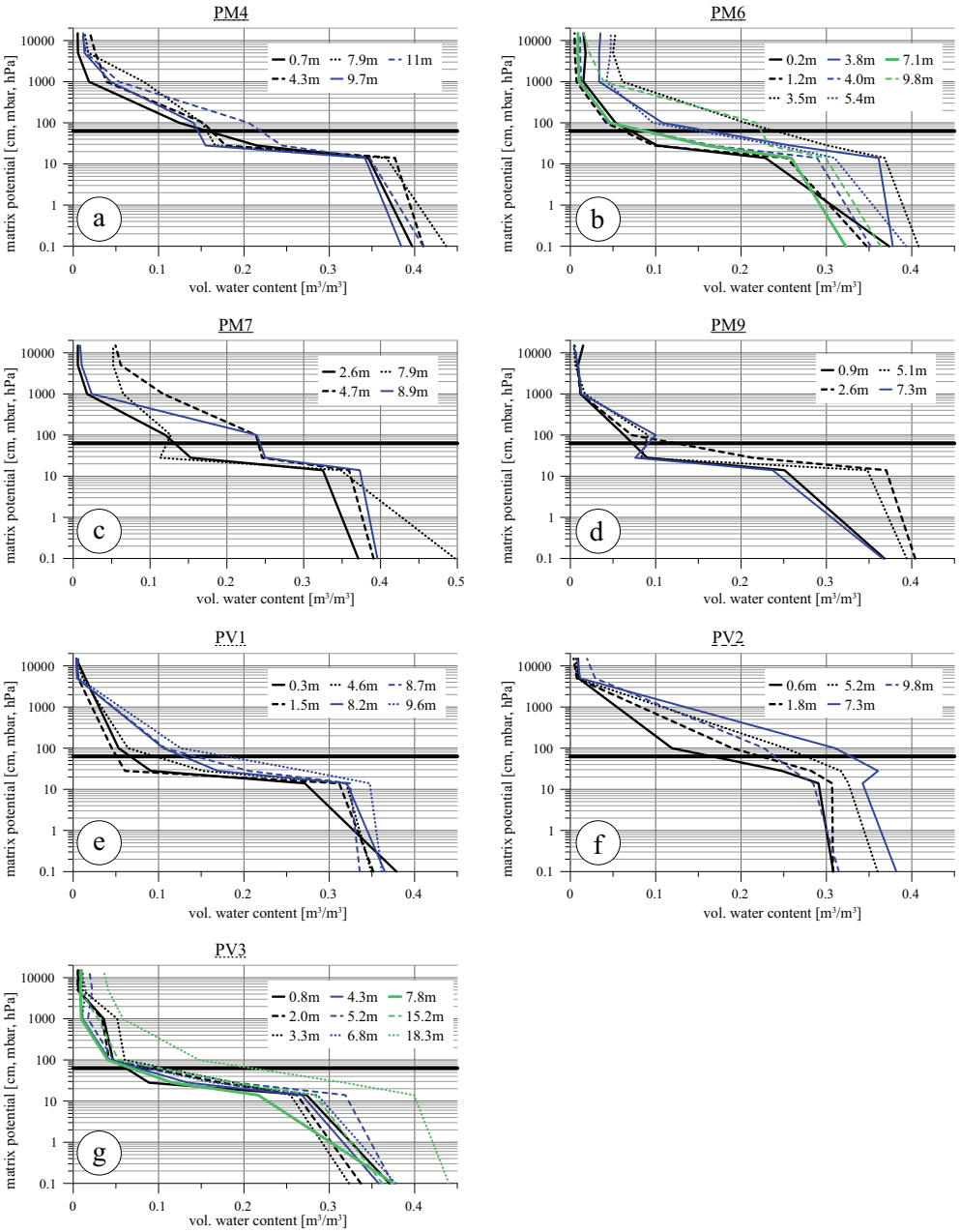

Figure 3.8: *Water retention curves for different depth levels for Pinjar area PM and PV boreholes. Note the increased soil water retention for some soil horizons.*

a reduced hydraulic conductivity that is likely due to their hydrophobic characteristics. The main portion of the soil profile, which includes materials of E- and C–horizon, are medium sands with high saturated hydraulic conductivity between 50 - 150 m/d. The B horizon material seems to vary depending on the clay content. Some “coffee rocks” had reduced saturated hydraulic conductivities of 10 - 30 m/d, but some brown layers don’t show any great decrease. The water retention of the B-horizon material tends to differ from the clean sand intervals as it has greater field capacity, which ranges between 20 - 30 % volumetric water content as opposed to 5 - 15 % for the

clean sands. The residual water fraction that cannot be used by plants is also greater in “coffee rock” and reaches 5 % compared to 1 - 2 % in clean sands. This suggests that the “coffee rock” could be a store of extra water in the vadose zone and make it available for plant consumption. Some clay materials, for example found at PV2 and PM6, indicate another type of ”coffee rock” layer, or a depositional clay. It could be that these layers are found close to the water table and represent another accumulation horizon that forms within the dynamic capillary fringe zone above the aquifer as has been described in the previous chapter (section 2.4.3). Whether these layers are also considered “coffee rock” depends on their origin. If they are depositional, such as the Guildford Clay, then they should be treated separately because the mineralogy will differ from the humic and Allophane-rich illuviation horizons.

In conclusion, the laboratory measurements provide a basis for understanding the hydraulic properties of the materials that are found in the Podosol soil profile of the Bassendean Sands, but they do not provide an insight into the flow patterns that occur in a natural inhomogeneous soil system. In this context, geophysical mapping techniques can play an important role in characterising the spatial distribution of those differing materials on a relevant scale.

3.2 Soil Dielectric Properties

In hydrogeophysics, agricultural, soil and plant sciences, researchers often seek quantitative water content distribution to better understand the vadose hydrologic system. Electromagnetic methods such as Ground penetrating Radar (GPR) or time-domain reflectometry (TDR) have been shown to be useful methods to map spatial water content distribution (*Huisman et al.*, 2003). For example *Hubbard et al.* (2002) bridge the gap between hydrogeophysics and agriculture by using GPR ground-wave analysis to spatially map the shallow water content in a vineyard, or *Steelman and Endres* (2010) monitor soil moisture distribution for different soils over an annual cycle including freezing and thawing events using multi-offset GPR. *Huisman et al.* (2002) compare mapping results from GPR ground wave and TDR and find that the GPR is better suited to measure variability with meter-scale correlation lengths. *Lambot et al.* (2006a) use air-launched Horn antennas to infer soil surface water content from reflected waves.

While GPR or TDR data can provide information about the physical properties of the soil, these methods do not directly measure water content. Quantitative interpretation of GPR or TDR data is based on evaluation of EM pulse propagation (*Huisman et al.*, 2003) or reflection characteristics (*Iskander and DuBow*, 1983). The phase velocity or reflectivity is used to derive the dielectric permittivity of the subsurface, while the attenuation of the signal is indicative of the electrical conductivity and the imaginary dielectric permittivity. Both of these quantities are sensitive to water content variations. The dielectric permittivity shows a strong dependency on water content and is therefore especially useful for inferring water content in unsaturated media. Water has a relative dielectric permittivity of 80, while a water-free mineral soil made of quartz, feldspar and other common soil constituents rarely exceeds values above 8 and is typically in the range between 2 - 5 (*Huisman et al.*, 2003). Hence, small amounts of water influence the dielectric property of a soil dramatically.

Despite the multitude of water content versus dielectric permittivity relationships that are readily available, most researchers recommend that site-specific calibration curves are produced. However, in professional practice and in the applied sciences, investigators typically use empirical relationships such as the Topp-relationship *Topp et al.* (1980), or a mixing law such as the complex refractive index model (CRIM). These simple relationships are sufficiently accurate to relate field derived permittivity measurements to water contents within the measurement errors in case of common soils. However, the soil profile under investigation in this study contains a water retentive accumulation and cementation horizon B(hs) that can contain a variety of minerals other than quartz as described previously. A recent study by *Josh et al.* (2011) demonstrated that small amounts of iron mineral precipitate can lead to greatly different dielectric properties for Australian soil from the Victorian desert. As no dielectric measurements on the accumulation horizons found in the Podosol soil profile could be found in the literature, I decided to investigate the electric and dielectric properties of Podosol horizons and compare them with the leached sand intervals of the A2 and E horizons, and the stained sand of the C horizons.

3.2.1 Theoretical Background: Electric And Dielectric Parameters

Electromagnetic field distribution in dielectric media is dominated by the processes of EM-energy diffusing and propagating through the material. Those processes are described by Maxwell's equations (*Maxwell*, 1865). The electrical material property that governs the diffusive behaviour is electric conductivity σ which describes materials' ability of charge transport (*Olhoeft*, 1998). Propagation, on the other hand, is governed by dielectric properties. The magnetic properties of most geological media are close to that of a vacuum; thus, magnetic properties of soils will not influence GPR or electrical measurements significantly. The process involved is a charge separation or polarization which facilitates storage of electric field energy. The dielectric constant, or dielectric permittivity ϵ, is the corresponding material property. Hence, ϵ describes a materials' ability to store the electric field energy under consideration of energy dissipation. ϵ can be expressed as a complex number $\epsilon^* = \epsilon' + i\epsilon''$. The real part ϵ' describes the effectiveness of energy storage, whereas the imaginary part ϵ'' contains energy dissipation that occurs during the polarization and relaxation process. In order to provide manageable values for dielectric permittivities, these values are generally expressed relative to the dielectric constant in a vacuum ϵ_0 ($8.854 \cdot 10^{-12}$ F/m) . If the applied electric field is alternating at a frequency in the radar range of several megahertz (MHz) to gigahertz (GHz), and the medium has a sufficiently low direct current (DC) conductivity, then the dielectric properties are dominant and waves propagate. Propagation can be described with the complex circular wavenumber (notation according to IEEE convention *Wave propagation Standards Committee and Society* (1997), derivation for example in *Balanis* (1982) or for GPR in *Knoll* (1996) or *Olhoeft* (1998)):

$$\gamma = ik = \alpha + i\beta \tag{3.1}$$

or the wavenumber k as

$$k^2 = \mu^*\epsilon^*\omega^2 + i\mu^*\sigma^*\omega \tag{3.2}$$

with $\omega = 2\pi f$ the angular frequency, μ^* and σ^* the complex magnetic permeability and conductivity, respectively, and β and α the phase and attenuation constants, respec-

tively. Note that measured parameters from the lab or the field are effective parameters denoted as ϵ_e written as

$$\epsilon_e' = \epsilon' + \frac{\sigma''}{\omega} \tag{3.3}$$

and

$$\epsilon_e'' = \epsilon'' + \frac{\sigma'}{\omega}. \tag{3.4}$$

By using $\epsilon_e^* = \epsilon_0 \left(\epsilon_{e,r}' - i\epsilon_{e,r}''\right)$ and $\mu^* = \mu_0$, and under consideration of low-loss (i.e. the loss tangent $\tan\delta = \frac{\epsilon_{e,r}''}{\epsilon_{e,r}'} << 1$) we obtain for the phase constant β and phase velocity ν:

$$\beta = \omega\sqrt{\frac{\mu_0\epsilon_e'}{2}\left(\sqrt{1+\tan^2\delta}+1\right)} = \omega\sqrt{\mu_0\epsilon_e'} \tag{3.5}$$

and

$$\nu = \frac{\omega}{\beta} = \frac{1}{\sqrt{\mu_0\epsilon_e}} = \frac{1}{\sqrt{\mu_0\epsilon_0}\sqrt{\epsilon_{e,r}'}} = \frac{c}{\sqrt{\epsilon_{e,r}}} \quad \text{[m/s]}. \tag{3.6}$$

The attenuation factor α includes the imaginary part and hence the loss tangent and is typically given as a coefficient α_c in Decibels per meter [dB/m]:

$$\begin{aligned} \alpha &= \omega\sqrt{\frac{\mu_0\epsilon_e'}{2}\left(\sqrt{1+\tan^2\delta}-1\right)} \\ &= \frac{\omega}{c\sqrt{2}}\sqrt{\sqrt{\epsilon_{e,r}'^2+\epsilon_{e,r}''^2}-\epsilon_{e,r}'} \quad \text{[Np/m]} \end{aligned} \tag{3.7}$$

and

$$\alpha_c = 8.686 \cdot \alpha \quad \text{[dB/m]} \quad . \tag{3.8}$$

The inverse of the attenuation factor $\frac{1}{\alpha}$ [m] is the skin depth which resembles the distance at which the initial wave amplitude A_0 is attenuated to $\frac{1}{e}A_0$. The attenuation coefficient is used to estimate depth of penetration of a radar system as part of the radar range equation.

At low frequencies, the imaginary electrical conductivity becomes negligible and the effective imaginary dielectric permittivity represents the real electrical conductivity because the dielectric losses are negligible. To verify whether dielectric losses are absent and $\epsilon_e'' = \sigma_{DC}/\omega$, one can investigate the slope of the double - logarithmic function $\epsilon_e''(f)$ at low frequencies. If that slope becomes -1, the measured parameter

represents the direct current (DC) conductivity (*Kaviratna et al.*, 1996; *Arcone et al.*, 2008). The DC-resistivity can then be calculated from the effective relative imaginary dielectric permittivity measured at a low frequency with

$$\rho_{DC} = \frac{1}{\epsilon_0 \epsilon''_{e,r} \cdot \omega}. \tag{3.9}$$

3.2.2 Dielectric Properties Of Mixed Media

Most soils are a mixture of solid minerals with air and water (with dissolved salts)in the pore space. Parts of the soil water are absorbed on the charged mineral surface, and clays can be hydrated and contain water in their crystal structure. For simple soils bulk dielectric properties are controlled by the volumetric water content, the grain dielectric permittivity, and the geometry of the grains and the porespace. Several ways of relating pore water to dielectric permittivity exist. The most prominent include empirical relationships derived for "average" common soils, mixing laws, and effective medium approaches. In this work, I will first investigate some of the most commonly used empirical relationships given by *Topp et al.* (1980) and *Roth et al.* (1992). To better understand some of the physical material properties involved in the dielectric response to water content, I will also test mixing laws that contain parameters that can give insight into pore space geometry and grain shape, or cementation and wettability.

Empirical Relationships

Numerous empirical relationships have been proposed in the literature. The most prominent is the Topp - relationship (*Topp et al.*, 1980). *Topp et al.* (1980) give two third-order polynomials that relate dielectric permittivity to water content and vice-versa based on coaxial transmission line measurements on different soils. Their equation 6 on page 580 provides relative dielectric real permittivity as a function of volumetric water content (i.e. $\epsilon'_{e,r}(\theta_v)$), while their equation 7 on page 580 is the water content as a function of relative dielectric permittivity. The latter is the equation most practitioners seek as GPR and TDR field measurements provide an estimate of dielectric permittivity. The two equations read as follows:

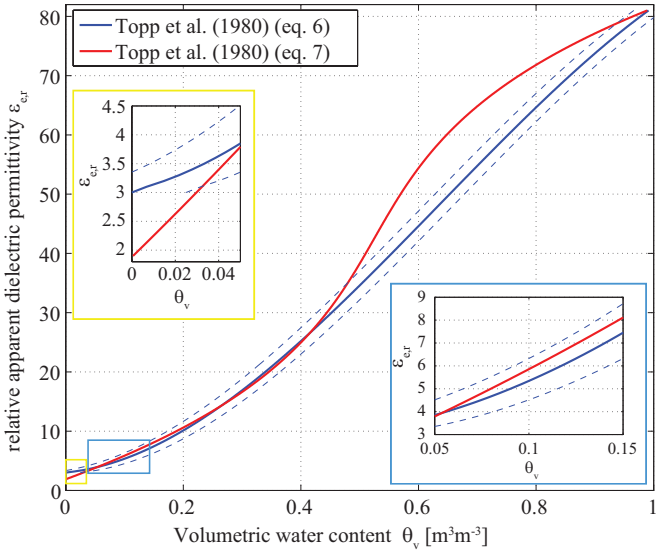

Figure 3.9: *Empirical derived Topp-relationship (Topp et al., 1980) relating apparent effective real dielectric permittivity to volumetric water content of soil mixtures. Note the discrepancy between the forward-relationship (i.e. $\epsilon'_{e,r}$ as function of θ_v, Topp Eq. 6) and the backward relationship (i.e. θ_v as function of $\epsilon'_{e,r}$, Topp Eq. 7) which is most severe at very low water contents below 3 v% and high water contents above 0.5 v%.*

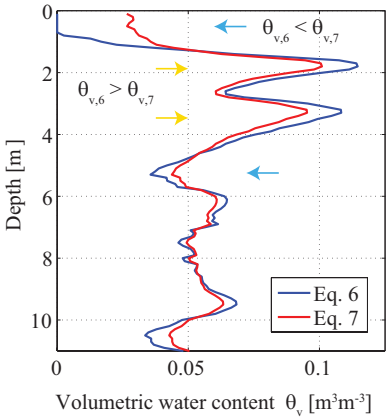

Figure 3.10: *Effect of Topp forward and backward relationship on example crosswell logging profile containing layers with different dielectric properties. Note that Topp Eq. 6 results in a sharper curve with higher gradients, while the curve from Eq. 7 is less defined.*

$$\epsilon'_{e,r} = 3.03 + 9.3\theta_v + 146.0\theta_v^2 - 76.7\theta_v^3 \quad \text{(Eq.6)} \tag{3.10}$$

and

$$\theta_v = -5.3 \cdot 10^{-2} + 2.92 \cdot 10^{-2}\epsilon'_{e,r} - 5.5 \cdot 10^{-4}\epsilon'^2_{e,r} + 4.3 \cdot 10^{-6}\epsilon'^3_{e,r} \text{(Eq.7)} \tag{3.11}$$

One would expect that one curve is close to the inverse of the other. Note that a true mathematical inverse of a third-order polynomial cannot be a third-order polynomial itself. Both equations were derived for the same dataset according to the authors. However, there is a large discrepancy between the two curves as shown in Figure 3.9; especially with large volumetric water contents above 0.4, where the curve given in equation 3.11 (Topp Eq.7) deviates from equation 3.10 (Topp Eq.6) towards higher dielectric permittivities. At a volumetric water content of approximately 0.7 the curves begin to converge and end up at the same dielectric permittivity for 100% volumetric water content (pure water). The section of the curve above 0.4 water content is important for soils with high clay contents and high porosities, which is less relevant in my

area of study. At very small water contents below 0.05, the curve from equation 3.11 approaches a dielectric permittivity value of 2, while equation 3.10 flattens off towards a dielectric permittivity value of 3. As a consequence any measured permittivities below 3, when combined with equation 3.10 predicts a water content of 0, while equation 3.11 predicts small water contents between 0 and 0.03. Between water contents of 0.05 and 0.3, equation 3.10 predicts larger water contents than equation 3.11 at any given permittivity value. When results from equation 3.10 and 3.11 are compared, for example in crosswell data as shown in Figure 3.10, the effect becomes clear as the inferred water content curves have less definition (smoother) when equation 3.11 is used for permittivity values between 2 and 10. This is due to the much steeper slope of the $\theta_v(\epsilon'_{e,r})$ - curve in that value range. In my work, whenever I used the Topp relationship to convert measured GPR velocity to water content, equation 3.10 was used by finding the roots of that third-order polynomial numerically with the Matlab function 'roots'. Equation 3.10 was used over 3.11 because in most materials I measured, either in the field, or in the coaxial transmission line, none showed relative dielectric permittivities below 2.75 (i.e. velocities were above 0.18 m/ns) when completely dry.

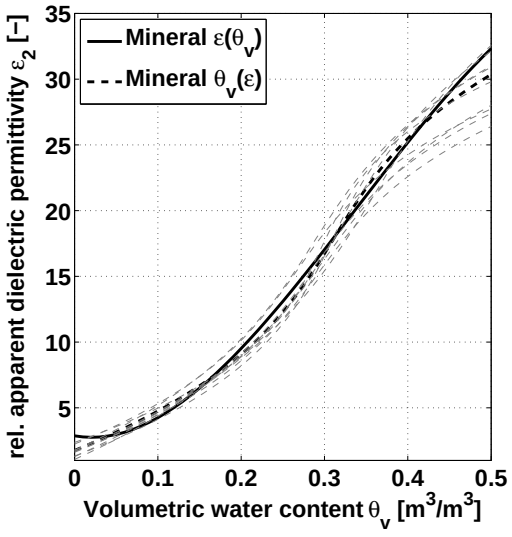

Figure 3.11: *Plots of third-order polynomials given in Roth et al. (1992) for mineral soils. Grey thin dashed curves are $\theta_v(\epsilon'_{e,r})$ relationship for single soils, and black thick curves are fitted to the whole dataset.*

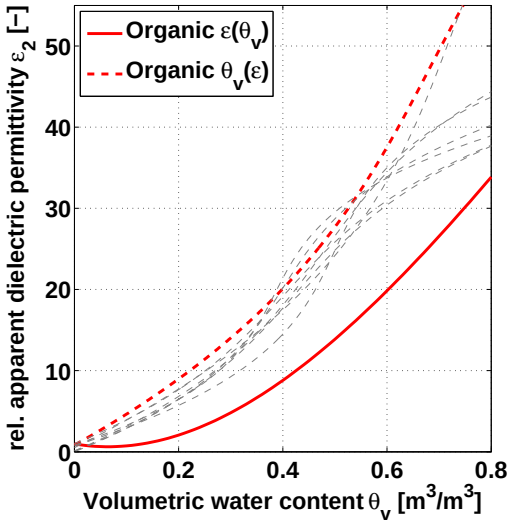

Figure 3.12: *Plots of third-order polynomials given in Roth et al. (1992) for organic soils. Grey thin dashed curves are $\theta_v(\epsilon'_{e,r})$ relationship for single soils, and red thick curves are fitted to the whole dataset. Note the discrepancy between $\theta_v(\epsilon'_{e,r})$-relationship for single and bulk soil, and between $\theta_v(\epsilon'_{e,r})$- and $\epsilon'_{e,r}(\theta_v)$-relationship.*

Several other researchers have derived various polynomials for different soils (*Roth et al.*, 1992; *Curtis*, 2001; *Steelman and Endres*, 2011). Most of the following analysis is with the empirically derived polynomials by *Roth et al.* (1992), because their paper is well cited and I initially intended to use this relationship as it provides third-order polynomial fits classified by mineral, organic and magnetic soils. The authors provide tables listing the polynomial coefficients for the $\theta_v(\epsilon'_{e,r})$ relationship. Those tables (i.e. in the original paper tables 2c, 3c and 4c for mineral, organic and magnetic soils, respectively) list the coefficients which produced the best fit for single soils, and additionally they give a bulk value that tries to represent a best fit for all soils of any one subclass. I have calculated and plotted the curves for single and bulk $\theta_v(\epsilon'_{e,r})$-coefficients for mineral, organic and magnetic soils in Figures 3.11, 3.12 and 3.13, respectively, as grey dashed lines for single soils, and dashed thick coloured lines for the bulk coefficient. Additionally, *Roth et al.* (1992) provide the bulk coefficients for the $\epsilon'_{e,r}(\theta_v)$-relationship under the respective plots (i.e. Figures 1, 2 and 3 in the original paper), which I plot as solid thick coloured line in Figures 3.11, 3.12 and 3.13. From those plots, it appears that the $\epsilon'_{e,r}(\theta_v)$ curves differ from the $\theta_v(\epsilon'_{e,r})$ curves, similar to what has been observed for the Topp equations discussed above. The behaviour of the mineral soil curves is similar to the Topp curves at water contents below 0.15. The curves I have reproduced in Figure 3.11 are similar to the curve shown in *Roth et al.* (1992) Figure 1. The organic soil curves I derived and plotted using the coefficients provided in the paper show a discrepancy between $\theta_v(\epsilon'_{e,r})$- and $\epsilon'_{e,r}(\theta_v)$-relationship. The solid red curve in Figure 3.12 predicts significantly lower permittivity values compared to the dashed curve. When compared to the curve shown in *Roth et al.* (1992), it becomes clear that neither of the two bulk curves match the one the authors show in their published Figure 2. In the case of the magnetic soils' coefficients provided in the paper, I also found significant differences between forward and backward relationships, and an inconsistency with what has been shown in *Roth et al.* (1992), Figure 2. Thus, it appears that the plots that are shown in the original publication *Roth et al.* (1992) were not created with the polynomial coefficients they provide. Due to this uncertainty, I decided not to use those relationships to compare with my data .

However, the publication by *Roth et al.* (1992) is valuable for my studies, as it provides some general insights into trends that are typical for the different soils. For

example, increasing organic content leads to low bulk dielectric permittivity of dry organic soils (i.e. $1 < \epsilon_{r,org,dry} < 2.5$) compared to the mineral soils (i.e. $2.75 < \epsilon_{r,org,dry} < 3.5$). This probably correlates with the lower bulk soil density due to the organic constituents which have a very low dielectric permittivity when dry.

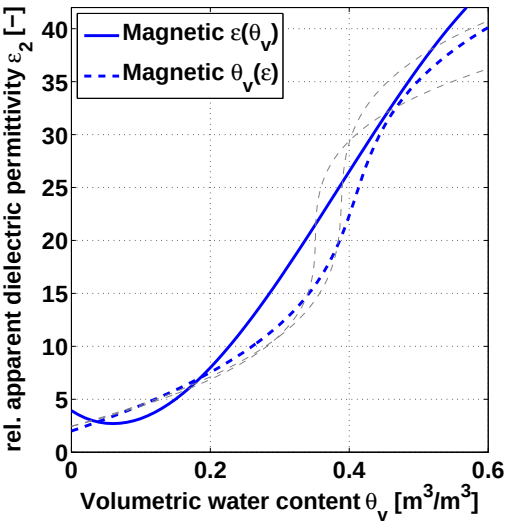

Figure 3.13: *Plots of third-order polynomials given in Roth et al. (1992) for magnetic soils. Grey thin dashed curves are $\theta_v(\epsilon'_{e,r})$ relationship for single soils, and blue thick curves are fitted to the whole dataset. Note the discrepancy between $\theta_v(\epsilon'_{e,r})$-relationship for single and bulk soil, and between $\theta_v(\epsilon'_{e,r})$- and $\epsilon'_{e,r}(\theta_v)$-relationship.*

Mixing Formula

Mixing equations are based on the principle that the bulk material property can be calculated as a combination of the individual components' properties. In most cases the bulk property is a weighted average of the constituents' properties. The Lichtenecker-Rother equation (*Lichtenecker and Rother*, 1931; *Brovelli and Cassiani*, 2008) is the simplest example and reads for dielectric properties:

$$\epsilon_b^\alpha = \sum_{i=1}^{n} \varphi_i \epsilon_i^\alpha \quad . \tag{3.12}$$

where ϵ_b the bulk dielectric permittivity (can be complex), ϵ_i the dielectric permittivity of the constituent i out of n constituents(e.g. solid grain, air, water, etc.), φ_i the volume fraction of constituent i and α ($-1 \leq \alpha \leq 1$ an exponent that can be used for fitting measured data. The boundary values -1 and 1 for α represent respectively the harmonic and arithmetic mean of the constituents properties under consideration of volume fraction (*Brovelli and Cassiani*, 2008). For layered media, the lower and upper boundaries represent transport perpendicular or parallel to the layering, respectively (equivalent to electrical circuit with components in series or parallel). For α

= 0.5, equation 3.12 reduces to the Complex Refractive Index Model (CRIM). This model is frequently used amongst the GPR community (*Roth et al.*, 1990; *Huisman et al.*, 2003; *Annan*, 2005; *Brovelli and Cassiani*, 2008). For a three-phase system air, water and solid mineral grains, the Lichtenecker-Rother equation for relative dielectric permittivities becomes (*Brovelli and Cassiani*, 2008)

$$\epsilon_{r,b}^{\alpha} = (1-\phi)\,\epsilon_{r,s}^{\alpha} + \theta_v \epsilon_{r,H_2O}^{\alpha} + (\phi - \theta_v)\,\epsilon_{r,air}^{\alpha} \tag{3.13}$$

and the volumetric water content can then be written as (*Strobach et al.*, 2011)

$$\theta_v = \frac{\phi(\epsilon_{r,air}^{\alpha} - \epsilon_{r,s}^{\alpha}) - \epsilon_{r,b}^{\alpha} + \epsilon_{r,s}^{\alpha}}{\epsilon_{r,air}^{\alpha} - \epsilon_{r,H_2O}^{\alpha}} \tag{3.14}$$

with $\epsilon_{r,air}$, $\epsilon_{r,s}$, ϵ_{r,H_2O} and $\epsilon_{r,d}$ the relative dielectric permittivities of air (i.e. 1), the solid phase, water (i.e. 80) and of the bulk medium (i.e. the measured quantity), and ϕ the porosity. The volumetric water content derived from bulk dielectric permittivity measurements becomes a function of the porosity, the parameter α and, if unknown, the solid (or grain) permittivity.

It has been shown by *Brovelli and Cassiani* (2008) that the exponent α (for $\alpha > 0$) is inversely proportional to Archie's cementation exponent m. Hence, it carries information on the geometry of the mixture, such as pore-space geometry, grain shape, bedding etc. *Brovelli and Cassiani* (2008) also show that α depends on the ratio of solid and water dielectric permittivity, and that α is inversely correlated with the solid matrix permittivity. This is a big drawback of that constitutive equation and led *Brovelli and Cassiani* (2010, 2011) to develop a model based on Archie's first and second law (*Archie*, 1942) for two- and three-phase systems, respectively. They use a weighted average of Hashin-Shtrikman (HS) bounds (*Hashin and Shtrikman*, 1962) to calculate bulk medium permittivity. The bulk permittivity HS lower (HSL)and upper (HSU) bounds are written for a two-phase system (i.e. pore phase with ϵ_p, and solid phase ϵ_s) as:

$$\epsilon_{HSL}\left(\epsilon_s, \epsilon_p, \varphi\right) = \epsilon_s + \frac{\varphi}{\left(\epsilon_p - \epsilon_s\right)^{-1} + \frac{1-\varphi}{3\epsilon_s}}, \tag{3.15}$$

$$\epsilon_{HSU}\left(\epsilon_s, \epsilon_p, \varphi\right) = \epsilon_p + \frac{1-\varphi}{\left(\epsilon_s - \epsilon_p\right)^{-1} + \frac{\varphi}{3\epsilon_p}}, \tag{3.16}$$

with the pore phase permittivity consisting of water and air reads as

$$\epsilon_p\left(\epsilon_a ir, \epsilon_w, s_w, n\right) = w\epsilon_{HSU}\left(\epsilon_a ir, \epsilon_w, \epsilon_w\right) + \left(1-w\right)\epsilon_{HSL}\left(\epsilon_a ir, \epsilon_w, s_w\right), \tag{3.17}$$

where s_w is the water saturation and w is a weight function given by

$$w = \frac{\epsilon_w}{\epsilon_{HSU}\left(0, \epsilon_w, s_w\right) \cdot s_w^{-n}}. \tag{3.18}$$

Brovelli and Cassiani (2010) derive the bulk medium permittivity ϵ_b as

$$\epsilon_b\left(\epsilon_s, \epsilon_p, \phi, m\right) = \left(\frac{3-\phi}{2}\phi^{(m-1)}\right)\epsilon_{HSU}\left(\epsilon_s, \epsilon_p, \phi\right) + \left(1+\frac{-3}{2}\phi^{(m-1)}\right)\epsilon_{HSL}\left(\epsilon_s, \epsilon_p, \phi\right). \tag{3.19}$$

I have changed the original order of quantities that appear in the brackets in ϵ_p and associated HS upper and lower boundaries, as well as in the term w as given in *Brovelli and Cassiani* (2010). The order written here is i) smaller valued quantity (e.g. ϵ_{air}), ii) larger valued quantity (e.g. ϵ_{H_2O}) and iii) the volume fraction of ii). The reason is to retain consistency with the general notation they give for the HS upper and lower boundaries (*Brovelli and Cassiani* (2010), p.235, equations 24 and 25) and to avoid confusion when assigning parameters that feed into a Matlab function. The Hashin-Shtrikman average (HSA) model provides a means to transfer Archie's law for bulk medium conductivity to dielectric permittivity . Although Archie's law was originally derived empirically, it has been shown that a self-consistent differential effective medium approach can lead to the same constitutive equation for a range of cementation exponents, and provide a physical foundation for the relationship (*Sen et al.*, 1981; *Brovelli and Cassiani*, 2010). The advantage of the Archie-type Brovelli-Cassiani Hashin-Shtrikman average constitutive equations over the Lichtenecker-Rother equation is that the exponents m and n have separate physical meanings describing the geometry and interconnectivity of pores and grains (e.g. Formation Factor, tortuosity), pore size and fluid distribution (e.g. wettability). A practical advantage is that the exponents are identical for the conductivity and dielectric permittivity measurements in the cases where the assumptions made by *Brovelli and Cassiani* (2010) are valid (i.e. solid dielectric permittivity $<<$ water dielectric permittivity, no grain surface conduction;

analogous to limitations of Archie's law). Hence, one set of measurements (e.g. water dependent electrical conductivity or dielectric permittivity) could provide microstructural features of the medium and therefore predict the behaviour of both electric and dielectric properties. This advantage has not been demonstrated on a sufficient amount of datasets to be considered entirely valid .

Dielectric measurements can typically recover DC electrical conductivity if frequencies were sufficiently low using the logarithmically linear slope of -1 part of the effective imaginary dielectric permittivity versus frequency curve (see section 3.2.1, equation 3.9). Therefore, frequency dependent dielectric measurements can provide a basis to test the claim that the cementation and saturation exponents derived from Archie's law for electrical conductivity and using the HSA-model for dielectric permittivity, result in the same parameters. Our dataset, was not large enough to test that approach .

The water content versus dielectric permittivity relationships introduced in this chapter were compared with the measured results from laboratory dielectric experiments described in the following sections. The data plots used the Topp-relationship equation 3.10 as it provided sufficiently robust results. Additionally, I used the Lichtenecker-Rother model to fit α-exponent, solid dielectric permittivity and porosity to the measured data pairs, and the HSA-model with fitted m, n, solid dielectric permittivity and porosity. Those mixing models were chosen as they are simple and provide some information on structure, pore space geometry and wettability.

3.2.3 Methods And Materials

The following sections deal with the dielectric measurements made on soil samples from the study area. The key objectives are to firstly contrast different soil horizons found within the podosol soil profile (namely leached sand versus accumulation horizons), and secondly to obtain insights into the dielectric properties of larger scale shallow materials. While the first objective is important for time-lapse studies, where temporal water content changes result in variations in dielectric properties, the secondary objective is aimed at better understanding the attenuation characteristics for large-scale data interpretation.

All soil samples were collected from the Bassendean or Spearwood dunes. The

Bassendean dunes are part of the Bassendean Sand Formation, while the Spearwood dunes belong to the Tamala Limestone Formation (refer to previous chapter, section 2.2) (*McArthur and Bettenay*, 1974; *Davidson*, 1995). The main characteristic of the Spearwood dunes is that they are younger and therefore have not been leached as extensively as the Bassendean sands. The distinctive B horizon is missing, and drillholes report limestone at a depth of about 4 - 10 m. Below a thin white sand layer on the surface, the quartz sand is coated with iron oxides which gives the sand a yellow to orange appearance. Prior to dielectric measurements, I initially thought that this coating might be the source of signal attenuation that was observed for the western part of east-west radar sections across the Gnangara Mound (*Strobach et al.*, 2010a). Further samples were collected north of Whiteman Park at the location M345 from the Bassendean Sand Formation (*Strobach et al.*, 2011). The soil profile is a podosol that shows distinct A, B and C horizons (Figure 2.11). In summary, the materials under investigation are (corresponding sample number in bracket):

- Tamala Formation
    - Leached sand from Spearwood dune (E)
    - Stained yellow-orange sand from Spearwood dune (A) (243-3, 254-2)
- Bassendean Formation
    - Leached sand (A/E) (250-(1-3), M345-3)
    - aeric indurated, cemented sand (”coffee rock”) (B(hs)) (CR-M345-1/2)
    - Stained sand below indurated horizon (C) (M345-5)
    - aquatic B - horizon (NG-CR-1?)
- Other surficial materials
    - Intradunal wetland material (organic?) (246-2)
    - Clay from below watertable TrRd East (Guildford?)(TrRd-Clay)
    - Track material (limestone?) (243-street)
    - Ferritic cemented sand (Mandalay Beach) (MB)

Pictures of the samples are shown in Figure 3.14.

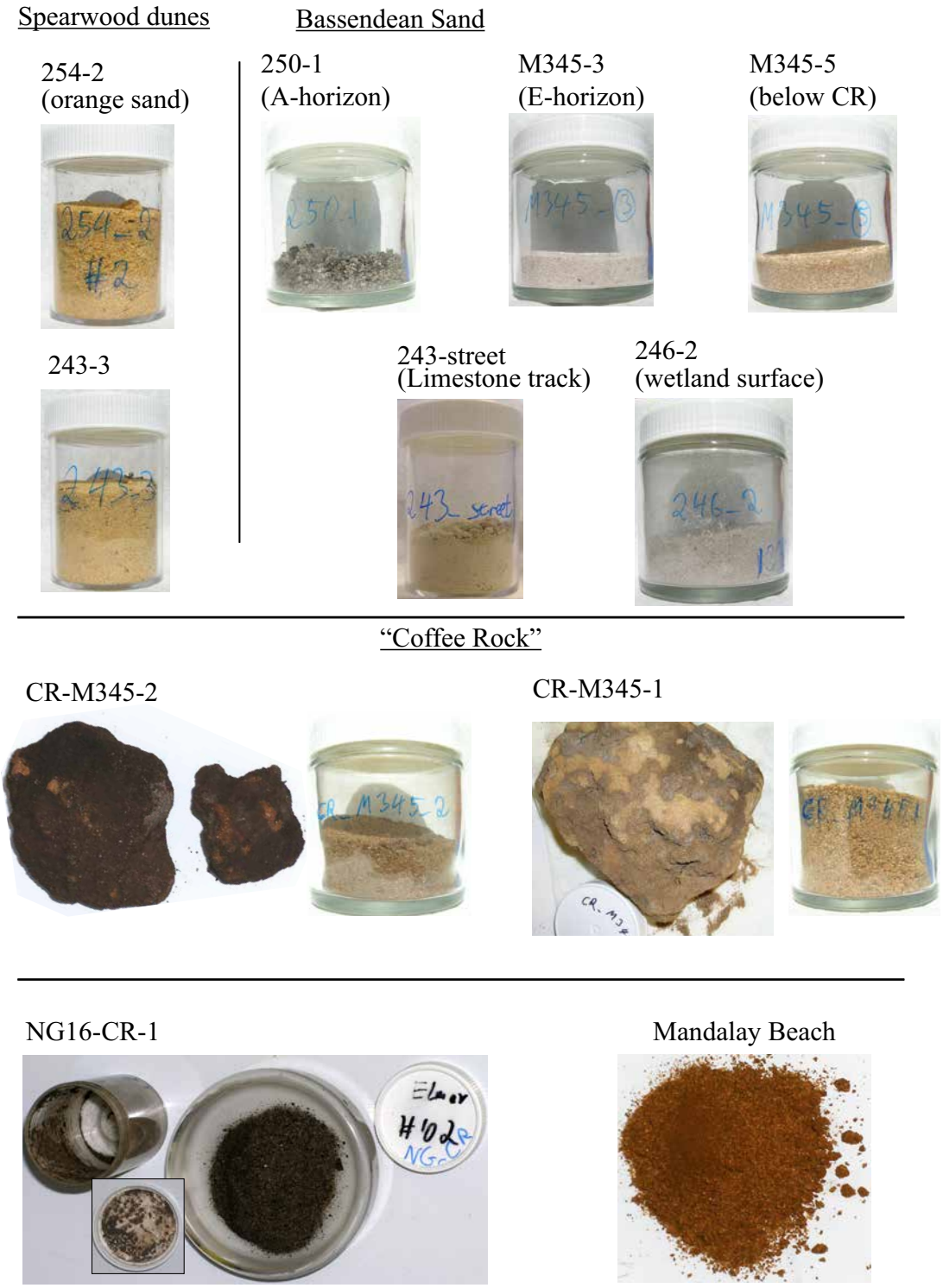

Figure 3.14: *Pictures of samples collected on the Gnangara Mound for dielectric lab measurements. Note that the cemented "coffee rock" material and Mandalay Beach ferricrete were broken up in order to fill the dielectric cell.*

3.2.3.1 Measurements In A Coaxial Transmission Line

Measurements were performed with a dielectric cell set up as a $50 - \Omega$ coaxial transmission line test jig (*Josh et al.*, 2009, 2011). The sample cell is a 40 mm long hollow

cylinder with outer and inner conductor diameters of 16 mm and 7 mm, respectively (Figure 3.15). The ends of the cell are connected to $50 - \Omega$ coaxial cables with a custom-made end-feed section. These coaxial cables are the connected to an Agilent E5070B network analyser, where the network analyser measures dielectric properties in the frequency range between 300 kHz and 3 GHz at discrete frequencies. The frequency steps were linearly distributed in the log-log space (e.g. $\mathrm{d}f_{0.3MHz} = 0.1$ MHz, $\mathrm{d}f_{30MHz} = 3.6$ MHz, etc.). Before soil samples were measured, the Agilent instrument was calibrated with a Teflon sample (a stable low loss sample) and no sample (air). Dielectric properties are inferred by the Agilent acquisition software, which automatically relates scattering (S-) parameters (reflection, i.e. S11, S22; and transmission, i.e. S12,S21) to dielectric properties (*Agilent*, 2012) using various approaches. The models used in this work are the fast transmission model ("model 3" in the Agilent software) for the real part of the dielectric permittivity, and a model described by *Baker-Jarvis et al.* (1990) for the imaginary part. The fast transmission model uses the transmission parameters S_{12} and S_{21} and iteratively estimates permittivity until the misfit between modelled and measured transmission parameters is minimised (*Agilent*, 2012). However, the imaginary part of the fast transmission model tends to show unexpected behaviour at frequencies starting from 200 - 300 MHz and up to 1 GHz (see Figures 3.16d, 3.18e (red box)). The values decrease with frequency in a way that that is unlikely. This behaviour is unphysical as the real and imaginary part should be coupled by the Kramers-Kronig relation (i.e. one is the derivative of the other). Hence I used "model 2" to obtain the imaginary part. This model uses reflection and transmission parameters S_{11}, S_{12}, S_{21} and S_{22} as described by *Baker-Jarvis et al.* (1990). Although the results for the imaginary part appear to be slightly improved using "model 2", the values at frequencies above some hundred MHz still show a similar behaviour to model 3. The staring point (in frequency) of the deviating behaviour correlates with the absolute values of the real dielectric permittivity. It appears that the lower $\epsilon'_{e,r}$, the lower the frequency at which $\epsilon''_{e,r}$ becomes unstable, which may indicate a lack of signal. Calibration and test measurements done on air, Teflon and Carbon Polymer samples displayed the same problem for measurement of higher frequency (more than several hundred MHz) imaginary dielectric permittivity (Figure 3.16). The relative dielectric permittivities of air and Teflon are given in the literature as 1 and 2.1,

respectively. Also, the test measurements do not appear to be valid at the low frequency end (i.e. below 1 MHz), but improves with increasing dielectric permittivity . Model 2 predicts a slightly different permittivity curve at the higher frequencies where the real values show a 'hump'. Note the same 'hump' for the field samples in Figure 3.18a. This irregular behaviour tends to be more profound in samples with high dielectric permittivity (i.e. Carbon Poly, samples with high water content). Model 3 on the other hand remains as a flat curve for the real dielectric permittivity (i.e. there is however a slight 'hump' evident in the Carbon Poly data) as would be expected for non-dispersive material. The very low loss characteristics of air, Teflon and dry sand results in very small values for the measured imaginary part, and these values are probably below the resolution limit of the measurement system. However, the test measurements appear to produce accurate calibrations and reliable results for measurements between 1 - 100 MHz where the Teflon results plots just slightly below the literature value.

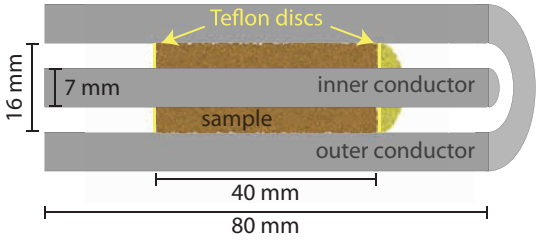

Figure 3.15: *Schematic of the coaxial cell used in the transmission-line dielectric experiment.*

In conclusion I could not find a definitive reason for the deviant system behaviour above approximately 200 MHz. For this reason, I typically used data at 100 MHz to compare real and imaginary dielectric permittivity at different water contents where the derived measurements for all samples showed reliable and consistent permittivity versus frequency curves. The real permittivity was extracted from "model 3" results, and the imaginary part from "model 2"' data as described above.

3.2.3.2 Sample Preparation And Characterisation

Homogenised samples were dried over night in a vacuum oven at 105°C . Loose material was then placed in sample containers, separately for each anticipated water content. The dry containers were weighed, and deionised water was trickled onto the sample and the weight was measured again to obtain a mass fraction of water. The samples were then homogenised once more to ensure even water distribution. The material was then placed into the dielectric cell between two Teflon discs. To

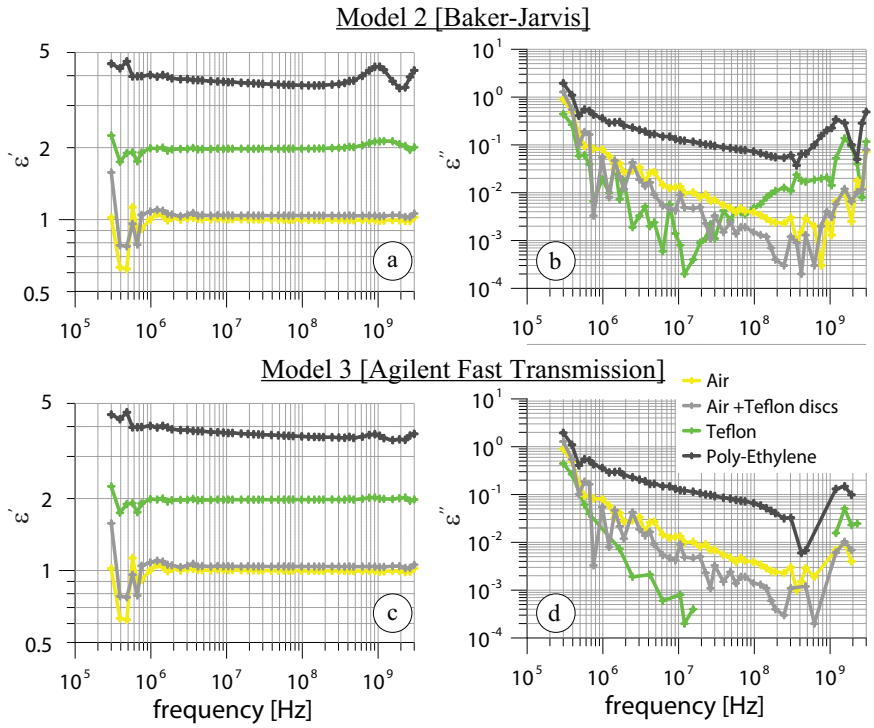

Figure 3.16: *Calibration results done on lossless empty coaxial cell (air) and Teflon filled cell, and lossy Poly-Ethylene. Permittivity values are derived by models 2 and 3 in the Agilent software. Model 2 shows a "hump" in real dielectric permittivity at around 1 GHz. Note the good agreement with Teflon literature value (approx. 2.1) and value in air of 1. The imaginary part is more problematic, due to very low loss and resultant low S/N.*

keep the loose material in place, I firstly compacted the sample with a steel rod. Five soil samples were tested at four to six different water contents ranging from entirely dry to almost saturated. Several more samples have been measured at smaller water contents below approximately 6 v%. Overall 38 sample and water content variations were measured for dielectric properties.

To obtain porosity, the bulk dry soil density measurements were done on 3 representative samples by weighing the dry samples in the coaxial cell and measuring sample volume (see Figure 3.17). From those densities, porosity ϕ was calculated using bulk soil density $\rho_{b,soil}$ and and grain density ρ_s of quartz (2.63 g/cm^3)

$$\phi = 1 - \frac{\rho_{b,soil}}{\rho_s} \quad . \tag{3.20}$$

The volumetric water content θ_v is calculated from measured gravimetric water content θ_m and porosity using

$$\theta_v = \theta_m \cdot \rho_s \cdot (1 - \phi) = \theta_m \cdot \rho_{b,soil} \quad . \tag{3.21}$$

Note that the uncertainty in estimating porosity is relatively large as it was not measured for every sample. If the error in soil density is 5%, this error will translates to an (approximate) $8 - 10\%$ error in porosity, and a 5% error in volumetric water content. Our density measurement for the different soils showed that the average soil density in the cell was 1.67 g/cm^3 with a standard deviation of 0.029 g/cm^3 ($< 2\ \%$) over three dry soils (i.e. samples 254-2, (orange sand), CR-M345-2 ("coffee rock") and M345-3 (leached sand), see Figure 3.17). In order to account for possible variation in porosity, the porosity was treated as an extra degree of freedom when fitting curves to the dielectric versus water content measurements (explained in further detail in section 3.2.4).

Note that in-situ density (i.e. field density) is probably less than the laboratory densities due to the compaction process that took place when preparing the dielectric cell. Some rough bulk density estimates were made with a simple measurement setup consisting of a hollow cylinder and a piston. Those measurements returned porosity values of around 0.4 (given grain density of 2.63 g/cm^3). But those measurements do not represent in-situ values because the loose dry sand was poured into the cylinder (i.e. less dense packing) and then slightly shaken and compacted with the piston. For materials with higher fractions of constituents other than quartz, a precise grain density analysis may become necessary. However, the materials of interest for this study consisted mainly of quartz.

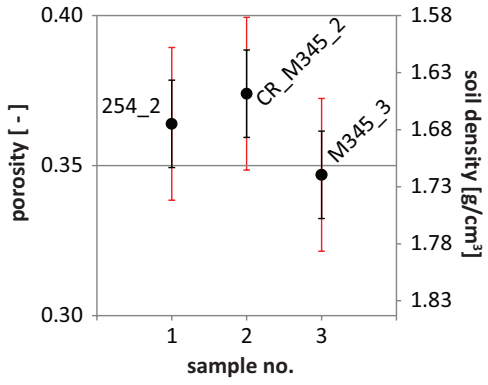

Figure 3.17: *Porosity measured for three dry and compacted samples in the coaxial transmission line. Porosity has been derived by assuming a grain density of 2.63 g/cm^3. Note that the "coffee rock" (CR-M345) and orange Spearwood dune sand (254-) samples show slightly increased porosity compared to the leached grey sand from M345.*

3.2.4 Data Interpretation

Real dielectric permittivity

The Lichtenecker-Rother (LR-) model and the HSA-model have both been implemented as functions into Matlab^{TM}. The measured data points were then fitted by a global grid search of minimum misfit between measured data and predicted data. I calculated the misfit using the root-mean-square error ($RMSE$) defined as

$$RMSE = \sqrt{\sum_i \left(\epsilon_{obs}(\theta_{v,i}) - \epsilon_p(\theta_{v,i})\right)^2} \tag{3.22}$$

with $\epsilon_{obs}(\theta_{v,i})$ the observed real effective dielectric permittivity (i.e. $\epsilon'_{e,r,obs}$) at volumetric water content $\theta_{v,i}$ and ϵ_p the predicted permittivity value. I called that misfit L2. For the LR model, I also tested a simple misfit defined as

$$L1 = \sum_i |\epsilon_{obs}(\theta_{v,i}) - \epsilon_p(\theta_{v,i})|. \tag{3.23}$$

The LR model has three degrees of freedom which are: the solid grain or matrix permittivity ϵ_s, porosity ϕ and fitting parameter α (see equation 3.13). For the three phase system, air and water relative dielectric permittivities were fixed at 1 and 80, respectively. Optimally, the porosity and grain permittivity are also known. Quartz grain dielectric permittivity has been measured and reported by various authors (note that mineral quartz is not fused quartz). Literature values range between 4.5 and 6.1 (e.g. *Stuart* (1955): 4.65 (1kHz), *Bottom* (1972): 4.5 - 4.6 (1kHz), *Knight* (1984); *Knight and Nur* (1987): (4.5-4.7), *Rzhevsky* (1971): 4.6 - 6.1)(cp. fused quartz 3.8). A realistic value for the sands studied is probably around 4.6 .

Other impurities such as clay minerals and iron hydroxides can introduce further complexity to the grain dielectric permittivity. Iron hydroxides, for example, have been demonstrated to contain additional water above 105°C due to their large surface area which influences the overall dielectric permittivity (*van Dam et al.*, 2002). Clay minerals such as Allophane are also potential carriers of additional bound water. As bound water that is only released above approx. 300°C remains a part of the material, the interpretation will ascribe it to matrix or grain dielectric permittivity. Hence, "coffee rock" as well as the stained orange sands, can be expected to contain some

of this additional water which is not accounted for in the volumetric water content term. Therefore, it is reasonable to keep the grain dielectric permittivity as a degree of freedom. In order to constrain the outcome I limited the possible range of grain permittivities between 2.4 and 8 for the LR data fitting (i.e. 2.4 representing organic material and 8 loamy sand with possible iron hydroxides). The porosity was limited to 32.5 $\%$ and 39.5 $\%$. The α - fitting parameter was allowed to take values between 0.35 and 0.65.

The HSA - model has four degrees of freedom: solid dielectric permittivity, porosity, cementation- (m) and saturation- (n) exponents. In order to further constrain the inversion, the ϵ_s of the LR model producing minimum misfit (i.e minimum RMSE, $\rightarrow \epsilon_{s,LR}$) was used as a basis for HSA grid search. A value of 1 was added and subtracted from $\epsilon_{s,LR}$ as a new search range for the solid dielectric permittivity. The porosity search range was kept identical to the porosity used in the LR fitting procedure, and m and n were limited to the intervals $[1.2, \quad 3]$ and $[1.2, \quad 4]$, respectively.

Attenuation

The attenuation factor predicts the damping that a wave experiences when propagating through a lossy material. Effective complex dielectric permittivity parameters (i.e. real and imaginary part) are used to calculate the attenuation factor according to equations 3.7 or 3.8.

To estimate losses associated with conduction phenomena, the low-frequency behaviour of the imaginary effective dielectric permittivity was investigated to verify the applicability of calculating resistivity using equation 3.9 (i.e. slope of $\epsilon''_{e,r}(f)$-curve -1).

3.2.5 Results And Discussion

3.2.5.1 Dielectric Measurements

The measurements of dielectric properties versus water content confirm that the dielectric permittivity increases with water content as shown in Figures 3.18, 3.21, 3.23 and 3.19. Both, the real and imaginary part are affected when pore water is introduced.

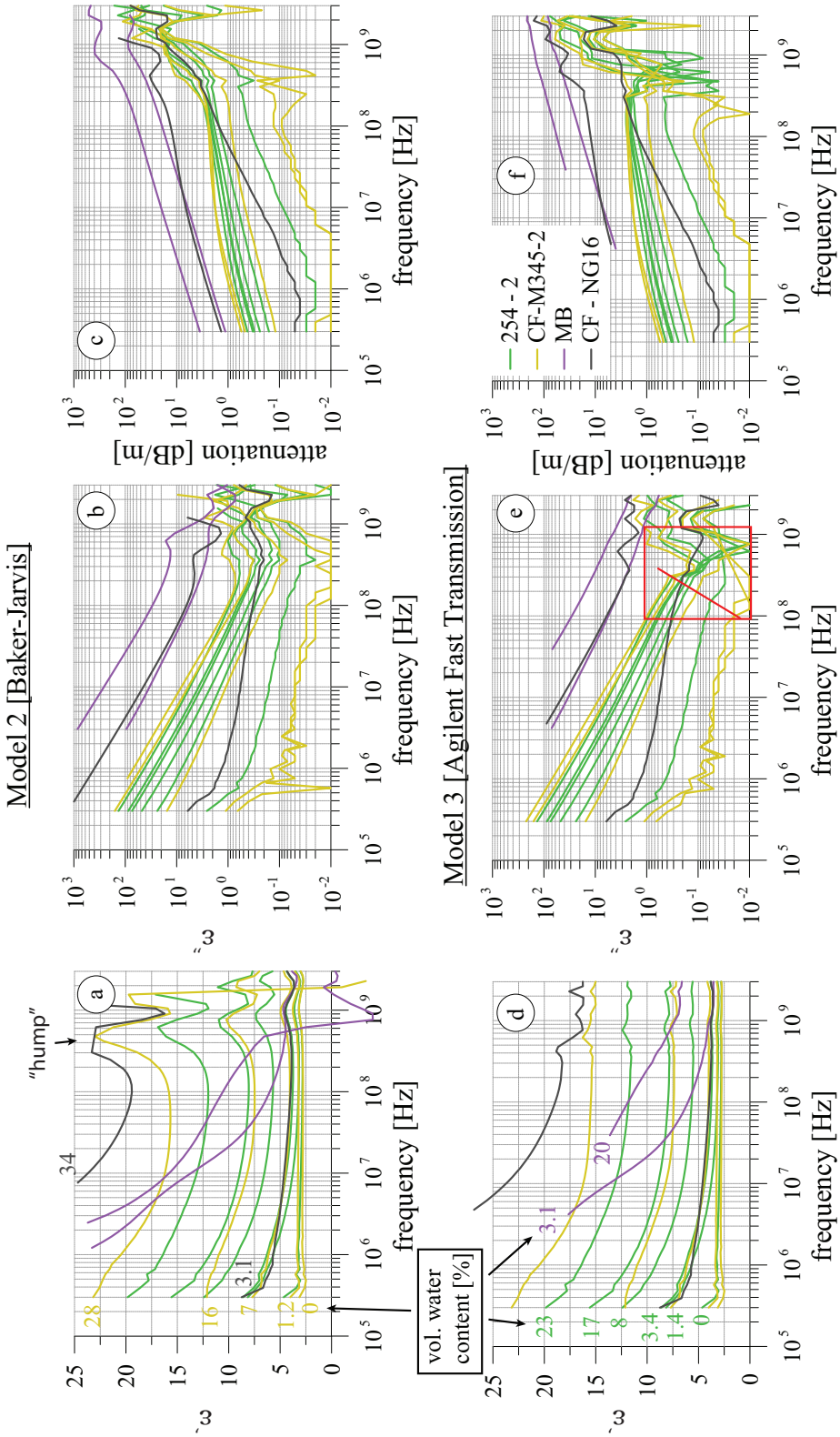

Figure 3.18: *Real (a ,d) and imaginary (b, e) dielectric permittivity and associated attenuation (c, f) versus frequency as obtained from Agilent Software's models 2 (upper) and 3 (lower) for four example soils at different water contents. Note the "hump" in (a) using model 2, which is greatly reduced using model 3 (d). Model 3 imaginary dielectric permittivity is unstable at frequencies above ≈ 100 MHz (red box in (e)). Irregular behaviour occurs at increased frequency with increasing dielectric permittivity (red line in (e)). Note the increase in both, real and imaginary dielectric permittivity with increasing water content, alongside increase in dispersivity.*

Real Dielectric Permittivity

Most materials tested show similar real relative apparent dielectric permittivity, as for example shown in Figure 3.19 (upper). For dry material, values are approximately 3 and increase to 15 - 18 for fully saturated samples. Two samples which show elevated values at given gravimetric water content are 243-street (limestone track material) and the MB (Mandalay Beach ferricrete). The limestone track material is of particular interest as it dominates large parts of the GPR 2D-lines described in the following chapter (i.e. section 4.2). A possible reason for increased dielectric permittivity could be calcite compounds which would be expected to increase soil density, which would increase vol. water content at any given grav. water content, but also result in increased matrix real dielectric permittivity (*Salat and Junge*, 2010).

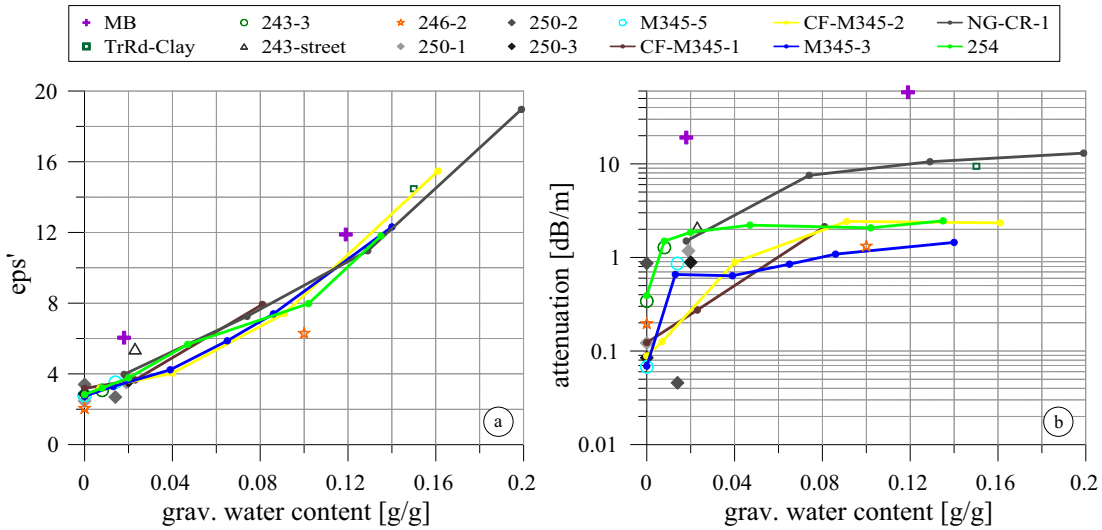

Figure 3.19: *Real dielectric permittivity (a) and attenuation (b) for all tested materials as a function of gravimetric water content. Values are extracted at 100 MHz.*

To retrieve fitting parameters for the LR- and HSA-models, I performed minimisation of L1 (LR only) and RMSE as described above in section 3.2.4 for individual soil samples (i.e. Figure 3.21), and for a collection of "coffee rock" (Figure 3.23, right) and sand samples 3.23, left). The resultant fitted parameters are listed in Table 3.1. In most instances, the HSA-model produced smaller RMS error which can be expected due to the extra degree of freedom introduced by a second exponent. The solid grain relative dielectric permittivities recovered by the LR-model are around 4 (i.e. 3.4 - 5.2 (L1) and 3.4 - 4.6 (L2)). The α-parameter ranges between 0.41 and 0.58. Note that a value of 0.5 is representative of the value used in the widely used CRIM-model. Most α-exponents were below 0.5 and only two "coffee rock" samples produced values above

0.5; thus, most samples are not particularly attenuative. The porosities associated with the best fits are all around 0.33, except for the NG16 clayey "coffee rock" which retrieved a value of 0.415. The explanation for such a high value is that the search range was modified for that sample towards higher porosities around 0.45 because of the high content of very fine material and the relative absence of sand particles. The accuracy of the chosen porosity constraint was not verified directly, but did not appear to be too abnormal and does not significantly alter any later interpretation. Nevertheless, this sample was included for the combined analysis of all "coffee rock" samples, and the porosity was constrained as for the sand samples, which might cause a higher misfit for the curve fitting (Figure 3.23, right).

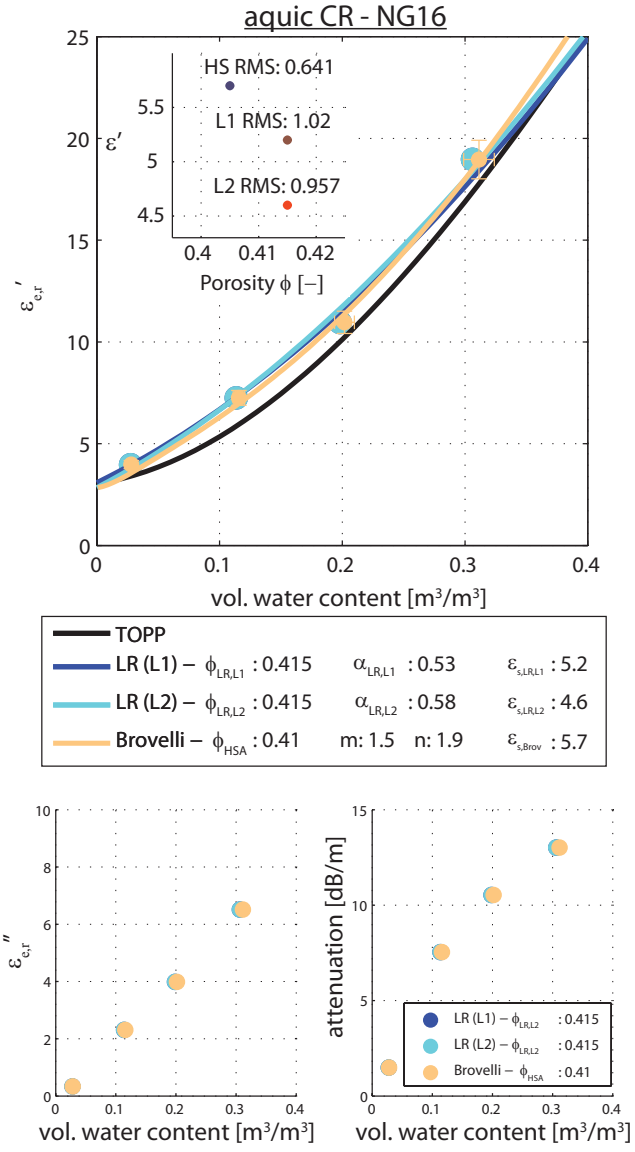

Figure 3.20: *Real (upper) and imaginary (lower left) dielectric permittivity, and associated attenuation (lower right) as a function of estimated volumetric water content for clayey sample NG16. Dielectric properties taken from the measurement at 100 MHz. Curves in upper graph represent the Topp-relationship (black), and different mixing models with parameters obtained by least-square inversion (see text). The small graph in upper plot shows the misfit associated with different ϵ' and porosity values for the different mixing laws. Note that for this sample, the porosity search range has been limited to values around 45% due to clay content and expected higher porosity.*

The HSA-model fitting results produced similar values to the LR-model. Results

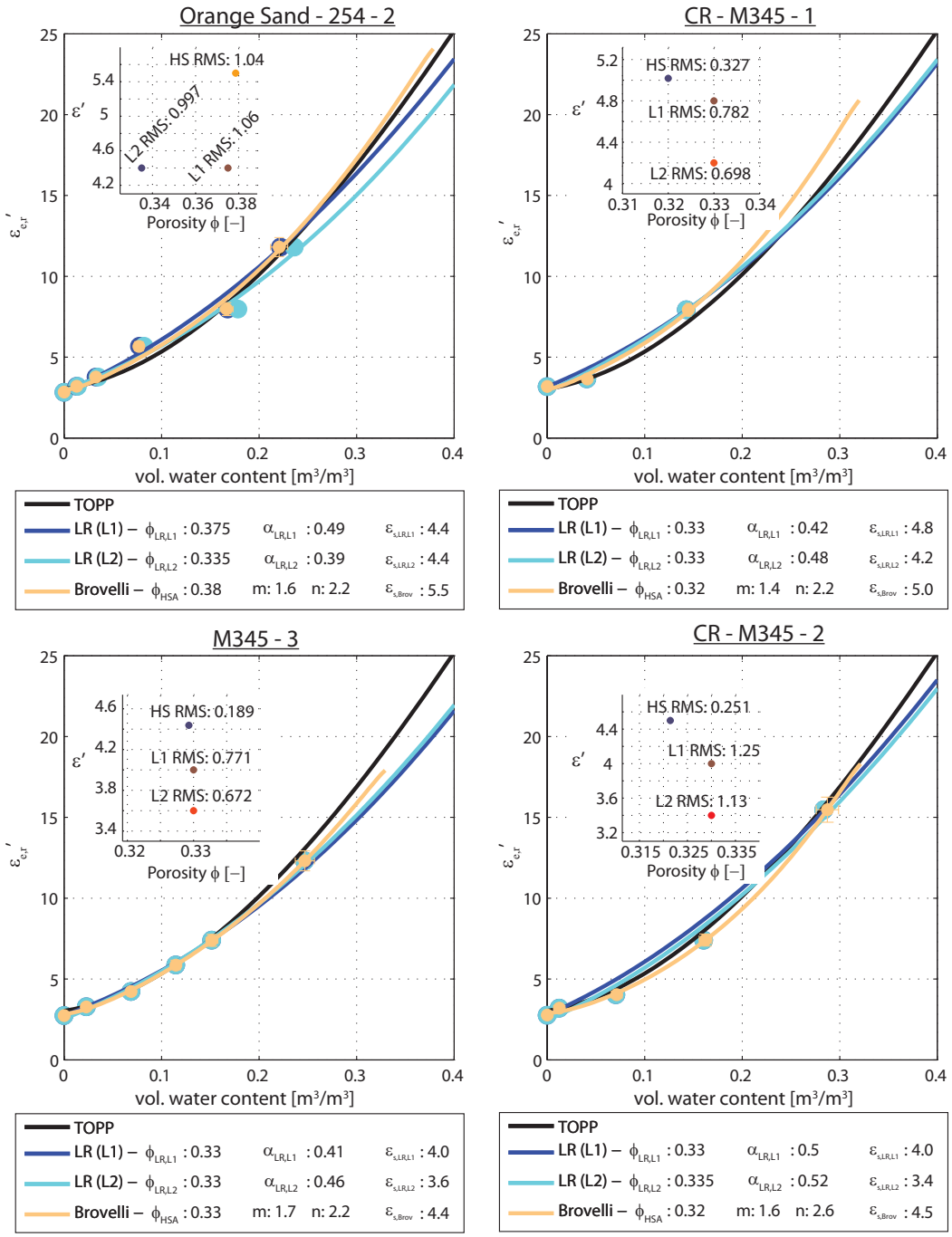

Figure 3.21: *Real dielectric permittivity as a function of estimated volumetric water content from measurement results at 100 MHz. Small graphs in upper left corners show the misfit associated with different ϵ' and porosity values for the different mixing laws. Fitting parameters include porosity and grain dielectric permittivity for both mixing models, and additionally α-exponent for the LR-model, and cementation and saturation exponents m and n, respectively, for the HSA-model by Brovelli and Cassiani (2010). Note the similar behaviour for sand samples (left) and "coffee rocks" (right). All soils plot around the Topp-curve in black (equation 3.10, Topp Eq. 6).*

for the solid grain permittivity are slightly higher between 4.4 and 5.5. Where the LR-model produced values around 4.4, the HSA-model showed values closer to 5. The petrophysical trends(that is where the models produced rather lower or higher val-

ues) are consistent in both models. The cementation exponent m ranged between 1.44 and 1.72 which compares well with values for example given in *Brovelli and Cassiani* (2010) (and references therein) for glass beads and sands. The fitting procedure produced saturation exponent n values between 1.89 and 2.55, with many values around 2.2. Also, these values appear to be reasonable when compared to n exponents recovered by *Brovelli and Cassiani* (2010). However, the porosities cited in *Brovelli and Cassiani* (2010) are higher than what was recovered in my case. This could be explained by reduced porosity due to cementation material, or decreased bulk soil density due to compaction during sample preparation. A 10 - 15 $\%$ difference in porosity between loose and densest packing is not unrealistic for sands (e.g. DIN 18126:1996-11, p.10). Another possible error associated with the porosity is the fact that soil packing can be influenced by water content (e.g. Proctor density, DIN18127:1997-11). The Proctor density is the highest dry density possible. Pore water plays an important role in the compaction process, and hence the Proctor density can only be reached if some water is present. This concept is used in civil engineering where compaction of building ground is optimised by adjusting water content of the soil that is to be compacted. Hence it is possible that the driest and wettest samples that were compacted in the coaxial cell were of a higher porosity compared to samples with intermediate water content, which are close to the Proctor density. For precise quantitative work it is better to measure the dry density for every experiment in order to fix the porosity (or saturation) in the interpretation phase. However,he objective of this study was to obtain a rough idea whether "coffee rock" and normal sands are very different in their dielectric properties as a function of water content. The results show that most samples, that is"coffee rock", clean sands and stained sands, share similar characteristics. Especially when compared to the Topp-relationship (i.e. equation 3.10, black curve in Figures 3.21 and 3.23), all of the investigated materials roughly follow the Topp-curve. Only few points deviate from the curve but without following any consistent trend. Given the possible errors associated with the dielectric measurements, vol. water content and the small amount of data points collected in the laboratory investigation, the Topp-relationship sufficiently represents the real dielectric permittivity versus volumetric water content relationship of the materials investigated for this study. The HSA-model which contains fitting parameters that carry physical meaning was able to produce model curves

that explain the data using physically reasonable parameters.

Imaginary Dielectric Permittivity

The effective imaginary relative dielectric permittivity as measured in the coaxial transmission line increases with water content as shown in Figures 3.18b, e, 3.22 and 3.23. Attenuation factors are plotted in Figure 3.19 (lower) for all samples, and the frequency dependency can be investigated for selected samples in Figure 3.18c and f. Note that the effective measured imaginary part is only an apparent measure of the imaginary dielectric permittivity as it includes the effects of (DC measurable) conductivity as described in equation 3.4 in section 3.2.1. However, it is an appropriate representation of all losses associated with an EM-wave propagating through the medium because the attenuation factor (equation 3.7) implicitly includes the conductivity term by using the effective (or apparent) imaginary dielectric permittivity.

The overall attenuation at the frequency range of interest for the GPR applications in this thesis (i.e. around 100 MHz), is low to very low for most of the materials tested. The sand samples show attenuation coefficients below 3 dB/m for all water contents. The dry samples have extremely low loss with attenuation values of less than 1 dB/m, which can be seen in the depths of investigation in actual GPR data over sand dunes. Attenuation of orange sand samples 254-2 increased with small amounts of introduced water and has attenuation values that are a factor of two higher compared to the other clean and stained sands tested. The limestone track material (labelled 243-street in Figure 3.19), shows attenuation similar to the yellow stained sand. The "coffee rock" samples CR-M345-1 and -2 are also relatively low loss, below 3 dB/m. The principal difference compared to the cleaner sands is the more gradual increase in attenuation with water content. While the sands show a sudden increase in attenuation from approximately 0.1 dB/m to 0.8 - 1.5 dB/m at very low water contents below 5 v%, the two "coffee rock" samples from M345 reach the same level at 8 - 10 v% water content. A possible explanation is that the first water is distributed on the large specific surface area created by the fine material, but is not yet interconnected and does not lead to a direct increase in conductivity. All the samples with low loss share the flattening of the attenuation curve with water content. It appears that the attenuation increases exponentially with small amounts of water in the pore space, and this increase then becomes more linear (e.g. Figure 3.19b). The samples that showed higher losses were

Table 3.1: *Results for curve fitting of LR- and HSA-models to water-content versus dielectric permittivity curves for different soil samples. Resistivities are estimated from low-frequency imaginary dielectric permittivity.*

	Lichtenecker - Rother Model								HSA - Model					vol. wat. /						
	L1				L2				L2						dry		medium		wet	
Sample	ϕ	ε_s	α	RMSE	ϕ	ε_s	α	RMSE	ϕ	ε_s	m	n	RMSE	resistivity						
M345-3 (E-horizon)	0.33	4	0.41	0.77	0.33	3.6	0.46	0.67	0.329	4.438	1.72	2.22	0.19	θ_v [-]	0	0.02	0.07	0.11	0.15	0.24
														ρ [Ωm]	19,470	2,670	1,956	1,153	728	384
254-2 (orange sand)	0.375	4.4	0.49	1.06	0.335	4.4	0.39	1.00	0.379	5.5	1.56	2.16	1.04	θ_v [-]	0	0.014	0.034	0.08	0.17	0.23
														ρ [Ωm]	23,240	2,517	1,259	811	686	442
CF-M345-1 (indurated)	0.33	4.8	0.42	0.78	0.33	4.2	0.48	0.70	0.32	5.018	1.44	2.21	0.33	θ_v [-]	0	0.04	-	-	0.14	-
														ρ [Ωm]	32,320	25,280	-	-	482	-
CF-M345-2 (indurated)	0.33	4	0.5	1.25	0.33	3.4	0.52	1.13	0.321	4.5	1.64	2.55	0.25	θ_v [-]	0	0.012	0.07	-	0.16	0.28
														ρ [Ωm]	91,800	53,800	3,880	-	375	270
NG16 (clayey CF)	0.415	5.2	0.53	1.02	0.415	4.6	0.58	0.96	0.405	5.7	1.49	1.89	0.64	θ_v [-]	-	0.031	-	0.13	0.22	0.34
														ρ [Ωm]	-	9,823	-	177	81	46
All CF	0.33	4.2	0.44	1.30	0.33	4	0.46	1.29	0.337	5.1	1.71	2.31	1.46							
All Sand	0.33	4	0.44	1.28	0.335	4	0.43	1.25	0.367	5.1	1.56	2.16	1.47							

the clayey "coffee rock" from NG16 and the ferric sample from Mandalay Beach. The clayey material collected at NG16 shows maximum attenuation values of 10 - 15 dB/m. The measured value at a water content of 3 v% reveals that the dry material has losses comparable to those of the sand sample. Losses then increase with water content and reach values that are one order of magnitude larger than those of the sand samples.

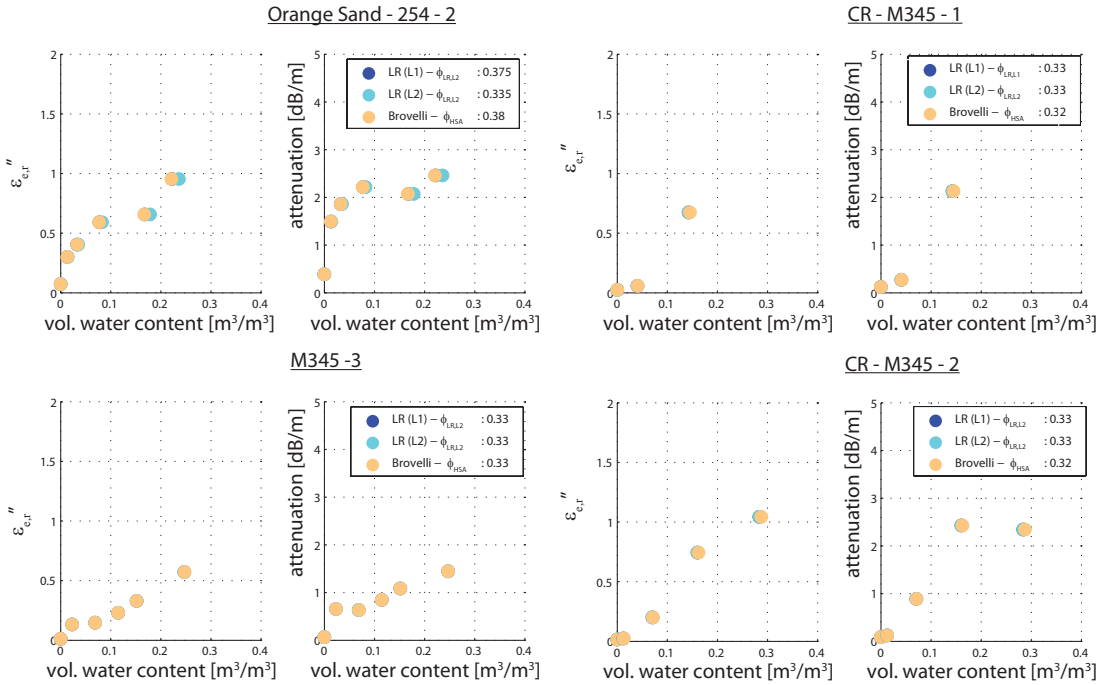

Figure 3.22: *Effective dielectric losses expressed by effective imaginary dielectric permittivity and associated attenuation as a function of water content for four soil samples at 100 MHz. Different colour symbols are plotted at volumetric water contents predicted by different mixing model porosities.*

The conductive part of the effective parameter measured is expected to increase with increasing water content along with the dielectric losses associated with a higher dielectric medium. Although the water used for wetting the samples was deionised and should be resistive, it can also start to bring ions back into solution that were precipitated on the grain surfaces during drying. Another effect that could be initiated by wetting is surface conductance. The deviation from the slope -1 in the log-log plot of imaginary part of permittivity versus frequency (e.g. deviation from dashed lines above approx. 1 MHz in Figure 3.24) constitutes the dielectric relaxation losses associated with water content at higher frequencies (i.e. not the effective, apparent measured losses, but the *real* contribution of the imaginary part of the dielectric permittivity). The dielectric loss component is rather small for all samples and losses can therefore be mainly attributed to conductivity.

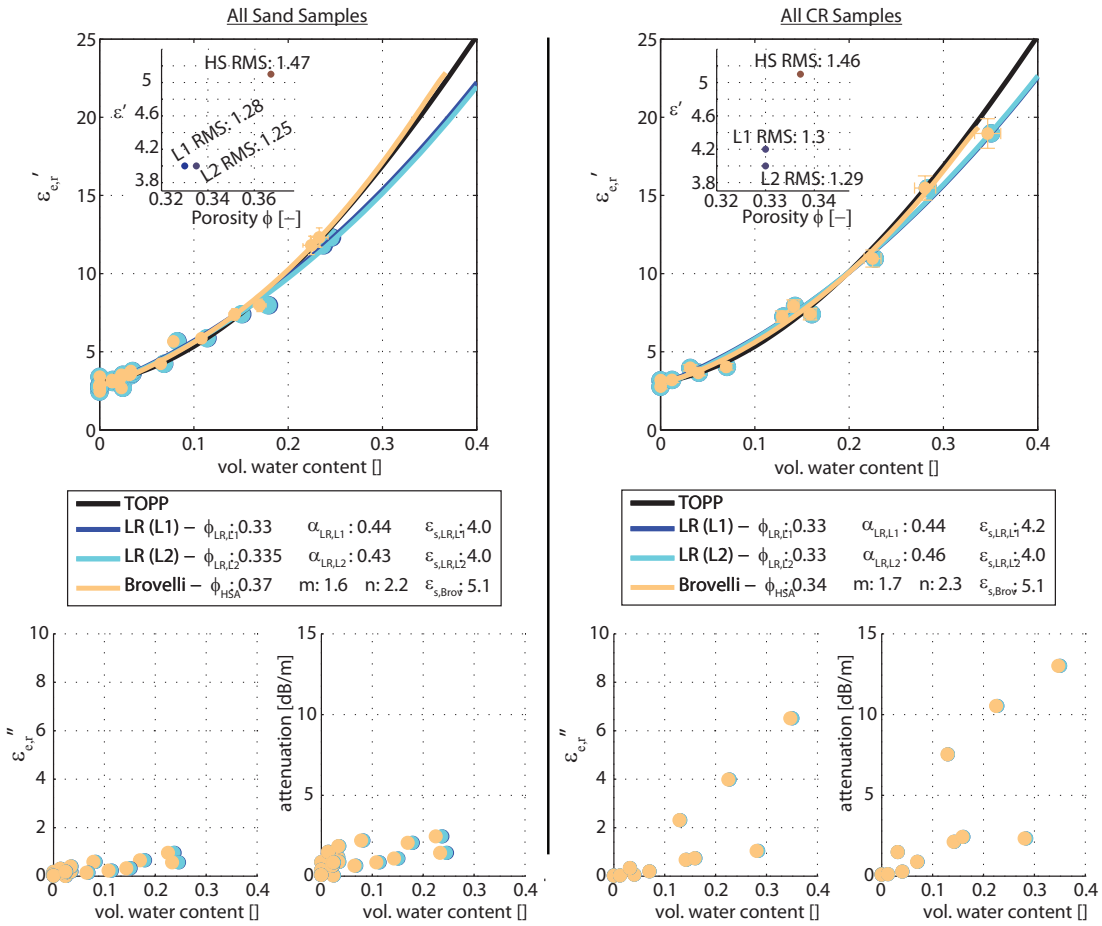

Figure 3.23: *Real dielectric permittivity as a function of water content for soil samples classified as sands (upper left) and "coffee rock" (upper right). Imaginary effective dielectric permittivity and attenuation are plotted below. Note the good correlation in fitting parameters between the different soils revealing great similarity between "coffee rock" and clean sands.*

3.2.5.2 DC Resistivity

A requirement for DC resistivity extraction from high-frequency AC measurements is that the log-log relationship between signal losses and frequency is linear and has a slope of -1 as described in the previous sections. The low-frequency end of the effective imaginary dielectric permittivity is plotted in Figure 3.24a, c, e, g, i, k. This plot demonstrates that the imaginary part follows a linear slope of -1 against frequency in the log-log space up to a frequency of approximately 500 kHz to 1 MHz for all samples that contain some water. Using equation 3.9 is therefore justified at low frequency. The DC resistivity calculated from the lowest frequency imaginary dielectric permittivity value at 300 kHz revealed values between 250 Ωm and almost 10^5 Ωm for highest and lowest water content, respectively. Only the conductive samples NG16 and MB showed lower resistivities between 46 - 177 Ωm and 7 - 67 Ωm at water contents

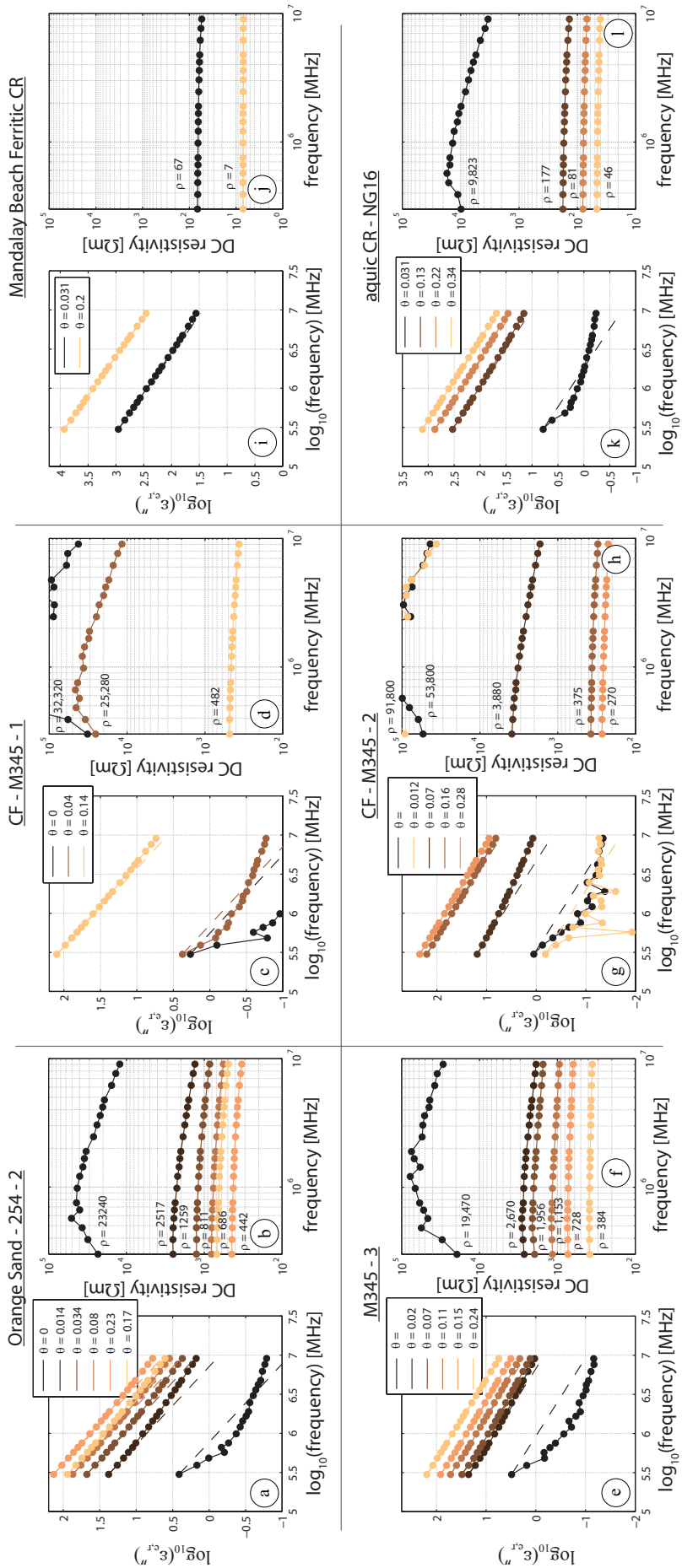

Figure 3.24: *Low-frequency portion of effective imaginary dielectric permittivity (a, c, e, g, i, k) and calculated DC resistivity using equation 3.9 for various water contents and soils. Note that a linear slope of -1 in the log-log space for imag. dielec. perm. leads to a constant DC-resistivity with frequencies, which is an indicator for low-frequency (DC) conductive losses dominate over dielectric relaxation losses.*

between 13 - 34 v% and 3 - 20 v%, respectively. Note that the frequency to which the linear slope of -1 persists is proportional to the electrical conductivity; that is the highly conductive samples show the slope of -1 up to 10 MHz, while the resistive drier samples only for the first measured frequencies (i.e. 300 - 500 kHz).

The very dry samples produce imaginary dielectric permittivity curves that are noisy and do not show any distinctive linear slope behaviour. Unlike the samples with some water content, the imaginary dielectric permittivity rapidly decreases with frequency for dry samples. It is unclear if the value at the lowest frequency represents the DC conductivity. As the measurement precision of the network analyser and the coaxial transmission line is not sufficient for such low loss samples there is not much use in using the imaginary data to calculate electrical conductivity. Problematic imaginary parts had already been observed for the air and Teflon samples shown in 3.16. According to Archie's second law, one would expect very high resistivities exceeding 10^6 Ωm for dry quartz sand. The only contribution to conductance is made by the grains, which are electrical insulators with extremely high resistivities.

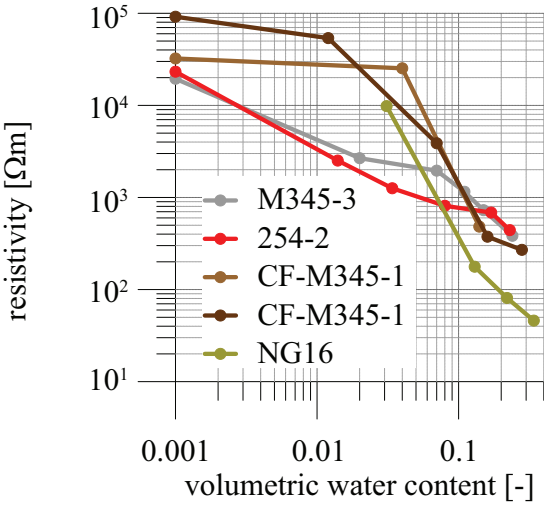

Figure 3.25: *DC-resistivity obtained from low-frequency portion of imaginary dielectric permittivity for different soil samples plotted against estimated volumetric water content.*

The resistivity versus water content curves presented in 3.25 show the somewhat delayed response of the "coffee rock" samples from M345 with increasing pore water, analog to what had been observed for the losses in the previous section. Dry resistivities of those samples appear to be higher compared to the sands. The clayey "coffee rock" from NG16 is more regular with a linear log-log relationship between resistivity and water content. Note that Archie's second law produces straight lines in this log-log representation where the cementation exponent m and the pore water electrical resis-

tivity shifts the curve up and down, and the saturation exponent n changes the slope of the curve. Thus, it is impossible to explain the measured curves for M345 "coffee rock" with Archie's law. A possible mechanism that could reproduce the observed curves is described in the previous section. The proposed process is that the first water that is introduced to the medium is distributed at the large specific surface area of the grain surfaces of fine material without being interconnected, which then suddenly changes when a secondary porosity starts to be filled with pore water. The underlying implication is that the losses observed at 100 MHz (described in previous section) are mainly associated with an electrical conduction mechanism and are not related to dielectric mechanisms.

3.3 Conclusions

Petrophysical characterisation of Materials from the Gnangara Mound study area included grain size distribution analysis, unsaturated and saturated hydraulic properties, and electric and dielectric properties. The main findings are that the indurated, cemented soil horizons in the aeric Podosol soil profile (i.e. the main focus of this study, in reference to samples CR-M345), have the following properties relative to the surrounding cleaner sands:

- Brown to black in colour due to iron mineral precipitates, Allophane clay minerals and humic components(vs. grey, white, cream leached quartz sand)
- Elevated content of fine grains in fine sand, silt and clay fraction (vs. well sorted medium sand)
- Higher soil water holding capacity at both, field capacity (≈15 - 25 v%) and wilting point (≈ 5 v%) (vs. $\approx 7 - 12$ v% and < 2 v% for clean sands)
- Reduced saturated hydraulic conductivity, but still around 10 m/d (vs. up to 150 m/d in other sands)
- Real dielectric permittivity behaviour with water content similar to both sets of materials, both follow Topp-relationship. Inversion using the Lichtenecker-Rother and a Hashin-Shtrikman average model based on Archie's law, provide

fitting parameters that are physically feasible and represent values typical for unconsolidated sand

- Imaginary effective dielectric permittivity (i.e. combined losses) is low for both materials and increases with water content, losses can be mainly attributed to electrical conductivity. The "coffee rock" has a slightly more gradual loss response to water content while the clean sands' losses increase immediately with small water content. Aeric "coffee rock" attenuation at field capacity is around 2 dB/m, while clean sands show values around 1 dB/m

- The DC-resistivity's are very high for clean and indurated dry sands. Water reduces the DC resistivity to a level of approx. 300 Ωm at saturation with deionised water. Unsaturated resistivities are several hundred to several thousand Ωm depending on water content. Peak values were considered unreliable due to noisy imaginary dielectric data

The clayey "coffee rock" sample taken from the saturated zone at NG16 showed higher electromagnetic losses at elevated water contents. Its conductivity is an order of magnitude higher than those of aeric "coffee rock" and clean sand samples at comparable water contents.

The losses observed in GPR field data associated with the orange sands from the Spearwood Dunes (i.e. sample 254-2) could be due to the slightly higher attenuation of 2 dB/m at intermediate water content compared to 1 dB/m for the grey leached sands of the Bassendean Dunes. However, these attenuation values are still relatively small and comparable to the aeric "coffee rock" from M345, which does not show considerable attenuation in the GPR field data (see following chapter).

Chapter 4

Spatial Characterisation Of Soil Horizons

To understand whether indurated sand layers can have a significant impact on infiltration characteristics on a hydrogeologic basin scale, it is necessary to understand the spatial extent and distribution of these soil horizons. Are these layers sufficiently extensive to be a barrier to vertical migration or a store of water during the dry season? Are the layers patchy and only locally significant? A geophysical, or non-invasive, approach was sought to answer this question due to the large area to be characterised (approximately 1000 sq km). Ground-penetrating Radar proved to be a powerful technique in the Gnangara Mound soil environment due to a combination of sensitivity to water content, high resolution and reasonable penetrating depth. Also, this geophysical method was relatively easy to deploy on the many dirt/sandy tracks off the main roads in the Gnangara area. Thus, GPR was chosen as the main investigative tool to map potential water retentive layers for the soil layer mapping project initiated by Water Corporation (with the Department of Exploration Geophysics, Curtin University). The GPR surveys were acquired at various spatial scales to map and sample the near-surface geological environment. Small-scale 3D surveys were performed in order to better understand the response of ”coffee rock” (a suspected water retentive layer) to surface common offset GPR. From those lessons, I derive a relatively simple workflow in order to analyse large-scale 2D GPR transects.

4.1 Interpretation Of Surface GPR Data

Theoretical background of the GPR methodology is provided in appendix A. I would like to refer the reader who is not familiar with the GPR technique to that part of the thesis before continuing with this chapter. In appendix A, I explain the basics of GPR: GPR system design, data acquisition, data processing and EM wave interaction with the earth.

In this section, I present a selection of interpretation techniques that can specifically be applied to common offset GPR reflection data, the type of data analysed in this chapter. The most obvious interpretation method (as used by most practitioners of GPR) is to investigate structures formed by reflections and/or diffractions and relate these to distinct depositional environments. *Neal* (2004) reviews the concept of adapting seismic stratigraphy analysis approach directly to GPR. In this methodology, a stratigraphy is build up based on radar surfaces, radar packages and radar facies. These radar elements are characterised based upon their appearance or spatial characteristics. For my thesis studies this type of analysis is only partially useful. Reflections and diffractions seen in GPR are often dominated by soil forming processes which are only partially dependent on the sedimentologic history of the background material. In the case of podosols, for example, most strong reflections originate from accumulation soil layers that have formed largely independent of depositional environment. Cemented sediments such as sandstones can produce reflections that are due to fractures or other non-stratigraphic structural features, which are also not related to the sedimentologic history of the rock. However, in other environments, where lithification preserved or even enhanced sedimentologic structure, or where sediments are not overprinted by major soil forming or deformation processes, the GPR stratigraphy interpretation is a valid method to understand the processes of deposition.

Within this context, it is interesting to note that *Neal* (2004) lists AGC-gain as a standard processing step. During my work with GPR data I omitted this processing step as it makes mis-interpretation more likely; for example due to over-exaggeration of migration artefacts. At times AGC is needed to enhance small amplitude reflections, which are typical for depositional features such as slight variations in porosity or grain orientation due to bedding. AGC gain further corrects for amplitude variations that are a result of changing ground coupling conditions due to, for example, undulating small-

scale topography or acquisition over low scrub. Reflectors that are expected to have a similar reflectivity appear with equivalent amplitude after AGC. However, the big disadvantage of using AGC is that variations in reflection strength and relative amplitudes are removed; thus, important attributes of the data that are useful for interpretation are lost. Examples of information loss are variations in attenuation above the reflector (i.e. as an indicator for conductivity) and for a series of reflectors their relative amplitude (e.g. a weak over a significant reflector appears just as strong overemphasising its importance). To have the best of both methodologies I only used AGC "on-the-fly", so it is not part of the processing steps, but is instead applied as a display option that can interactively be turned on and off to assist viewing.

Another feature that can relate to significant structure are diffractions occurring from rough surface reflections. An example is uneven erosion of "coffee rock" layers or buried pipes and conduit structures in civil engineering applications. In contrast to a rough interface, very continuous and "clean" reflections indicate a smooth surface and a clear interface as is often the case for a water table in coarse grained sediments (gravel). Note, however, that this is a frequency dependent phenomenon, that is the diffractors which indicate surface roughness may disappear at low frequencies.

An interesting study in relation to identifying structural elements has been presented by *Moysey et al.* (2006) who present a semi-automated classification scheme for radar facies identification based on neural networking and image attributes such as texture.

The hydrogeologically most relevant features in common offset (CO) GPR data should be characterised by relatively strong reflection strength. Strong reflections are produced by high impedance contrasts. For the sandy near-surface environment of the Gnangara Mound, high contrasts in dielectric impedance will be produced by interfaces that have a high contrast in water content (i.e. dry vs. wet). A strong impedance contrast also results in a strong contrast in velocity. Amplitude and velocity analysis are therefore potentially the most powerful tools for identifying critical layers and may be used to quantify their hydrogeologic significance.

4.1.1 Amplitude Analysis

The characteristics of the reflected energy from a layer measured on the surface is controlled by i) the impedance contrast between the layer and its surroundings, ii) the thickness of the layer relative to the wavelengths, iii) the interface characteristics and iv) the electromagnetic properties of the stratigraphy above the interface of interest. The definition of a single confined layer effectively results in a three layer case to be modelled because a layer has to be bound by an upper and lower interface. When the EM (radar) wave hits the upper interface, some energy is reflected and some transmitted, based on the impedance contrast between layer 1 and layer 2. That transmitted energy then hits the second interface, and again some is reflected and some transmitted. The overall energy radiated back upwards to the receiver can therefore be calculated based on impedance contrasts. Snell's law or Fresnel's equation describe reflectivity which becomes for the transverse electric field component and for normal incidence on a simple interface (i.e. wavefront parallel or ray direction orthogonal to reflector):

$$R_{TE} = \frac{\sqrt{\epsilon_{r,1}} - \sqrt{\epsilon_{r,2}}}{\sqrt{\epsilon_{r,1}} + \sqrt{\epsilon_{r,2}}} = \frac{v_2 - v_1}{v_2 + v_1} \tag{4.1}$$

$\epsilon_{r,1}$ and $\epsilon_{r,2}$ are the relative dielectric permittivities of upper and lower layer, respectively, and ν the layer velocities. $\sqrt{\epsilon_r}$ is admittance (i.e. 1/impedance). For a thin bed, where layer thickness is much smaller than wavelength, upper and lower boundary are not evident anymore and the reflected wavelet appears to originate only from one interface.

As the layer thickness increases, reflections from interface 1 and 2 interfere with each other. The overall reflected signal of a thin layer is therefore wavelength dependent, or frequency dependent. The amplitude versus angle (AVA) equation for a three-layer case can be found in *Bradford and Deeds* (2006) and shows that the reflectivity is also dependent on the angle of incidence of the impinging wavefront (cp. Snell's law). This has to be taken into consideration when multi-offset amplitudes are investigated. For this study, the characteristics of a thin-bed reflection can be an important consideration as the layers under investigations are thin relative to the wavelength of a 250 MHz antenna in dry material.

The biggest challenge in amplitude analysis is the fact that in order to calculate

the impedance of one deep layer, the impedances and attenuation characteristics of the materials above that layer interface need to be known as well. A reflectivity sequence can only be built up if the attenuation of layers above is correctly assumed or known. This ambiguity is a barrier to the practical application of impedance inversion to large scale datasets.

Lastly, a very recent publication by *Schmelzbach et al.* (2012) noteworthy, as the authors are the first to attempt impedance inversion of surface CO GPR reflection data. They have developed a workflow analogous to seismic impedance inversion (a standard procedure performed upon seismic reflection data) to obtain GPR impedance cross-sections. At the beginning of this project we had a similar idea, but found that the input parameters necessary (i.e. high resolution dielectric well logs) were not available on the relevant scale. *Schmelzbach et al.* (2012) reiterate this concern and further point out that low-frequency reflection information is necessary to successfully apply their workflow. They estimate that their approach of impedance inversion, despite having supplementary data such as dielectric permittivity logs, is limited to GPR with nominal frequencies less than or equal to (approximately) 100 MHz. Because GPR antennas are typically narrow band, this also limits the resolution (approx. $\lambda/4$). For high-velocity areas and thin layers, such as the unsaturated sands of the Podosol soil on the Gnangara Mound, impedance inversion would be challenging (at best) and likely would not provide the necessary resolution.

4.1.2 Velocity Estimation

Radar wave velocity estimation is usually based on travel-time analysis of some type. For CO data, one can derive the velocity from i) the moveout of diffraction hyperbolae, ii) from the travel-time of a reflection originating from a known depth, or iii) direct ground-wave analysis (if Tx-Rx separation large enough).

In i), two ways of deriving velocity are possible. The first involves matching a theoretical hyperbola to observed hyperbola. GPR software packages typically include a facility to interactively plot and adjust a theoretical curve. The problem with that approach is non-uniqueness due to different sizes of the diffracting object. A large cylindrical diffractor (e.g. large pipe) in high-velocity medium can produce similar diffraction hyperbola as a smaller pipe in lower velocity medium. Furthermore, the

angle between survey line and the strike of the pipe widens the apex of the hyperbola for acute angles, while the apex width is minimal for a mostly orthogonal or 90 degree angle. The second option of velocity determination from diffraction hyperbola is data migration. For this, migration velocities are adjusted until hyperbolae are migrated to a point.

Analysis based on ii) (travel time to a reflector) can be applied in small scale surveys where the depth to a reflector is known. From the two-way travel t_r of the reflection in the radargram, and the depth z_r to the reflector, the average interval velocity to the reflector is $v_{int} = 2z_r/t_r$. Interval velocity of the unsaturated zone can then be used as an indicator for soil water retention properties. This type of analysis requires strict assumptions and is difficult to apply on large-scale data in natural environments due to sparse borehole or other data. One key parameter needed for this type of analysis is depth to reflector, which can be determined by drilling, or for large scale by geospatial information such as layer (i.e. reflector) elevation level and the topography. In the case of distinct reflectors, the point of reflection will be well defined. For diffuse interfaces such as a water table this point will vary depending on the height of the capillary fringe and transition zone. To obtain the depth of reflection from direct field evidence can also be challenging because the water table measured in a borehole with a dipper represents the gravimetric water table, that is the pressure level where the soil cannot hold water against gravitational forces, which is not necessarily the point of radar reflection. Above the gravimetric water table is the capillary fringe which contains water that is sucked up by the matrix potential of the soil and this is where radar reflections typically occur (*Gloaguen et al.*, 2001). Above the capillary fringe is a transition zone. The height of capillary fringe and transition zone depends on the soil matrix potential. As this can and will change laterally, the point of reflection changes as well.

If we assume that the point of reflection is known with decimetre accuracy and further that the level of the reflector does not change laterally, the depth to that reflector is then only determined by surface topography. As the depth to reflectors is typically not great in GPR applications (i.e. 1 - 20 m), precise knowledge of elevation is crucial for accurate velocity determination from known reflector depths. While very high-precision (i.e. centimetre accurate) elevation information can be obtained on a test-site scale, large-scale data acquisition that is practical and cost-effective will probably only

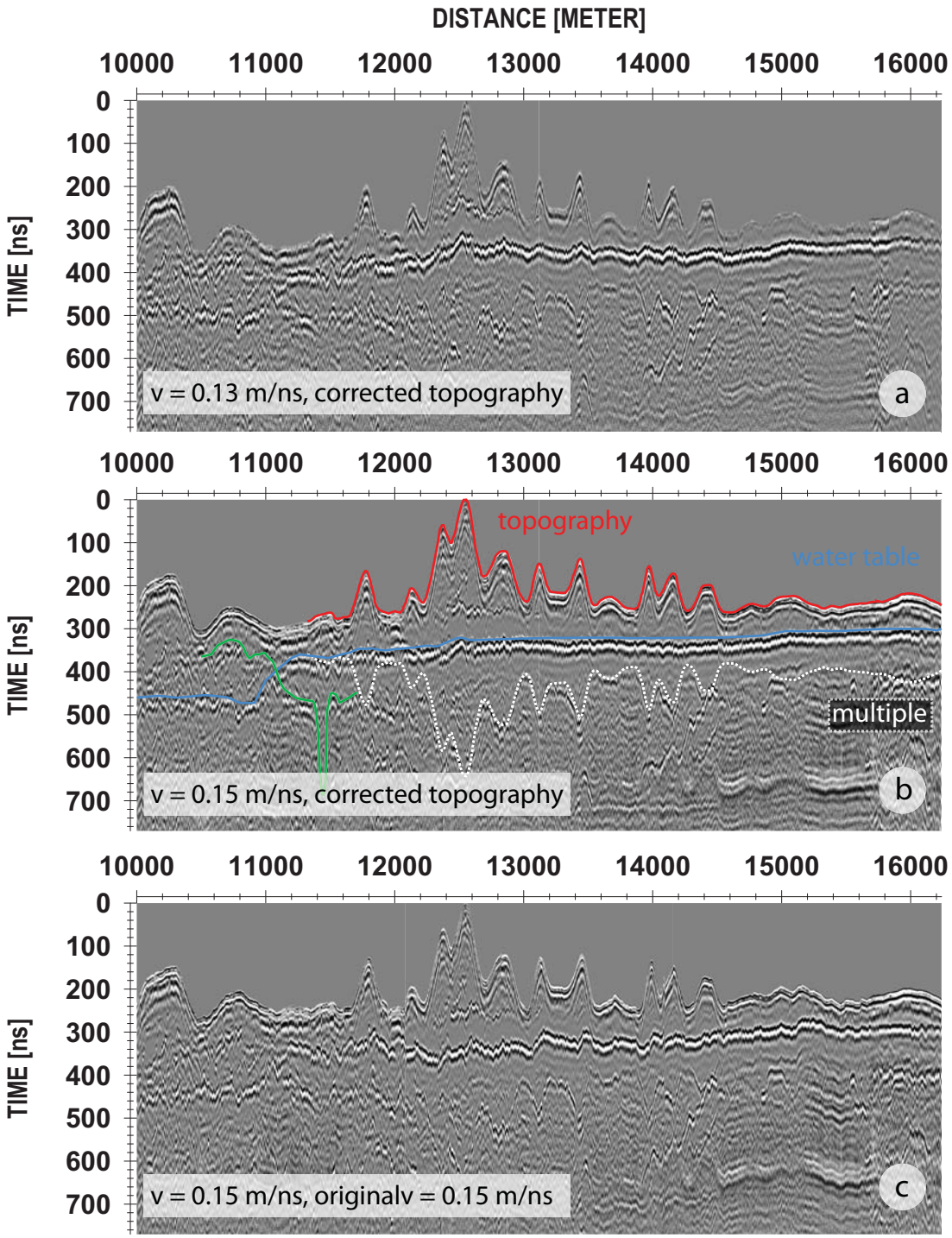

Figure 4.1: *Tuart Rd GPR transect with (a) correct topography but incorrect velocity, (b) correct velocity and topography and (c) incorrect topography and correct velocity. A strong water table reflection (blue line) and its multiple reflected at the surface (dashed white line) are shown in (b). The water table multiple appears as a "mirror-image" of the topography after topography correction, identical to what has been proposed for a water-table multiple by Botha et al. (2003) in a dune environment, and predicted for the case of a water table by Nobes et al. (2005) who observe "mirror-image" multiples of a brine layer functioning as "mirror" and multiples of layers within the ice above the brine layer. The green solid line is an unidentified, undulating reflector. It is hypothesised that this layer might cause the large hydraulic gradient interpreted between 10.8 and 11.2 km.*

provide decimetre to meter accurate topographic information. This tends to result in large uncertainties in velocity estimates.

Both of these uncertainties, variation of the point of reflection, position of reflector and inaccurate topography result in errors that may exceed the expected lateral interval velocity variations.

One approach to derive approximate large-scale velocity estimates with topography errors of less than one meter is to adjust the ground velocity until a reflector that is believed to be flat on the relevant scale, flattens out. Figure 4.1 shows a 50 MHz example from Tuart Road (northern Gnangara Mound) where the water table reflection flattens with realistic velocity of 0.15 m/ns (Figure 4.1b). It also shows that correct topography is crucial. The topography which was supplied by the contractor (differential GPS) did not match the topography needed to produce a flat water table reflection when a static shift is applied with a reasonable velocity. Better topography correction was extracted from a LiDAR dataset and used regionally to flatten the water table reflection. Note, however, that while the water table appears flat on a hundred meter to kilometre scale, it is quite variable on a one to ten meter scale. In conclusion, it is questionable whether any velocity estimation based on depth to a known reflector is an appropriate technique to calculate lateral changes in water content on a large scale (certainly in my study area), which is the final objective when soil water retention is studied.

The third method iii) to quantify ground velocity is based on identifying direct ground wave first arrival time t_g, and calculating velocity with $\nu = \Delta x_{\text{Tx-Rx}}/t_g$. This method works for Tx-Rx antenna separation on the order of the wavelength of the transmitted wave and above. To identify the correct arrival, a short multi-offset (e.g. common shot point) gather should be acquired and the direct ground wave arrival identified from the radargram (i.e. linear moveout in CSP-gather as indicated in Figure 4.14). Antenna separation can be tuned based on the CSP result to obtain a separation where the air wave and ground wave are well separated, and interference with deeper reflections does not occur. This method has been applied successfully by many researchers and on large scales (*Hubbard et al.*, 2002; *Grote et al.*, 2010a; *Steelman et al.*, 2010; *Steelman and Endres*, 2011). The only downside is that the effective sampling depth, that is the volume of earth that the measurement is representative of, is difficult to

predict (*Galagedara et al.*, 2003; *Grote et al.*, 2010b). Depth of penetration is also limited and deeper strata cannot be characterised well, if at all. The sampled depth depends on the frequency, antenna separation and the velocity structure. Waveguide phenomena and refracted energy can further complicate matters in regards of sampled depth. Uncertainty exists also in absolute velocity determination due to inaccuracies in travel-time picking; similar to issues found in my time-lapse studies 6.

The following sections provide case studies that demonstrate the application of some of the aforementioned approaches to analyse 2D and 3D GPR surveys. After some initial characterisation of GPR reflections based on direct geologic evidence and qualitative analysis, basin scale 2D datasets provide an example of large-scale spatial variability of the GPR ground response. Geological and hydrogeological interpretation of the data is provided. Different analysis schemes were tested on a small-scale 3D survey at Whiteman Park prior to being used on larger 2D datasets.

4.2 Case Studies From The Gnangara Mound

As part of this chapter I will show some exemplary GPR 2D sections and several 3D examples which provide a basis for large scale interpretation. The first example is from Rocla mine site (see chapter 2, Figure 2.12) followed by two large-scale 2D transects Tuart and Clover Roads which span the entire Gnangara Mound. This section is finalised with a 3D GPR cube acquired at Whiteman Park which provides the basis for large scale amplitude analysis.

4.2.1 "Coffee Rock" Imaging At Rocla Mine Site

The Rocla mine site provides direct geological evidence for the existence and spatial characteristics of accumulation horizons in the Bassendean Sand formation. In order to better understand the GPR response of those layers, a 2D 250 MHz GPR transect was measured over the cleared area behind the mining face as shown in Figure 4.2 (upper right). The GPR profile shows that the clean sand interval above the first accumulation horizon does not produce significant GPR reflections. The first GPR reflections are from a depth where the "coffee rock" would be expected based on the mine face observation. In general, the "coffee rock" reflections are characterised by a multitude of diffractions, which correlates well with the rough interface seen at the mine face (i.e. erosional surface, pipe structures). Below the interface, the radargram is also characterised by diffractions and clutter, creating a noisy appearance.

However, reflected signal strength varies throughout the profile. At a horizontal position of around 200 m (along survey line) a clear reflection is absent. The geologic transect shows that at this approximate position, a clear cemented "coffee rock" layer is absent while the sands show a slight change in colour from greyish white to a cream colour. Where the profile direction changes from a northern direction to an eastern acquisition direction at a position of 650 m (along survey line), the radargram shows a stronger ground response. The reflections appear to originate from internal bedding that was not clearly visible at the north-south part of the profile (interpreted bedding reflections are indicated in Figure 4.2, lower). It is possible that the polarization of the antenna and the direction of acquisition cause the different structural appearance of the GPR images. The north-south section could strike parallel to the bedding, while

the east-west acquisition runs perpendicular to the strike of the bedding plane which increases reflectivity at the given polarization and emphasises structural characteristics. This is consistent with the internal bedding of aeolian sand dunes under the current (and presumably past) predominant westerly wind direction.

Another transect was acquired at a revegetation site where an excavator dug a trench over the GPR profile (Figure 4.3). The data shown in Figure 4.3 (middle and lower) is acquired with the Mala 500 MHz shielded antenna. Note that the 250 MHz antenna produces a similar result but lacked resolution in the very near-surface due to direct wave interference. The comparison between the sediments and the GPR response shows that only a minor change in lithology at approximately 1.5 m depth produces a strong GPR reflection. The sediments looked very similar in the field, with only minor colour variations (i.e. cream above and light brown to slightly orange below). Water content measurements showed that on average, the water content increases with depth. Volumetric water contents within the first half meter are below 3 v% and then increase to values between 4.5 - 5 v% below. The changes in reflectivity of that horizon cannot be directly related to the structures seen in the sediment. Overall, the colour changes within the soil profile are probably due to slight iron mineral precipitation, and/or humic material deposition (e.g. fine brown line at horizontal position between 3 - 4 m and 1.7 m depth).

The geological and direct petrophysical measurement evidence from the Rocla mine site supports two major findings:

- "Coffee rock" accumulation horizons are a major source of GPR reflections in the Bassendean Sand soil. The reflection of eroding horizons is characterised by a multitude of GPR diffractions at the layer top, and diffractions /clutter within soil below the upper interface.

- an ambiguity exists between strong GPR ground response and potential hydraulic significance of layers because minor precipitation bands can create large reflection amplitudes. Whereas, the reflection strength of "coffee rock" layers varies laterally and can be weak. Shallow ground conditions and a possible dependency on acquisition direction create further uncertainty in reflection strength interpretation.

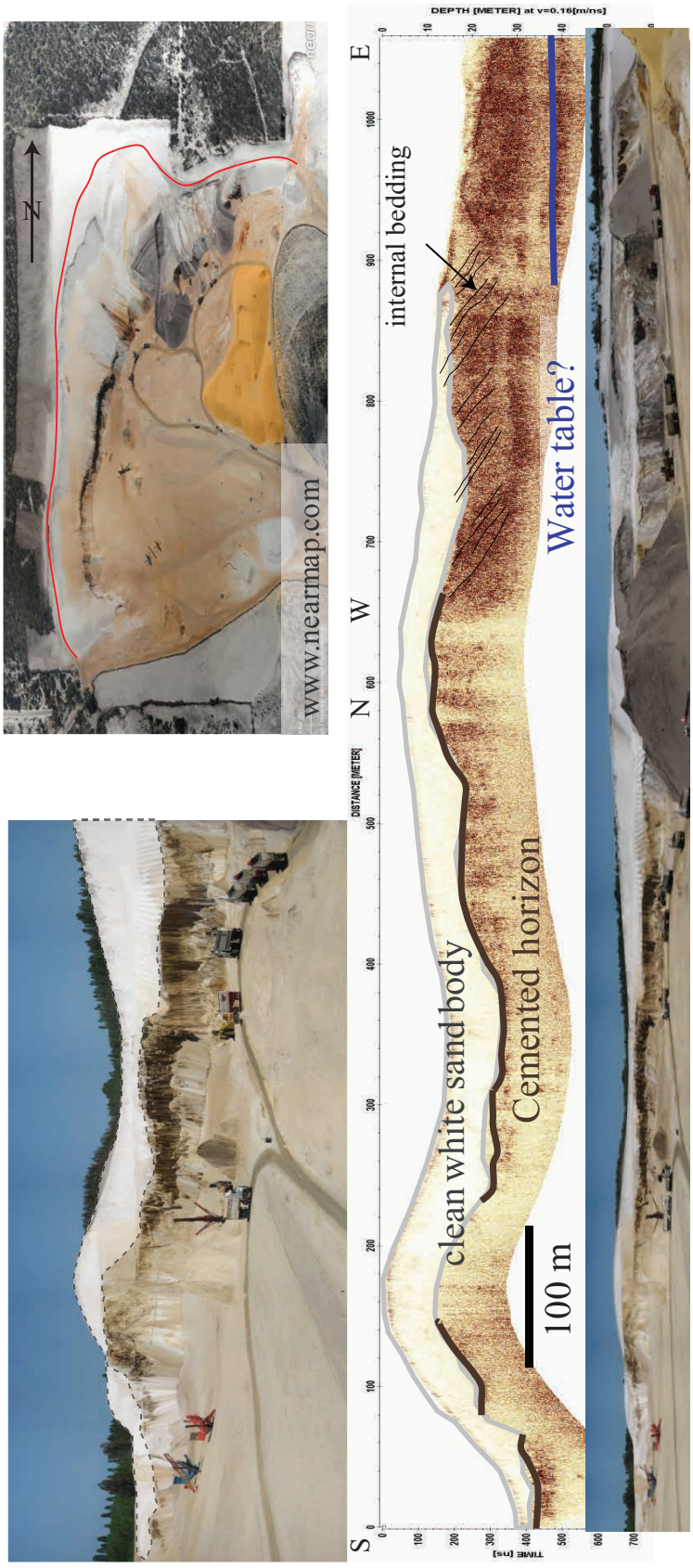

Figure 4.2: *The Rocla mine site north of Whiteman Park provides direct evidence of "coffee rock" characteristics and imaging potential of GPR.*

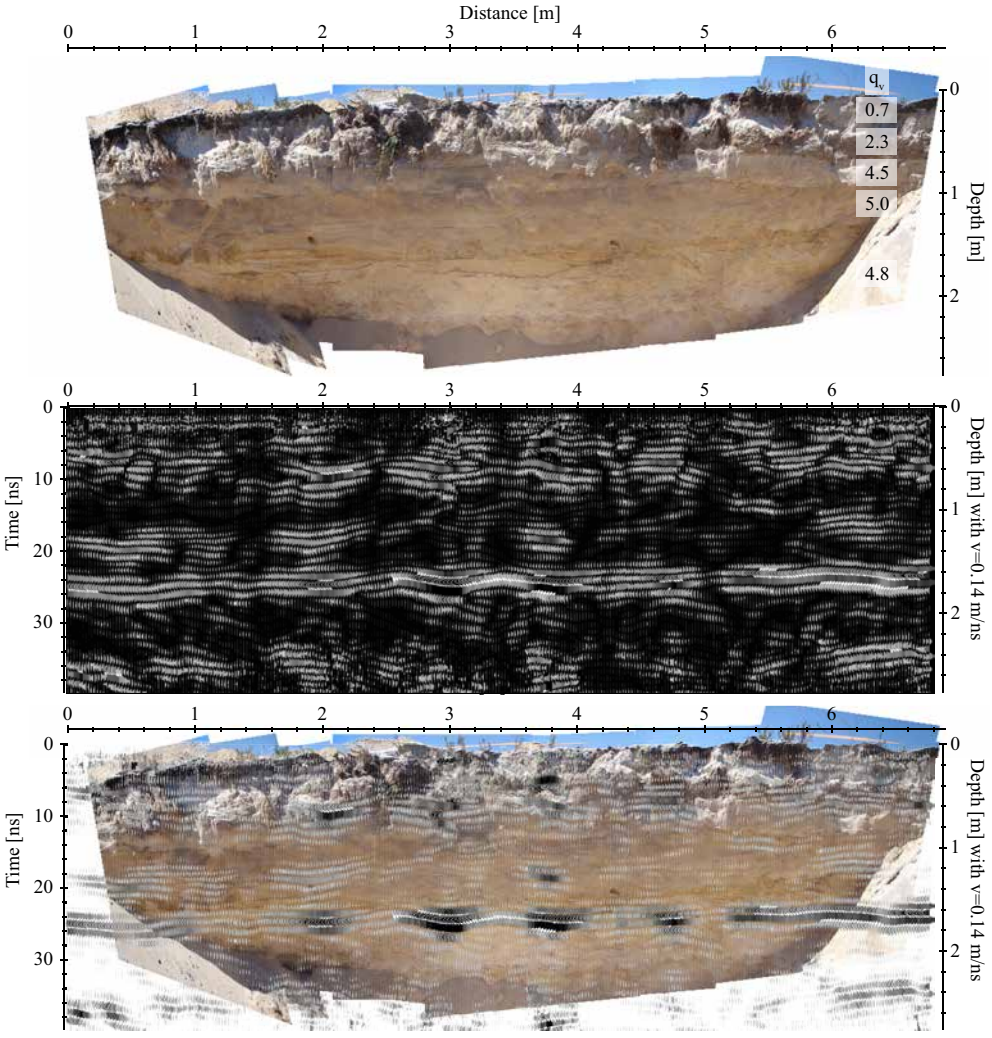

Figure 4.3: *Trench dug by excavator at revegetation site at Rocla mine site (upper) and corresponding 500 MHz GPR profile (middle) and GPR overlay (lower). A slight change in material colour produces a strong GPR reflection.*

4.2.2 The Tuart And Clover Road Transects

In this section I present two 2D GPR cross-sections that were acquired along Tuart and Clover Roads, in the Yeal area, northern Gnangara Mound. Both sections transect the Gnangara Mound in a west-east orientation, stretching from the Spearwood dunes in the west to the Bassendean dunes in the east. The dune systems dominate the landscape by forming major topographical features. Topography is well represented by the topography corrected GPR sections shown in Figures 4.4 and 4.6a. These particular transects were chosen because they feature most of the near-surface geological elements found on the Gnangara Mound.

Note that the processing of the GPR data displayed in this section was aimed at preserving relative amplitudes. That is, the same time-varying gain function based on spherical divergence was applied to all traces equally (i.e. multiplication with t^2). Thus, amplitude information is preserved not only within one profile, but hypothetically throughout all profiles. Further prior processing was done in ReflexW (*Sandmeier*, 2012) and included in this order: static correction, de-spiking, DC-shift removal, trace-interpolation, 2D-median filtering, background removal and stacking of traces. After applying gain, a static correction was performed by adding additional two-way time $t_{\text{topo, i}}$ in the front of each trace based on its topographic position h_i, a reference height (maximum height of full profile) h_{max} and the velocity of the first interval v_1 (i.e. average interval velocity above water table):

$$t_{\text{topo, i}} = 2\frac{h_{\text{max}} - h_i}{v_1}. \tag{4.2}$$

Correct topography and velocity information is essential to be able to interpret elevation level and topology of subsurface reflectors. At the large scale of the profiles, that is tens of kilometres, a single layer approximation of unsaturated velocity provides an adequate first-order estimate sufficient for further interpretation. The velocity was chosen as 0.15 m/ns which resulted in a roughly flat water table reflection in the eastern part of the cross-sections.

Large-scale features which are present at both profiles are i) absence of ground response (i.e. reflections, diffractions, clutter etc.) in the western part where the Spearwood dunes overly aeolian carbonates of the Tamala Limestone; ii) a transition zone

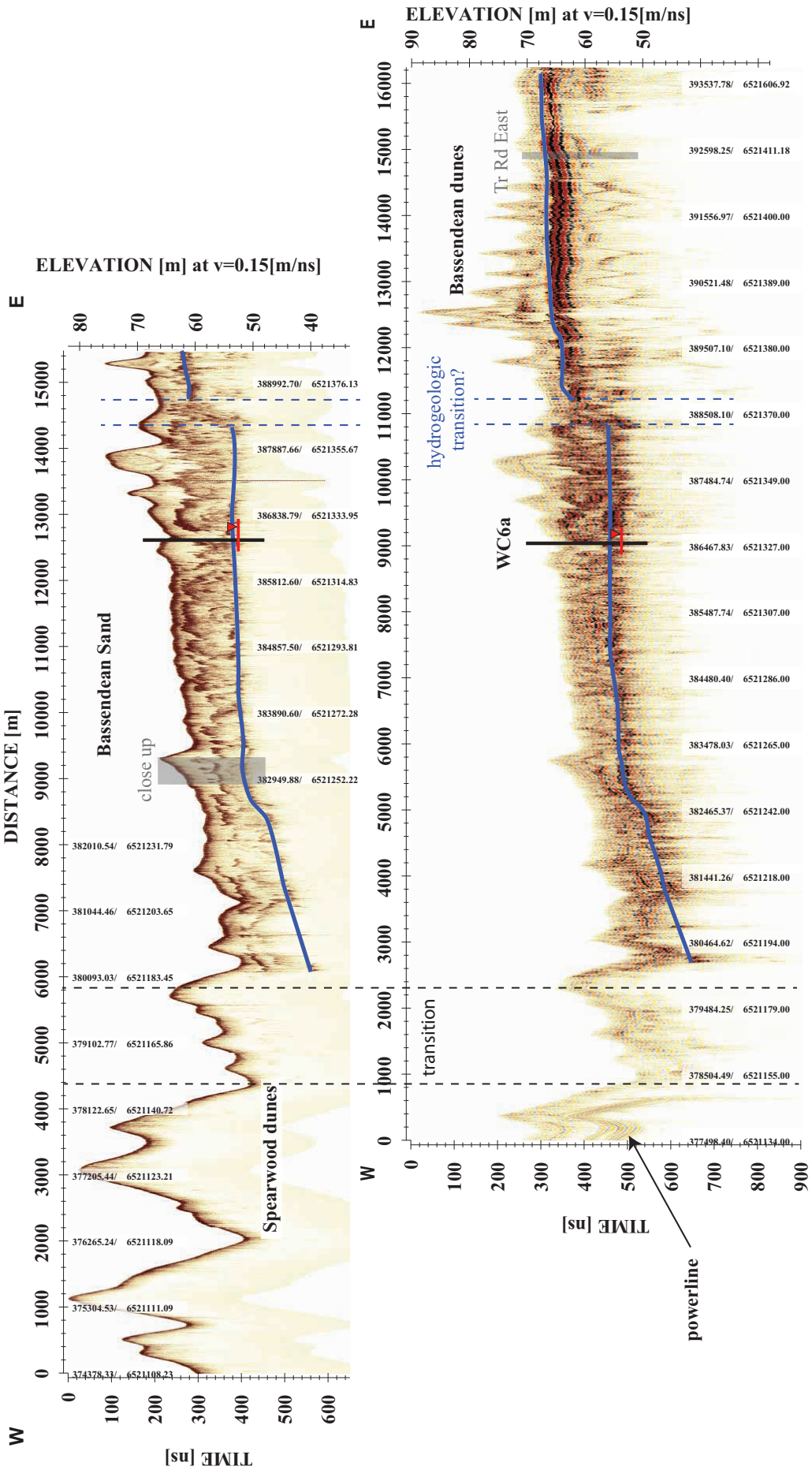

Figure 4.4: *The Tuart Road GPR transect acquired with 250 MHz (upper) and 50 MHz antennae (lower). The main features interpreted in this cross-section are i) the Spearwood Dunes in the west with low GPR energy return, ii) the central Bassendean Sand with various unsaturated zone reflectors and a weak reflection response from the water table, iii) a step in water table position and iv) a strong water table reflection and reflectors below the water table in the east.*

between Spearwood dunes and Bassendean Sand/Bassendean dunes where ground response is attenuated in contrast to iii) the strong reflectors found in the unsaturated part of the Bassendean Formation. Further to the east, feature iv) is a step-like increase in water table position, from an elevation of approximately 58 m above sea level (masl), to a level of approximately 62 masl. The eastern part of both transects show reflectors below the water table reflection. These features and other significant hydrogeological aspects are examined in the following sections in more detail.

Regional water table

The interpreted GPR water table reflection within the Bassendean Sand, indicated with a blue line in Figures 4.4 and 4.6, appears at a level that is consistent with the regional water level used for PRAMS derived from shallow boreholes (see for example Figures 4.22, 4.23 and 4.24 where PRAMS water table is displayed as dashed blue line, and the coloured symbol plots are roughly located at the GPR interpreted water table position for Tuart Rd, Airfield Rd and Clover Rd, respectively). One significant difference is the step in water table reflection that occurs at the eastern part part of the profile. At Tuart Road, this step occurs at a lateral position of 14.3 - 14.7 km (250 MHz) and 10.8 - 11.2 km (50 MHz) (Figure 4.4a and b, respectively), which is at eastings between 388450 - 388850 mE and a northing of 6521370 mN (in GDA94, MGA Zone 50). A similar step is evident in the Clover Road transect where it occurs at a profile position of 12.9 - 13.3 km (390835 - 391230 mE/6517240 mN). The height of that step is approximately 4 m. Note that another transect is shown in the following section in Figure 5.6 that also shows the same step further north at a position of 384500 - 384930 mE/6526200 mN (note that the radargram in Figure 5.6 is oriented east-west, i.e. the start of the line at 0 m represents the eastern end of the profile). My interpretation of this unusual change or step is that either a layer with reduced hydraulic conductivity intersects the water table at those positions, or a general lithologic change results in lower hydraulic conductivity towards the east.

The 50 MHz data from Tuart Road corroborate the theory that a layer intersects the water table where the water table reflection appears to change vertical position. Figure 4.1 shows a horizon, indicated as green solid line, coming from below the water table in the east, intersecting the water table at the abovementioned step, and comes out and above the water table in the west. However, this layer does not appear to be

electrically conductive as it does not greatly attenuate the GPR signals and in some places deeper reflections are visible (below this layer). It is not conclusive whether it is a layer (i.e. finite thickness), or a lithologic interface. The 50 MHz data from Tuart Road show a signal return from below the reflection, which is in parts roughly parallel to the upper reflection and it might indicate a lower layer interface. The approximate thickness of this layer would be 7 m based on an approximate saturated GPR velocity of 0.6 m/ns. The signal strengths from both upper and lower layer reflections are weak. The reflector is undulating and shows an approximate topography with a maximum amplitude of 8 m.

To confirm this apparent step in water table position and to better understand the geological origin of a potentially large hydraulic gradient, a drilling program that targets this horizon within the lateral intervals defined above would confirm or refute my interpretation; however, the resources available for my work did not allow such a diversion.

Central Bassendean Sands

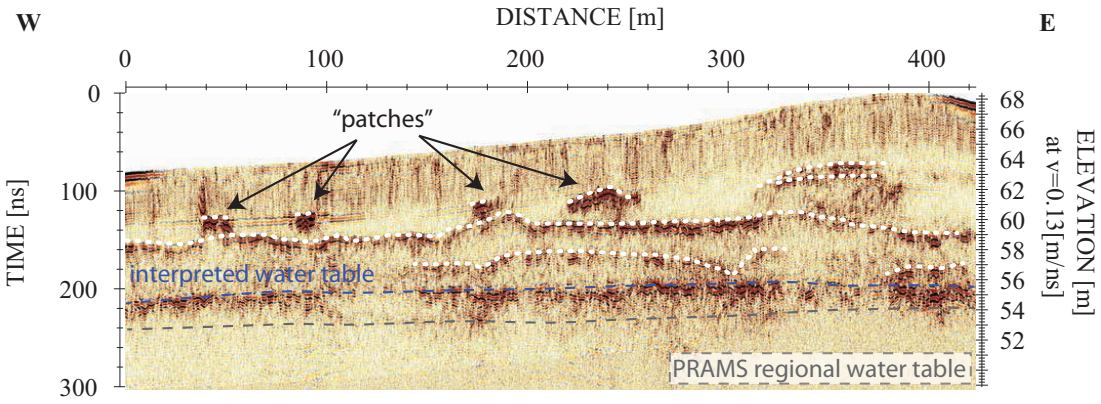

Figure 4.5: *Close-up of 250 MHz Tuart Rd GPR transect (grey box in Figure 4.4a), central Bassendean Sand formation. It shows unsaturated reflectors, probably Podosol soil horizons, which are "patchy" and show several reflection levels either indicating several interfaces, or distinct upper and lower layer boundaries.*

The GPR response in the central part of the Bassendean Sand formation is characterised by strong, undulating and discontinuous reflectors in the unsaturated zone. In contrast, the Spearwood dunes do not seem to provide much in the way of interpretable GPR responses that are continuous on a larger scale.

The lateral extent of soils with these characteristic vadose zone reflectors is approximately 9 - 10 km. This portion of the Bassendean Sand is of main interest: i) from a groundwater recharge perspective due to the intermediate depth to water table, well-drained sands, and natural vegetation which leads to high recharge estimates in the current VFM (compare, for example Figure 2.10); and ii) from an ecological perspective due to the pristine Banksia woodland preserved in this area.

The large-scale transects measured with 250 MHz GPR antenna shown in Figures 4.4a and 4.6a provide sufficient resolution and depth penetration to characterise those reflections. Note that the wavelength of the 50 MHz in those high-velocity sands is too large to provide adequate resolution in the unsaturated zone. In this central part of the Bassendean Sands, the water table is flat at an approximate depth of around 10 m based on an average topographic level of 60 - 70 masl (i.e. water table at 50 - 60 masl). While the topography is relatively flat at the Tuart Road transect, Clover Road intersects several dunes where depth to water table depends on dune height but can be up to 25 - 30 mbNS. Water table elevation drops towards the west and the reflection is lost even with the 50 MHz data due to the higher attenuation under the Spearwood dunes. The interpreted water table position is reasonable within the certainty of the GPR depth estimation (see for example WC6a measured water level indicated in Figure 4.4, and the PRAMS water table prediction in Figures 4.5,4.22 and 4.24).

Figures 4.5 (migrated) and 4.6b, c (not migrated but downsampled to 1 m trace increment) are close-ups that show the typical reflection response of unsaturated zone layers of the central part of the Bassendean Sand. Several levels of strong reflectors are present in the radargrams. The Tuart Road example in Figure 4.5 shows ”patches” of strong reflectors as the shallowest, significant ground response. They occur at an approximate depth of 3 - 4 mbNS. Their overall appearance is similar to the western patch of ”coffee rock” at Whiteman Park that will be discussed in section 4.2.3.

Below those ”patches”, a more continuous reflection appears. This reflector has some topography (independent of the natural surface topography), which becomes particularly obvious on a larger scale. Below that reflection follows a second reflection which might originate from the lower interface of the earlier reflection. Below those horizons is what I interpret to be the water table response. It is characterised by a multitude of diffractions, which in the given example in Figure 4.5 do not migrate to

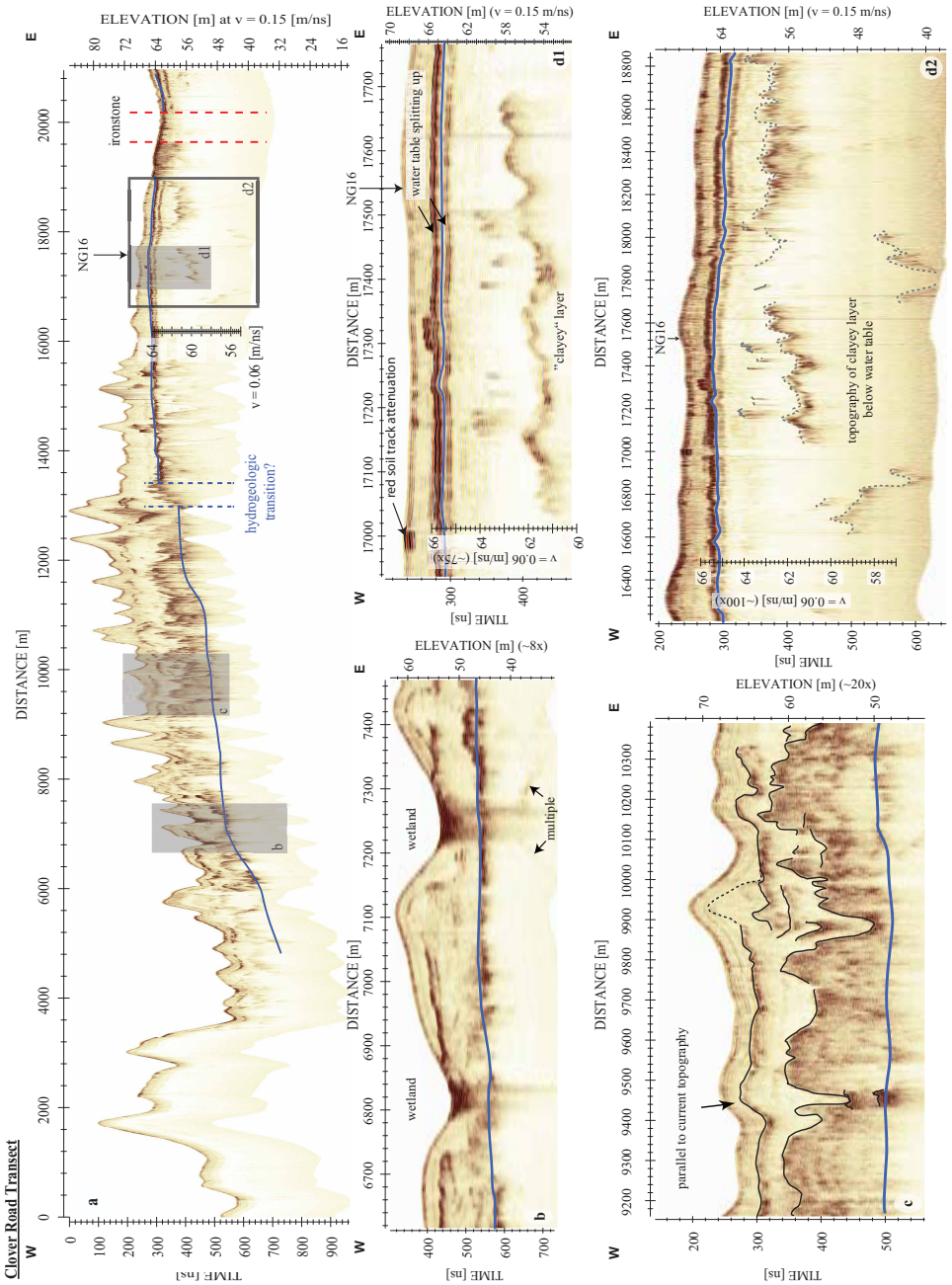

Figure 4.6: *GPR transect along Clover Road spanning the central Gnangara Mound (a). Close-ups (b), (c), (d1) and (d2) present typical features found in the Bassendean Sand formation: intradunal wetlands (b); layer parallel to topography and deeper layers showing their own topography and several levels of reflection (c); a splitting of water table reflection, and layers below the water table that show topography in (d1) and (d2).*

a point (undermigrated), possibly due to deficient migration velocity. This could indicate an increase in velocity with depth. As the shallow diffraction hyperbolae have migrated reasonably well, the chosen velocity of 0.15 m/ns is appropriate for the units above the water table.

Figure 4.6c shows slightly different reflectors. The first significant reflection originates from a depth of approximately 2 mbNS and strictly follows the current topography. Below that horizon are several levels of reflections which have their own topography with a maximum vertical amplitude of 8 - 10 m. Those reflections consist of a multitude of diffractions, most of which occur on the top of the layer. Some diffractions, however, are found below the upper interface creating the impression of a change in lithology rather than a confined layer. My current interpretation is that those horizons represent the upper interface of older Podosol horizons with an erosional surface. Note that those have been already described in Figure 2.12 for the Rocla mine site at the southern Gnangara Mound, and in the literature by *Thompson* (1992). The diffractions below the upper part of the interface might originate from pipe-like structures reaching into indurated or stained sand. From field and GPR observations alone it is somewhat speculative on how and when those horizons formed, and how they developed. A possible explanation is that they formed around a paleo water table, possibly during the last transgression. Thus, they would have been flat and then, after water tables dropped, eroded by eluviation and illuviation and ion mobilisation and precipitation processes. Another explanation is that they formed in the unsaturated zone under a different topography, that is a paleo topography, and initially were parallel to that topographic surface. The Bassendean dune system has experienced several glaciation (cold) and interglaciation (warm) periods, which in these latitudes would have lead to changes both in average temperatures and rainfall. In any case, the surface topography and the Podosol horizons have had enough time to develop into what is now a complex spatial arrangement. A third explanation is that not all reflectors originate from Podosol accumulation horizons (i.e. ”coffee rock”). Some reflections could be paleo surfaces, that is paleo A-horizons, or deposits from other features that formed at the surface, such as wetlands.

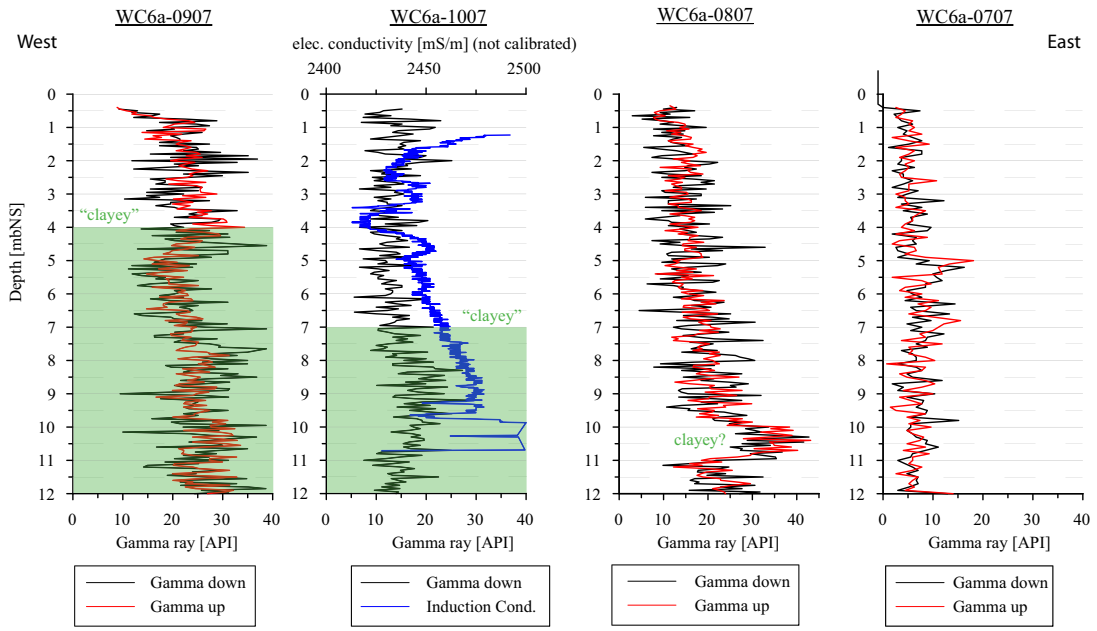

Figure 4.7: *Natural gamma ray and electrical conductivity (induction-) logging results at boreholes WC6a. Green shading indicates borehole section described as brown clay and sand intervals (Robertson et al., 2008). Low gamma emission demonstrates that the material is likely not related to clay minerals of depositional origin (e.g. Kaolinite, Montmorillonite, Smectite), that typically shows higher gamma response. Thus the horizon is probably a Podosol soil horizon (i.e. "coffee rock").*

WC6a

A small-scale 3D GPR survey was performed at boreholes WC6a in order to analyse the 3D configuration of the vadose zone GPR reflector identified from the large-scale data at the central Bassendean Sand formation as described above. The WC6a test-site position is indicated on Figure 4.4, site coordinates are 386412mE/6521312mN. The lithological borehole logs from the two western holes (i.e. four holes in EW strike, borehole locations are plotted in Figure 4.9a, b) describe shallow, clayey deposits, indicated with green shading over the geophysical borehole logs in Figure 4.7. Borehole WC6a-09/07 (westernmost) contained "brown gritty clays and sands" between 4 and 16 mbNS (*Robertson et al.*, 2008). WC6a-10/07 (next to the east), the shallowest hole, encountered "brown clay and sand" between 7 and 12 mbNS, embedded within "white sand". Natural gamma ray logs were performed in all four wells. Induction logging was done in the shallowest well 10/07 only as it is the only borehole without shallow steel casing. Note that the induction technique is strong in contrasting conductive layers from resistive layers. In a very resistive environment such as the unsaturated sand, the induction technique does not necessarily provide the resolution capability

necessary to distinguish between slight changes in electrical conductivity. Note that the measurements were not calibrated, thus the scales given in Figure 4.7 do not provide absolute conductivity values, while API units for gamma ray data are based on the conversion provided by the AusLog software.

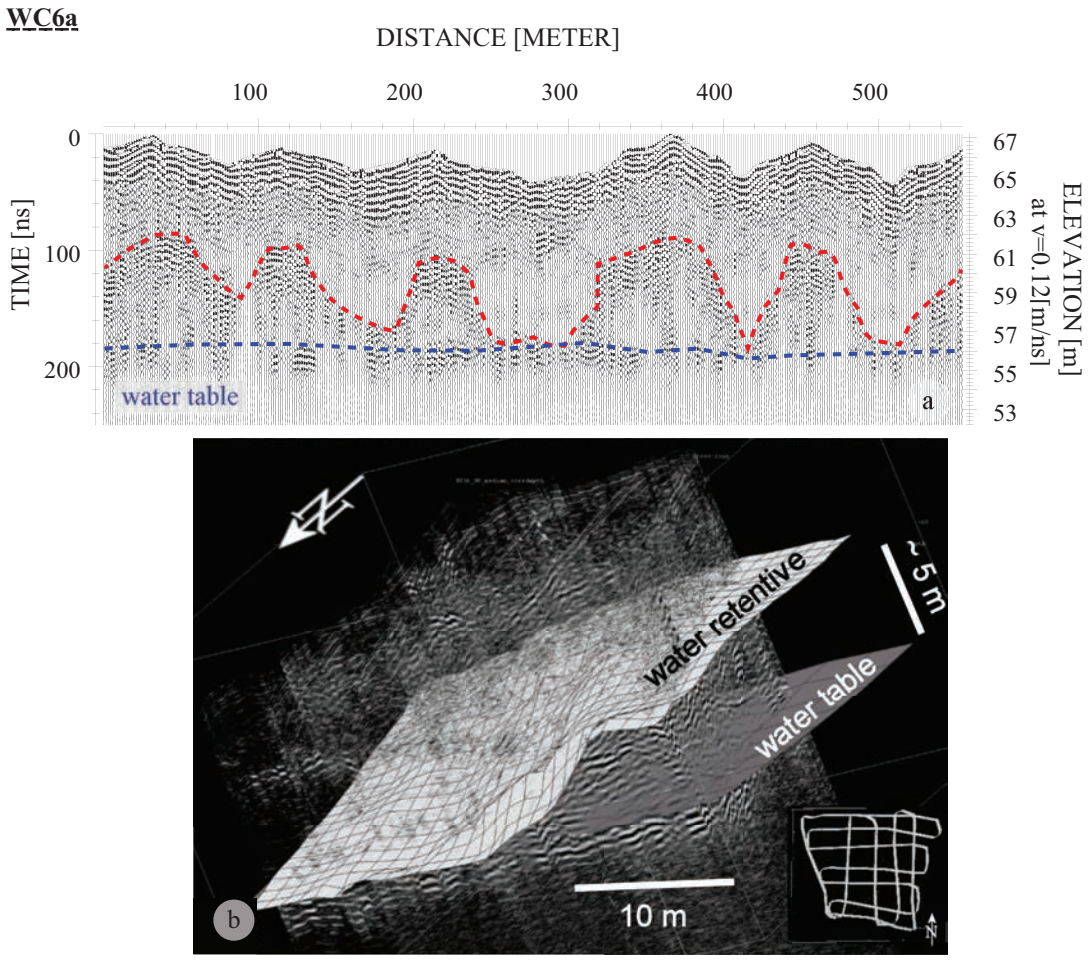

Figure 4.8: *2D snake-like data acquisition (a) displayed in 3D (b) at boreholes WC6a (Tuart Road) showing dipping reflector within the unsaturated central Bassendean Sand formation, and an irregular water table reflection.*

The geophysical logs do not clearly confirm the driller interpretation. Depositional clays would be expected to show an increase in natural gamma ray radiation and increased electrical conductivity. Neither are observed on the geophysical logs. Hole WC6a-08/07 shows a slight increase in gamma ray emission between 10 and 11 mbNS. Note, however, that the gamma counts shown here are below 40 counts, which is a small number compared to depositional clay that produces values between 150 and 200 in this environment as measured in deeper well section (*Robertson et al.*, 2008)). The induction log at WC6a-10/07 shows a gradual increase in conductivity

with depth below 5 m, however this might be due to the approaching water table at 10 mbNS. The gamma log at that well also shows a slight increase in counts below 7 mbNS. WC6a-09/07 shows a very small increase in gamma counts between 3 and 5 mbNS. However, the gamma and electrical response of vadose zone layers is not significant and almost unresolved by the geophysical logging tool used.

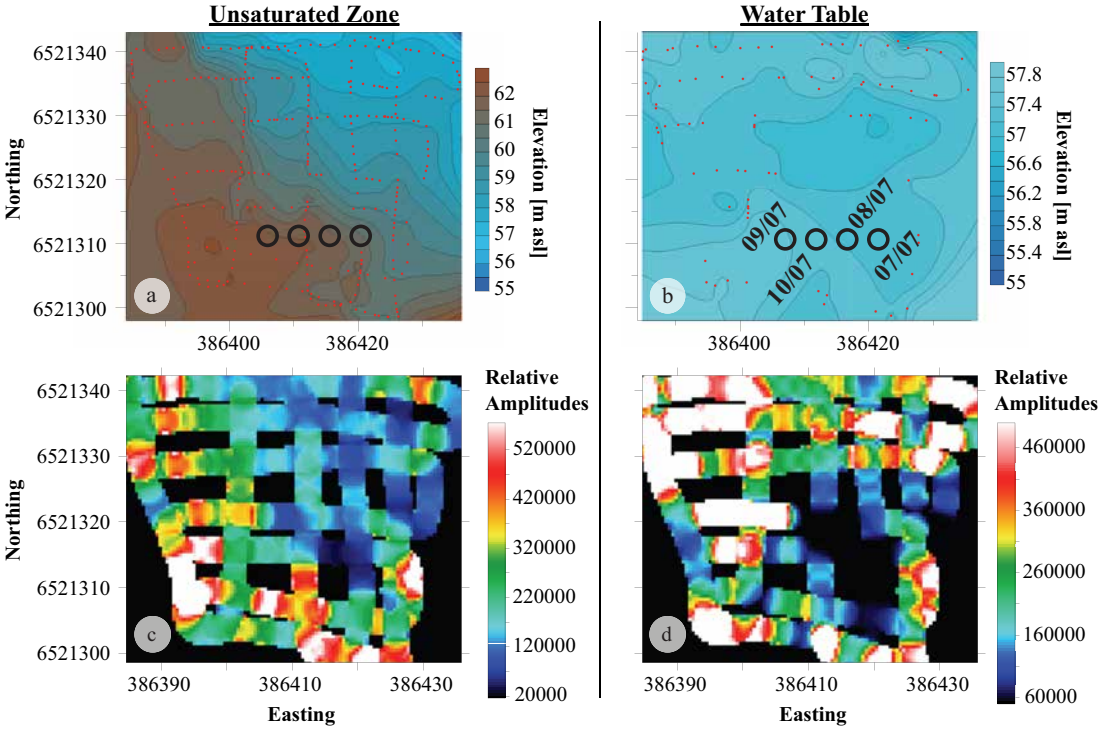

Figure 4.9: *Surface topology of unsaturated reflector (a) and water table reflection (b) at WC6a (central Tuart Road) reveal a northeast dipping vadose zone horizon. Summed absolute amplitudes of unsaturated zone (c) and water table reflection interval (d) show a good correlation which could indicate that attenuation rates are the cause of low amplitude signal return.*

Pseudo-3D GPR results are presented in Figure 4.8. GPR data were acquired using 250 MHz shielded antenna which was dragged over the drill pad in a snake-like manner (see lower left bird's eye view in Figure 4.8b). Survey size is approximately 40 x 40 m. Topography was measured simultaneously using an RTK-GPS mounted on the radar antenna. Elevation information was used to introduce topography to the radargram as previously described in equation 4.2. Other processing steps are similar to the processing flow outlined previously. One particular processing step, FX-Deconvolution, became necessary due to strong radio signals transmitted by the RTK base station (i.e. GPS corrections). The base station was placed too close to the survey area which lead to strong noise signals that, despite the antenna shielding, contaminated the radargram at a similar frequency range as the GPR signal. FX-deconvolution proved effective in

removing these unwanted energy bands while preserving the ground response.

The survey extent and line density is sufficient to resolve the spatial orientation of the reflector of interest. Figure 4.8b and 4.9a reveal that the layer reflection is dipping towards the north-east with an approximate average dip angle of $10°$. Local dip is greater between $10° - 20°$. The 3D orientation is somewhat consistent with the drilling report, which stated the shallowest "clayey" material at the most western position (i.e. at 4 mbNS), followed by increased depth to that layer towards the east (i.e. 7 mbNS). In the northeastern corner of the survey, the layer coincides with the water table reflection.

The interpreted water table reflection resulted in an approximately flat interface at a topographic position of 56 masl (Figure 4.9b). The reflector depths compares well with the gravimetric water table measured at the shallowest borehole (i.e. 10/07). From this survey, it became evident that the water table reflection strength varies, even at a small scale (see Figure 4.9d). Reflections occur at around the expected position, and when picked result in a flat reflection. However, a clear water table such as has been observed for example at Whiteman Park is missing (see following section, e.g. Figure 4.12a). The measured reflected amplitude from a reflector is determined by two main factors: i) the reflectivity of the interface (i.e. impedance contrast), and ii) the losses the wave experiences between source/receiver and point of reflection (see section A). Low reflectivity could be a result of an extensive capillary fringe with a smooth gradient in water content as describe in section A.2 (*Bano*, 2006). This would be a reasonable explanation for the geologic setting where a cementation horizon with indurated sand below extends to the water table. The capillary rise might be increased due to the increased matrix potential of those materials which could lead to a smoother gradient compared to a well sorted clean sand. The second explanation for low signal amplitudes are high attenuation rates, for example due to the drill pad surface (limestone track material), or clayey material that was spread over the drill pad during drilling (e.g. drilling mud or recovered clay material from deeper strata). Some areas where water table reflection is absent or very weak coincide with weak unsaturated zone response which would support attenuation as the cause for low signal return (see for example area 6521310 - 6521330 mN / 386410 - 386425 mE in Figures 4.9 c and d).

The main outcome of this study that improves our understanding of unsaturated flow and recharge in this soil environment is the 3D topology of the vadose zone re-

flector. It is clear that a significant soil horizon exists at WC6a, revealed by drilling, borehole logging and GPR. This material, either being an aquitard (i.e. clay) or a capillary barrier (i.e. "coffee rock" with high matrix potential, compare funnelled flow, *Miyazaki* (2006)) will influence the local unsaturated flow field. Due to the layer's dip, flow will be guided in dip direction, in this case to the north-east, towards the water table. This can have a profound influence on groundwater recharge rates as a dipping layer does not perch water as would, for example, a flat or U-shaped horizon.

Intradunal Wetlands

Another interesting geological feature intersected by the Clover Road transect are the wetlands as labelled in Figure 4.6b. They show a very strong ground response that, due to having relative amplitudes preserved, appears similar to ringing in the current GPR data representation. This wetland response is somewhat unexpected as in most cases, Western Australian wetlands are associated with either clays, or high salt concentrations. Thus, GPR typically does not perform well in these environments. These wetlands are found in between dune systems and probably were groundwater dependent, but are now supported by rainfall. The wetlands are not connected to a freely flowing superficial water system (i.e. rivers), which explains why clays are not transported and deposited in them. The soil found at these wetlands consists of very fine, grey material. Although no detailed analysis has been performed it appears to be very high in organic content, and could be peat. It could also consist of very fine quartz which was produced by diatomites (i.e. diatomaceous earth). Both materials would explain the low loss associated with them as they do not contain attenuating minerals, and possess very high porosity. In the case they are dry, one would expect to find very good GPR penetration.

I hypothesise that those intradunal wetlands could be a relict from a time when the water table was approximately 8 m above its current level, which would have created discharge or through-flow lakes after the wet season. In their current state, they might experience temporary water logging due to the low hydraulic conductivity of the sediments found there. They are therefore still favourable environments for plants as the soils can potentially store large amounts of plant available water, and they occur in depressions, which means that the depth to water table is minimal; thus, providing larger plants with a steady water supply.

At both wetlands, distinct reflections occur towards the east which continue for approximately 200 m and then fade out. Whether those reflections are somewhat connected to the wetlands is unclear. One could infer that possibly the predominant wind direction is from the west (sea-breeze and the direction of oncoming weather patterns), which would blow fine materials out of the wetland onto the adjacent dune. Eluviation and illuviation of fine material could then lead to accumulation bands which create strong GPR reflections. Another explanation could be that those reflections represent the previous water table level. The large-scale profiles tend to show an upper reflector level at a position that could represent a previously flat horizon. One could speculate that after the water table has dropped sometime after the last transgression, this horizon, which would have been around the water table, started to erode. Another alternative is that these horizons have previously been parallel to the paleo-surface topography and represent a Podosol horizon.

Davidson and Yu (2006) describe perched water above ”coffee rock” at swamps and damplands, especially in the southern Perth region. In the case of those intradunal wetlands, which would fit their description, a clear sign of layers which could provide for water perching is missing in the GPR section. However, some internal layering is evident within the wetland deposits, which could be an indication of its depositional origin.

Another aspect associated with these two wetlands are dispersive diffractions. They indicate a shallow waveguide, which in this case must originate from the shallow peaty soil. An alternative explanation for waveguide phenomena are limestone tracks, which are commonly used as road surface at the northern Gnangara Mound. However, this part of Clover Road is not paved and the surface either consists of loose sand, or the grey wetland deposits. Exploiting this waveguide phenomena will be further discussed in the a later section. Note that the large-sale data set described here (i.e. Tuart Rd, Clover Rd) was not used for waveguide dispersion analysis as the data quality was not deemed sufficient to recover reliable dispersion curves. In addition, very similar dispersion was observed for the wetlands in the northern Yeal area (refer to the September SII diffractions discussed in the following chapter, Figure 5.6).

Eastern Bassendean Sands

I would now like to discuss the eastern part of the GPR transects, which are shown in

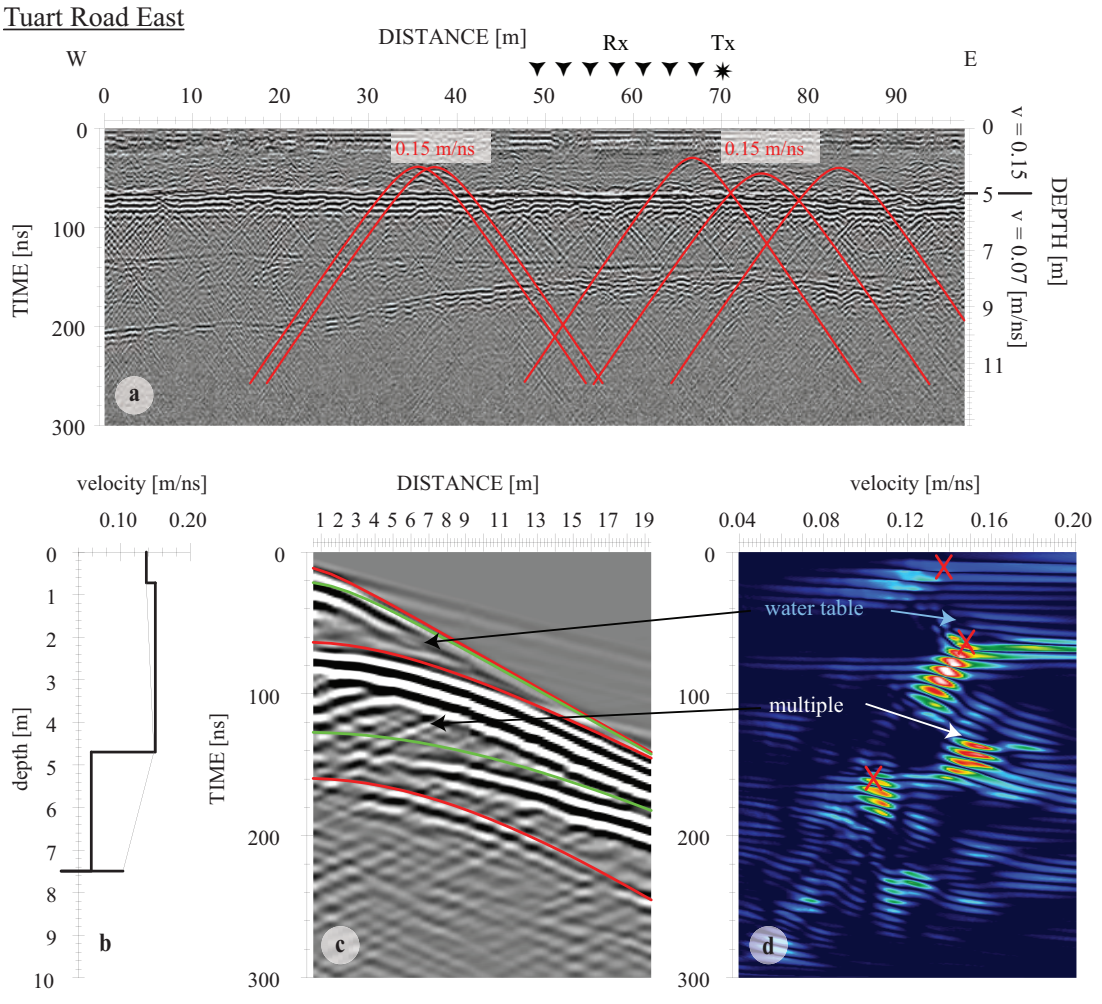

Figure 4.10: *Common offset 2D GPR transect collected at eastern Tuart Road (a) showing reflections from the water table and a layer below. A common shotpoint multioffset gather (c) and its semblance plot (d) reveal a velocity profile (b) with unsaturated velocities of approx. 0.15 m/ns, depth to water table of 4.7 mbNS, saturated velocity of 0.06 m/ns and a second reflector depth of 7.5 m. Note the good correlation between velocities obtained by matching diffractions in (a) and the multi-offset analysis.*

Figures 4.6 d1, d2 and 4.10a. The original 250 MHz Tuart Rd transect does not reach very far to the west; therefore, I collected some additional data at the far east end of Tuart Road. A part of this eastern transect is shown in Figure 4.10a. This transect was collected on August 4th, 2010, during winter, alongside a common shot point (CSP) gather shown in Figure 4.10c.

As previously described, the water table experiences a step, with a higher topographic level in the east. In the east, the water table appears flat, and is characterised by a clear and distinct GPR reflection for both, 50 and 250 MHz data. The 250 MHz Clover Road GPR transect shows that the water table reflection is splitting up. Time difference between first and second reflection arrival is increasing towards the east. On a local scale, the secondary reflection is strictly parallel to the primary reflection.

While both are flat on a large scale, they show small-scale undulations, which can be explained by local surface topography (i.e. not layer topography) at that scale. This small-scale topography, which is mainly found on sand tracks, is not captured by the GPS and cannot be corrected based on measured elevation. Thus, a notionally flat layer reflection appears ”bumpy”. My preliminary interpretation for this splitting of reflection is the existence of an accumulation horizon marking the uppermost level of the dynamic water table. The water table is known to vary by approximately 1 m throughout the seasons (*Yesertener*, 2002). The accumulation could for example be a precipitation band formed by redox reactions occurring due to changing water table levels. It could also be formed by microbial metabolism and subsequent chemical variations, or by microbe material itself. A purely inorganic mechanical explanation could be that a washout and illuviation zone around the dynamic water table produces vertical variability of porosity. In that case, the upper reflection could be due to water content variations associated with different matrix potentials. A similar horizon was interpreted at Whiteman Park. Further geophysical examination and speculation of the nature of this horizon is covered in chapter 6, see for example Figure 6.4. The layer which was at around the water table in July became submerged in August. A crosswell radar tomographic profile from August revealed that the layer has a higher velocity than the saturated sand below, which indicates decreased porosity. Attenuation, however, appeared to be higher compared to the comparable saturated zone below. For NG16 (see Figure 4.6d1, d2; Figure 6.2), I would claim that the lower reflection is the water table reflection, and the upper reflection originates from a layer as discussed above. Thus, the reflection splits up where the water table falls well below the upper accumulation horizon, as would be the case in late summer (the time when the Clover Rd 250 MHz data were collected). This also explains why the Tuart Road data from August does not show pronounced splitting up because the water table and upper reflection horizon position would coincide.

Regardless of origin or make-up I do not believe that this accumulation horizon is of significance for groundwater recharge from the unsaturated zone, nor for plant available water as long as ground water levels do not drop significantly. However, it might be of significance for other ecohydrologic problems such as acid sulfate soils in case groundwater levels decline until the layer is unsaturated and exposed to oxygen

(i.e. oxidisation of pyrite leads to sulfuric acid release into the environment), or for groundwater contamination where saturated hydraulics are important for contaminant re-distribution.

Another notable feature in the eastern Bassendean Sands is a reflector within the saturated zone. It is shown in Figures 4.6d1 and d2 labelled as ”clayey layer”, and in Figure 4.10a. Note that an additional elevation axis has been plotted in these figures according to the estimated velocity for saturated sands. At the eastern Tuart Rd profile in Figure 4.10, this reflector allowed a velocity estimation for the saturated zone, as a clear reflection appeared in the common shotpoint gather (Figure 4.10c). The velocity profile is consistent with the 2D surface GPR, resulting in a high velocity unsaturated zone of approximately 0.15 m/ns, the saturated zone with low velocity of approximately 0.06 m/ns, and based on that interval velocity profile, a reflector at 7.5 mbNS. Below that reflector, no further energy ascribed to reflectors below that layer are evident.

The layer below the water table is described as ”clayey”. I chose this classification based on drilling information which was obtained during drilling of NG16 borehole, which is intersected by the Clover Road transect as labelled in Figure 4.6. During drilling, a hard layer was encountered by the cable tool drill rig at the expected depth of that reflector. The first few meters were drilled only by barrel collection, while the driller had to use a ram to penetrate through the layer. As most of the broken-up material was either going into water suspension, or being pressed to the sides, only few chips of cohesive, clayey material were recovered. This is the NG16 ”coffee rock” investigated in chapter 3 for its dielectric properties (it showed high attenuation). It has to be noted that the final drill report did not mention this layer as clay, which demonstrates how inaccurate such drilling methods are. The recovered material was described as ”weak to moderate ferruginous cementation (coffee rock)”. However, this interpretation is a result of information taken from other sites. This misrepresentation is due to the lack of material recovered as mentioned before. The material that I have seen was cohesive when wet, that is plastically deformable, which I would interpret as high clay content. After drying it became friable. It contained black mineral grains, and some magnetic needle shaped grains, which indicates heavy minerals. Auger drilling at Tuart Road also encountered a hard layer at expected reflector depths. The auger

could not penetrate this layer, and no material was recovered. Drilling reports from two private wells northeast of NG16 mention a 2 m thick clay layer. It is likely that those reports describe the same material as well.

This reflector is characterised by showing topography, and possibly different levels, as Figure 4.6d1 and d2 show. The uppermost level shows patches of strong reflectors, similar to what has been described for one type of unsaturated reflectors (compare Whiteman Park site, and Tuart Road Figure 4.5). The continuous reflector below these patches seems to be discontinuous, maybe interrupted by a different level. In between the reflection fades out and returns at a deeper level. Where the shallow reflection exists and the deeper reflection disappears, it is not possible based on the data to tell whether the reflector is absent or its reflectivity very low, or whether attenuating material such as dispersed clay or more saline water prevent the EM-energy from achieving depth penetration necessary to image the deeper layer. Figure 4.6d2 reveals that both, shallow and deeper reflector go missing in the west. The 50 MHz data available at Tuart Road also shows the same layer behaviour, including discontinuities. So the GPR signals either lacked depth of penetration from strong attenuation above the horizon, or the reflecting interface/layer is absent.

From the minimal knowledge and recovered material available, it is difficult to interpret if the layer is of depositional or postdepositional origin. It would be useful to understand the continuity of this layer in order to understand the saturated hydrogeologic regime in the northern Yeal area. Other more careful drilling programs, for example at central Yeal wetlands, Tangletoe Swamp (see chapter 6) or Bambun Lake identified different water levels separated by clayey material. This material has been interpreted as Guildford Clay, which suggests a depositional origin. The GPR response of these materials, however, is quite different. As will be shown in the following chapter, the Tangletoe clay perches the water table, not only hydraulically, that is it produces a confined aquifer and large gradients in piezometric heads, but also physically separates saturated zones from each other. This has produced an unsaturated interval below the clay, and a hanging saturated zone above (Figure 6.3). The borehole radar (i.e. crosswell and vertical profiling) from Tangletoe clearly demonstrates that no EM-energy propagates through the clay layer. At Lake Bambun and central Yeal wetland borehole radar performance was the same. Whereas at NG16

the vertical radar profile shows that EM-waves were transmitted beyond this clayey layer (see Figure 6.2 left). The recorded amplitude is reduced. However, the degree of reduction is expected to be greater for a saturated clay, and in its form could be explained by reflection/transmission losses. The crosswell data (Figure 6.2 right) show the layer as attenuative, but waves still propagate through the layer. The traveltimes were even reduced indicating a faster horizon and possibly reduced porosity (see for example Figure 6.181a). Those findings indicate that a non-depositional clayey "coffee rock" horizon exists. The clay minerals could be allophane or humic substances, which might be less attenuative than the typical depositional clays such as kaolinite or smectites. Although the dielectric lab experiments showed an increased attenuation for the NG16 "coffee rock", the lowest estimated resistivity was around 50 Ωm. This is a reasonably resistive value where some GPR depth penetration might be expected.

Another significant layer property is thickness. Although reflections in the vertical radar profile at NG16 did not resolve the layer thickness, the zero offset profiling suggests a layer of 0.6 m thickness (*Strobach et al.*, 2012a). This is in contrast to Tangletoe and central Yeal wetlands, where layer thickness is of the order of meters (i.e. $>$ 1.5 m at Tangletoe, and several meters at central Yeal wetlands). It is furthermore possible that the clayey drilling chips collected at NG16 are not representative of the whole layer. They might come from a thin band or nodules that constitute a fraction of his horizon.

My current interpretation is that those layers are in origin and physical characteristics similar to the reflectors found within the unsaturated zone of the central Bassendean Sand formation. They show a topography, are "patchy", discontinuous, have topology, and possibly show several levels. They are furthermore at a similar elevation level compared to the unsaturated reflectors further to the west (i.e. between 55 and 65 masl). The profound difference is that the water table is above those layers in the east, thus they are submerged within the saturated zone. This would have a big impact on their development after formation. A reasonable scenario is that the horizons were formed as part of a Podosol soil development, starting out as unsaturated accumulation horizons, which started to erode and migrate to greater depth. A succession of varying climates, sand dune formation and erosion, transgression and regression cycles during the Pleistocene resulted in a complex, inhomogeneous layer distribution including

multiple levels of buried and eroded soil horizons. In the last 10,000 years or so climate was approximately stable and the groundwater mound filled up to its pre-European settlement level (i.e. overfull groundwater system). Thus, for the last 10,000 years or so, it is reasonable to suppose that the soil horizons in the central Bassendean soil were in the vadose zone, while the eastern horizons were submerged, leading to erosion in the west, and preservation in the east. This would explain why the eastern layers have somewhat different characteristics (i.e. containing clay fraction that allows plastic deformation which has not been observed for the friably cemented unsaturated "coffee rock" horizons).

4.2.3 Whiteman Park Test Site

This small 3D GPR case-study from Whiteman Park provides a basis for interpreting large-scale GPR data. Three methods that aim to extract the characteristic of a water-retentive soil horizon are tested and compared: i) travel-time analysis of flat reflector below soil horizon, ii) reflection strength of reflector below soil horizon and iii) reflection strength of soil horizon (i.e. overall vadose zone response).

4.2.3.1 Introduction

The Whiteman Park area has been chosen by Water Corporation and Edith Cowan University (Ray Froend, Muriel Davies) to test the influence of winter-pumping on vegetation. Neutron moisture monitoring access tubes have been installed at seven test-sites. The soils from the Whiteman Park area have been described by *Bertuch and Froend* (2006). The soil profile is the typical aeric podosol described in section 2.4. Geophysical measurements were performed at site 4 where a brown, indurated sand horizon, that is "coffee rock", is at a depth of approximately 2 m. Measurements of gravimetric water content by Froend (personal communication) reveals that the "coffee rock" layer has an elevated gravimetric water content of approximately 5 w% to 10 w% above the clean sand background. The depth to water table is around 4 - 5 mbNS depending on pumping activity. Time-lapse neutron logging at the site showed the indurated sand interval as high neutron count layer. Temporal variations of soil moisture are further discussed in chapter 6. Some of the results from the 3D GPR investigation have been published by *Strobach et al.* (2011).

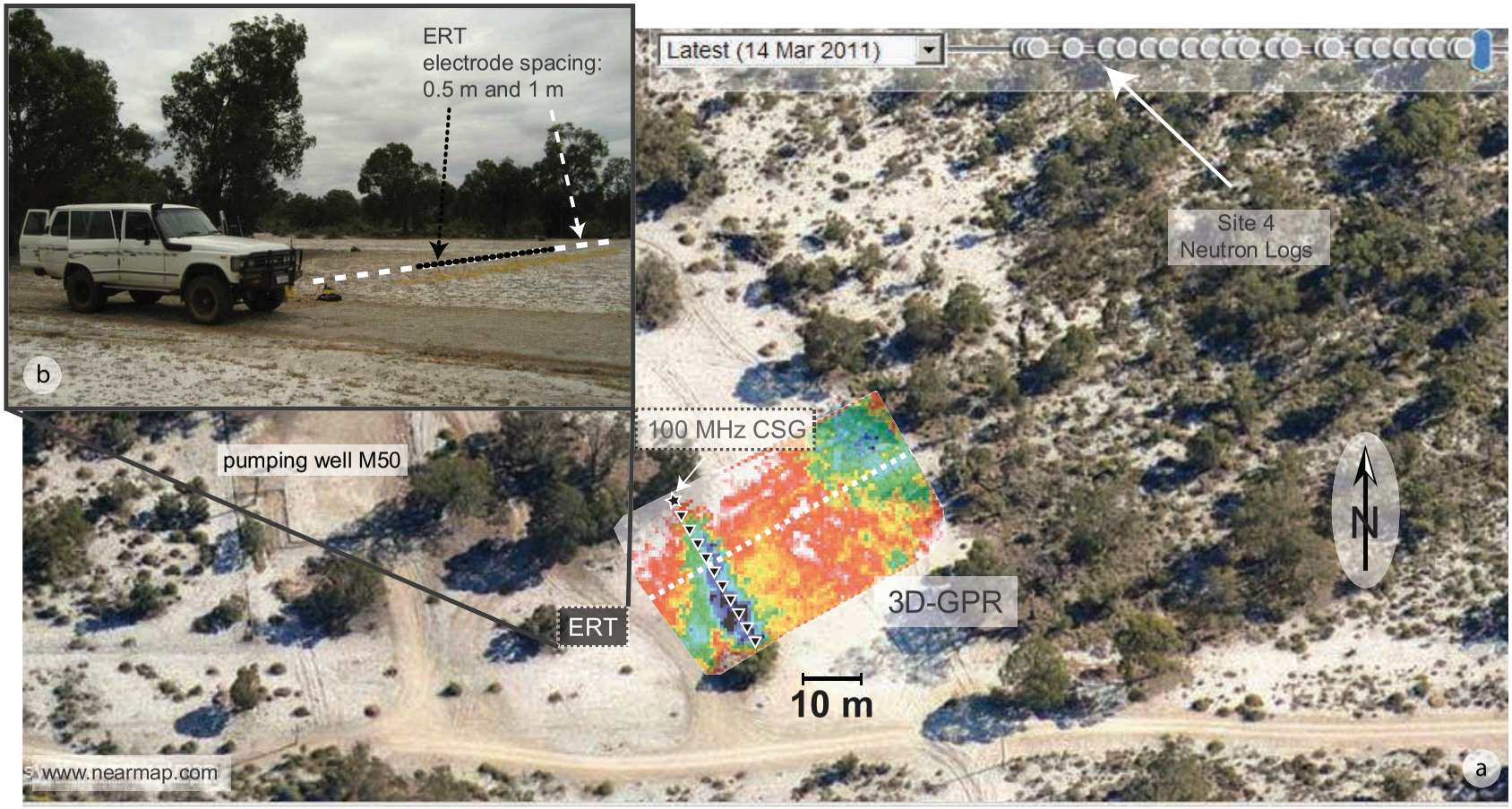

Figure 4.11: *Location map of Whiteman Park test site 4, showing location of 3D GPR survey area, GPR walkaway and 2D electrical resistivity imaging transect and neutron logging borehole location.*

4.2.3.2 Experimental Procedure

Pseudo 3D GPR measurements were performed on November 24, 2009 at a clear area southwest of the neutron logging observation boreholes at site 4 (Figure 4.11). Measurements were performed with the Mala ProEx 2 and a 250 MHz shielded antenna. The GPR system was triggered at 0.1 s time intervals. A real-time kinematic (RTK) GPS system (Thales ZMax) was mounted on the GPR antenna and provided centimetre accurate positioning. The pseudo 3D GPR spans an area of approximately 50m x 25m. It consists of 25 parallel lines with a crossline spacing of approximately 1 m. The inline spacing, that is the spatial trace increment, was resampled to 0.1 m. A multi-offset common-shotpoint gather (CSG) was acquired along the crossline direction at an inline position of approximately 10 m.

Further geophysical characterisation of the site included geoelectric imaging parallel to the inline direction of the GPR survey within the center of the 3D GPR area. This experiment was performed one year later on October 21, 2010 with a Supersting, 8 channel resistivity meter. 56 electrodes were available and acquisition was done with 1 m electrode spacing to cover the whole length of the 3D GPR study area, and at 0.5 m over anomaly A to increase resolution over that anomaly. The dash-interval in Figures 4.11b and 4.13a indicate sections with 1 m (long dashes) and 0.5 m (short dashes) electrode spacing. The measurement geometry was Dipole-Dipole and inverse Schlumberger array. Those were chosen in order to obtain maximum possible sensitivity in the vertical direction from the Schlumberger array, and high lateral sensitivity from the Dipole-Dipole. A problem with data quality was high noise floor due to high contact resistance (dry sand). In order to obtain the best outcome possible, all datasets were combined (i.e. 4 datasets, 3091 data points). Inversion was performed in DC2DInvRes [1]. Inversion parameters were kept at default values. Inversion results were compared with a commercial software package from Advanced Geoscience. However, I found that results were similar and therefore prefer the open source code DC2DInvRes.

4.2.3.3 Observation And Description Of GPR Reflectors

GPR reflection profiles show a clear reflection from the water table at an arrival time of around 60 ns. Inline GPR radargrams are shown in Figures 4.12a and 4.13a. Figure

[1] by Thomas Guenther, www.resistivity.org

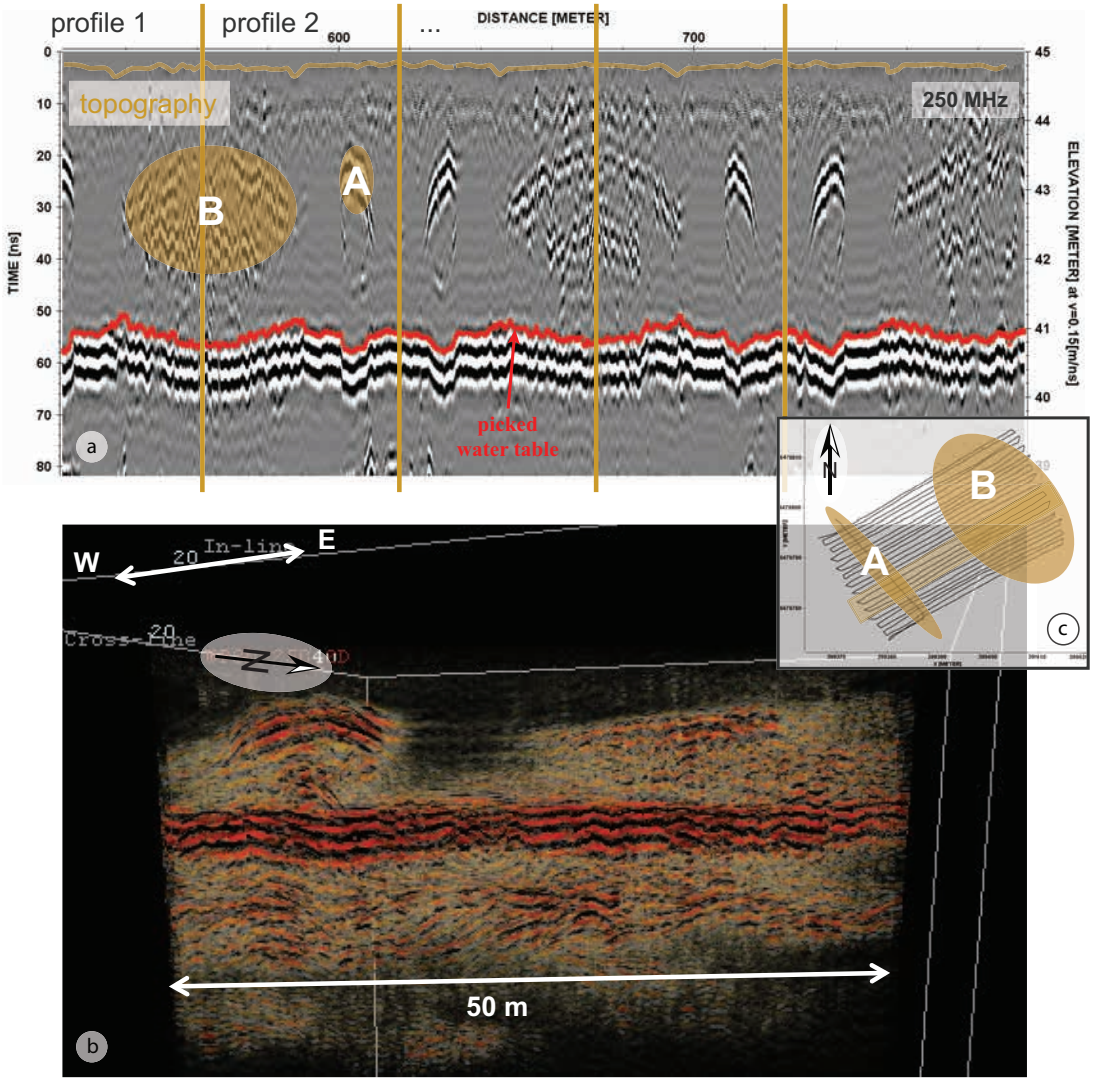

Figure 4.12: *Several exemplary GPR transects (a) showing increase in water table reflection time under anomalies A and B despite topographic correction. (b) shows a view to the northeast through a transparent 3D GPR cube (displayed in OpendTect) revealing anomalies A and B and a 10 m wide hole in between. Measured GPR lines are shown in (c), approximate spatial extent of anomalies A and B is shown in brown shading.*

4.12a shows an undulating water table reflection. Note that this cross-section has been topographically corrected with an average interval velocity of 0.155 m/ns that has flattened out parts of the water table reflection. The magnitude of reflection undulations is up to 10 ns. GPR acquisition intersected two main areas where energy was reflected from the unsaturated zone labelled anomaly A and B in Figures 4.12a and 4.13a. In Figure 4.13a anomaly A starts at a horizontal position of 6 m and reflections arrive between 15 and 25 ns. This area coincides with clear kinks in water table reflection time towards later times. The reflection from anomaly A is continuous and domes up in the central part. Half diffraction hyperbolae are evident at the sides indicating an abrupt

change in reflectivity. For some cross-sections a reflection from the lower boundary appears. The travel times of the lower boundary and upper boundary reflections coincide at the edge of a body that creates an ellipsoidal appearance, which can be seen in Figure 4.13a (note that this radar cross-section was measured in 2010 together with electrical resistivity imaging (ERI) acquisition). Anomaly B starts at approximately 25 m and continues to the end of the profile. The reflection is diffuse and characterised by a multitude of diffraction hyperbola. Between 25 m and 30 m the reflection appears as a single reflector that gradually splits up towards the end of the line. At the southern lines, two clear reflection events are obvious from upper and lower layer interface, while the northern profiles show a diffuse thick reflection arrival masked by various diffractions. The distinct patch of "coffee rock" labelled anomaly A at the western part of the profile has an elongated shape with an axis striking approximately northwest-southeast (see Figures 4.12c and 4.15c and d). The multi-offset common shotpoint gather (CSG) shown in Figure 4.14b was acquired along that axis to capture the reflection from the "coffee rock". Anomaly B appears as a larger slab of "coffee rock" which is cut off towards the west parallel to the strike of anomaly A (Figure 4.15c and d). The middle part of the profile does not contain significant reflectors above the water table. This is interpreted as a soil profile built up by clean sands .

The Whiteman Park test site provides a range of representative types of unsaturated zone radar response, which will be used in the following to test different methods aimed at extracting physical properties of the unsaturated zone.

4.2.3.4 Towards Quantitative Analysis

The following analysis is based on the major observations of the previous section: that is that the arrival time of water table reflection is increased under strong reflectors within the unsaturated zone (i.e. "coffee rock" patch and slab). This can be explained by a great decrease in velocity within the "coffee rock" layer. Decrease in velocity is equivalent with increase in dielectric permittivity which can be explained by increased water content (cp. Chapter 3). These layers are therefore potentially significant hydrogeologic barriers. The objective is to develop a simple processing flow that can identify hydrogeologically significant layers for large-scale GPR data sets with fairly simple heuristics. It has to be stressed that the following analysis is purely based on

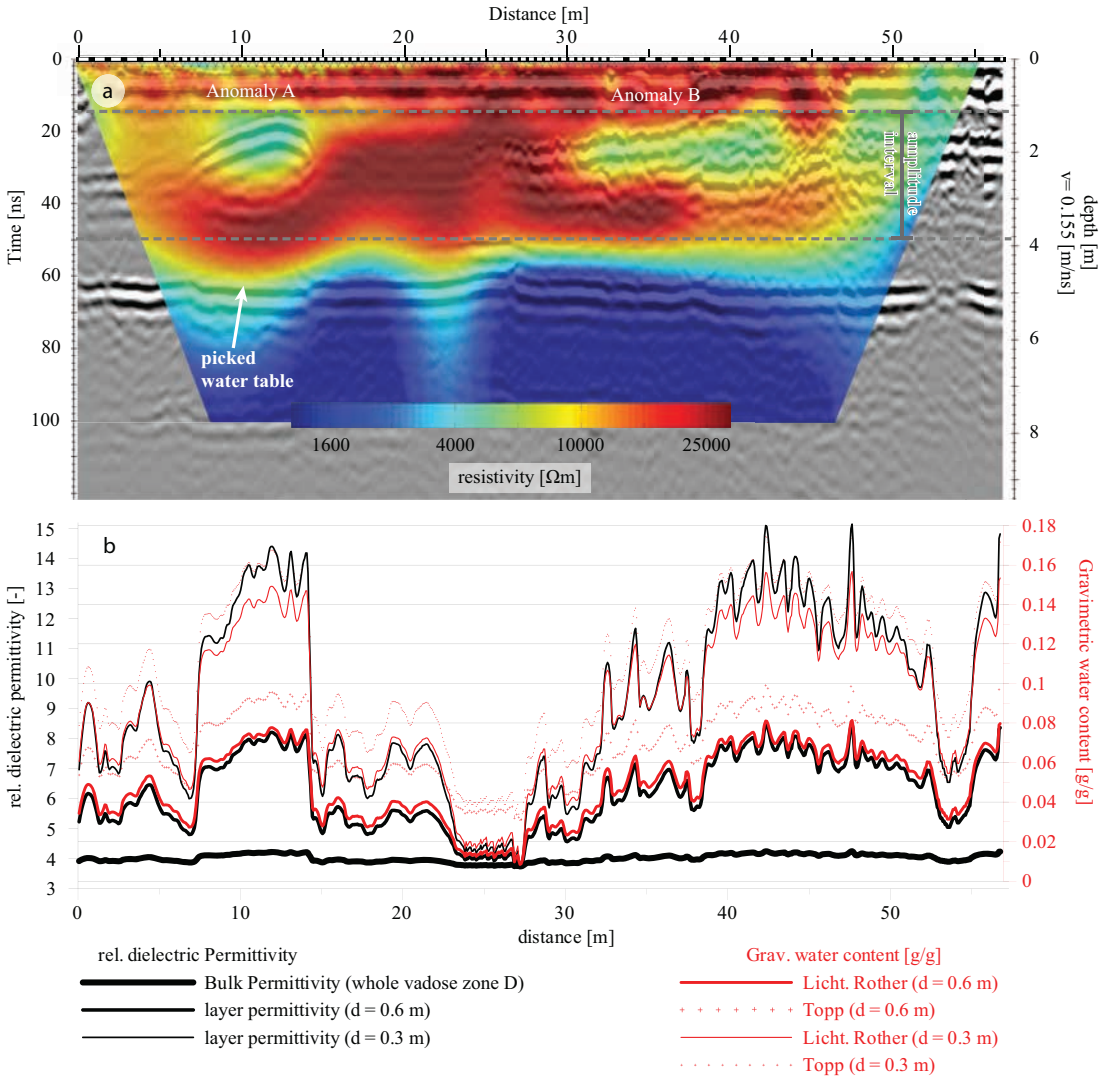

Figure 4.13: *(a) GPR transect with transparent DC resistivity overlay from tomographic electrical resistivity imaging, (b) interval dielectric permittivity (black) and gravimetric water content (red) transect estimated from travel time of water table reflection at known depth. Thick curves are for full unsaturated interval, medium curves for a 0.6 m thick layer, and thin curves for a 0.3 m thick layer in homogeneous background. refer to text for details.*

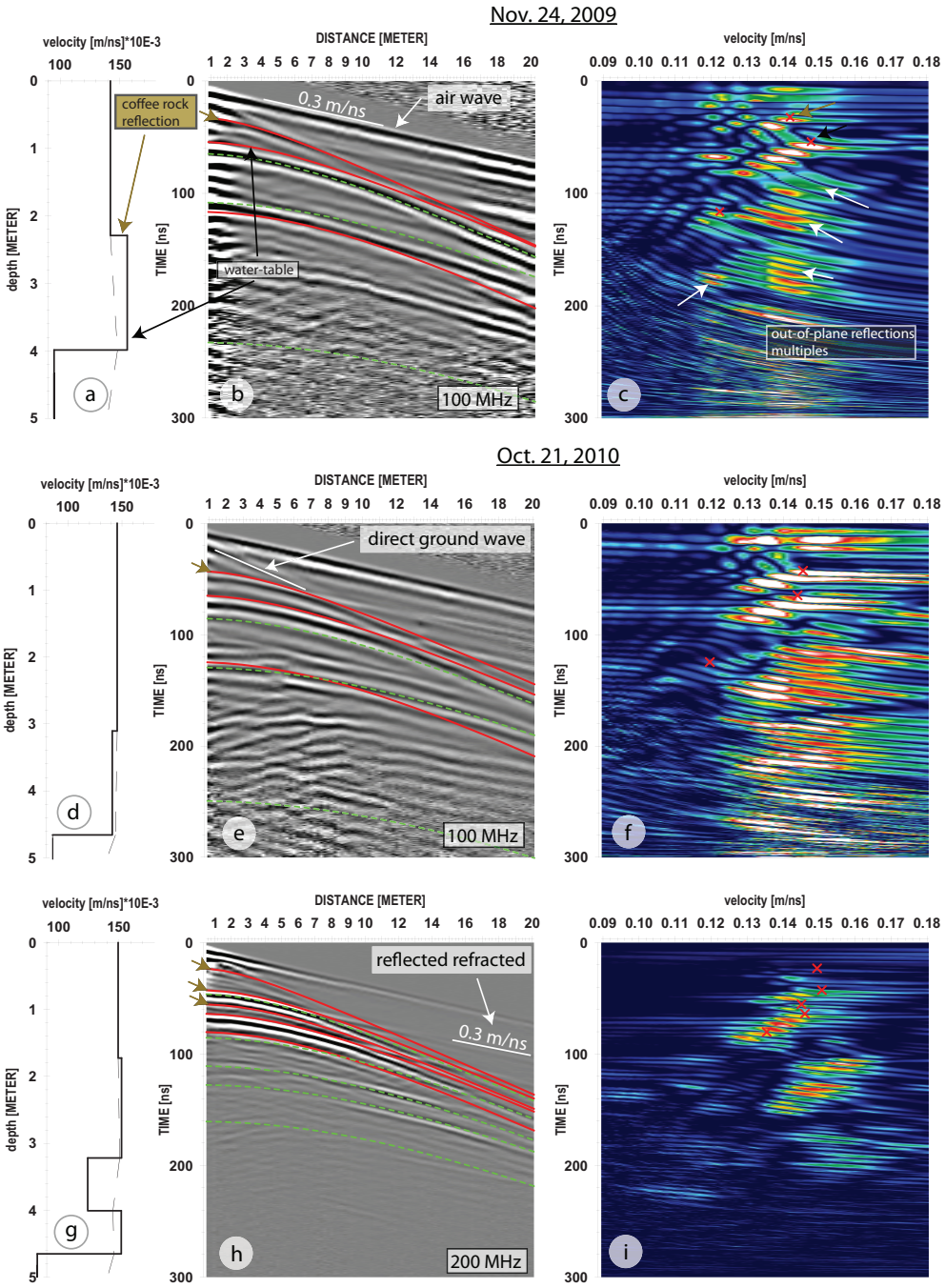

Figure 4.14: *CSP gather over anomaly A performed on the day of 3D GPR (b) and the ERI (e), (h) surveys; velocity profiles in (a), (d) and (g) are obtained from semblance analysis shown in (c), (f) and (i). Note the increased resolution of the 200 MHz data in (e) compared to the 100 MHz data in (h).*

GPR information and "reasonable" assumptions about the layer properties. I will test two approaches of quantitatively capturing water bearing layers. One is based on reflection strength or reflectivity, which I compare with a more elaborate estimation of layer dielectric permittivity based on travel time delay.

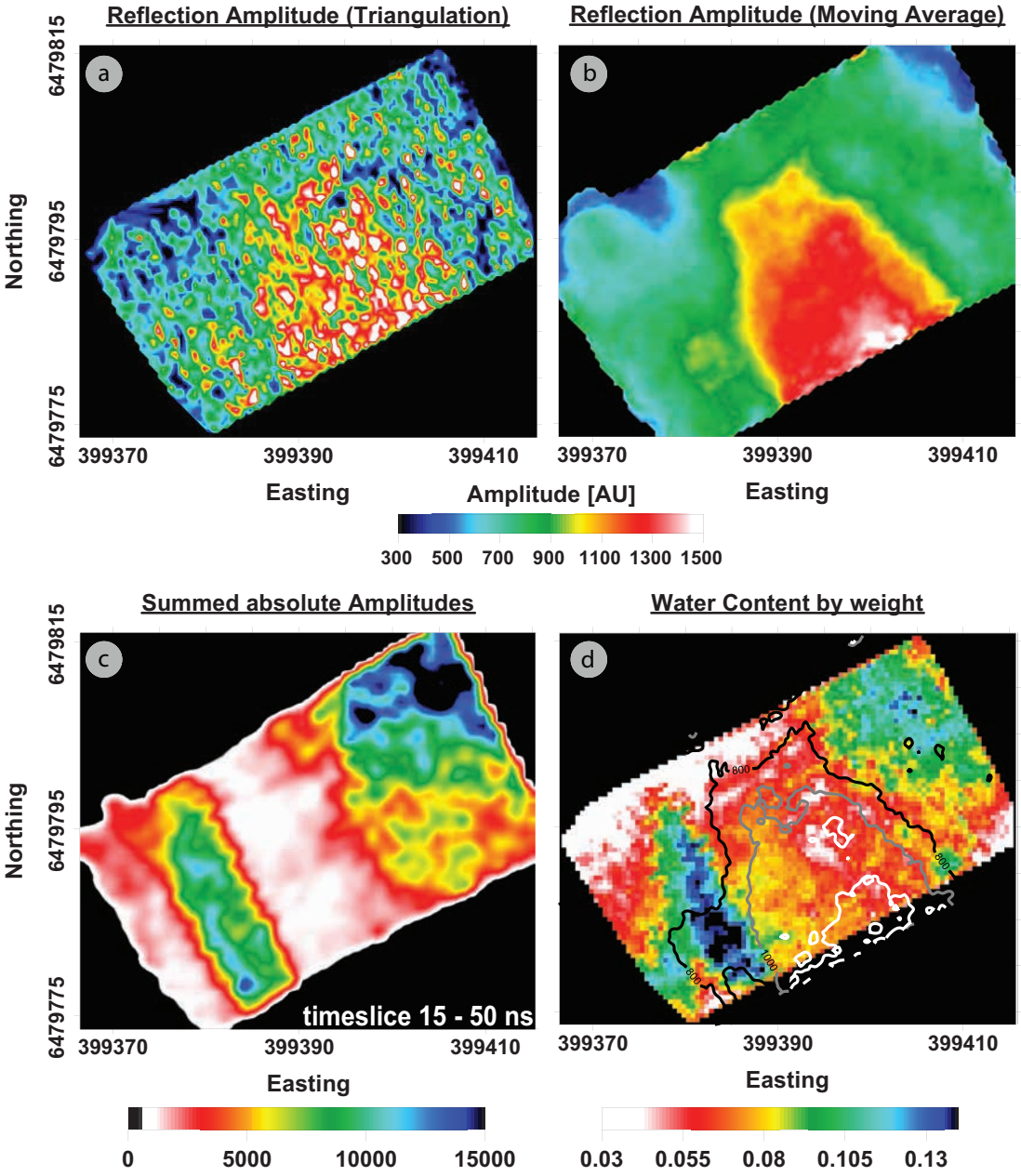

Figure 4.15: *Unsaturated zone characterisation based on water table reflection strength (a) and (b), unsaturated zone response (c) and water table travel time (d) demonstrates that reflectivity of vadose zone reflectors and travel time show good spatial correlation. Comparison of triangulation (a) and moving average gridding (b) of water table reflection amplitudes reveals that amplitude picking produces noisy results represented by (a), thus a smoothing gridding operator is necessary (b). Water table reflection strength, however, is spatially not as well correlated with the unsaturated zone water content as estimated from the travel time (c).*

To verify and laterally map the hydrogeologic significance of the reflectors within

the unsaturated zone at this site, I will estimate the layer velocity based on the travel time delay below the layer to infer layer dielectric permittivity and water content. This approach is similar to work done by *Gloaguen et al.* (2001), *Grote et al.* (2005) and *Lunt et al.* (2005). We know from this site and other direct field observation that the cemented soil horizons are typically 0.1 - 0.6 m thick. This thickness is called d. By further assuming a sequence of i) high velocity ν_b in interval above the layer (i.e. clean sand), ii) a low velocity ν_d within the layer and iii) the high velocity ν_b below the layer followed by iv) the water table (see Figure 4.16), we can write the total vertical two-way traveltime for normal incidence through all layers to the water table as

$$t_{twt,D} = \sum_i t_i = 2 \sum_i \frac{d_i}{\nu_i} = \frac{2}{c} \sum_i d_i \sqrt{(\epsilon_{r,i})} \quad . \tag{4.3}$$

with d_i, ν_i are thickness and velocity of the layer i, respectively, and c the speed-of-light in vacuum. For the three layer case (background medium and retentive layer) we obtain for the travel time t_d in the layer, and layer velocity ν_d

$$t_d = 2\frac{D-d}{\nu_0} + \frac{d}{\nu_d} = \frac{2}{c}(D-d)\sqrt{\epsilon_{r,b}} + d\sqrt{\epsilon_{r,d}} \tag{4.4}$$

$$\text{and} \quad \nu_d = \frac{2d}{t_d - \frac{2(D-d)}{\nu_b}} \quad \text{or} \quad \epsilon_{r,d} = \frac{c^2}{\nu_d^2}. \tag{4.5}$$

with D the total depth to reflector and $\epsilon_{r,b}$ and $\epsilon_{r,d}$ the relative dielectric permittivity of background and layer, respectively.

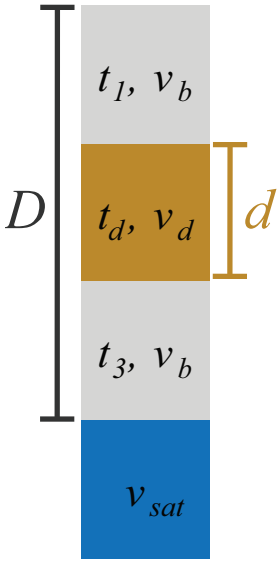

Figure 4.16: *Layer model used for calculating travel time t_d within soil horizon with thickness d surrounded by homogeneous soil, thickness of total unsaturated zone is labelled D.*

An average background velocity of $\nu_b = 0.155$ m/ns has been determined from

diffraction hyperbolae from various depth levels where the unsaturated layer is absent. Note that the velocity model obtained from semblance analysis of the multi-offset gather (Figure 4.14c) also predicts an average velocity of around 0.15 m/ns for the full unsaturated zone. For calculating layer velocity using equation 4.4, D has to be determined at every position. This is done by assuming a flat water table which is at a constant horizontal position, and by accurately measuring topography. The water table position is determined at a cross-section interval without reflection above the water table and using the background velocity of 0.155 m/ns. The depth to water table is then topographically corrected based on that velocity and equation 4.2. Note that the depth to the water table and the background velocity do not greatly influence the layer velocity. In this analysis, the main parameter that controls the layer velocity is the layer thickness d. A very thin layer for example results in extremely low layer velocity ν_d, while a thick layer produces small velocity contrasts between layer and background. The graph in Figure 4.13b shows the influence of layer thickness on layer rel. dielectric permittivity estimate (black lines) for a selected transect. The thick black line at values around 4 shows the dielectric permittivity estimated without a layer (i.e. homogeneous background velocity). Estimated permittivity values do not vary significantly in the case no layer is introduced and range between 3.9 and 4.3. In contrast, there is a good correlation between high dielectric permittivity and the occurrence of reflection above water table. The layer existence can therefore be assumed to be the cause of the increase in total travel-time. By including a layer with finite thickness d, large contrast in dielectric permittivity is introduced throughout the profile. The next thinner black line in Figure 4.13b is the permittivity prediction for a 0.6 m thick layer. Note that this results in overestimation of dielectric permittivity where no layer contributes to the overall travel-time for example between 15 and 27 m. Permittivities now range between 4.5 and 8. The thinnest layer (i.e. thinnest black line) with $d = 0.3$ m produces the highest permittivity anomaly of 14 - 15. To obtain water content estimates from dielectric permittivities I used Topp's equation (i.e. equation 3.10) and the Lichtenecker-Rother (LR) model given by equation 3.12 with a porosity of 40 $\%$, solid matrix permittivity of 5.5 and α exponent of 0.55. Note that the laboratory measurement results were not yet available at the time of this study, so these values were the best guess at the time (*Strobach et al.*, 2011). Due to the large uncertainty attributable

to layer thickness, and the relatively good agreement between laboratory results and the Topp-curve, I decided that the analysis would not be improved by including the knowledge from lab experiments. The increased solid dielectric permittivity for the LR equation was originally chosen to represent the fine material which could have had a higher dielectric permittivity than quartz. The volumetric water contents were then translated to gravimetric water content in order to compare to values reported by Froend (personal communication). Water contents were then gridded on a regular 25 cm grid using a kriging algorithm (see example for $d = 0.4$ m in Figure 4.15d).

The water content analysis described above is not very accurate. However, the main message is that the layer produces a significant increase in the traveltime of water table reflection below. In order to estimate the overall traveltime, I had to make simplistic assumptions (i.e. flat reflector, constant background velocity) and provide accurate topography information that prevent this type of analysis for large scale application being truly useful. Despite this issue, due to the good correlation between layer reflection and increase in traveltime, I will now try to quantify the reflection strength from layers above the water table and correlate this map with the travel-time map. I chose the simplest possible algorithm to estimate the energy that is reflected from interfaces within the unsaturated zone by summing absolute amplitudes within that time interval on a trace by trace basis. As we will see later, there is some justification why that could potentially represent the overall significance of that layer. In order to obtain realistic amplitude information, an application of amplitude preserving exponential gain to each trace plus migration and topographical corrections were applied to the data. The migration algorithm successfully collapsed diffraction hyperbola and did not lead to strong artefacts such as migration smiles. This is further evidence for an appropriate velocity estimate of 0.155 m/ns. The upper 15 ns were not used for interpretation due to strong direct air and ground wave arrival and the topography correction. A value of 50 ns was the lower limit at which no water table reflection energy occurred for all profiles. Absolute amplitudes were then summed for an interval between 15 and 50 ns as indicated in Figure 4.13a and gridded using kriging shown as map in Figure 4.15c. Maps c and d in Figure 4.15 show that areas of high reflected energy compare favourably with high water content areas.

The last analysis, which was considered simple and possibly effective in providing

information about the distribution of material or reflectors within the unsaturated zone, was analysis of reflection strength from the water table. Reflection strength in this context is not the reflectivity of the water table reflector. The idea is that layers above the water table reflect parts of the emitted energy back to the surface, and only portions are transmitted (i.e. proportional to the reflectivity of the layer, compare to equation 4.1). The process of reflection and transmission occurs twice, firstly for downgoing, and then again for upgoing waves. A further consideration was the possibly higher electrical conductivity which would further attenuate EM energy due to fine grains in the clay fraction and elevated water content. Several approaches that estimate reflection strength were tried including maximum peak and trough, RMS amplitude and envelope which all resulted in nearly identical maps. Here I show a result which was obtained by picking the maximum envelope (i.e. Hilbert transform) of the water table reflection (map a and b in Figure 4.15, isoline overlay of b in d). Although the general trend is similar to the other two types of analysis, the spatial noise was greater. The same kriging parameters that were used in c and d did not provide a reasonable image. A triangulation method was tested which resulted in a similar noise level compared to the kriging. Finally, a moving average gridding resulted in an acceptable parameter distribution map that represented the general spatial trends. Some high-energy areas have been smoothed out by this approach, especially in the eastern area. The overall result shows increased energy in the central part where no reflective layer reduces the transmitted energy. The overall correlation between areas with layers (best represented in map c) and the water table reflection strength is not as good as overall reflection strength and time delay (i.e. maps c and d).

Multi-Offset GPR

The objective of multi-offset common-shot point gathers (CSPGs) is to obtain vertical velocity distribution based on the curvature or moveout of subsurface reflection arrivals. CSPGs were acquired over the 3D GPR test-site area at Whiteman Park on three occasions. They are a reliable surface GPR method to confirm velocities obtained from diffraction hyperbola analysis in common offset data, and at Whiteman Park to validate the layered earth assumptions made in regards to layer interval velocity estimation based on water table reflection time as described in the previous section (i.e. layered earth model in Figure 4.16).

The interpretation of CSPGs is based on i) direct wave slope analysis, or ii) reflection hyperbola moveout analysis, or iii) refracted wave analysis. Slope analysis of direct waves is usually simple, except for the case where shallow waveguides produce dispersion. In the case of dispersive direct wavefields, the area around the direct wave arrivals is typically muted and a slant stack, that is a transformation into the frequency-slowness domain, is performed (*Park et al.*, 1998; *Van der Kruk et al.*, 2006). Modal wave propagation models can be used to invert the observed dispersion curves. Chapter 5 will further discuss this interpretation scheme. An interpretation of ii) reflection moveout is done with semblance analysis. The hyperbolic moveout equation and stacking is used to produce a velocity versus time image. Peak values indicate velocities which produce maximum semblance, that are those velocities that produce flat reflectors when hyperbolic moveout (or normal- moveout) is applied. Starting from the shallowest reflection, an interval velocity profile is built up using Dix's formula to convert moveout velocities to interval velocities (*Dix*, 1955). Care has to be taken that for a minimum phase wavelet (i.e. the normal GPR wavelet without deconvolution, opposed to a zero-phase wavelet), the maximum in the semblance plot does not coincide with the layer interface position. The correct position is situated at the true first arrival, which is compared to the maximum in the semblance plot towards slightly higher semblance velocity and at earlier time. See for example *Booth et al.* (2010) who propose a backshifting method that is implemented into ReflexW (*Sandmeier*, 2012). In this work I manually interpreted the correct position. CSPG analysis is strongly dependent on reflected wavefields being present in the data. This implies that gradual permittivity changes that do not produce a reflection cannot be captured by this method. In that case, this method will produce an average interval velocity above the next deeper reflection. To resolve a layer, reflections from upper and lower layer interface have to be distinguishable. Thus, the combination of velocity and antenna frequency (i.e. wavelength) provides theoretical bounds for the minimum resolvable layer thickness, which is approximately half a wavelength.

The antennas available for CSPGs at Whiteman Park are unshielded with center frequencies of 100 MHz and 200 MHz. A 100 MHz CSPG was done over the western "coffee rock" patch anomaly A on the same day as the 3D GPR acquisition (November 24, 2009; Figure 4.14b). On October 21, 2010, the day of resistivity measurements, a

CSPG was acquired with 100 MHz and 200 MHz antennae (4.14e and h, respectively). The direction is northwest and initially intended to be over anomaly A, but probably missed it by a few meters and ended up in between anomalies A and B. Three additional CSPGs were performed on August 8, 2011 with 200 MHz frequency shown in Figure 4.17b, e and h. All had a northwest strike, one over anomaly A (called west), a second over the clean sand interval (middle) and the third over anomaly B. The examples illustrate potential vertical resolution that can be obtained by 100 MHz versus 200 MHz antennae (Figure 4.14), and associated uncertainty and possible pitfalls due to multiple and out-of-plane reflections (4.17), as will be further discussed in the following.

For the Whiteman Park test site the higher frequency antennas of 200 MHz are preferable as they provide higher resolution and sufficient depth of penetration. For other sites with deep unsaturated zones (e.g. High Hill Road in chapter 6), a combination of low and high frequency is necessary to achieve the desired resolution and depth of penetration. Figure 4.14a and b are the results from a 100 MHz experiment, which show, when compared to Figure 4.17a and b collected at the same location, that the lower frequency does not resolve upper and lower interface, while the 200 MHz data reveal distinguishable reflections from top and bottom of the layer. Note that the layer response in the surface CO data was comparable on both dates.

A source of misinterpretation in CSPGs are out-of-plane reflections, reflections from surface targets and multiples. All Whiteman Park examples show several events in the semblance plot after the water table reflection arrival (i.e. Figures 4.14c, f, i and 4.17c, f, i). Those events have equivalent, or higher semblance velocity when compared to the water table reflection. This would imply that there are layers below the water table with velocities comparable to or faster than those of the vadose zone, which is physically unreasonable at this site. In fact, this observation is unreasonable for most sites, because in the case of a hanging water table (which would be the only geologic situation where unsaturated velocities could occur below the saturated zone) one would typically expect an impermeable layer below the first saturated zone. In most cases those are clay layers with high electrical conductivity. Those layers would dissipate the EM energy and reflections from below would be attenuated and therefore remain undetected at the surface. An example of this geologic situation is the Tangletoe test site (see Figure 6.3).

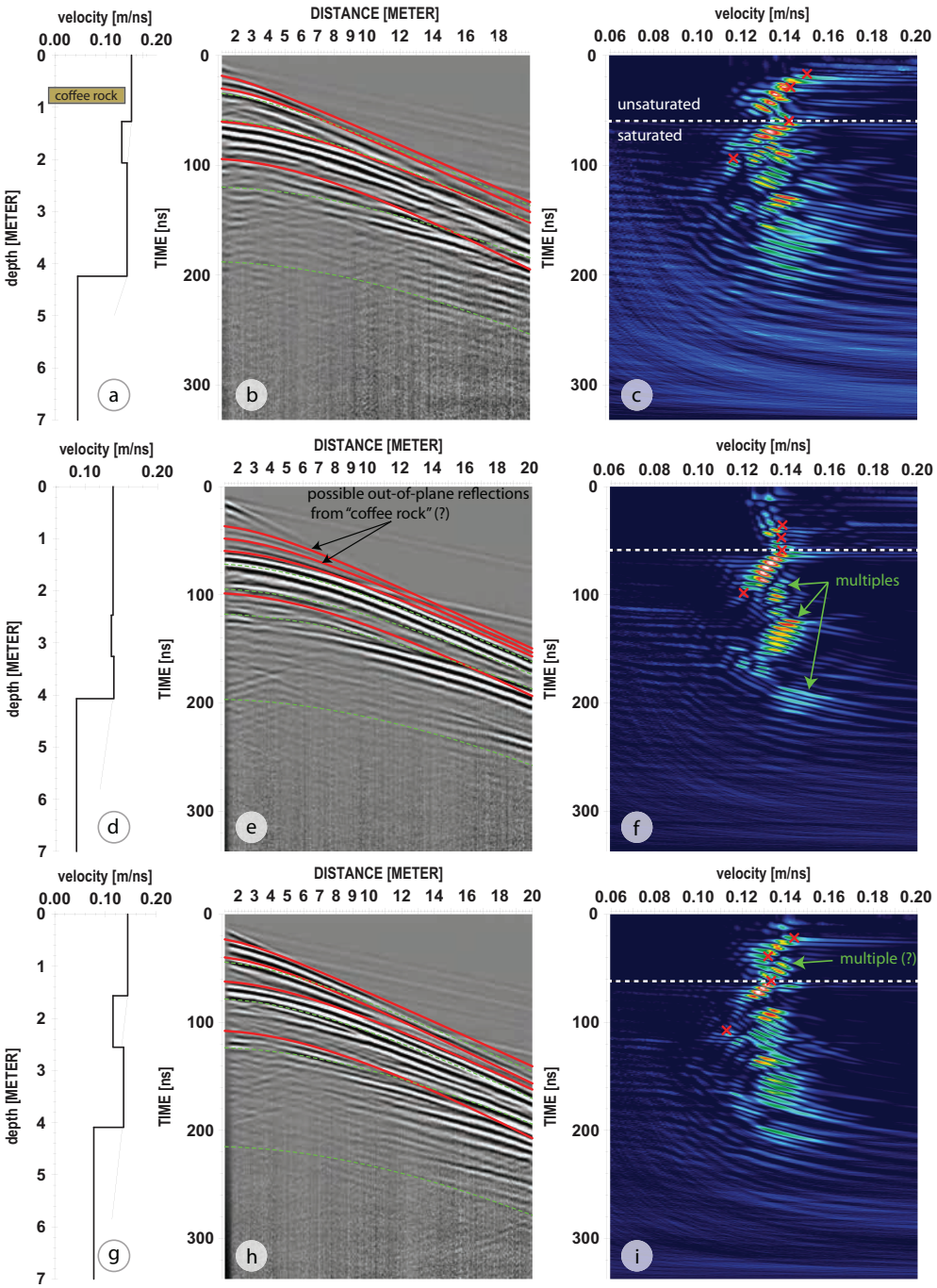

Figure 4.17: *Semblance analysis (right) of common shot point gathers (middle) and resultant velocity profiles (right) at 3D Whiteman Park survey site, over the western anomaly A (upper), the clean sand interval in the central survey area (middle) and over anomaly B in the east (lower). Note the weak unsaturated zone reflection at the central clean sand interval (e), while (b) and (h) show strong reflections leading to low velocity vadose zone horizons (a) and (g).*

The high velocity events that appear at late times in the Whiteman Park CSPGs can either be out-of-plane reflections that originate for example from the side boundary of a ”coffee rock” patch, or reflections from surface targets or multiples. Theoretically predicted multiples are indicated as dashed green lines in the semblance plots. This

type of prediction makes identification possible. Typically, only the strongest reflectors produce noticeable multiples. A good example is shown in Figure 4.18e where the water table reflection is very strong due to absence of reflections within the unsaturated zone. The water table multiple, indicated with a dashed grey circle, arrives at twice the traveltime (i.e. 120 ns) of the first water table reflection (i.e. 60 ns), and at the same semblance velocity (i.e. approx. 0.14 m/ns). Note that in this Figure, the unnormalised correlation is plotted instead of semblance. The unnormalised correlation is similar to the semblance, but the energy is not normalised (*Sandmeier*, 2012). It therefore allows distinguishing between strong significant events, and weak reflections in case the input data provide true relative amplitudes. It is obvious from the semblance images that out-of-plane reflections and multiples are quite common in these low-loss environments and even appear in the unnormalised correlation. Due to the rapid decrease in amplitudes below the water table, it can be challenging to identify reflections that originate from below the water table in unnormalised semblance plots. In most cases, derived velocity from below-water table reflections was highly uncertain due to interference with stronger unsaturated multiples. Interpretation was then purely based on the semblance response as reflections were not clearly visible on the CSPGs.

The 200 MHz CSPGs in Figures 4.17b, e and h show the significance of unsaturated zone "coffee rock" layers on the GPR response at the Whiteman Park test site. The corresponding unnormalised semblance images in Figures 4.18d, e, f further show that the weak reflection in the middle transect (Figure 4.18e) is not as significant compared to reflections in the western and eastern patches of "coffee rock"in Figure 4.18d and f, respectively. The energy visible in the semblance plot of the middle CSPG(Figures 4.17f and 4.18b) is possibly an out-of-plane reflection from the "coffee rock" patch, and does not result in a significant low-velocity layer (Figure 4.17d). As resolution was sufficient to resolve upper and lower layer interface of anomalies A and B in CSPGs (Figures 4.17b and h), the resultant interval velocity profiles shown in Figures 4.17a and g include a low-velocity horizon between approximately 1.3 and 2 mbNS over anomaly A (a), and between 1.5 and 2.5 mbNS over anomaly B (g). While these estimates for the unsaturated zone are prone to error, the most certain average interval velocity and depth estimate can be derived from the strong groundwater table reflection. In many applications it is sufficient for depth to water table estimation, or for

migration velocity. However, in this example, the interpretation of interval velocities revealed low-velocity layers in the unsaturated zone where ”coffee rock” is expected. The layer thicknesses appear slightly too large compared to neutron moisture data derived from close-by boreholes (see Chapter 6, Figures 6.13 and 6.20a) which could be due to inaccurate hyperbola determination from the semblance plots. Note that by reducing layer thickness for example by shifting the hyperbola that originates from the lower layer interface towards earlier times, the layer interval velocity would decrease, which would probably be more realistic. However, this does not affect the interval velocity recovered below the layer. Note that the interval velocity below the layer is very similar to the uppermost interval. This confirms the assumptions made in the previous section in regards of the layered earth model for layer velocity calculation from water table reflection time.

Electrical resistivity imaging

The direct current (DC) electrical resistivity imaging showed areas of increased electric conductivity that correlate well with the occurrence of ”coffee rock” reflectors. The overall electrical resistivity of the vadose zone is very high with values of several thousand Ohm-meter (Ωm). The clean sands that surround the water retentive soil horizons show resistivity values between 10,000 - 30,000 Ωm. The water retentive soil layers have less resistivity, between 2,000-5,000 Ωm. These values have the same order of magnitude as the DC-resistivity estimation from the low-frequency end of the dielectric measurements derived in section 3.2.5.2 for very dry, and slightly moist material. For a ”coffee rock” with water contents above 10 $v\%$, the laboratory measurements would have predicted resistivities of less than 1,000 Ωm. There is a slight discrepancy between observation and expectation. However, the resistivity tomography was not constrained to result in a structured model with large resistivity gradients (smooth inversion). Thus, the inversion resulted in a smoother model with possibly a larger anomaly with smaller resistivity contrast and therefore overestimates ”coffee rock” resistivities and layer thickness. Overall, the ”coffee rock” is rather resistive and does not attenuate the GPR signal greatly which is supported by the high water table reflection amplitudes (i.e. low GPR wave attenuation) beneath these layers.

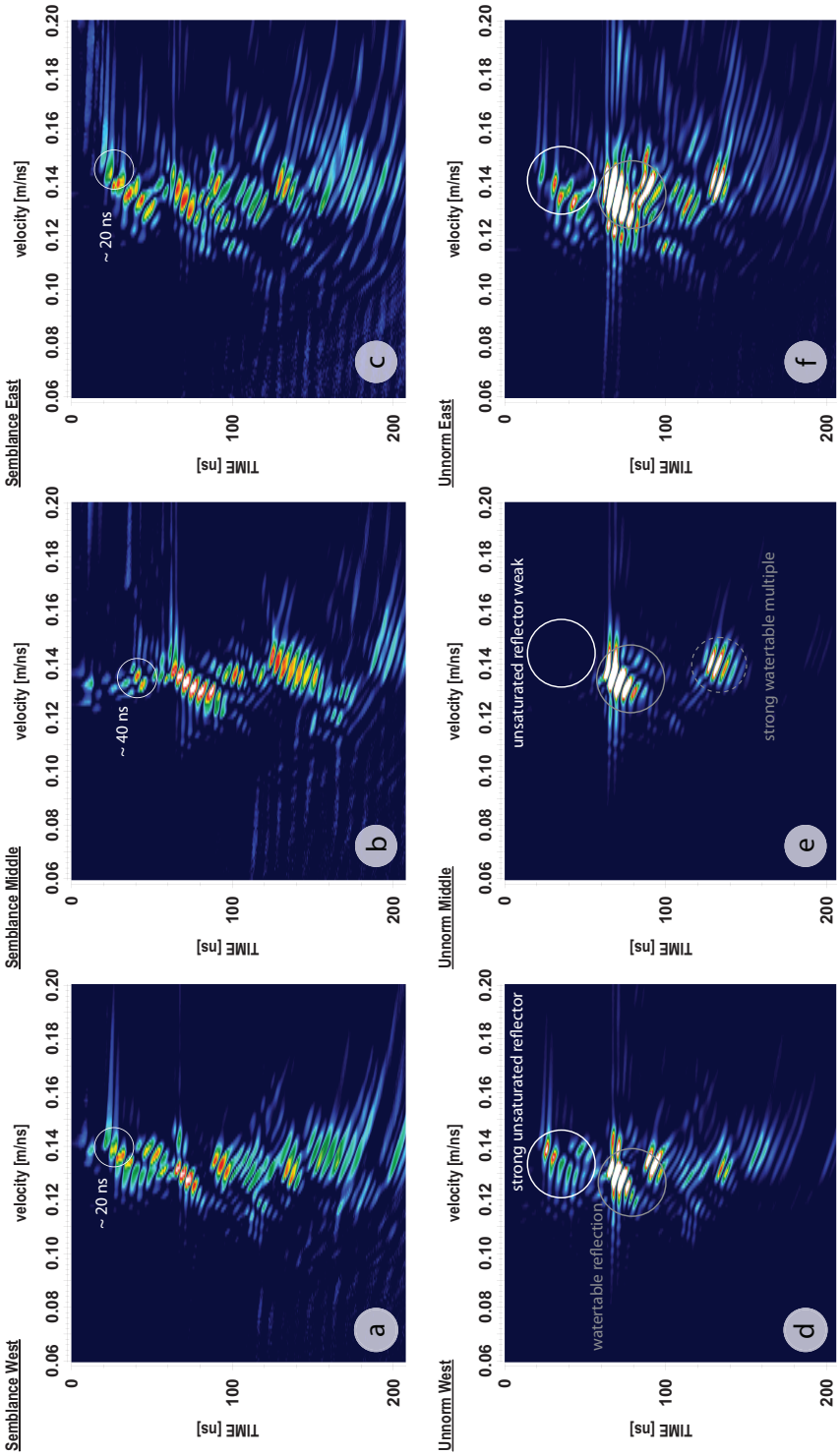

Figure 4.18: *Comparison between semblance (a, b, c) and unnormalised correlation (d, e, f) images. Note the difference in energy of unsaturated zone reflections in semblance plot compared to the unnormalised correlation result for the middle section in (b) and (e), respectively.*

4.2.3.5 Conclusion

The 3D investigation at Whiteman Park provides a useful insight into some aspects of GPR interpretation based on common offset surface reflection profiles and common-shot point gathers. This case study also enhances the knowledge and understanding of "coffee rock" response to GPR waves. The following conclusions can be drawn from this example:

- "coffee rock" produces a strong reflection in GPR data
- layer velocity of water retentive layer is greatly reduced
- "coffee rock" distribution is patchy, and properties change on a 10 m scale
- bulk vadose zone water content can be estimated from travel time analysis of GPR reflector based on the assumption of geologically flat water table
- total reflection strength from unsaturated zone reflectors correlate well with interval velocity and can provide a simple tool to laterally map spatial distribution and significance of "coffee rock" layers
- reflection strength from the water table is influenced by vadose zone layers, but not as strongly as expected. It probably does not provide a high-certainty analysis technique for large-scale characterisation of unsaturated zone properties
- "coffee rock" at Whiteman Park shows high resistivity and does not attenuate radar waves significantly
- multi-offset data acquisition can be used as an additional technique to quantify unsaturated zone interval velocity, resolution limitations are frequency dependent, and the highest frequency antenna available for this study might be too low to resolve 0.2 - 0.4 m thick layers with high certainty

4.3 Large-Scale Reflector Analysis

In the previous section, two example radar profiles have been interpreted in terms of geologic and hydrogeologic characteristics, with special focus on reflectors within the

unsaturated zone and the water table reflection. In this section I attempt to visualise and derive the larger-scale characteristics of those reflectors in respect to their potential hydrogeologic influence on groundwater recharge. Many aspects of the following analysis are based on the learnings from the small-scale survey at Whiteman Park.

4.3.1 Dataset

The data to be analysed in the following were acquired by GeoForce (now Groundprobe Ltd.) and Baigent, both local contractors in Perth; and some of it myself. All the datasets were measured with the shielded 250 MHz Mala antenna. The GeoForce data were acquired in three stages before 2007 and covers the whole of the Gnangara Mound area (note that stages 1 and 2 were also acquired with the Mala 50 MHz unshielded rough terrain antenna).

As mentioned previously, the data were provided with coordinates and topography. The precision and spatial resolution of the GPS topography that was provided with the GPR transects shows great deviation from the DEM provided by Water Corporation. The discrepancy between DEM and GPR-trace topography was inconsistent and too difficult to correct. Some GPR/GPS transects revealed a possibly linear trend in misfit compared to the DEM topography. This trend could be related to daily variations in satellite positioning. The absolute GPR elevations were tens of meters above or below the actual elevation level. In some instances, jumps occurred within the GPS data. In any case, the accuracy and precision of the GPR/GPS elevation is insufficient for high-accuracy depth to water estimation analogous to the Whiteman Park 3D example. Instead of correcting the elevation data by filtering, I used the DEM and Digital Surface Model (DSM) LiDAR data provided by Water Corporation. Using these data for topographic correction proved to produce better results compared to the original data (see for example Figure 4.1). Another advantage using large-scale DEM/DSM GIS information is the self-consistency of these datasets. For the purpose of this study, these elevation models suffice to roughly estimate depth to reflector.

4.3.2 Analysis Based On Reflector Configuration

In a first order attempt to capture the spatial extent and significance of layers within the unsaturated zone, the first reflection event was picked from the radargrams. The depth

to that first reflector was then calculated using velocities of 0.13 m/ns, 0.145 m/ns and 0.16 m/ns in order to cater for possible lateral velocity variations and uncertainty (symbol position in profiles Figure 4.19 are with 0.145 m/ns, grey lines above and below are with higher and lower ground velocity, respectively). Topography and water table information was extracted from the DEM/DSM and water table grids provided by Water Corporation (see grids in Figure 2.1 and for the GPR line positions in Figure 4.20a, b, c). Depth to first reflection represents the upper clean sand interval, which is assumed to be characterised by the water retention properties of the clean sand (i.e. impact on groundwater flow and recharge is minimal). The philosophy behind this type of analysis is that it represents a conservative approach in identifying areas of potential recharge impediment. Because the first reflector is not yet characterised for its significance, and deeper reflectors are not taken into consideration, layer influence on recharge is rather over- than underestimated. Identification of a shallow reflector leads to the interpretation of a potential water retentive soil profile, although the reflector might be insignificant. On the other hand, where depth to first reflector is large, or where the first reflector coincides with or originates from the water table, are high-certainty maximum recharge potential areas. As opposed to a shallow first reflector and deep water tables, which result in higher potential water retention .

To obtain a quantity that can describe the influence on recharge based on the concepts stated above, I combined the parameters reflector depth R_1, and separation between water table and reflector R_2 into a *zero-order* retention potential coefficient RP_0:

$$RP_0 = \log\left(\frac{\sqrt[4]{R_1^2 + R_2^2}}{\arctan^2(\frac{R_1}{R_2})}\right). \tag{4.6}$$

This equation was chosen based on the cross-plot of water table depth versus picked reflector depth (Figure 4.21). The $\sqrt{R_1^2 + R_2^2}$-term is the length, and the $\arctan(\frac{R_1}{R_2})$-term the angle from the vertical when considering the cross-plot points as vectors. The smaller the angle, the larger is the discrepancy between depth to reflector and water table depth (i.e. shallow reflector, deep water table) which results in a higher retention potential (i.e. larger RP_0-value). Due to the logarithm, RP_0 can become negative. However, equation 4.6 does not provide deeper physical meaning and was solely chosen based on its applicability. The y-axis in Figure 4.21 is the depth to water table instead of the distance between first reflector and water table. This is in order to

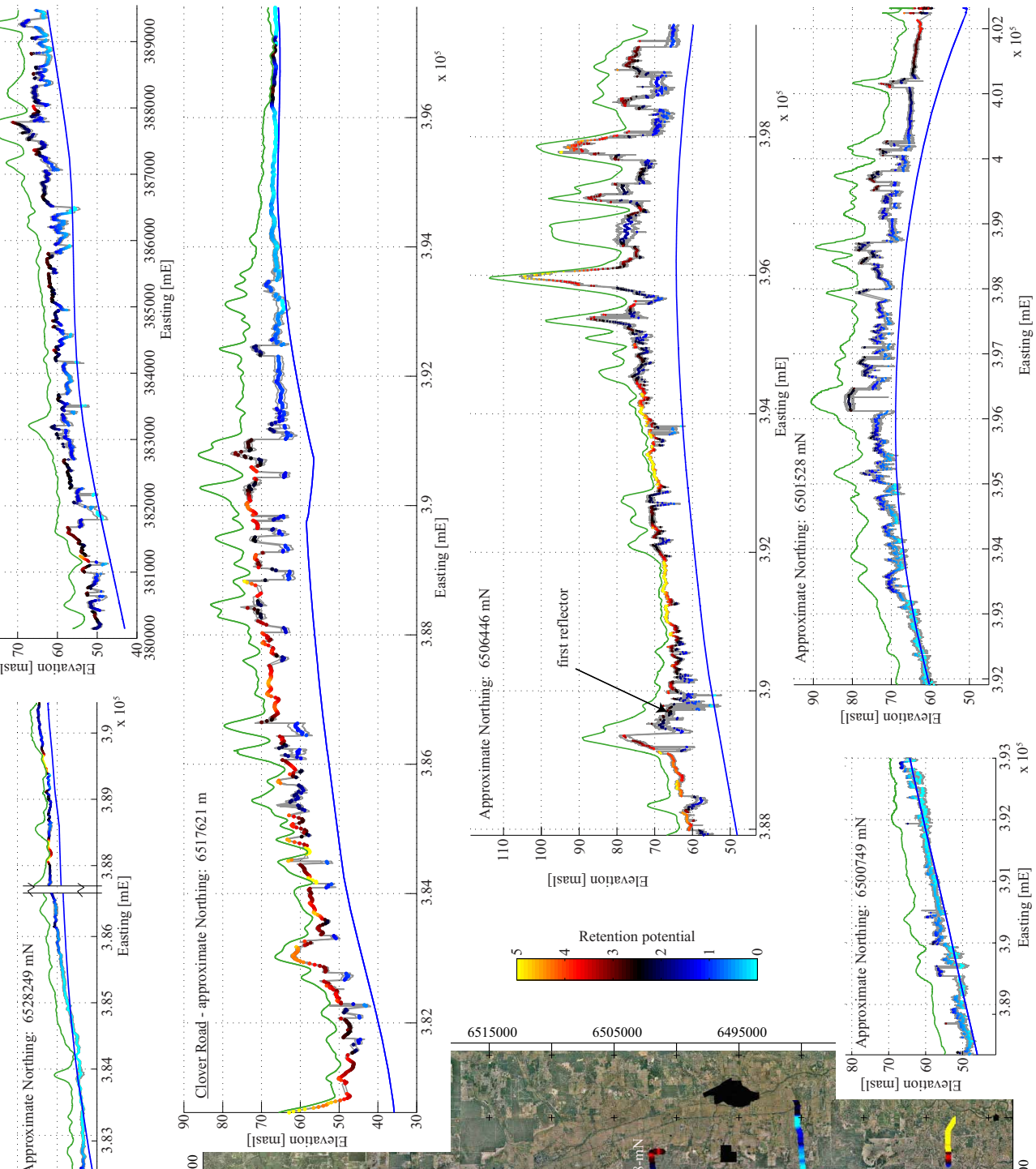

Figure 4.19: *Map of zero-order retention potential (left) and example radar profiles that illustrate the lateral distribution and variability of depth to first reflector. Symbol locations in the profile plots represent reflector position using a ground velocity of 0.145 m/ns for depth estimate and topography correction, and extracted topography values from DEM/DSM data (green line). The grey lines represent reflector position calculated for upper and lower ground velocity limits of 0.16 and 0.13 m/ns, respectively. Profile plot symbol colour is calculated using equation 4.6 (see also Figure 4.21). Note that profile sections where signal return was insufficient have been disregarded from interpretation (i.e. the western part of the study area).*

display points that plot around the line with a slope of -1 are those where the picked first reflection is close to the water table.

Results and Discussion

Figure 4.20d shows the spatial distribution of first-reflector depth, based on a ground velocity of 0.145 m/ns. The map and profiles in Figure 4.19 show the resultant retention potential in a hot-cold colour map with hot colours (yellow, red) signifying high retention potential, and cold colours (cyan, blue) high recharge potential. The grey lines in the profile plots represent upper and lower layer position estimates based on low and high ground velocities, respectively (i.e. 0.13 and 0.16 m/ns). As those grey lines are an indication for depth inaccuracy, we can infer from these plots that variations in ground velocity, either laterally or temporal, have little effect on the interpretation.

The central mound area, that is the Pinjar area and north up to Tuart Road, are dominated by shallow reflectors and deep water tables. This indicates high retention potential in the *zero-order* retention potential classification scheme. The areas north of Tuart Road and south of Pinjar on the other hand have shallower water table and the first reflection is deeper. The colour map in Figure 4.19 should be interpreted such that cyan colours are areas where the first reflection likely represents the water table, which means that a window exists for infiltrating water. Dark blue colours are already characterised by an impeding layer which is well separated from the water table, but at depths of more than approximately 5 mbNS (i.e. depending on the water table depth). Red and yellow colours indicate shallow and superficial reflectors, respectively. The yellow colours on the Clover Road transect for example represent the reflector parallel to the surface which has been described beforehand. In this case this reflector is missing, such as is the case for most of Tuart Road, the first reflector is slightly deeper, shows topography, is patchy, and thus creates slightly small retention potential values.

The certainty of identifying large retention potential using this analysis scheme is poorer than correctly identifying high recharge potential. Although a clear and significant GPR reflector exists in the near-surface, it might not be significant for groundwater recharge. The radargram reflection profiles have shown that in the case where a shallow reflector exists, several deeper unsaturated zone reflections follow. Although they

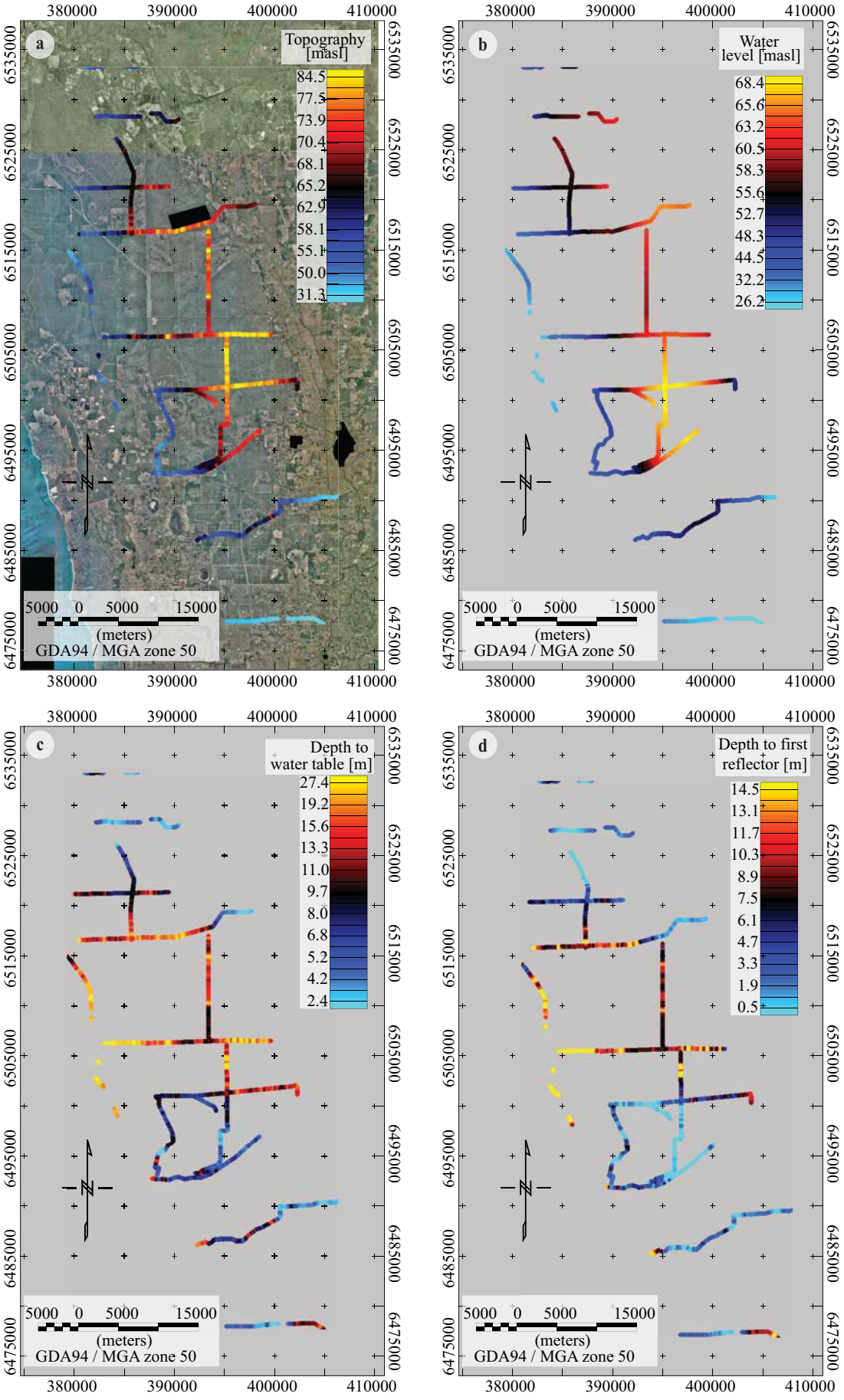

Figure 4.20: *Grids of extracted DEM topography (a), water table (b), depth to water table (c) and reflector depth (d) for large-scale GPR transects. The constellation of depth to first reflector and its distance to the water table (i.e. combination of (c) and (d)) has been used to define a zero-order water retention potential to laterally characterise the soil profile for recharge windows and impedance zones.*

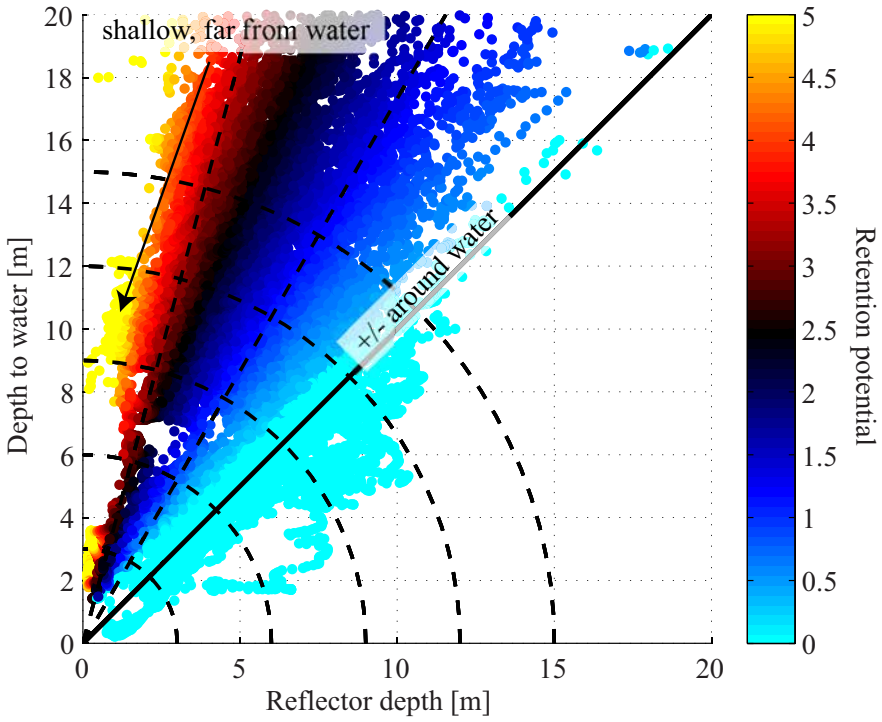

Figure 4.21: *Crossplot showing distribution of water table versus reflector depths determined for the stage 2 GeoForce dataset (i.e. Tuart Road, Clover Road, etc.). The symbol colour represents the retention potential as defined by equation 4.6. The dashed lines and circles are possible limits for a classification scheme which considers data points as vectors and defines limits based on angle to vertical and vector length, respectively. Those are meaningful values as they define separation between first reflector and water table (i.e. angle) and depth to water table (i.e. length).*

might also be insignificant for recharge, the likelihood of some influence on recharge is greater than otherwise. The areas that are concerned with uncertainty have to be further investigated in terms of different levels of layers, and their possible significance on water retention and recharge impediment. This will be the objective of the following section where analysis is based on amplitudes.

Conclusions

The depth to the first GPR reflector represents the soil interval that contains clean sands without noticeable internal structure and absence of GPR reflections. Because small changes have been shown to be able to produce strong reflections, the absence of shallow reflections where deeper reflections are present is a high-certainty indicator for a clean sand interval. Where shallow reflectors exist, it is not certain whether they influence water infiltration (and hence recharge), or if they are of minor importance for the unsaturated flow regime. Thus, we can be more confident of identifying higher recharge zones, but less confident in identifying zones that inhibit recharge.

The profiles at Gnangara Mound show several areas where the water table constitutes the first reflector within the soil profile. This occurs where the water table is shallow, or significant reflectors are patchy or absent (cyan/blue symbols in Figure 4.19). On the contrary, the area between Pinjar (south) and Tuart Road (north) has been identified to contain shallow reflections and deep water table, providing the possibility of water retention and reduced recharge.

4.3.3 Analysis Based On Reflection Amplitudes

Based on the findings from the 3D survey at Whiteman Park (see section 4.2.3), an analysis of the large-scale unsaturated zone reflection response based on cumulative amplitudes is presented. The analysis will be done on example profiles Tuart, Airfield and Clover Road.

The Whiteman Park 3D survey demonstrated that the summed unsaturated zone amplitudes were spatially well correlated with the unsaturated zone velocity and therefore moisture content and water retention. Due to the extent and data size of the large-scale 2D radargrams, the processing was modified to make the analysis manageable. In the small-scale investigation, the 2D radargrams were migrated in order to move

diffracted energy to its point of origin. For large-scale profiles of several tens of kilometres, migration is challenging due to lateral and vertical velocity variations (compare for example discussion for Figure 4.5 where deeper diffractions did not collapse). Appropriate migration thus requires a 2D velocity profile, which would be a laborious task to obtain. The most efficient 2D migration algorithm, the fk-Stolt migration, has the limitation of constant velocity. Thus other, less efficient migration such as Kirchhoff migration would become necessary. After I performed some careful analysis on smaller scale sections, using 2D velocity profiles as input for Kirchhoff migration, I found that the interpretation of the profile is not necessarily improved. As expected, diffraction hyperbolae collapse to a point, and reflector dips are corrected. But this is only crucial in 3D radar surveys, where the objective is to locate structures from time- or depth slices. An example from the literature is the 3D GPR cube from Shark Bay shown in *Jahnert et al.* (2012) which would have been contaminated by diffractions without 3D migration, and reflector dips could have been affected by false moveout. Most reflectors at the Gnangara Mound are not steeply dipping, and the large-scale data are 2D rather than 3D. Consider for example the WC6 reflector, which showed local dip between $10° - 20°$, and represents one of the steeper dipping interfaces. Diffraction hyperbolae, on the other hand, are a common feature in radargrams. I found that they are also indicative of the reflector and can aid interpretation without contaminating other parts of the data. Compare for example the two types of reflectors A and B at Whiteman Park, where A was characterised by a distinct, flat reflection with two diffractions originating from the sides of the slab, while reflector B showed a multitude of diffractions which gave the reflector its characteristic appearance.

If migrating 2D profiles is not a necessity from an imaging perspective, migration is perhaps not necessary at all for large-scale amplitude estimation. For the scale of interest in this study, that is hundreds of meters to several tens of kilometres, the resolution of GPR radargrams does not have to be on a decimetre scale. In fact, the large-scale radargrams shown in Figures 4.4 and 4.6 have already been downsampled from 4 cm to 1 m trace increments by stacking traces. These profiles show that the main, sub-horizontal reflection events are preserved, while diffracted energy has been largely removed by the stacking process. Therefore, stacked sections are adequate for further analysis of bulk vadose zone reflection response without the significant concern

of overemphasising diffracted energy.

To obtain bulk summed amplitudes from the unsaturated zone, I processed the data with a simple processing flow that preserves relative amplitudes. In order to compare different lines with each other, relative amplitudes should not only be consistent within one profile, but also throughout different datasets. I chose to use a spherical divergence compensation twice (i.e. amplitude at time t multiplied with t^2). This gain function resulted in satisfactory energy enhancement for events arriving at late times. Results are comparable to the automatic "energy decay"-gain in ReflexW (gain function determined based on average low-frequency envelope of all traces of profile). To reduce file size, I stacked traces to 3 m spatial increments, and downsampled the time sampling to 1 ns. Thus temporal aliasing occurs for frequencies above 500 MHz, which are beyond the bandwidth of the 250 MHz antenna used for data acquisition. Spatial aliasing is not a problem for the objective of this study, as reflectors in the tens of meter range are accurately captured with a 3 m trace increment.

Further processing prior to gaining and stacking included: DC-shift removal, static correction, 2D median-filtering and background removal. The final stacked profile was topography corrected using a constant velocity of 0.15 m/ns according to equation 4.2. Processed profiles were exported from ReflexW and imported into Matlab for further analysis. To obtain absolute energy return from the unsaturated zone, I manually picked what I believed to be reflections from or close to the water table. Regional minimum water table information (i.e. the summer 2005 grid provided by Water Corporation, see Figure 2.1) was extracted in order to aid in identifying the correct approximate water level. I then summed the envelope (Hilbert transformation function in Matlab) values within the unsaturated zone interval starting at a depth of 1.2 mbNS and the water table (see red line in Figure 4.22). This step is equivalent to summing absolute amplitudes (compare Whiteman Park example).

Additionally, the energy within the first 1.2 mbNS is summed and within an interval of 3 m below the picked water table position. The energy within the upper 1.2 mbNS is largely contaminated by air- and direct wave arrivals. Background removal is meant to reduce the early-time record to energy that represents near-surface reflections. In practice with large-scale data the background removal was rarely successful in removing air- and ground wave energy. As street or track surface materials change, so does the

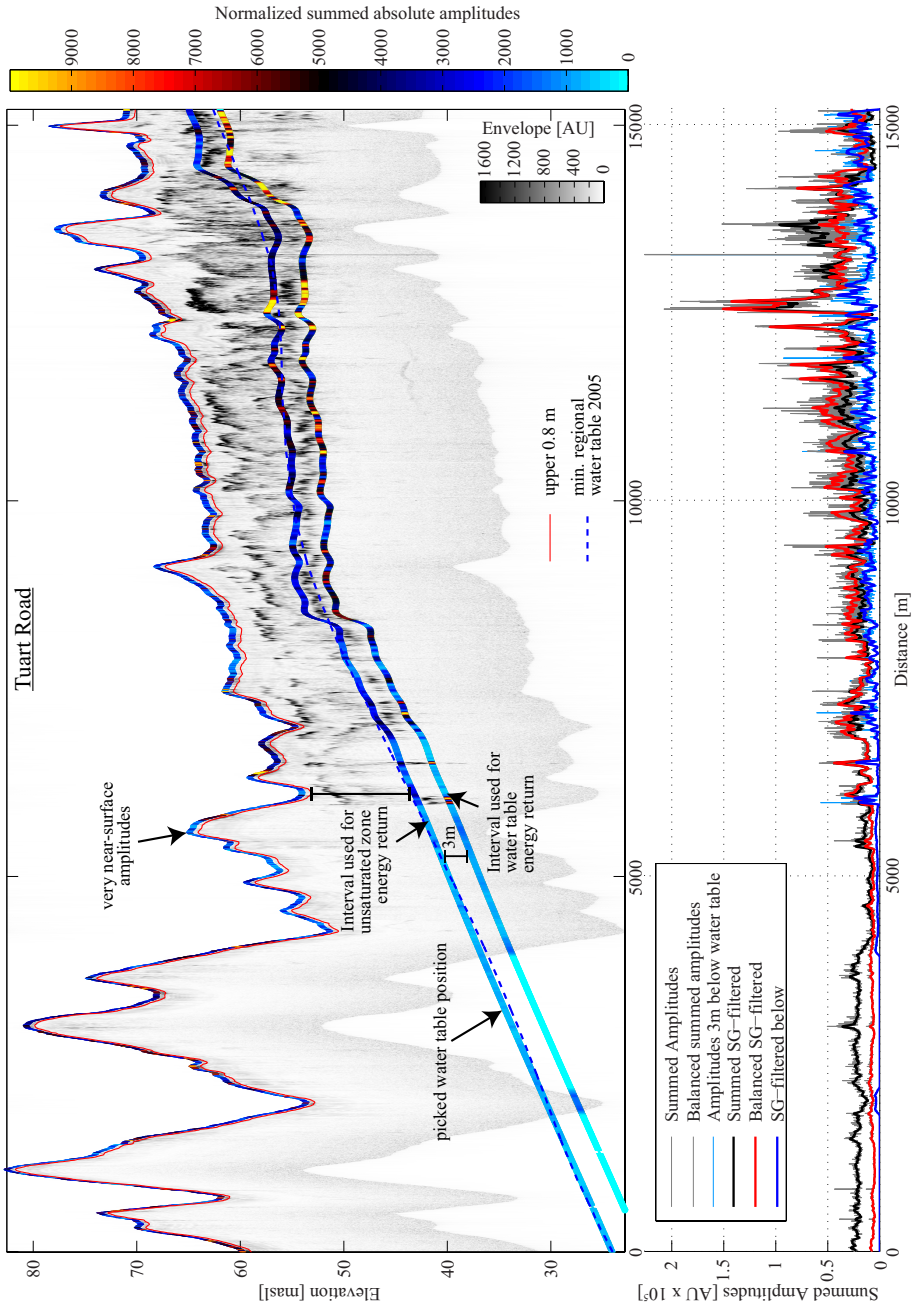

Figure 4.22: *Amplitude analysis of Tuart Road transect represented as coloured scatter plot (upper) of summed envelope values of the upper meter, the unsaturated zone and the area 3 m below the interpreted water table position. The PRAMS min. water table 2005 is shown as dashed blue line which correlates well with the interpreted GPR water table position. The lower graph shows the filtered unsaturated zone response with (red) and without (black) balancing based on unsaturated zone thickness before (grey, cyan) and after Savitzky-Golay filtering (black, red, blue). Note the effect of balancing in the western part of the profile where the noise of a large unsaturated zone without reflectors accumulates to relatively high unsaturated zone response. Amplitude values are in arbitrary units (AU) which represent the value (i.e. voltage) digitised by the Mala radar system.*

antenna coupling and the direct ground wave arrival time. To circumvent this problem, I reduced the background removal to spatial intervals where direct- and air arrivals appeared to be consistent on a kilometre scale. On a smaller scale, variations in direct/air arrival are then indicative of areas with different ground conditions, as for example the wetlands on Clover Road (see Figure 4.24). Another feasible approach for background removal is fk-filtering (reject the energy band around 0 wavenumber in fk-spectrum). While this filtering procedure typically removes air- and ground-wave energy effectively, it is a delicate process and artefacts are easily introduced. However, I applied the fk background removal after the average subtraction which further improved the image.

After retrieving amplitude versus distance curves for the abovementioned intervals (see lower graphs in Figures 4.22, 4.23 and 4.24) further filtering was applied to smooth the result. Different moving average filters were tested and the Savitzky-Golay filter produced best result (Matlab function "sgolayfilt"). This filter smoothes the data while preserving extreme values unlike normal moving average or median filtering.

Another post-processing step is to balance energy based on the thickness of the unsaturated zone interval (i.e. summed energy is divided by the interval thickness). This step was tested in order to reduce the accumulation of noise energy for example below sand dunes (i.e. large unsaturated zone).

Prior to presenting results obtained from amplitude analysis, I will briefly discuss some challenges of this method and propose potential solutions. The EM energy that returns to the surface in reflection GPR is determined by i) sequence of impedance contrasts in the subsurface for example due to layering (i.e., this is what we want to measure) and ii) attenuation due to energy loss. Laterally varying ground conditions, such as changing surface materials (e.g. limestone track versus clean sand track) or subsurface material properties (e.g. dispersed clay in "coffee rock" layers, different water contents) can introduce different degrees of attenuation. Thus, some areas produce generally stronger ground response compared to others. In the radar cross-sections, we have observed this effect for example due to changing formations (e.g. Spearwood dunes versus Bassendean Sand) or changing sediments within one formation (e.g. wetlands can show enhanced or weakened ground response compared to clean dune sand). By applying a constant gain function to all environments, the sig-

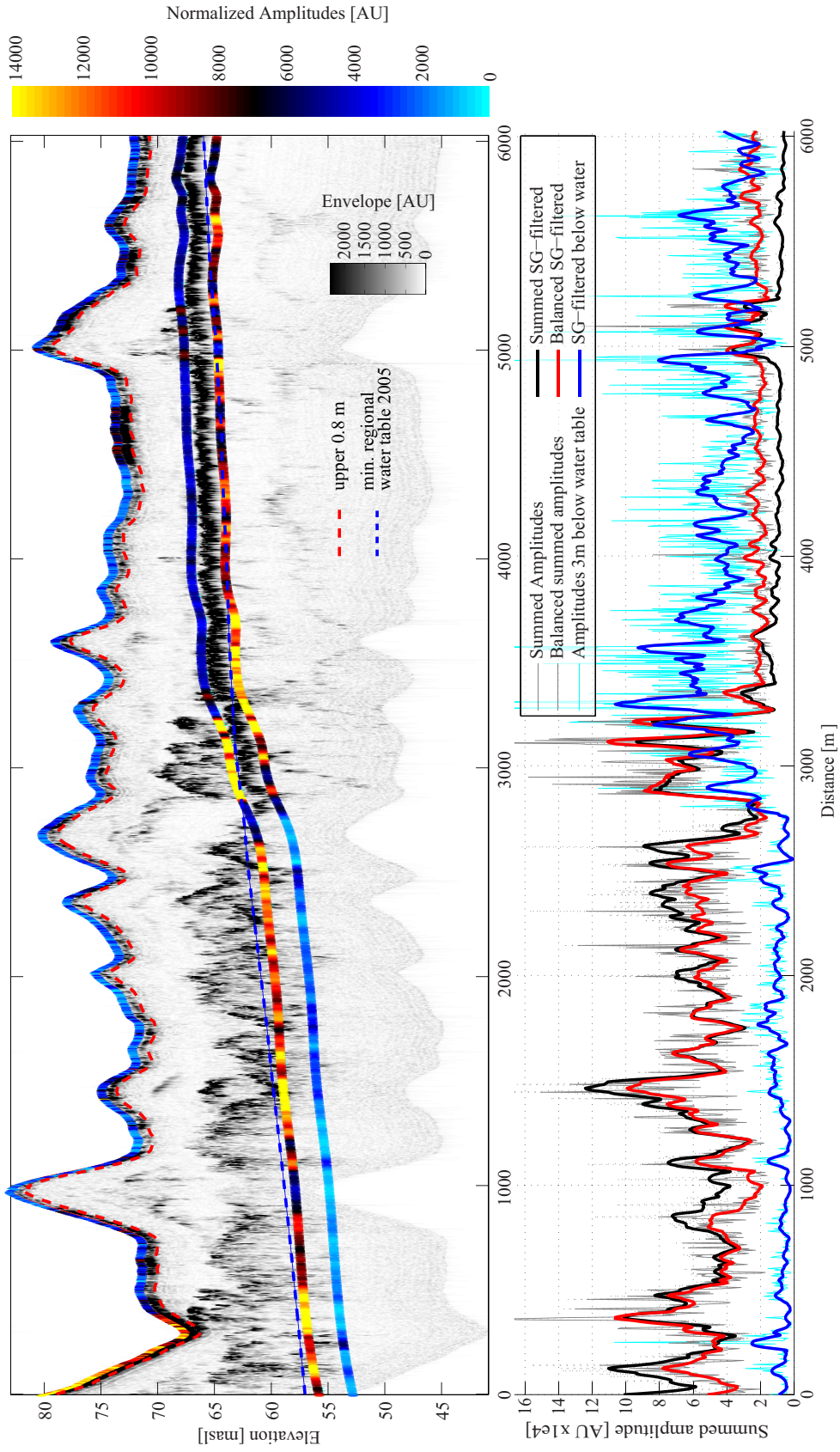

Figure 4.23: *Amplitude analysis for the Airfield Road transect analog to Figure 4.22. Note the increase in water table response in the eastern part of the profile where the unsaturated zone response is small, which is a strong contrast to the western part of the profile where unsaturated zone response is strong while water table response is weaker.*

nificance of reflectors can be greatly underestimated in lossy areas, when compared to areas where sediments are electrically resistive and have low dielectric permittivity.

One way to decrease the errors related to this problem is to compare the unsaturated zone response with the water table reflection response as already done in section 4.2.2 for the test-site WC6a. This comparison can be indicative of higher attenuation rates related to attenuation within the very shallow subsurface or the deeper unsaturated zone. However, some ambiguity exists when interpreting the strength or significance of the water table reflection. A weak water table response can either indicate unsaturated zone attenuation, or reduced reflectivity for example due to a gradual interface transition. As previously discussed, a gradual moisture content gradient in the capillary fringe might result in frequency dependent reflectivity up to the point where no reflection occurs above some threshold frequency (*Bano*, 2006). Another reason for low reflectivity from the water table is due to gradual increase in water content throughout the entire unsaturated zone, which results in low impedance contrast at the water table although the transition of the interface is abrupt. Despite these ambiguities, one can in general identify co-occurrence of weak response from the unsaturated zone and the water table, and classify sections with this constellation as areas with low fidelity. In the case of a strong unsaturated zone response and a weak or absent water table reflection, one could assume that the reflector is attenuative, and therefore hydrogeologically more significant due to elevated clay content. The significance of those areas could be interpreted as potentially more influential for unsaturated flow.

Results And Discussion

The results of smoothed interval amplitude analysis are presented as coloured scatter plots in Figures 4.22, 4.23 and 4.24 (upper) above the envelope transect for Tuart, Airfield and Clover Roads, respectively. Symbol position of i) the very near-surface, ii) the unsaturated zone and iii) the interval below water table are plotted at the position of i) the surface elevation, ii) the water table and iii) 3 m below the water table (see Figure 4.22 upper). Note that amplitudes in these figures are normalised relative to the maximum value of each interval. The Tuart and Airfield Road scatter plots are those obtained after balancing energy based on interval thickness, while the Clover Road unsaturated zone scatter plot is the unbalanced result.

Below these transects are the line scatter plots which show the effect of filtering and

energy balancing (Figures 4.22, 4.23, 4.24, lower). Unfiltered unsaturated zone data are shown in grey, while the filtered balanced and unbalanced curves are displayed in red and black, respectively. Those plots represent the true summed energy as recovered from the envelope transect. The effect of amplitude balancing becomes evident from these plots. The western part of Tuart Road for example contains mainly noise (i.e. Spearwood dunes), which accumulates and produces some energy due to the great thickness of the unsaturated zone interval (black line in Figure 4.22 lower). This is corrected, or balanced, by taking into account unsaturated zone thickness (red curve). For Clover Road the unsaturated zone in the eastern part is very small, resulting in an overestimate of amplitudes relative to the areas with normal unsaturated zone thicknesses (red curve in Figure 4.24 lower). Thus amplitude balancing is not appropriate for this part of the profile. Figure 4.25 shows the different amplitude intervals on a map as coloured symbol scatter plots (amplitudes not normalised).

Amplitude analyses of the three example profiles demonstrate good agreement with the findings of the initial first-reflector depth analysis. Areas which had a low retention potential, such as the eastern part of Clover Road, are again identified as low-retention areas as no major reflectors exist above the water table. The cumulative amplitude analysis in the central area shows lateral variation in reflector significance (compare to the depth-to-reflector analysis which showed more continuous shallow reflector for example at Clover Road). So while the two approaches seem to deliver similar results, especially in the low retention potential areas, there are some difference in the areas that may have retention potential.

Similar to the first reflector analysis, areas with high recharge potential are readily identified with high certainty. That is, in case of no reflection energy within the unsaturated zone, but with high reflection response from the water table, the certainty of having a clean sand without significant layers above the water table is very high. This is for example the case for eastern part of Clover and Airfield Road (cyan colours in the unsaturated zone plots in Figures 4.25b). To identify these areas correctly, it is important not to balance amplitudes relative to the unsaturated zone thickness (i.e. divide estimated value by unsaturated zone thickness).

Analogous to the cross-plot classification for the reflector depth analysis, one can produce a cross-plot based on water table energy return and unsaturated zone energy

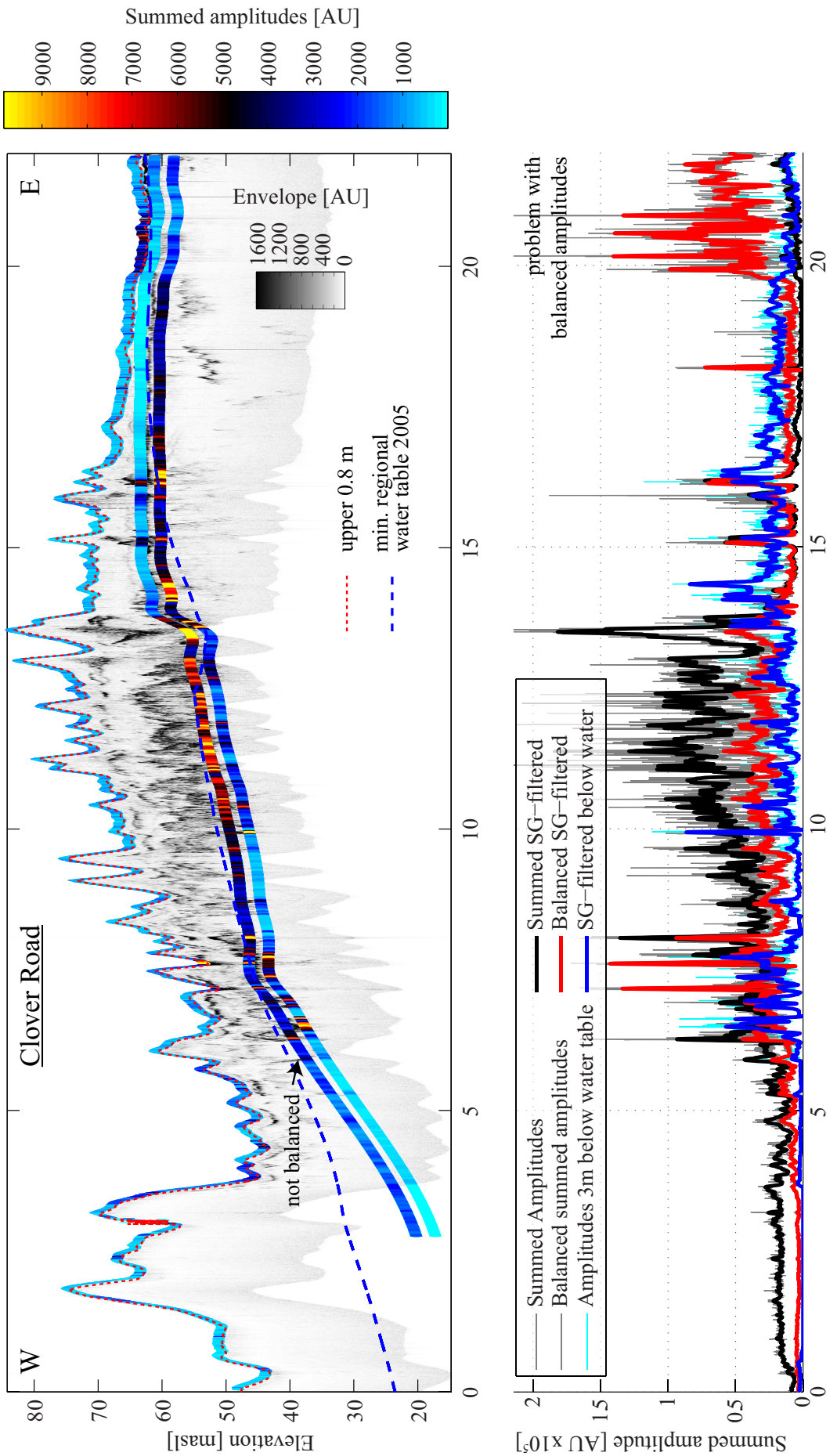

Figure 4.24: *Amplitude analysis for the Clover Road transect analog to Figure 4.22. Note the false effect of balancing energy based on unsaturated zone thickness in the eastern part of the transect where the water table is close to the surface and balanced energy is greatly emphasised.*

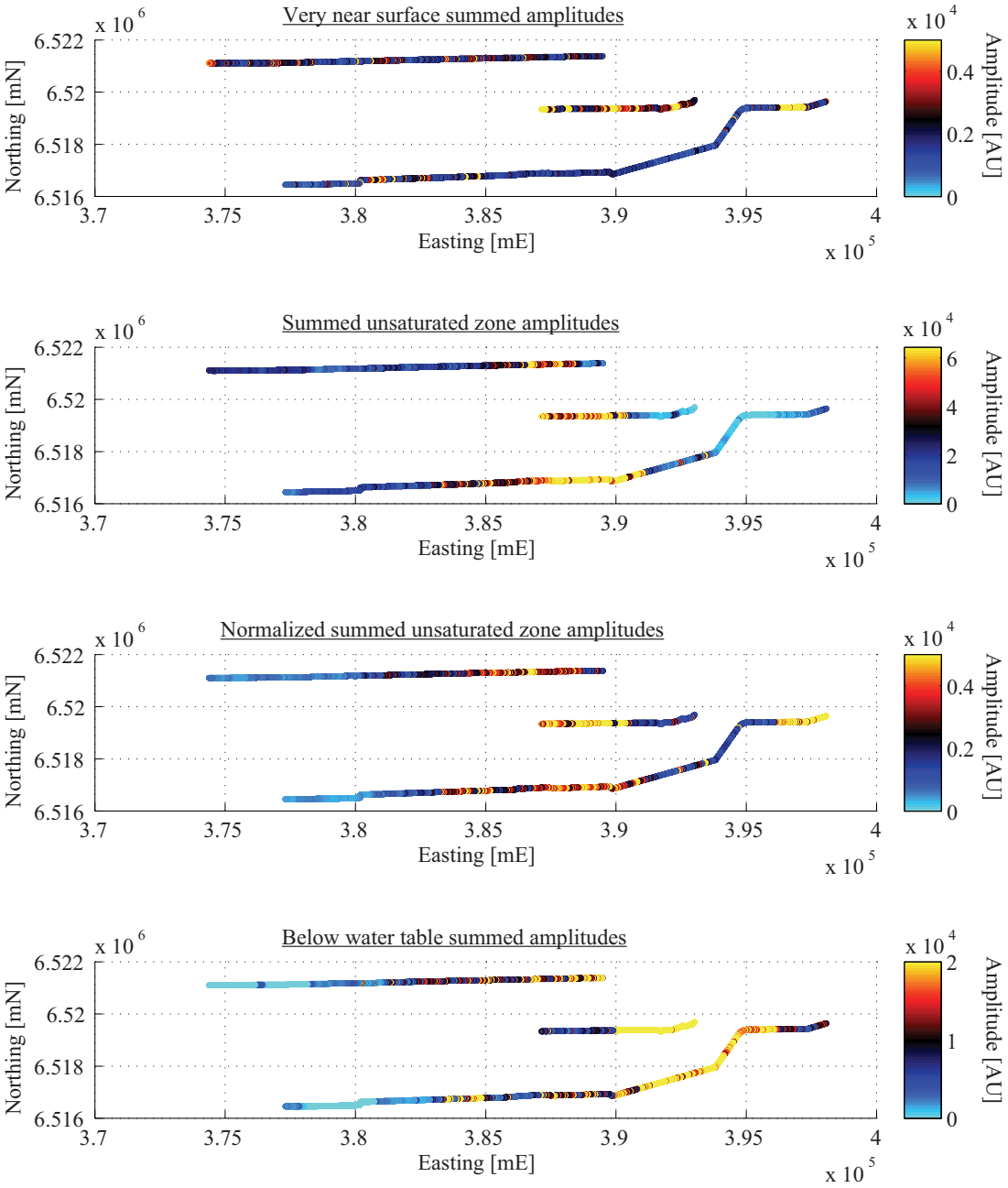

Figure 4.25: *Amplitude maps showing from north to south Tuart, Airfield and Clover Road summed envelope results for intervals 0 - 1.2 m (a), 1.2 m - above water table ((b), balanced in (c)) and 3 m below the water table (d).*

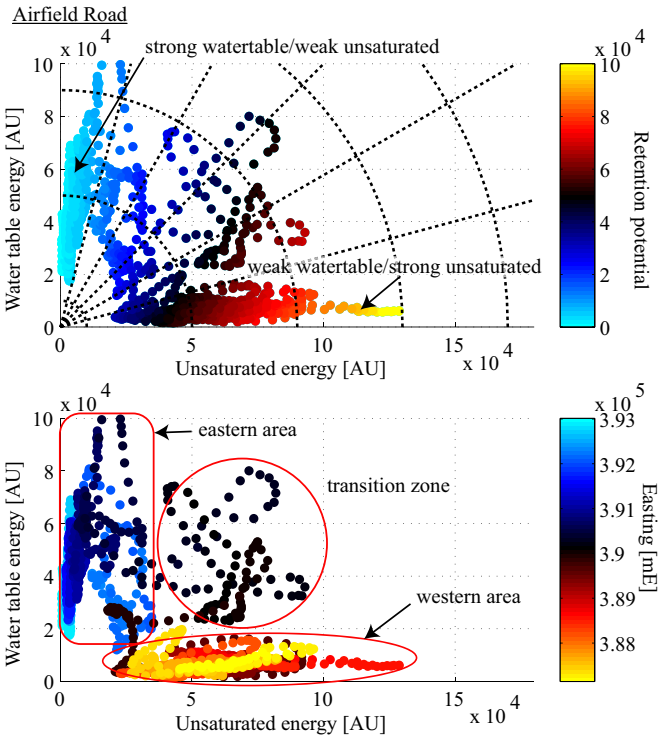

Figure 4.26: *Crossplot showing summed envelope values of water table versus unsaturated zone response from Airfield Road example. Colourmap represents proposed amplitude-based retention potential RP_1 (upper) or easting (lower). Warm colours (yellow/red) for RP_1 represent a constellation where a strong unsaturated response coincides with a weak water table response indicating high retention potential, and cold colours (cyan/blue) representing high recharge potential for areas where weak unsaturated zone response coincides with strong water table response. The upper plot shows the spatial occurrence of high retention potential in the west (warm colours) and high recharge potential in the east (cold colours).*

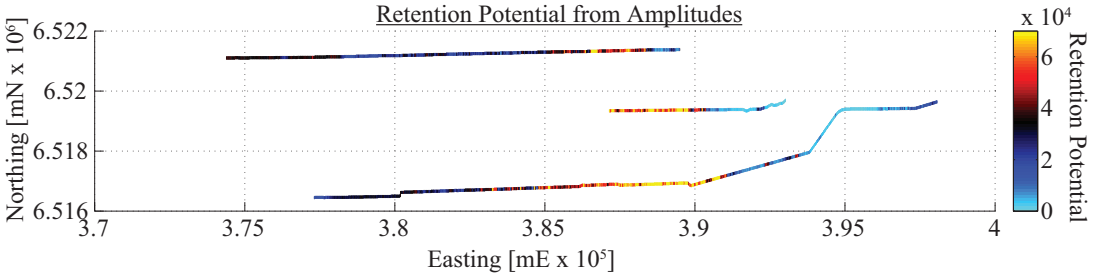

Figure 4.27: *Map of RP_1 amplitude retention parameter distribution for Tuart, Airfield and Clover Roads. Note the higher retention potential in the central area when compared to the eastern section where the water table is the first significant reflector in the radargrams.*

return as shown in Figure 4.26 (upper). The symbol colour here is again derived from the angle and length of a vector described by the plotted data pair (compare with RP_0 derived from reflector position, Figure 4.21, equation 4.6). To obtain a retention potential for amplitudes which is founded on the above stated considerations, I defined RP_1 as

$$RP_1 = \arctan\left(\frac{A_{\text{Unsat}}}{A_{\text{Sat}}}\right) \cdot \left(\sqrt{A_{\text{Unsat}}^2 + A_{\text{Sat}}^2}\right)^{0.6} \tag{4.7}$$

with A_{Unsat} and A_{Sat} the absolute summed energy for unsaturated and water table response, respectively. In the case the energy return from around the water table is strong and the unsaturated zone response is weak, RP_1 is small. Areas where a strong unsaturated zone response coincides with weak water table response, RP_1 becomes largest. The symbol scatter plot in Figure 4.26 is an example for the Airfield Rd transect where the western part is characterised by high retention potential, and the eastern part beyond the "step" in water table has low unsaturated zone retention potential.

Figure 4.28 (lowermost) shows an alternative approach to determine unsaturated zone response from amplitudes by weighting depth and amount of layers in the vertical profile. This proposed method should be understood as an outlook and preliminary attempt in order to identify the need to automatically extract reflector occurrence and number of reflectors. Figure 4.28 shows (upper to lower) i) the envelope, ii) summed envelope and iii) weighted summed envelope of the Clover Road transect. The lowest value (i.e. deepest value for each trace) in the summed envelope section (middle) is identical to the summed energy values shown as scatter plot in Figure 4.24 for the unsaturated zone. The lowermost section in Figure 4.28 shows a weighted summed envelope (or abs. amplitude) plot where the summed value A at depth d_n is calculated according to

$$A(d_n) = \sum_{i=0}^{n} \frac{1}{d_i} A(d_i). \tag{4.8}$$

The weighting with $\frac{1}{d}$ introduces an evaluation of the strength, depth, and number of reflectors present in the profile. The wetlands that have been discussed previously, for example, appear as dark blue (i.e. high energy) starting from shallow depth all the way to the water table. That implies that several strong reflection events starting at

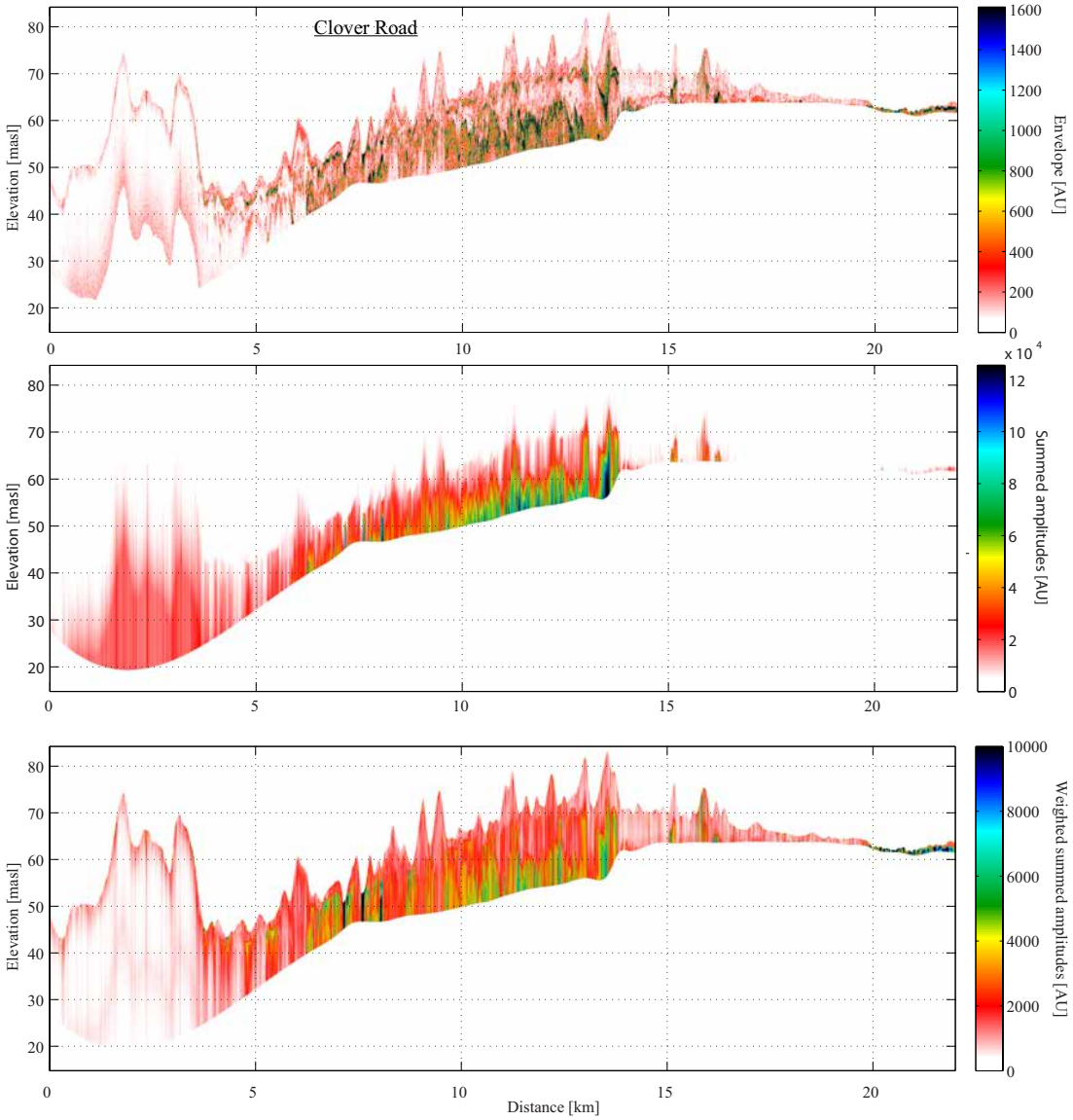

Figure 4.28: *Clover Road transects representing the envelope (upper), the vertical development of summed envelope values (middle), and an alternative, weighted summed envelope calculated using equation 4.8 (lower). The weighed summation is an alternative to the simple summation and includes information on layer position within the profile, and the amount of layers and their significance.*

shallow depth keep the weighted energy high. Other areas where only shallow reflectors exist and no reflectors are encountered at greater depths gradually fade out. Those sections provide a visual representation of reflector constellation and characteristics. Whether it is possible, or reasonable, to extract one single unsaturated zone value out of those sections is beyond the scope of my work.

Conclusion

The analysis of amplitudes appears to be vital in evaluating the significance of vadose zone reflectors. Amplitudes are the best indicator for the absolute energy return from any one interval, which provides an upper limit for a summed reflectivity sequence. To obtain a summed absolute energy reflected from intervals, I chose to calculate the Hilbert transform (i.e. envelope) of wiggle traces, and integrate those over predefined intervals (i.e. summation). Intervals were chosen to represent i) very shallow ground response (i.e. upper 1 m) due to remaining ground and air wave energy which does not represent shallow reflections, ii) unsaturated zone response (i.e. energy below 1 mbNS and down to picked water table) and iii) the water table response (i.e. 3 m below water table, energy return from or close to the water table). On a large scale, this is a simple method that enables rapid extraction of information from GPR profiles, yet it provides a meaningful quantitative outcome for interpretation.

On a large scale, GPR transects are typically oversampled in every respect and can be greatly downsampled in time (i.e. Nyquist frequency) and space. I found that 3 m trace increments and 1 ns sampling interval was sufficient to capture the large-scale amplitude characteristics of 250 MHz data. The spatial stacking removed diffractions and thus migration was found to be redundant as accurate reflector dip is not needed for large-scale amplitude interpretation.

Lateral variations in conductivity are the major perceived weakness of this simple analysis approach. Analogous to the zero-order first-reflector depth analysis, one can devise qualitative statements about certainty involved in this type of interpretation based on the following classification:

1. Profile sections with weak energy return from the unsaturated zone but strong water table reflections

   $\rightarrow$ maximum potential recharge areas (compare to sections where water table is

first significant reflector)

2. Areas with generally weak energy return from unsaturated zone and water table

   → definite interpretation is not possible due to ambiguity:

   - no reflectors are present in the profile, and water table reflection is weak due to for example gradual permittivity increase (i.e. capillary fringe) (those would be high recharge areas)
   - near-surface electric conductivity attenuates the signal (those areas might produce surface runoff; conductivity increase might be locally confined for example to street)
   - dispersed clay in the profile reduces energy return but does not produce reflections (this would influence unsaturated flow)

3. Profile sections with very strong unsaturated zone reflector(s) and absence of reflections from below is a sign of

   - a clear interface that is electrically conductive (i.e. possible clay)
   - interface with very high reflectivity (i.e. strong contrast due to high water content)
   - several intermediate to strong interfaces
   - significant layers in unsaturated zone but absence of clear interfaces at depth (e.g. gradual/diffuse interface)

   → All of the above are reliable indicators for hydrogeologic significance.

To capture these features, one can compare the very shallow interval response, the unsaturated interval response and the water table response to interpret hydrogeologic significance from occurrence and/or co-occurrence or absence of GPR reflectors.

Three example profiles in the northern Yeal area show that the results from amplitude analysis are similar to the outcomes of first reflector depth analysis. The central part of Tuart and Clover Road appear as potentially water retentive, while the eastern part has few significant unsaturated zone reflectors and the first significant reflection originates from the water table. The western part (i.e. Spearwood dunes) is in both

cases characterised by weak or absent reflectors, most likely due to increased attenuation. Thus, it is difficult to draw conclusions from this part of the profile. The unsaturated zone response in the central Bassendean Sand area varies, which can be explained by the "patchiness" of "coffee rock" reflectors, the number of reflectors and their topography.

This section provided an outlook towards possible interpretation schemes for large-scale GPR data. To implement these schemes in a more robust way requires further research and direct observation from boreholes to calibrate vadose zone energy response models.

4.4 Conclusions

In this chapter, the case studies illustrate spatial features of vadose zone GPR reflectors on the Gnangara Mound at local and semi-regional scales. Reflectors originate from various soil layers, for example "coffee rock" (i.e. Podosol accumulation horizon), paleosurfaces or other depositional materials (i.e. peat, clay or heavy mineral bands) (i.e. as discussed in chapter 2) and the water table. Unsaturated zone reflectors are found to be discontinuous on various scales, that is distinct "patches" can be found on a small scale (i.e. tens of meters), and layers are interrupted on a larger scale (i.e. hundreds of meters). On a hundred meter scale, reflectors show a pronounced topography. This leads to the preliminary conclusion that the layers' impact on large scale groundwater recharge is small, even though it is likely that they locally influence the seasonal vertical water infiltration characteristics, for example by promoting preferential flow.

Several reflections reveal vertical layering. Several reflections at different depth are either a sign of discrete layers (i.e. upper lower reflection) or several layers. Several reflections of accumulation horizons can be interpreted as an indicator for stacked paleo-podosol accumulation horizons. In some areas, a layer parallel to the current topography might be a sign for recent formation of podosol B-horizon. The topography of deeper layers could be presumed to represent a horizon parallel to a paleo-topography, thus they could be paleo-accumulation horizons which are currently subject to erosion.

The small-scale pseudo 3D GPR surveys at Whiteman Park and WC6a provided a basis for interpreting large scale amplitudes. At Whiteman Park, it has been shown that

a good spatial correlation exists between overall reflection response of the unsaturated zone, and the dielectric permittivity distribution that is determined by reflector arrival time analysis. The WC6a site showed that low energy in the unsaturated zone response correlated with low energy return from the water table indicates that the vadose zone response is probably influenced by shallow (i.e. surficial) variations in attenuation rates controlled by electrical conductivity.

A zero-order approach in evaluating hydrogeologic significance of vadose zone reflectors is to determine the depth of the first reflector. In case the first reflector is close to the depth of expected water table, the recharge potential is high. If the first reflector is shallow, the zero-order recharge potential is low. However, one shallow reflector might be insignificant.

Amplitude analysis can reveal whether several reflectors impede unsaturated flow in a first-order attempt to obtain a recharge potential map. A simple processing and analysis scheme is proposed for large-scale 2D GPR data that enables identification of areas where the unsaturated zone shows several or significant reflectors (i.e. high unsaturated zone energy return, high retention potential) and contrast those to areas where little energy reflects from the unsaturated zone while the water table is a strong first reflector (i.e. high certainty high recharge potential). To account for possible underestimation of unsaturated zone response due to increased attenuation rates, it is proposed to compare the energy return from around the water table laterally. In case both, unsaturated zone and water table response are weak, one might disregard those areas, or label them as potentially water retentive.

Based on the zero- and first-order analysis, it is found that areas at the central Bassendean Sand formation where the water table is at depth between 8 mbNS (topographic low) to 35 m (dune crest) have the highest water retention potential. Those areas should be further investigated for example by targeted drilling, time-lapse infiltration surveys, hundred meter scale pseudo 3D GPR surveys and additional intermediate scale 2D GPR lines .

Chapter 5

Waveguide Properties Recovered From Shallow Diffractions In Common Offset GPR

The contents of this chapter have been published in Journal of Geophysical Research - Solid Earth (*Strobach et al.*, 2013) and have been reproduced by permission of American Geophysical Union. This work is relevant for the broader hydrogeophysical community due to the novel methodology aimed at extracting very shallow water content distribution using waveguide dispersion phenomena. In the context of the objectives of this dissertation, the outcomes provide insight into the lateral and temporal changes of very shallow dielectric property distribution, which might be needed in the reflector analysis described in the previous chapter. Due to the novelty of the method, I concentrated on proving the validity of the proposed analysis scheme, and to explore the characteristics of dispersion results obtained using this method. The available field data provided the trigger and an objective for the work, and to give a real-world verification or proof of concept of the analysis scheme. However, planning and performing field experiments that utilise the method in order to gain a better understanding of, for example, hydraulic subsurface properties is the next step which could not be performed due to time restrictions. A useful application of the waveguide dispersion analysis would be to complement other radar measurements by supplying shallow water content distribution which is difficult to obtain for example from borehole radar methods (i.e. as explained in chapter 6). The technique could be especially useful for monitor-

ing ephemeral infiltration after extreme rainfall events and on a short time scale. Yet, the main scientific impact of the presented work is on demonstrated methodology; and secondary on hydrogeologic findings.

ABSTRACT

Near-surface heterogeneities produce diffractions in common offset GPR data from the Gnangara Groundwater Mound, north of Perth, Western Australia. These diffracted wavefields can be enhanced and show a dispersion pattern if they propagate along a waveguide caused by a low-velocity surface layer, such as moist sand on top of dry sand. Until now, GPR waveguide dispersion has been analysed and inverted using common midpoint data. Using numerical modelling, we demonstrate that the same dispersion information can also be recovered from a diffracted electromagnetic wavefield recorded with common offset geometry. Frequency-slowness analysis of shallow diffractions in common offset GPR field data reveal high resolution dispersion curves. Inverting picked dispersion maxima to modelled curves (i.e. modal wave propagation in waveguide layer) allows estimation of waveguide height and velocities of waveguide and the underlying material. Data analysis in the frequency-wavenumber domain provides an alternative technique for extracting dispersion curves. Preliminary results validate this approach which could be favourable in large scale applications due to minimal processing requirement and inherent yet adjustable spatial averaging. The differences between waveguide parameters recovered from two surveys appear to be consistent with seasonal changes in moisture content and lateral changes due to variations in depositional environment. Our approach presents a new method to quantify the shallow dielectric permittivity structure of the subsurface from common offset gathers, the most commonly acquired type of GPR data. Potential applications of this method include estimation of shallow moisture distribution, early target identification for UXO detection, concrete slab characterisation, pedological investigations or planetary exploration.

5.1 Introduction

The near-surface moisture distribution is of great interest for several earth-related disciplines such as agriculture, plant ecology, civil engineering, soil science and hydrogeology. Since the dielectric permittivity is largely controlled by water content, measurements of the relative dielectric permittivity of the medium can provide information about soil moisture (*Huisman et al.*, 2003). A Ground-penetrating Radar (GPR) system consists of an arrangement of antennas that can emit and receive electromagnetic pulses in the radar frequency range of 1 MHz to several GHz. These pulses propagate through low-loss materials until they are reflected or diffracted by interfaces and objects that exhibit contrasts in conductivity and electric permittivity. The propagation velocity is inversely proportional to the square-root of the relative dielectric permittivity and hence moisture content can be inferred (*Huisman et al.*, 2003). Several authors have examined methods for quantifying very near-surface dielectric permittivity from

GPR common offset (CO) gather (COG) based on velocity or reflectivity determination. A COG represents point measurements at a constant spatial sampling interval. With bistatic systems, which is composed of separate transmit and receive antennas, a COG is acquired with a constant antenna separation (hence common offset). In the case of a monostatic system, where the transmit and receive antenna are the same, the offset is zero.

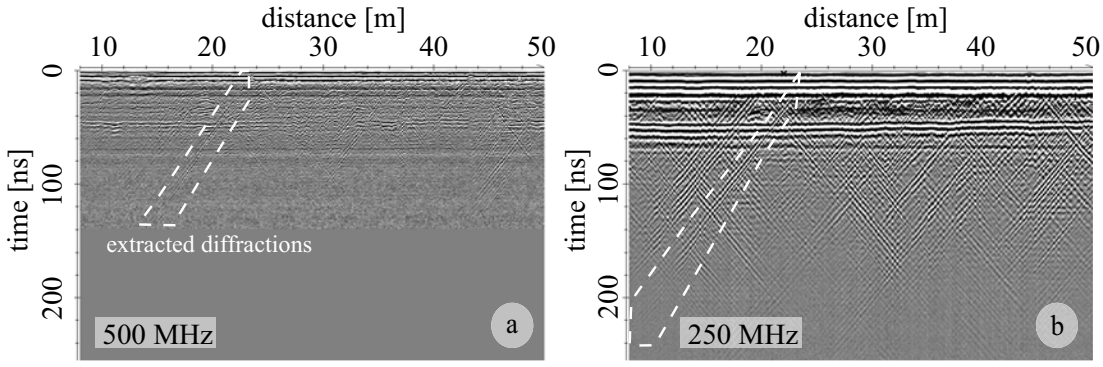

Figure 5.1: *Common offset field example from the May 2011 survey showing argyle-like pattern created by dispersive diffraction hyperbolae originating from shallow diffractors within a low-velocity waveguide (western Lexia West site). Diffraction onsets are first seen from up to 14 m ahead of the diffractor for the 250 MHz data in (b) which can be explained by low-loss propagation of waveguide modes.*

The most common type of GPR systems are based on ground-coupled and air-launched techniques (*Pettinelli et al.*, 2007; *Lambot et al.*, 2006b; *Grote et al.*, 2010b; *Huisman et al.*, 2003). These approaches, however, tend to lack depth of penetration (e.g. air-launched) or seldom provide a conclusive layered earth model (e.g. bistatic constant offset). Multi-offset methods such as common midpoint (CMP - variable antenna separation) or common shotpoint (CSP) gather provide an alternative method of determining dielectric properties of the shallow subsurface by analysing the arrival times of the direct ground-wave. Alternatively, a 1D velocity model can be derived from reflections using semblance analysis. The length of time required to acquire CMP and CSP gathers with a GPR system that consists of a single transmit and receive antenna pair, typical of most commercial systems available at present, precludes its widespread use. Also, several of the bistatic systems commercially available are prescriptive about the antenna spacing that can be used during acquisition and thus making acquisition of multi-offset data impossible.

After collecting and analysing many hundreds of kilometres of GPR data with a bistatic COG configuration, we noticed that numerous diffractions in the data, originat-

ing from roots, stones and other sub-wavelength unconformities, had signals enhanced by waveguide phenomena (e.g. Figure 5.1). As these diffraction signals are measurable from significant distances from the diffraction location, they can be analysed with a multi-offset data analysis approach, as used in the CMP or CSP method. However, to do this requires an understanding of how the diffracted COG-GPR signal behaves in near-surface waveguides, which we investigate in Section 5.2.

Waveguide effects in GPR data were first described and quantified by *Arcone* (1984) who applied modal propagation theory to explain the phenomenon. Subsequent authors refined the approach by introducing inversion schemes to obtain geological models (*Busch et al.*, 2012; *Strobbia and Cassiani*, 2007; *Van der Kruk et al.*, 2006; *Van der Kruk*, 2006; *Van der Kruk et al.*, 2009a, 2010). Until now, the use of the waveguide dispersion observed in the diffraction hyperbola of COGs to compute dielectric properties has largely been ignored, or unreported. *Arcone et al.* (2003) observed these signals as ”diagonal streaks”, which they identified as backscattered modes travelling in a surface layer. From the slope of these streaks they concluded that they were waveguide modes excited by diffractors. *Cassiani et al.* (2006) noticed similar diffractions in their GPR data. *Van der Kruk et al.* (2010) observed that these diffractions were dispersive and, in their example, originated from shallow boulders. *Steelman et al.* (2010) identified dispersive scattering events in their CO data and say that ”inverse analysis [. . .] should yield physical property measurements analogous to that obtained from CMP soundings”.

In this work, we show, using Finite-Difference Time-Domain modelling, that diffraction hyperbolae observed in CO-GPR data, where a shallow waveguide exists, exhibit the same dispersion characteristics as would be recovered from the CMP or CSP survey geometries. We then demonstrate that shallow soil properties can be derived from dispersive diffractions in CO data acquired at a sandy soil environment (e.g. Figure 5.1). Dispersion curves are extracted from i) frequency-slowness domain (i.e. slant stack, *Park et al.* (1998)) and ii) frequency-wavenumber spectrum. Waveguide parameters are estimated by inversion and the parameter space investigated. Observed curves are matched using a waveguide layer model (*Van der Kruk et al.*, 2006).

Table 5.1: *Waveguide, underlying layer and diffractor parameters used for the synthetic study. Cutoff frequencies for fundamental ($f_{c,0}$) and higher modes ($f_{c,m}$) are calculated from waveguide parameters using equation 5.1.*

	ν [m/ns]	ε_r	h [m]
layer 1	0.300	1	2.00
FDTD layer 2	0.128	5.5	0.50
FDTD layer 3	0.173	3	3.00
FDTD diffractor	0.060	25	0.40
$f_{c,0}$: 44 $f_{c,1}$: 234	$f_{c,3}$: 424	$f_{c,3}$: 613	
FDTD Δt:	0.04 ns	Receiver ΔX_r: 0.1 m	
FDTD Δx:	0.025 m	CO shot ΔX_{CO}: 0.1 m	

5.2 Synthetic Example

Dispersion images in the slowness-frequency domain can be calculated from radargrams with the method described by *Park et al.* (1998) and adapted by *Van der Kruk et al.* (2006). By picking maxima of fundamental and higher modes from trace-normalised dispersion images, we can obtain dispersion curves. In the following synthetic example we compare the dispersion images for CSP and CO configurations and show that dispersion curves recovered from i) the direct and diffracted wavefield, and ii) sampled with a CO and CSP geometry, are identical after two-way traveltime adjustment. We will discuss some characteristics of the dispersion images obtained from diffractions sampled with COGs.

5.2.1 Forward Modelling

The full electromagnetic wavefields are simulated by forward modelling using a 2D Finite-difference time domain (FDTD) scheme included in the Software package ReflexW (*Sandmeier*, 2012). We compare results from i) the direct CSP wavefield with the CSP diffracted wavefield, and ii) the diffracted wavefield sampled as COG with the CSP results. Our FDTD analysis is for the transverse electric TE (Ey-) field components. The model consists of 3 layers representing a waveguide: (i) an air layer underlain by (ii) a low-velocity horizon (waveguide-layer) which is itself underlain by (iii) a high-velocity layer (Figure 5.2a, d). We embed a diffractor in the low-velocity layer (layer 2) to create the diffracted energy. The diffractor is a circular area with a diameter of 0.4 m and a relative dielectric permittivity of 25. This is significantly higher

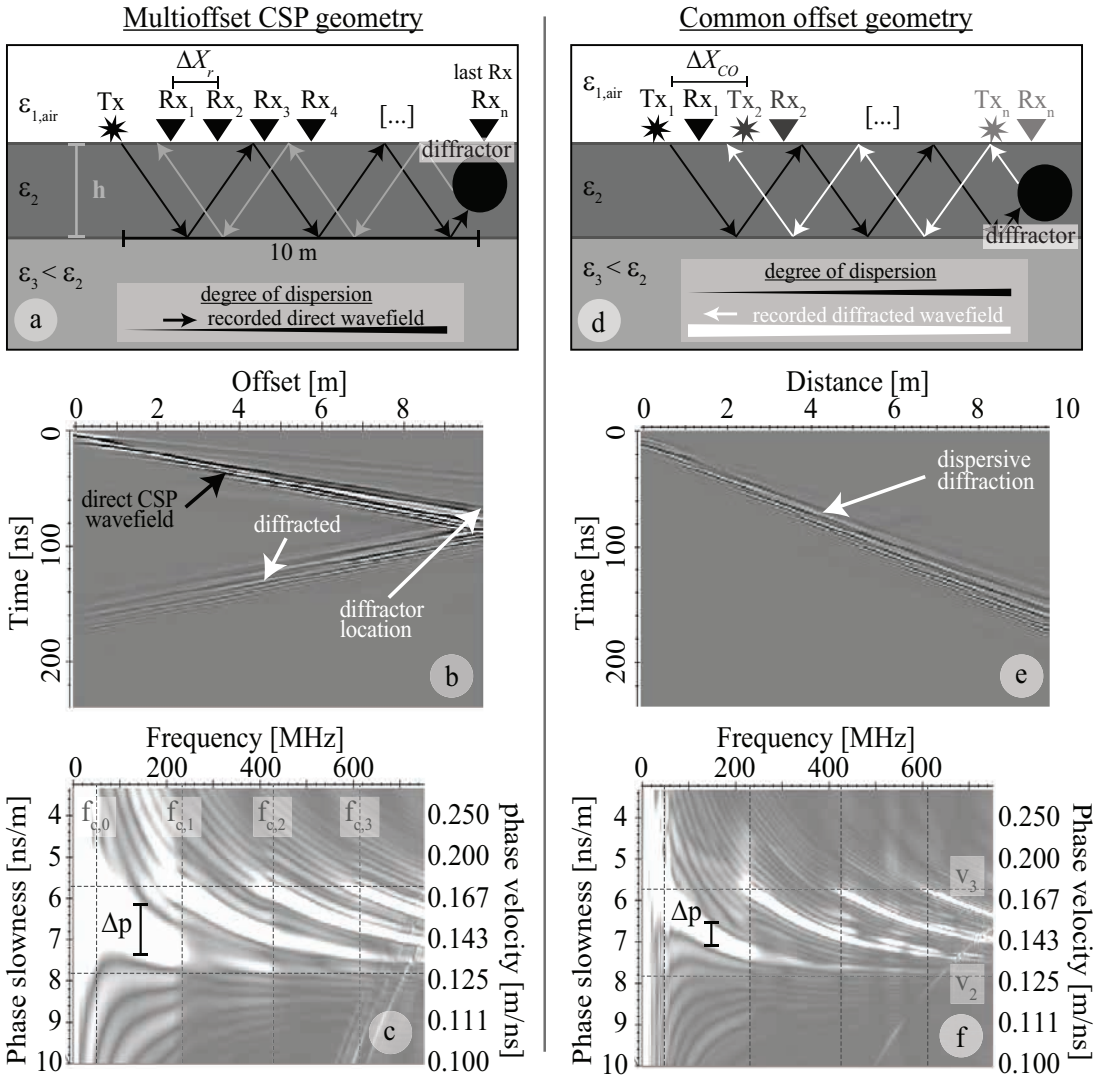

Figure 5.2: *Waveguide model used for FDTD modelling corresponding: (a) common shot point, and (d) common offset geometry. Shot (transmitter Tx) and receiver (Rx) positions are shown as stars and triangles, respectively. Greyscale density represents relative dielectric permittivity with white being the lowest (i.e. $\epsilon_{air} = 1$) and black (diffractor) the highest value (i.e. $\epsilon_{diff} = 25$). Ray-paths of a direct and diffracted phase travelling in the waveguide layer are displayed in black and grey/white, respectively. For the CSP geometry, dispersion can be derived from waves either following the black (direct) or grey (diffracted) ray-paths, while the CO mode samples white rays (diffracted). Synthetic common shotpoint and common offset gathers are shown in (b) and (c), respectively; and their corresponding dispersion images in (c) and (f). FDTD modelling parameters are given in table 1. Note the increased resolution p (length of black bars) of the slowness maxima obtained in (f) due to the increased effective spread length. Phase slownesses in (f) have been calculated with two-way traveltime. All plots are trace-normalised.*

than the low-velocity layer which is given a dielectric permittivity of 5.5 yielding a strong impedance contrast. A high permittivity circular object could, for example, represent a water saturated tree root.

Time and space discretisation (i.e. Δt and Δx) for the FDTD modelling was set to 0.04 ns and 0.025 m, respectively (see Table 5.1). This discretisation is sufficiently

small to prevent numerical dispersion in time and space (see Figures 5.3 and 5.4). Model boundaries were set to the largest exponential absorbing boundaries possible in ReflexW. Modelling parameters for the synthetic study are summarised in Table 5.1.

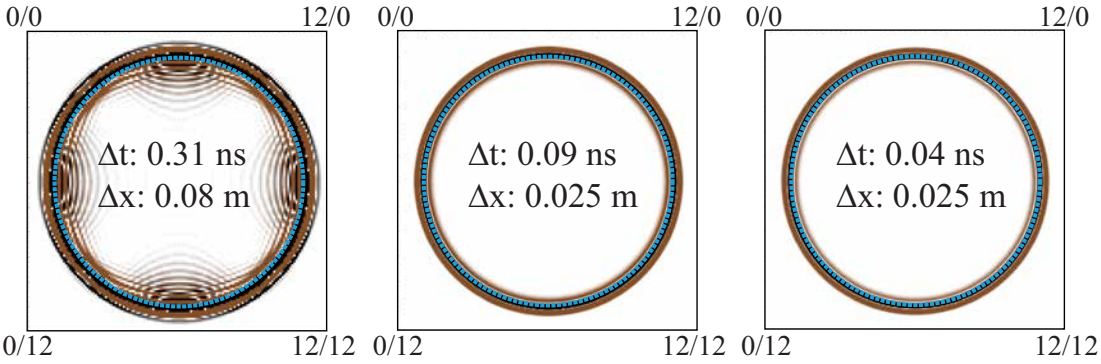

Figure 5.3: *Effect of angular numerical dispersion (i.e. propagation velocity dependent on direction) tested by placing point source in the center of homogeneous FDTD model and observing deviation from a circle after 50 ns for different discretisation. Note that even for the coarsest discretisation parameters (i.e. $\Delta t = 0.31$ ns, $\Delta x = 0.08$ m), angular dispersion is not occurring. However, frequency dispersion is obvious at the horizontal and vertical axes. Thus, frequency dispersion is dependent on angle. Realisations with a fine FD discretisation do not show any sign of either, angular or frequency dispersion.*

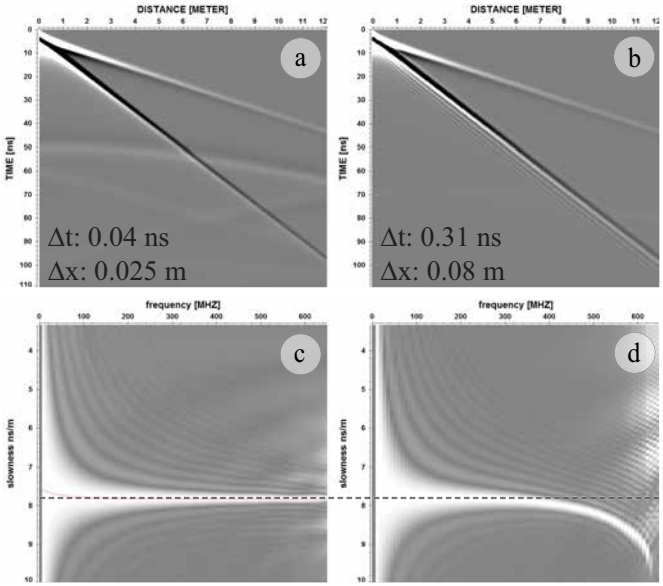

Figure 5.4: *Numerical frequency dispersion for a two-layer model (i.e. air and one layer). Graphs (a) and (b) are common shot gathers for fine and coarse FD discretisation, respectively. Figures (c) and (d) are the corresponding dispersion images. Frequency dispersion occurs for the coarsely modelled case (b) and (d) at frequencies above approximately 400 MHz, while the fine sampling used in this study in (a) and (c) does not produce noticeable numerical frequency dispersion.*

The ground-arrivals in the modelled radargram of the CSP gather exhibit characteristics of a dispersive direct ground-wave arrival (Figure 5.2b). Note the diffracted, left dipping wavefield in Figure 5.2b that originates at a position of 10 m (i.e. diffractor location) at approximately 50 ns. Figure 5.2e shows the diffracted wavefield sampled with a CO survey configuration which we want to compare with the CSP geometry results. Note that the travel-time curve of the diffracted CO arrivals is linear,

not hyperbolic. The presence of a waveguide results in lateral wave propagation and hence the move-out of the diffraction arrivals appear as if the diffractor is at "zero" depth. This observation means that single-frequency phase velocity vp can be approximated from the slope of those diffraction events after applying narrow bandpass filters (*Van der Kruk et al.*, 2009b). The move-out function is linear and can be written as $\nu_p = 2dx/dt$. Hence, the characteristics of shallow diffracted wavefields are inherently similar to direct ground-arrivals observed on CMP- or CSP gathers with the exception of a factor of two. Figure 5.2e shows the synthetic COG with diffracted arrivals to the right of the diffractor. Traces have been re-sorted so that the diffractor is now located at $x = 0$. Dispersion images of both wavefields and sampling methods reveal very similar dispersion images (Figure 5.2c, f). Picked maxima of the dispersion images from both survey geometries are displayed in Figure 5.5. In addition, the dispersion curve recovered from the CSP diffracted wavefield (dispersion image not shown here) is also shown in Figure 5.5. The critical frequencies $f_{c,m}$ for mode m displayed as dashed vertical lines in Figures 5.2c, f and 5.5 (values are listed in Table 5.1) were calculated using the equation given by *Van der Kruk et al.* (2006) for the TE modes:

$$f_c = \frac{c \cdot \left[2\pi m + \Phi^{TE}\left(\Theta_{c,23}\right)\right]}{4\pi h\sqrt{\epsilon_2 - \epsilon_3}} \tag{5.1}$$

with Φ^{TE} the phase component for the critical angle $\Theta_{c,23}$ for mode propagation that can be written as

$$\Phi^{TE}\left(\Theta_{c,23}\right) = \tan^{-1}\left(\frac{2\sqrt{\epsilon_2 - \epsilon_3}\sqrt{\epsilon_2 - \epsilon_{\text{air}}}}{\epsilon_{\text{air}} + \epsilon_2 - 2\epsilon_3}\right) \quad . \tag{5.2}$$

Note that ϵ_{air} is ϵ_1 in the model shown in Figure 5.2, h is the height of the waveguide and c the velocity of light in vacuum.

5.2.2 Characteristics Of Synthetic COG Dispersion Images

The CO dispersion curves provide an apparent higher resolution of the slowness compared to the CSP gather (see for example Figure 5.2c vs. 5.2f) after correcting for two-way travel. The slowness resolution for a CSP geometry is given by the half distance between neighbouring minima (half the width of slowness maxima) $\Delta p = 2\pi/\omega L$, where L is the spread length (*Forbriger*, 2003). Thus, the mathematical explanation

for the apparent increase in resolution for CO geometry is the two-way time correction that multiplies Δp with a factor 0.5. The physical reason can be explained by assuming that the dispersive wavefield is back-scattered by the diffractor and continues to disperse along the waveguide as indicated in Figure 5.2. The wavefield therefore effectively covers twice the distance in the waveguide. This means that the diffractor can be considered as an equivalent source emitting a dispersive wave-field, sharing some characteristics of a time-varying frequency sweep that has low frequencies at the beginning and higher frequencies at later times. Thus, for the CO field configuration, the phase velocities at each frequency have greater travel time to separate, and consequently the apparent resolution of the dispersion images can appear superior compared to a dispersion image of a CSP gather with equivalent maximum spread length. We determined Δp from the dispersion images of synthetic two-way time corrected CO diffraction hyperbola at different frequencies and obtained estimates for the spread length between 17.8 m and 19.5 m. The farthest CO pair is 10 m away from the diffractor. The effective spread length L_{eff} for CO diffraction hyperbolae is, as predicted, almost doubled.

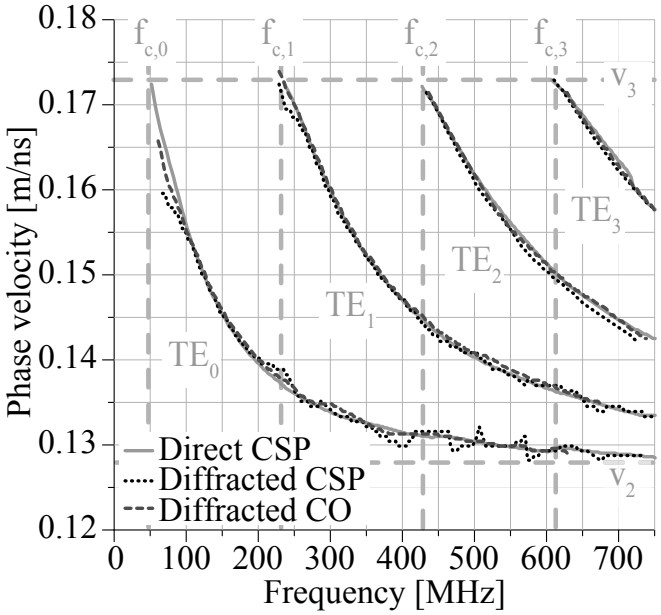

Figure 5.5: *Dispersion curves derived from FDTD modelling corresponding to direct waves (solid lines), diffracted wavefields sampled with CSP geometry (dotted lines) and with CO geometry (dashed lines). A good match between dispersion curves is observed for fundamental and higher order modes. Minor variations are due to numerical inaccuracies from converting into frequency-slowness domain.*

The additional travel distance in the waveguide means that signal-to-noise ratio of the dispersion image is potentially reduced and the aliasing frequency and consequently the aliasing velocity are increased compared to an equivalent offset CSP or CMP gather. Spatial aliasing is especially prevalent in slow waveguides (e.g. water above ice) and for frequencies at the higher end of the radar band. Additional prob-

lems can occur when other wavefields with similar moveout such as diffractions from deeper targets cause interference. For example, deeper diffractions with dispersive diffraction legs have the potential to make CO dispersion analysis more complicated. Note that horizontal reflectors such as a water table would tend to be more problematic in multi-offset dispersion analysis compared with CO dispersion analysis because in CO data it produces zero slowness in the slowness-frequency domain (i.e. slope of flat reflection in CO profile is zero, hence velocity goes towards infinity). Steeply dipping reflectors may also cause interference when interpreting dispersive diffractions in the frequency slowness domain. The influence of other wavefields on dispersion images is certainly an important consideration and may form a basis for future research on analysis of dispersive diffractions.

5.3 Field Experiments And Results

5.3.1 Field Observations

In this section, we show that the dispersion analysis of diffracted wavefields described in the previous section can be applied to two CO datasets collected on the Gnangara Mound, north of Perth, Western Australia in May and September 2011. The datasets were acquired with the Mala ProEx 2 system with 250 MHz and 500 MHz shielded antennas. Measurements were triggered at 0.025 m intervals using an encoder wheel. Field measurements on May 6th 2011 were acquired at Lexia West (LXA-W) after 18 mm of precipitation was recorded at a close-by climate observatory over the preceding week[1]. Shallow infiltration after rainfall resulted in a layer of moist sand trapped between an air layer above and dry sand below. In the time between the May and September experiments, cumulative rainfall of approximately 550 mm increased the background moisture content (*Strobach et al.*, 2012a). The measurements on September 21st 2011 are from the northern Yeal area and were also preceded by a period of rainfall with approximately 35 mm precipitation starting on September 16th after 12 days of dry and sunny conditions. The May 2011 dataset is taken from a 100 m long profile, while the September 2011 data were extracted from a larger scale investigation spanning approximately 5 km. Both sites are situated on the Bassendean Sand forma-

[1] http://www.bom.gov.au/climate/data/

tion that is dominated by vegetated dunes with wetlands common at the depressions (*Davidson*, 1995). The shallow material at both areas consists of an A-horizon which is a mixture of leached quartz sand and dispersed organic material. Below is a leached E-horizon typical for podosolic soils on the Gnangara Mound (*Prakongkep et al.*, 2009). It is characterised by well sorted medium grained quartz sand of pale white to grey colour. The September profile intersected a wetland that contains peat-like material in the A-horizon.

Figure 5.1 shows CO radargrams collected in May 2011 with the 500 MHz and 250 MHz antennae. The sections are characterised by numerous lines running diagonal through the radargram with positive and negative slopes creating an argyle pattern. We interpret those events to originate from diffractors embedded in a shallow waveguide. Although radiation pattern of modern GPR systems emit some energy forward (i.e. lateral waves, *Chen* (2012), a strong response from shallow diffractors is not expected to be detectable several wavelength ahead of the target in low-loss dielectric environment. A waveguide, however, captures EM energy and facilitates lossless wave propagation. Diffracted energy can then have equivalent or higher amplitudes at late times compared to reflected waves from greater depth. The apex of those diffraction hyperbolae (i.e. where the straight lines meet) is close to zero time, which indicates very shallow diffractors. Tree roots, buried rocks, patches of hydrophobic sand or boulders (*Van der Kruk et al.*, 2010) are all known and identified potential sources of shallow diffractors. We investigated soil conditions in the field and identified elevated moisture within the first approximately 30 cm. Shallow diffractions appear to be correlated with vegetation and shallow excavation revealed dry spots associated with grasstree roots (Xanthorrhoea). We hypothesise that dry spots within a wet soil might reasonably function as diffractors for the electromagnetic waves.

CO data in Figure 5.1 show diffracted energy at up to 15 m distance from the diffractor at arrival times of up to 240 ns for the 250 MHz data. The horizontal reflector at approximately 45 ns is interpreted as the reflection from the water table or the capillary fringe. Depth to water was measured at a close-by well (LXA-W) to be 3.9 m below surface level. This leads to an average interval velocity of approximately 0.17 m/ns for the sand above the water table.

The September 250 MHz data from northern Yeal (Figure 5.6) showed two types

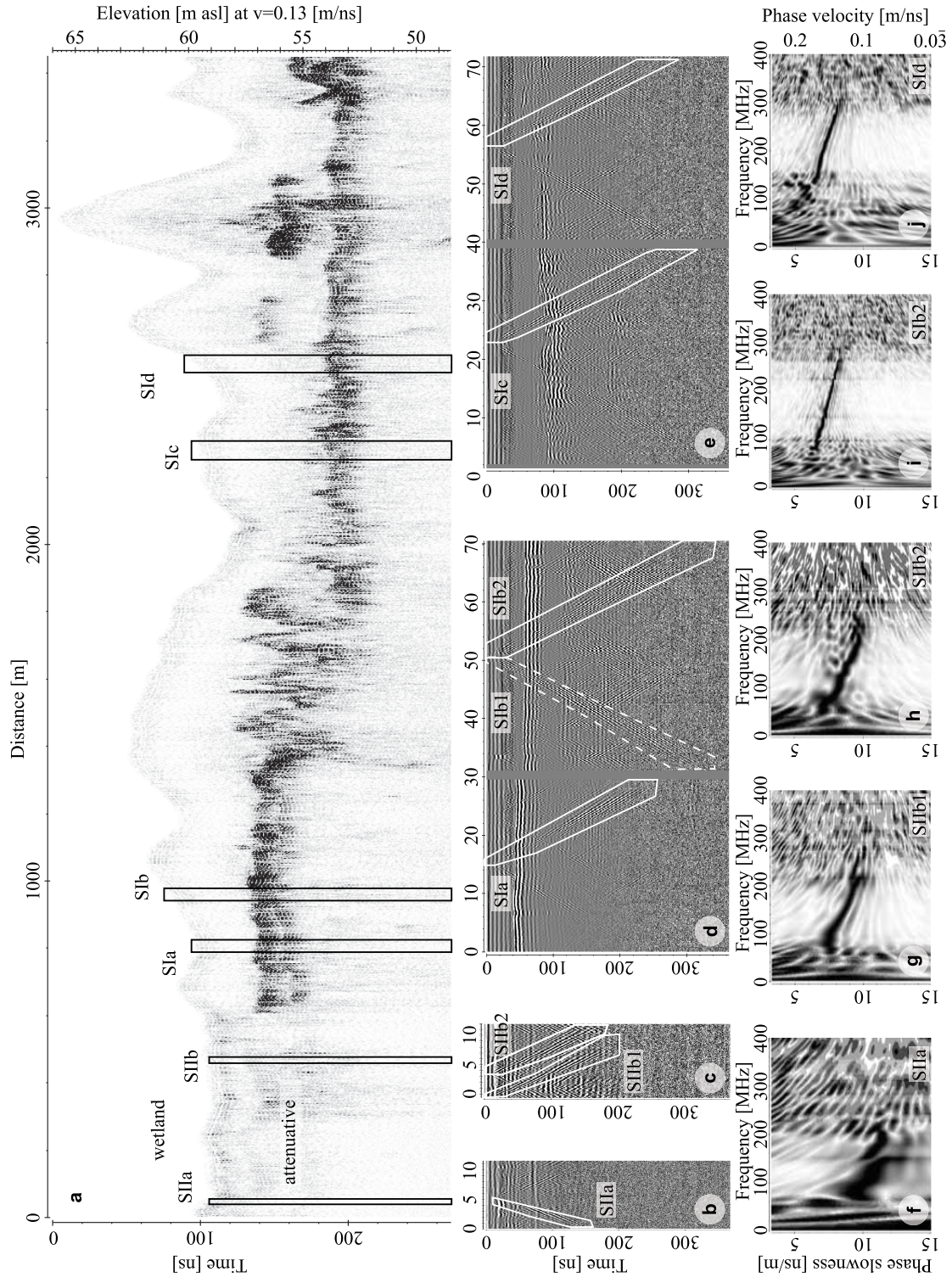

Figure 5.6: *Radargram with corrected topography (a) for the common offset field example from the September 2011 survey (north Yeal). Boxes indicate locations of extracted sections with dispersive diffractions (b) - (e). Diffractions are labelled SIa-d (clean sand) and SIIa-b (wetland). Examples of dispersion images are shown in (f) - (i). Note the attenuation in (a) associated with the wetland at 0 - 600 m and the difference in dispersion images (SI vs. SII).*

of dispersive diffractions. The first type represents strong dispersive diffractions that can be observed up to 18 m ahead of the diffractor at arrival times of 300 ns. These are denoted as September I (SIa - SId) in Figure 5.6d and 5.6e and are associated with clean sands below the vegetated dunes. The second type, called September II (SIIa and SIIb), are associated with the lower wetlands spanning the first 600 m of the profile shown in Figure 5.6a. Diffractions SIIa and SIIb in Figure 5.6b and 5.6c, respectively, are weak and detectable up to 5 m (120 ns) and 8 m (200 ns) ahead of the diffractor, respectively. The section of the radargram across the wetland area shows increased attenuation which is likely to be a consequence of an increased fraction percent of damp loamy sand and a peat-like surface layer. Two-way travel time to the water table in the Yeal area is dependent on topography and can vary between 40 ns and 200 ns. Exact water table position is not known here, however it is a relatively flat interface. The interval velocity required to create a flat water table reflection after topographic correction is approximately 0.13 m/ns. This value of 0.13 m/ns is generally consistent with velocities estimated from deeper hyperbolic diffractions that originate close to the water table. Note that the step in the water table level between 1300 m and 1800 m is currently interpreted as a hydrologic transition and not due to lateral velocity variations.

5.3.2 Data Processing

We extracted single diffraction legs from the COGs shown in Figure 5.1 and Figure 5.6. The diffraction legs are marked with white lines in both figures. Single diffractions were chosen for dispersion analysis based on their dispersive character, signal to noise ratio and the absence of interfering wavefields. Further processing was performed in ReflexW and included a DC-shift removal (subtraction of average trace amplitudes within a late time window) and application of a time dependent gain function calculated from the mean amplitude decay of all traces. We then muted the area above and below the diffraction leg with a cosine taper window of 5 ns. Processed data are shown in Figures 5.6b, c, d, e, 5.7a, c, e. This simple processing flow was designed to minimise the impact of the processing on the phase characteristics of the signals. Phase-slowness spectra were then calculated using a slant stack as described by *Park et al.* (1998) and shown in Figures 5.6f-j and 5.7b, d, f. Dispersion curves are then extracted by picking

maxima from the dispersion images.

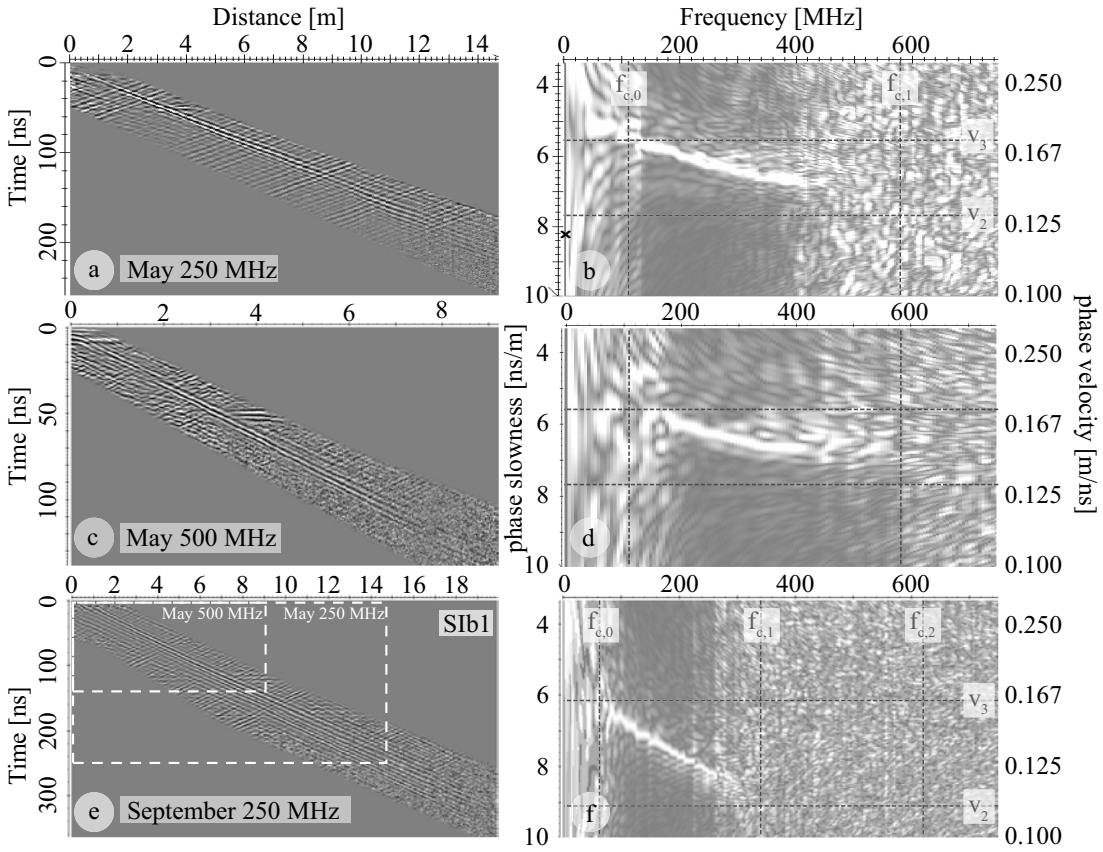

Figure 5.7: *Field CO gathers from (a) May 250 MHz (white box in Figure 1), (c) May 500 MHz and (e) September 250 MHz (SIb1), and corresponding dispersion images (b, d, f); cutoff frequencies and upper and lower layer velocities calculated from model results are shown as dashed lines. Note the different scales in (a, c, e). Dashed white boxes in (e) indicate the data extent in (a) and (c).*

An interesting alternative to calculating frequency-slowness distribution, as above, is to perform dispersion analysis in the frequency-wavenumber (fk-) domain. An example of fk-analysis is given for the May 250 MHz dataset in Figure 5.8. The fk-spectrum makes it possible to identify energy associated with the move-out of the diffractions due to characteristic fk-slope. Phase velocity for the CO data is calculated from frequency and wavenumber picks with $\nu_{fk} = 2f/k$. The fk-spectrum was calculated from radar sections without muting. The fk-analysis, offers the potential for semi-automated extraction of dispersion curve without the need to mute data. This method could be used for larger scale mapping. The size of the analysed window provides a method of averaging over larger radar cross sections.

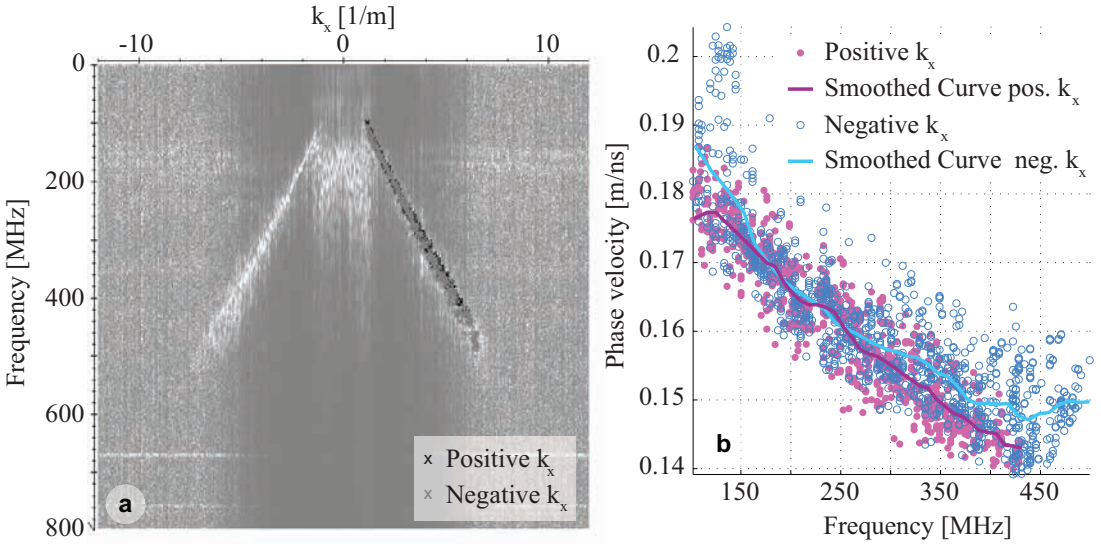

Figure 5.8: *fk-spectrum of the entire 250 MHz profile (May 2011, 100 m) shows energy bands associated with dispersive diffractions (a). Phase velocity versus frequency plot (b), symbols denote values obtained for automatic picking results (i.e. fk-spectrum maxima), in magenta for positive and in blue for negative wavenumbers (i.e. black and grey crosses in (a), respectively). Solid curves in (b) are calculated with an averaging operator and downsampling by interpolation.*

5.3.3 Waveguide Dispersion: May Versus September

The 250 MHz and 500 MHz data from May 2011 present similar dispersion images (Figure 5.7b and 5.7d). The 250 MHz data tend to have better signal to noise ratio and a thinner dispersion curve indicating higher slowness resolution. We estimate effective spread lengths Leff from the half-width p of the slowness maxima at several frequencies and obtain values between 18 m and 24 m for the 250 MHz data, and between 8 m and 17 m for the 500 MHz data. The maximum offset at which diffracted energy appears above the noise floor for CO data is half the effective spread length. This results in good correlation between the maximum distance at which diffraction energy was observed in the field data (i.e. 8 and 15 m for 500 and 250 MHz, respectively) and the predicted spread length from dispersion slowness resolution.

The picked dispersion curves from May are shown in Figure 5.9. Their velocities range between 0.143 m/ns and 0.176 m/ns for frequencies between 130 MHz to 450 MHz.

To examine the method of picking dispersion curves from the fk-spectrum, we transformed the 100 m long 250 MHz radar section into the frequency-wavenumber domain without muting (Figure 5.8a). The diffractions appear in the fk-spectrum as clouds of energy with a linear slope. Positive and negative wavenumbers represent the

left and right diffraction legs, respectively. The resolution of those energy clouds is poor and a continuous curve is not evident. Automatic picking of fk-maxima as facilitated in ReflexW reveals clouds of data points after transformation to the velocity-frequency domain (Figure 5.8b, Figure 5.9). Diffraction curves were extracted from those clouds by moving average filtering and interpolating to downsampled and regularly spaced frequency points. Note, however, that the continuity of the diffracted energy in the fk-spectrum can be increased by muting unwanted data. This results in dispersion curves which are highly comparable to those picked from the frequency-slowness domain dispersion images.

Dispersion images resulting from our type SI diffractors within the September 250 MHz data show a slightly increased effective spread length between 22 m and 35 m compared to the May data. Their dispersion characteristics are plotted in Figure 5.9 and reveal velocities between 0.12 m/ns and 0.155 m/ns. The frequency range where a dispersion curve can be identified is between approximately 70 MHz and 260 MHz. For a similar frequency range, the SII diffractions in the wetland area show lower velocities of between 0.085 m/ns and 0.107 m/ns for SIIa and between 0.102 m/ns and 0.145 m/ns for SIIb. Their resolution is generally decreased consistent with the maximum distance at which diffracted energy is above the noise floor (see Figure 5.6f-h). The SIIa dispersion image appears to contain two dispersion curves. The first dispersive energy band ranges between 75 MHz to 155 MHz, and the second curve lies at frequencies from 140 MHz to 210 MHz.

5.3.4 Waveguide Parameter Inversion

We have applied inversion methods to recover waveguide parameters from our field data. The code we used is that developed by Jan Van der Kruk (*Van der Kruk et al.*, 2006; *Van der Kruk*, 2006). Waveguide parameters are recovered from the field experiments by minimising the misfit between forward modelled and picked dispersion curves using a combined local and global optimisation. The global optimisation is based on several iterations of local minimisation probing a variety of starting models (simplex search method). In order to test a large parameter space and obtain a better understanding on the model convergence, we performed the global optimisation twice. The first optimisation covered a coarsely sampled but larger parameter space. The ob-

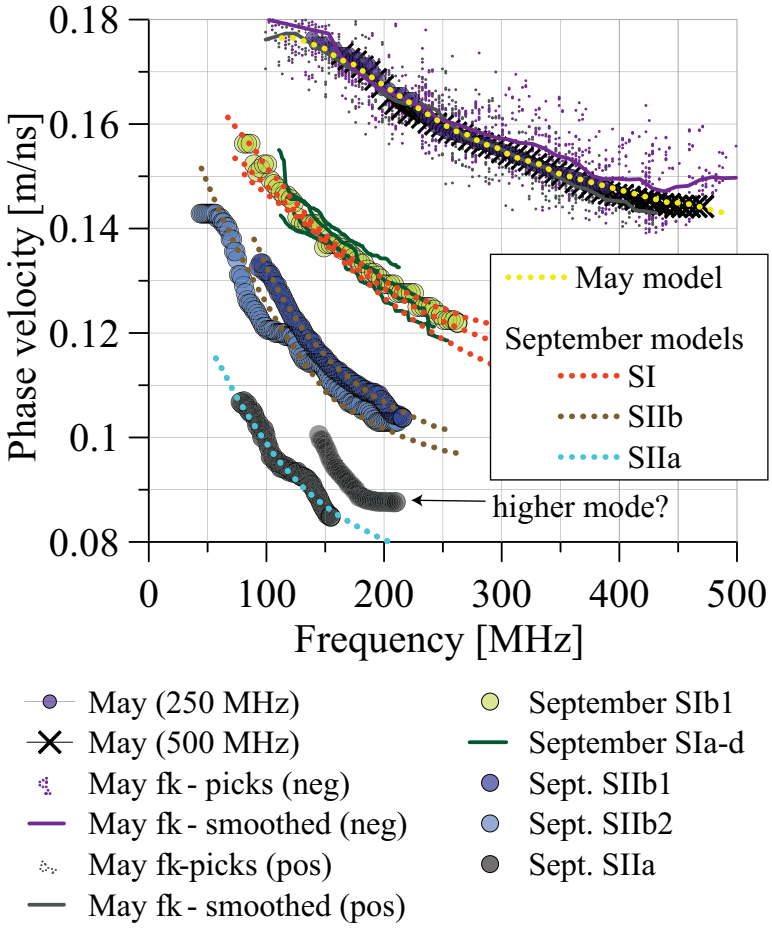

Figure 5.9: *Dispersion curves derived from field data (coloured symbols and solid lines), and predicted curves using the model results of inversion (dotted lines) given in Table 5.2 and 5.3. Note the great difference in dispersion characteristic from different date and location.*

jective was to find constraints for starting values for the second optimisation. Results of the inversion process are shown in Figures 5.10, 5.11 and 5.12 for the second optimisation. The cost function that is to be minimised is defined as the L1-norm. The forward model is based on modal wave propagation (*Arcone*, 1984; *Arcone et al.*, 2003; *Van der Kruk et al.*, 2006). All measured dispersion curves were assumed to represent the fundamental TE mode (TE0), except for the higher frequency dispersion curve in SIIa which was inverted as the first higher mode (TE1). Table refTab:WG2 lists the parameters derived from the curve matching.

5.3.5 Inversion Results

This section summarises the modelling results from inversion which are summarised in Table 5.2. In May, a waveguide of 0.2 m thickness and relative dielectric permittivity values of above five (i.e. $\epsilon_{2,\text{may}} \approx 5.3$) and for the halfspace below of 3 (i.e.

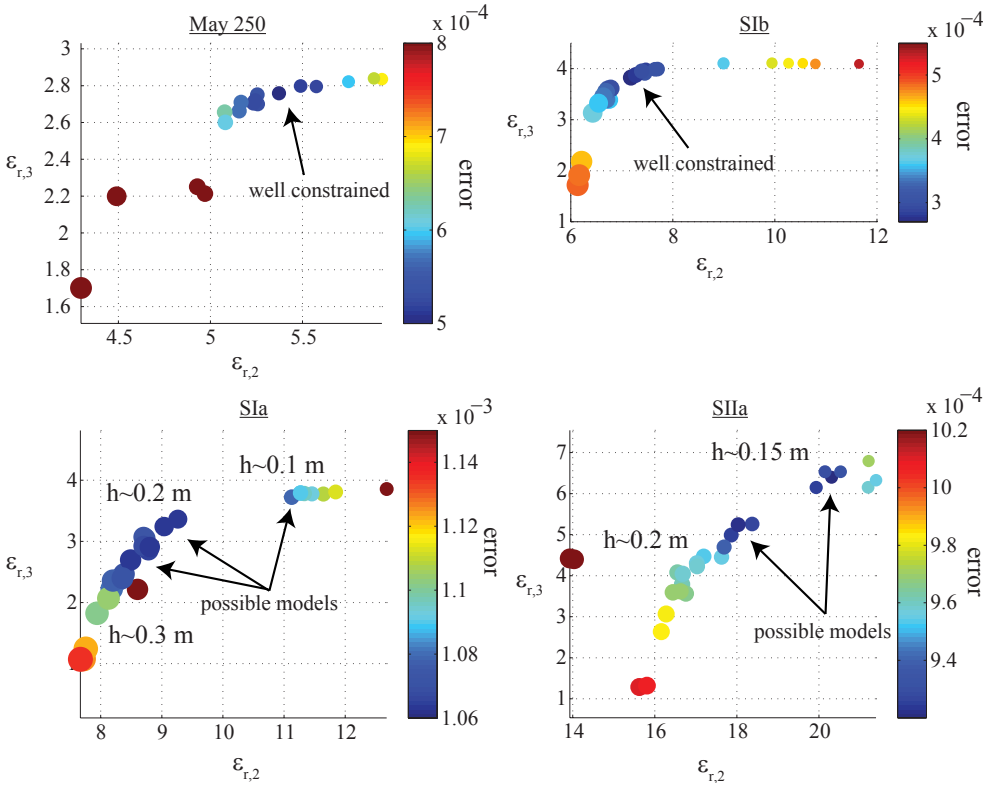

Figure 5.10: *Inversion L1 misfit (blue low, red high values) between model and observed dispersion curves shown as a function of waveguide parameters ϵ_3, ϵ_2. Circle size indicates waveguide height h. Arrows indicate inversion results with low misfit for different sets of parameters illustrating non-uniqueness.*

$\epsilon_{3,\text{may}} \approx 2.8$) provided a suitable fit between field and model data. According to the complex refractive index model (CRIM) for a quartz sand with 40 % porosity and relative dielectric permittivity for quartz of 4.4, those values correspond to volumetric water contents [v%] of 8 v% and 0.2 v% for waveguide layer and lower halfspace, respectively. The field and model dispersion curves are shown in Figure 5.9. Inversion results for dispersion curves derived from fk-clouds and smoothed curves are almost identical. That means that our method of smoothing and interpolating phase-velocity versus frequency picks represents the trend within the data cloud well. Inversion results for positive and negative wavenumbers (right and left diffractions), however, differ slightly. That is expected because the extracted dispersion curves reveal a different trend. While the positive (fk+) dispersion curve is similar to the curves picked from the dispersion image, the negative (fk-) curve probably includes outliers at the low and high frequency end.

The type SI diffractions from the September 2011 data generally predict lower layer velocities compared to May, while the waveguide thickness varied between 0.1

Table 5.2: *Waveguide and underlying halfspace parameters and theoretical cutoff frequencies $f_{c,0}$ and $f_{c,1}$ of fundamental and first higher mode, respectively, listed for a selection of field data dispersion curves obtained by inversion (Van der Kruk, 2006). The L1 value represents the misfit between modelled and measured dispersion curves. Dispersion curves from May extracted from 250 MHz data were compared using a slant stack (May 250) (Park et al., 1998), and using fk-method. The automated picking in fk domain resulted in velocity versus frequency clouds (i.e. fk-cloud) that were smoothed using averaging and interpolation (fk-curve) for positive (+) and negative (-) wavenumbers independently (see Figure 5.9).*

			May			
	ε_2	ε_3	h [m]	L1	$f_{c,0}$	$f_{c,1}$
May 250	5.4	2.8	0.20	5.02E-04	103	568
May 500	5.3	2.7	0.21	5.20E-04	96	539
fk-cloud +	6.3	2.9	0.13	3.14E-03	128	754
fk -curve +	6.0	2.9	0.15	6.67E-04	120	688
fk -cloud -	4.6	2.5	0.31	4.37E-03	75	409
fk -curve -	4.6	2.6	0.31	1.20E-03	79	422
			September			
	ε_2	ε_3	h [m]	L1	$f_{c,0}$	$f_{c,1}$
SIa	8.5	2.7	0.22	1.06E-03	45	328
	11.1	3.7	0.12	1.08E-03	79	539
SIb1	7.3	3.3	0.26	8.04E-04	60	348
	8.6	3.8	0.19	7.17E-04	75	435
SIb2	7.2	3.8	0.25	2.73E-04	76	402
	9.9	4.1	0.12	4.32E-04	104	623
SIc	9.2	3.0	0.20	7.74E-04	50	351
	12.3	4.1	0.10	4.83E-04	92	616
SIIa TE_0	20.3	6.4	0.16	9.20E-04	45	296
	17.9	5.0	0.22	9.25E-04	31	221
SIIa TE_1	16.8	7.2	0.54	7.82E-04	19	109
	16.7	2.2	0.56	7.29E-04	6	77
SIIb1	12.8	4.3	0.20	1.20E-03	46	303
SIIb2	12.0	3.3	0.21	4.09E-04	37	279

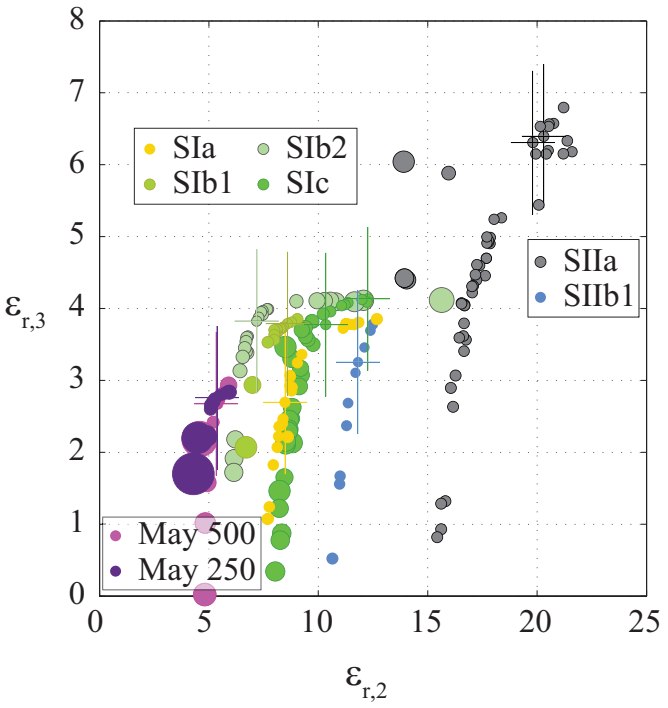

Figure 5.11: *Halfspace dielectric permittivity ϵ_3 plotted against waveguide layer permittivity ϵ_2 and symbol size indicating misfit illustrates trace of conversion to best fit model which is highlighted with a cross. Note the non-uniqueness of SIIa (i.e. two clusters of small grey circles fit the dispersion curves equally well) and insensitivity of SIIb1 (blue circles).*

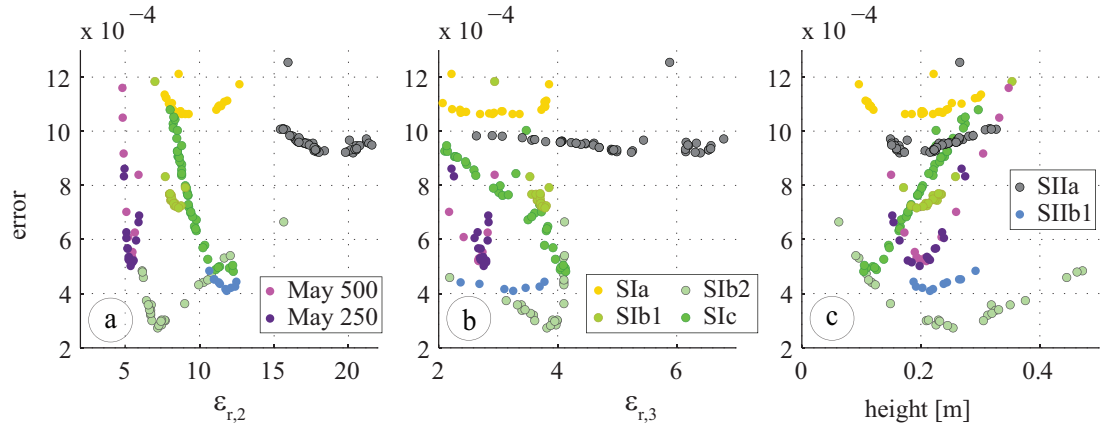

Figure 5.12: *Inversion L1 misfit plotted against waveguide parameters ϵ_2 (a), ϵ_3 (b) and h (c). For waveguides where misfit is constant throughout the parameter space, sensitivity for that parameter is low, for example SIa, SIIa and SIIb1 (yellow, blue and grey symbols, respectively) are insensitive to ϵ_3. On the contrary May 250 and 500 inversion results are sensitive to all three waveguide parameters revealed by great increase in misfit due to small variations in waveguide parameters.*

m and 0.25 m (i.e. $h_{SI} = 0.1 \ldots 0.2$ m). Relative dielectric permittivities for waveguide layer were around 7.5 for the 0.25 m thick waveguide, and between 8.5 and 11 for the thinner waveguide prediction ($\epsilon_{2,SI} = 7.5 \ldots 11$). Models with lower halfspace permittivities around 3 (thicker waveguide) and 4 (thinner waveguide) resulted in a good fit with the observed dispersion curves (i.e. $\epsilon_{3,SI} = 3 \ldots 4.1$). Those values correspond to volumetric water contents of approximately 13 - 20 v% and 2 - 5 v% for waveguide layer and lower halfspace, respectively. The possible SIIb models predict a waveguide with similar dielectric permittivities as the SI model with smaller waveg-

uide height. Waveguide permittivities are around 12 (i.e. $\epsilon_{2,SIIb} = 12.0 \ldots 12.8$) and halfspace permittivities were similar to the SI values (i.e. $\epsilon_{3,SIIb} = 3.3 \ldots 4.0$) for a waveguide of around 0.2 m thickness (i.e. $h_{SIIb} = 0.2$ m). Dispersion curves from SIIa diffractions result in the highest dielectric permittivity model predictions for both, waveguide and halfspace. The possible models are a waveguide with a height of 0.2 m when dielectric permittivities are 17.9 and 5 for waveguide and halfspace, respectively (i.e. model 1: $\epsilon_{2,SIIa} = 17.9$, $\epsilon_{3,SIIa} = 5.0$, $h = 0.22$ m). The alternative model is a thinner waveguide of 0.16 m thickness, and layer permittivities of 20.3 and 6.4 for waveguide and halfspace, respectively (i.e. model 2: $\epsilon_{2,SIIa} = 20.3$, $\epsilon_{3,SIIa} = 6.4$, $h = 0.16$ m). Water contents inferred for the waveguide are high (i.e. above 35 v%). Separate analysis of the possible higher order mode (i.e. TE1 inversion) also resulted in a non-unique solution with models predicting waveguide permittivities close to 17, and halfspace permittivities of 2.2 or 7.2. A joint inversion of fundamental and higher mode did not improve our results.

Note that the theoretical cut-off frequencies calculated using equation 5.1 which correspond to May and September models are reported in Table 5.2 and 5.3 and are displayed as vertical lines in Figure 5.7b, d, e. The first higher mode (i.e. TE1) in the May data is predicted at 580 MHz. This falls outside of the bandwidth of the antennas used for the measurement and hence this higher mode is not evident in the dispersion images of the common offset datasets. The critical frequency for the TE1-mode in the September SI models is above 330 MHz. The dispersion images, however, do not show evidence of that higher mode.

5.3.6 Discussion of inversion procedure

Key inputs for effective inversion of waveguide dispersion data are the range and density of frequencies selected (*Bikowski et al.*, 2012). We have presented inversion results based on best fit to all data points that could reasonable be extracted from the field experiments (see Figure 5.9). The number of phase velocity frequency data pairs was between 50 and 130 (i.e. as picked from the dispersion images), and around 800 for the fk-cloud data. Thus the frequency range that produced the final inversion result is that of the data shown in Figure 5.9 and discussed in the previous section. Figure 5.10 shows inversion results for ϵ_2 plotted against ϵ_3 in a scatter plot where the colour of the

symbol represents L1 error and the symbol size is proportional to the waveguide height h. Figure 5.11 illustrates the conversion path for the waveguide dielectric properties only. Symbol size represents misfit in this plot. In Figure 5.12a-c, misfit is plotted against the waveguide parameters ϵ_2, ϵ_3 and height, respectively, in order to better visualise the model sensitivity for each parameter. The inversion for May data seems to be well constrained and we did not encounter non-uniqueness issues within the parameter space used for inversion. We found, however, that minimisation for some diffractions in September resulted in two models that both minimise the cost function to a sufficient degree as illustrated in Figure 5.10 (i.e. SIa and SIIa models) and Figure 5.11 (cluster of symbols with same circle size, e.g. SIa (yellow), SIIa (grey) and SIIb1 (blue) circles). Two physically reasonable waveguide geometries result in low misfit (i.e. blue symbols in Figure 5.10, small circles in Figure 5.11). The waveguides differ in dielectric permittivity and waveguide height. The two waveguide constellations that fit the data are i) a thin waveguide with high waveguide and halfspace dielectric permittivities and corresponds to ii) a thicker waveguide with lower dielectric permittivities. While both models can produce dispersion curves with similar shape, this ambiguity is frequency limited. The lower limit is the higher cutoff frequency, which is typically determined by the thinner waveguide model (see Table 5.2). At higher frequencies, the TE0 dispersion curves will diverge as each model converges to the velocity given by the layer below the waveguide. The second difference between the two models is the incidence of the first higher mode which also is at higher frequencies for the thinner waveguide. For the SI data, the thinner waveguide predicts a higher mode at around 350 MHz and the thicker waveguide between 450 and 600 MHz. The dispersion images SI of the September field data, however, do not show any signs of a higher mode and the signal to noise ratio at above approximately 300 MHz appears too low for signal detection.

In a recent publication, *Bikowski et al.* (2012) investigate the influence of frequency range used for dispersion inversion on recovered parameter certainty. They find that by removing phase velocity data points at the lower frequency end, the lower halfspace permittivity result becomes uncertain. By removing data points at the high frequency end, however, the certainty of waveguide layer permittivity and height is affected. Those findings suggest that dispersion curves from May are better defined

	v [m/ns]	ε_r	h [m]	c_{H2O}[a] [v%]
layer 1	0.300	1	2.00	-
May, layer 2	0.130	5.3	0.20	8.1
May, layer 3	0.179	2.8	-	0.2
$f_{c,0}$: 106		$f_{c,1}$: 581		
Sep. SI, layer 2	0.110	7.5	0.26	13.6
Sep. SI, layer3	0.165	3.3	-	2.0
$f_{c,0}$: 57		$f_{c,1}$: 339		
Sep. SIIb2, layer 2	0.087	12	0.21	22.7
Sep. SIIb2, layer3	0.165	3.3	-	2.0
$f_{c,0}$: 37		$f_{c,1}$: 279		
Sep. SIIa, layer 2	0.067	20.3	0.16	35.8
Sep. SIIa, layer3	0.119	6.4	-	11.0
$f_{c,0}$: 45		$f_{c,1}$: 296		

[a] estimated with CRIM model (porosity 0.4, $\varepsilon_{r,s}$ 4.4)

Table 5.3: *Waveguide and underlying halfspace parameters and volumetric water content c_{H20} for inverted dispersion curves shown in Figure 5.9. Model parameters are derived using inversion of fundamental TE mode for dispersion curves extracted from the field examples May and September.*

for their waveguide permittivity and height due to high frequency information, which is consistent with the findings here. *Van der Kruk et al.* (2006) and *Strobbia and Cassiani* (2007) found similar lack of sensitivity and non-uniqueness related to waveguide height and dielectric properties.

The SIIa curve shows a second mode in the dispersion image (Figure 5.6f), but it is not clear that this is a higher order mode. A joint inversion using the lower frequency part as TE0 and the higher frequency part as TE1 did not decrease the misfit and the predicted model is unrealistic with dielectric permittivity values below 1 (local minimisation is unconstrained) and a waveguide height of 2 m (results not shown here). An alternative explanation for the second mode is disturbance introduced by interface roughness (compare *der Kruk et al.* (2012)) or lateral changes in waveguide properties.

Cutoff frequency prediction for fundamental and higher order modes might be useful to interpret inversion results. One might favour the models that predict higher cutoff frequencies (thinner waveguide) as we could not observe higher modes in the dispersion images.

Apriori knowledge can provide further constraints for the parameter space used for inversion. In a inhomogeneous geologic environment and at large scales, however, additional information might be difficult to obtain. Certainty and uniqueness could be improved by introducing the frequency-slowness magnitude (i.e. amplitude) of dispersive modes into the inversion process as already proposed by *Van der Kruk* (2006).

5.3.7 Effect Of Rainfall On Waveguide Properties

We have interpreted the waveguide analysis and inversion results and summarised key outcomes in Table 5.3. The soil moisture derived from the May 2011 data is typical for the period immediately after early precipitation in sandy environments following an otherwise extended dry summer period. The uppermost layer is moist sand underlain by dry sand. Towards the end of the wet season in September, the dispersion characteristics changed significantly for the sand part of the profile (SI diffractions). The waveguide again occurred after extensive rain which was preceded by a period of dry conditions. Intermittent rain persisted during data acquisition. When compared to the May 2011 results, the soil moisture in the waveguide is higher and the sand below is slightly moist rather than dry. The derived dielectric permittivity for the halfspace in the thick SI models appears quite low (i.e. $\epsilon_{3,SI_1} \approx 3.3$, $\nu = 0.165$ m/ns, $c_{H2O} \approx 2\ \%$) and more realistic for the thin waveguide model (i.e. $\epsilon_{3,SI_2} \approx 4$, $\nu = 0.15$ m/ns, $c_{H2O} \approx 5\ \%$). Diffractions found on wetland soils reveal the highest water content. In particular diffraction SIIa predicts volumetric water contents between 0.35 and 0.4, depending on the choice of model and porosity used for the CRIM. The peat like surface layer is very rich in organics and may have a porosity of up to 60 %. It is likely that this material can take up and temporarily hold large amounts of water. Here porosity is expected to be much larger than other mineral soils and high water content is unlikely to equate to full saturation of these more peaty soils.

The velocities and moisture contents derived from waveguide properties are reasonable within the framework of other field observations made on the Gnangara Mound (*Strobach et al.* (2012b,a) and references therein). That is, in May 2011 high velocities above 0.17 m/ns are common for the extremely dry sands down to several meters.

5.4 Conclusions

A high dielectric permittivity layer embedded into lower dielectric layers above and below leads to a waveguide for radiated electromagnetic energy (i.e. radar waves). These trapped waves travel and disperse within the shallow low-velocity waveguide with very low loss. Heterogeneities within the shallow waveguide produce diffractions in ground-penetrating radar data. In common offset radargrams, this diffracted

energy appears as straight lines with dispersive pattern. The dispersion characteristics of those diffracted events contain the same dispersion information as the direct waves sampled with a common midpoint or common shotpoint geometry. The linear moveout of common offset diffractions, however, is twice the slope and spatial aliasing therefore occurs at lower frequencies compared to the common shot geometry for a given spatial sample interval. The dispersiveness of the common offset diffracted wavefields is consistent with two-way travel which means that the diffractor we investigated scatters an already dispersive wavefield. Hence, the resolution of maxima in common offset dispersion images is higher compared to resolution obtained from a common shot gather with equivalent offset. Thus, after two-way time adjustment, a multi-offset data analysis method can be used on common offset data to compute dielectric properties of the near subsurface.

Common offset diffraction hyperbolae from two field campaigns have been analysed for their dispersion characteristics. To extract dispersion characteristics, two methods have been compared. The slant-stack method provides frequency-slowness dispersion images which reveal high resolution after extracting single diffracting legs and muting unwanted data. For rapid dispersion characterisation, a data transformation to frequency-wavenumber domain can offer an alternative method which does not require muting and offers adjustable spatial averaging. Preliminary results validate this approach.

We successfully recover waveguide parameters from our field data by inversion, using modal wave propagation in a single-layer waveguide model. Waveguide velocities can be linked to dielectric permittivity and layer water content. The examples illustrate the sensitivity of this method to subtle variations in waveguide properties due to seasonal changes in water content and lateral variations due to different soil material. The seasonal changes in waveguide dielectric properties are attributed to water content variations related to rainfall. Lateral variations are likely due to differences in water retention properties of the surface soil horizon. With this new interpretation scheme, soil moisture distribution can be derived for the shallow subsurface on large scales.

Shallow diffractions in GPR data are common in near surface settings and can have many origins. Suitable diffractions may result from tree roots with high dielectric permittivity or dry pockets within partially water saturated sands. The dispersive char-

acteristics of diffractions in shallow waveguides have been demonstrated as a new way of extracting information from common offset ground penetrating radar data, the most commonly acquired data. We see many potential scientific applications for our work. Possible applications include estimation of shallow moisture distribution for example during infiltration experiments, soil characterisation in agriculture, monitoring of surficial thawing of permafrost, early target identification in UXO detection and terrestrial or extraterrestrial pedological investigations.

Chapter 6

Temporal Variations In Soil Moisture

Water retentive soil horizons have an influence on unsaturated flow on the Gnangara Groundwater Mound, north of Perth, Western Australia. To investigate unsaturated flow regimes, borehole radar techniques were deployed which can provide estimates of soil moisture variations during an annual recharge cycle. Zero Offset crosswell Profiling and Vertical Radar Profiling measurements were performed on a monthly basis before, during and after annual rainfall in 2011. Time-lapse experiments show interval velocity decreases which are consistent with expected increase in vadose zone water content.

Zero Offset Profiles (ZOP) show high repeatability but suffer accuracy of absolute velocity estimates for closely spaced boreholes. While Vertical Radar Profiles (VRPs) have lower precision, they provide an independent and robust method to derive interval velocities based on local slope analysis of first-break arrival times. The mismatch between VRP- and ZOP-derived absolute ground velocities in the saturated zone is used as correction for the ZOP profiles. The highly repeatable and corrected ZOPs form the basis for water balance analysis.

Time-lapse experiments from six test-sites reveal three vadose zone infiltration regimes: I) Full recharge potential after 200 mm rainfall, II) delayed wetting below 2 m depth and impeded recharge and III) dry soil and no water content changes below 7 m depth, possibly no or negligible flux to the water table.

Results from time-lapse borehole radar are in good agreement with time-lapse Neutron logging observations made in previous years at comparable test-sites. A simple water balance can be derived from the time-lapse borehole radar for regime III which

reveals an evapotranspiration rate of 620 mm during the study period which compares favourably with previous studies.

Before presenting the results from my research, the chapter starts out with a brief introduction to groundwater recharge and how geophysics can be applied to study hydrologic processes, followed by an overview over the two techniques borehole radar and neutron logging and a compilation of previous recharge studies performed on the Gnangara Mound.

6.1 Geophysical Techniques In Groundwater Recharge Studies

Scanlon et al. (2002) and *De Vries and Simmers* (2002) discuss scale-dependent processes of groundwater recharge and techniques to measure the amount of water that replenishes an aquifer. As most processes are scale-dependent, so are the monitoring procedures that are applied to capture spatial and temporal variability. Techniques are either aimed on directly monitoring infiltration (e.g. unsaturated zone moisture dynamics, seepage and discharge from rivers) or indirectly inferring recharge from environmental indicators (e.g. water table fluctuations, environmental tracers, forced tracers). I have pursued an approach featuring geophysical techniques, for more detail on classical hydrogeologic methods used for recharge studies, I refer the reader to the beforementioned publications and references therein, or one of the numerous hydrogeologic text books such as *Sharma* (1989), *Fetter* (2001) or *Healy* (2010).

Geophysical techniques have become more popular in recent decades (largely due to technological changes in electronics and wider availability of these technologies) and can contribute where contrasts in material properties develop in time or space due to hydrologic processes, which are significant enough to change the bulk physical properties of the subsurface to a measurable extent. They can be used as a mapping tool and provide physical property distributions and thus structural information important for unsaturated or saturated flow modelling. Geophysical techniques may also be employed in a time-lapse mode to monitor changes in fluid distribution in the subsurface. The United States Geological Survey published a review article by *Ferre et al.* (2007) in which the authors discuss a variety of geophysical techniques that

have been successfully used to qualitatively or quantitatively characterise groundwater recharge. The case studies provided in that publication demonstrate that almost every imaginable physical property could be exploited for groundwater recharge investigation. The prominent include density (i.e. gravimetry), elastic parameters (seismic), dielectric properties (TDR, GPR), electrical properties (ERT, EMI, TEM, spectral IP), electrokinetic phenomena (SP, seismoelectric), proton precession (NMR), hydrogen density (Neutron logging) and temperature. However, the first step of planning a geophysical survey is a clear understanding of the hydrogeologic objective. That is, what are the temporal and spatial hydrogeologic characteristics that are investigated, and which geophysical methods can provide the spatial and temporal resolution on a relevant scale with appropriate accuracy?

The methods used in this thesis cover several aspects of groundwater recharge. The spatial characterisation of water retentive layers that possibly influence groundwater infiltration discussed in chapter 4 have the objective to refine a vertical flux model by introducing layers and spatial variability into a more complex soil profile than initially sought to be implemented into WAVES and the VFM. The spatial scale ranges from meters (i.e. in depth) to tens of kilometres (i.e. laterally). The only remote sensing method that could provide data at the desired vertical and lateral resolution and coverage given the soil environment and cost and time constraints is common offset surface GPR. Vertical resolution is maximised by borehole logging, using methods such as lithologic, gamma ray, Neutron-Neutron, GPR and induction conductivity measurements.

In this chapter, I present time-lapse borehole techniques to capture snapshots of soil moisture depth profiles to infer infiltration characteristics to better understand the influence of water retentive soil layers on vertical flux on a test-site scale. Thus the vertical resolution and temporal variations are of principal importance, whilst the lateral variations are captured by investigating site-specific infiltration at various test sites. The temporal scale of the investigation is determined by climatic factors such as rainfall in winter and a long dry period in summer. As vertical flux is inhibited by high matrix potential, for example in dry sands, the soil profile has to be initially wetted before transient flow occurs at short time-scales and without considerable storage. Due to the extensive drying of the Gnangara Mound soil profile in summer, the time scale

of water infiltration after the first annual rainfall introduces changes on a monthly scale if the entire bulk unsaturated zone is considered. This is the time-frame targeted in this study. To capture the full natural infiltration cycle, a baseline measurement is done before annual rainfall starts, and subsequent measurements during the rainfall period. After one or two months, the soil profile is moist and precipitation is then largely flowing according to the unsaturated hydraulic conductivity at or close to the soils' field capacities. I would like to mention that the mechanisms involved in the initial wetting and transient flux are probably more complicated due to preferential flow phenomena (*Miyazaki*, 2006). The geophysical methods used in this study cannot resolve preferential flow paths. However, data analysis and conclusions drawn from the study acknowledge and include the potential presence of preferential flow.

From a hydrogeologic perspective, the approach taken in this study is classified as an indirect flux measurement within the unsaturated zone to characterise direct recharge. Direct recharge means that the precipitation infiltrates where it occurred (i.e. no surface runoff). The geophysical measurements are considered indirect because they require conversion from physical property to water content. A direct method is for example a lysimeter where water content changes are determined by weight changes of a full soil profile, or a direct seepage measurement based on flow. Interpretation of unsaturated infiltration studies can for example be based on water budget calculations; for example by using the zero flux plane technique (*Sharma et al.*, 1991). Alternatively, unsaturated flow parameters (e.g. van Genuchten parameters, unsaturated hydraulic conductivity) can be estimated from transient flow and recharge can be directly calculated using Darcy's law. However, this typically requires high temporal resolution to capture transient flow, and a soil that is close to its field capacity when precipitation occurs. Such measurements were not attempted during this study.

As has been described in earlier chapters, GPR is a geophysical technique suitable to quantify water content with high accuracy. Because the spatial characterisation of soil variability was also performed with GPR, it appeared to be a reasonable approach to also use a GPR-based technique to investigate the temporal variations using borehole radar, as this acquisition geometry would supplement the surface GPR and possibly provide useful insights into wave-propagation characteristics in a more direct fashion (i.e. attenuation analysis, velocity profiles). The classical geophysical technique used

to monitor vadose zone dynamics, is Neutron logging, and is used to compare and evaluate the approach I used with borehole radar.

6.2 Introduction To Geophysical Techniques

6.2.1 Borehole Radar

Time-lapse BHR measurements in the vadose zone have been applied successfully in many hydrogeophysical investigations. *Hubbard et al.* (1997) detect permeable pathways, *Deiana et al.* (2007) and *Looms et al.* (2008) monitor migration of forced infiltration fronts through soil, *Day-Lewis et al.* (2003) image tracer transport in fractured rock, *Chang et al.* (2004) use attenuation and traveltime tomography for monitoring of a salt tracer plume in soil and *Alumbaugh et al.* (2002) investigate accuracy and repeatability of moisture contents estimates from cross-borehole GPR measurements in the unsaturated zone. Studies performed by *Binley et al.* (2001) and *Farmani et al.* (2008) are similar to this study as they monitor natural infiltration on a seasonal basis with crosswell radar.

For bi-static antennae, various borehole acquisition geometries can be applied. In case of two adjacent wells, crosswell measurements can be performed as a vertical scan where the relative position of the antenna pair remains constant, or as a multi-offset gather where one antenna moves relative to the other. For a vertical scan, two geometries are possible: i) the zero vertical offset profiling (ZOP) where both antennae are lowered simultaneously into the adjacent wells while their midpoints are at the same horizontal level (*Rucker and Ferre*, 2003) (schematic in Figure 6.1, data examples in Figures 6.2 (right), 6.3 (right), 6.4, 6.5b), or ii) a constant offset profiling geometry where the antennae are kept at a constant offset, but horizontally shifted. Vertical scans are the fastest way to obtain a 1D tomographic velocity profile.

The most elaborate acquisition method is the multi-offset geometry. Data acquisition involves moving one antenna at small increments in hole A (e.g. 0.05 - 0.1 m) , while the second antenna remains at a constant position in the other hole B. The resulting radargram represents one shot position in hole B. The previously fixed antenna is then moved by a typically larger space increment of approximately 0.25 - 0.5 m in hole B, and the moving antenna repeats sampling in hole A creating a second shot gather,

and so forth. The procedure is then reversed by keeping antenna position fixed in hole A and moving shot by shot in hole B. Analysis of first-arrival times of the resulting shot gathers from hole A and B can provide 2D images of velocity and conductivity distribution by tomographic inversion by ray-tracing and amplitude attenuation, respectively (*Binley et al.*, 2001; *Chang et al.*, 2004; *Farmani et al.*, 2008).

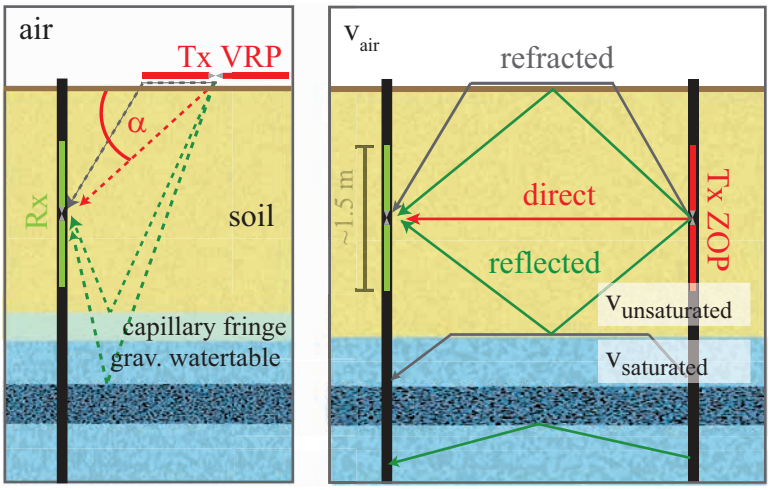

Figure 6.1: *Schematic showing possible ray paths for VRP (left) and ZOP (right) borehole radar acquisition geometries including arrivals of air- and unsaturated refracted (grey) (i.e. large well separation), reflected (green) and direct (red) waves.*

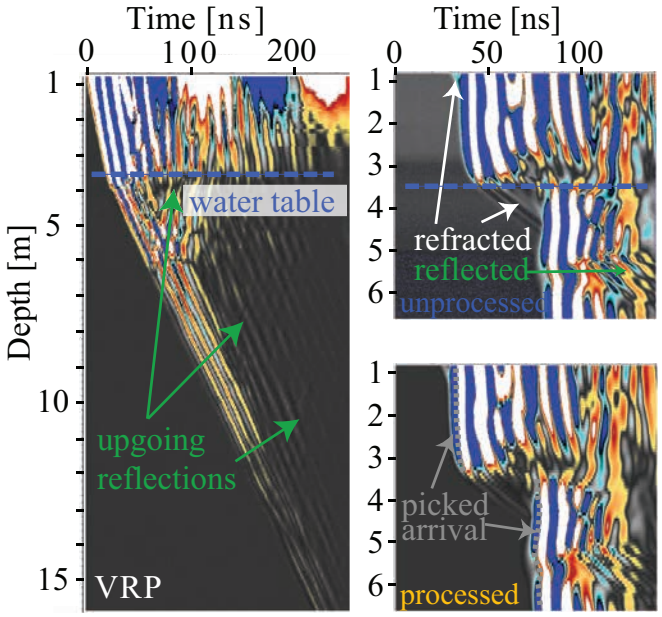

Figure 6.2: *VRP (left) and ZOP (right) profiles from NG16. Upper right ZOP is data before despiking and DC-shift removal. Note the clear unsaturated zone refracted wave in the ZOP data, and the reflections from an attenuating layer at approx. 5.5 mbNS visible in VRP (upgoing waves) and ZOP (hyperbolic).*

If only one borehole is available, BHR can be performed as a vertical radar profile (VRP, analogous to vertical seismic profiling). In this geometry, one antenna remains at a fixed position on the surface while the second antenna, typically the receiver, is lowered into the well. A data examples are given in Figures 6.2 (left), 6.4 (right), 6.5d and 6.6. The surface antenna is typically placed such that the radiation and sensitivity pattern of transmitting (Tx) and receiving antenna (Rx), respectively, are well coupled

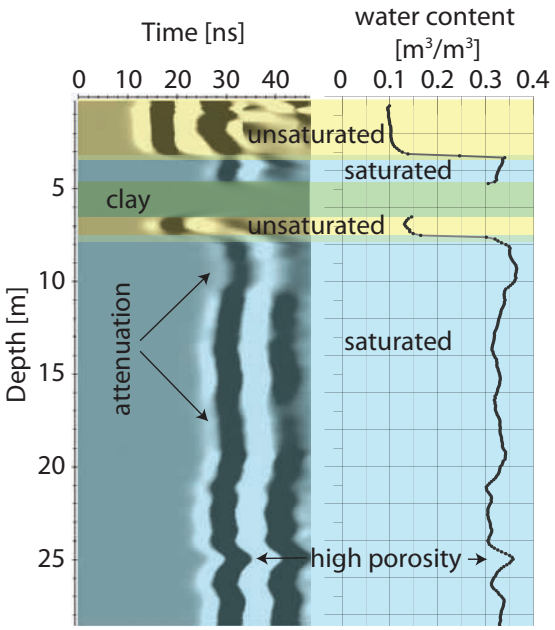

Figure 6.3: *ZOP from the TGT test-site (left) and corresponding water content profile (right). A hanging water table is revealed by a sequence of i) high velocity (first 3 mbNS, unsaturated zone I), ii) low velocity (saturated zone I), iii) attenuating layer, no signal recorded at 4.5 - 6.5 mbNS, iv) high velocity (unsaturated zone II, $\approx 1\ m$), and v) low velocity (saturated zone II). Within the saturated zone, ZOP can provide information on elec. conduct. (e.g. attenuation due to clay), and on porosity (i.e. higher velocities $\rightarrow$ lower water content $\rightarrow$ lower porosity).*

(*Tronicke and Knoll*, 2005), that is the long axis aligns with the hole (copolarized). A true zero-offset (i.e. antenna midpoint at well) is not desirable as the antennae are null-coupled in that setup. An equivalent zero-offset VRP has the tip of the antenna close to the borehole and the midpoint is therefore away from the hole. VRPs can provide 1D interval velocity information or 2D tomographic and migrated images from multioffset VRP (*Boeniger et al.*, 2006). As discussed by *Tronicke and Knoll* (2005), air-refracted energy occurs at offset VRPs and has to be accounted for. *Clement and Knoll* (2006) and *Cassiani et al.* (2004) use straight-ray based tomographic inversion to find a smooth layered earth model from VRP travel times. This method is based on absolute travel times and therefore zero-time correction is needed. Calculation of local gradients of travel times (*Cassiani et al.*, 2008) is an alternative method to determine interval velocity without any zero-time correction.

Precise recovery of subsurface properties from BHR can be challenging and care has to be taken to avoid artefacts and false velocity estimation (*Peterson*, 2001). Phenomena such as energy travelling from antenna tip to tip at high ray angles (*Irving et al.*, 2007), time-variation of zero-time (*Peterson*, 2001), borehole deviation, waveform distortion and refracted energy can lead to under- or overestimation of true ground velocity. Depending on the objective of the study, incorrect velocity estimates can alter the outcome severely, or little. My studies demonstrate that incorrect absolute velocities have a significant impact on water content estimates, but the effect on time-lapse differential moisture content curves (the curves representing the change in water con-

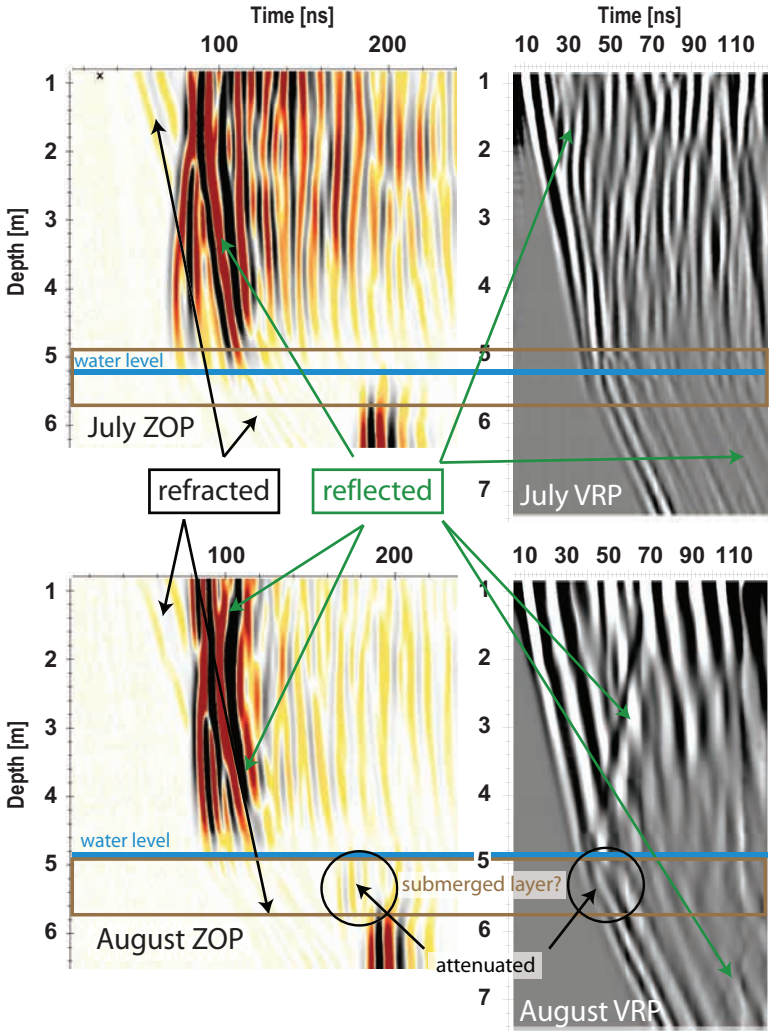

Figure 6.4: *ZOP data example from Whiteman Park, site 4 from July (upper) and August (lower) showing refracted energy which is clearly separated from direct arrival due to low amplitude and large well separation. Change in water table depth measured with dipper (blue line) has a strong effect on ZOP radargram. Note the additional layer submerged in August with higher velocity, and higher attenuation compared to the direct wave arrivals below. This layer is not obvious in the July data.*

tent between subsequent experiments) is less severe as the first order effects of the error cancel. Furthermore, a water balance calculation that includes decreasing and increasing velocity (i.e. wetting and drying) cycle seems to be unaffected. Systematic errors resulting in underestimation of cumulative water content changes during wetting are compensated during the drying due to overestimation of cumulative water content change.

In my study I concentrated on ZOP and VRP geometries for BHR experiments as these are the most likely practical solutions.

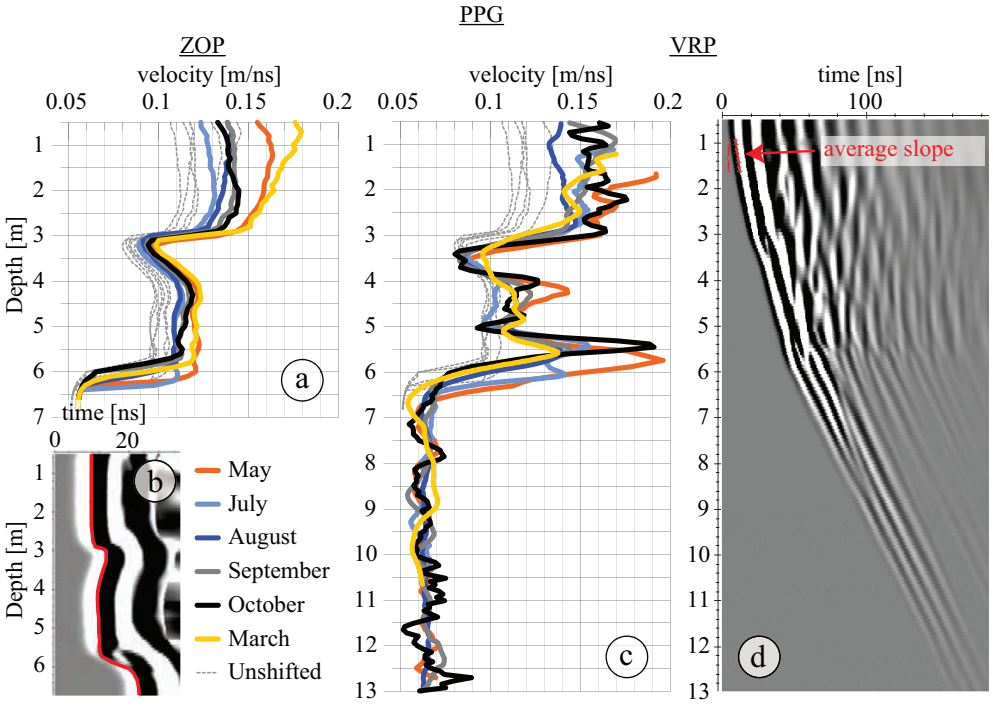

Figure 6.5: *Zero-offset crosswell profiling (b) and Vertical Radar Profiling (d) data examples from the Pinjar Piggery test site. Depth profiles represent velocities that were derived from equation 6.1 for the ZOP case, and equation 6.2 for the VRP example. Red lines in (b) and (d) indicate the picked zero-crossing for traveltime and slope analysis. The time-lapse velocity curves in (a) and (c) show high velocities in May 2011 before infiltration occurred, and reduced velocities during the winter month, followed by drying in March 2012. Note that the ZOP curves (a) are repeatable with low inherent noise, while the VRP curves (c) show higher noise level and are prone to inaccuracy from 0 - 2 m depth. Dashed grey curves in (a) and (c) are initial ZOP velocities which have been zero-time corrected to match VRP results (coloured curves in (a)).*

6.2.2 Neutron Logging

Neutron logging is an alternative technique that is capable of precise measurement of moisture content profiles in a borehole. For Neutron measurements, a Didcot Neutron probe[1] as displayed in Figure 6.7 has been used. The probe consists of a 50 mCl Americium-Beryllium fast Neutron source which emits fast (also called epithermal) neutrons that collide with the atomic nuclei of the soil. Hydrogen atoms (soil water) are the main contributor in elastic scattering as these atoms most closely match the mass of the neutron, slowing these fast neutrons. Slowed neutrons eventually reach a lower, "thermal" energy level. Slow neutrons are detected by a boron triflouride (BF_3) detector. Thus Neutron logging is a powerful geophysical logging technique to measure soil moisture. *Bell* (1987) wrote a "Neutron probe practice" report[2] where the

[1] http://nora.nerc.ac.uk/5845/1/IH_079.pdf
[2] http://nora.nerc.ac.uk/5629/1/IH_019.pdf

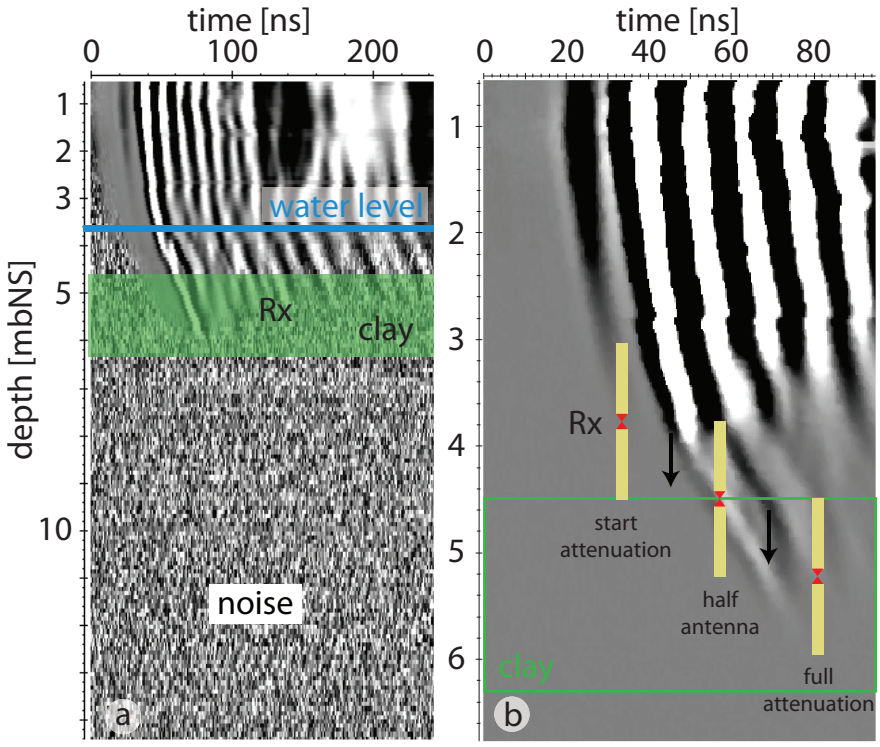

Figure 6.6: *VRP data example from TGT showing loss of energy below clay layer. Radargram in (a) is displayed with AGC-gain and tracenormalisation revealing that no energy penetrates the clay. Amplitudes in (b) are preserved. Some energy apparently "leaks" into the clay layer probably due to the finite antenna length and maybe as guided wave in the hole. Note that the depth axis represents the antenna midpoint, thus the upper part of Rx records attenuated energy although its lower part reaches into the clay.*

author summarises best practice in data acquisition and processing for hydrogeologic investigations. Other useful references and case studies include *Kramer et al.* (1992); *Flint and Flint* (1995); *Flint et al.* (2001); *Ferre et al.* (2007).

The neutron instrument provides raw neutron counts within given time interval, typically registered counts per second (cps). The counts can then be normalised (ncps) to a reference reading by placing the probe into a bucket of water. Normalisation can be important due to instrument drift, for example due to temperature variations, or the long-term decrease in radioactivity of the neutron source. The next step is to calibrate neutron counts against water content. Raw relative neutron counts are linearly related to water content, while each soil has a unique slope and x-axis intercept. A common calibration is performed in-situ by repeating neutron readings under varying environmental conditions during different seasons (*Bell*, 1987). Neutron logging is then accompanied by direct soil sampling, which provides gravimetric soil moisture profiles for calibration. The direct sampling procedure, however, can be problematic for ex-

ample due to compaction as a result of the sampling process. By plotting measured volumetric water content against neutron counts, a calibration curve is obtained, which typically reveals a linear relationship between the two quantities. The linear slope of the calibration curve typically increases with finer soil texture (*Bell*, 1987) (i.e. sands $\rightarrow$ small slope ($\approx$ 0.8 m^3/m^3/ncps), loam $\rightarrow$ intermediate slope ($\approx$ 0.87 m^3/m^3/ncps), clays $\rightarrow$ highest slope ($\approx$ 0.95 m^3/m^3/ncps). Thus, the variation in slopes throughout greatly differing soils is not huge. Further discussion on this will be part of section 6.5.4.

The minimum count, that is the counts for dry material or the x-axis intercept, is smallest for clays (0.012 ncps), slightly higher for loam (0.018 ncps) and highest for sands and gravel (0.05 ncps). Note that those values are relative counts. For the probe used here, the reference counts are usually between 600 and 700. The counts for dry material are therefore expected to be between 10 cps (clay) and 30 - 40 cps (sand).

Figure 6.7: *Neutron logging in the field with Didcot Neutron moisture probe.*

6.3 Measurement Campaigns On The Gnangara Mound

6.3.1 Previous Studies On The Gnangara Mound

The vadose zone time-lapse BHR measurements performed during this study are the first of their kind to be carried out in Australia. Previous recharge and soil moisture studies solely employed Neutron logging techniques to obtain time-lapse moisture pro-

files at well locations. Several campaigns were performed on the Gnangara Mound, either to derive recharge rates, or to monitor soil moisture for ecologic studies. For example, *Sharma et al.* (1991) presents time-lapse moisture profiles from the Pinjar area to derive recharge and evapotranspiration rates for the late 1980s. Since 2000, a series of time-lapse Neutron logging has been performed by Kel Baldock for Department of Water of Western Australia, Water Corporation and Edith Cowan University as previously mentioned in chapter 3. Measurement campaigns that I am aware of are listed in Table 6.1. However, the results from those studies have not been reported or published. In this section, some of this data are presented in order to compare to the borehole radar measurements (as it is not published elsewhere), and to draw some conclusions from observations that could not be made from the BHR study alone due to limitations in observation timespan. The largest time-lapse Neutron dataset came to my attention after the time-lapse BHR was finished in late 2011. These data are from boreholes located in the Pinjar area covering the winters from 2002 - 2004. Two example datasets are shown by *Silberstein et al.* (2009), who also refer to the larger dataset. In that report, the authors compare model results from the Vertical Flux Model with Neutron moisture measurements. Beforehand data from Whiteman Park covering the winter of 2009 and 2010 were available to me. While writing this thesis, I discovered that the Whiteman Park dataset I was given is incomplete and that further data exist from 2006 onwards (*Froend et al.*, 2010). Another big dataset came to my attention when meeting Kel Baldock in March 2012. For the soil layer mapping project, 62 sites have been logged on one occasion in winter 2007. Although most datasets have not yet been fully analysed, I found it important to list all campaigns for future reference, as a unified data management system is not yet in place, and information about the Neutron campaigns are not publicly available to date.

6.3.2 Climate During Time-Lapse Experiments

Rainfall and evapotranspiration values[3] during the study period are plotted in Figure 6.9. Rainfall from previous years where Neutron logging campaigns took place is displayed in Figure 6.10. Average annual rainfall is approximately 800 mm for 2011. Previous years showed variable rainfall where 2002 and 2010 were extremely

[3] http://www.bom.gov.au/climate/data/

Table 6.1: *Neutron logging campaigns performed on the Gnangara Mound.*

Location	Years	Repeat rate	Comments
Central Gnangara Mound	1985 - 1987	3 - 4 month (?)	8 sites north of Pinjar (?), Banksia woodland on Bassendean Sand (4 upslope, 4 downslope); Sharma et al. (1991)
Pinjar Area	2002 - 2004	(bi-)monthly	Pinjar Area, PM4, PM6, PM7, PM9, PV1, PV2, PV3, PV4; Water Corp, or R. Silberstein (CSIRO)
Vegetation Sensitive Areas	Summer 2007	monthly	4 repeats Feb. - May, 17 sites incl. Pinjar ; Water Corp. and ECU (?)
Soil Layer mapping	Winter 2007	once	63 locations on Gnangara Mound; Water Corp.
Wetland Investigations	2007/08 - 2009	monthly	Bindiar, Joondalup, Nowergup; Dept. of Water, Josephine Searle
Whiteman Park	2006 (?) - 2009 - 2011	(bi-)monthly	Sites 1 - 7; Ray Froend (ECU)
Pinjar Area	Mar-12	once	11 sites: PPG, HHW, HHWW, HHWE, PV2, PV3, PM4, PM6, PM7; Curtin University, Elmar Strobach

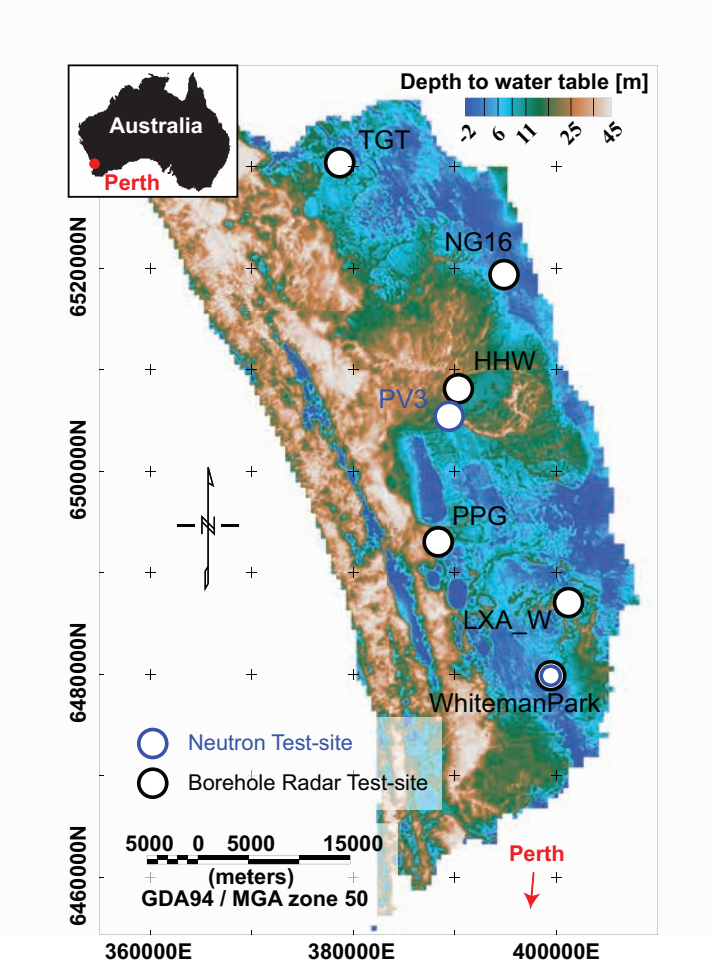

Figure 6.8: *Map of Gnangara mound showing test-sites where time-lapse BHR (black circles) and Neutron logging (blue circles) was performed. Neutron logging sites are selected as they are close to the BHR sites, and show inhibited infiltration similar to BHR results.*

dry years with total rainfall between 400 - 500 mm. Annual pan evapotranspiration is around 1800 mm. This value, however, is not the actual evapotranspiration that occurs in natural bushland setting. *Farrington et al.* (1989) and *Farrington et al.* (1990) measure evapotranspiration directly with ventilated chambers for Banksia woodland and dampland on the Gnangara Mound, respectively. They obtain average values of 666 mm/year (1985 - 1986, 77 % of rainfall) and 814 mm/year (1987 - 1988, 109 %) for Banksia woodland and dampland, respectively. *Sharma et al.* (1991) apply the zero flux plane technique to calibrated time-lapse neutron logs and derive recharge rates between 5 % and 20 % from eight test sites between 1985 and 1987. Those values are equivalent to 95 % and 80 % evapotranspiration rate based on annual rainfall records, respectively.

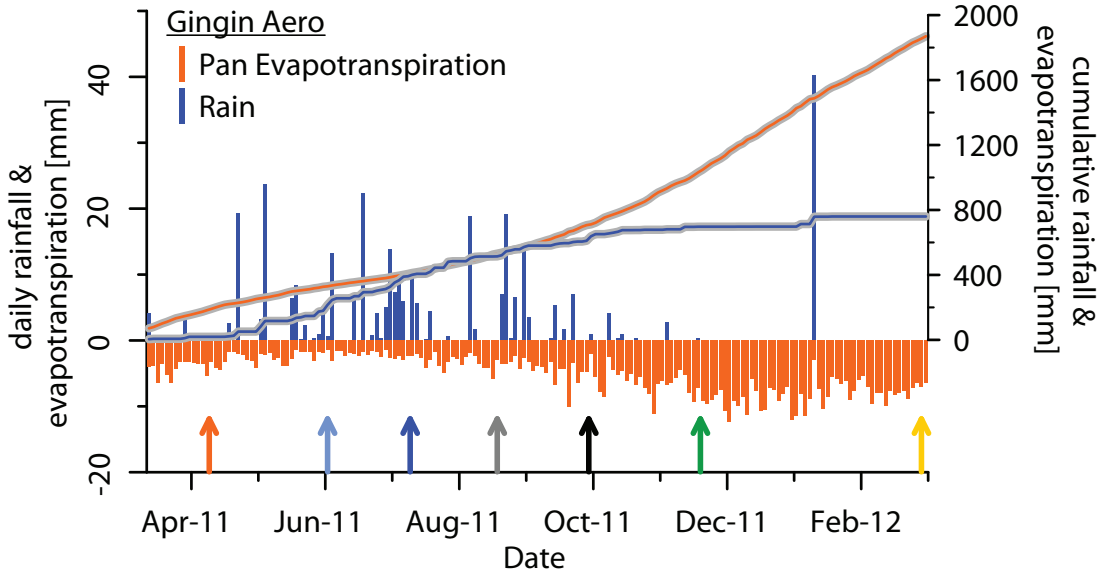

Figure 6.9: *Daily and cumulative rainfall and evapotranspiration 2011 shown as bar chart and line plots, respectively in blue and orange. Coloured arrows indicate dates when borehole radar time-lapse experiments were performed (HHW) before, during and after winter rainfall. Rainfall and evapotranspiration data are from BoM Gingin Aero climate observatory.*

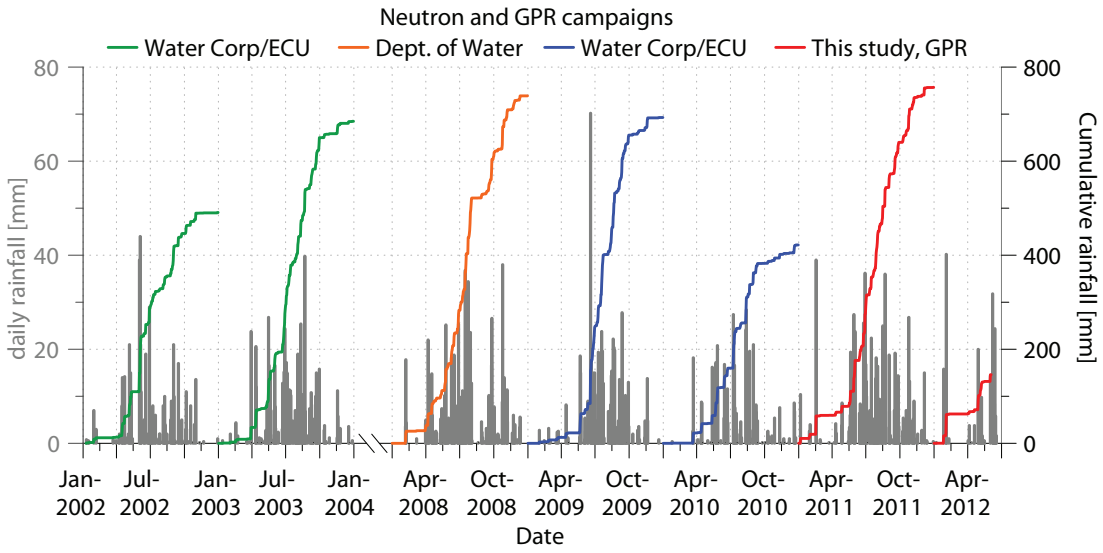

Figure 6.10: *Daily and cumulative rainfall for years with neutron data (green, orange and blue curves) and this study (red lines). Note the large variability throughout the years. 2002 and 2010 were exceptionally dry with annual precipitation below 500 mm.*

6.4 Test Sites And Field Experiments

6.4.1 Test Sites

The BHR data were acquired at six test-sites that were chosen to provide a range of geologic situations present at the Gnangara Mound. The depth to water table map in Figure 6.8 shows the test-site locations as black circles. All the sites are characterised

as medium to high groundwater recharge areas according to the VFM model. Site characteristics are listed in Table 6.2. The most important hydrogeologic parameters for groundwater recharge estimation are the soil properties (e.g. unsaturated hydraulic conductivity, clean or indurated sand), depth to water table, vegetation and rainfall. Sites Lexia West (LXAW), Tangletoe (TGT) and North Gnangara 16 (NG16) have shallow water tables; Pinjar Piggery (PPG) and Whiteman Park Site 4 (WP) have intermediate depth to water table and High Hill Road West (HHW) a deep water table (Figure 6.18 3a-f). Sites PPG, HHW and WP show inhomogeneous soil profiles with indurated sand layers above the water table (*Searle and Bathols*, 2009; *Bertuch and Froend*, 2006). NG16 has a clayey layer below the water table (*Pigois*, 2010; *Strobach et al.*, 2012b) and NG16 and WP have an additional radar reflector at around the water table, which has not been identified from drilling. TGT has a more complex geology with a locally perched water table above a clay layer (*McHugh and Hammond*, 2011), an unsaturated horizon below the clay, followed by a second water table (regional water table) (Figure 6.3). For BHR crosswell acquisition, the borehole separation is of great importance. WP has the largest borehole separation (11.5 m) followed by NG16 (4.8 m). TGT has a nest of 4 aligned holes of which combinations with separations of 1.95 and 3.54 m were used for crosswell experiments. LXAW also has 3 holes in triangular arrangement with separations of 2 m, 4.05 m and 5.74 m. Closely spaced wells are PPG (1.15 m) and HHW (0.98 m).

In addition to the BHR test-sites, time-lapse neutron data are investigated that have been acquired close to the radar sites in previous years. The test-site PV3 is approximately 3 km to the southwest of HHW (blue circle in Figure 6.8). It has similar features as the HHW site with 2 indurated sand intervals and a deep water table. The Whiteman Park Neutron data have been acquired in the same borehole as the crosswell BHR, WP site 4.

6.4.2 Data Acquisition

BHR data were collected before, during and after the main recharge period from autumn to spring 2011 (see timeline in 6.9). The BHR data were acquired with the Mala ProEx 2 system and bistatic 100 MHz slimhole antennae. Measurements were triggered with a calibrated trigger wheel in constant distance increments of 1.5 cm. I

Table 6.2: *List of Borehole Radar test-site characteristics that influence data acquisition (i.e. borehole separation) and groundwater infiltration (i.e. indurated soil horizons, vegetation, depth to water table). Site-specific cumulative and sequential rainfall ($\sum P$ and ΔP_s, respectively) from different weather observatories are listed alongside soil water storage calculated with equation 6.4 from BHR derived soil water contents.*

Test-site		High Hill Rd W	NG16 Airfield Rd	Lexia West	Whiteman Park S4	PPG	Tangletoe
Date (month #)		5, 6, 8, 9, 10, 12, 3	4, 7, 8, 9	5, 7, 8, 9	4, 7, 8, 9	5, 6, 8, 9, 10, 3	5, 7, 8
Borehole separation [m]		0.98	4.85	2 (4.05)	11.5	1.17	1.95 (3.54)
Depth to watertable [m]		11.5	4 - 3.5	4 - 3.5	4.8 - 5.5	5.8 - 6.4	3.4 - 3.6
Vegetation		+	-	+	+	-/o	o
Indurated Sand intervals in vadose zone [m bNS]		[1.2 - 1.5] [2.9-3.5] [5.7-6.2] [9.2-9.8]	-	o (below 2 m?)	[1.7 - 2.3]	[2.6-3.5] [4.4-4.7]	-
Weather Station		Gingin Aero	Gingin Aero	WP	WP	Mariginiup	Gingin Aero
Measurement #	**[mm]**						
1st	ΣP	19	7	25	3	46	19
2nd	$\Sigma P / \Delta P_s$	216 / 197	246 / 239	261/236	288/285	269.4/223	246/227
3rd	$\Sigma P / \Delta P_s$	392 / 176	407 / 161	471/210	471/183	460/191	484/239
4th	$\Sigma P / \Delta P_s$	514 / 122	521 / 114	611/140	612/141	591/131	-
5th	$\Sigma P / \Delta P_s$	637 / 123	-	-	-	697/106	-
6th	$\Sigma P / \Delta P_s$	696 / 59	-	-	-	-	-
2nd	$\Delta S_{s,BHR}$	140[a] (111)[b] / 72[b] (63)[b]	98	136 (130)[b]	163	275[a] (236)[b] / 142 (118)[b]	147 (139)[b]
3rd	$\Delta S_{s,BHR}$	86[a] (80)[b] / 85 (79)[b]	-25	46 (216)[b]	24	-63[a] (-56)[b] / -27 (-23)[b]	15 (-4)[b]
4th	$\Delta S_{s,BHR}$	59[a] (49)[b] / -15 (-15)[b]	-14	-5 (-5)[b]	-5	-53[a] (-49)[b] / -29 (-26)[b]	-
5th	$\Delta S_{s,BHR}$	85[a] (72)[b] / -5 (-5)[b]	-	-	-	-3[a] (-4)[b] / -6 (-5)[b]	-
6th	$\Delta S_{s,BHR}$	-76[a] (-69)[b] / -37 (-35)[b]	-	-	-	-	-
7th	$\Delta S_{s,BHR}$	-166[a] (-139)[b] / -70 (-63)[b]	-	-	-	-226[a] (-177)[b] / -101 (-75)[b]	-
Comment		naturally vegetated	not vegetated, close to elevated street, possible runoff onto test-site	naturally vegetated but thinned at site, trees at close distance	naturally vegetated, winter pumping trial	poorly vegetated, some reestablished vegetation after logging of pine trees	gap in vegetation, natural vegetation close

[a] values for full unsaturated zone [b] unshifted ZOP results (HHW, PPG) or alternative well pair (TGT_{AC}, $LXAW_{BC}$)

chose a small measurement interval instead of stacking during acquisition as the data contained spikes that could be effectively removed by 2D median filtering (see Figure 6.2 right upper vs. lower, *Strobach et al.* (2012b)). I used VRP and ZOP geometries as described in the previous section. The center feedpoint of the dipole antenna is used as the midpoint. The closest VRP antenna midpoint offset position is 1 m away from the well, which is the distance from cable head to antenna midpoint.

Time-lapse neutron data were also acquired on the Gnangara Mound on several occasions for different purposes. All data were collected by Kel Baldock (HydroSmart) with Didcot neutron probes, serial numbers N0098 and N0126. The N0098 was used approximately until 2007. Afterwards readings from the N0126 were adjusted to match counts of the N0098 using a correction factored determined by *Kel Baldock (pers. comm.)*. Data available were collected for Water Corporation Ltd. and Edith Cowan University (ECU) in 2002 - 2004 and 2009 - 2011, at Pinjar and Whiteman Park areas, respectively. Rainfall for the years under investigation is plotted in Figure 6.10. The spatial sampling interval is 0.25 m and counts are averaged over a 16 s time window. Time-lapse experiments were performed on a monthly or bi-monthly basis.

6.5 Discussion Of Geophysical Methodology

6.5.1 Borehole Radar Accuracy And Repeatability

The precision of the BHR instrumentation and experimental procedure can be very high; that is measurements on any one day are highly reproducible. Dense spatial and temporal sampling also contribute to the precision of measurements. Significant instrument drift within the duration of the experiments as described by *Peterson* (2001) is not observed with the Mala RAMAC system . That means zero-time corrections are assumed constant during a single scan. Figure 6.12 demonstrates good repeatability of ZOP measurements from the saturated zone for time-lapse experiments. *Alumbaugh et al.* (2002) investigate accuracy and precision from repeatability of multi-offset cross-well BHR tomography experiments and the comparison to calibrated Neutron logs. They estimate the system measurement precision and obtain an average error of 0.5 % in moisture content estimation. However, their methodology does not provide an error estimate for ZOPs.

Absolute velocity estimation is prone to inaccuracy, partially due to systematic errors in defining time-zero/arrival time or the source-receiver origins. The accuracy of measured interval velocities depends firstly on the physics of electromagnetic wave propagation in an inhomogeneous medium, and secondly on the method applied to extract absolute traveltimes. Accuracy of absolute interval velocity and layer thickness resolution in ZOP BHR is controlled by:

i) zero-time correction and picking accuracy

ii) borehole separation (i.e. increasing separation $\rightarrow$ increasing traveltime $\rightarrow$ less effect of t_{corr} and picking accuracy) and accuracy of borehole geometry (i.e. possible unknown deviation)

iii) material dielectric properties (i.e. high dielectric permittivity $\rightarrow$ greater traveltime, e.g. higher precision in saturated zone)

iv) measurement frequency and antenna properties (i.e. higher frequency $\rightarrow$ smaller antennae and shorter wavelengths $\rightarrow$ higher resolution)

v) wavefield and propagation stability (i.e. interfering wavefields, refracted energy, dispersion, lossy materials)

Some of the aspects of the above are contrary to each other; for example larger borehole separation results in smaller traveltime errors in regards of picking and zero-time correction, but may also lead to refracted energy and hence overestimation of interval velocity and loss of layer resolution. The accuracy of water content estimation is dependent on how representative the mixing model or empirical relationship is when applied to the velocities. Ideally, a local relationship between dielectric permittivity and volumetric water content is established for every stratigraphic unit or soil horizon. I have measured this relationship for many representative samples in a coaxial transmission line as described in chapter 3. I found that the (empirical) Topp relationship fits the data sufficiently well within its error bounds and the measurement errors related to the inaccuracies described above tend to outweigh the error of water content derivation. Thus, I used the Topp-relationship as described in equation 3.10 (original Topp equation 6).

In summary, data acquisition during steady conditions has high precision. However, absolute values are prone to systematic errors that introduce inaccuracy in absolute travel times, and therefore water content. Long term time-lapse experiments can recover identically shaped curves, but possibly suffer from systematic shifts in the absolute values.

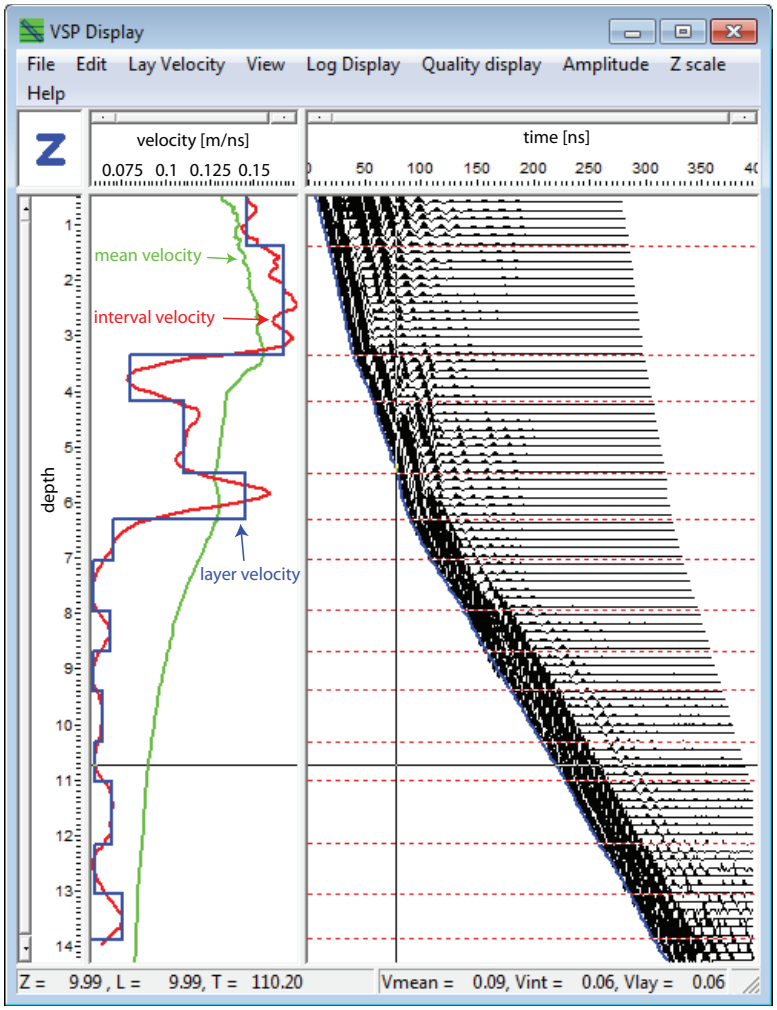

Figure 6.11: *VRP velocity analysis in RadexPro "Advanced VSP display" module based on interval velocity determination by local slope calculation (red line) and layered earth inversion (blue line) by interactively picking interface depths. Green curve is the mean velocity.*

6.5.2 BHR Data Processing: Repeatability And Accuracy Investigated

In order to preserve the waveform of the first arrival wavelet, processing has been kept relative simple. After assigning the acquisition geometry to the collected radargrams, several 1D and 2D median filters were applied in order to remove spikes before DC

shift removal (*Strobach et al.*, 2012b), zero-time correction, resampling to 0.1 ns and stacking of the data to a uniform trace spacing of 0.1 m. Zero-time correction and first break picking were based on the zero-crossings as they mostly resemble the group velocity and picking proved very repeatable for time-lapse traveltime determination, revealing smooth curves with low inherent noise (for example Figure 6.12).

However, I found that zero-time determination in air depends on antenna separation. *Peterson* (2001) recommends to measure several distances and fit a linear function to the picks, with the constant term in that function (y-intersect) is the zero-time correction. The slope of the curve should be the velocity of air, that is 0.3 m/ns, and hence zero-time correction becomes $t_{\text{corr.}} = t_{\text{obs.}} - \frac{x_{\text{air}}}{v_{\text{air}}}$ with x_{air} the distance between antenna in air and $t_{\text{obs.}}$ the observed arrival time in air. I found that a linear function does not fit the picks at separations smaller 5 m due to large changes in waveform (which I ascribe to intermediate to near-field changes in the EM radiation). It is noted that picking peaks (*Buursink et al.*, 2002) or instantaneous amplitudes (*Harbi and McMechan*, 2011) suffers the same problem. I found that true first-arrival determination, both with manual and automated amplitude and frequency thresholding, exhibits a mismatch between close and distant zero-time corrections. For very close separations, one source of error are near-field effects. For a borehole antenna of length D, the reactive near-field is dependent on the wavelength λ and extends radially to a distance $R_{\text{ReacNF}} = 0.62\sqrt{\frac{D^3}{\lambda}}$ and the radiating near-field has a radius of $R_{\text{RadNF}} = 2\frac{D^2}{\lambda}$ (*Balanis*, 1982). In air with velocity $v_{\text{air}} = 0.3$ m/ns) and an antenna of 1.5 m length with a center frequency f of 100 MHz (i.e. $\lambda = \frac{v_{\text{air}}}{f} = 3$ m), the reactive and radiating near fields become $R_{\text{ReacNF}} = 0.66$ m and $R_{\text{RadNF}} = 1.5$ m, respectively. Hence, all zero-time correction measurements in air were theoretically done in the far field. Picking at 3 m separation throughout all experiments resulted in improved agreement between time-lapse ZOP velocity curves in the saturated zone where no change is expected .

To increase the accuracy of changes in the unsaturated zone, ZOP curves were matched by L2-norm minimisation of time-lapse traveltimes in the saturated zone. The curves in Figure 6.12 from different months have been matched and reveal a high degree of repeatability. At HHW, saturated curve matching showed that the velocities in the unsaturated interval below 7 mbNS did not change throughout all experiments and the curves are almost identical (Figure 6.15 left) (*Strobach et al.*, 2012a). While

this matching procedure greatly increased the precision, the absolute accuracy of the traveltimes might still be poor, that is curves might be shifted to greater or smaller values based on a constant time-shift; thus another means is used to later correct.

After picking ZOP traveltimes $t_{\mathrm{i}}^{\mathrm{z}}(d)$, the ZOP interval velocities $v_{\mathrm{i}}^{\mathrm{z}}(d)$, as a function of depth d between Tx and Rx in boreholes separated by x^{b}, are calculated by:

$$v_{\mathrm{i}}^{\mathrm{z}} = \frac{x^{\mathrm{BH}}}{t_{\mathrm{i}}^{\mathrm{z}}}. \tag{6.1}$$

VRP interval velocity calculations were performed with RadexPro and is based on slope analysis within a moving window. As such linear curves were fitted to the traveltimes over a depth interval (picks and slope indicated in Figure 6.5d, example screenshot in Figure 6.11). Note that for offset VRP, the separation x^{v} between Tx on the surface and Rx in the hole is related to depth by $x^{\mathrm{v}}(d) = \sqrt{(x^{\mathrm{s}})^2 + d^2}$ where x^{s} the shortest distance between surface antenna and the hole. A smoothed interval velocity curve is obtained by determining the average slope from travel times versus separation within a window consisting of n discrete travel times centred around depth level d_i by calculating

$$v^{\mathrm{v}}(d_i) = \frac{1}{n+1} \sum_{j=i-\frac{n}{2}}^{i+\frac{n}{2}-1} v^{\mathrm{v}}(d_j) = \frac{1}{n+1} \sum_{j=i-\frac{n}{2}}^{i+\frac{n}{2}-1} \frac{x^{\mathrm{v}}\left(d_{j+1}\right) - x^{\mathrm{v}}\left(d_j\right)}{t^{\mathrm{v}}\left(d_{j+1}\right) - t^{\mathrm{v}}\left(d_j\right)}. \tag{6.2}$$

The smoothing of the curve depends on the window size. A value of 0.6 m has been used in my analysis. Note that the window size either has to be adjusted at the beginning and the end of the curve, or the curve has to be mirrored in order to obtain reasonable values without end-effects. Interval velocities derived from shallow depths are the least accurate due to the small gradients used for slope analysis (Δx^{v} and Δt^{v} both small) and fewer traveltimes used. Additional factors that decrease accuracy close to the surface are refracted airwaves, energy travelling from antenna tip-to-tip and near-field effects. Refracted energy tends to be a minor problem in this study as our offset were chosen to be small and refracted energy is not expected (*Tronicke and Knoll*, 2005). At increased depth, near-field effects and refracted energy are expected to be less of a problem, and Δd and Δt are maximal. Then, the slope or gradient analysis is a robust method to recover absolute interval velocities. Although this method is independent from absolute traveltimes, and the absolute accuracy is increased, I found

that the precision and repeatability is less when compared to the ZOP derived interval velocities (Figures 6.5c, 6.15, 6.14, 6.13).

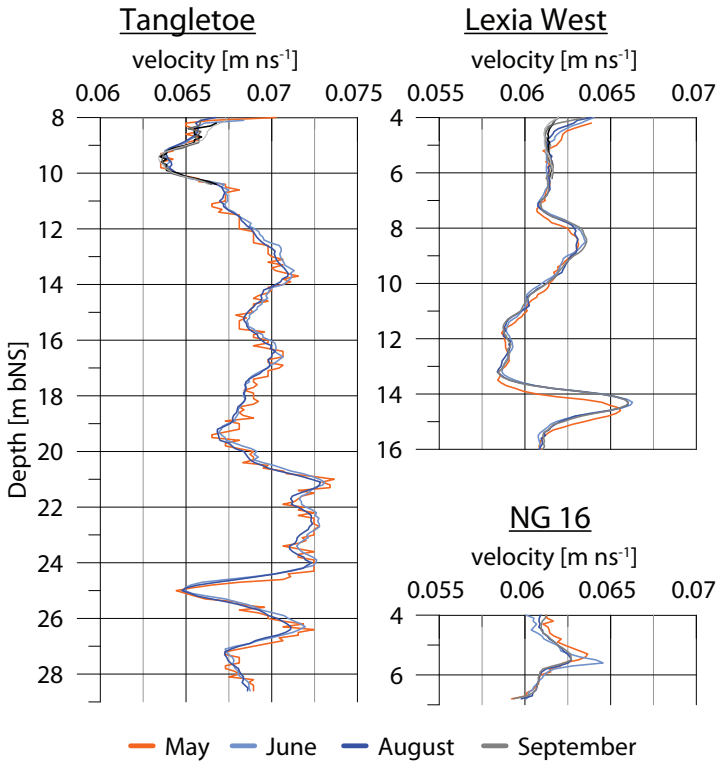

Figure 6.12: *Time-lapse zero-offset crosswell radar velocity profiles for the saturated zones at three sites demonstrate high repeatability. Only at Lexia West is a vertical shift evident in the May data which was likely caused by triggering errors of the acquisition system.*

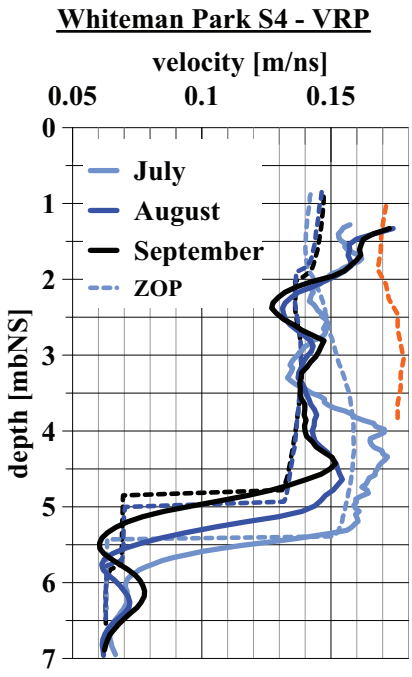

Figure 6.13: *Comparison between VRP derived time-lapse velocity profiles (solid lines) and ZOP profiles (dashed) for the Whiteman Park test site. Note the lower vertical resolution in the ZOP data due to large well separation.*

Sites with short x_{BH} such as HHW and PPG showed mismatch between ZOP and

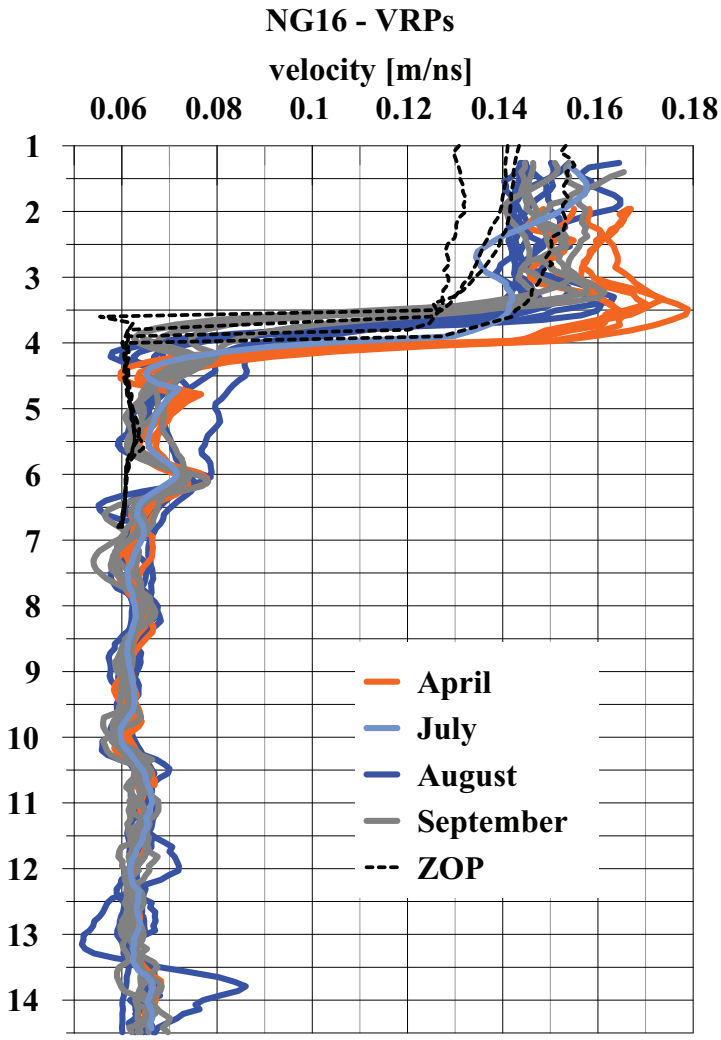

Figure 6.14: *Velocity profiles derived from VRPs with offsets between 1 - 4.75 m at NG16. As no trend with offset was obvious from the results, curves are plotted identical for any one month. Dashed black curves are ZOP results, see also Figure 6.18.*

VRP derived velocities. I believe that absolute interval velocities derived by slope analysis of VRP data are more reliable for depths greater 2 - 3 m as they are independent of the type of errors associated with short well separation in ZOP. Thus VRP velocities are used to correct ZOP velocities as shown in Figures 6.15 and 6.5a, c where grey dashed curves represent the unshifted ZOP velocities. The shift was performed in the time-domain by a constant time shift of arrival times for the full profile.

In *Strobach et al.* (2012b) and *Strobach et al.* (2012a) various explanations for the observed discrepancy between ZOP and VRP velocities are proposed. One reason could be deviating wells. Uncorrected increased borehole separation leads to underestimation of velocity due to increased traveltime and vice versa. This could explain the lower unsaturated velocities determined from constant well separation in case well separation increases with depth. The effect of deviating wells can be large, especially for short well separations. For a 1 m separation (i.e. HHW), a deviation that leads to

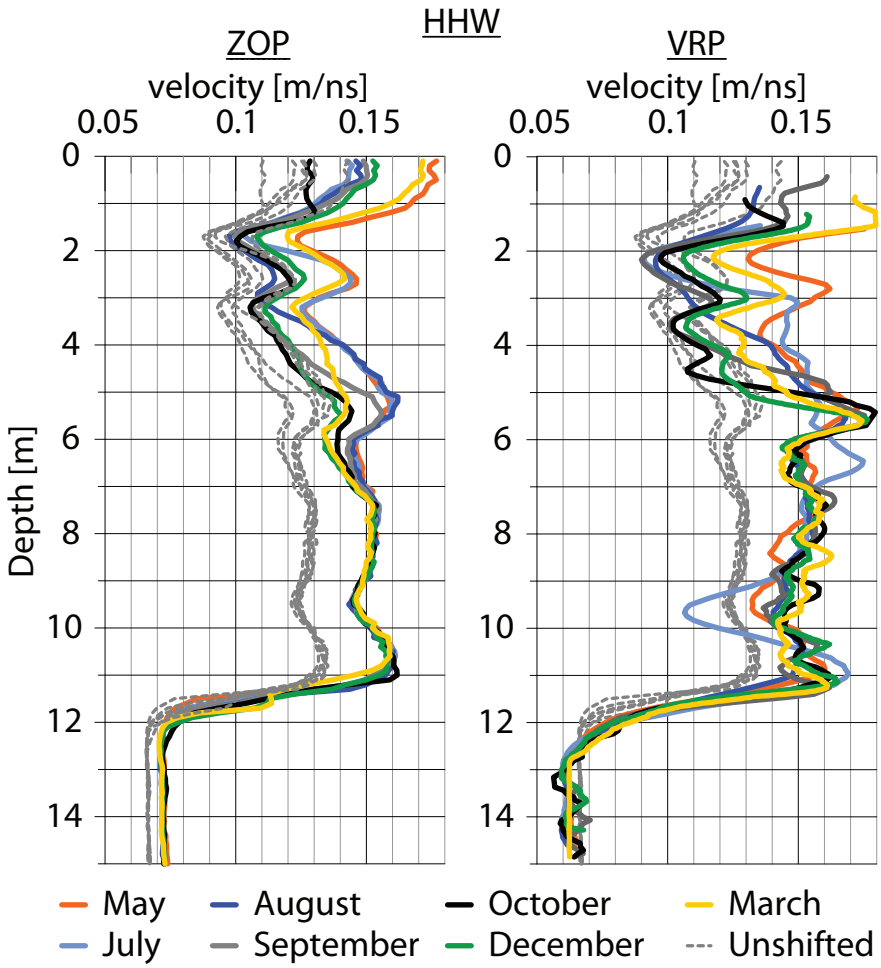

Figure 6.15: *Time-lapse velocity profiles from the High Hill Road test site. While ZOP profiles show high repeatability below 7 mbNS, the VRP curves are more noisy in that depth interval. VRP velocities above 2 m depth were not reliable, however, below 2 mbNS both techniques show the same trend. The dashed grey curves represent initial velocity estimates for ZOPs.*

0.15 m increase in distance over the depth, predicts the observed velocity discrepancy. Another explanation for observing different velocities from VRP and ZOP measurements is anisotropy. ZOPs sample a horizontal, and VRPs a vertical velocity. In the HHW case, this would imply higher vertical velocity. In a depositional soil environment, (sub-)horizontal layering would lead to higher horizontal velocity, which tends to contradict the observation.

Both explanations do not explain the misfit that exists between saturated and unsaturated ZOP- and VRP-derived velocities at HHW. After shifting the ZOP curves to the VRP level, the saturated ZOP velocities exceed the VRP estimates (i.e. 0.07 vs. 0.06 m/ns). Although this shift doesn't seem dramatic, it is a discrepancy of 2.4 ns in traveltime, despite the short well separation. A possible explanation for this phenomenon are near-field effects. According to the reactive and radiating near-field

equations (see above), the reactive near-field is between 0.9 m and 1 m for unsaturated velocities between 0.15 m/ns and 0.13 m/ns, respectively; and between 1.35 m and 1.5 m for saturated velocities between 0.07 m/ns and 0.06 m/ns, respectively. Note that the VRP predicts the greater contrast (i.e. 0.9 m versus 1.5 m). Measurements at HHW are therefore at the boundary between reactive and radiating near-field in the unsaturated zone, and clearly within the reactive near-field in the saturated zone. This would produce a complex effect on group and phase velocities. To discuss the exact influence on velocity determination is beyond the scope of my work and needs to be a subject of future research.

6.5.3 Implications For ZOP And VRP Geometry

6.5.3.1 Vertical Radar Profiling

For the VRP geometry, the depth of investigation often depends on soil characteristics of the test-site and the depth to water table. All sites tested showed sufficient S/N for reliable slope analysis to several meters below the water table. VRP data examples are shown in Figures 6.2 (left), 6.4 (right), 6.5d for NG16, WP and PPG, respectively. The clay at TGT attenuated the EM energy and no signal penetrated beyond five meters (see Figure 6.6). Figures 6.15 and 6.5c display VRP derived time-lapse velocity profiles for HHW and PPG, respectively. As described previously, the VRP slope analysis is unreliable at shallow depths. I also found that picking zero-crossings in VRPs created unrealistic velocities in the near surface down to three meter depths. True first arrival picking revealed more plausible velocities from 1.5 - 2 mbNS onwards. Interfaces that produce reflections (upgoing wavefields) then create interference with the first arriving down-going wavelet. Extreme slope values can be the result. FK-filtering can remove upgoing from downgoing wavefields with appropriate signal conditioning, but this did not greatly improve the results. A typical example is the reflection from the water table, which is a strong contrast interface. All profiles showed an increase in velocity just above the water table. As most ZOP profiles did not show that effect, it is likely that this is an artefact introduced by interference with an upgoing wavefield from an interface with negative reflectivity. Numerical modelling confirms that interfering waves that are 2π phase shifted will result in higher velocity estimation from slope analysis just above the interface. Anomalous velocities at interfaces should be therefore discarded

from interpretation.

The precision or repeatability of VRPs can be estimated from intervals where no change with time is expected. That is the case at the HHW test-site between 7 - 11 m depth, and for the saturated zone at all sites. For the purpose of this study, it is sufficient to keep the precision analysis qualitative. The VRP unsaturated repeatability appears to be around 0.005 m/ns, or approximately 3.5 %. The ZOP precision is about an order of magnitude higher. Received S/N can be low in the saturated zone due to attenuation and scattering due to shorter wavelengths; thus, repeatability tends to be lower compared to the unsaturated zone. For the unsaturated zones at HHW and PPG, VRP repeatability is smaller compared to the ZOPs. However, the general trends at HHW are similar.

The VRP velocity profiles from WP displayed in Figure 6.13 provide a higher vertical resolution compared to the ZOPs (dashed lines). This is due to the large well separation of 11.5 m. The absolute velocities are comparable in the saturated zone at 0.062 m/ns (ZOP) and around 0.065 m/ns (VRP). When the water table was rising in August/September, a secondary layer between 5 and 5.7 mbNS produced higher saturated velocities compared to the 0.0625 m/ns below. Figure 6.4 (lower left and right) reveals that this layer has higher attenuation compared to the fully saturated interval below. It is possible that this horizon is an accumulation horizon with reduced porosity (hence lower dielectric), and that it contains electrically conductive material such as dispersed clay minerals. In July when the capillary fringe is at this layer, it is neither obvious in the ZOP nor the VRP data (Figure 6.4 upper).

In the unsaturated zone, the WP ZOP velocity profile results are smoothed and don't resolve the "coffee rock" layer at around 2 mbNS. The velocity profiles merely show a kink at that position. The VRPs on the other hand do resolve the water-retentive horizon. The unsaturated VRP velocities above 2 m are higher for the VRP. It is possible that the ZOP velocity estimates are too low, but the relative differences are consistent between ZOP and VRP results. Both show a decrease in velocity for the upper 2 m in July while unsaturated velocities below remain high. The August and September data for both geometries show reduced velocities below 2 m.

At NG16, VRP velocity interpretation was difficult as shown in Figure 6.2. VRP profiles were acquired with offsets between 1 and 8 m from the logged borehole. Fig-

ure 6.2 shows all the VRP results (each colour represents one month). Note that in July, only a 4.85 m offset VRP was performed. The August 1 m offset data show great deviation from the other curves (i.e. between 4 and 6 m and 12, 13 and 14 m depth). In general no clear time-lapse trends are evident in the unsaturated zone when comparing data from same offset (not explicitly shown in Figure 6.2 as colours are only unique for every month). When looking at the results from all offsets and comparing the different months the curves reveal a trend, which is similar to the ZOP observation (i.e. highest velocity in April, lower velocity in July and August, and September slight increase from August). An explanation for the poor performance of the VRPs at NG16 is not apparent. When estimating velocity from travel-times rather than local slopes, the results look more promising (not shown here). However, such analysis requires accurate zero-time correction which is problematic when dealing with close offsets in the near-field of the antenna.

6.5.3.2 Zero Offset Profiling

Crosswell ZOP measurements revealed strong first arrival waveforms over the full profile lengths at all sites. The only exception is the clay band at TGT between 5 - 6.5 mbNS, which attenuated the signals below the signal to noise ratio (S/N) (Figure 6.3). Well pairs at test sites LXAW, TGT, HHW and NG16 facilitated crosswell measurements throughout several meters of the saturated zone. The time-lapse curves, as shown in Figure 6.12, were very repeatable after the matching procedure described in section 6.5.2, revealing high precision for ZOP measurements. Sites with larger well separation showed ZOP velocities that typically matched the VRP results but suffered from lack of resolution (i.e. NG16, WP) (*Strobach et al.*, 2012b,a). Critically refracted air-arrivals showed very low amplitudes compared to the direct ground arrival and did not alter the first arriving wavelet significantly. Hence, I picked the true first ground arrival based on the first zero-crossing. Slope analysis of the critically refracted air-waves (*Rucker and Ferre*, 2003) corroborated the results obtained from direct ground arrivals.

At WP, refracted energy above and below an indurated sand horizon at 2 mbNS masks the layer's low velocity characteristic (*Strobach et al.*, 2012b). The curves show a kink at the upper position of that horizon, but do not fully resolve the cemented

horizon as a low-velocity layer that would be expected due to high water content (i.e. as identified by *Bertuch and Froend* (2006), Figure B.95 and *Strobach et al.* (2011), see Figures 6.4, 6.13 and 6.18 (1d)).

NG16 has a clayey layer below the water table (*Strobach et al.*, 2012a). It is characterised by higher velocities but relatively small amplitudes in the ZOP data. *Strobach et al.* (2012a) derive a 0.6 m thick layer centred around 5.7 mbNS. Higher velocity layers tend to be resolved at larger borehole separation due to refracted arrivals travelling along these interfaces (*Strobach et al.*, 2012b). FDTD modelling suggests that the low amplitude observed in ZOP data could be a result of complex wave propagation in a leaky (i.e. high velocity) waveguide structure. This would mean that the layer material is not attenuating the EM waves. This would also explain that the amplitudes for VRP data below that layer are not attenuated.

LXAW and TGT have boreholes with different separations. By assuming that lateral changes are small at the test-site locations, results from different well separation may be used to gain insight into the method's performance. At LXAW, the 2 m spaced wells $Wa-Wb$ consistently show higher velocities compared to the well pair $Wb-Wc$ which are 4 m separated (Figure 6.18 (1e)). The wells at TGT, that is TGT_A and TGT_B (1.95 m separation), show lower velocities compared to TGT_A and TGT_C (3.54 m separation) (Figure 6.18 (1b)). Thus, no clear trend in performance of the method can be inferred from those test-sites. At both sites, VRPs produced results that are in favour of the higher velocity well pairs. However, both sites have shallow water tables and the VRP results are therefore not very reliable above the water table. A possible explanation for the observed differences is that lateral velocity variations or well deviation are present at one of the two sites.

The sites HHW and PPG show a clear trend. Both sites have well spacing's around 1 m and ZOP velocities are consistently less compared to VRP velocities. As both sites have a deeper water table, the VRP velocity derivation is expected to be reliable at the deeper interval. At HHW, ZOP velocities between 7 and 11 mbNS did not change throughout the experiments (Figures 6.15 and 6.17). The ZOP velocity was originally centred around 0.125 m/ns and has been corrected to the VRP level of around 0.15 m/ns (grey vs coloured curves in Figure 6.15). At PPG, ZOP velocities were changing in time throughout the whole vadose zone. The VRPs had a similar trend compared to

the ZOPs. The most reliable VRP data were identified between 4 - 5 m depth where up-going energy, reflecting from the cemented sand, did not interfere significantly with the direct arrivals. ZOP curves were shifted from a 0.1 m/ns velocity level, to 0.12 m/ns (grey vs coloured curves in Figure 6.5a, c).

6.5.4 Neutron Logging

Quality control of neutron measurements involves taking reference measurements in a reference environment of high hydrogen density. Reference measurements are typically made in a bucket filled with water; however, it is also possible to choose a material with high hydrogen density such as polyethylene. Due to possible water leakages into the probe, reference measurements were made in the polyethylene shield provided with the probe before each measurement campaign. The field campaigns in 2002 - 2004 were done with the probe N0098. Reference measurements proved very stable with counts around 620 - 625 cps. Some measurements have been made in water through a PVC-pipe which resulted in 628 cps. Data from 2008 onwards were collected with the N0126 probe. The reference measurements for this probe were quite different and varied considerably. Counts between around 550 and 580 cps were recorded in the polyethylene shield. The variations of counts with the N0098 probe are within the specified measurement precision of the tool. Precision is for example influenced by the statistical variation in radioactive decay. Longer acquisition times improve the precision. The N0126 reference measurements might be flawed, as the resultant raw counts did not exhibit the same shifts. The datasets were not normalised as the N0098 reference measurements appeared to be sufficiently similar, and the N0126 reference varied too much and would have possibly introduced additional errors.

However, the available neutron data have two problems. The first is that the data could only be collected in dry boreholes due to concerns of potential water leakage into the probe (*Kel Baldock, pers. comm.*). Thus, data for repeatability analysis from the saturated zone are not always available. The second problem is a lack of information on how volumetric water content relates to neutron counts. The implications of this deficiency are not as far-reaching as one might expect at first. *Bell* (1987) points out that for time-lapse investigations where annual changes are observed and water balances calculated, the absolute accuracy of neutron count versus volumetric water content re-

lationship is not crucial for a successful outcome. Note that the same is true for the time-lapse radar where GPR velocities are transformed into water content as will be shown later. For neutron counts, the slope of the linear relationship between counts

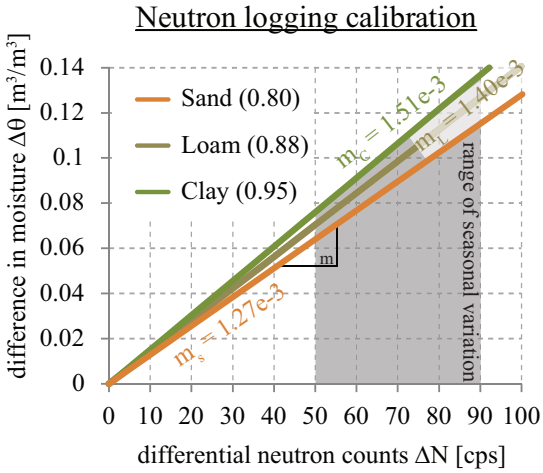

Figure 6.16: *Differences in neutron-derived water content for different soil type. Slope values given by Bell (1987) (i.e. 0.8, 0.88, 0.95) for relative counts are transferred to m_c, m_l and m_s valid for absolute raw counts by assuming a reference count value of 625 cps. Note the small discrepancy in water content differences for the different soils.*

and water content are the only factor influencing the interpretation of water balance calculations. However, those slopes are quite similar throughout different materials, and are mainly influenced by texture (clay vs. loam vs. sand) (*Bell*, 1987). The graph in Figure 6.16 shows the differences in water content estimation based on differences in observed neutron counts for sand, loam and clay as determined by *Bell* (1987) (note that those plots have been called calibration curves in *Bell* (1987)). We can see that the error in water content estimation that occurs for a difference of 80 counts (e.g. variation between summer and winter), differs by only 2 % for clay and sand textures, the extreme cases. Note that typical seasonal moisture variation results in 60 - 70 cps differences. Thus, the maximum error that is anticipated for differential moisture content estimates is between 1 - 2 % when using an imprecise empirical relation. Note that the difference in water content derived from neutron count difference is higher for clayey and loamy soils than for sands due to the greater slope in the linear relationship between water content and neutron counts. That means if we compare sand intervals with loam intervals and assume the same slope, the water content difference in loam horizons could be underestimated by only a negligible percentage.

6.6 Hydrogeologic Analysis And Implications

The previous sections have covered geophysical aspects of time-lapse borehole radar and neutron logging data. Precise moisture profiles can be derived from ZOP BHR. Such data can be interpreted to better understand hydrogeologic infiltration characteristics. Additionally, the neutron logging data are investigated for two purposes. It firstly provides a comparison dataset to analyse the unsaturated flow characteristics based on temporal changes in soil moisture content with depth. Secondly, as the neutron profiles were performed over several recharge cycles, they can potentially provide information on long-term water balance. This is of particular interest to differentiate soil horizons, and derive storage for water-retentive horizons and clean sand intervals separately. The outcome of this analysis can potentially answer the question whether water-retentive soil horizons store additional water which is available for plants.

6.6.1 Time-lapse Infiltration From Borehole Radar

The aim of this section is to demonstrate a methodology using results obtained from the BHR time-lapse studies at different sites to produce a classification of different infiltration regimes based on vadose zone moisture content development during the recharge period 2011.

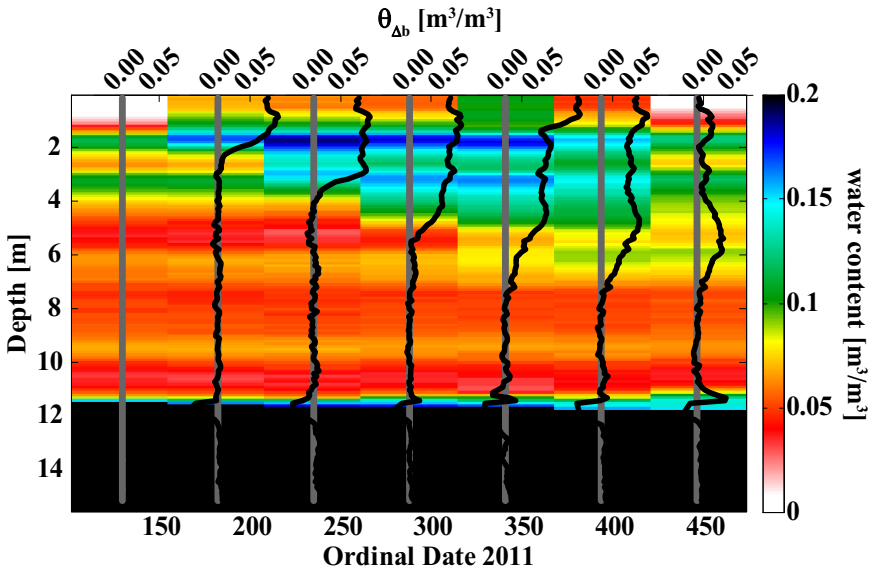

Figure 6.17: *Pseudocolour plot of time-lapse water contents at HHW site where x-axis represents time, and y-axis depth. Line plots of baseline difference water contents $\theta_{\triangle b}$ depict the downward movement of the infiltration front.*

For water infiltration analysis, two sets of temporal gradient curves are calculated from water content profiles. The first type are differences to baseline moisture curves $\theta_{\Delta b}(d)$ with θ for volumetric water content, Δb to indicate baseline difference and d for depth. These curves represent the changes in moisture content relative to the driest profile before rainfall (i.e. April or May data). An example is given as overlay in Figure 6.17. The integral

$$\Sigma S_{\mathrm{b,BHR}} = \int_{d_1}^{d_2} \theta_{\Delta b}(d)\,\mathrm{d}d \tag{6.3}$$

over depth intervals $[d_1\ d_2]$ of those difference profiles represents the cumulative storage ΣS, the expression of cumulative water content change relative to the baseline month.

The second type of gradient curves are sequential difference water content curves $\theta_{\Delta s}(d)$ obtained by calculating differences of successive moisture profiles (Figure 6.18 2a-f). Those curves portray changes in water content between subsequent surveys. Positive values represent wetting (i.e. storage), zero values no change and negative values drying. The integral

$$\Sigma S_{\mathrm{s,BHR}} = \int_{d_1}^{d_2} \theta_{\Delta s}(d)\,\mathrm{d}d \tag{6.4}$$

over the unsaturated part of those sequential difference profiles should directly provide information about the storage or loss of water in the vadose zone relative to the previous month (cumulative sequential difference). This can be useful for water balance calculation (*Sharma et al.*, 1991; *Farmani et al.*, 2008) and to detect the depth intervals where changes occur.

At most sites wetting occurred on the second (PPG, NG16, TGT) or second and third repeat (WP, LXAW) (Figure 6.18 2a-f). On the fourth repeat in September, the sequential difference curves showed either no change, or slight drying. HHW is the only test site that showed different infiltration characteristics. Wetting proceeds down to 7 m and the changes progress until October. In December, drying started above 5 mbNS while minimal wetting continued between 5 - 6.5 mbNS. The wetting during the first 3 measurements was delayed compared to all other test-sites. It appears that in 2011 only minimal or no recharge took place at HHW, the results of which will be

further discussed in section 6.6.3.

In order to compare test-sites with each other the analysis is restricted to the unsaturated zone interval, which is vadose for all test-sites and repeats. The limiting factor is the shallowest water table, which is at TGT at a depth of 3.3 m (see Figure 6.18 1a-f, 2a-f). Although the overall infiltration behaviour of the full unsaturated profiles are not captured by restricting analysis to this depth limit, this method allows investigation of the influence of retentive layers at shallow depth only and the results can then be compared to all sites investigated. In Figure 6.19 (upper) cumulative water contents within a depth interval between 1 - 3.3 mbNS are plotted against the date. The lower graphs in Figure 6.19 contains cumulative sequential difference plots for the same depth interval, calculated with equation 6.4. The black lines and dots show the HHW data, which has the highest overall water content within that interval due to two water retentive layers. HHW also shows the greatest delay in wetting within the first three meters. This is well represented by the increase in cumulative sequential water content difference graphs (Figure 6.19, lower) from 0.072 m^3/m^2/72 mm in June, to 0.085 m^3/m^2/85 mm in August. The June value is low compared to the other sites, while the August value is higher and indicates delayed wetting.

The infiltration behaviour at the different sites leads to a classification based on wetting response to rainfall. **Regime I** is described by wetting of the full profile occurring after 200 - 250 mm of rainfall in June at sites PPG, NG16 and TGT (red, yellow and grey dots and lines in Figure 6.19). After initial wetting, rainfall events may lead to transient flow and ephemeral increase in the water content during infiltration. Examples are the June data at PPG, or the October data at HHW, where rainfall just before the measurements lead to higher water content in the first meter (see Figure 6.18 1c, 2c, 1f, 2f). Dry periods can lead to intermittent loss of water within the first meter due to evapotranspiration. At Regime I sites, the initial wetting probably produced a moisture content equivalent to the soils' field capacity. Such behaviour provides a reason why later measurements did not detect further wetting.

Regime II is characterised by initial wetting of the full profile, whereas, the upper two meters are experiencing no further changes by the third repeat; while below two meters there is a further increase in water content in August after another ≈ 200 mm of rainfall (LXAW and WP, blue and green dots and lines in Figure 6.19). Regime II

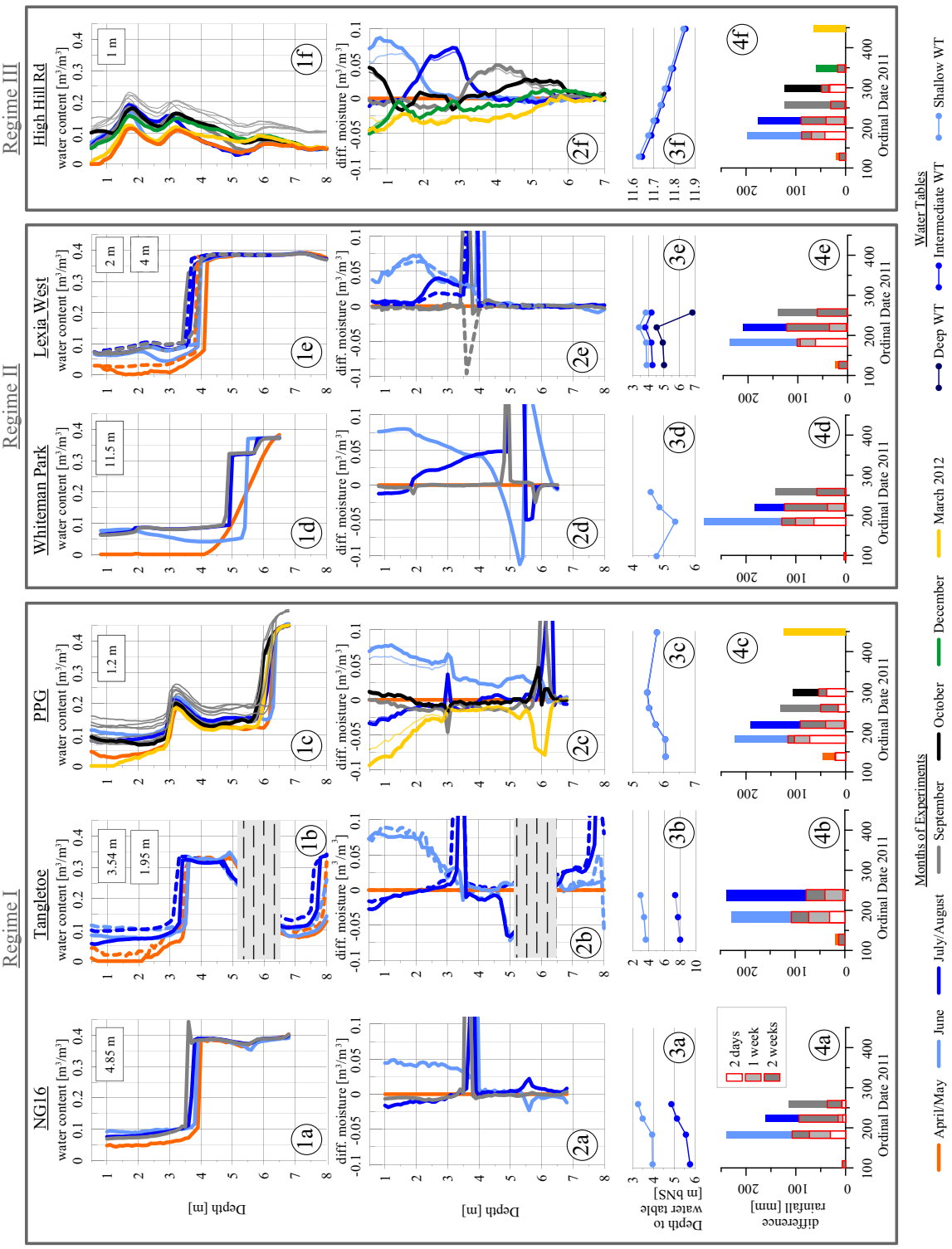

Figure 6.18: *Compilation of borehole radar results classified by infiltration Regimes I - III. Figures (1) are water content profiles, (2) sequential difference water content $\theta_{\Delta s}$ plots which show wetting (positive values) and drying (negative values) relative to the previous month, (3) are depth to water table (dipper) and (4) rainfall charts of cumulative rainfall between subsequent repeats, cum. rainfall 2 weeks, 1 week and 3 days before measurement are outlined in red and filled in dark grey, light grey and white, respectively. Note that all sites have very similar rainfall amounts before equivalent measurement days.*

describes a delayed wetting response.

HHW represents **Regime III** with extremely delayed response and overall high water content due to the retentive soil layers.

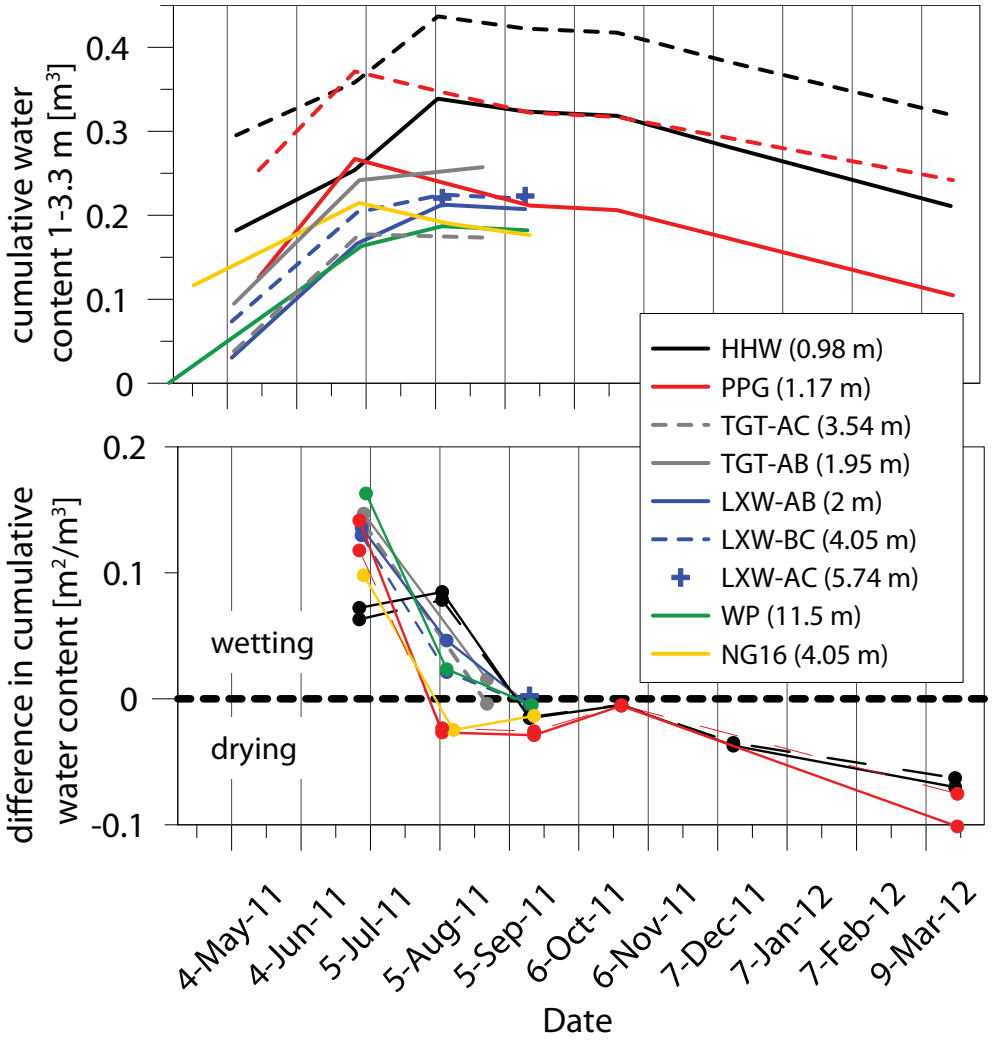

Figure 6.19: *Upper: Site-specific cumulative water content of depth interval 1 - 3.3 mbNS as a function of time. Lower: temporal derivative of upper graphs, positive values stand for wetting, zero means no change and negative values drying. Note the three Regimes: I) all changes at first repeat and no change or drying afterwards (red, yellow, grey), II) most change at first repeat, further change second repeat, afterwards no change or drying (green, blue) and III) some change at first repeat, same change second repeat, and no more change or drying afterwards (black).*

6.6.2 Time-Lapse Infiltration From Neutron Logging

Time-lapse neutron logging data from previous years provides baseline information on infiltration behaviour independent of the GPR investigations. The neutron data presented in this section is mostly kept in units of raw absolute counts, as calibration data to obtain absolute water content were not available. In qualitative terms, neutron

count values between 20 - 60 cps represent dry sections with water contents around 5 v%. The expected field capacity of the sands is at approximately 8 - 10 v% water content, which equates to neutron counts of around 80 - 100 cps. Fully saturated intervals (i.e. $\approx$ 30 - 40 v% $\rightarrow$ vol. water content = porosity) show counts around 350 - 400 cps.

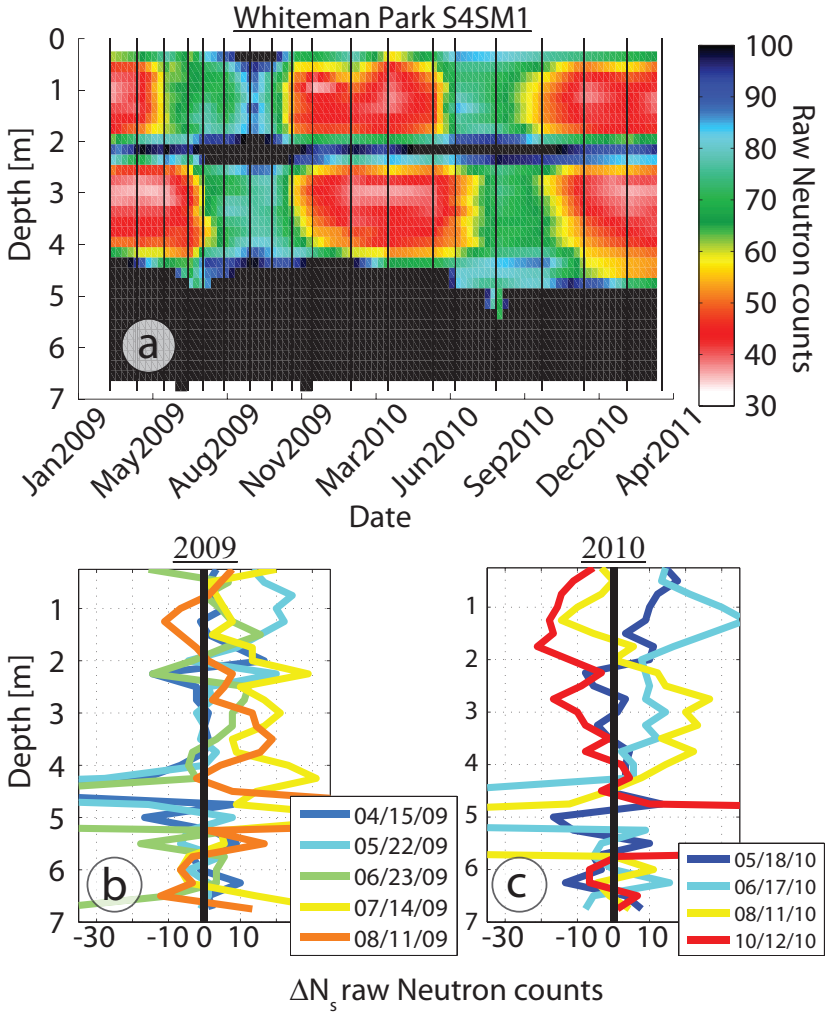

Figure 6.20: *Pseudocolour time-lapse representation of raw Neutron counts from WP, measurement dates are indicated by black vertical lines in (a). Sequential difference curves of wetting cycles from 2009 and 2010 are shown in (b) and (c), respectively. In (b) and (c) positive counts represent wetting and negative counts drying. Both years show delayed wetting below the water retentive horizon at 2 mbNS, equivalent to Regime II.*

Raw neutron count data are shown in Figures 6.21a and 6.20a for sites PV3 and WP and was re-gridded (i.e. interpolated) in time to obtain regular time intervals for illustration purposes only. Black vertical lines indicate dates of measurements. Further raw neutron counts images are shown in appendix B (e.g. Figures B.2, B.6, B.10, etc.).

Relative changes in neutron counts with time reveal the mechanisms of recharge.

The raw time-lapse neutron count profiles have been treated identical to the BHR data in that baseline and sequential difference curves were calculated and called ΔN_b and ΔN_s, respectively. Baseline difference images and curves are shown in appendix B. The baseline graphs were transformed to water content based on a constant linear relationship between difference in moisture and difference in counts. The slope was chosen as $1.33 \cdot 10^{-3}$ $m^3/m^3/\Delta N$, which lies in between the literature value for sand and loam (*Bell*, 1987) (see Figure 6.16). Sequential difference images are shown in appendix B, Figures B.3, B.7, B.11, etc. Selected sequential difference curves are shown for winter months of 2002/2003, and 2009/2010 in Figures 6.21b,c and Figures 6.20b,c, for PV3 and WP respectively.

The time-lapse neutron data reveal similar infiltration regimes as proposed in the previous section 6.6.1. However, comparing historic neutron data with 2011 GPR results is challenging due to differences in annual rainfall patterns (Figure 6.10). Although a calibration to absolute water contents would be desirable, the raw counts still show that recharge is influenced by climatic and soil conditions.

The WP Neutron data confirmed the GPR interpretation. It appears that Regime II infiltration, that is delayed wetting, is occurring in 2009 and 2010, as shown in Figure 6.20. In both years there was a slight delay in infiltration below the cemented soil horizon. Note that the winter of 2010 had exceptionally low rainfall with annual precipitation of 470 mm (Whiteman Park climate station), while 2009 was an average year with almost 700 mm (Figure 6.10). The Neutron data reveal a general trend of lower Neutron counts in 2010 compared to 2009. This indicates that the water balance within a thin vadose zone of less than four meters is significantly influenced by variations in rainfall.

Other sites that behave like Regime II can be found in the appendix B. For example, time-lapse logs from other sites at Whiteman Park show similar infiltration behaviour. To clearly distinguish Regime I from Regime II, one has to closely inspect the cumulative rainfall between subsequent measurements, or alternatively compare data from proximate sites and from the same time under the assumption that rainfall was similar for both sites.

The test-site PV3 close to HHW has an extensive vadose zone with a deep water table. Figure 6.21a reveals a water retentive soil horizon at around 4.5 mbNS and

between 9 and 12.5 mbNS. While 2002 was a dry year with below average rainfall of 490 mm (Gingin Aero climate observatory), which was preceded by a sequence of drier years 2001 and 2002 (630 and 570 mm, respectively), 2003 was slightly wetter with 680 mm. The infiltration behaves very similar to what was observed at HHW with BHR. In 2001, the wetting front gradually moves downwards as depicted in Figure 6.21b,c. Below 12 meters, no changes are obvious in 2002/2003 (Figure 6.21b), and Neutron counts within that depth interval are generally low (65 - 75). Although it is possible that the soil is already at its field capacity and no more stable wetting could therefore be expected, the 2003/2004 data show how the wetting front moves further than in 2002 and elevates the soil moisture to what I believe to be the field capacity (or slightly above) between depths of 12.5 and 17 mbNS (Figure 6.21c). It is unlikely that major downward movement of water took place in 2002/2003 as one would expect that the soil's matrix potential would attract some of the passing water and elevate the recorded neutron counts, which certainly happened in 2003/2004.

Scanlon et al. (2002) points out that a lack of change in moisture content has been misinterpreted as no flow. In our case, the changes of the subsequent year indicate that if considerable amounts of water had infiltrated it would have increased the soil water content. The migration of water to depths beyond 12 m is delayed in 2003/2004 and the infiltration front reaches the water table in February 2004. The last measurement in September 2004 shows that the moisture between 12.5 and 16.5 mbNS normalises to pre-2003 infiltration. This can mean that either the soil returns to its field capacity and water flow in 2004 was above field capacity, or that some other mechanism draws water from the system such as deeper roots or microorganisms.

The second objective of neutron logging data investigation is the analysis of water storage and loss within water-retentive horizons, and to compare these to clean sand intervals. The petrophysical analysis of unsaturated soil properties (i.e. water retention, see section 3.1) revealed that water-retentive soil horizons might provide some additional water available for plant consumption. While the field capacity of these layers was elevated at around 20 - 25 v% water content, and the wilting point is at around 5 v%, results in 15 - 20 v% of water potentially available for plants. The clean sands only provide an estimated 8 - 12 v% of available water due to lower field capacity. To investigate this effect in time-lapse neutron logging data, I plot the baseline

difference time-lapse neutron logging data as curves for each depth interval as shown in the appendix Figures B.5, B.9,B.13, etc. The lowest neutron count per depth interval throughout the monitoring period, that is the driest measurement at any given depth level, was chosen as the baseline value (note that this is different to the baseline data calculated with the driest month as baseline in order to avoid negative values). The amplitude of those baseline difference depth interval time-lapse curves reveals the maximum difference in neutron counts (or water content) throughout the full observation period. Thus, this amplitude is indicative of how much water has entered and later left the soil interval. In case of high amplitudes, large amounts of water entered the soil horizon and left again, while lower amplitudes mean only small amounts of water entered and left. Note that those amplitudes do not provide information on how much water is permanently stored in the soil interval. To illustrate the amount of water that is permanently in that interval, I colour-coded the curves based on the baseline value. That means red/orange colours represent sections which have a low baseline count (low water content, non-retentive), while green/blue colours indicate depth levels of high baseline counts (higher water content and water retentive or saturated zone). If water-retentive layers store and release more plant-available water compared to the surrounding sands, one would expect that the blue curves show higher amplitudes than the red and orange curves.

At first, I identified the PM7 site as a potential candidate for this behaviour. While the baseline difference image in Figure B.12 appears to show that the water-retentive horizons at around 3.5 - 4.2 mbNS and 6.0 - 6.5 mbNS have a higher difference between maximum counts in winter, and minimum counts in summer. The Graph in Figure B.13 shows that although the difference is there, it is not dramatic. The overall estimated amplitude of difference in water content throughout both recharge and drying cycles is around 8 and 12 v%. Note that the baseline values are depicted in black in Figure B.12, or where the curves in Figure B.13 are at zero water content difference. The curves show that the measurements in April 2004 showed the lowest absolute counts for almost all depth intervals. The wetting and drying periods 2002/2003, reveal that the non-retentive intervals show some variation in regards of lowest water content difference. While some sections have the lowest difference value around zero, which means that they were as dry as in April 2004, other intervals do not reach that

value and show minimum water contents around 2 v%. This means that the drying in 2004 might have been more intense compared to 2003.

Retentive horizons at other sites such as PM4, PM6, PV1 and PV3 show less annual variations in water content compared to the non-retentive profile sections. PV4b, while missing the 2002 wetting cycle, appears to have a retentive horizon that was depleted in 2001, and did not recharge with water in 2002, but then recharged in 2003. This can be explained by the low rainfall in 2002, and the great depth of this horizon. As evident from other sites, the infiltration front in 2002 did not reach the same depths as the infiltration in 2003. At PV4b, the recharging of the layer at 9 - 12 mbNS probably severely impeded recharge in the wet year 2003, indicated by the dry horizon below 12.5 mbNS.

Another feature at PM7 is a time-delay in wetting and drying of the water-retentive horizons relative to the non-retentive layers. The delayed wetting response in water-retentive horizons is not as large as the delay in drying at this site. While there is some delayed wetting, the maximum water contents are reached at approximately the same times in retentive and non-retentive depth levels. The maximum drying, on the other hand, is delayed significantly by several months. Other sites such as PM4, PM6, PV1 and PV3 show a similar trend. At these sites the retentive horizons show a delay in both, wetting and drying.

While the lag in wetting can be explained by a gradually moving wetting front (i.e. initiated by subsequent rainfall events), the drying delay may be due to the drying mechanism involved in the different horizons. If plants extract water evenly throughout the soil profile the expectation is that drying occurs at the same time for all depth levels; simultaneously in retentive and non-retentive horizons. A delayed response may indicate that plants use water preferentially from non-retentive horizons and only secondary from retentive layers; perhaps due to the cementation found in many retentive layers preventing roots from developing.

6.6.3 Discussion On Infiltration Observation

I found that by correcting initial ZOP velocity estimates to VRP velocity levels, the certainty of absolute water content estimates can be increased. The effect of this correction is for example shown in the cumulative water content curves in Figure 6.19

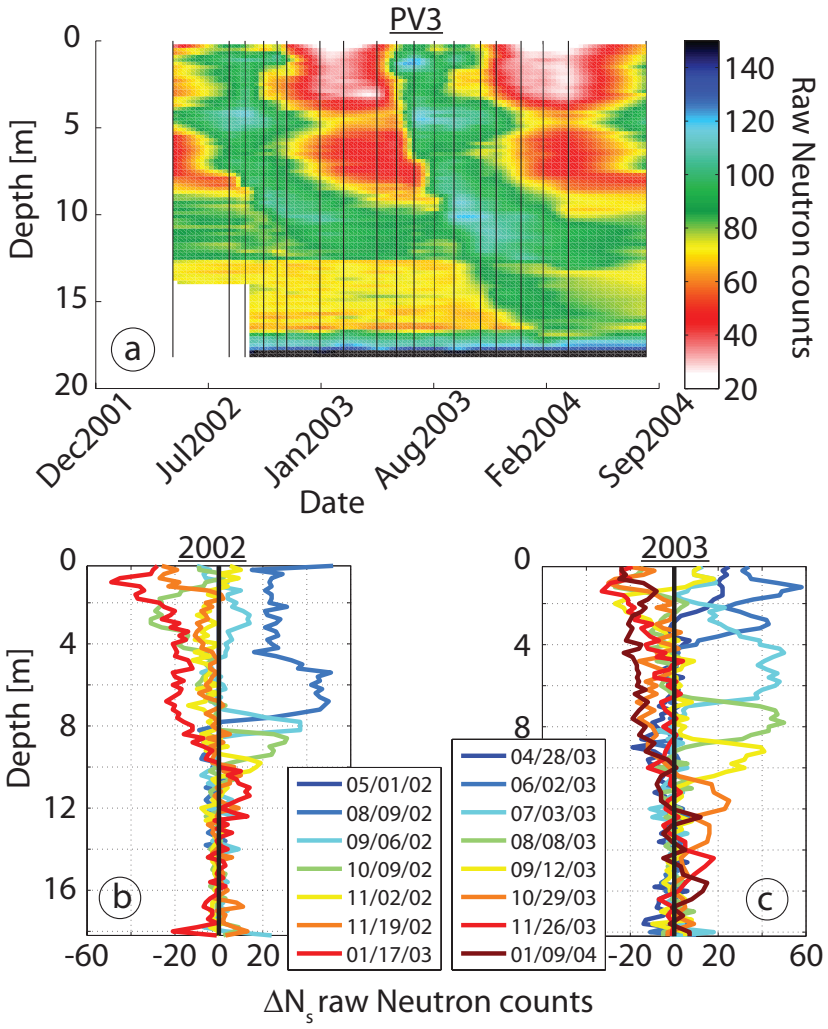

Figure 6.21: *Pseudocolour time-lapse representation of raw Neutron counts from PV3 measured at dates indicated by black vertical lines (a) and sequential difference curves of wetting cycles from 2002 and 2003 in (b) and (c), respectively. In (b) and (c) positive counts represent wetting, while negative counts drying between subsequent measurements. Both years show delayed wetting below the water retentive horizons at 4.5 mbNS equivalent to Regime II, and severely delayed wetting below retentive horizon between 9 and 13 mbNS in 2003, and no changes below that horizon in 2002 (Regime III). Note that measurements in 2002 started in May and first repeat was in August, while in 2003, measurements were done every month between April and November. Hence the sequential difference curves represent change between different lengths time intervals.*

(upper) for the depth interval 1 - 3.3 mbNS (dashed vs. solid lines). While the applied correction has a great influence on absolute water content, the influence in sequential difference curves is minor as will be shown by the following examples. Sequential difference curves derived for corrected and uncorrected ZOP water content estimates are plotted in Figure 6.18 for HHW and PPG (thick (corrected) vs. thin (uncorrected) curves in plots 2c and 2f). Although the curves differ, that is the thin or uncorrected curves show smaller variation in water content difference between subsequent measurements, the difference does not influence the interpretation of those curves. Ta-

ble 6.2 lists the cumulative sequential difference values obtained from the corrected and uncorrected (in brackets) data for the entire unsaturated zone at HHW and PPG. It can be seen that values only vary by a few millimetre, with a maximum of 40 mm for the first repeat at PPG. while Figure 6.19 (lower) shows the effect of velocity correction on sequential curves for the limited depth interval 1 - 3.3 mbNS (solid/corrected, dashed/uncorrected). These graphs and values demonstrate that the sequential change of moisture content is not very sensitive to absolute water content correction.

However, sequential difference values are sensitive to noise, especially spikes in the data, thus requiring high repeatability/precision. The first correction step described in section 6.5.2 (i.e. matching saturated zone data) is therefore critical for baseline and sequential difference analysis. The same general statements hold true for neutron, or any other type of time-lapse data.

In order to evaluate the soil moisture variations in a hydrogeologic sense, environmental factors have to be considered such as: vegetation (i.e. type and abundance) at the test site, cumulative rainfall between subsequent experiments, rainfall immediately before the experiments and near-surface soil properties . Table 6.2 summarises some of these characteristics for the test sites under investigation. For water balance estimations, factors such as vegetation at the test site and cumulative rainfall are most important. However, if shallow soil conditions yield surface runoff from the test-site to neighbouring soil, recharge at the site will be underestimated.

Regime I was identified at sites where vegetation was either absent (NG16, PPG) or reduced (TGT). Infiltration appears to be rapid as the sands are likely still moist from the previous winter. Soil evaporation, that is evaporation from solar radiance and heating of the shallow subsurface without the influence of vegetation, does not reach depths of more than approximately 0.5 - 1 m. The water content at field capacity below approximately 1 m is therefore not lost during the summer time. Thus, soils are pre-wetted when the first rain falls, and water will quickly drain and elevate water contents above field capacity. Due to the long times between sampling, a period of approximately one month, more detailed interpretation is not possible.

Regime II sites had intact native vegetation (WP, LXAW). The pre-wetting of the unsaturated zone below 2 m depth in June can be explained by preferential flow. Before the main wetting front penetrates the full profile, flow will be channelled along path-

ways predefined by roots, hydrophobic sand and burrows. As a result, the soil moisture distribution is predicted to be somewhat inhomogeneous. The measured water contents are lower compared to those observed once the main wetting front saturates the dry residuals in August. A second explanation for delayed infiltration is the cemented, indurated sand horizon at WP between 1.7 and 2.3 mbNS. In this case if the cemented surface has some dip, it might function as a capillary barrier and flow might be directed out of the crosswell radar plane between the wells. *Strobach et al.* (2010b) found indications of dipping layers at several locations at the Gnangara Mound. At LXAW no distinct horizon is evident, neither from drill reports (*McHugh*, 2011) nor from the GPR signature. However, a slight increase in water content seems to be evident below 2 mbNS, and this depth is also where initial low water contents were recognised.

Another possibility is surface runoff. The site is proximate to the Lexia wetland complex and on the surface is a layer rich in organic material. Although topography is not known with centimetre accuracy, it seems that the topographic level at well locations A and B is slightly elevated (solid lines in Figure 6.18 1e and 2e). In combination with a less permeable surface layer, runoff to the sides is possible. However, the well pair B C (i.e. dashed lines in Figure 6.18 1e and 2e) are not elevated, but show less water content, which contradicts the surface runoff hypothesis.

Regime III at HHW is a combination of a vegetated test-site and several indurated and cemented soil horizons. Neutron logging and VRPs from the two adjacent holes indicate that the first few meters contain several water-retentive layers. Their position is generally shallower in well Wb compared to Wc which indicates dipping structures. Surface common offset GPR confirms that observation. It is therefore possible that preferential flow follows the dips as proposed in *Strobach et al.* (2010b). The top soil layer is also rich in organic material, which is likely a remnant from a previous wetland in that area (*Searle and Bathols*, 2009); thus, making surface runoff to the adjacent sand track possible. At this site the water table did not rise. Thus, there was no seasonal recharge at this site (see Figure 6.18 3f). In fact, the water table declined by 20 cm while all the other sites showed an increase in local water table elevation. This is consistent with recharge from infiltration (*Scanlon et al.*, 2002). The Neutron data described above also backs the hypothesis of no recharge in some years for a similar site as previously discussed.

6.6.4 Towards A Water Balance Evaluation

As only negligible amounts of water reached the water table at the HHW test site, a water balance can be calculated based on this assumption. The simplified water balance equation for the case of no flux to the water table and neglecting runoff from or to the site can be written as

$$P = ET + \Delta S \tag{6.5}$$

with P the precipitation, ET evapotranspiration and ΔS the water storage in the soil (*Scanlon et al.*, 2002). Quantities are typically given as rates in millimetre per time interval. The rates given here are calculated based on the time interval between subsequent field experiments in days. ΔS_s is the sequential water storage in the soil calculated with equation 6.4. Note that for the other sites, the water fluxes to the saturated zone would appear in this equation. As those values are not known, the evapotranspiration rate cannot be calculated. The results for HHW are plotted in Figure 6.22. Note that data were extrapolated from 1 mbNS to zero depth because the missing interval would have had a great influence on evapotranspiration estimates indicated by dashed red and black lines opposed to solid lines in Figure 6.22. This figure also shows the results of the uncorrected ZOP data (dotted lines) which initially overestimates total evapotranspiration due to underestimation of the change in stored water in the unsaturated soil. However, the cumulative annual evapotranspiration is almost identical to the corrected curves. While the wetting periods are overestimated by uncorrected velocities, the drying periods are equivalently underestimated. For annual evapotranspiration that includes wetting and drying the accuracy of absolute water content in the profile becomes less important than is the case for sequential difference curves. The overall evapotranspiration estimated from the ZOP experiments is 620 mm. This value compares well with values found in the literature. *Farrington et al.* (1989) derived 666 mm annual evapotranspiration with annual rainfall of 865 mm in similar Banksia woodland vegetation. *Sharma et al.* (1991) find evapotranspiration values with the zero flux plane technique between 600 and 700 mm for different test sites at native Banksia woodland on the central Gnangara Mound for 1987 when annual precipitation was 742 mm (i.e. similar to study period 2011). Note that our measurements did not span a full year and

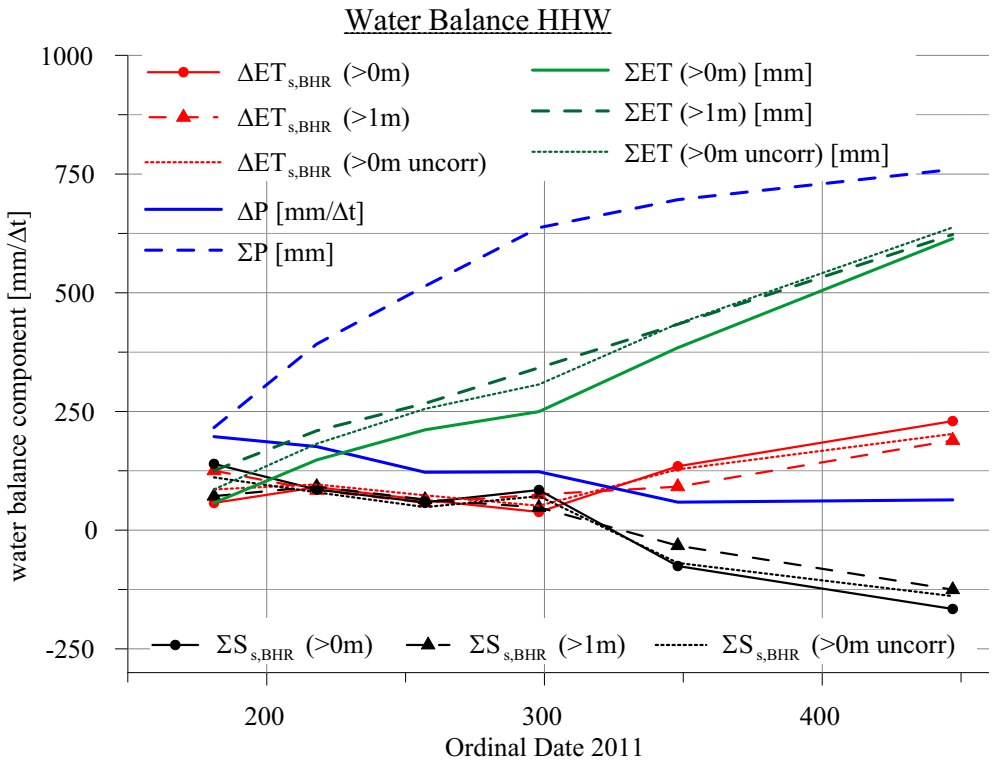

Figure 6.22: *A water balance calculation for HHW under the assumption of negligible flux below 7 mbNS. Sequential difference evapotranspiration estimates $\Delta ET_{s,BHR}$ are given for the unsaturated zone from 0 - 11.5 mbNS (solid red line and dots) and and 1 - 11.5 mbNS (dashed red line and triangles) and also for the unshifted ZOP data (dotted red line). Cumulative storage $\sum S_{s,BHR}$ is plotted in black. Note the cumulative evapotranspiration estimate $\sum ET$ for shifted and unshifted ZOP results (green solid and dotted lines, respectively) yields a similar value of 600 mm for a full wetting-drying cycle.*

some evapotranspiration can be expected for the months of April and May.

6.7 Conclusions

Borehole radar techniques were successfully employed for time-lapse monitoring of rainfall infiltration into a layered sandy soil during an annual recharge cycle in Mediterranean climate. Zero vertical offset profiling ZOP and zero offset vertical radar profiling VRP measurements were performed on a monthly basis. Soil moisture profiles reveal infiltration characteristics at six test sites located on the Gnangara Mound, north of Perth, Western Australia.

High repeatability of long-term time-lapse ZOPs in the saturated zone demonstrates that this technique can achieve high precision for the saturated case. A similar precision is expected for the long-term unsaturated zone ZOPs as indicated by high repeatability of measurements performed in short succession. The resolution is determined

by the antenna length, the antenna frequency, and the separation of boreholes. Initial absolute velocity estimates derived from in-hole radar travel times exhibited inconsistencies associated with zero-time correction inaccuracies, and problems with repeatability. However, it is possible to match zero time corrections based on travel times in the saturated zone where saturation and travel time can be expected to remain constant throughout all experiments. This matching greatly improves repeatability of the entire ZOP profiles. Larger discrepancies between VRP and ZOP velocity estimates were observed at sites with small well spacing. Explanations for the inconsistency are inaccuracies in well separation or borehole deviation, high uncertainty in zero-time correction, and near-field effects; all of which are less influential on VRP velocity calculation. Hence, the zero-offset VRPs provide a robust, independent measure of interval velocity which does not require zero-time correction. The ZOP curves can be shifted to the velocity level provided by the VRP profiles in order to improve the accuracy of absolute values of velocity. The matching techniques provide a workflow for correcting ZOP data for closely spaced wells. For larger well separation, accuracy is sufficient and no matching is necessary. However, the resolution of ZOP measurements with larger well spacing suffers due to refracted energy and an increased Fresnel zone. Layers with higher dielectric permittivity (low velocity) within a low dielectric permittivity (high velocity) background are especially difficult to resolve with ZOPs between distant wells.

While VRPs maintain high resolution power because refracted energy is less important, they were less repeatable than ZOPs. They suffer from interference with upgoing wavefields, which leads to large and erroneous slope estimates. However, the general velocity structure could be resolved from VRPs and they provide an independent measure of absolute interval velocities and information on depth of penetration, reflectivity of layers and the exact location of layers. While this work clearly indicates that time-lapse ZOPs provide higher repeatability, it is strongly recommended to measure both VRP with ZOP to compare and possibly match results.

The time-lapse moisture curves revealed different infiltration characteristics for the various test-sites. Three regimes were identified. Regime I shows simple infiltration behaviour where the initially dry unsaturated zone in May is transformed into a wet soil at its field capacity after approximately 200 mm of rainfall in June/July. Regime

II is characterised by initial pre-wetting in June/July and saturation to field capacity after approximately 400 mm precipitation in August. One site showed no change in the unsaturated zone below 7 mbNS and was categorised into an infiltration Regime III. While no change in water content doesn't in itself demonstrate no-flow (*Scanlon et al.*, 2002; *Sharma et al.*, 1991), time-lapse Neutron data from a similar site confirms that large flux is likely to increase the water content at all depths. The falling water table further substantiates that only minimal or no recharge occurred from the winter rainfall cycle in this area.

Under the assumption of no-flow to the water table, evapotranspiration can be derived based on a water balance calculation. For the site HHW, a cumulative value of 620 mm is obtained for the 10 month observation period (84 % of total precipitation).

A comparison between time-lapse Neutron logging and crosswell radar data show that both exhibit similar infiltration behaviour. The crosswell radar technique, however, has some advantages over neutron logging. Some advantages include: i) it is non-hazardous unlike the radioactive source employed for neutron logging, ii) the measurements represent a larger volume of earth (i.e. between borehole), iii) full waveform of BHR can provide information on discrete interfaces (i.e. reflections/refractions), iv) the calibration to water contents is robust for simple soils, and v) GPR additionally provides electrical conductivity (i.e. attenuation analysis).

Although a more detailed investigation of the existing neutron data is required to entirely evaluate their information content and compare those to time-lapse BHR results, the historic neutron data already revealed some additional information that the short duration of the borehole radar surveys could not provide. That is, the water-retentive horizons do not appear to provide extra plant available water over a two year time period. This is inferred from their water balance, which is similar to the non-retentive horizons. However, these horizons tend to influence the infiltration and recharge, especially for deep vadose zones, by impeding flow. Truly perched water over "coffee rock" horizons, however, could not be demonstrated.

Chapter 7

Thesis Conclusions

The work presented in this dissertation provides new insights into the shallow subsurface soil structures and hydrogeologic processes involved in shallow unsaturated flow induced by rainfall infiltration on the Gnangara Mound north of Perth, Western Australia. These findings are facilitated by hydrogeophysical methods and measurements. A substantial part of this dissertation deals with the critical discussion, improvement and development of hydrogeophysical remote-sensing and borehole techniques such as ground-penetrating radar, electrical resistivity tomography and neutron logging. The key outcomes and advances from a methodological viewpoint are:

- **GPR is a powerful technique to image the unsaturated zone of the sandy Bassendean soil on the Gnangara Mound, Swan Coastal Plain in southwestern Western Australia.**

  - Podosol accumulation soil horizons are largely electrically resistive; thus, electromagnetic waves can penetrate with low loss and allow imaging of the strata below. The dielectric permittivity versus water content relationship for accumulation and clean sand intervals are similar. Both show a reasonable fit with the Topp-relationship.

    A Hashin-Shtrickman average Archie-type mixing law provides cementation and saturation parameters analogous to Archie's unsaturated electric conductivity mixing law. Both clean sands and friably cemented "coffee rock" material have low cementation exponents m between 1.4 and 1.7 and saturation exponents n between 2.2 and 2.6, these values are consistent with

literature values for unconsolidated sandy soil.

- Elevated water content of accumulation horizons explains the vertical impedance contrasts and resulting reflections in GPR profiles. Any additional contribution to reflectivity is probably due to change in texture due to illuviation.
- Common offset GPR is suitable for large-scale mapping and multi-offset GPR has been done to obtain vertical velocity distribution.
- Diffraction hyperbolae moveout analysis in common offset GPR data is useful to determine lateral near-surface EM velocity variations. A new technique has been developed and applied that allows recovery of the shallow dielectric permittivity structure based on dispersion analysis of diffracted energy captured within a waveguide structure.
- To determine the potential influence of water retentive vadose zone layers on recharge, two analysis schemes are developed for rapid characterisation and classification of large-scale 2D GPR. The first is based on vertical reflector configuration (i.e. unsat. reflector depth relative to the water table), this is obtained by picking first reflection arrival time. The second method determines energy return from unsaturated zone intervals (i.e. sum of amplitudes) and compares this response to the energy reflected from the water table to detect layer characteristics that may be indicative of hydrogeologic significance.

- **Borehole radar time-lapse measurements produce repeatable and accurate water content profiles.**
  - Experiments demonstrate that the precision of time-lapse zero-offset crosswell radar experiments can be improved by matching saturated zone intervals where temporal variations are not expected.
  - Inaccuracies due to problems with zero-time correction and near-field antenna effects are reduced by analysing vertical radar profiles, which are less precise, but not impacted by zero-time correction inaccuracies and antennas near-field effects.
  - Resolution, accuracy and precision (i.e. repeatability) of crosswell GPR is shown to have a dependence on borehole separation. This can be explained

by considering wavefront propagation characteristics: larger separation → larger Fresnel zone (smaller resolution/spatial precision) → longer travel time (higher precision/accuracy). The same is true for frequency (and therefore antenna length) where a higher frequency (shorter antenna) will increase precision and accuracy due to higher certainty in zero-time determination and increased spatial resolution.

- Borehole GPR is a feasible alternative to neutron logging. Advantages include: i) non-radioactive source, yet easy and fast to measure, ii) measurement away from borehole, i.e. bulk property of interval between two wells is characterised (i.e. 1 - 10...30 m) rather than the disturbed ground around the borehole, iii) the full-waveform allows interpretation of distinct layers based on characteristics of wave propagation (i.e. guided waves, refracted and reflected waves), iv) several acquisition geometries possible (i.e. ZOP, multi offset VRP, multi-offset crosswell tomography) to characterise subsurface in 2D/3D, v) recovery of both, dielectric and electrical conductivity soil properties, and vi) simple relationship between dielectric properties and water content makes calibration to water content unnecessary, especially in time-lapse experiments.

Many hydrogeologic objectives can be addressed by interpretation of geophysical measurements. Hydrogeologic significance is manifest in the subsurface physical properties, for example the capacity of soil horizons to store or transport water, which has an influence on unsaturated flow. The geophysical techniques that may be used to address these problems are 2D and 3D surface GPR and time-lapse borehole GPR or time-lapse neutron logging. These tools allow to determine the spatial layer distribution (vertically and laterally) and provide estimates of layer water content, and water content changes throughout a recharge cycle (water balance). The main hydrogeologic findings in this thesis were:

- **Layers locally influence the unsaturated flow regime.**

  - Friably cemented sand has a reduced hydraulic conductivity, and increased

water retention potential on a laboratory scale; thus, it could be influential in water infiltration and storage on a field scale as well.

- Field scale time-lapse borehole measurements (i.e. borehole radar and neutron logging) show that the layers with elevated water content seem to influence wetting front development. As findings are based on a limited set of study sites, it is not yet clear that conclusions can be applied more broadly across the entire Gnangara Mound recharge area.
- Climate (i.e. rainfall) has a profound influence on moisture content dynamics of the vadose zone. Recharge seems to be absent in some locations during drier years.

- **Indurated sand horizons probably do not provide additional plant available water compared to the clean sand soil intervals (i.e. previously unaccounted loss due to extra storage).**
  - Time-lapse neutron logs from Whiteman Park, the Pinjar area and several wetlands do not conclusively show that water retentive horizons have a higher annual variation in water content compared to the clean sand intervals (i.e. their water balance is similar). This should have implications for groundwater recharge as the water balance of the bulk soil including the retention horizons is similar to the clean soil.

- **Spatial reflector distribution is "patchy" on a large scale. Reflector significance seems to vary throughout the central Gnangara Mound.**
  - Large parts of the investigated transects have no significant impeding soil horizons. This conclusion is based on the assumptions that reflectors are most influential for groundwater recharge if they are strong and close to the surface.
  - However, multiple levels of shallow and often strong but patchy reflectors were identified in the deep unsaturated zone of the central part of the Gnangara Mound.
  - Towards the east of a possible hydrogeologic transition (i.e. where water

table shows a step) there appear to be no major reflection events in the unsaturated zone, which leads to the interpretation of high recharge potential.

7.1 Recommendations for future research

This work represents the first significant effort in applying shallow geophysical methods for groundwater recharge investigation on this scale on the Gnangara Mound, and amongst a few studies worldwide to target such a large area with terrestrial (i.e. not ice) ground penetrating radar. Thus, this work is exploratory, and many aspects deserve more research. Based on the experience gained in this study, I suggest the following studies for future investigation:

- **Test-site scale investigations:**
  - Based on the large scale data, identify areas in the central mound that show different layer constellations within close vicinity of each other and target these with shallow drilling. Nests of boreholes, for example arranged in a grid with approx. 5 m spacing provide infrastructure for borehole radar experiments.
  - Other environmental factors to be considered are vegetation at the test site. Different extremes could be targeted (i.e. densely vegetated Banksia bushland versus recently logged pine plantation).
  - Time-lapse experiments could be performed on a weekly basis starting just before the annual rainfall season, and repeated until changes are only due to ephemeral infiltration events (i.e. until July/August).
  - After strong rainfall events, some selected sites could be measured with a high temporal repetition rate (i.e. hourly to daily) to retrieve in-situ unsaturated hydraulic conductivity estimates from transient flow events. Another alternative is to perform a forced infiltration experiment, for example by irrigation.
  - Crosswell experiments should be performed with higher antenna frequency than performed in this study, for example between 250 - 400 MHz.

- To obtain site-specific recharge, it should be considered to stay close to a climate observatory, or monitor rainfall at the site during the observation period.

- To obtain 2D water distribution in between boreholes, multi-offset cross-well gathers could be considered. Preliminary tests have shown that the wavelength of 100 MHz signals in dry sands in combination with standard ray-based tomographic inversion does not provide sufficient resolution to obtain additional 2D information. Full-waveform inversion is an alternative approach to increase resolution. However, this method is computationally expensive and subject to current research and development. Despite the future potential of full-waveform inversion, I recommend to use ZOPs and VRPs, higher antenna frequency and measurement between several parallel boreholes to obtain 2D information.

→ The anticipated outcome of those test-site studies are to obtain definite comprehensive understanding of how different soil profiles influence unsaturated flow, especially in the context of guided (funnelled) flow along capillary barriers and associated "fingering flow", preferential flow through "pipe" structures in accumulation horizons, influence of layering on refracted flow and the influence of surficial hydrophobic sand patches.

→ Unsaturated hydraulic parameters can then replace the current simplified homogeneous unsaturated zone model.

- **Proposed subregional scale investigations:**

  - Although some profiles intersect the critical areas at the central Bassendean Sand formation, the GPR line density is too sparse in the area between Pinjar and Tuart Road. Further 2D GPR lines would increase certainty of extrapolating unsaturated zone properties in between existing lines.

  - In my view it is very important to understand the 3D properties (i.e. topology)of GPR reflectors. The 3D investigations at Whiteman Park and WC6a demonstrated that layer distribution and topography can be quite inhomogeneous and complex. The 2D transects also confirm this observation. However, the scale of 3D surveys need to be increased. I would recom-

mend to acquire a pseudo 3D dataset with approx. 30 - 50 parallel lines and a spacing between 5 - 10 m, and profile length between 200 - 300 m (parameters depending on the local variability of soil horizons). Due to the dense natural bushland at the areas of interest, I recommend to use copolarized endfire antenna configuration with a frequency between 100 - 200 MHz (i.e. 50 MHz is probably too low).

- The test-site scale investigations and results from drilling as proposed above would enable the refinement of large-scale 2D data interpretation and/or re-interpretation.
- Another point of interest are the layers that appear below the water table in the area east of where the step in the water table occurs. Drilling should specifically target areas where these horizons appear as strong reflectors, and areas where they disappear to confirm whether they are continuous or not.
- Analogous to the unsaturated layer characterisation, the topography of layers below the water table could be investigated on a similar 3D arrangement as described above.

References

Agilent (2012), *Agilent 85071E Materials Measurement Software*, Agilent Technologies. (Cited on page 56.)

Alumbaugh, D., P. Chang, L. Paprocki, J. Brainard, R. Glass, and C. Rautman (2002), Estimating moisture contents in the vadose zone using cross-borehole ground penetrating radar: A study of accuracy and repeatability, *Water Resour. Res*, *38*(12), 1309. (Cited on pages 178 and 191.)

Annan, A. P. (2005), Gpr methods for hydrogeological studies, *Water Science and Technology Library*, *50*, 185–213. (Cited on pages 51, 244 and 246.)

Archie, G. (1942), The electrical resistivity log as an aid in determining some reservoir characteristics, *Trans. AIMe*, *146*(99), 54–62. (Cited on page 51.)

Arcone, S. (1984), Field observations of electromagnetic pulse propagation in dielectric slabs, *Geophysics*, *49*, 1763. (Cited on pages 151 and 164.)

Arcone, S., P. Peapples, and L. Liu (2003), Propagation of a ground-penetrating radar (gpr) pulse in a thin-surface waveguide, *Geophysics*, *68*(6), 1922. (Cited on pages 151 and 164.)

Arcone, S., S. Grant, G. Boitnott, and B. Bostick (2008), Complex permittivity and clay mineralogy of grain-size fractions in a wet silt soil, *Geophysics*, *73*(3), J1–J13. (Cited on page 46.)

Baker-Jarvis, J., E. Vanzura, and W. Kissick (1990), Improved technique for determining complex permittivity with the transmission/reflection method, *Microwave Theory and Techniques, IEEE Transactions on*, *38*(8), 1096–1103. (Cited on page 56.)

Balanis, C. (1982), *Antenna Theory: Analysis and Design, 2nd Edition*, J. Wiley, New York. (Cited on pages 44 and 194.)

Bano, M. (2006), Effects of the transition zone above a water table on the reflection of gpr waves, *Geophys. Res. Lett*, *33*, L13,309. (Cited on pages 98, 137 and 246.)

Bell, J. (1987), Neutron probe practice, report 19 (third edition), *Tech. rep.*, Institute of Hydrology. (Cited on pages 182, 183, 184, 203, 204, 211 and 318.)

Bertuch, M., and R. Froend (2006), Winter drawdown trial - whiteman park, soil characterisation report, *Tech. rep.*, Edith-Cowan University, School of Natural Sciences, Perth, Western Australia. (Cited on pages 106, 189, 202, 280 and 321.)

Bikowski, J., J. A. Huisman, J. A. Vrugt, H. Vereecken, and J. van der Kruk (2012), Integrated analysis of waveguide dispersed gpr pulses using deterministic and bayesian inversion methods, *Near Surface Geophysics*, *in press, available online*, doi:doi: 10.3997/1873-0604.2012041. (Cited on pages 168 and 169.)

Binley, A., P. Winship, R. Middleton, M. Pokar, and J. West (2001), High-resolution characterization of vadose zone dynamics using cross-borehole radar, *Water Resources Research*, *37*(11), 2639–2652. (Cited on pages 178 and 179.)

Boeniger, U., J. Tronicke, K. Holliger, and A. Becht (2006), Multi-offset vertical radar profiling for subsurface reflection imaging, *Journal of Environmental & Engineering Geophysics*, *11*(4), 289–298, doi:10.2113/JEEG11.4.289. (Cited on page 180.)

Booth, A., R. Clark, and T. Murray (2010), Semblance response to a ground-penetrating radar wavelet and resulting errors in velocity analysis, *Near Surface Geophysics*, *8*(3). (Cited on page 118.)

Botha, G., C. Bristow, N. Porat, G. Duller, S. Armitage, H. Roberts, B. Clarke, M. Kota, and P. Schoeman (2003), Evidence for dune reactivation from gpr profiles on the maputaland coastal plain, south africa, *Geological Society, London, Special Publications*, *211*(1), 29–46. (Cited on pages 81 and 310.)

Bottom, V. (1972), Dielectric constants of quartz, *Journal of Applied Physics*, *43*(4), 1493–1495. (Cited on page 60.)

Bradford, J., and J. Deeds (2006), Ground-penetrating radar theory and application of thin-bed offset-dependent reflectivity, *Geophysics*, *71*(3), K47–K57. (Cited on page 78.)

Bradford, J., W. Clement, and W. Barrash (2009), Estimating porosity with ground-penetrating radar reflection tomography: A controlled 3-d experiment at the boise hydrogeophysical research site, *Water Resources Research*, *45*(null), W00D26. (Cited on page 248.)

Brooke, B., M. Preda, R. Lee, M. Cox, J. Olley, T. Pietsch, and D. Price (2008), Development, composition and age of indurated sand layers in the late quaternary coastal deposits of northern moreton bay, queensland, *Australian Journal of Earth Sciences*, *55*(2), 141–157. (Cited on page 25.)

Brovelli, A., and G. Cassiani (2008), Effective permittivity of porous media; a critical analysis of the complex refractive index model, *Geophysical Prospecting*, *56*(5), 715–727. (Cited on pages 50 and 51.)

Brovelli, A., and G. Cassiani (2010), A combination of the hashin-shtrikman bounds aimed at modelling electrical conductivity and permittivity of variably saturated porous media, *Geophysical Journal International*, *180*(1), 225–237. (Cited on pages 51, 52, 65, 66 and 309.)

Brovelli, A., and G. Cassiani (2011), Combined estimation of effective electrical conductivity and permittivity for soil monitoring, *Water Resources Research*, *47*(8), W08,510. (Cited on page 51.)

Busch, S., J. V. der Kruk, J. Bikowski, and H. Vereecken (2012), Quantitative conductivity and permittivity estimation using full-waveform inversion of on-ground gpr data, *Geophysics*, *77*, H79–H91. (Cited on page 151.)

Buursink, M., J. Lane Jr, W. Clement, and M. Knoll (2002), Use of vertical-radar profiling to estimate porosity at two new england sites and comparison with neutron log porosity, in *Proc. of SAGEEP*, vol. 2. (Cited on page 194.)

Cassiani, G., C. Strobbia, and L. Gallotti (2004), Vertical radar profiles for the characterization of deep vadose zones, *Vadose Zone J.*, *3*(4), 1093–1105, doi: 10.2113/3.4.1093. (Cited on page 180.)

Cassiani, G., C. Strobbia, M. Giustiniani, N. Fusi, G. Crosta, and P. Frattini (2006), Monitoring of hydrological hillslope processes via time-lapse ground-penetrating radar guided waves, *Bollettino di Geofisica Teorica ed Applicata*, *47*(1-2), 125–144. (Cited on page 151.)

Cassiani, G., N. Fusi, D. Susanni, and R. Deiana (2008), Vertical radar profiles for the assessment of landfill capping effectiveness, *Near Surface Geophysics*, *6*, 133–142. (Cited on page 180.)

Chang, P.-Y., D. Alumbaugh, J. Brainard, and L. Hall (2004), The application of ground penetrating radar attenuation tomography in a vadose zone infiltration experiment, *Journal of Contaminant Hydrology*, *71*(1-4), 67 – 87, doi:DOI:10.1016/j.jconhyd.2003.09.011. (Cited on pages 178 and 179.)

Chen, C. (2012), Lateral waves in ground penetrating radar applications, in *Ground Penetrating Radar (GPR), 2012 14th International Conference on*, pp. 39–41, IEEE. (Cited on pages 158 and 246.)

Claerbout, J., and S. Fomel (2008), *Image estimation by example: Geophysical soundings image construction: multidimensional autoregression*, Citeseer. (Cited on page 251.)

Clement, W. P., and M. D. Knoll (2006), Traveltime inversion of vertical radar profiles, *Geophysics*, *71*(3), K67–76, doi:10.1190/1.2194527. (Cited on page 180.)

Cox, M., M. Preda, and J. Harbison (2002), Importance of indurated sand layers to groundwater flow in quaternary coastal settings, moreton bay, in *Balancing the Groundwater Budget: International Association of Hydrogeologists Groundwater Conference*, pp. 12–17. (Cited on pages 22 and 26.)

Curtis, J. (2001), Moisture effects on the dielectric properties of soils, *Geoscience and Remote Sensing, IEEE Transactions on*, *39*(1), 125–128. (Cited on page 49.)

Daniels, D. (2005), *Ground penetrating radar*, Wiley Online Library. (Cited on pages 244 and 247.)

Davidson, W. (1995), *Hydrogeology and groundwater resources of the Perth Region, Western Australia*, Bulletin 142, Western Australia geological Survey. (Cited on pages 7, 12, 16, 54 and 158.)

Davidson, W., and X. Yu (2006), Perth regional aquifer modelling system (prams) model development: Hydrogeology and groundwater modelling, *Department of Water, Western Australia, Hydrogeological record series*, *HG 20*. (Cited on pages 7, 12, 13, 14, 16, 17, 18, 19, 20, 21, 22, 100 and 306.)

Day-Lewis, F., J. Lane Jr, J. Harris, and S. Gorelick (2003), Time-lapse imaging of saline-tracer transport in fractured rock using difference-attenuation radar tomography, *Water Resources Research*, *39*(10), 1290. (Cited on page 178.)

De Vries, J., and I. Simmers (2002), Groundwater recharge: an overview of processes and challenges, *Hydrogeology Journal*, *10*(1), 5–17. (Cited on page 175.)

Deiana, R., G. Cassiani, A. Kemna, A. Villa, V. Bruno, and A. Bagliani (2007), An experiment of non invasive characterization of the vadose zone via water injection and cross-hole time-lapse geophysical monitoring, *Near Surface Geophysics*, *5*(3), 183–194. (Cited on page 178.)

der Kruk, J. V., N. Diamanti, A. Giannopoulos, and H. Vereecken (2012), Inversion of dispersive gpr pulse propagation in waveguides with heterogeneities and rough and dipping interfaces, *Journal of applied Geophysics*, *81*, 88–96. (Cited on page 170.)

Dix, C. H. (1955), Seismic velocities from surface measurements, *Geophysics*, *20*(1), 68–86. (Cited on page 118.)

Farmani, M., H. Keers, and N. Kitterød (2008), Time-lapse gpr tomography of unsaturated water flow in an ice-contact delta, *Vadose Zone Journal*, *7*(1), 272–283. (Cited on pages 178, 179 and 206.)

Farrington, P., E. Greenwood, G. Bartle, J. Beresford, and G. Watson (1989), Evaporation from banksia woodland on a groundwater mound, *Journal of Hydrology*, *105*(1-2), 173–186. (Cited on pages 187 and 218.)

Farrington, P., G. Watson, G. Bartle, and E. Greenwood (1990), Evaporation from dampland vegetation on a groundwater mound, *Journal of Hydrology*, *115*(1-4), 65–75. (Cited on page 187.)

Ferre, T. P., A. M. Binley, K. W. Blasch, J. B. Callegary, S. M. Crawford, J. B. Fink, A. L. Flint, L. E. Flint, J. P. Hoffmann, J. A. Izbicki, M. T. Levitt, D. R. Pool, and B. R. Scanlon (2007), Geophysical methods for investigating ground-water recharge, *Ground-water recharge in the arid and semiarid southwestern United States: U.S. Geological Survey Professional Paper*, *1703*, 375–412. (Cited on pages 175 and 183.)

Fetter, C. (2001), *Applied Hydrogeology (4th Ed.)*, Prentice Hall, Columbus, Ohio. (Cited on page 175.)

Flint, A., L. Flint, E. Kwicklis, G. Bodvarsson, and J. Fabryka-Martin (2001), Hydrology of yucca mountain, nevada, *Reviews of Geophysics*, *39*(4), 447–470. (Cited on page 183.)

Flint, L., and A. Flint (1995), Shallow infiltration processes at yucca mountain, nevada: Neutron logging data 1984–1993, *Tech. rep.*, Geological Survey, Denver, CO (United States). (Cited on page 183.)

Forbriger, T. (2003), Inversion of shallow-seismic wavefields: I. wavefield transformation, *Geophysical Journal International*, *153*(3), 719–734. (Cited on page 155.)

Froend, R. H., M. Davies, W. Stock, M. Martin, C. Robertson, D. Eamus, and K. Smettem (2010), Environmentally sympathetic groundwater production: is it possible to maintain abstraction in areas with vulnerable phreatophytic vegetation?, in *Proceedings of Groundwater 2010: The Challenges of Sustainable Management, Canberra, Australia*. (Cited on page 185.)

Galagedara, L., G. Parkin, and J. Redman (2003), An analysis of the ground-penetrating radar direct ground wave method for soil water content measurement, *Hydrological Processes*, *17*(18), 3615–3628. (Cited on page 83.)

Gloaguen, E., M. Chouteau, D. Marcotte, and R. Chapuis (2001), Estimation of hydraulic conductivity of an unconfined aquifer using cokriging of gpr and hydrostratigraphic data, *Journal of Applied Geophysics*, *47*(2), 135–152. (Cited on pages 80 and 114.)

Grote, K., S. Hubbard, J. Harvey, and Y. Rubin (2005), Evaluation of infiltration in layered pavements using surface gpr reflection techniques, *Journal of Applied Geophysics*, *57*(2), 129–153. (Cited on page 114.)

Grote, K., C. Anger, B. Kelly, S. Hubbard, and Y. Rubin (2010a), Characterization of soil water content variability and soil texture using gpr groundwave techniques, *Journal of Environmental & Engineering Geophysics*, *15*(3), 93. (Cited on page 82.)

Grote, K., T. Crist, and C. Nickel (2010b), Experimental estimation of the gpr groundwave sampling depth, *Water Resources Research*, *46*(10), W10,520. (Cited on pages 83 and 150.)

Harbi, H., and G. McMechan (2011), Modeling 3d porosity and permeability from gpr data in the ellenburger dolomite, central texas, *Geophysics*, *76*, J35. (Cited on page 194.)

Hashin, Z., and S. Shtrikman (1962), A variational approach to the theory of the effective magnetic permeability of multiphase materials, *Journal of Applied Physics*, *33*(10), 3125–3131. (Cited on page 51.)

Healy, R. (2010), *Estimating groundwater recharge*, Cambridge University Press. (Cited on page 175.)

Hendrickx, J., and M. Flury (2001), Uniform and preferential flow mechanisms in the vadose zone, *Conceptual models of flow and transport in the fractured vadose zone. Natl. Acad. Press, Washington, DC*, pp. 149–187. (Cited on page 39.)

Hubbard, S., J. Peterson, E. Majer, P. Zawislanski, K. Williams, J. Roberts, and F. Wobber (1997), Estimation of permeable pathways and water content using tomographic radar data, *The Leading Edge*, *16*, 1623. (Cited on page 178.)

Hubbard, S., K. Grote, and Y. Rubin (2002), Mapping the volumetric soil water content of a california vineyard using high-frequency gpr ground wave data, *The Leading Edge*, *21*(6), 552–559. (Cited on pages 42 and 82.)

Huisman, J., J. Snepvangers, W. Bouten, and G. Heuvelink (2002), Mapping spatial variation in surface soil water content: comparison of ground-penetrating radar and time domain reflectometry, *Journal of Hydrology*, *269*(3), 194–207. (Cited on page 42.)

Huisman, J. A., S. S. Hubbard, J. D. Redman, and A. P. Annan (2003), Measuring soil water content with ground penetrating radar: A review, *Vadose Zone J.*, *2*(4), 476–491, doi:10.2113/2.4.476. (Cited on pages 42, 43, 51, 149, 150 and 244.)

Irving, J. D., M. D. Knoll, and R. J. Knight (2007), Improving crosshole radar velocity tomograms: a new approach to incorporating high-angle traveltime data, *Geophysics*, *72*(4), J31–J41. (Cited on page 180.)

Iskander, M., and J. DuBow (1983), Time-and frequency-domain techniques for measuring the dielectric properties of rocks: a review, *Journal of Microwave Power*, *18*(1), 55–74. (Cited on page 43.)

Jahnert, R., O. de Paula, L. Collins, E. Strobach, and R. Pevzner (2012), Evolution of a coquina barrier in shark bay, australia by gpr imaging: Architecture of a holocene reservoir analogue, *Sedimentary Geology*. (Cited on pages 132 and 303.)

Josh, M., B. Clennell, and A. Siggins (2009), Practical broadband dielectric measurement of geological samples, in *SPWLA 50th Annual Logging Symposium*. (Cited on page 55.)

Josh, M., M. Lintern, A. Kepic, and M. Verrall (2011), Impact of grain-coating iron minerals on dielectric response of quartz sand and implications for ground-penetrating radar, *Geophysics*, *76*, J27. (Cited on pages 43 and 55.)

Kaviratna, P., T. Pinnavaia, and P. Schroeder (1996), Dielectric properties of smectite clays, *Journal of Physics and Chemistry of Solids*, *57*(12), 1897–1906. (Cited on page 46.)

Knight, R. (1984), The dielectric constant of sandstones. 5 hz to 13 mhz, Ph.D. thesis, Stanford University. (Cited on page 60.)

Knight, R., and A. Nur (1987), The dielectric constant of sandstones, 60 khz to 4 mhz, *Geophysics*, *52*(5), 644–654. (Cited on page 60.)

Knoll, M. (1996), A petrophysical basis for ground penetrating radar and very early time electromagnetics: Electrical properties of sand-clay mixtures, Ph.D. thesis, University of British Columbia. (Cited on pages 44 and 246.)

Kramer, J., S. Cullen, and L. Everett (1992), Vadose zone monitoring with the neutron moisture probe, *Ground Water Monitoring & Remediation*, *12*(3), 177–187. (Cited on page 183.)

Kundzewicz, Z., L. Mata, N. Arnell, P. Döll, P. Kabat, B. Jiménez, K. Miller, T. Oki, Z. Sen, and I. Shiklomanov (2007), *Freshwater resources and their management*, chap. Climate Change 2007: Impacts, Adaptation and Vulnerability. Contribution of Working Group II to the Fourth Assessment Report of the Intergovernmental Panel on Climate Change, pp. 173–210, Cambridge University Press, Cambridge, UK. (Cited on page VII.)

Kung, K. (1990), Preferential flow in a sandy vadose zone: 1. field observation, *Geoderma*, *46*(1), 51–58. (Cited on page 39.)

Lambot, S., L. Weihermüller, J. Huisman, H. Vereecken, M. Vanclooster, and E. Slob (2006a), Analysis of air-launched ground-penetrating radar techniques to measure the soil surface water content, *Water Resources Research*, *42*(11), W11,403. (Cited on page 42.)

Lambot, S., E. Slob, M. Vanclooster, and H. Vereecken (2006b), Closed loop gpr data inversion for soil hydraulic and electric property determination, *Geophys. Res. Lett*, *33*(21), L21,405. (Cited on page 150.)

Lichtenecker, K., and K. Rother (1931), Die herleitung des logarithmischen mischungsgesetzes aus allgemeinen prinzipien der stationären strömung, *phys. Z*, *32*, 255–260. (Cited on page 50.)

Looms, M. C., K. H. Jensen, A. Binley, and L. Nielsen (2008), Monitoring unsaturated flow and transport using cross-borehole geophysical methods, *Vadose Zone Journal*, *7*(1), 227–237, doi:10.2136/vzj2006.0129. (Cited on page 178.)

Lunt, I., S. Hubbard, and Y. Rubin (2005), Soil moisture content estimation using ground-penetrating radar reflection data, *Journal of Hydrology*, *307*(1), 254–269. (Cited on page 114.)

Maxwell, J. (1865), A dynamical theory of the electromagnetic field, *Philosophical Transactions of the Royal Society of London*, *155*, 459–512. (Cited on page 44.)

McArthur, W. M., and E. Bettenay (1974), The development and distribution of the soils of the swan coastal plain, western australia, *Soil Publication, CSIRO, Melbourne*, *No. 16*. (Cited on pages 14 and 54.)

McHugh, S. (2011), Perth shallow groundwater systems investigation: Lexia wetlands, *Department of Water, Western Australia, Hydrogeological record series*, *HG 44*. (Cited on page 217.)

McHugh, S., and M. Hammond (2011), Perth shallow groundwater systems investigation: Tangletoe swamp, *Department of Water, Western Australia, Hydrogeological record series*, *HG 49*. (Cited on page 189.)

Miyazaki, T. (2006), *Water Flow in Soils, Second Edition*, CRC Press, Taylor & Francis Group. (Cited on pages 99 and 177.)

Moysey, S., R. Knight, and H. Jol (2006), Texture-based classification of ground-penetrating radar images, *Geophysics*, *71*(6), K111–K118. (Cited on page 77.)

Neal, A. (2004), Ground-penetrating radar and its use in sedimentology: principles, problems and progress, *Earth-science reviews*, *66*(3), 261–330. (Cited on pages 76 and 244.)

Nobes, D., E. Davis, and S. Arcone (2005), "mirror-image" multiples in ground-penetrating radar, *Geophysics*, *70*(1), K20–K22. (Cited on pages 81 and 310.)

Olhoeft, G. (1998), Electrical, magnetic, and geometric properties that determine ground-penetrating radar performance, in *Proc. 7th Int. Conf. on Ground-Penetrating Radar (The University of Kansas, Lawrence, KS, USA, 27–30 May)*, pp. 177–82. (Cited on page 44.)

Park, C., R. Miller, J. Xia, et al. (1998), Imaging dispersion curves of surface waves on multi-channel record, *Expanded Abstract: Soc. Explor. Geophys*, pp. 1377–1380. (Cited on pages 118, 151, 152, 160, 166 and 305.)

Peterson, J. (2001), Pre-inversion corrections and analysis of radar tomographic data, *Journal of Environmental and Engineering Geophysics*, *6*, 1. (Cited on pages 180, 191 and 194.)

Pettinelli, E., G. Vannaroni, B. Di Pasquo, E. Mattei, A. Di Matteo, A. De Santis, and P. Annan (2007), Correlation between near-surface electromagnetic soil parameters and early-time gpr signals: An experimental study, *Geophysics*, *72*(2), A25. (Cited on page 150.)

Pigois, J.-P. (2010), North gnangara bore completion report, *Department of Water, Western Australia, Hydrogeological record series*, *HR 277*. (Cited on page 189.)

Prakongkep, N., B. Gilkes, and B. Singh (2009), Understanding soil processes controlling landscape acidity and heavy metal mobilisation in aquic podosols on the swan coastal plain, *Tech. rep.*, Department of Environment and Conservation of Western Australia. (Cited on pages 22, 25, 26 and 158.)

Robertson, C., R. Woods, W. Bartley, and M. Martin (2008), Yeal area groudnwater investigation: Review of drilling program, infrastructure Planning Branch, Water Corporation, IPB Report No. A4-1853. (Cited on pages 95, 96 and 311.)

Roth, C., M. Malicki, and R. Plagge (1992), Empirical evaluation of the relationship between soil dielectric constant and volumetric water content as the basis for calibrating soil moisture measurements by tdr, *Journal of Soil Science*, *43*(1), 1–13. (Cited on pages 46, 48, 49, 50 and 308.)

Roth, K., R. Schulin, H. Flühler, W. Attinger, et al. (1990), Calibration of time domain reflectometry for water content measurement using a composite dielectric approach, *Water Resour. Res*, *26*(10), 2267–2273. (Cited on page 51.)

Rucker, D. F., and T. P. A. Ferre (2003), Near-surface water content estimation with borehole ground penetrating radar using critically refracted waves, *Vadose Zone Journal*, *2*(2), 247–252, doi:10.2113/2.2.247. (Cited on pages 178 and 201.)

Rzhevsky, V. (1971), *The physics of rocks*, Mir. (Cited on page 60.)

Salama, R., E. Bekele, T. Hatton, D. Pollock, and N. Lee-Steere (2002), Sustainable yield of groundwater of the gnangara mound, perth, western australia, in *International Conference on Balancing the Groundwater Budget, 12-17 May, 2002, Darwin, IAH Australia - Northern Territory Branch*, pp. 1–21, CSIRO. (Cited on page 16.)

Salama, R. B., R. Silberstein, and D. W. Pollock (2005), Soils characteristics of the bassendean and spearwood sands of the gnangara mound (western australia) and their controls on recharge, water level patterns and solutes of the superficial aquifer, *Water, Air, & Soil Pollution. Focus*, *5*(1-2), 3–26. (Cited on pages 15 and 306.)

Salat, C., and A. Junge (2010), Dielectric permittivity of fine-grained fractions of soil samples from eastern spain at 200 mhz, *Geophysics*, *75*(1), J1–J9. (Cited on page 63.)

Sandmeier, K. J. (2012), *ReflexW Version 5.5, Windows™ 9x/NT/2000/XP-program for the processing of seismic, acoustic or electromagnetic reflection, refraction and transmission data*. (Cited on pages 88, 118, 121 and 152.)

Sawkins, D. N., W. H. Verboom, J. S. Pate, and W. Australia. (2011), *Native vegetation in Western Australia is actively involved in soil formation / by Doug Sawkins, William H. Verboom and John S. Pate*, i, 27 p. : pp., Dept. of Agriculture and Food, [South Perth, W.A.] :. (Cited on pages 24 and 25.)

Scanlon, B., R. Healy, and P. Cook (2002), Choosing appropriate techniques for quantifying groundwater recharge, *Hydrogeology Journal*, *10*(1), 18–39. (Cited on pages 175, 212, 217, 218 and 221.)

Schmelzbach, C., J. Tronicke, and P. Dietrich (2012), High-resolution water content estimation from surface-based ground-penetrating radar reflection data by impedance inversion, *Water Resources Research*, *48*(8), W08,505. (Cited on page 79.)

Searle, J., and G. Bathols (2009), Bore completion report for the shallow groundwater system investigation stage 2, *Department of Water, Western Australia, Hydrogeological record series*, *HR 276*. (Cited on pages 189 and 217.)

Sen, P., C. Scala, and M. Cohen (1981), A self-similar model for sedimentary rocks with application to the dielectric constant of fused glass beads, *Geophysics*, *46*(5), 781–795. (Cited on page 52.)

Sharma, M. (1989), *Groundwater recharge*, Balkema Rotterdam. (Cited on page 175.)

Sharma, M., M. Bari, and J. Byrne (1991), Dynamics of seasonal recharge beneath a semiarid vegetation on the gnangara mound, western australia, *Hydrological processes*, *5*(4), 383–398. (Cited on pages 177, 185, 187, 206, 218 and 221.)

Silberstein, R., A. Barr, G. Hodgson, D. Pollock, R. Salama, and T. Hatton (2009), A vertical flux model for the perth groundwater region, *Department of Water, Western Australia, Hydrogeological record series*, *HG 33*. (Cited on pages 19, 20, 31 and 185.)

Singh, B., and S. Wong (2010), Acid sulfate soils in the perth metropolitan area of western australia, in *19th World Congress of Soil Science, Soil Solutions for a Changing World, 1 – 6 August 2010, Brisbane, Australia*. (Cited on page 22.)

Skjemstad, J., A. Waters, J. Hanna, and J. Oades (1992), Genesis of podzols on coastal dunes in southern queensland. iv. nature of the organic fraction as seen by 13c nuclear magnetic resonance spectroscopy, *Soil Research*, *30*(5), 667–681. (Cited on page 27.)

Steelman, C., and A. Endres (2010), An examination of direct ground wave soil moisture monitoring over an annual cycle of soil conditions, *Water Resources Research*, *46*(11), W11,533. (Cited on page 42.)

Steelman, C., and A. Endres (2011), Comparison of petrophysical relationships for soil moisture estimation using gpr ground waves, *Vadose Zone Journal*, *10*(1), 270–285. (Cited on pages 49 and 82.)

Steelman, C., A. Endres, and J. Van der Kruk (2010), Field observations of shallow freeze and thaw processes using high-frequency ground-penetrating radar, *Hydrological Processes*, *24*(14), 2022–2033. (Cited on pages 82 and 151.)

Strobach, E., B. Harris, J. Dupuis, A. Kepic, and M. Martin (2010a), Gpr for large-scale estimation of groundwater recharge distribution, in *13th International Conference on Ground Penetrating Radar (GPR), Lecce, Italy*, pp. 1–6, IEEE. (Cited on pages 5, 54 and 303.)

Strobach, E., B. Harris, J. Dupuis, A. Kepic, and M. Martin (2010b), Ground-penetrating radar for delineation of hydraulically significant layers in the unsaturated zone of the gnangara mound, wa, in *21st ASEG Conference Extended Abstracts*, pp. 1–4, CSIRO. (Cited on pages 5, 217 and 303.)

Strobach, E., B. D. Harris, J. C. Dupuis, A. W. Kepic, and M. W. Martin (2011), Estimation of water content in partially saturated soil horizons with ground-penetrating radar, in *73rd EAGE Conference and Exhibition, 23-25 May 2011, Vienna*. (Cited on pages 5, 51, 54, 106, 115, 202, 303 and 304.)

Strobach, E., B. D. Harris, J. C. Dupuis, A. W. Kepic, and M. W. Martin (2012a), Time-lapse borehole radar measurements in a sandy groundwater system during a winter recharge cycle, in *14th International Conference on Ground Penetrating Radar (GPR), Shanghai, China*, pp. 1–6. (Cited on pages 105, 157, 171, 194, 197, 201, 202 and 303.)

Strobach, E., B. D. Harris, J. Christian Dupuis, A. W. Kepic, and M. W. Martin (2012b), Cross well radar and vertical radar profiling methods for time lapse monitoring of rainfall infiltration, in *22nd ASEG Conference Extended Abstracts*, pp. 1–4. (Cited on pages 171, 189, 191, 194, 197, 201, 202, 303 and 304.)

Strobach, E., B. D. Harris, J. C. Dupuis, and A. W. Kepic (2013), Waveguide properties recovered from shallow diffractions in common offset gpr, *Journal of Geophysical Research: Solid Earth*, *118*(1), 39–50, doi:10.1029/2012JB009448. (Cited on pages 5, 148 and 304.)

Strobbia, C., and G. Cassiani (2007), Multilayer ground-penetrating radar guided waves in shallow soil layers for estimating soil water content, *Geophysics*, *72*(4), J17–29, doi:10.1190/1.2716374. (Cited on pages 151 and 170.)

Stuart, M. (1955), Dielectric constant of quartz as a function of frequency and temperature, *Journal of Applied Physics*, *26*(12), 1399–1404. (Cited on page 60.)

Thompson, C. (1981), Podzol chronosequences on coastal dunes of eastern australia, *Nature*, *291*, 59–61. (Cited on pages 22 and 24.)

Thompson, C. (1992), Genesis of podzols on coastal dunes in southern queensland. i. field relationships and profile morphology, *Soil Research*, *30*(5), 593–613. (Cited on pages 22, 24, 25, 26, 27 and 94.)

Thompson, C., E. Bridges, and D. Jenkins (1996), Pans in humus podzols (humods and aquods) in coastal southern queensland, *Soil Research*, *34*(1), 161–182. (Cited on page 26.)

Topp, G. C., J. L. Davis, and A. P. Annan (1980), Electromagnetic determination of soil water content: Measurements in coaxial transmission lines, *Water Resour. Res.*, *16(3)*, 574–582. (Cited on pages 43, 46, 47 and 308.)

Tronicke, J., and M. D. Knoll (2005), Vertical radar profiling; influence of survey geometry on first-arrival traveltimes and amplitudes, *Journal of Applied Geophysics*, *57*(3), 179–191. (Cited on pages 180, 195 and 246.)

van Dam, R. L., W. Schlager, M. J. Dekkers, and J. A. Huisman (2002), Iron oxides as a cause of gpr reflections, *Geophysics*, *67*(2), 536–545. (Cited on page 60.)

Van der Kruk, J. (2006), Properties of surface waveguides derived from inversion of fundamental and higher mode dispersive gpr data, *Geoscience and Remote Sensing, IEEE Transactions on*, *44*(10), 2908–2915. (Cited on pages 151, 163, 166, 170 and 305.)

Van der Kruk, J., R. Streich, and A. G. Green (2006), Properties of surface waveguides derived from separate and joint inversion of dispersive te and tm gpr data, *Geophysics*, *71*(1), K19–29, doi:10.1190/1.2168011. (Cited on pages 118, 151, 152, 155, 163, 164 and 170.)

Van der Kruk, J., H. Vereecken, and R. W. Jacob (2009a), Identifying dispersive gpr signals and inverting for surface wave-guide properties, *The Leading Edge*, *28*(10), 1234–1239, doi:10.1190/1.3249780. (Cited on page 151.)

Van der Kruk, J., C. Steelman, A. L. Endres, and H. Vereecken (2009b), Dispersion inversion of gpr data recorded across freezing and thawing induced waveguides, *Geophysical Research Abstracts*, *11*. (Cited on page 155.)

Van der Kruk, J., R. W. Jacob, and H. Vereecken (2010), Properties of precipitation-induced multilayer surface waveguides derived from inversion of dispersive te and tm gpr data, *Geophysics*, *75*(4), WA263–273, doi:10.1190/1.3467444. (Cited on pages 151 and 158.)

Van Gestel, J., and P. Stoffa (2001), Application of alford rotation to ground-penetrating radar data, *Geophysics*, *66*(6), 1781–1792. (Cited on page 248.)

Veihmeyer, F., and A. Hendrickson (1931), The moisture equivalent as a measure of the field capacity of soils, *Soil Science*, *32*(3), 181–194. (Cited on page 40.)

Veihmeyer, F., and A. Hendrickson (1949), The application of some basic concepts of soil moisture to orchard irrigation, in *Proc. Wash. State Hort. Assoc*, vol. 45, pp. 25–41. (Cited on page 40.)

Verboom, W., and J. Pate (2006), Bioengineering of soil profiles in semiarid ecosystems: the 'phytotarium'concept. a review, *Plant and soil*, *289*(1), 71–102. (Cited on pages 23, 24 and 25.)

Verboom, W., and J. Pate (2012), Exploring the biological dimension to pedogenesis with emphasis on the ecosystems, soils and landscapes of southwestern australia, *Geoderma*. (Cited on pages 23, 24 and 25.)

Wave propagation Standards Committee, A., and P. Society (1997), Ieee standard definitions of terms for radio wave propagation, std. 211-1997, *Tech. rep.*, The Institute of Electrical and Electronics Engineers, Inc., New York. (Cited on page 44.)

Xu, C., M. Canci, M. Martin, M. Donnelly, and R. Stokes (2008), Perth regional aquifer modelling system (prams) model development: Application of the vertical flux model, *Department of Water, Western Australia, Hydrogeological record series*, *HG 27*. (Cited on pages 9, 17, 19, 20, 31 and 306.)

Yesertener, C. (2002), Declining water levels in the gnangara and jandakot groundwater mounds (stage i), *Hydrology and Water Resources Branch*, *HR 199*. (Cited on pages 17 and 102.)

Yilmaz, Ö. (2001), *Seismic data analysis*, Society of Exploration Geophysicists. (Cited on pages 245 and 248.)

Zhang, L., and W. Dawes (1998), Waves - an integrated energy and water balance model, *Technical Report 31/98*, CSIRO Land and Water, Canberra, Australia. (Cited on page 20.)

Author Index

Every reasonable effort has been made to acknowledge the owners of copyright material. I would be pleased to hear from any copyright owner who has been omitted or incorrectly acknowledged.

Appendix A

GPR Theory and Application

Ground-penetrating radar (GPR) is a non-invasive remote sensing technology that uses electromagnetic (EM) waves in the radar frequency range to probe the subsurface. The GPR method has rapidly evolved alongside computer and electronics development. Since the early 1990s, commercial GPR systems are widely available and have been used in various applications such as civil engineering, pedology, sedimentology, hydrogeophysics, archaeology, agriculture, extraterrestrial exploration (i.e. moon, planets), UXO detection, forensic investigations, mineral exploration and cryospheric studies.

The following sections target a readership that is new to the GPR technique. Physical principles of GPR have been covered in various books, reviews and scientific articles. *Daniels* (2005) is a comprehensive summary of the technique and provides a wealth of case studies from various disciplines. Other useful references for geoscientists include *Huisman et al.* (2003); *Annan* (2005); *Neal* (2004) and references therein. As those references and other books dealing with fundamental electrodynamics provide all the necessary derivations, I decided not to repeat these books, but instead provide the inexperienced reader with the implications the physics provide for practical field applications. In the following I will summarise the main elements of GPR: system design, data acquisition and wave interaction with the earth are outlined. Note that more specific interpretation methods for surface GPR measurements are discussed in chapter 4.

A.1 GPR Systems

Different types of surface and borehole GPR systems are successfully in use. I will concentrate on bistatic systems where one antenna is used as a transmitter Tx while a second antenna Rx receives electric signals. A pulse generator sends an electric signal to the Tx antenna which then radiates electromagnetic energy. The generated pulse can have various forms depending on the system design. Signals typically achieved in GPR systems are impulses, stepped frequency and continuous wave. The system used in this study is the Mala ProEx2 and antennae with nominal center frequencies of unshielded bowtie 100 and 200 MHz, loaded dipole 50 MHz surface and 100 MHz borehole, and shielded bowtie 250 and 500 MHz. The Mala is an impulse radar system, thus I will concentrate on this type of signal in the following. The electromagnetic energy radiated from an impulse radar looks in the time domain like a sinus except for having a steeper, narrower appearance and is called a wavelet. The energy in frequency domain is distributed around a center frequency (the peak power in frequency spectrum)

and a bandwidth which depends on the radar system design (i.e. pulse rise, antenna characteristics). Typical GPR systems have a bandwidths that spans several octaves. The generated source wavelet is in principle similar to a seismic impulse wavelet for example created by explosives, a sledgehammer or other impact source and which is recorded in the far-field.

The energy radiated by the Tx antenna is aimed to be emitted into the ground. Thus, in GPR the antenna is typically coupled to the ground in order to avoid energy transmission loss which would occur due to the strong dielectric interface of air and soil. Coupling is achieved by placing the antenna elements close to the ground. The distance should not exceed approximately 1/8 - 1/4 of a wavelength in air. In surface applications, further care has to be taken to prevent EM energy radiating in all directions. A typical bowtie antenna in air, for example, would radiate energy equally down towards the ground and up into the air. Although coupling to the higher dielectric ground already reduces the relative amount of energy radiated into air, reflections from surface objects can still be stronger compared to subsurface target reflections. To prevent energy to be radiated upwards, antenna are typically shielded. The shield not only prevents energy radiation, it also protects the Rx antenna from recording unwanted environmental noise. While this is less of a problem in remote Australian bushland, it can be a major noise source in built-up areas and reduces signal-to-noise ratio and therefore effective depth of penetration.

A.2 Wave Interaction With The Earth

For ground-penetrating radar, the EM energy is aimed to be radiated into the ground in a beam as narrow as possible. In case the ground physical properties allow for the EM energy to propagate as a wave (i.e. resistive environment), the energy will be transmitted through the ground until it hits a discontinuity in dielectric properties (i.e. layer interface, ground disturbance, caves, pipes, roots). Depending on the shape and size of the discontinuity relative to the wavelength (i.e. frequency), and the contrast in dielectric property, the wave is then reflected, diffracted and/or scattered or transmitted. Wavefields that are reflected back to the surface are called upgoing waves and are recorded by the receiver. Transmitted waves are downgoing and can only be directly recorded with borehole radar or other transillumination acquisition geometries (e.g. on a mine face).

The wave-like behaviour of energy propagation in the radar frequency range bears a striking resemblance to acoustic and elastic wave interaction with the earth. Seismic wave phenomena in earth have been studied in detail by physicists and seismologists during the last two centuries, and by the oil exploration industry during the second half of the twentieth century. Because the seismic method is the main tool for hydrocarbon exploration, society has invested a great deal of resources to not only study the theory of elastic and acoustic wave-interaction with the earth, but also to develop processing software and flows and interpretation tools (*Yilmaz*, 2001). Most of those tools can be directly adapted to GPR data processing and interpretation. There are, however, some discrepancies between GPR and seismic methods which I will discuss in the following.

The first difference lies within the physics of wave propagation. The GPR uses electromagnetic waves to sample the subsurface. Their behaviour is described by Maxwell's equations. The subsurface properties that determine GPR wave propagation are the complex dielectric permittivity and electrical conductivity distribution. Some

of the basic principles have been described in chapter 3. A possible solution of the Maxwell differential equation for the electric vector field $\vec{E}$ can take the form of a wave equation (i.e. for the case of low loss and high frequencies) (*Knoll*, 1996) and as a function of time t and depth z reads

$$\vec{E}(z,t) = \left|\vec{E_0}\right| e^{-\gamma z} e^{i\omega t} = \left|\vec{E_0}\right| e^{-\alpha z} e^{i(\omega t - \beta z)} \tag{A.1}$$

with $\gamma = \alpha + i\beta$ the complex propagation constant, and α and β the attenuation and phase constants, respectively (see equations 3.5 and 3.7). E_0 represents the initial electric field strength which is damped by $1/e$ over the distance $1/\alpha$, also called the skin depth (compare damped oscillation).

Although seismic waves follow different physical laws (e.g. Hook's law, stress-strain relations), the solution of the differential equation looks very similar to the EM case. The main difference lies within the physical properties that govern the seismic wave propagation because they are of elastic nature such as bulk- and shear modulus and density of the material. Although the physical properties that determine wave propagation are vastly different for seismic and EM waves, both types of waves travel through the ground with a finite velocity and a magnitude (i.e. phase and amplitude) both of which can be measured by sensors (i.e. geophones/hydrophones or antennae).

In principle, both, velocity and amplitude are related to the intrinsic material properties. However, velocities mainly depend on the intrinsic physical properties of the material (i.e. how energy is passed on, from one point to the next), while the amplitudes or amplitude reduction (i.e. attenuation) in addition controlled by what I call here extrinsic factors such as geometric spreading losses and constellation of subsurface inhomogeneities (i.e. layers, diffractors, scatterers).

Considering the lossless case, that is waves are not damped by energy dissipation, energy attenuation is solely based on the geometric configuration. The initial radiated energy packet dampens as energy is distributed (spread out), for example over a half-spherical area of a 3D wavefront. The beam that was mentioned earlier which surface GPR systems try to emit aims at reducing those spreading losses. Current technology, however, is not producing true beams (or rays) and the resultant radiation pattern for example from dipole sources such as bowtie antennae produces a radar footprint whose area is dependent on distance from the source (see *Annan* (2005); *Tronicke and Knoll* (2005)). They also emit lateral waves (*Chen*, 2012) which makes for example waveguide analysis of CO GPR described in section 5 is possible. Spreading losses are frequency independent. The second type of extrinsic attenuation (i.e. not energy dissipation) is due to reflection and transmission losses. For a layered earth, or where inhomogeneities are larger than the wavelength, reflectivity and transmissivity can be described by impedance or admittance contrast. Equations are given for example in *Annan* (2005). Reflection losses for distinct interfaces are in principle frequency independent. However, there exists a frequency dependency for gradual interfaces such as the transition zone above the capillary fringe of a water table in sand. *Bano* (2006) showed that a reflection from the water table might be undetectable or absent for high frequencies if the transition zone is larger than half the radar wavelength. Knowledge about reflection and transmitted signal strength are crucial in quantitative GPR interpretation but their estimation can be problematic.

A third type of losses are scattering and diffraction losses which occur due to small inhomogeneities (sub-wavelength). Those losses are frequency dependent be-

cause low frequencies (long wavelengths) might not be influenced by small inhomogeneities, while higher frequencies are scattered or diffracted which can result in clutter or diffraction hyperbolae in common offset data.

Energy dissipation, or intrinsic attenuation, occurs due to electric conduction and/or dielectric losses (relaxation losses) in the EM case (displacement of elec. charges/ions). The seismic analog is inelastic behaviour (displacement of matter). For both, seismic and EM, heating of the material can be a consequence of intrinsic attenuation (cp. microwave or friction heat).

In the case of intrinsic attenuation for lossy materials, the phase-amplitudes are dampened proportional to their frequency, which can be readily derived from equation A.1. This is due to the fact that wavelength λ is inversely proportional to frequency f for a given velocity ν:

$$\lambda(f) = \frac{\nu}{f} \tag{A.2}$$

as long as the material is non-dispersive (i.e. rel. dielectric permittivity is identical for all frequencies, $\nu = c/\sqrt{(\epsilon_r)} = \text{const.}$). Thus, the number of cycles per distance interval (i.e. wavenumber) increases with frequency which results in greater attenuation per distance interval. Note that reflected energy recorded on the surface has to travel twice through the ground, thus the number of cycles which experience intrinsic attenuation is also doubled.

Considering all losses related to the radar system, antenna ground coupling, geometric losses, material losses, scattering and clutter losses and reflection losses, we obtain the radar range equation for example given by *Daniels* (2005). In practical applications, however, most of the parameters that control total loss are unknown and radar performance prediction becomes an educated guess at best. Only in the case of surface conductors such as moist clays (smectites etc.) or wet salt lakes one can make the valid assumption that depth of penetration will be negligible. Dry salt in salt domes, clean dry quartz sand dunes, freshwater lakes, ice-sheets and the atmosphere are all natural environments where GPR depth of penetration will be large. However, most terrestrial surface materials are made up of soil. Soil is a mixture of all imaginable materials, and they are mixed up in an on all scales inhomogeneous mass. Thus, in most relevant environments, prediction of radar performance becomes an art, and electric material characterisation is the only means of narrowing down on GPR performance prediction.

The concepts of reflectivity and transmissivity and intrinsic attenuation will appear again later on in this chapter as they are of interest for the study presented here.

A.3 Data Acquisition

Another specialty of GPR contrasting it to seismic has to do with data acquisition. While seismic data is typically recorded with multiple receivers, GPR is still widely acquired with one transmitter and one receiver only (one channel systems). In most mapping applications, data is collected as common offset (CO) gathers (COG). In this acquisition mode, Rx and Tx antennas are kept at constant separation and moved over the ground and a radargram is produced. Commercial antennae, especially shielded, are often placed in sealed casing and the distance and position between Rx and Tx cannot be adjusted. Shielded encased antennae are typically arranged co-polarised

broadfire with their antenna axis perpendicular to the acquisition direction (i.e. if x is line direction, they emit and receive the Ey or transverse electric (TE) field components, sometimes called the yy-configuration) (*Van Gestel and Stoffa*, 2001). This arrangement is most sensitive to structures that strike perpendicular to the acquisition direction. Unshielded lower frequency antennae are typically built like "snakes" (e.g. Mala 50 MHz rough terrain antenna). Those antennae are co-polarised endfire, oriented parallel to acquisition direction (i.e. emit and receive Ex or transverse magnetic (TM) field components, also called xx-configuration). Multi-channel GPR systems have recently become commercially available (up to 32 channel). Currently, they are mainly used with higher frequency antennae (i.e. above 400 MHz) for 3D applications mainly for archaeology or road mapping. Those antennae are currently arranged within a grid, not in line to capture far offsets. *Bradford et al.* (2009) collected a 3D data cube with multifold GPR using four receiving antennae and offsets between 1 and 16 m with 1 m increments in between receivers (4 repeat surveys) and 0.15 m source intervals. For large scale 2D mapping, this geometry would require 16 antennae to be pulled behind a vehicle at once which is probably only realistic for the xx-configuration.

Measurements are triggered either at constant time intervals, or with a triggering wheel at constant distance increments. The latter is the preferred method as it does not require a time-to-distance conversion and directly provides sampling at constant distance increments (personal remark: the first undertaking of my PhD was building a custom-made triggering wheel, which unfortunately failed for some of the first surveys). The distance increment has to be chosen based on maximum possible resolution considerations (i.e. wavelength, Fresnel zone) and the Nyquist theorem to avoid spatial aliasing. Temporal sampling obeys to the Nyquist theorem as well, and the cycle (period) of the maximum frequency within the bandwidth of the antenna should be at least represented by two data points in time (i.e. sampling interval $\Delta t_s <= 1/(2f_{\max})$, e.g. 250 MHz antenna with frequency content up to 400 MHz or $\Delta t = 2.5$ ns requires minimum sampling of 800 MHz or $\Delta t_s <= 1.25$ ns). However, GPR data is typically oversampled, both in time and space, which is mainly due to sufficient data storage capabilities and the ability of the system to deal with high sampling demands. I noticed that although theoretically oversampled 2D data appears to contain detail that makes interpretation for example of diffraction hyperbolae easier. I follow the philosophy that I collect data at small spatial increments with few stacks, and then stack the data later on as part of the processing flow. The advantage (and partially drawback) of CO GPR is that data acquisition is rapid and can cover long transects quickly. That means, however, that interpretation in natural environments can be time consuming and overburden the interpreter. In comparison to seismic, a 20 km GPR transect that images to a depth of 10 m is equivalent to a 1000 km seismic profile imaging to 2 km.

Multioffset data acquisition follows the same field geometry as in seismic. Radar common midpoint (CMP) gathers are often referred to as wide angle reflection and refraction (WARR) profiles. Although most researchers call multioffset data acquisition CMP, they usually actually perform a common shot point (CSP) experiment. This is the acquisition geometry I primarily used as part of test-site characterisation.

A.4 GPR Processing

2D CO GPR processing is mostly analogous to poststack seismic data processing which is treated exhaustively in the literature (e.g. *Yilmaz* (2001)). A typical 2D GPR

processing flow includes the following operations:

- Trace-header editing, geometry (xyz-coordinates)
- Interpolate skipped (zero) traces
- Despiking (1D-median over 3 samples with threshold control)
- zero-time correction based on air wave arrival and Rx-Tx separation
- moveout correction for shallow reflections in case of large Tx-Rx separations (e.g. the 50 MHz Mala snake has an offset of 4 m) for example based on a constant ground velocity as facilitated in ReflexW "dynamic correction" (caution, it changes the frequency content by distorting the wavelet)
- DC-shift removal (based on late-time DC-shift)
- wavelet smoothing, e.g. bandpass-filtering or 1D moving median or average
- Background removal (see detail below)
- Relative amplitude preserving Gain (divergence compensation, or exponential decay function)
- velocity determination (e.g. diffractions, see next section)
- migration (e.g. fk-Stolt (fast), Kirchhoff migration, diffraction stack)
- if wanted: spectral whitening/blueing or deconvolution
- if necessary: spatial filtering, e.g. 2D median
- if wanted AGC-Gain (small and large amplitudes not distinguishable)
- spatial downsampling, e.g. stacking
- temporal resampling (down/up sampling by interpolation)
- topography correction

A waveform specific to GPR CO data is the strong direct air- and ground arrivals which appear as flat events. They typically do no change dramatically throughout short profiles and are removed by background removal techniques. Depending on the antenna frequency, these first onsets have a duration of up to 50 ns (i.e. for zero-offset) which means that they mask most reflected arrivals within that time interval. Some later arrivals that appear as flat events can relate to surface reflections for example originating from a vehicle at constant distance, or a wall or fence parallel to acquisition direction. Those events are removed by either spatial filtering in the time-distance (x-t) domain or in the frequency-wavenumber (fk) domain. Time-distance background removal can be done by calculating an average trace within a t-x window (or the whole profile) which is then subtracted from every trace individually. This filter will also remove DC-shift in case DC-shift is constant. Otherwise it has to be applied after DC-shift correction, which is the preferred option. Filtering in the fk-domain can be superior, especially when lateral variations in air- and groundwave are apparent in the data. Energy of

continuous and flat reflections in a CO dataset is accumulated where wavenumbers are close to zero. In a multi-offset gather, those are infinite velocities with apparent zero moveout. This part of the fk-spectrum is notch filtered over all frequencies and under application of an appropriate taper. Some adjustments are typically necessary until satisfactory results are achieved. I found that it is crucial to produce a rectangular notchfilter area which is centred around zero wavenumber to avoid artefacts in the data.

A peculiarity in CO data are shallow dispersive diffraction which will be further discussed in section 5. They are usually easily identifiable in the fk-spectrum based on their characteristic velocity range and their large amplitudes (Figure A.1 upper right). Dispersive diffractions cannot be efficiently collapsed by migration algorithms, but instead can be removed by muting in the fk-domain as shown in Figure A.1.

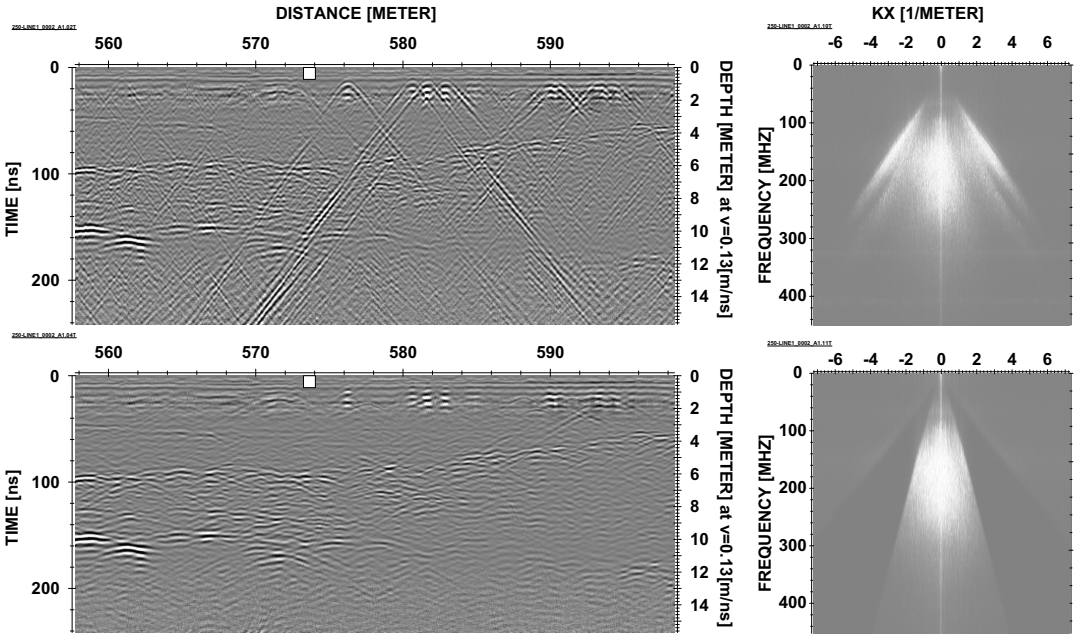

Figure A.1: *CO-radargram contaminated by strong shallow diffractions showing signs of dispersion (upper left) and the associated fk-spectrum (upper right). Dispersive diffractions can be effectively removed from the radargram (lower left) by muting parts of the fk-spectrum (lower right).*

A.5 Interpretation Of Subsurface Material Parameters

This section has deliberately been called *interpretation* rather than *calculation* of material parameters. Although the derivation of certain physical parameters will always be based on some sort of calculation, the derived value is at best an approximation of reality and typically only allows *interpretation* of real property distribution rather than providing a definite result.

To derive physical parameter distribution in the subsurface, geophysicists have to make assumptions towards i) designing a simplified earth model (e.g. 1D layered earth, 2D, 2.5D), ii) adjustment and smoothing of the model until it fits the observed data within the data error bounds (i.e. inversion), iii) estimate the error bounds and iv) using an empirical or model-based relationship between physical property (e.g. dielectric permittivity, electrical conductivity, density, elastic property, etc.) and the desired property (e.g. water content, hydraulic conductivity). The physical parameter model

that fits the observations is therefore based on many simplifying assumptions, each carrying a great degree of uncertainty and possibly non-uniqueness. It is crucial to build an interpretation workflow that minimises uncertainty and non-uniqueness. To increase certainty, additional background knowledge for example from drilling (direct information) and subsequent geophysical logging (calibration, supporting parameters) and geologic interpretation are necessary to bring the outcome to a satisfactory certainty level. Another rule typically demands to find the simplest model possible (Occam's razor). This, however, should be rephrased to "find the simplest model that satisfies the apriori knowledge", which in modern days can result into a *simplest*, but very complex model.

Between *Theory* and *Practice*

"In theory there is no difference between theory and practice. In practice there is." - Yogi Berra

In order to extract useful information from a subsurface image for management purposes, one not only has to derive a model, but also estimate uncertainty. In geoscience, however, quantitative uncertainty, or certainty, analysis is challenging. As described above, in theory, it is possible to quantify mathematical certainty for example associated with inversion processes (e.g. misfit), or to investigate the model space for non-uniqueness which is inherent for example in potential field inversion. But in practice, mathematical uncertainty does not reflect the real uncertainty. *Claerbout and Fomel* (2008) write in the introduction to their book:

"*The difference between theory and practice is smaller in theory than it is in practice.* [...] There is a well-developed *theory* about the difference between theory and practice, and it is called "geophysical inverse theory"".

Several elements in the workflow that produce a geophysical image of subsurface property distribution lead to uncertainty that cannot be readily calculated. Those include the applicability or appropriateness of the theory or the model used for parameter transformation and/or datapoint interpolation/extrapolation. Uncertainty associated with human interaction, that is interpretation, is difficult to quantify (e.g. inclusion/rejection of datapoints, choice of dataset, dealing with contradicting observations, development of hypothesis).

In geosciences, the uncertainty associated with human interpretation of, for example, seismic or radar reflection profiles is not well published in the literature as far as I am aware. In seismic exploration, typically a team of geologists, geophysicists and petroleum engineers combine sedimentary process based modelling with geophysical analysis and mechanical modelling to jointly interpret geology and identify possible targets in a combined effort. This process is employed to maximise certainty and reduce risk. In GPR, however, interpretation is often limited to a very small amount of people that typically are either geologists **or** soil scientists **or** geophysicists, but often not a mixture of those. As a result, interpretation uncertainty is often not well studied nor communicated. Geophysicists for example tend to derive material properties up to a detail where it is firstly highly uncertain whether it represents reality (although in theory the model fits the data perfectly), and secondly impractical for other scientists.

Interpreters with less geophysical knowledge might misinterpret processing artefacts as structural features (e.g. migration artefacts) or incorporate areas of low sensitivity into their model. However, results of an elaborate geologic interpretation including mechanisms of formation/deposition, although lacking detail and quantification of material properties, can be more useful for process modelling on a relevant scale than centimetre accurate derivation of material properties at one small test-site. Thus, the combination of people with different backgrounds and competencies will result in the best outcome possible by minimising uncertainty that is challenging to quantify.

Appendix B

Neutron Data

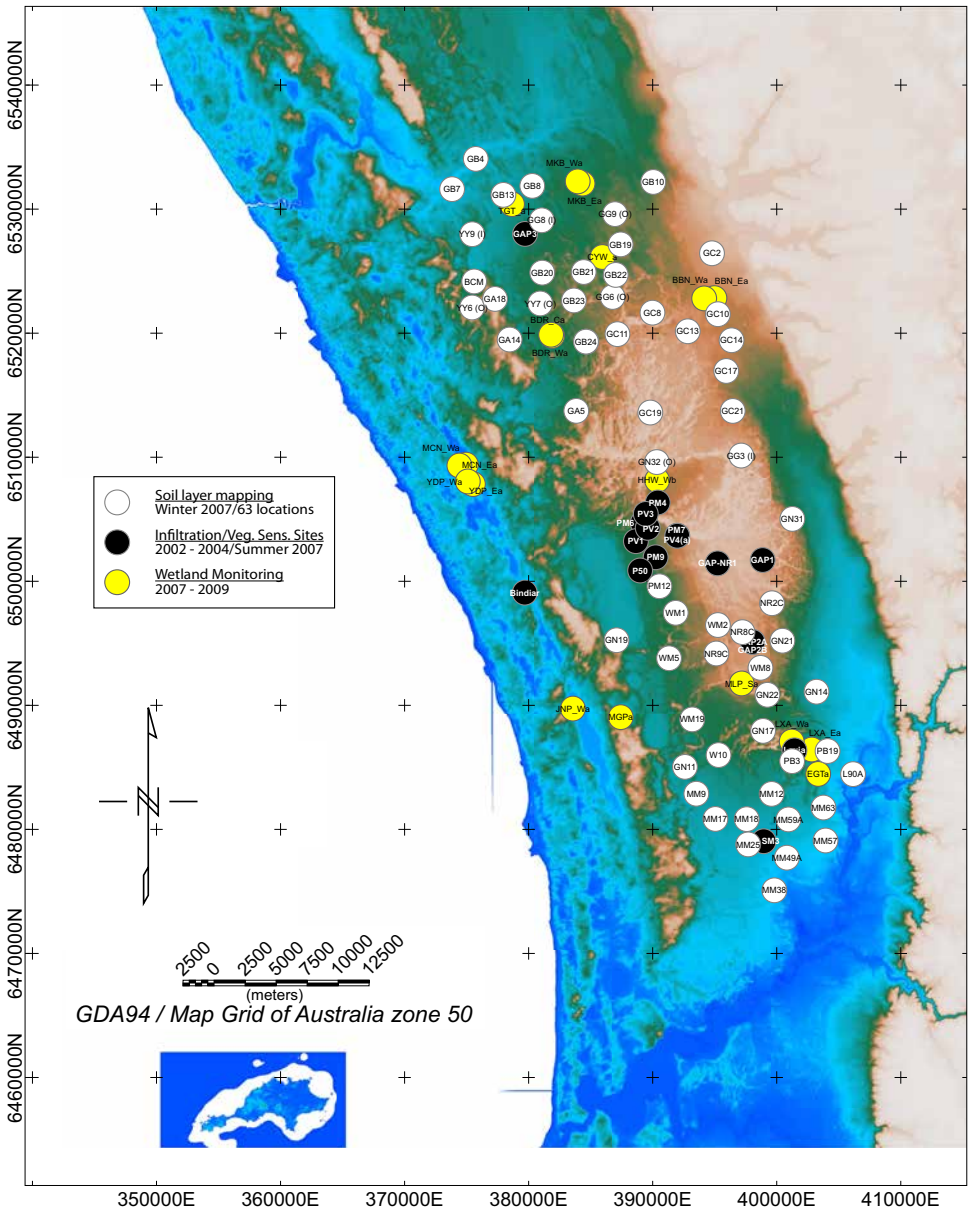

Figure B.1: *Location of neutron logging campaigns listed in Table 6.1. The following time-lapse neutron logs are from the Vegetation sensitive sites, Pinjar area (2002-2004) (black circles) and from Whiteman Park (around SM3) and wetland monitoring between 2007 and 2009.*

B.1 Pinjar area

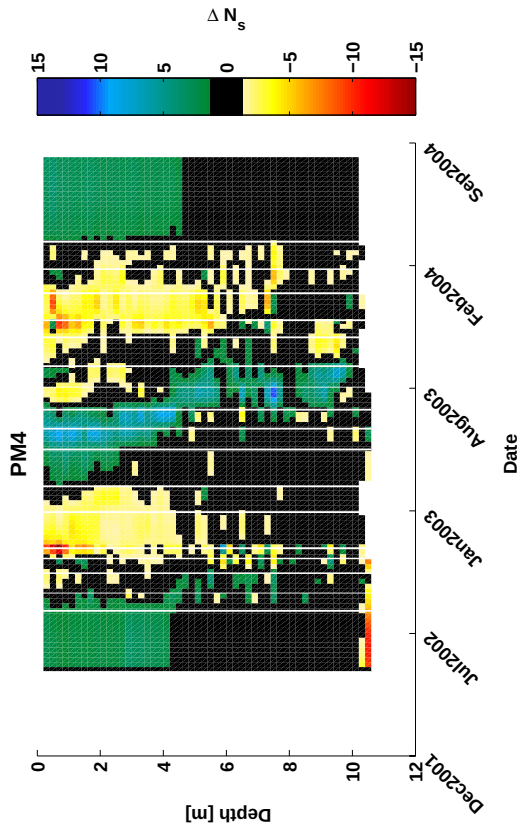

Figure B.3: *PM4 - Sequential difference in raw neutron counts.*

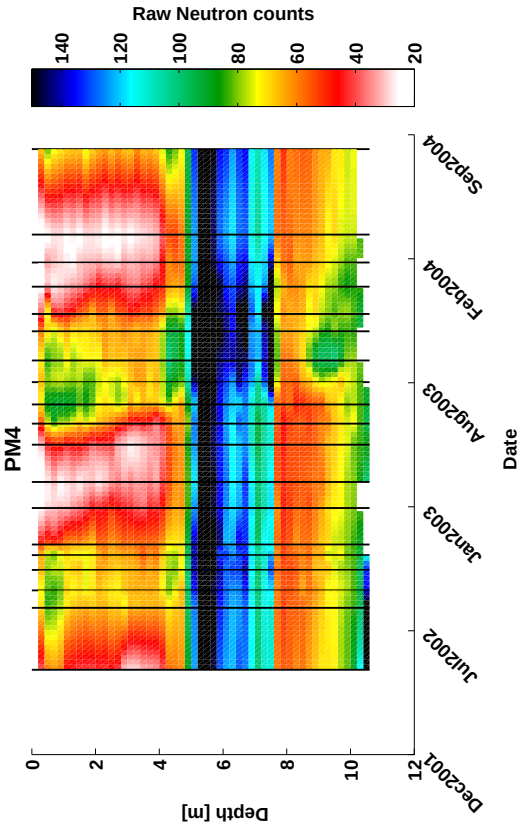

Figure B.2: *PM4 - Gridded raw time-lapse neutron counts.*

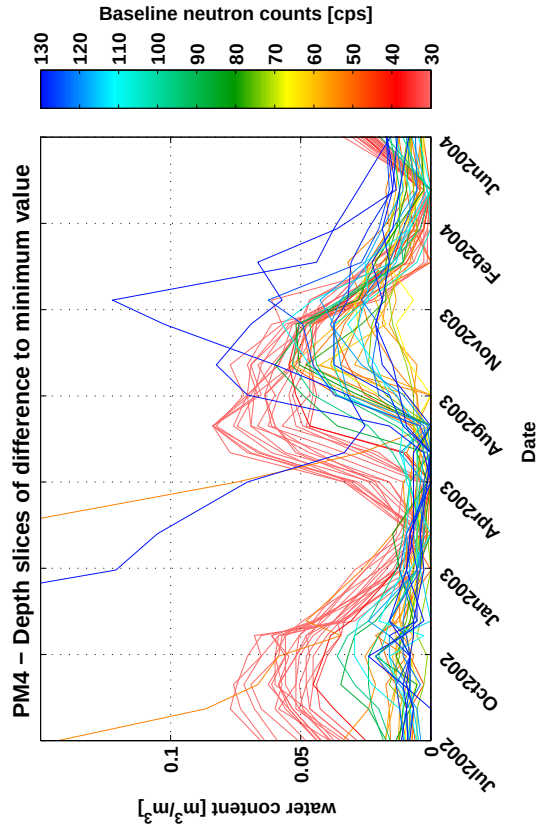

Figure B.5: *PM4 - Difference of estimated water content to driest month for individual depth levels. Colour indicates raw counts on baseline date.*

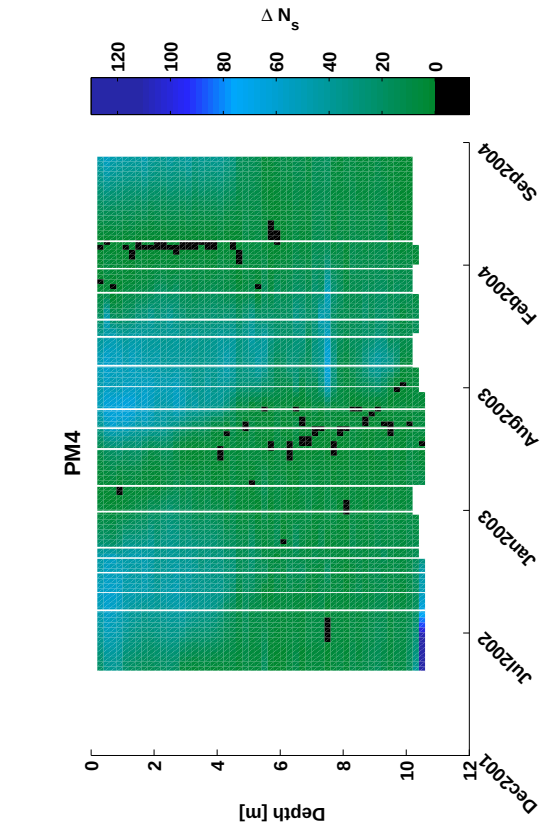

Figure B.4: *PM4 - Baseline difference of raw time-lapse neutron counts.*

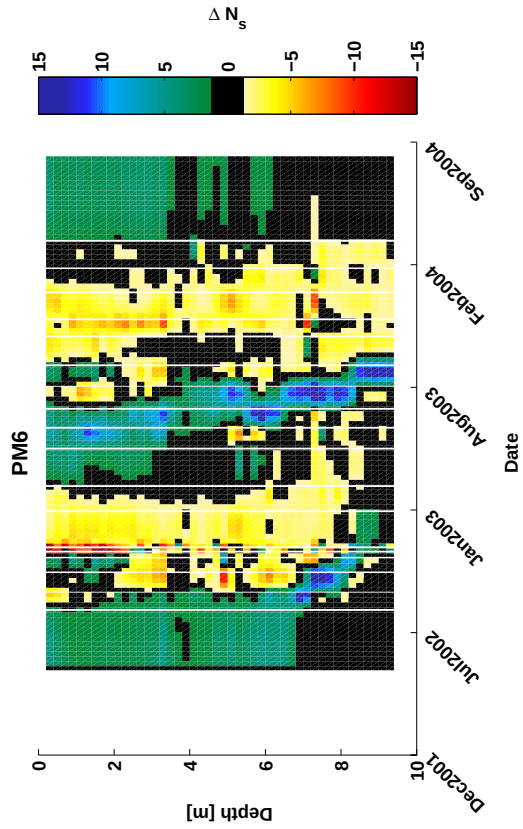

Figure B.7: *PM6 - Sequential difference in raw neutron counts.*

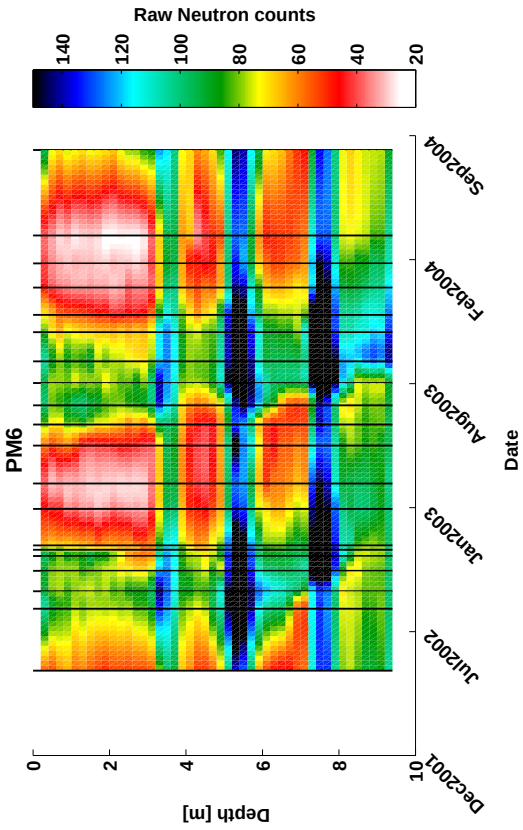

Figure B.6: *PM6 - Gridded raw time-lapse neutron counts.*

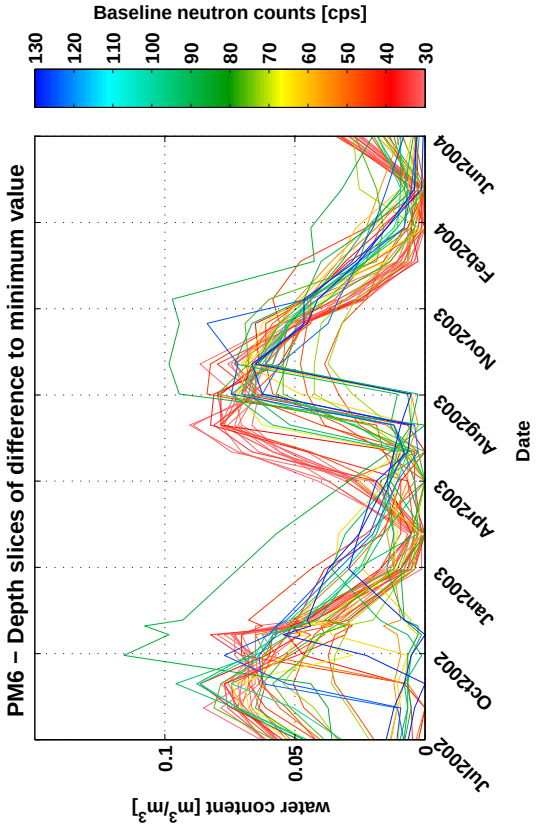

Figure B.9: *PM6 - Difference of estimated water content to driest month for individual depth levels. Colour indicates raw counts on baseline date.*

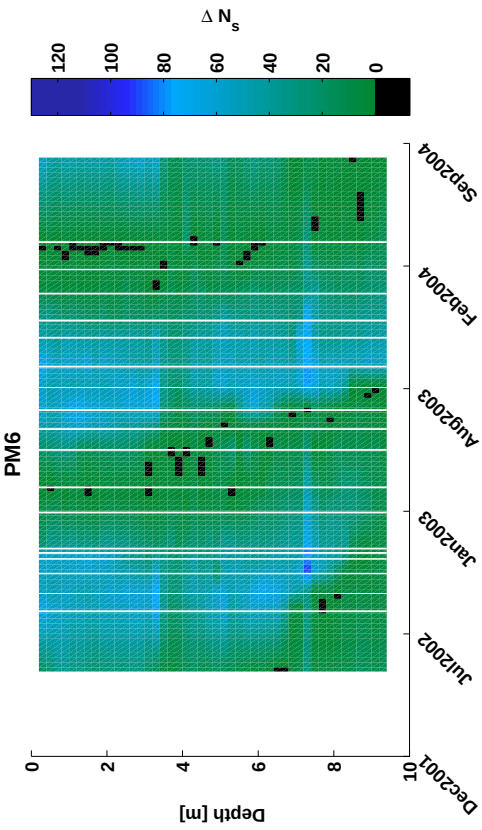

Figure B.8: *PM6 - Baseline difference of raw time-lapse neutron counts.*

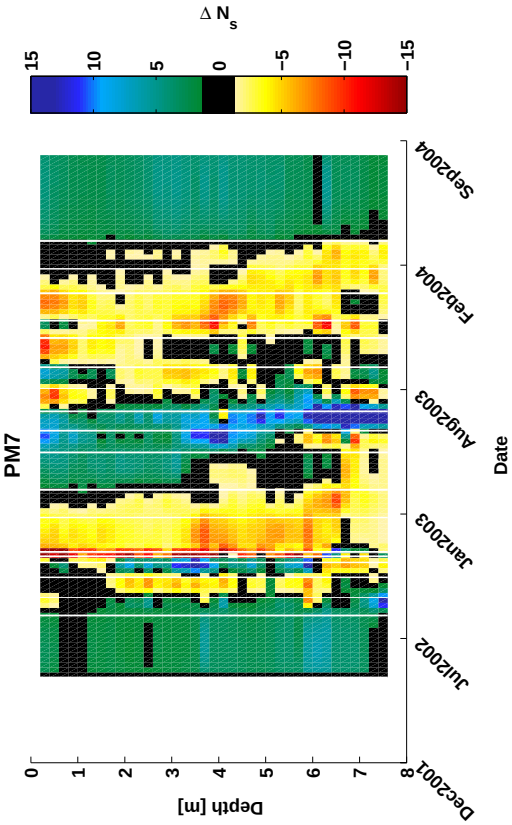

Figure B.10: *PM7 - Gridded raw time-lapse neutron counts.*

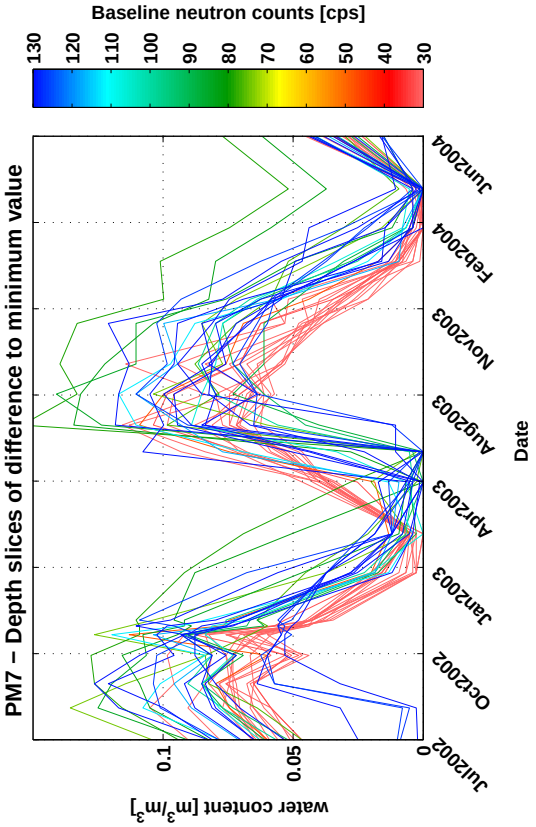

Figure B.11: *PM7 - Sequential difference in raw neutron counts.*

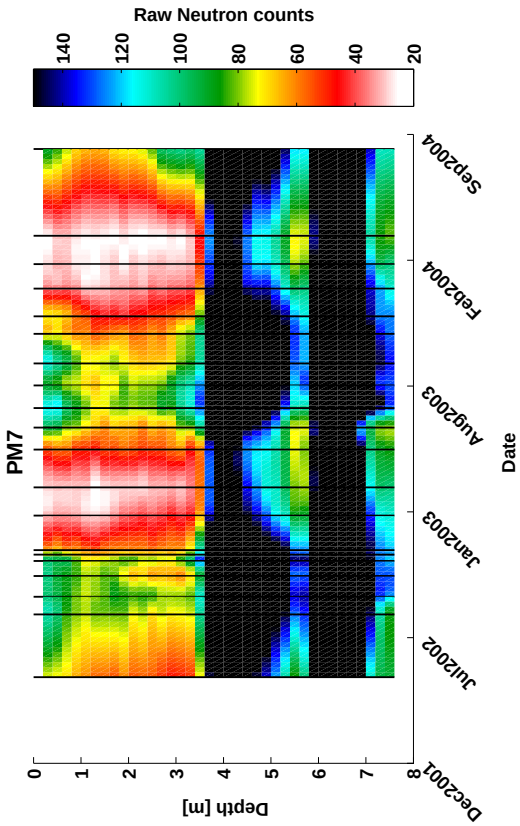

Figure B.12: *PM7 - Baseline difference of raw time-lapse neutron counts.*

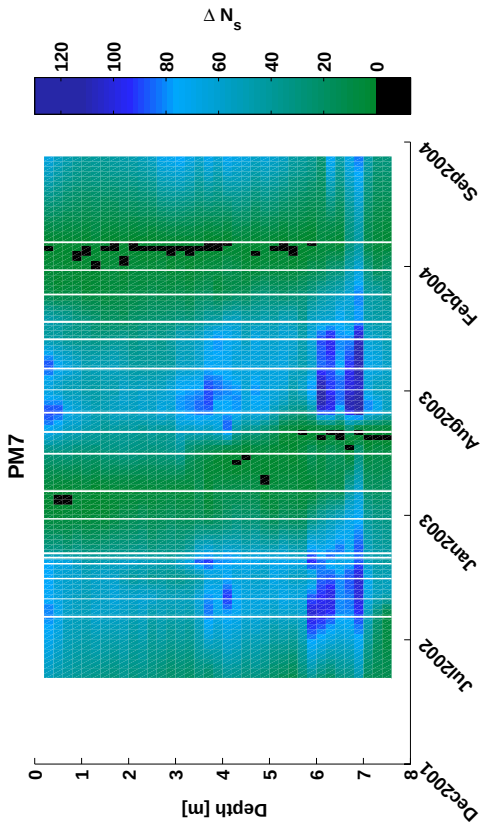

Figure B.13: *PM7 - Difference of estimated water content to driest month for individual depth levels. Colour indicates raw counts on baseline date.*

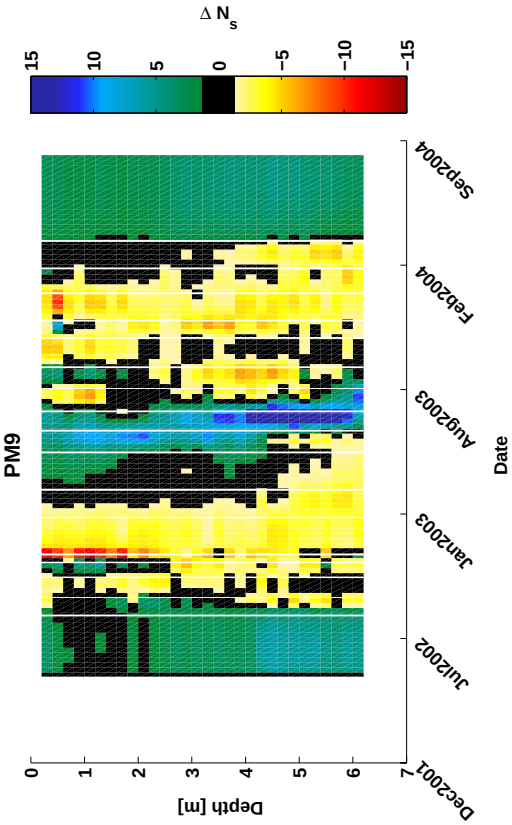

Figure B.15: *PM9 - Sequential difference in raw neutron counts.*

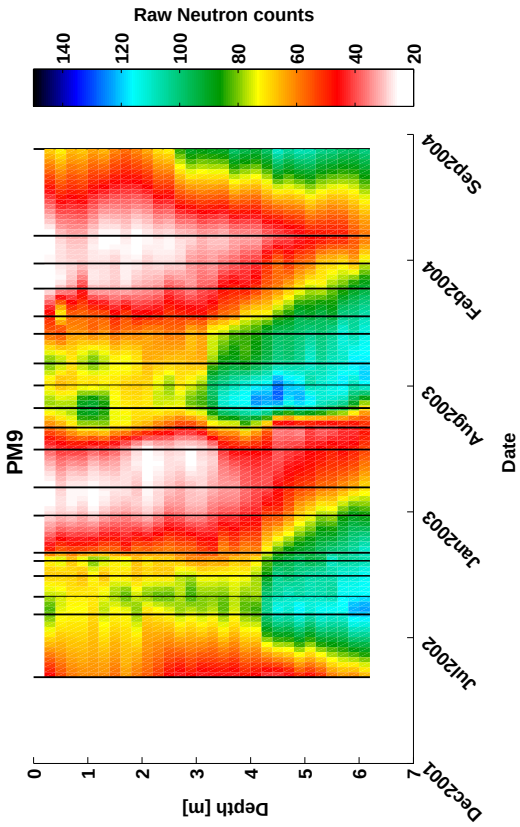

Figure B.14: *PM9 - Gridded raw time-lapse neutron counts.*

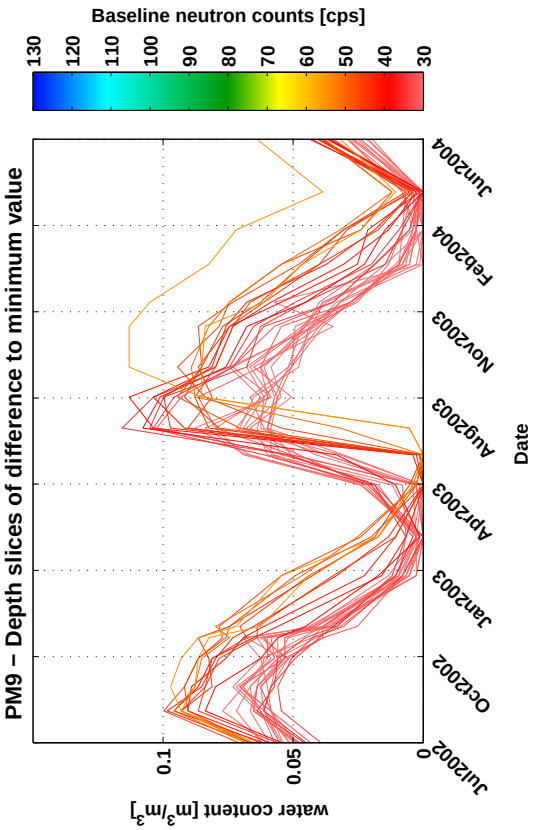

Figure B.17: *PM9 - Difference of estimated water content to driest month for individual depth levels. Colour indicates raw counts on baseline date.*

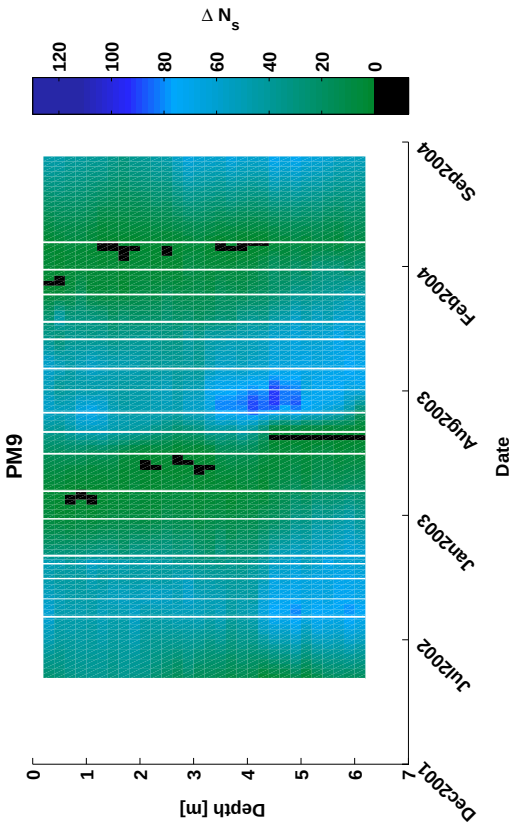

Figure B.16: *PM9 - Baseline difference of raw time-lapse neutron counts.*

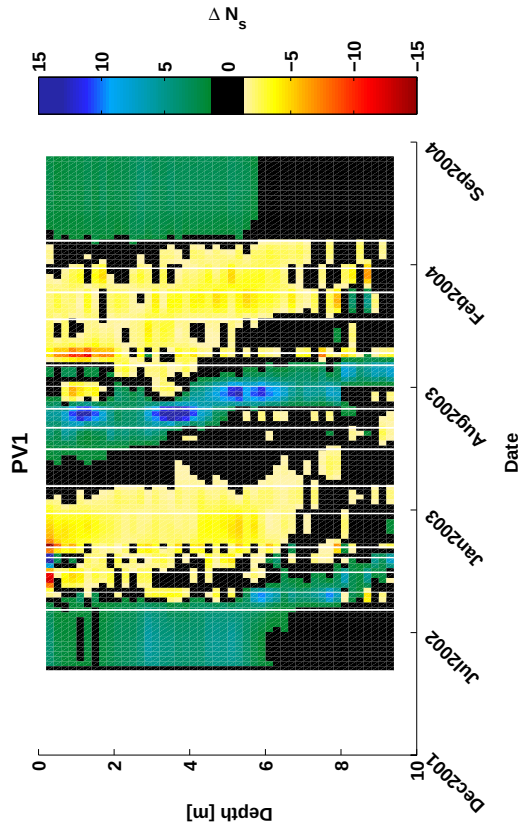

Figure B.19: *PV1 - Sequential difference in raw neutron counts.*

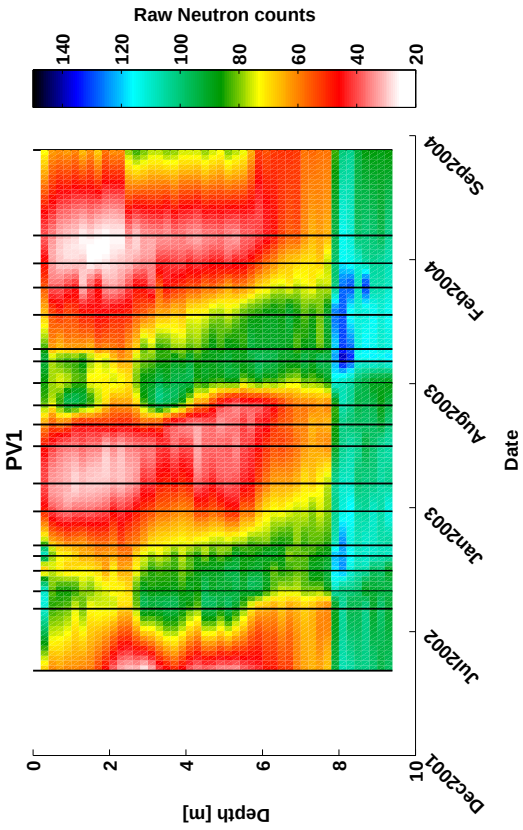

Figure B.18: *PV1 - Gridded raw time-lapse neutron counts.*

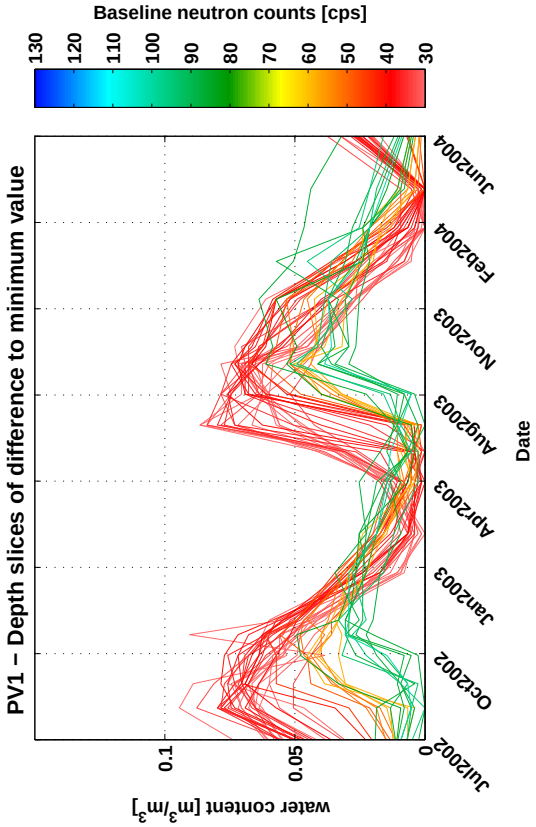

Figure B.21: *PV1 - Difference of estimated water content to driest month for individual depth levels. Colour indicates raw counts on baseline date.*

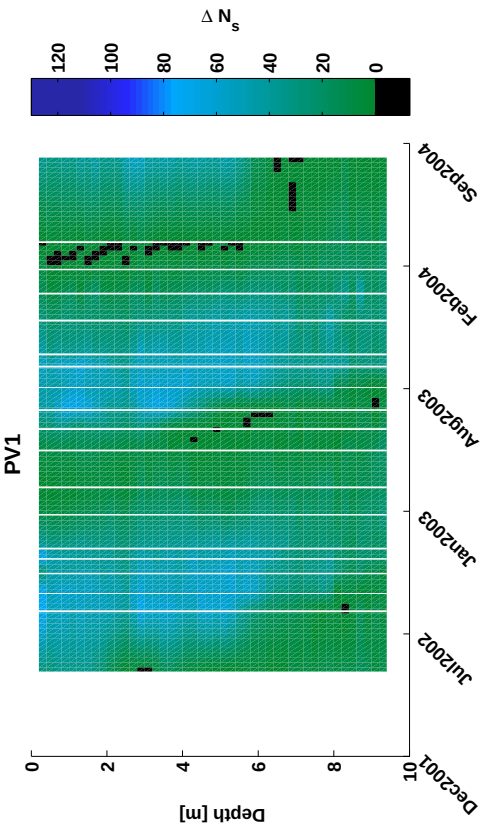

Figure B.20: *PV1 - Baseline difference of raw time-lapse neutron counts.*

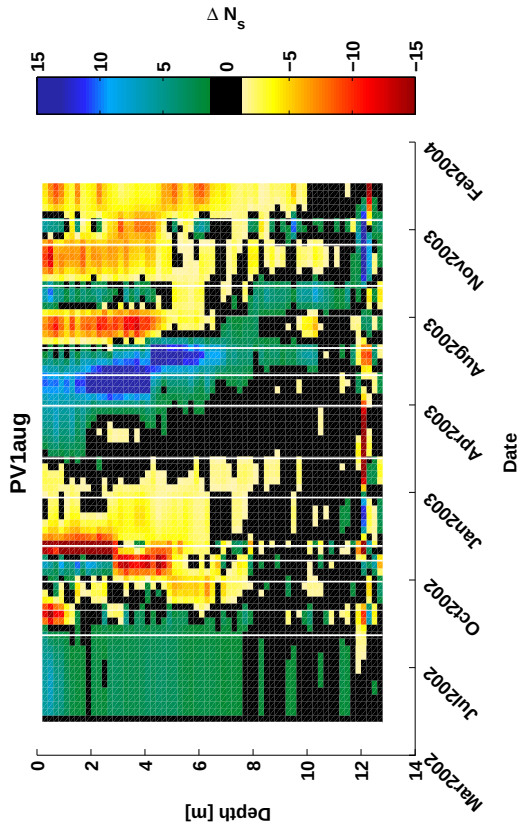

Figure B.22: *PV1aug - Gridded raw time-lapse neutron counts.*

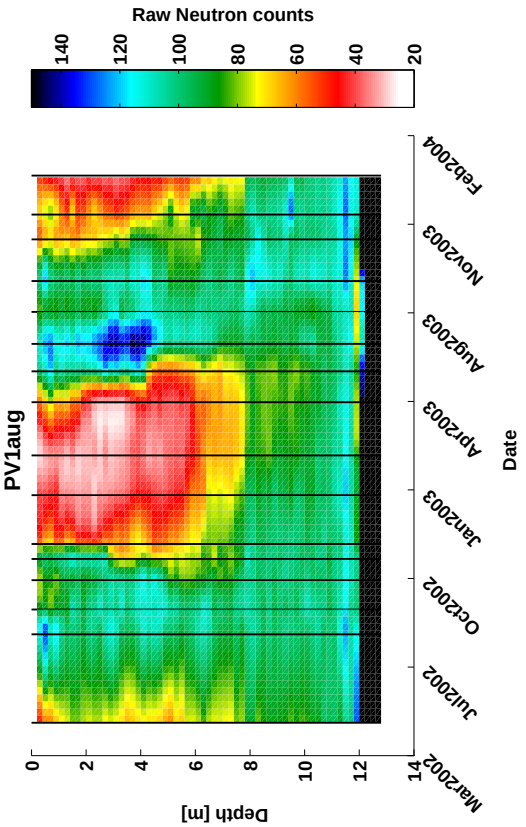

Figure B.23: *PV1aug - Sequential difference in raw neutron counts.*

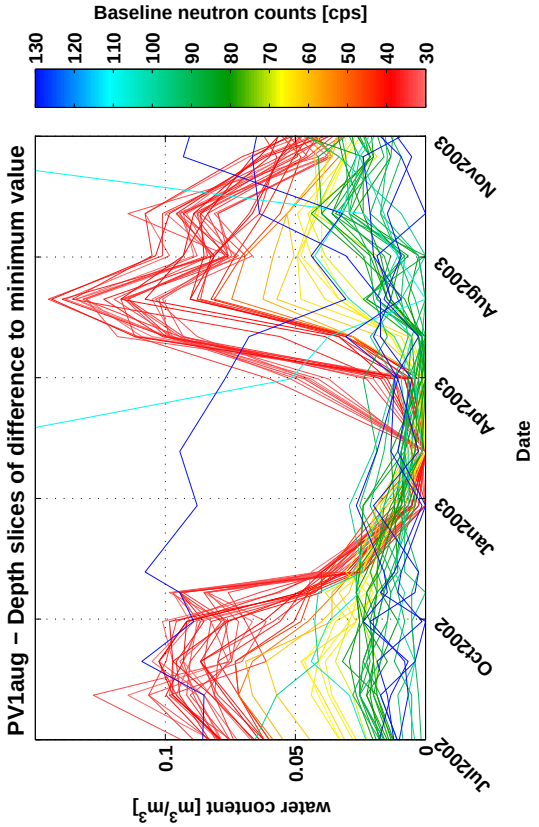

Figure B.25: *PV1aug - Difference of estimated water content to driest month for individual depth levels. Colour indicates raw counts on baseline date.*

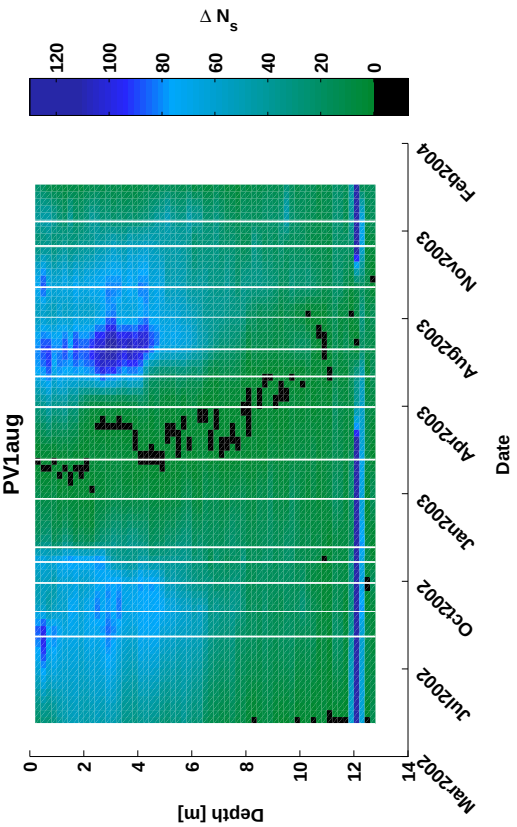

Figure B.24: *PV1aug - Baseline difference of raw time-lapse neutron counts.*

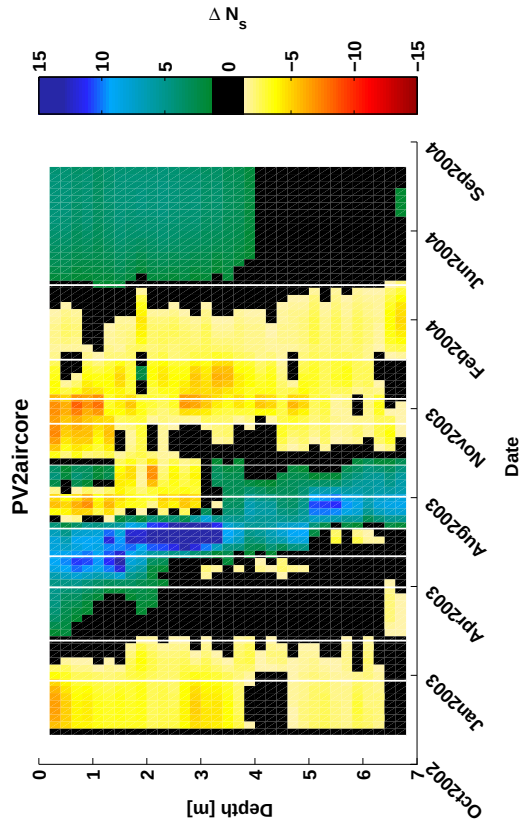

Figure B.26: *PV2aircore - Gridded raw time-lapse neutron counts.*

Figure B.27: *PV2aircore - Sequential difference in raw neutron counts.*

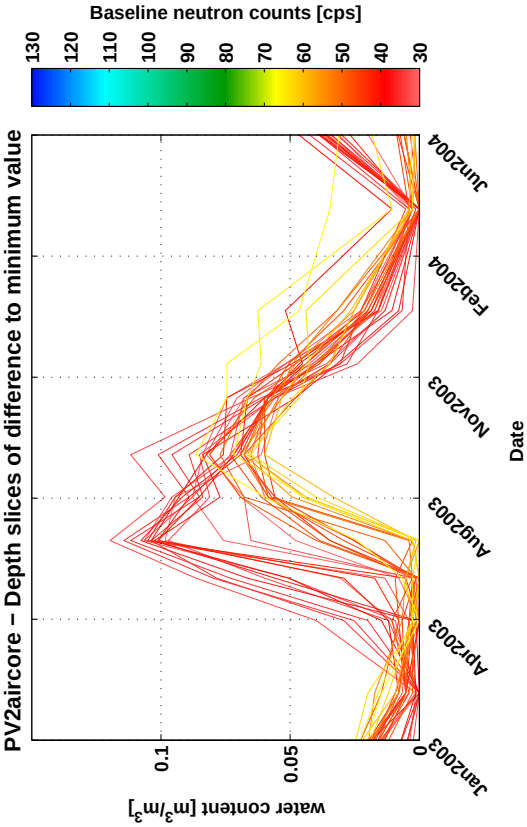

Figure B.29: *PV2aircore - Difference of estimated water content to driest month for individual depth levels. Colour indicates raw counts on baseline date.*

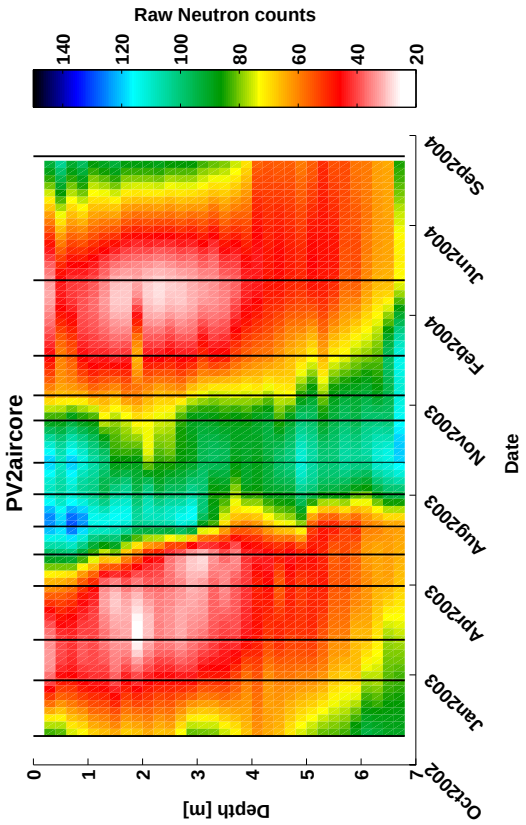

Figure B.28: *PV2aircore - Baseline difference of raw time-lapse neutron counts.*

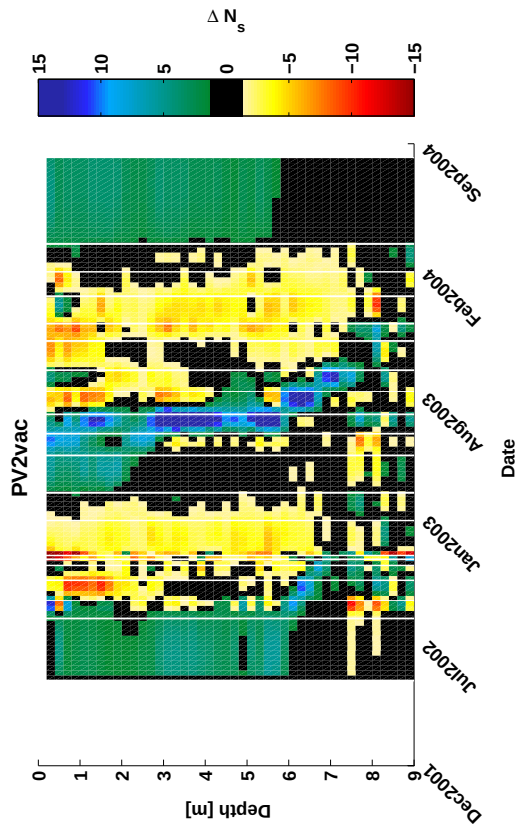

Figure B.31: *PV2vac - Sequential difference in raw neutron counts.*

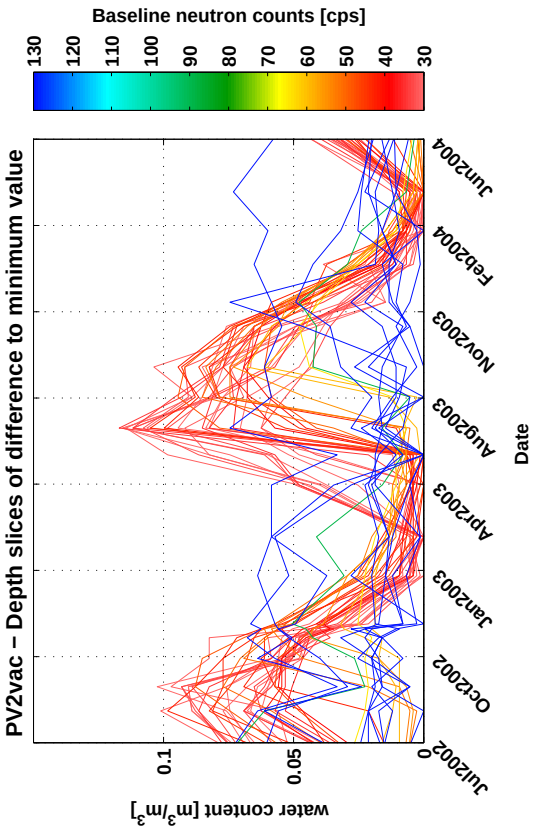

Figure B.33: *PV2vac - Difference of estimated water content to driest month for individual depth levels. Colour indicates raw counts on baseline date.*

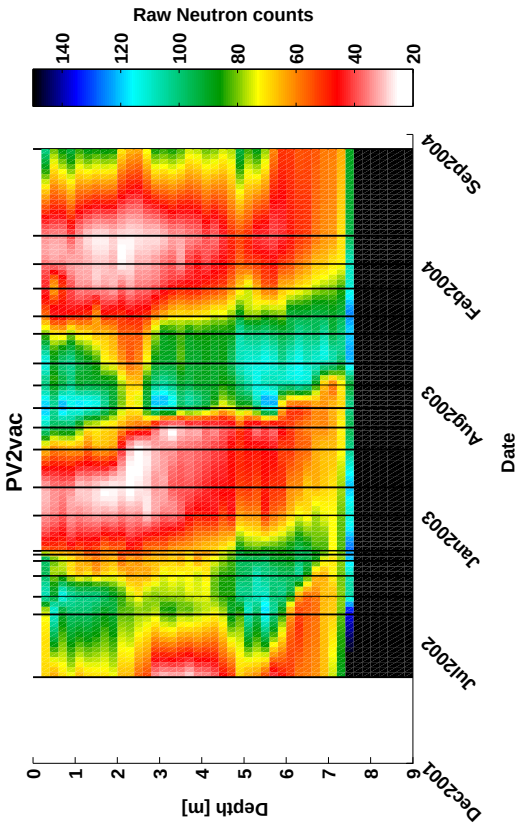

Figure B.30: *PV2vac - Gridded raw time-lapse neutron counts.*

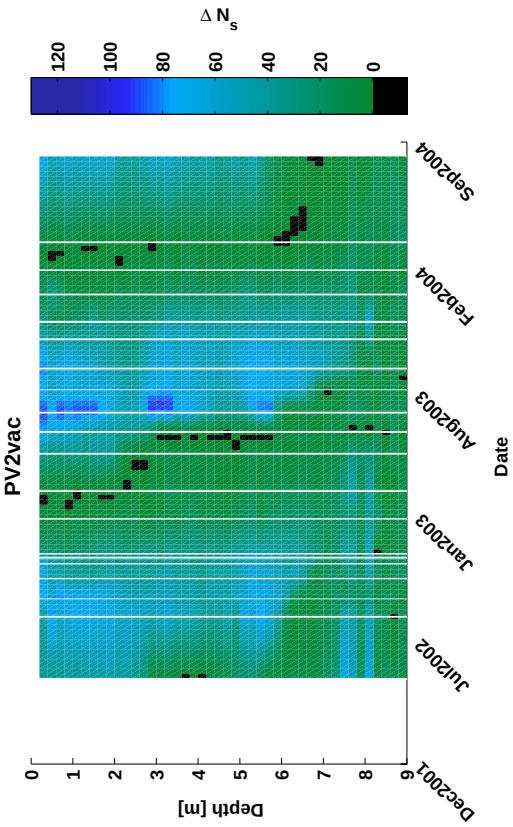

Figure B.32: *PV2vac - Baseline difference of raw time-lapse neutron counts.*

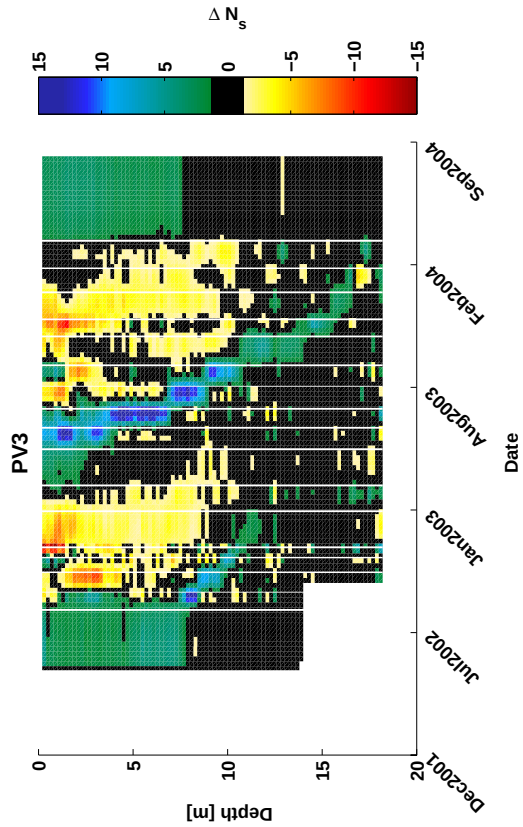

Figure B.35: *PV3 - Sequential difference in raw neutron counts.*

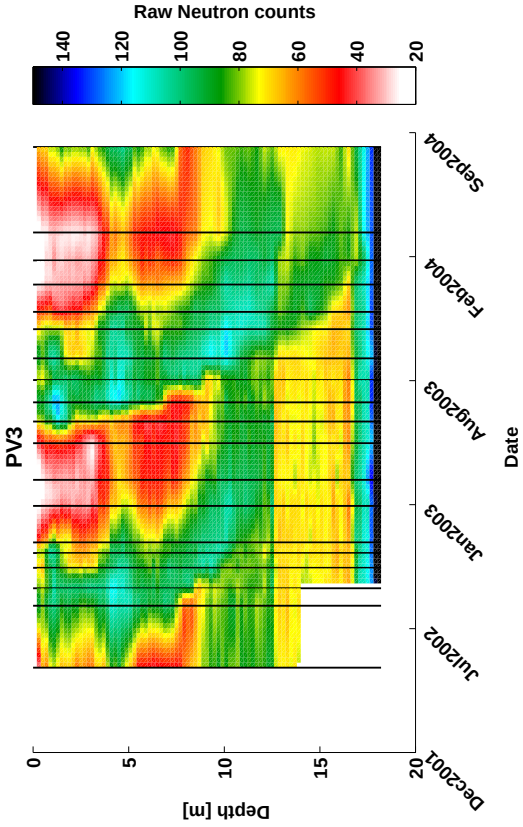

Figure B.34: *PV3 - Gridded raw time-lapse neutron counts.*

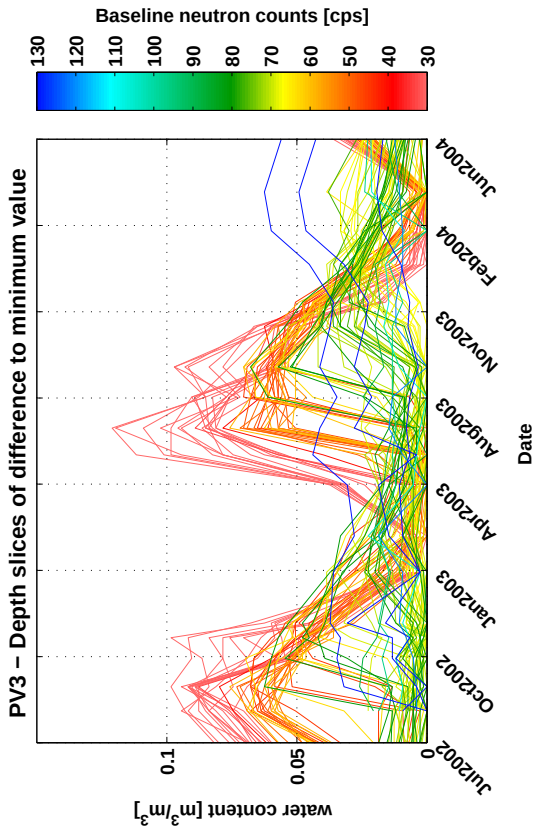

Figure B.37: *PV3 - Difference of estimated water content to driest month for individual depth levels. Colour indicates raw counts on baseline date.*

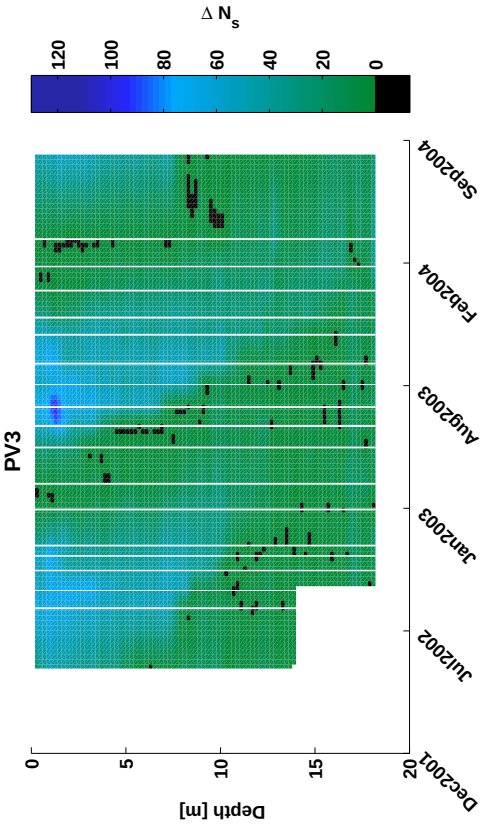

Figure B.36: *PV3 - Baseline difference of raw time-lapse neutron counts.*

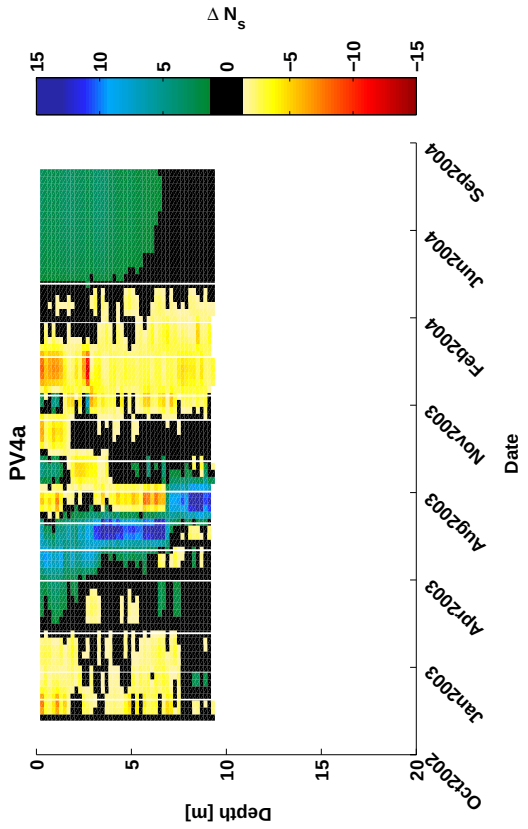

Figure B.39: *PV4a - Sequential difference in raw neutron counts.*

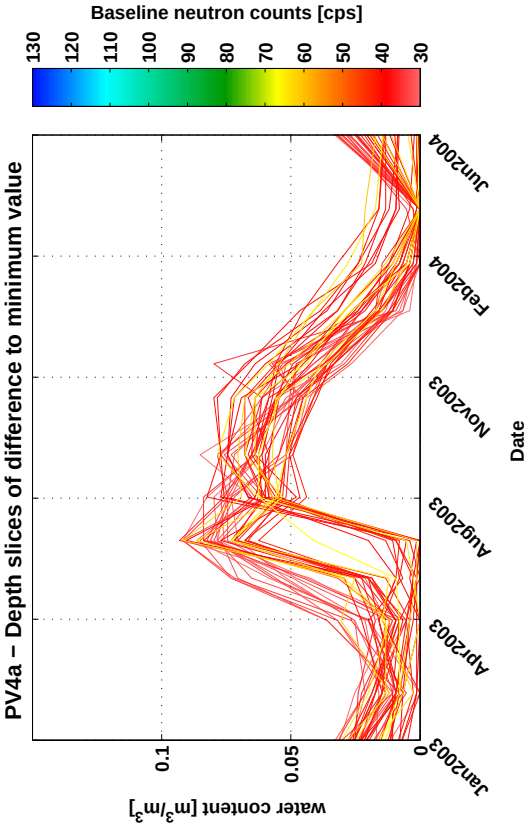

Figure B.41: *PV4a - Difference of estimated water content to driest month for individual depth levels. Colour indicates raw counts on baseline date.*

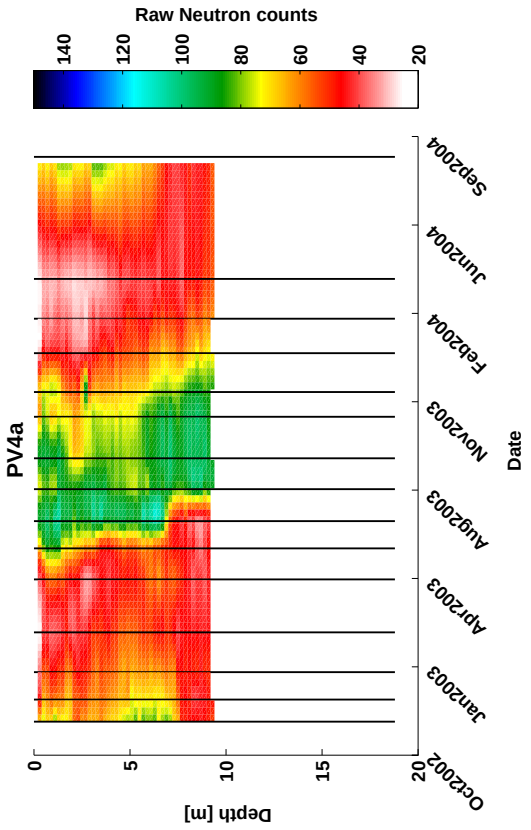

Figure B.38: *PV4a - Gridded raw time-lapse neutron counts.*

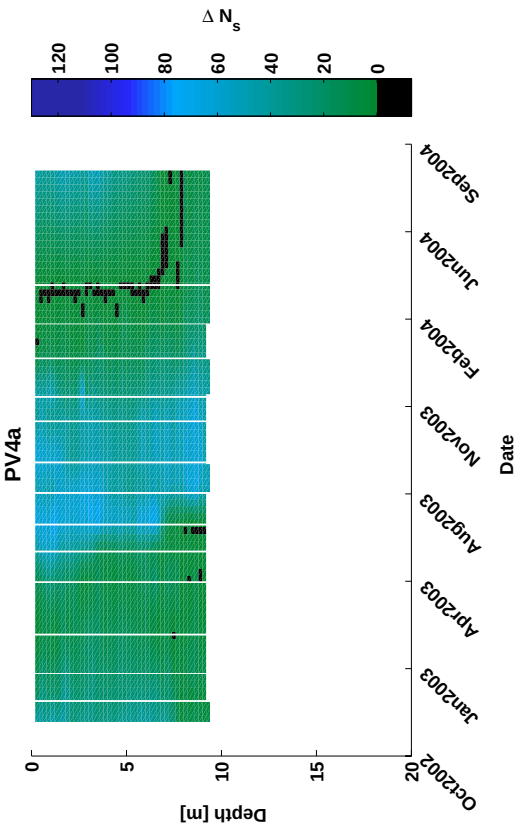

Figure B.40: *PV4a - Baseline difference of raw time-lapse neutron counts.*

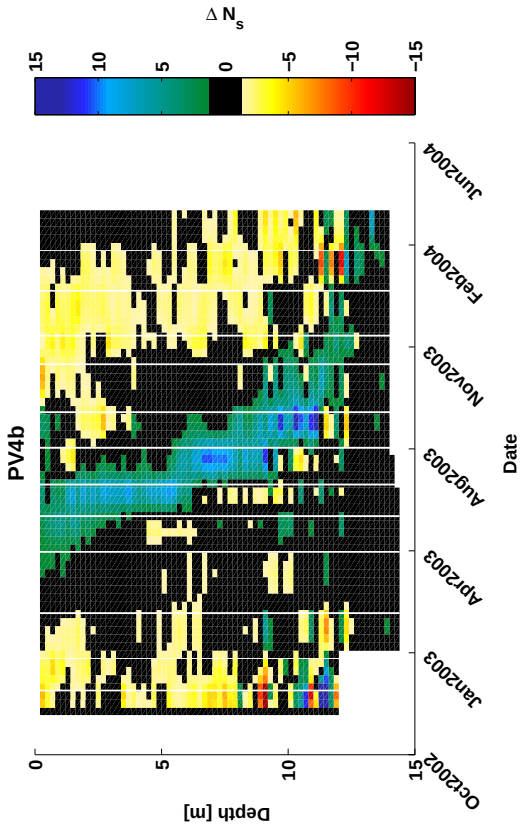

Figure B.42: *PV4b - Gridded raw time-lapse neutron counts.*

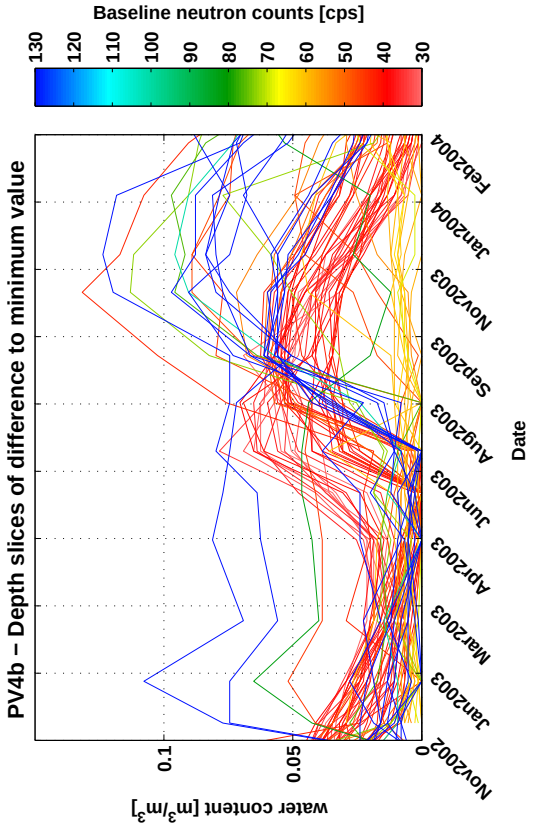

Figure B.43: *PV4b - Sequential difference in raw neutron counts.*

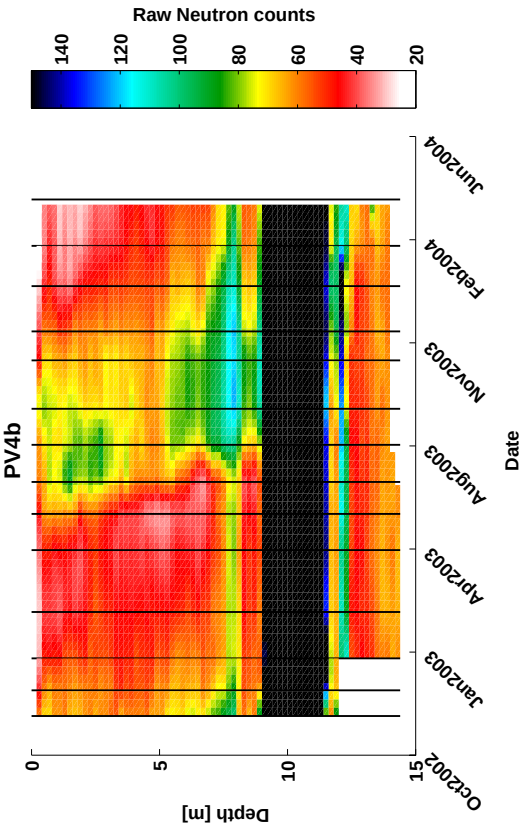

Figure B.44: *PV4b - Baseline difference of raw time-lapse neutron counts.*

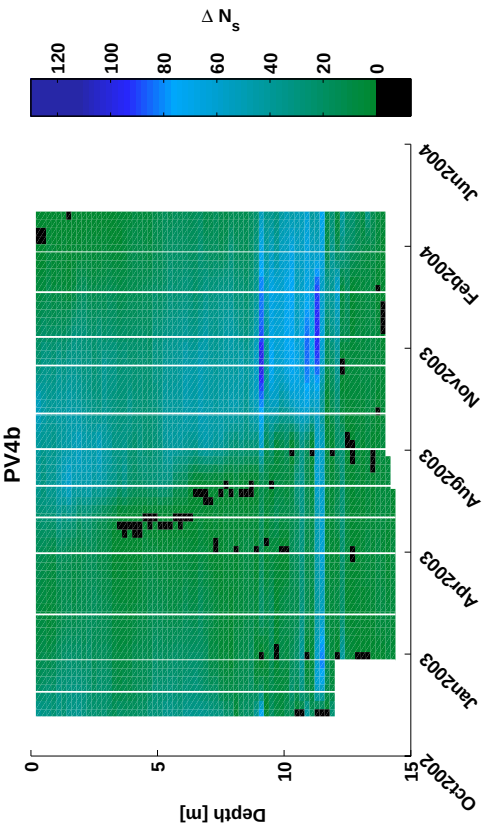

Figure B.45: *PV4b - Difference of estimated water content to driest month for individual depth levels. Colour indicates raw counts on baseline date.*

B.2 Dept. of Water, wetland investigation

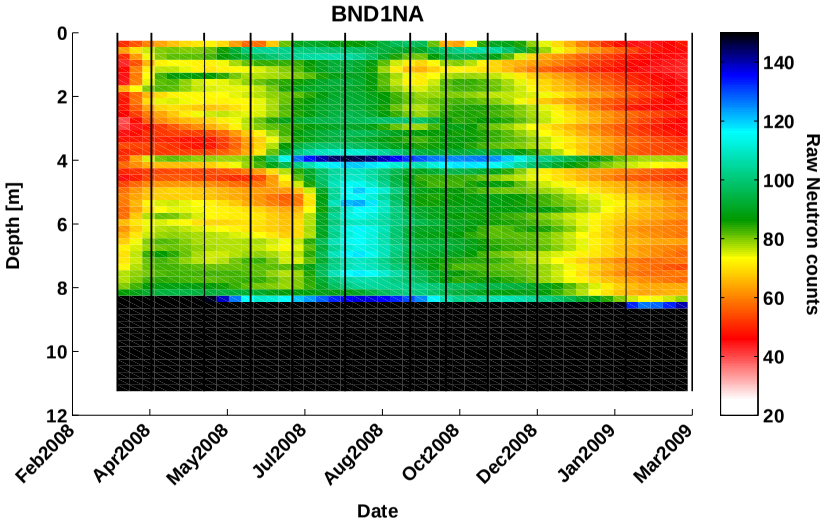

Figure B.46: *BND1NA - Gridded raw time-lapse neutron counts.*

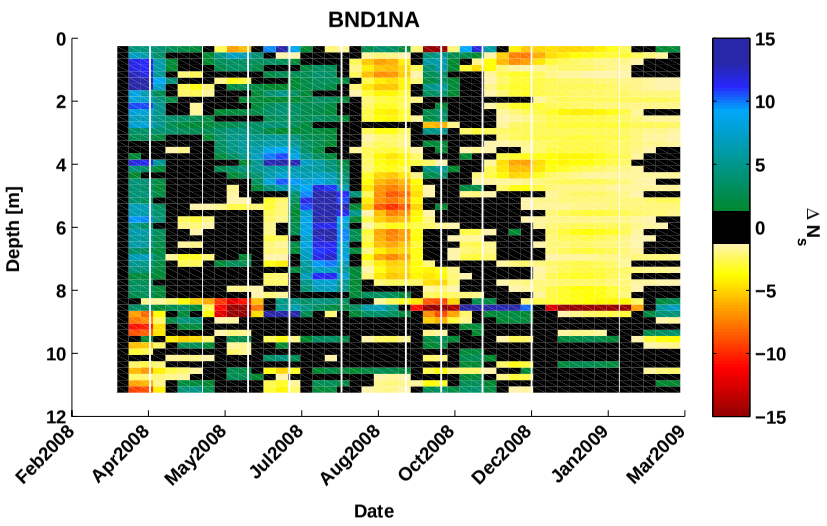

Figure B.47: *BND1NA - Sequential difference in raw neutron counts.*

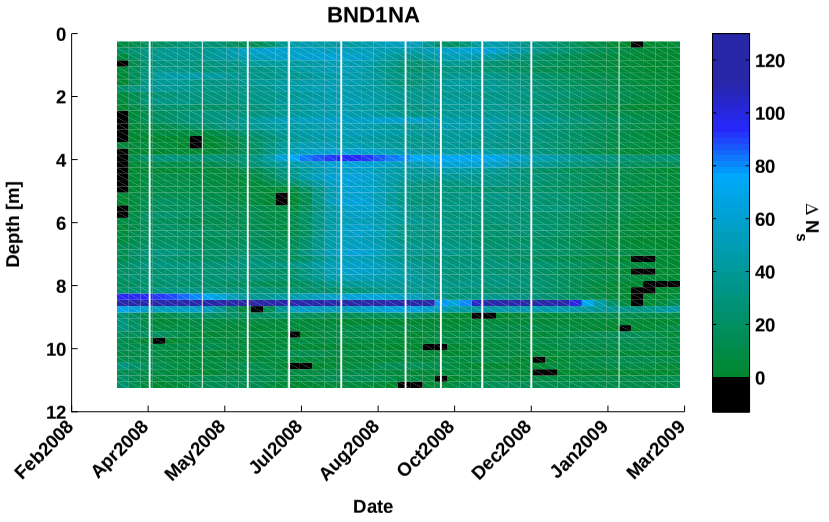

Figure B.48: *BND1NA - Baseline difference of raw time-lapse neutron counts.*

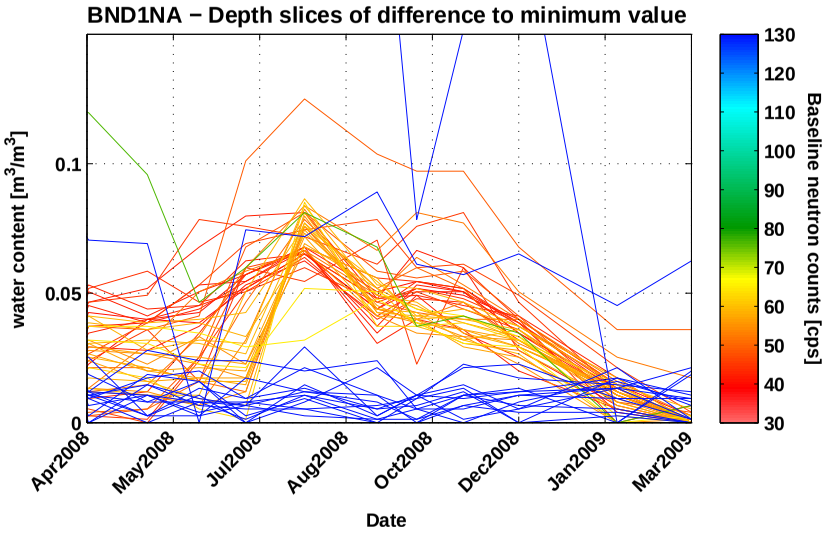

Figure B.49: *BND1NA - Difference of estimated water content to driest month for individual depth levels. Colour indicates raw counts on baseline date.*

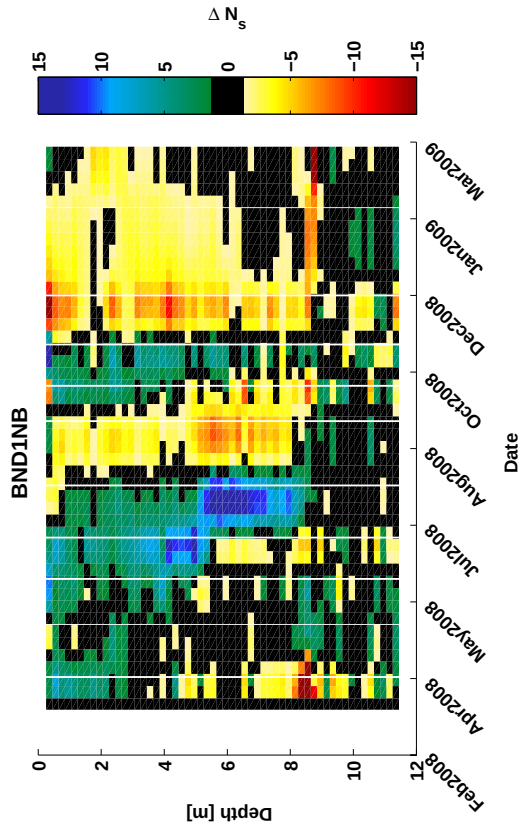

Figure B.51: *BND1NB - Sequential difference in raw neutron counts.*

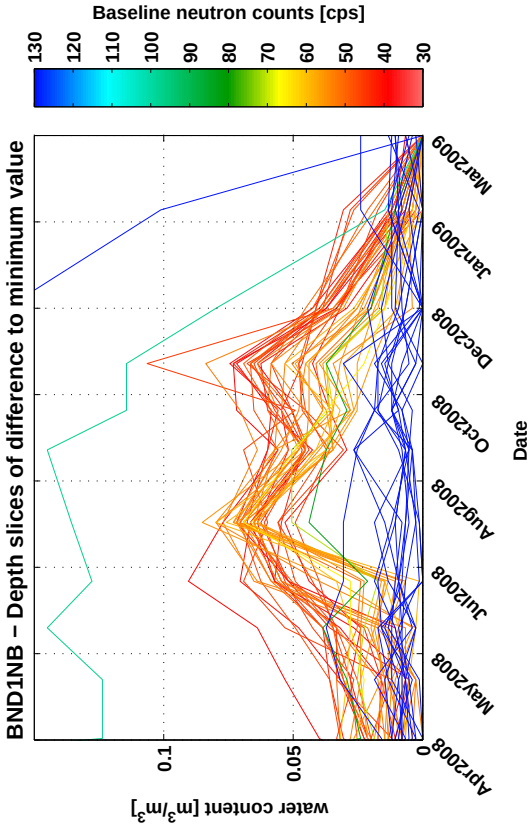

Figure B.53: *BND1NB - Difference of estimated water content to driest month for individual depth levels. Colour indicates raw counts on baseline date.*

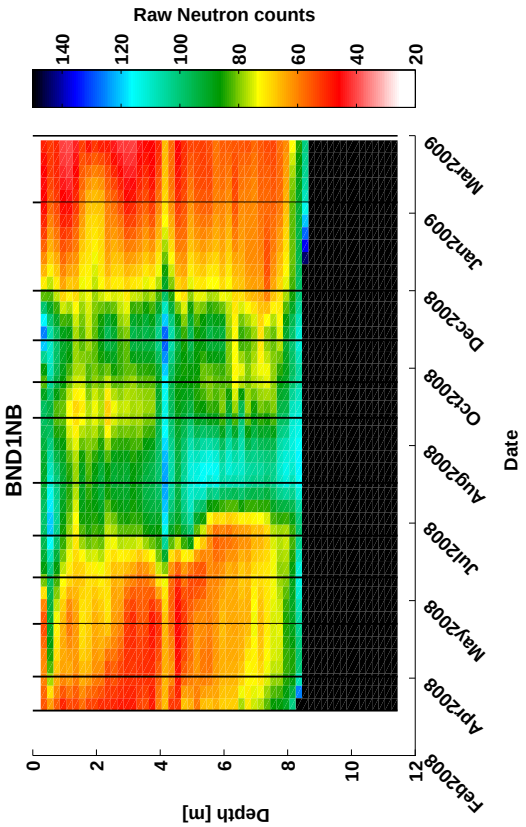

Figure B.50: *BND1NB - Gridded raw time-lapse neutron counts.*

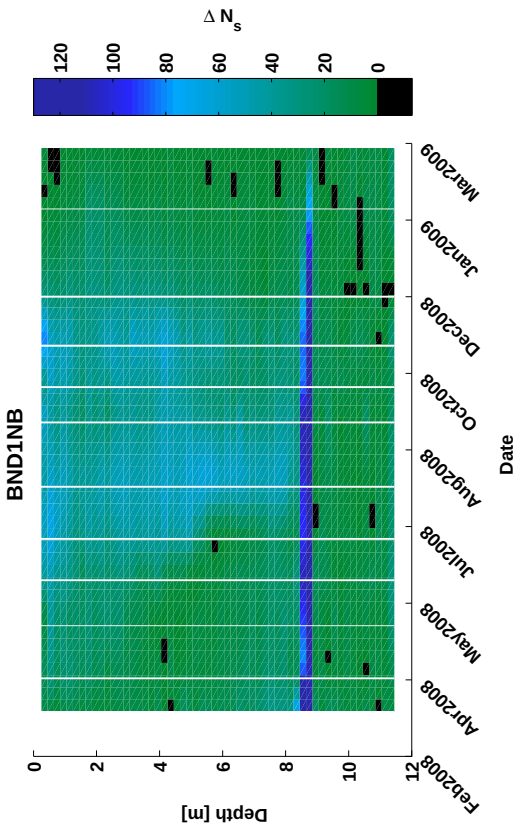

Figure B.52: *BND1NB - Baseline difference of raw time-lapse neutron counts.*

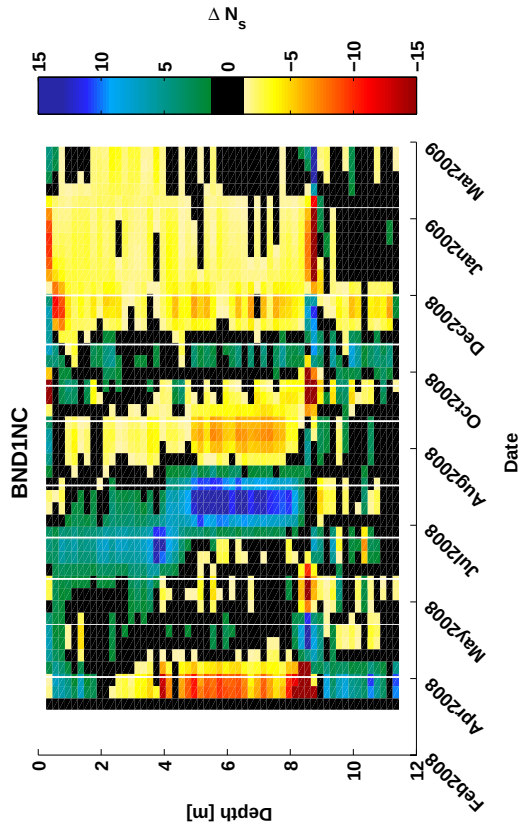

Figure B.55: *BND1NC - Sequential difference in raw neutron counts.*

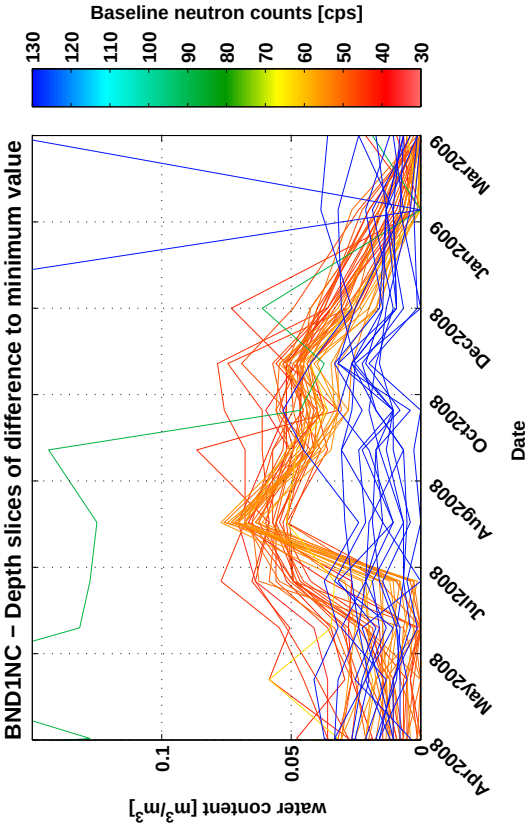

Figure B.57: *BND1NC - Difference of estimated water content to driest month for individual depth levels. Colour indicates raw counts on baseline date.*

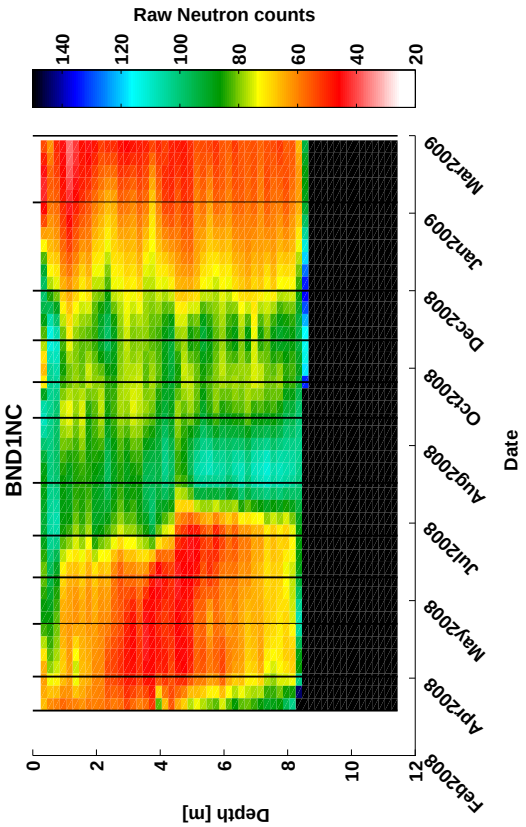

Figure B.54: *BND1NC - Gridded raw time-lapse neutron counts.*

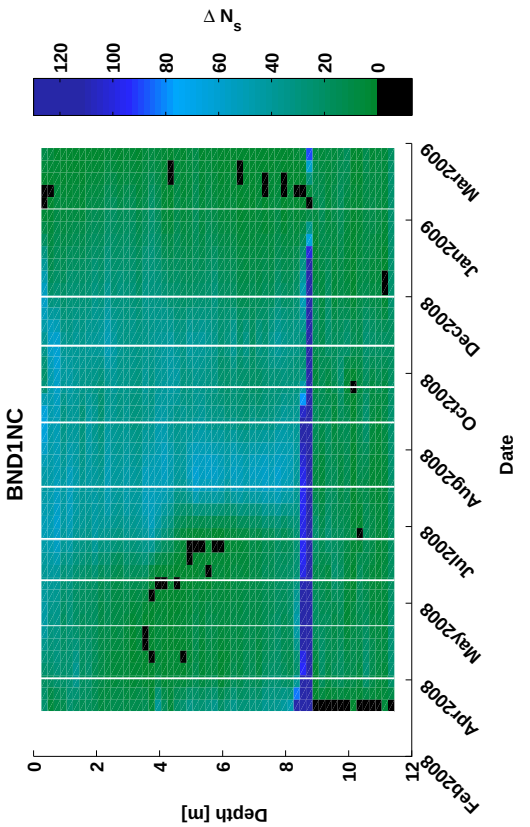

Figure B.56: *BND1NC - Baseline difference of raw time-lapse neutron counts.*

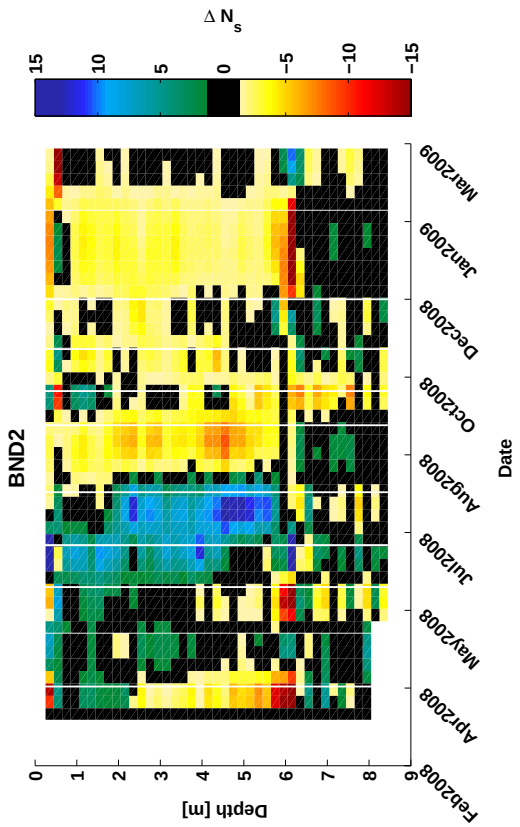

Figure B.58: *BND2 - Gridded raw time-lapse neutron counts.*

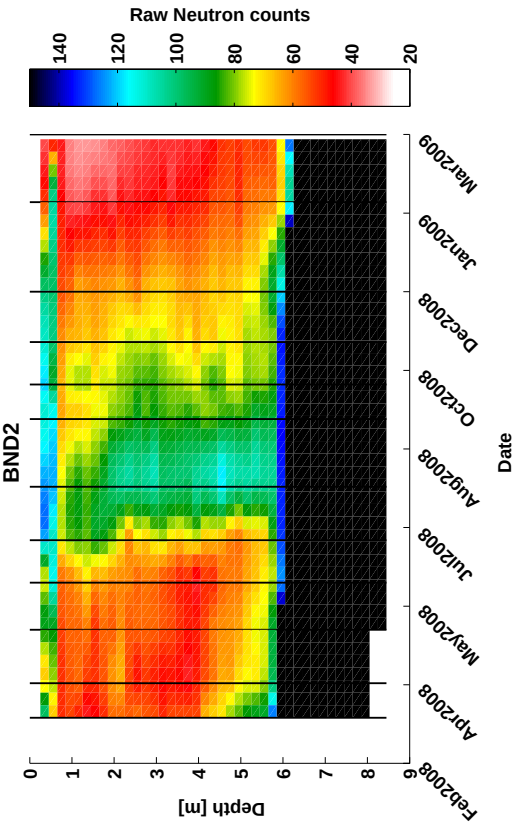

Figure B.59: *BND2 - Sequential difference in raw neutron counts.*

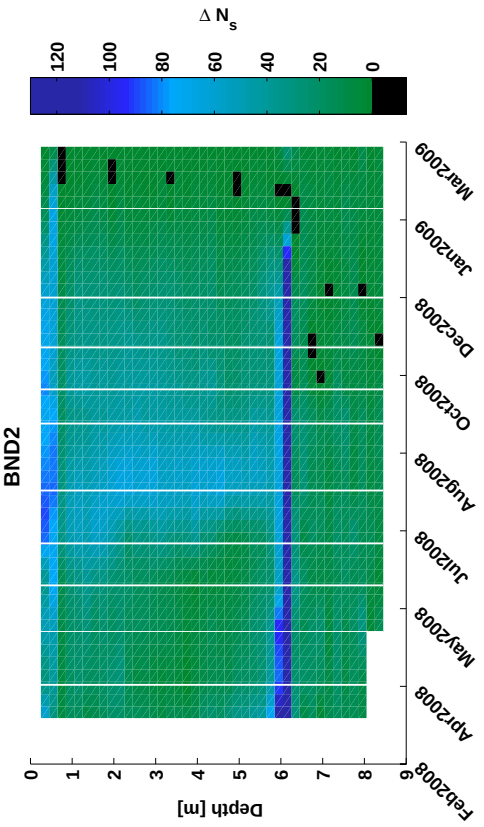

Figure B.60: *BND2 - Baseline difference of raw time-lapse neutron counts.*

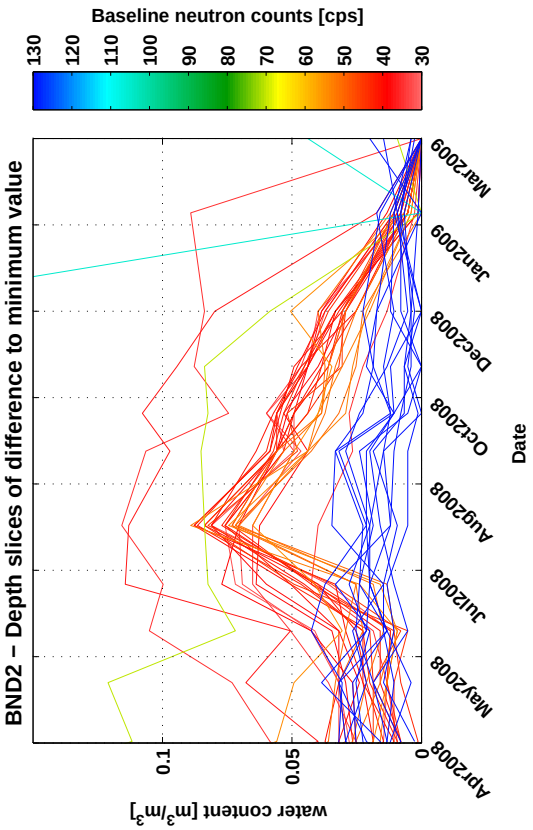

Figure B.61: *BND2 - Difference of estimated water content to driest month for individual depth levels. Colour indicates raw counts on baseline date.*

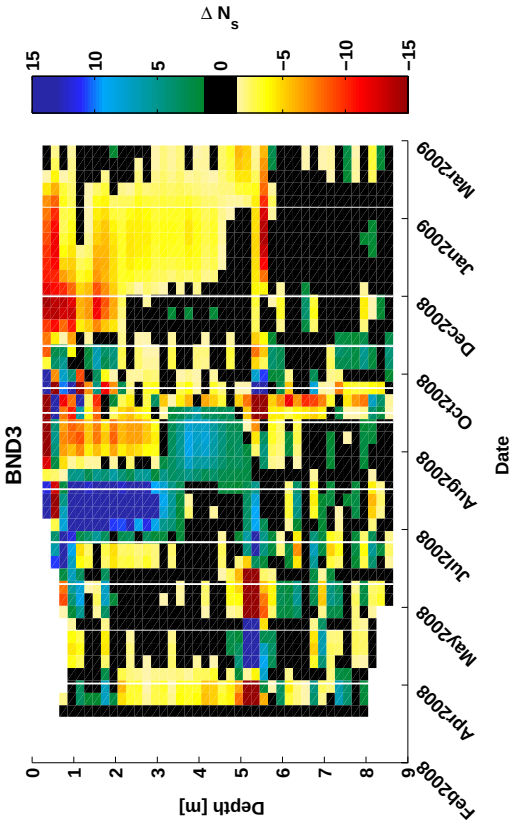

Figure B.62: *BND3 - Gridded raw time-lapse neutron counts.*

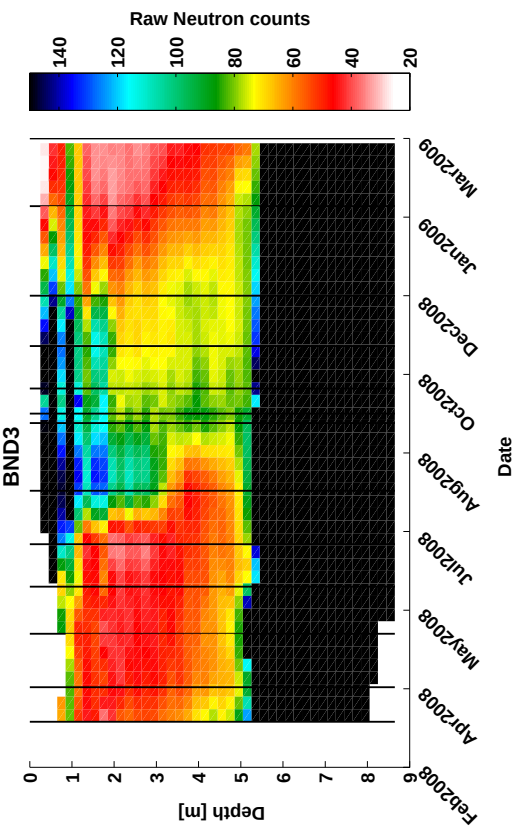

Figure B.63: *BND3 - Sequential difference in raw neutron counts.*

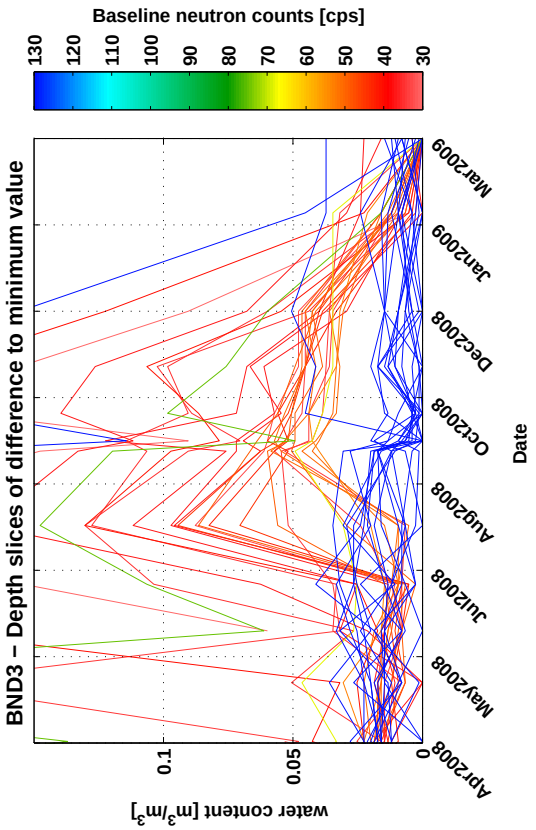

Figure B.65: *BND3 - Difference of estimated water content to driest month for individual depth levels. Colour indicates raw counts on baseline date.*

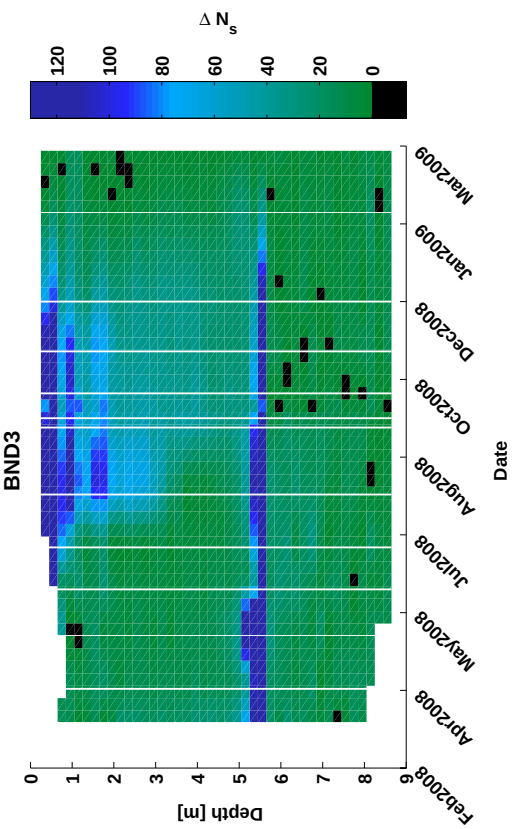

Figure B.64: *BND3 - Baseline difference of raw time-lapse neutron counts.*

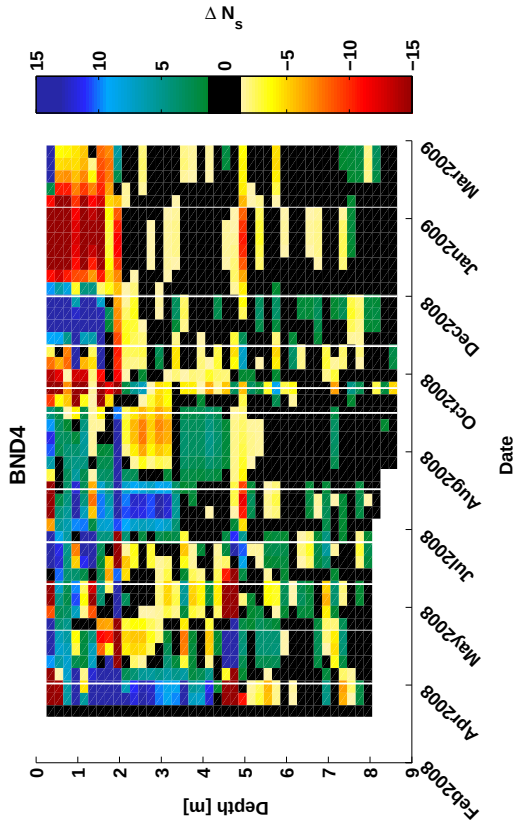

Figure B.66: *BND4 - Gridded raw time-lapse neutron counts.*

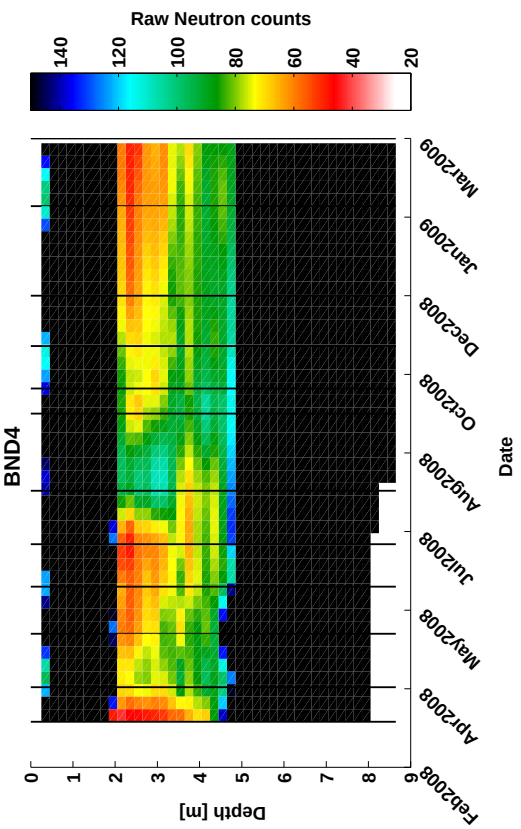

Figure B.67: *BND4 - Sequential difference in raw neutron counts.*

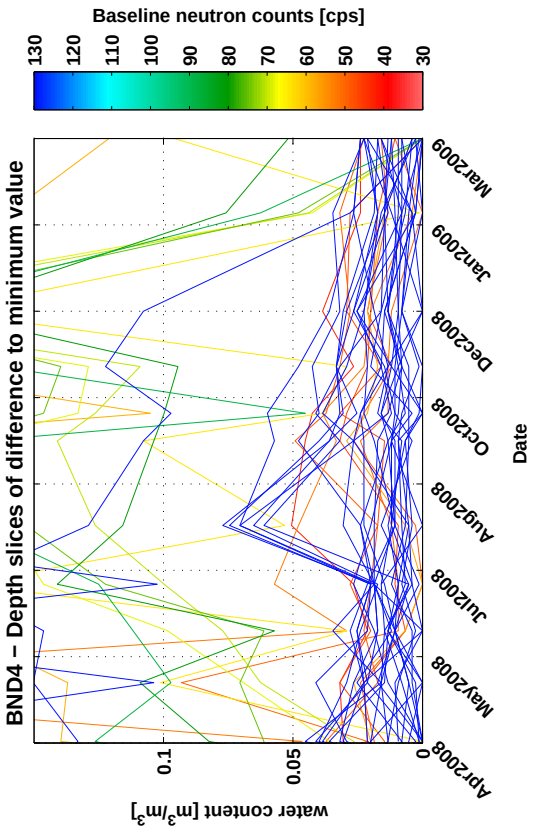

Figure B.69: *BND4 - Difference of estimated water content to driest month for individual depth levels. Colour indicates raw counts on baseline date.*

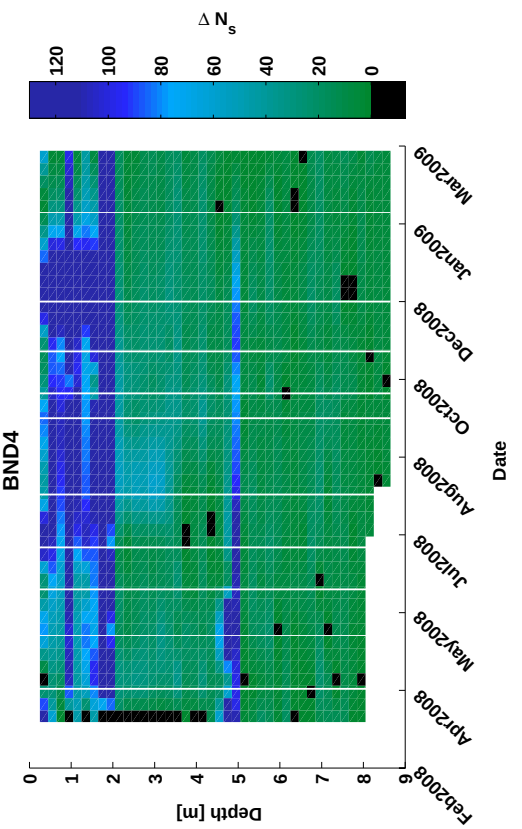

Figure B.68: *BND4 - Baseline difference of raw time-lapse neutron counts.*

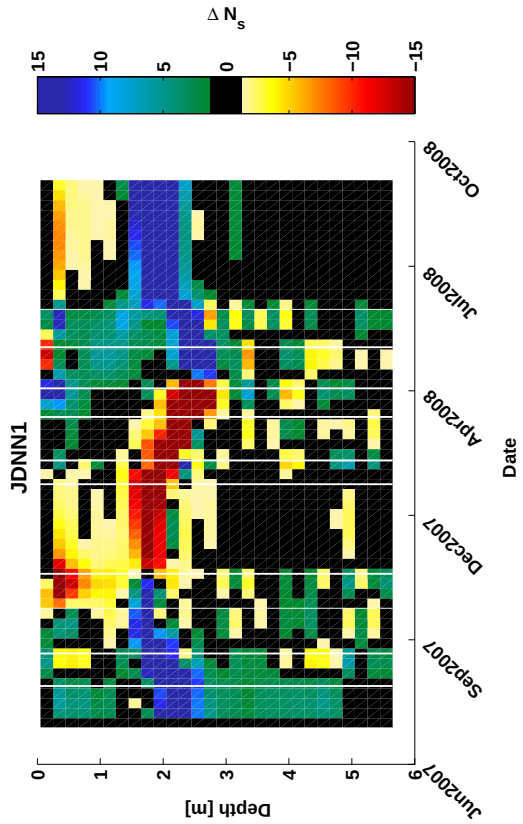

Figure B.71: *JDNN1 - Sequential difference in raw neutron counts.*

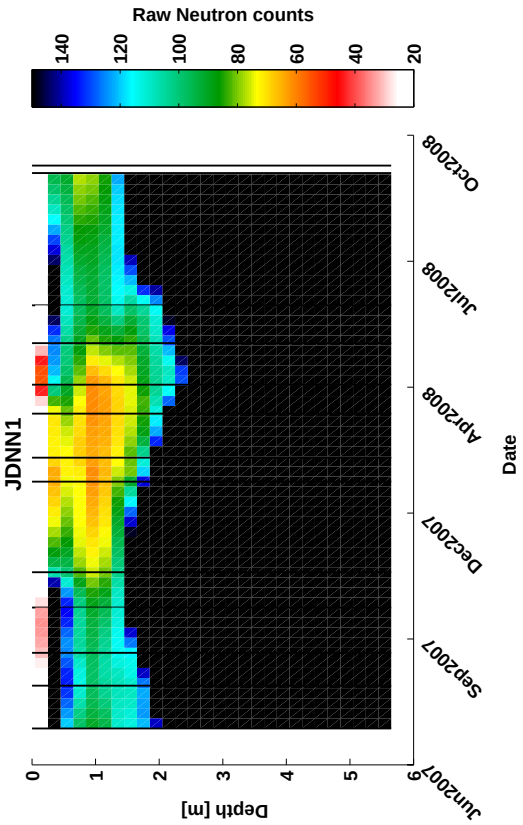

Figure B.70: *JDNN1 - Gridded raw time-lapse neutron counts.*

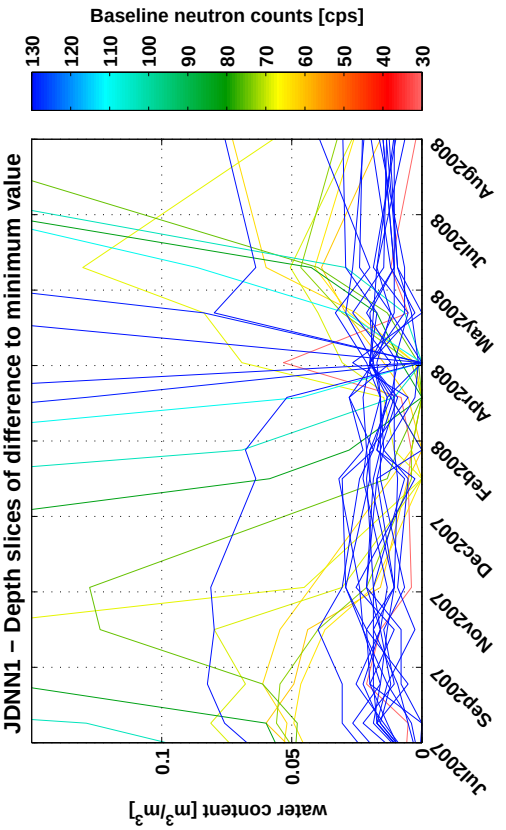

Figure B.73: *JDNN1 - Difference of estimated water content to driest month for individual depth levels. Colour indicates raw counts on baseline date.*

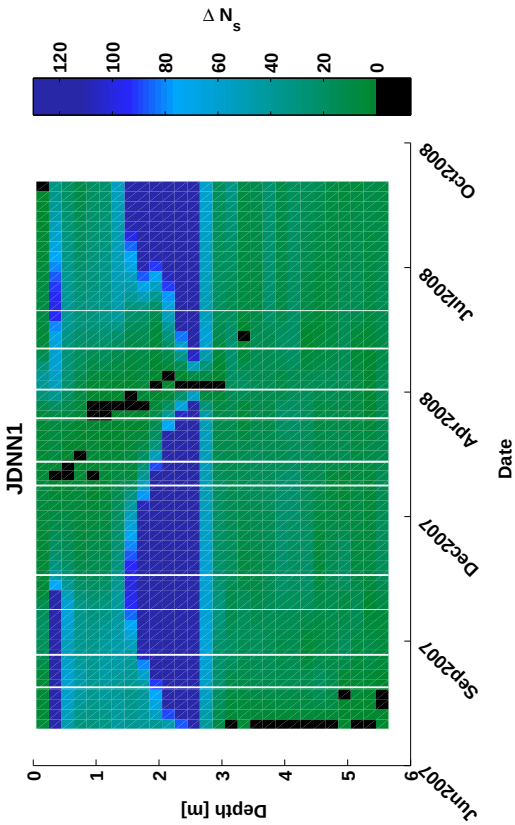

Figure B.72: *JDNN1 - Baseline difference of raw time-lapse neutron counts.*

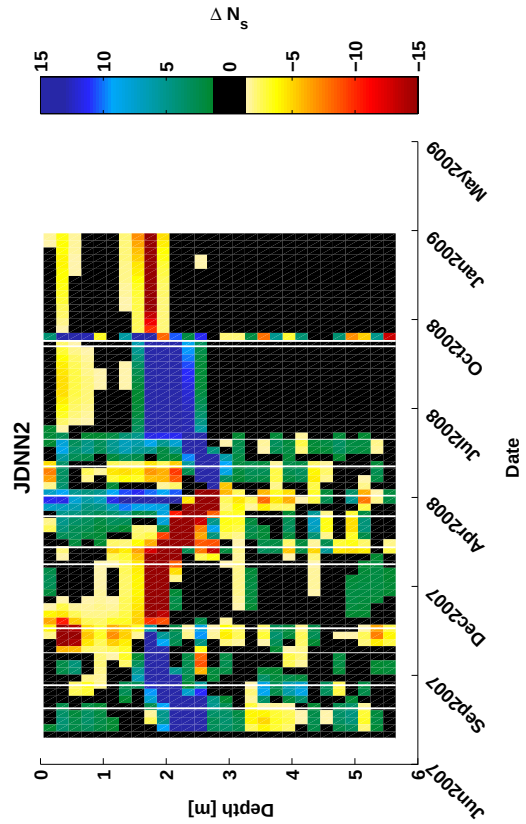

Figure B.74: *JDNN2 - Gridded raw time-lapse neutron counts.*

Figure B.75: *JDNN2 - Sequential difference in raw neutron counts.*

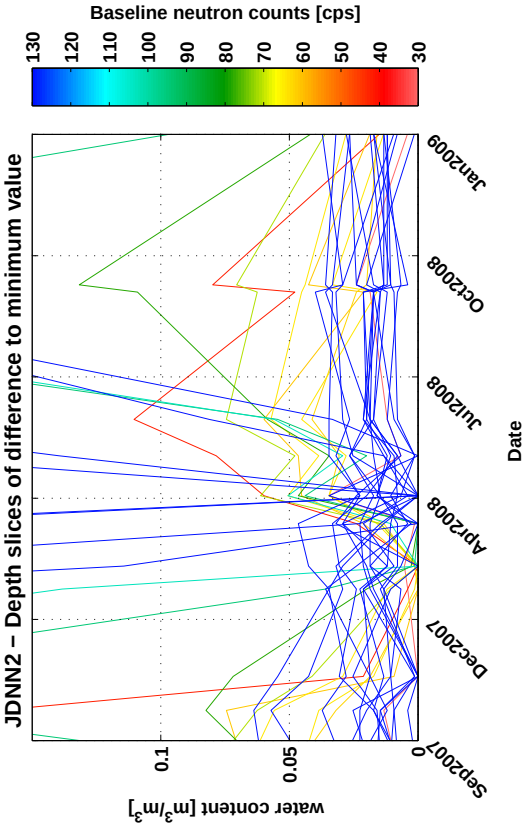

Figure B.77: *JDNN2 - Difference of estimated water content to driest month for individual depth levels. Colour indicates raw counts on baseline date.*

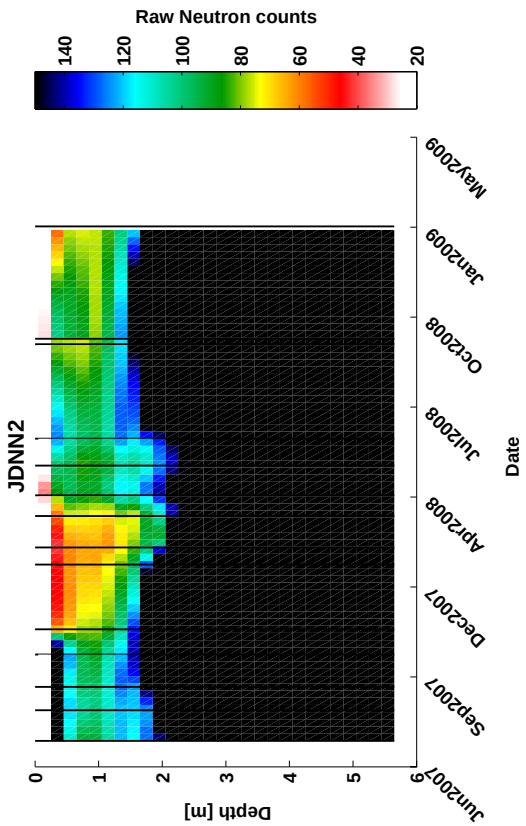

Figure B.76: *JDNN2 - Baseline difference of raw time-lapse neutron counts.*

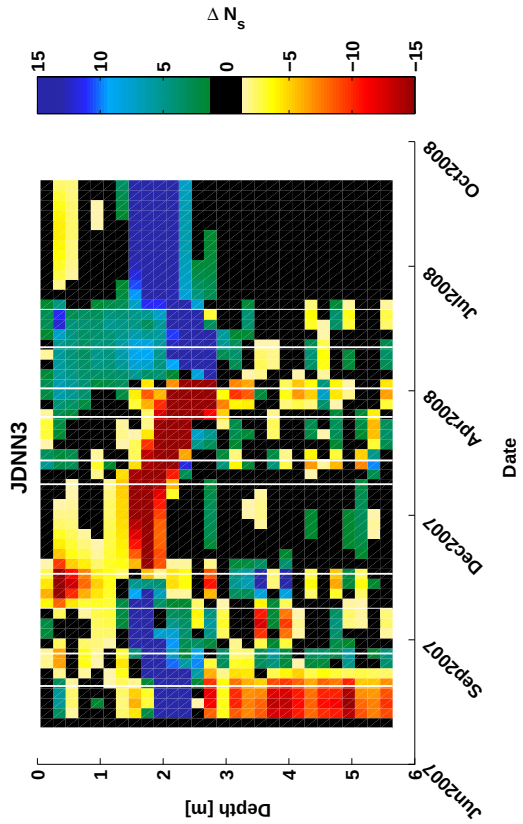

Figure B.78: *JDNN3 - Gridded raw time-lapse neutron counts.*

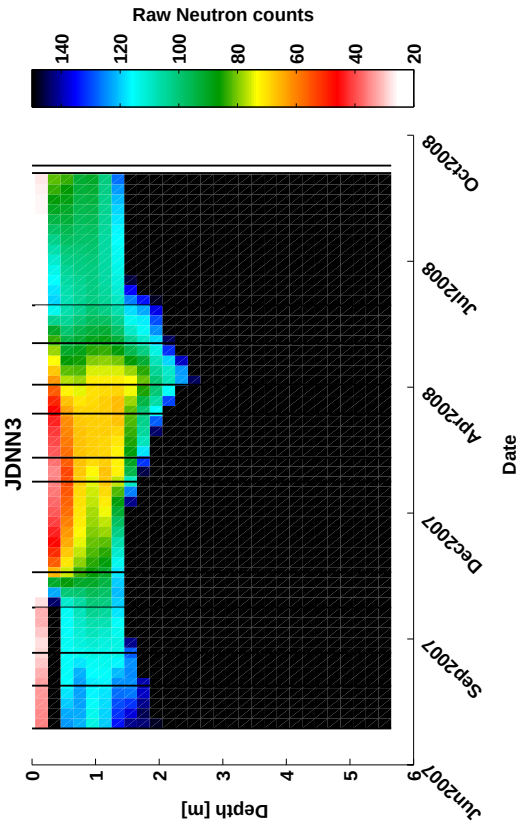

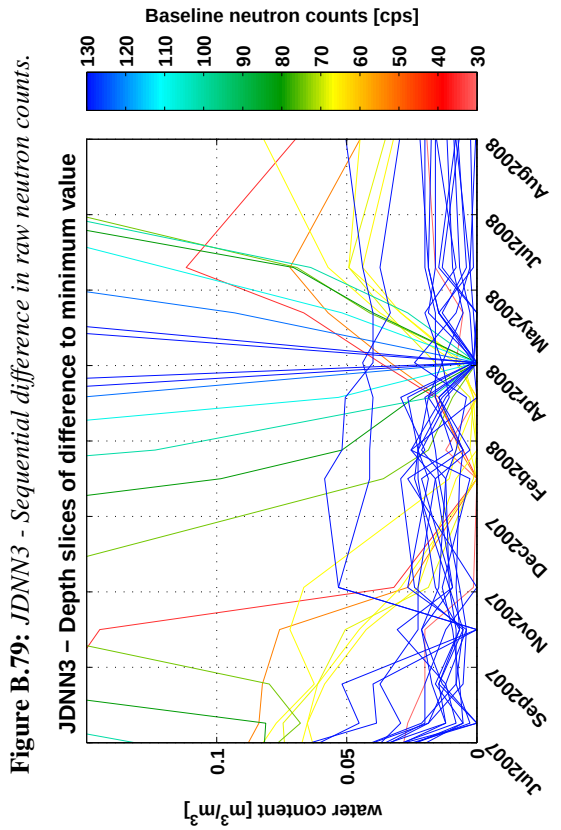

Figure B.79: *JDNN3 - Sequential difference in raw neutron counts.*

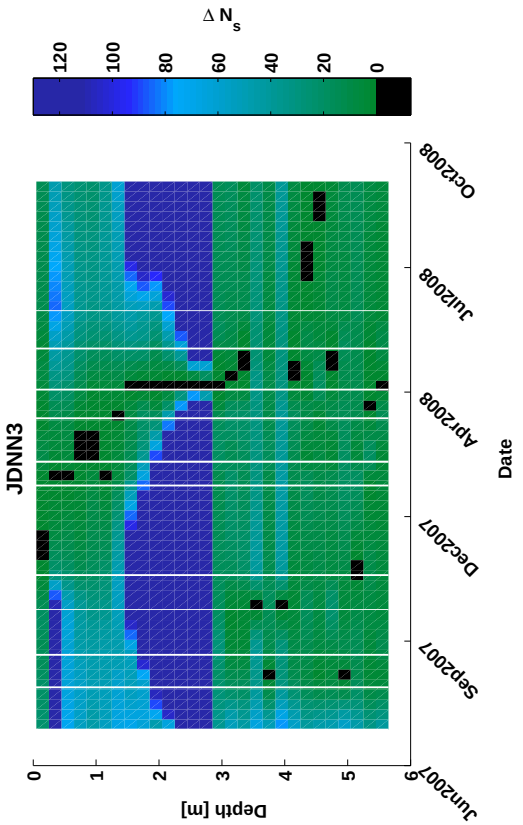

Figure B.80: *JDNN3 - Baseline difference of raw time-lapse neutron counts.*

Figure B.81: *JDNN3 - Difference of estimated water content to driest month for individual depth levels. Colour indicates raw counts on baseline date.*

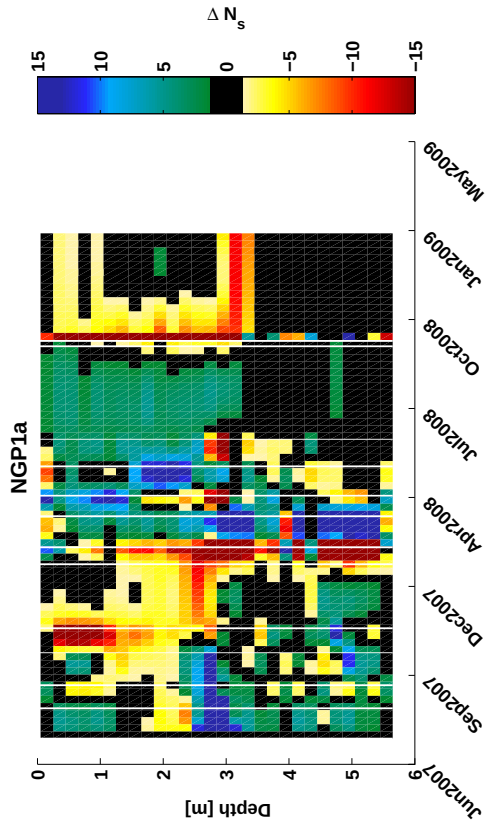

Figure B.82: *NGP1a - Gridded raw time-lapse neutron counts.*

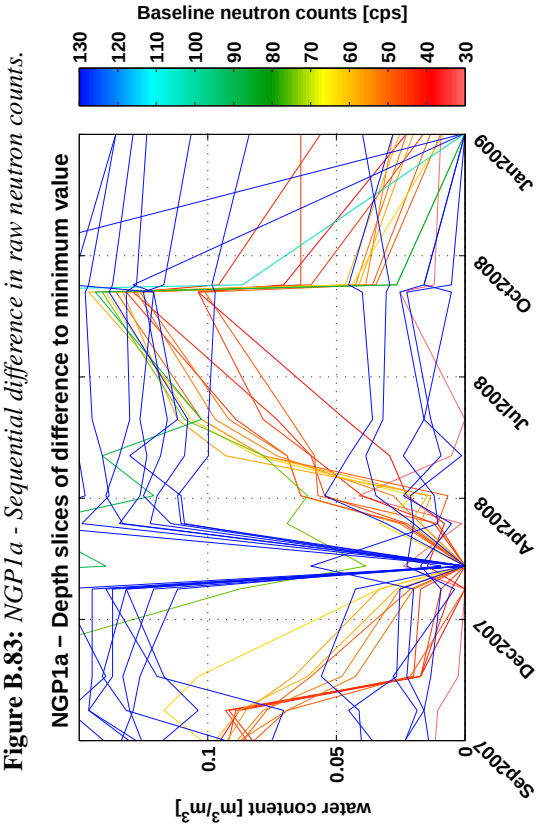

Figure B.83: *NGP1a - Sequential difference in raw neutron counts.*

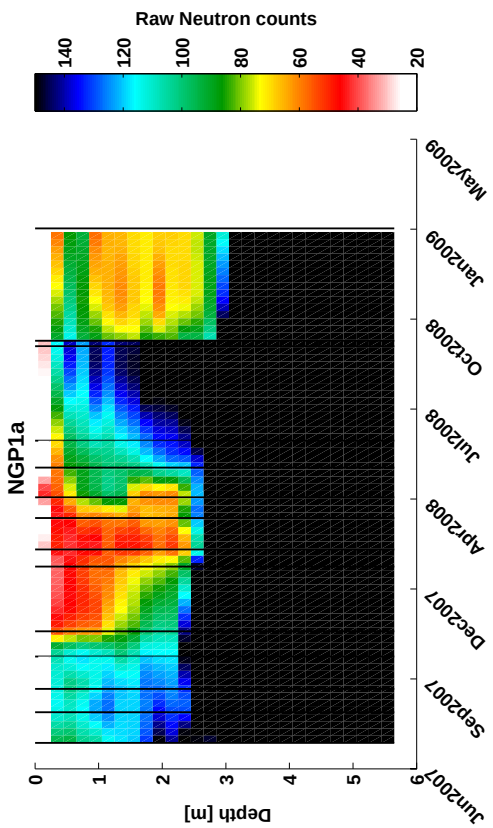

Figure B.84: *NGP1a - Baseline difference of raw time-lapse neutron counts.*

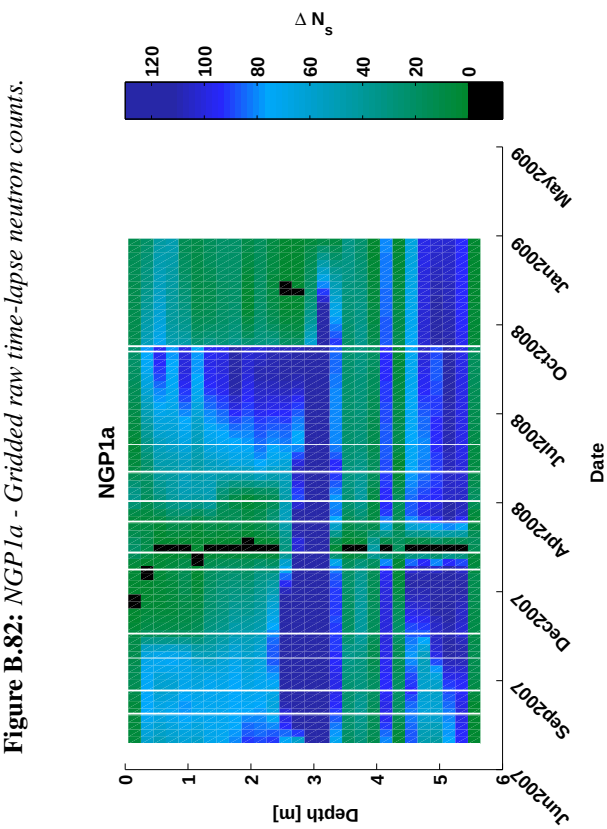

Figure B.85: *NGP1a - Difference of estimated water content to driest month for individual depth levels. Colour indicates raw counts on baseline date.*

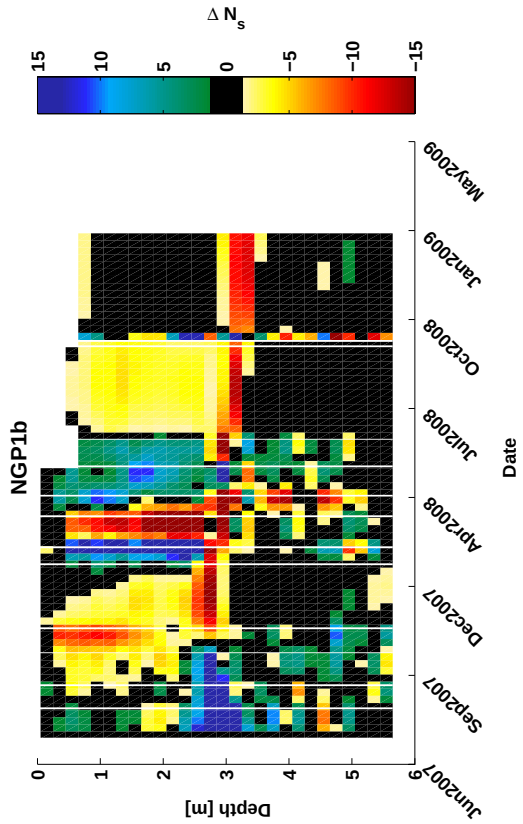

Figure B.87: *NGP1b - Sequential difference in raw neutron counts.*

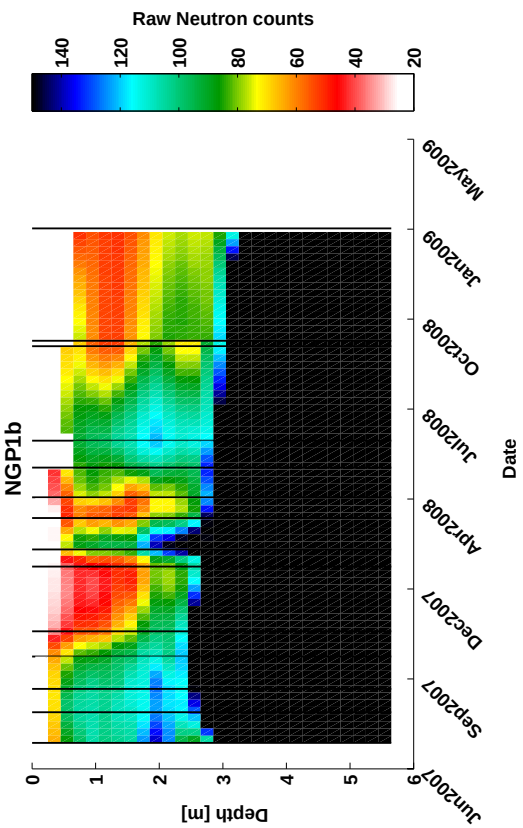

Figure B.86: *NGP1b - Gridded raw time-lapse neutron counts.*

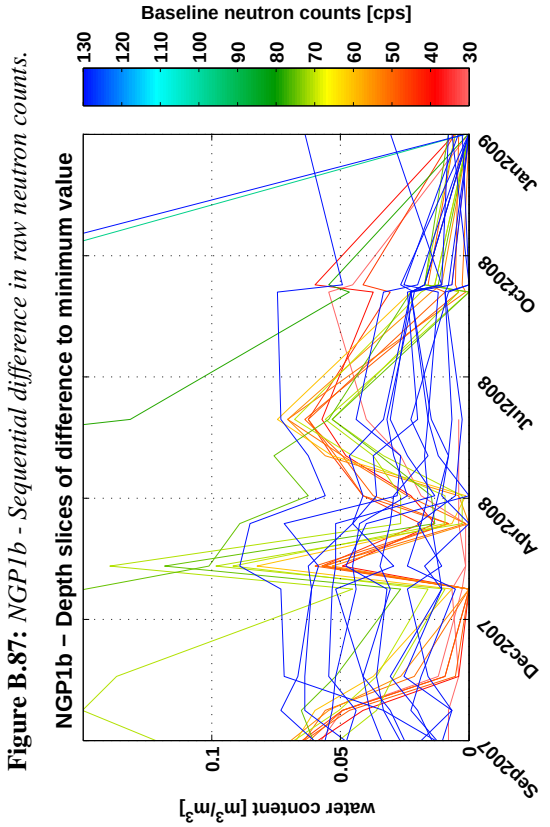

Figure B.89: *NGP1b - Difference of estimated water content to driest month for individual depth levels. Colour indicates raw counts on baseline date.*

Figure B.88: *NGP1b - Baseline difference of raw time-lapse neutron counts.*

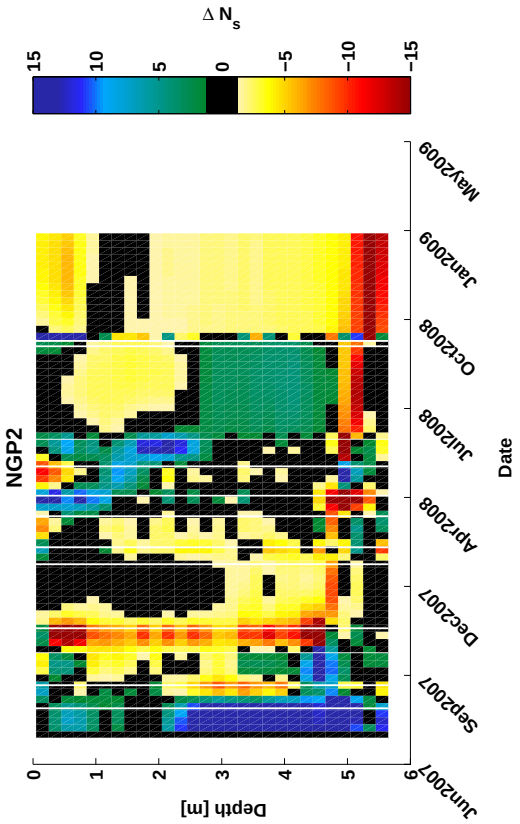

Figure B.90: *NGP2 - Gridded raw time-lapse neutron counts.*

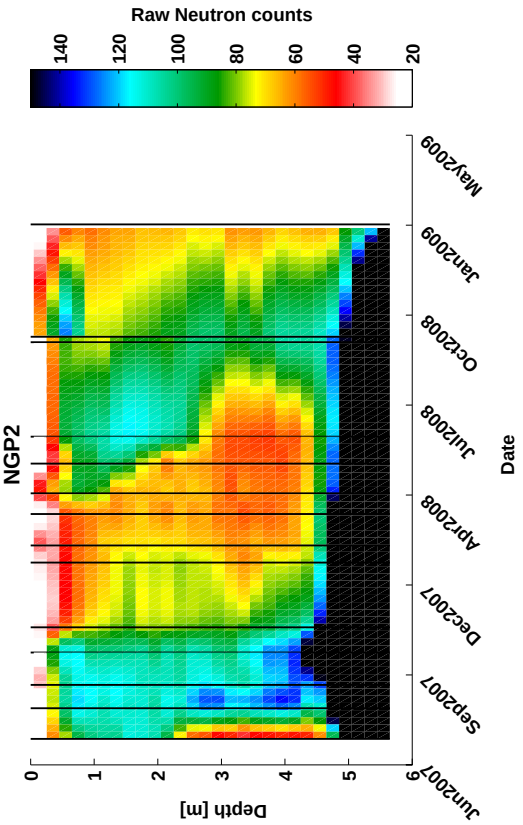

Figure B.91: *NGP2 - Sequential difference in raw neutron counts.*

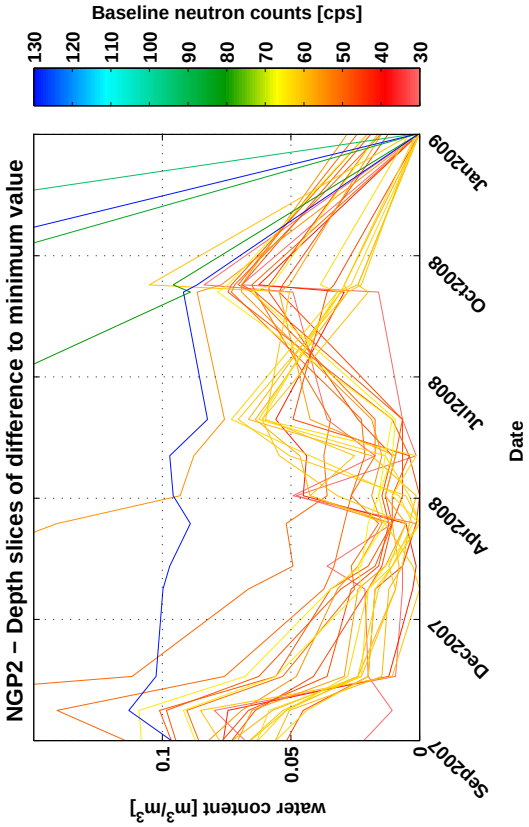

Figure B.93: *NGP2 - Difference of estimated water content to driest month for individual depth levels. Colour indicates raw counts on baseline date.*

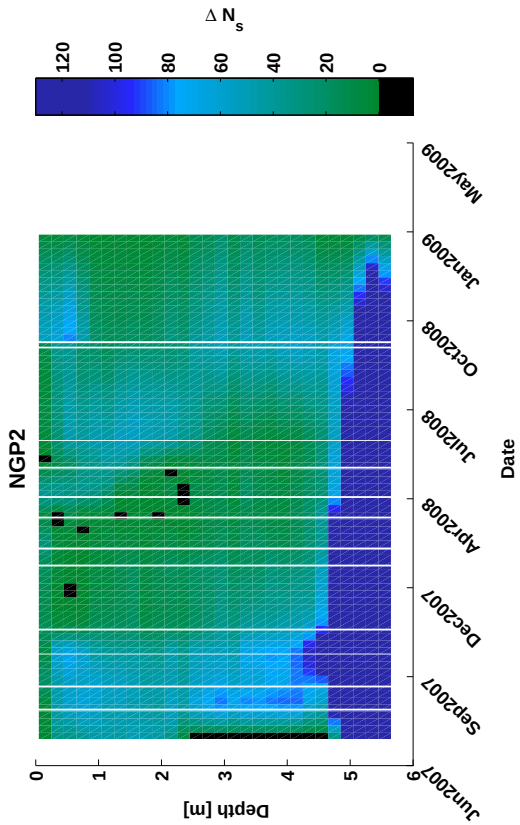

Figure B.92: *NGP2 - Baseline difference of raw time-lapse neutron counts.*

B.3 Whiteman Park

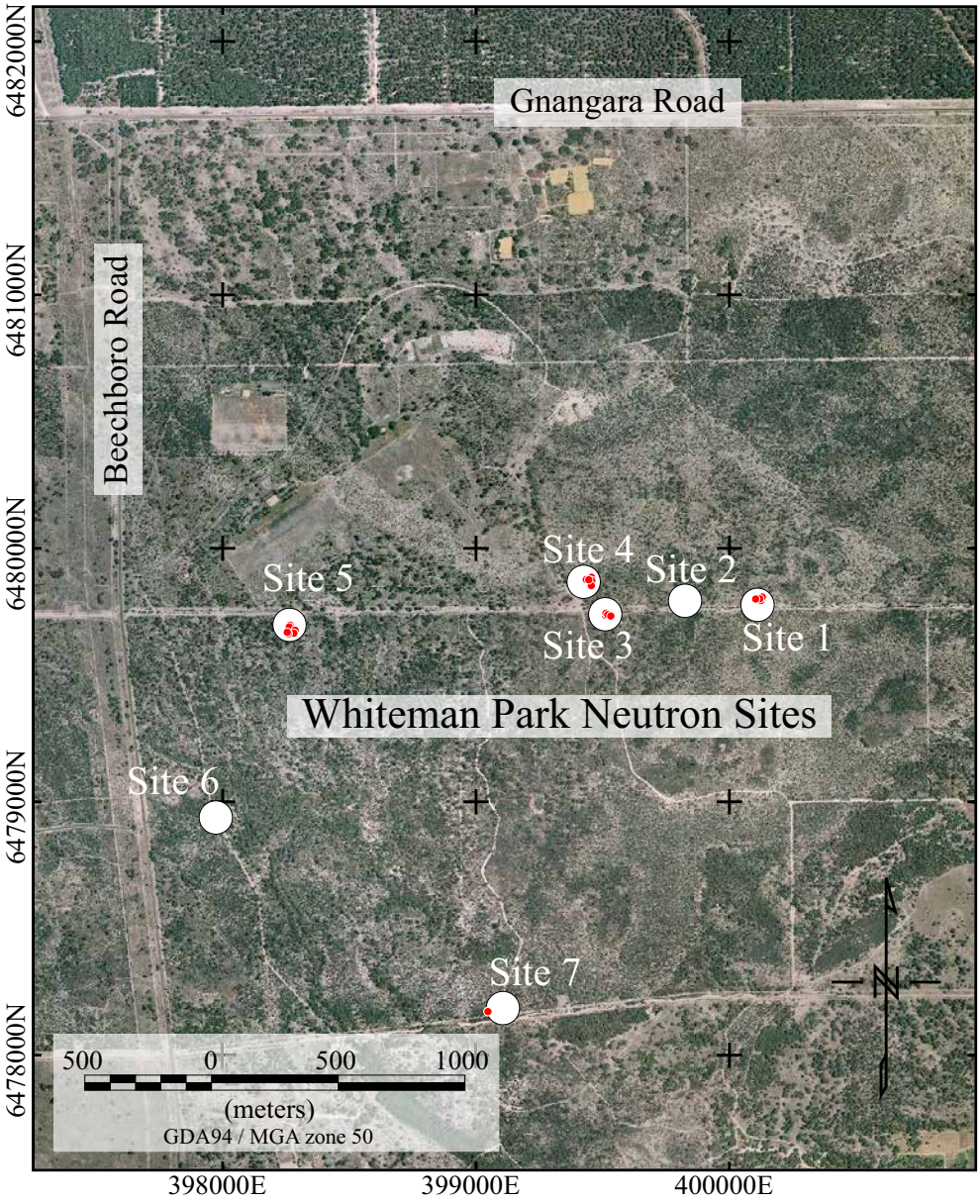

Figure B.94: *Whiteman Park test site locations for time-lapse monitoring of water infiltration. Sites have been set up by Water Corp. and Edith Cowen Unviersity (Ray Froend) to monitor soil moisture and plant response during winter pumping trial, 2006 - 2011.*

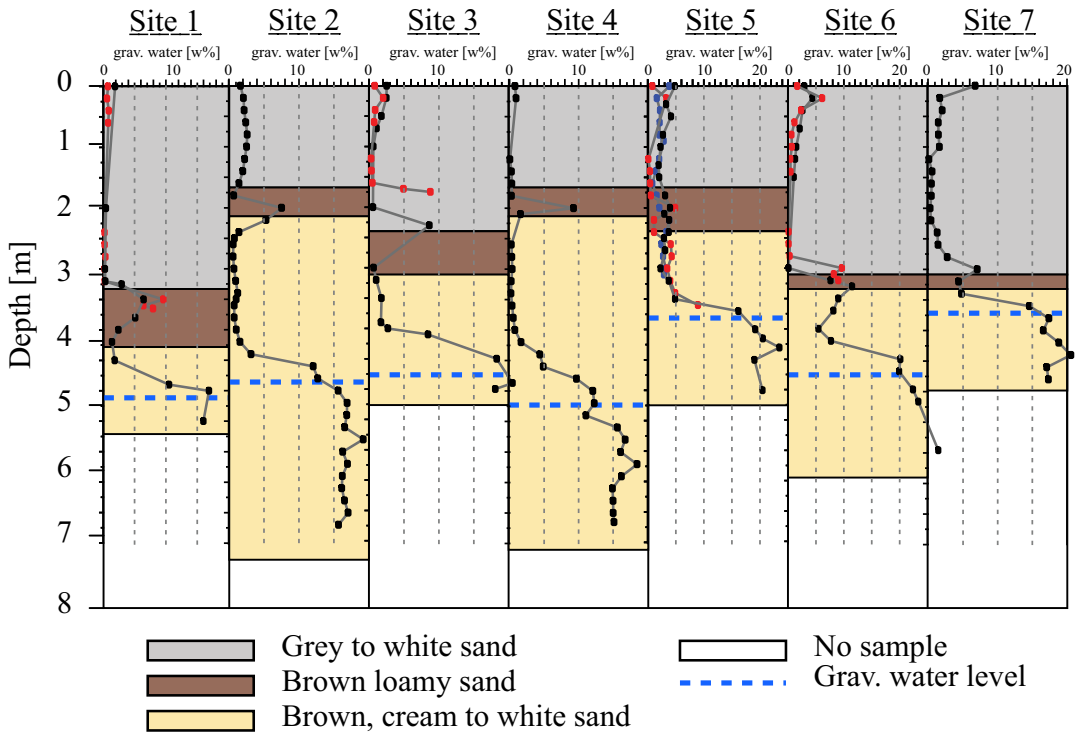

Figure B.95: *Whiteman Park site characteristics from shallow drilling and gravimetric water content analysis done by Muriel Bertuch (Bertuch and Froend, 2006).*

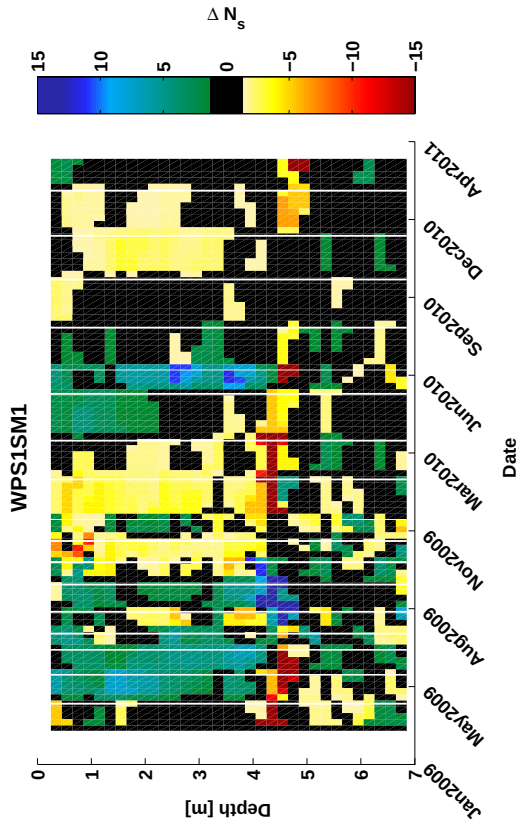

Figure B.96: *WPS1SM1 - Gridded raw time-lapse neutron counts.*

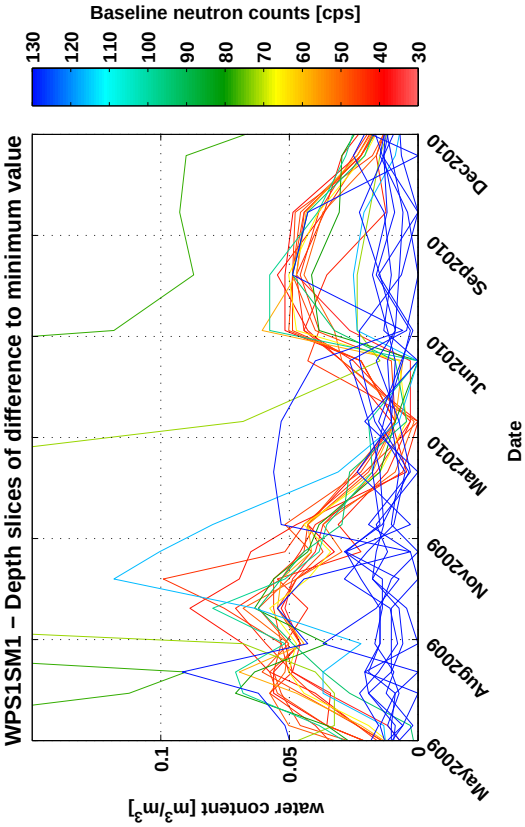

Figure B.97: *WPS1SM1 - Sequential difference in raw neutron counts.*

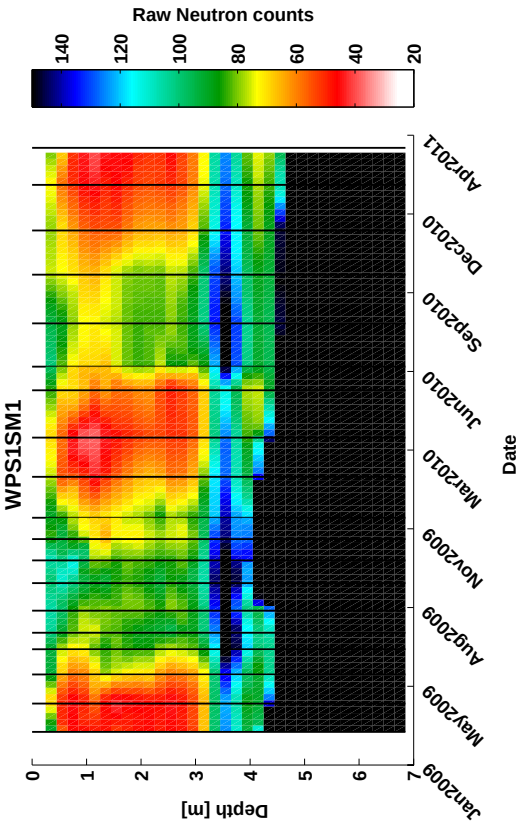

Figure B.98: *WPS1SM1 - Baseline difference of raw time-lapse neutron counts.*

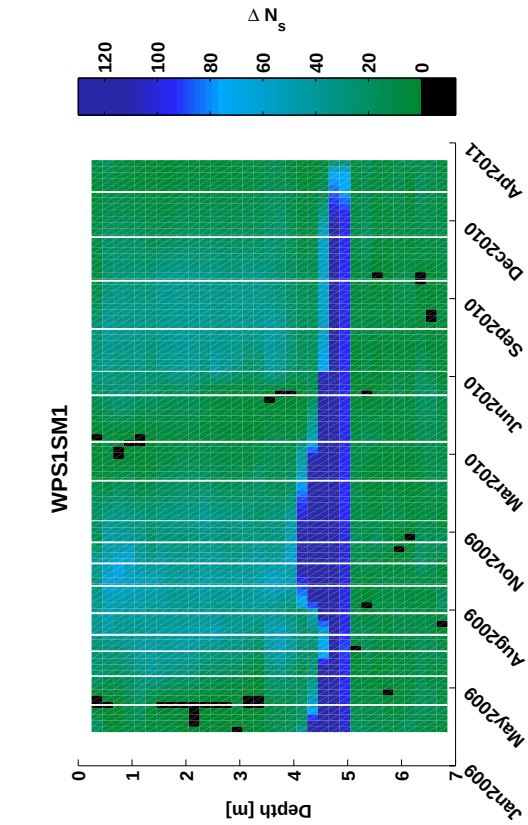

Figure B.99: *WPS1SM1 - Difference of estimated water content to driest month for individual depth levels. Colour indicates raw counts on baseline date.*

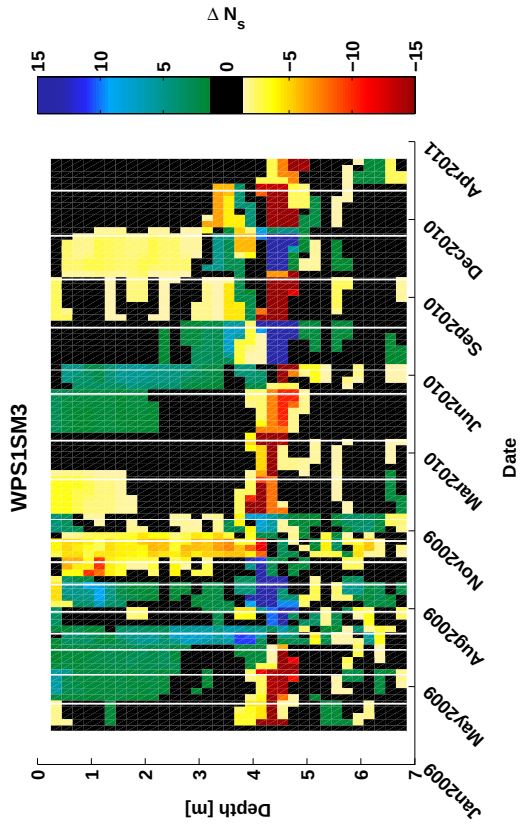

Figure B.100: *WPS1SM3 - Gridded raw time-lapse neutron counts.*

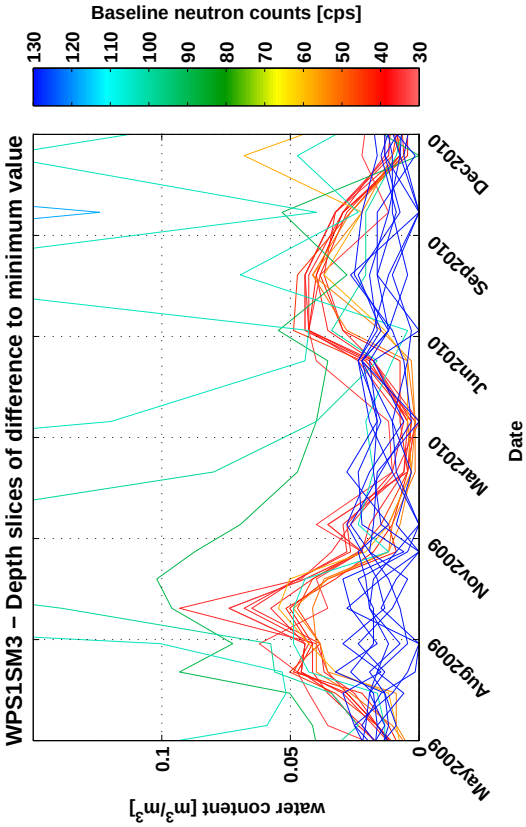

Figure B.101: *WPS1SM3 - Sequential difference in raw neutron counts.*

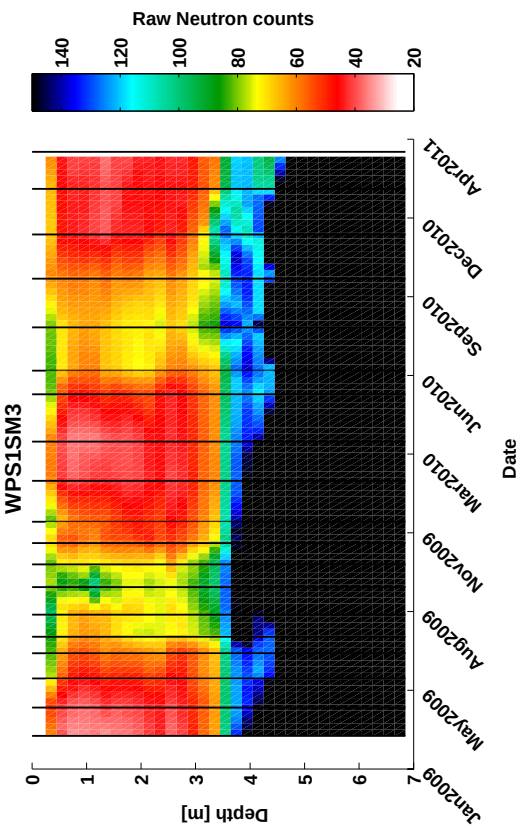

Figure B.102: *WPS1SM3 - Baseline difference of raw time-lapse neutron counts.*

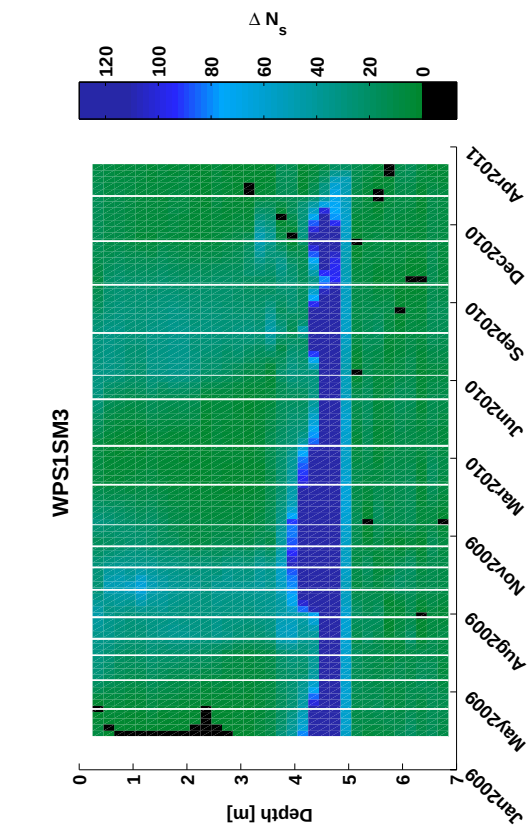

Figure B.103: *WPS1SM3 - Difference of estimated water content to driest month for individual depth levels. Colour indicates raw counts on baseline date.*

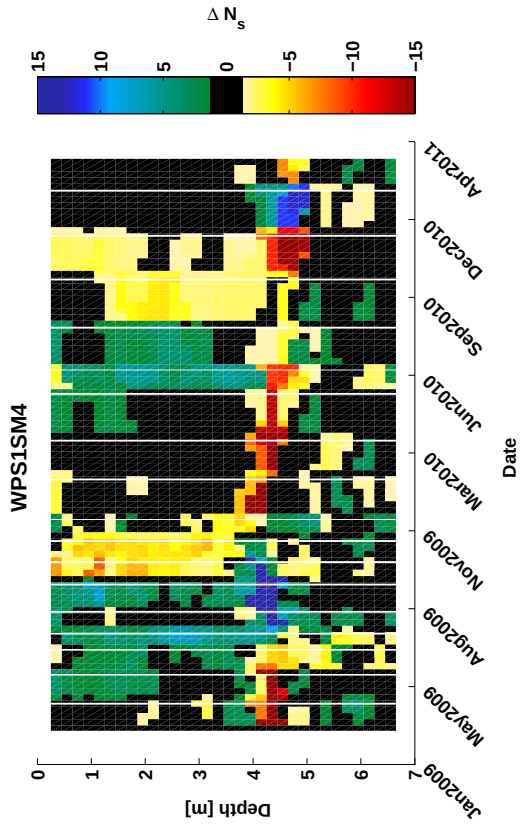

Figure B.104: *WPS1SM4 - Gridded raw time-lapse neutron counts.*

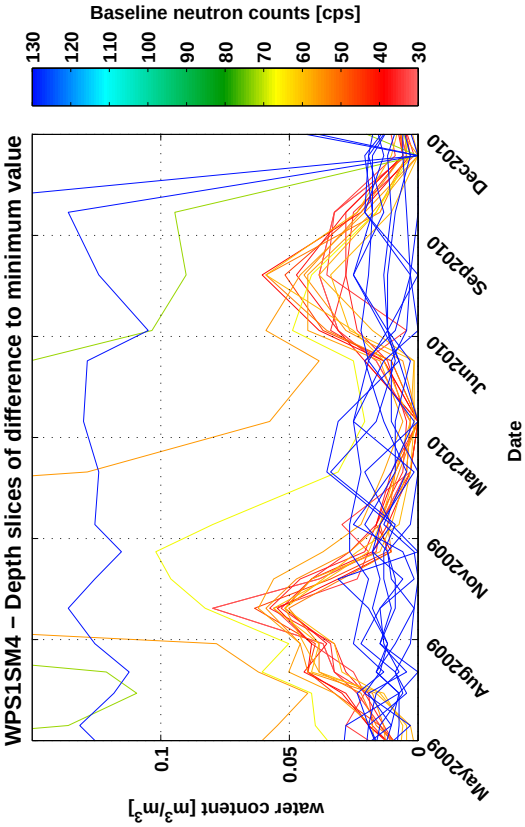

Figure B.105: *WPS1SM4 - Sequential difference in raw neutron counts.*

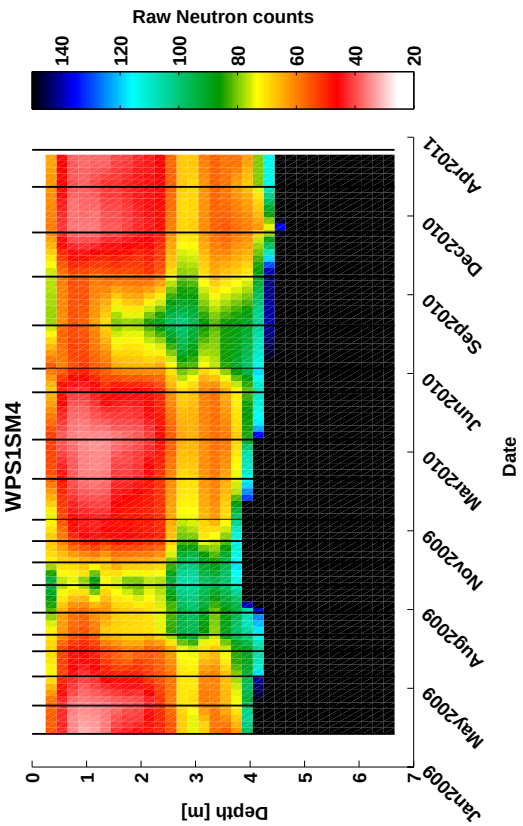

Figure B.106: *WPS1SM4 - Baseline difference of raw time-lapse neutron counts.*

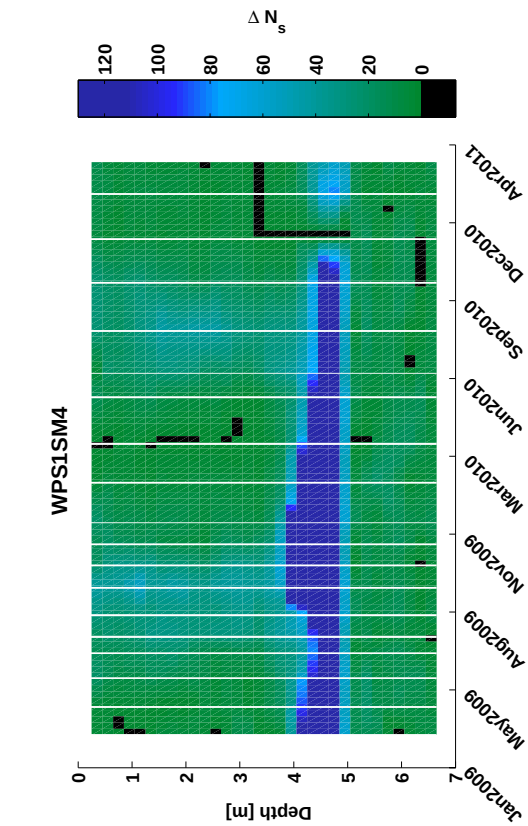

Figure B.107: *WPS1SM4 - Difference of estimated water content to driest month for individual depth levels. Colour indicates raw counts on baseline date.*

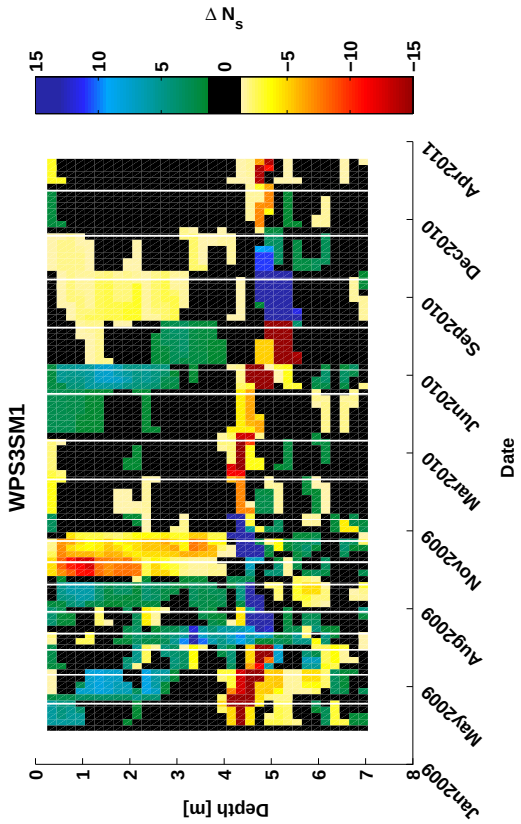

Figure B.108: *WPS3SM1 - Gridded raw time-lapse neutron counts.*

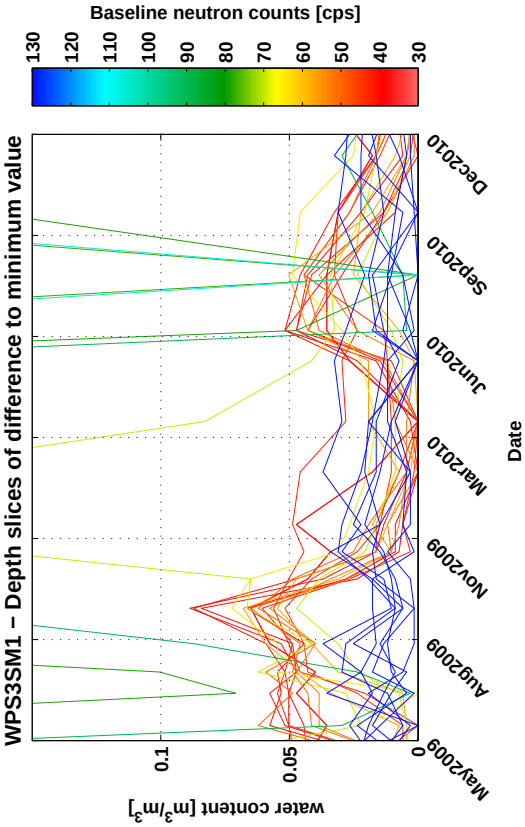

Figure B.109: *WPS3SM1 - Sequential difference in raw neutron counts.*

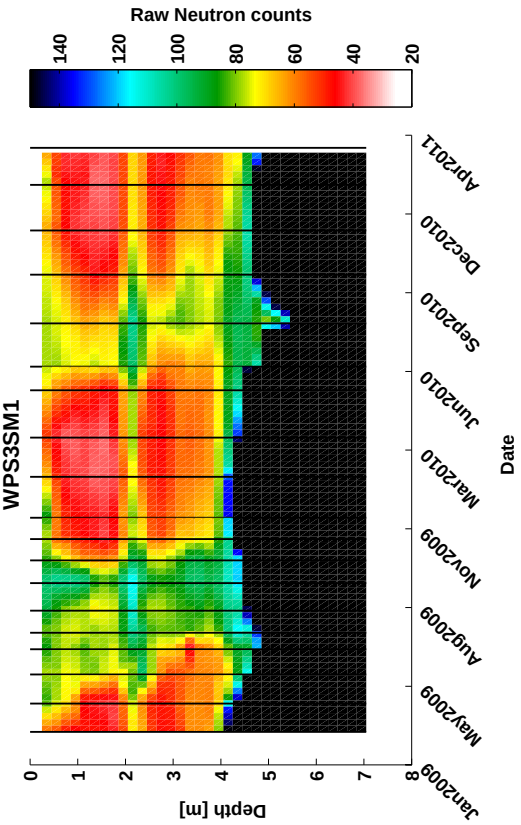

Figure B.110: *WPS3SM1 - Baseline difference of raw time-lapse neutron counts.*

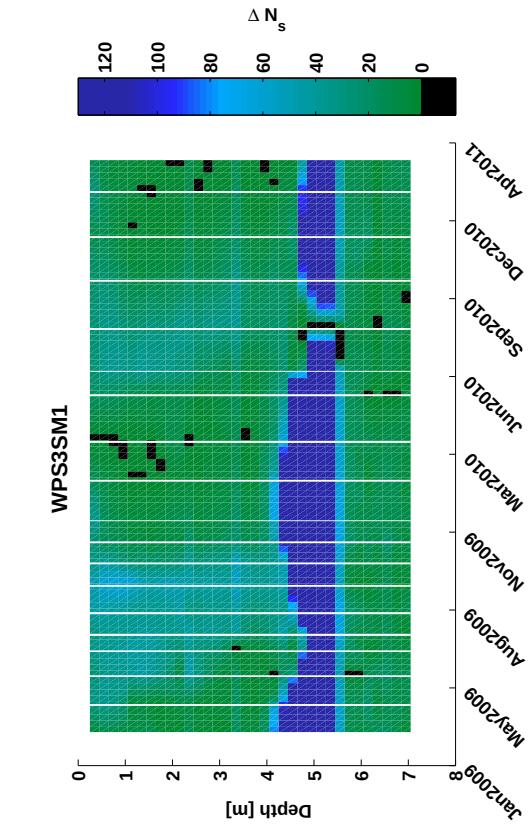

Figure B.111: *WPS3SM1 - Difference of estimated water content to driest month for individual depth levels. Colour indicates raw counts on baseline date.*

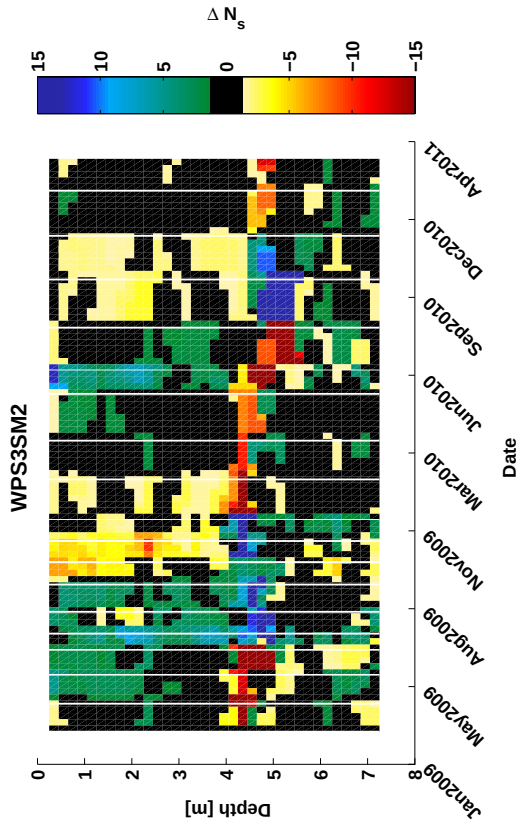

Figure B.112: *WPS3SM2 - Gridded raw time-lapse neutron counts.*

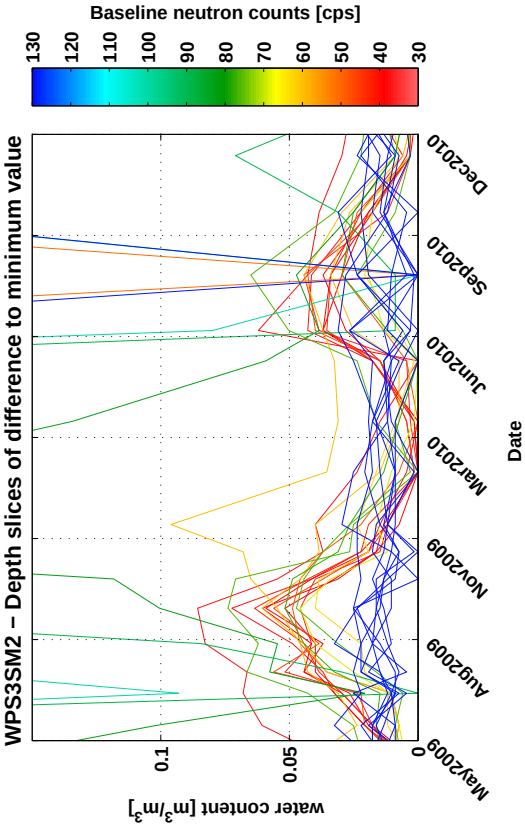

Figure B.113: *WPS3SM2 - Sequential difference in raw neutron counts.*

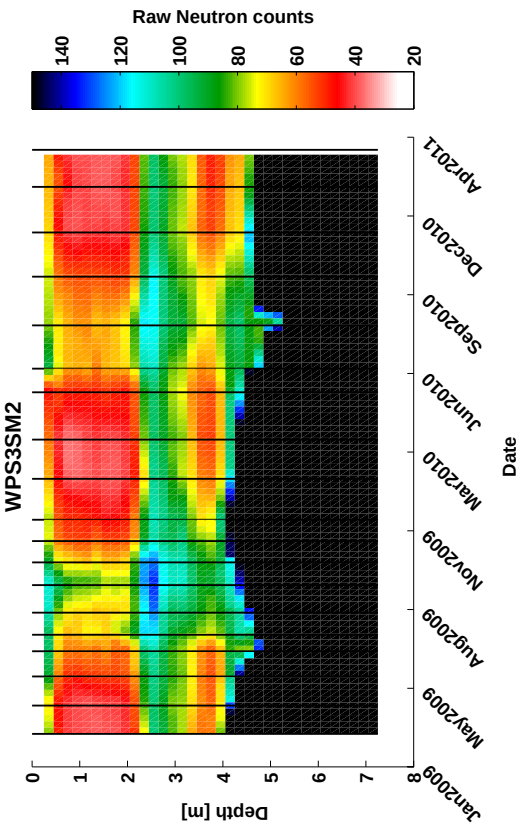

Figure B.114: *WPS3SM2 - Baseline difference of raw time-lapse neutron counts.*

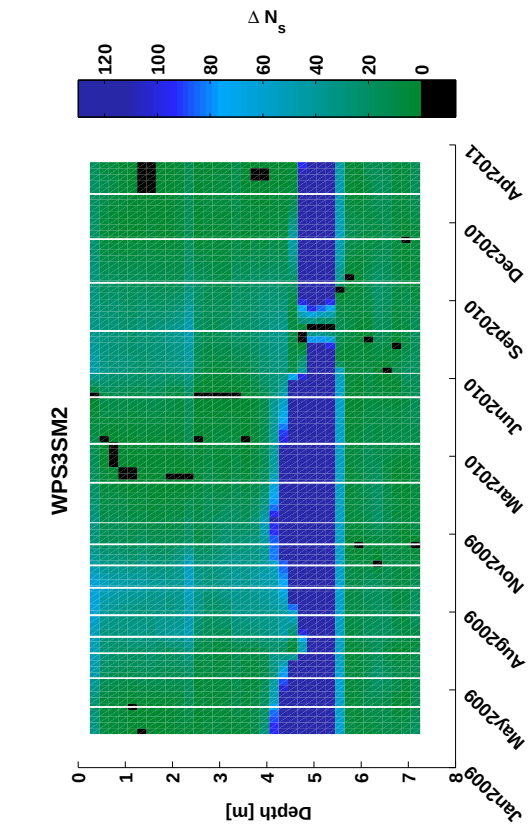

Figure B.115: *WPS3SM2 - Difference of estimated water content to driest month for individual depth levels. Colour indicates raw counts on baseline date.*

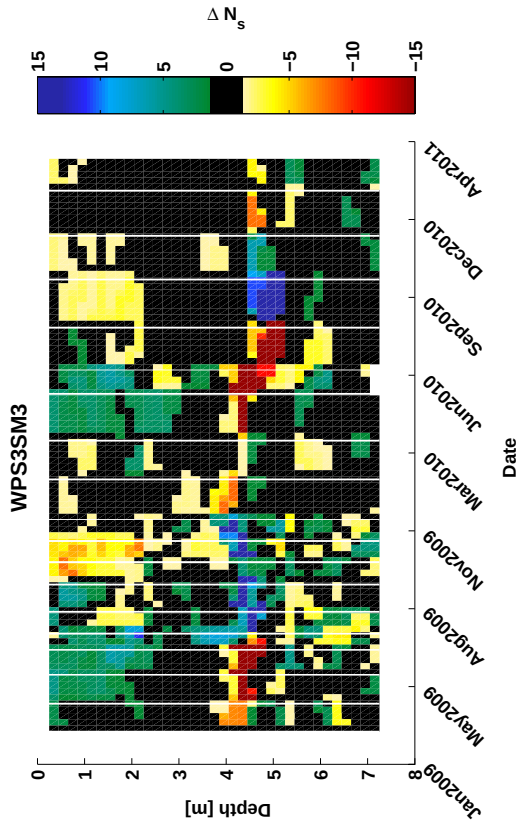

Figure B.116: *WPS3SM3 - Gridded raw time-lapse neutron counts.*

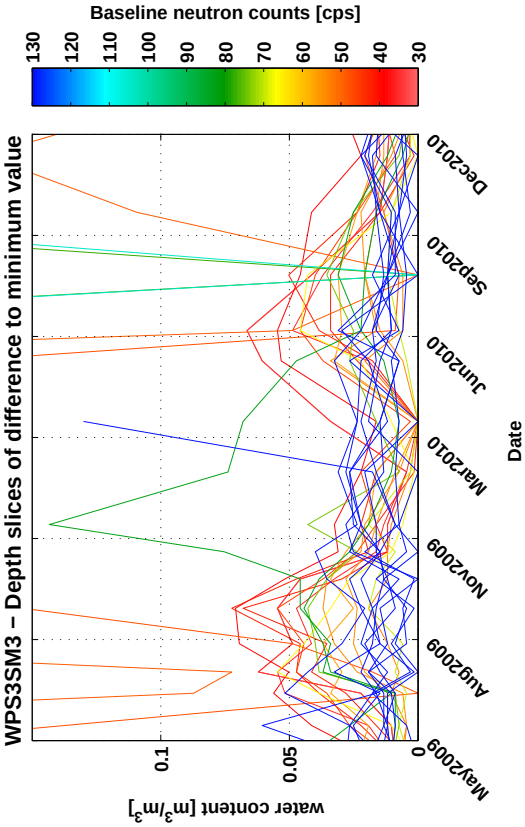

Figure B.117: *WPS3SM3 - Sequential difference in raw neutron counts.*

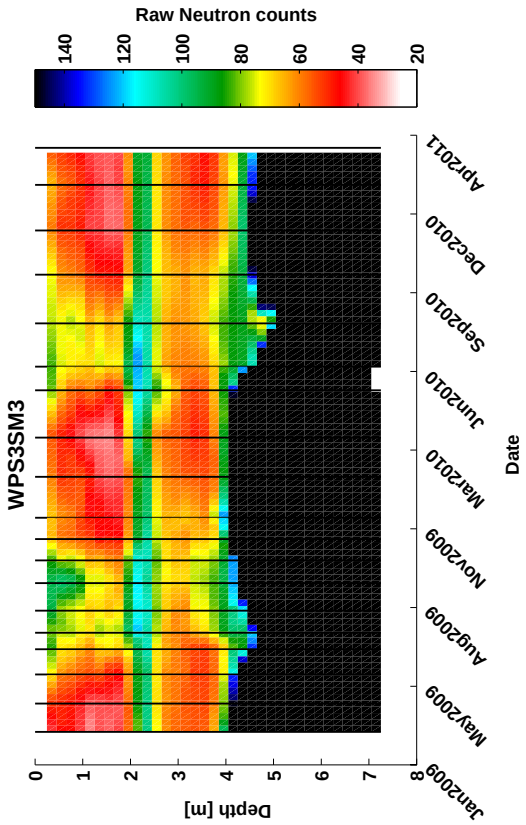

Figure B.118: *WPS3SM3 - Baseline difference of raw time-lapse neutron counts.*

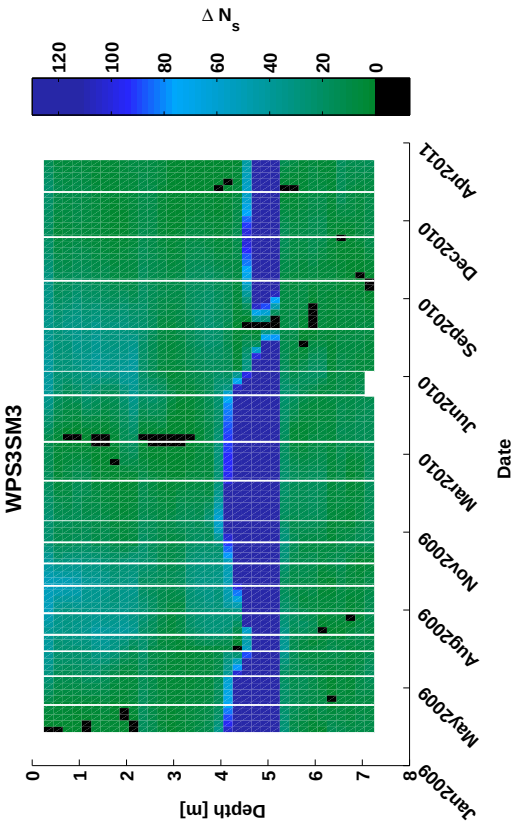

Figure B.119: *WPS3SM3 - Difference of estimated water content to driest month for individual depth levels. Colour indicates raw counts on baseline date.*

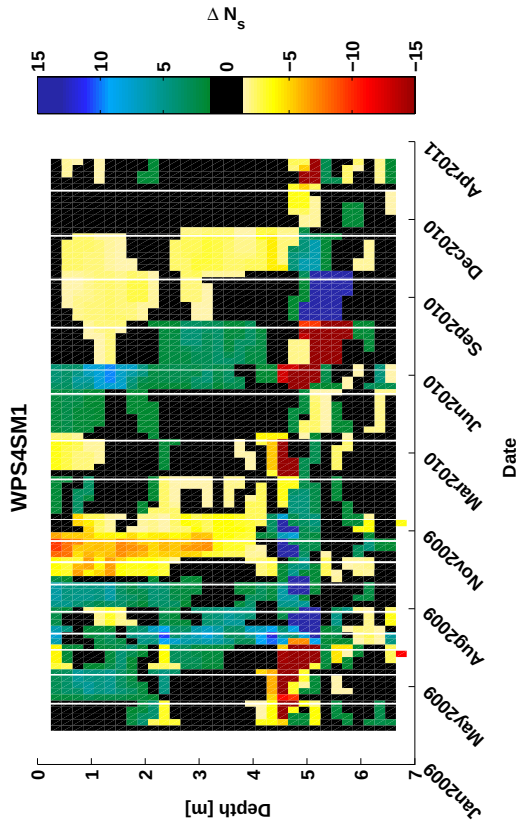

Figure B.120: *WPS4SM1 - Gridded raw time-lapse neutron counts.*

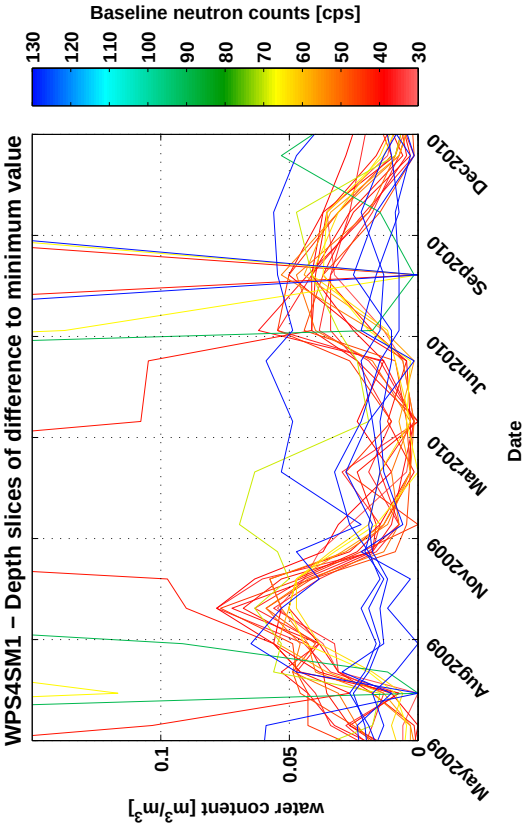

Figure B.121: *WPS4SM1 - Sequential difference in raw neutron counts.*

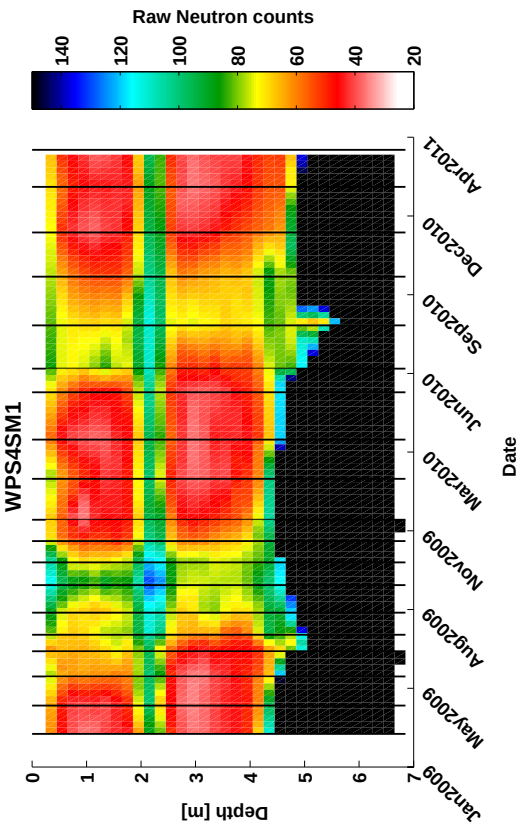

Figure B.122: *WPS4SM1 - Baseline difference of raw time-lapse neutron counts.*

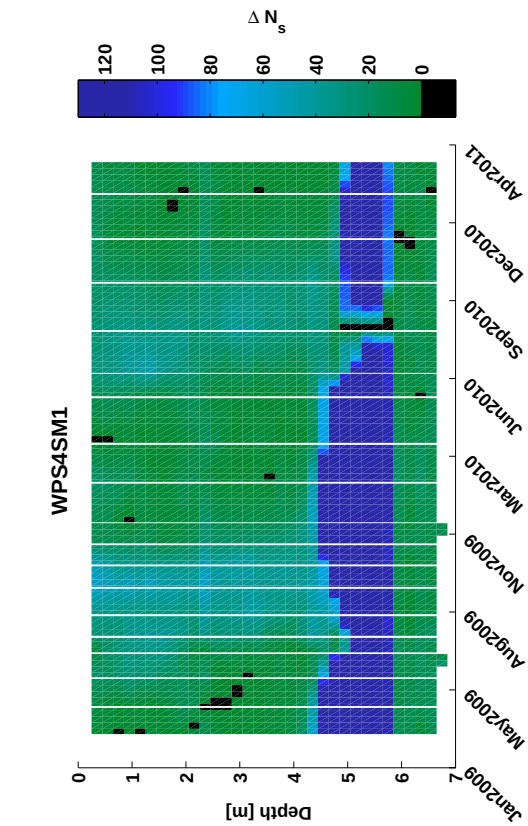

Figure B.123: *WPS4SM1 - Difference of estimated water content to driest month for individual depth levels. Colour indicates raw counts on baseline date.*

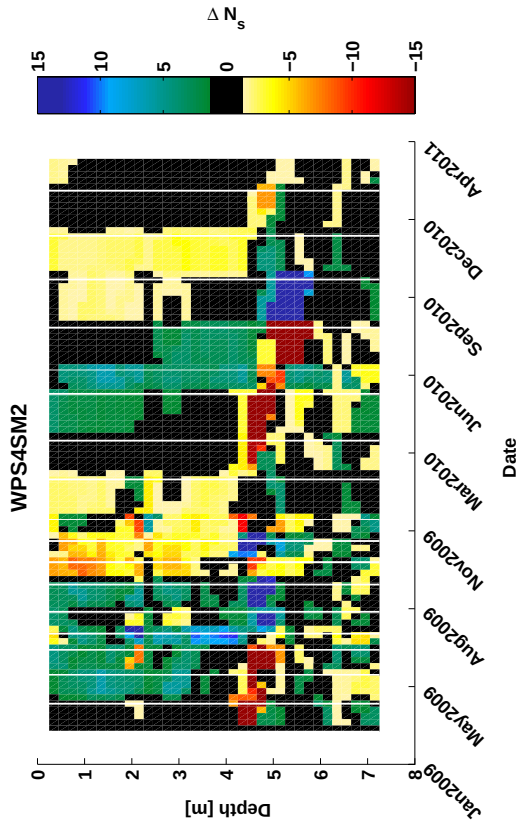

Figure B.124: *WPS4SM2 - Gridded raw time-lapse neutron counts.*

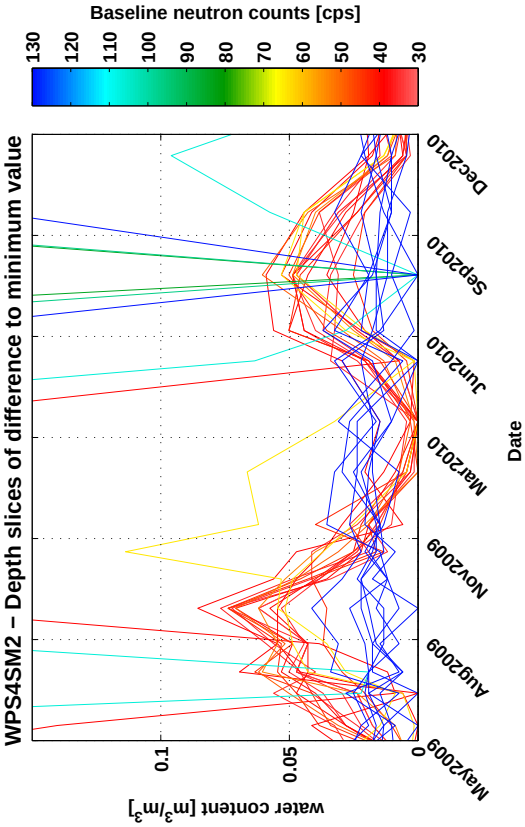

Figure B.125: *WPS4SM2 - Sequential difference in raw neutron counts.*

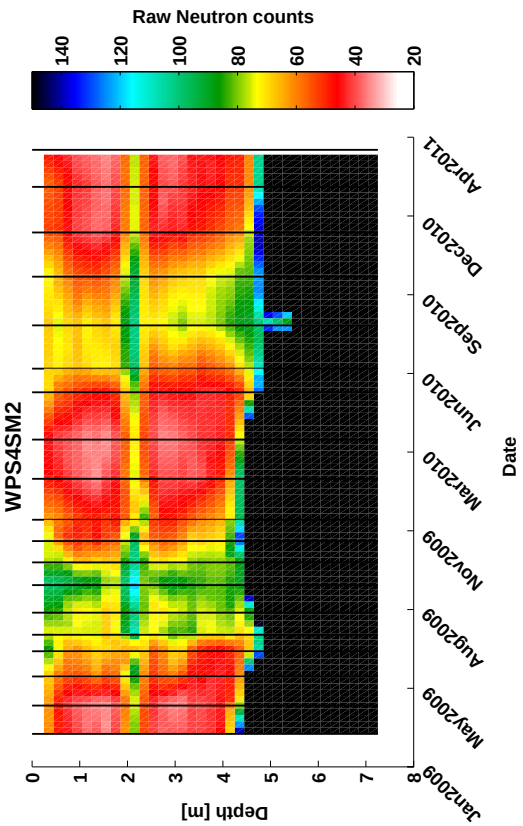

Figure B.126: *WPS4SM2 - Baseline difference of raw time-lapse neutron counts.*

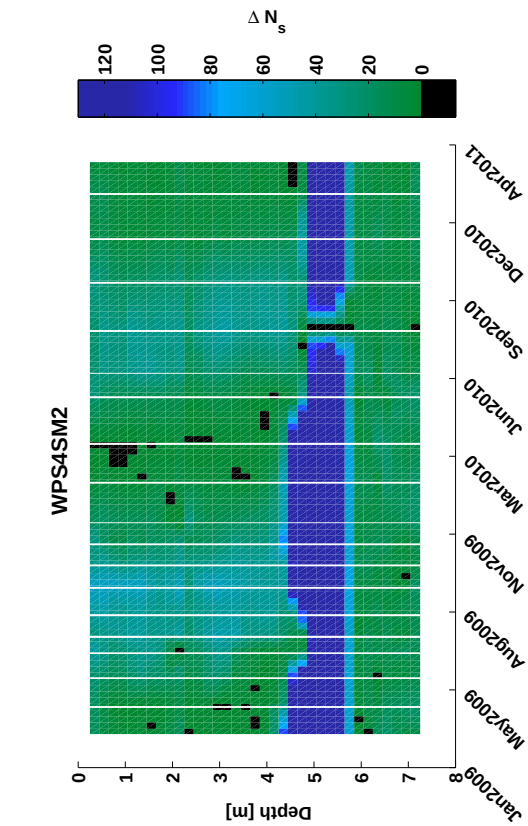

Figure B.127: *WPS4SM2 - Difference of estimated water content to driest month for individual depth levels. Colour indicates raw counts on baseline date.*

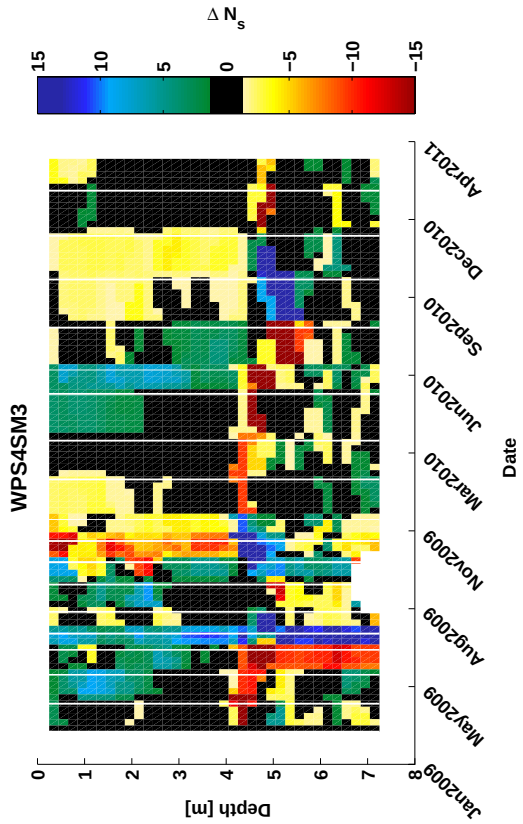

Figure B.128: *WPS4SM3 - Gridded raw time-lapse neutron counts.*

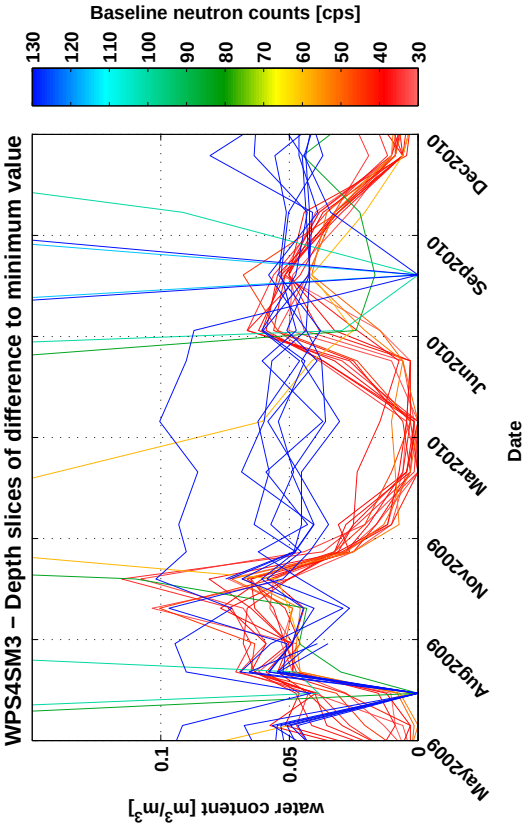

Figure B.129: *WPS4SM3 - Sequential difference in raw neutron counts.*

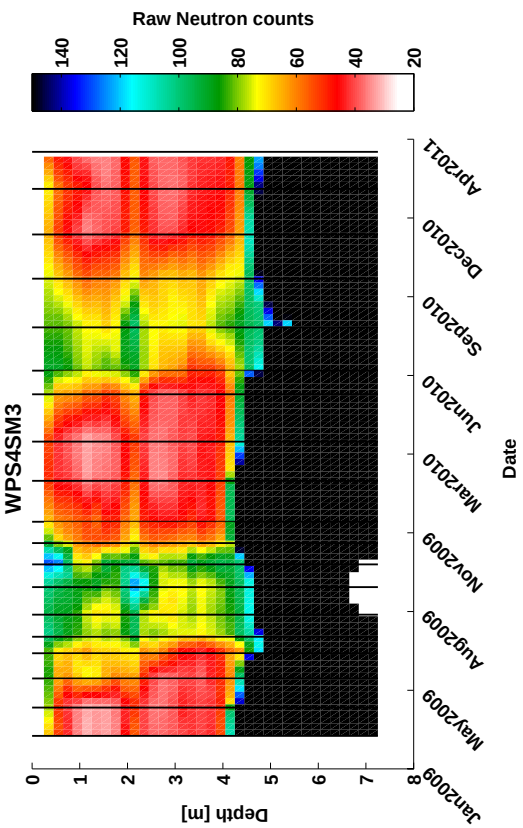

Figure B.130: *WPS4SM3 - Baseline difference of raw time-lapse neutron counts.*

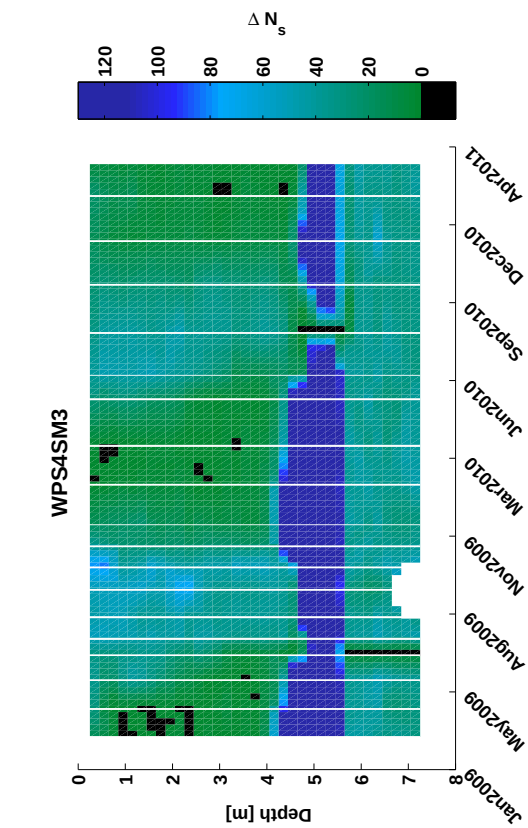

Figure B.131: *WPS4SM3 - Difference of estimated water content to driest month for individual depth levels. Colour indicates raw counts on baseline date.*

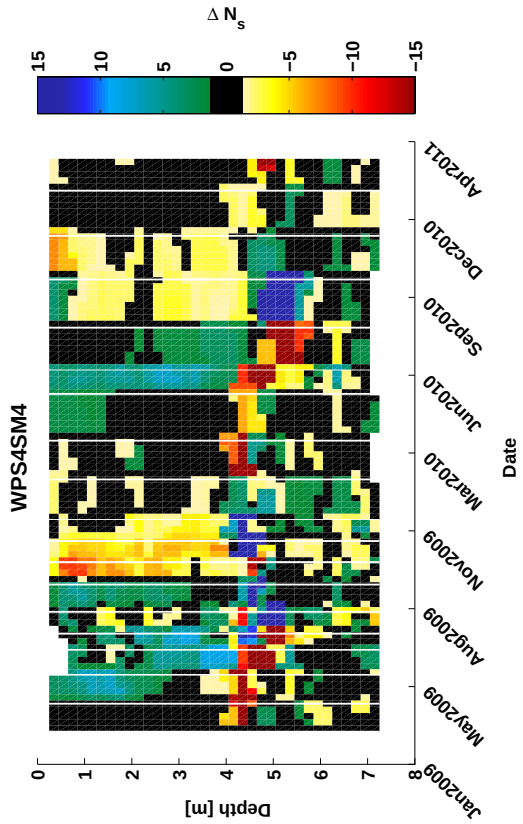

Figure B.132: *WPS4SM4 - Gridded raw time-lapse neutron counts.*

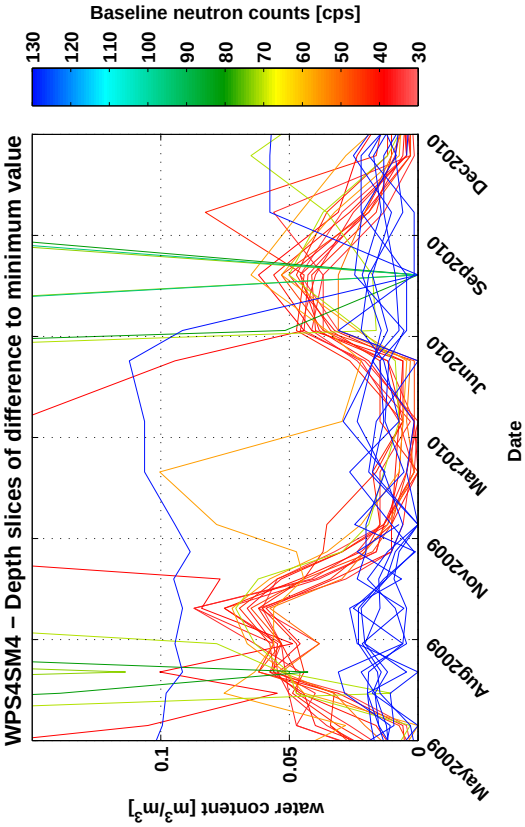

Figure B.133: *WPS4SM4 - Sequential difference in raw neutron counts.*

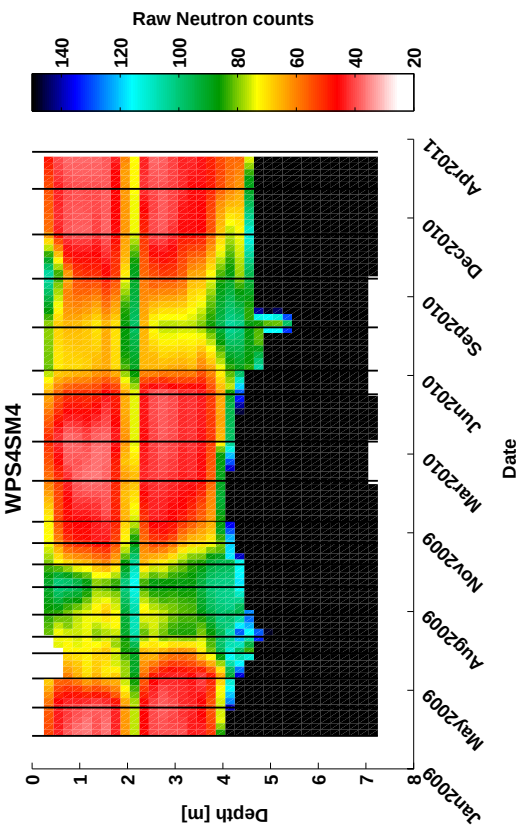

Figure B.134: *WPS4SM4 - Baseline difference of raw time-lapse neutron counts.*

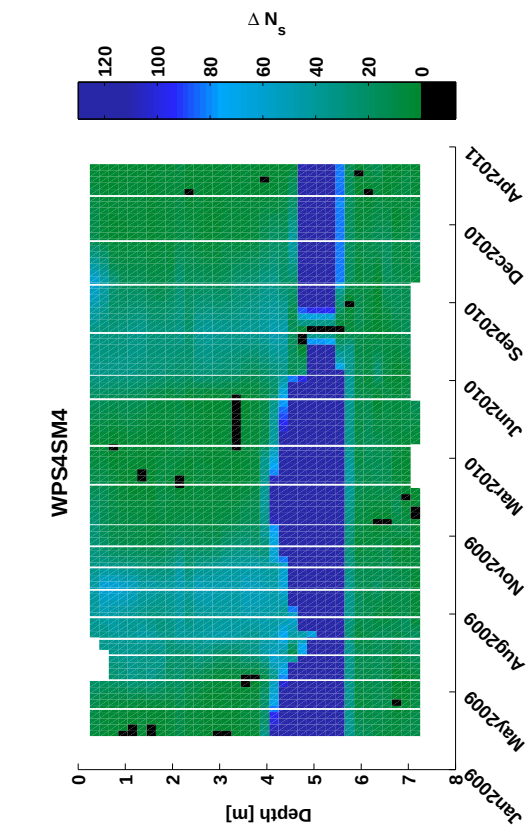

Figure B.135: *WPS4SM4 - Difference of estimated water content to driest month for individual depth levels. Colour indicates raw counts on baseline date.*

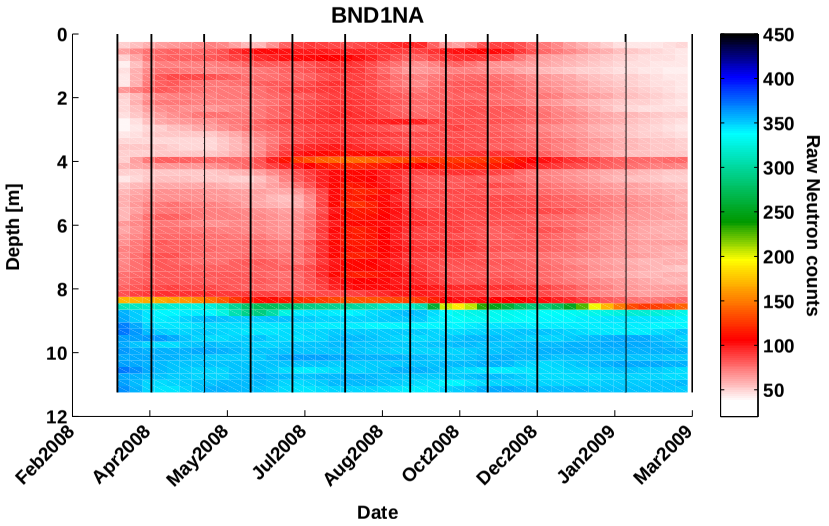

Figure B.136: *BND1NA - Gridded raw time-lapse neutron counts. Colour scaled for saturated zone.*

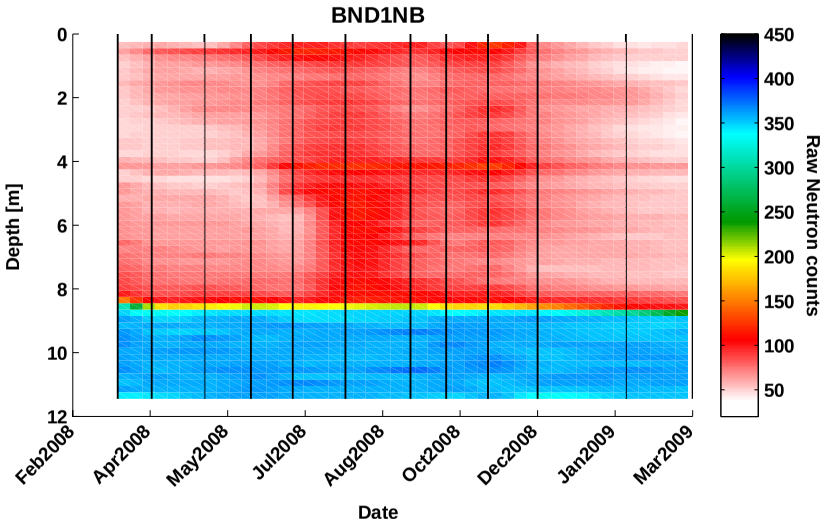

Figure B.137: *BND1NB - Gridded raw time-lapse neutron counts. Colour scaled for saturated zone.*

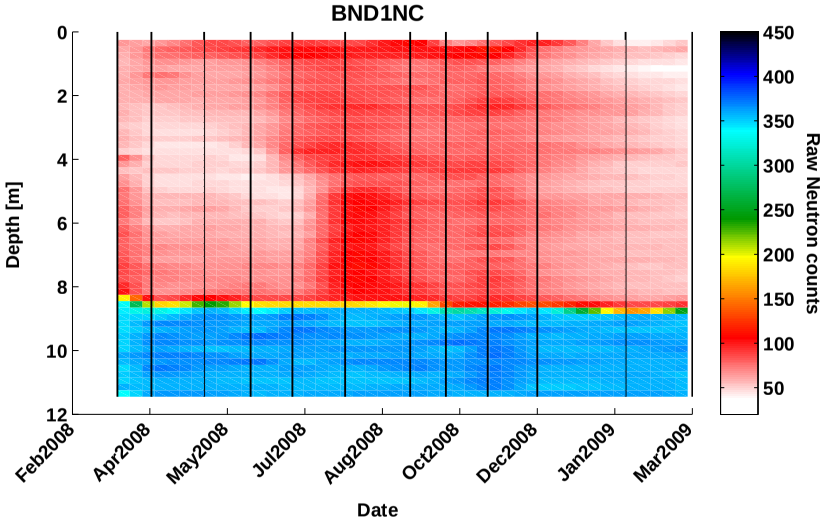

Figure B.138: *BND1NC - Gridded raw time-lapse neutron counts. Colour scaled for saturated zone.*

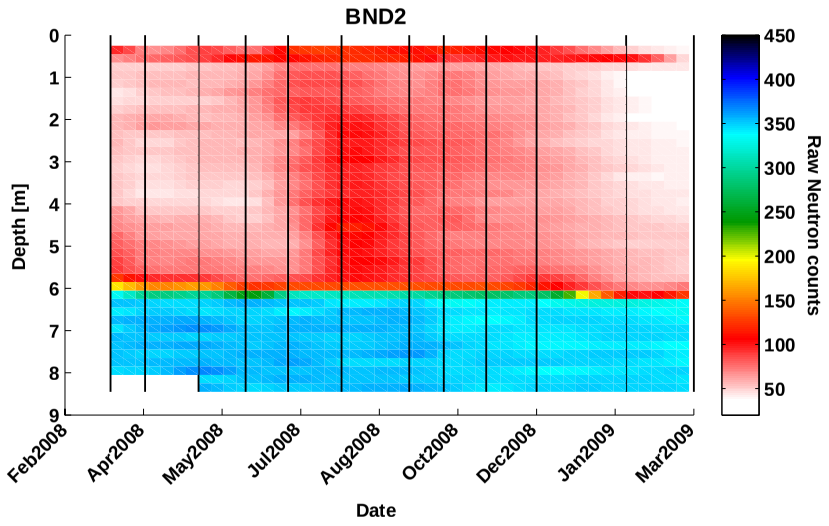

Figure B.139: *BND2 - Gridded raw time-lapse neutron counts. Colour scaled for saturated zone.*

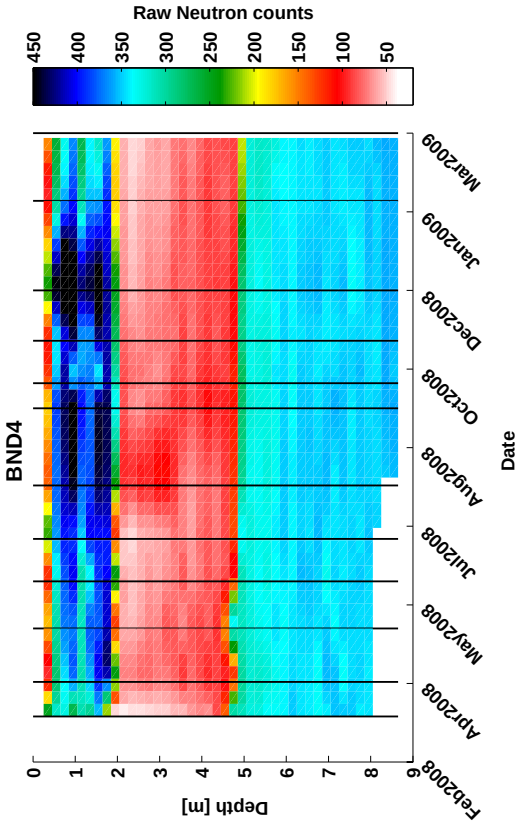

Figure B.141: *BND4 - Gridded raw time-lapse neutron counts. Colour scaled for saturated zone.*

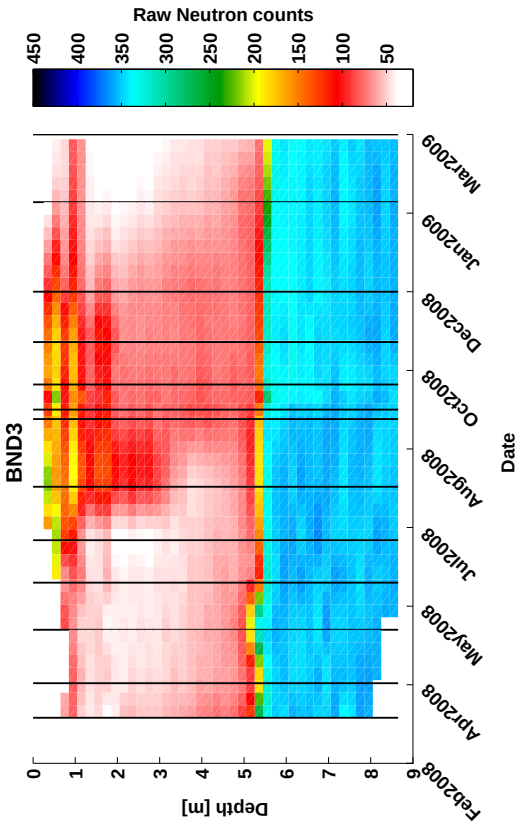

Figure B.140: *BND3 - Gridded raw time-lapse neutron counts. Colour scaled for saturated zone.*

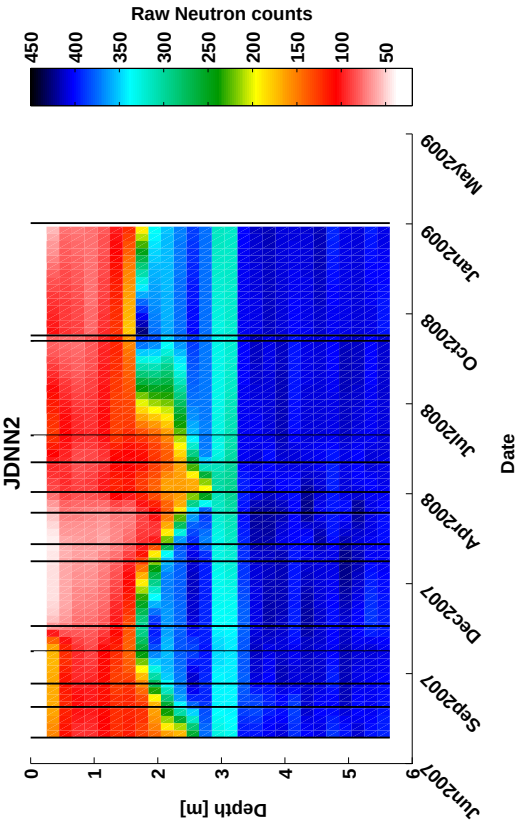

Figure B.143: *JDNN2 - Gridded raw time-lapse neutron counts. Colour scaled for saturated zone.*

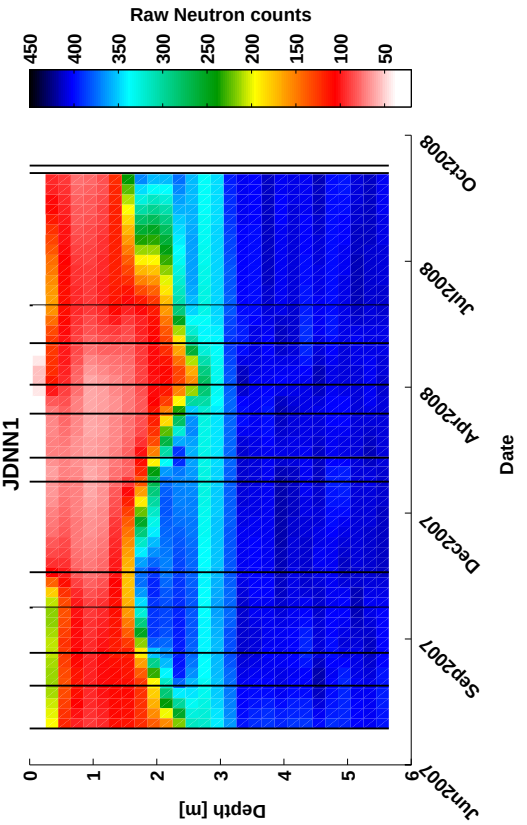

Figure B.142: *JDNN1 - Gridded raw time-lapse neutron counts. Colour scaled for saturated zone.*

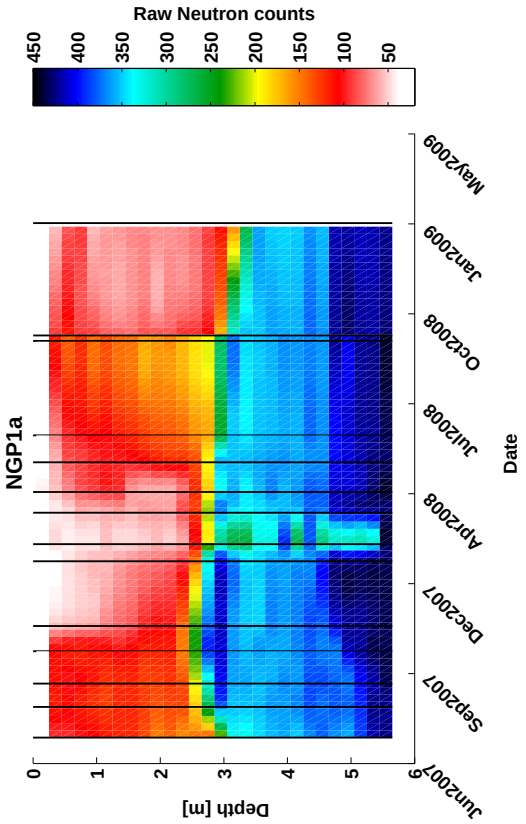

Figure B.145: *NGP1a - Gridded raw time-lapse neutron counts. Colour scaled for saturated zone.*

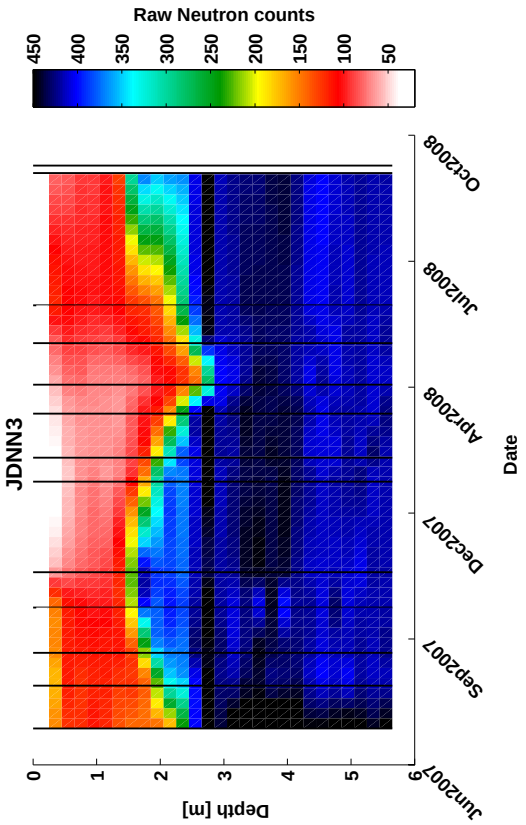

Figure B.144: *JDNN3 - Gridded raw time-lapse neutron counts. Colour scaled for saturated zone.*

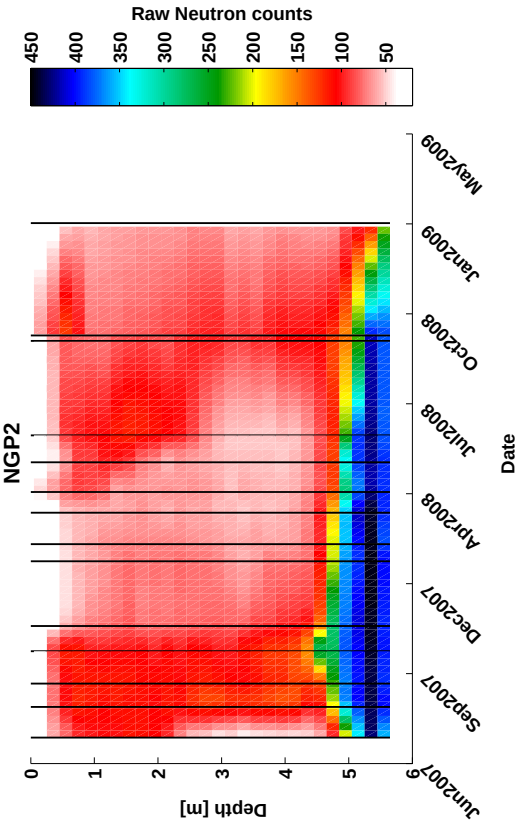

Figure B.147: *NGP2 - Gridded raw time-lapse neutron counts. Colour scaled for saturated zone.*

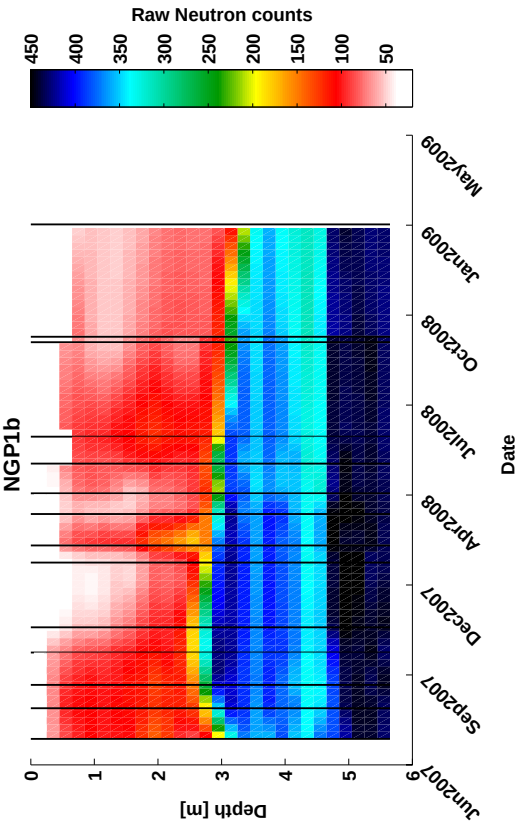

Figure B.146: *NGP1b - Gridded raw time-lapse neutron counts. Colour scaled for saturated zone.*

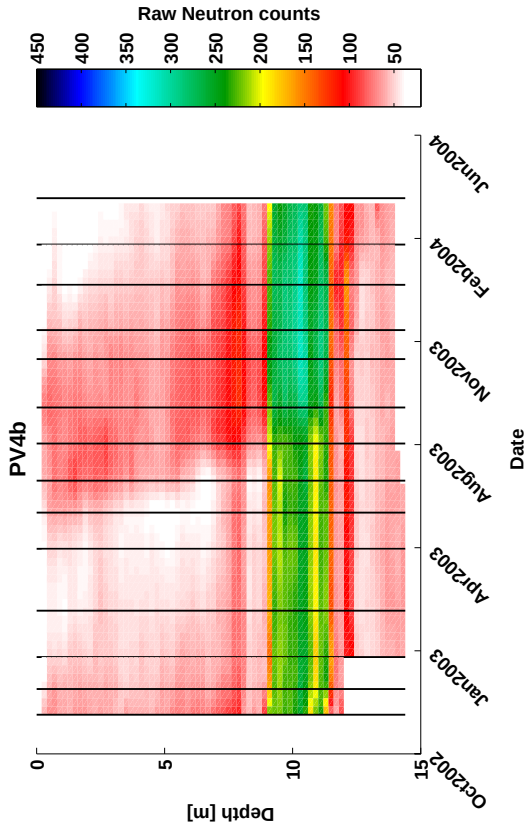

Figure B.149: *PV4b - Gridded raw time-lapse neutron counts. Colour scaled for saturated zone.*

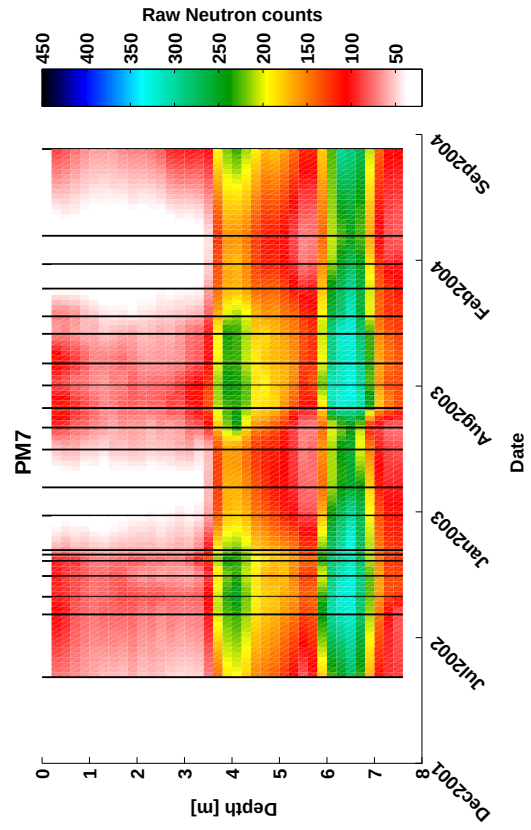

Figure B.148: *PM7 - Gridded raw time-lapse neutron counts. Colour scaled for saturated zone.*

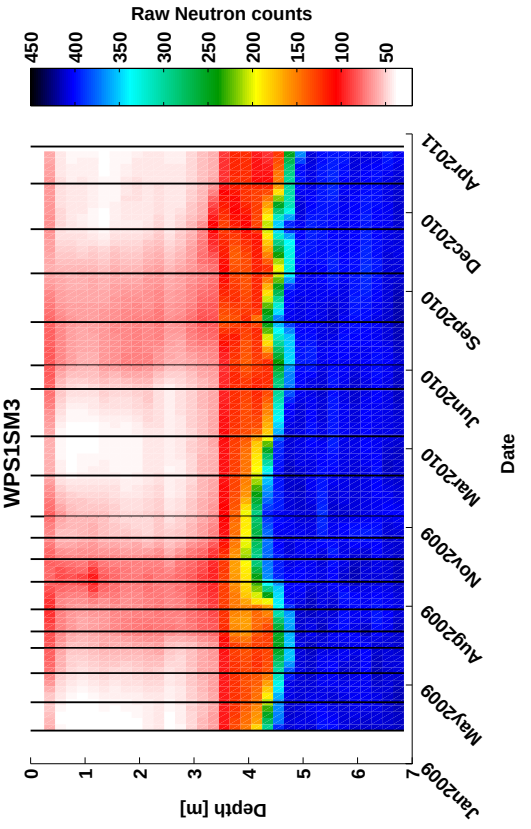

Figure B.151: *WPS1SM3 - Gridded raw time-lapse neutron counts. Colour scaled for saturated zone.*

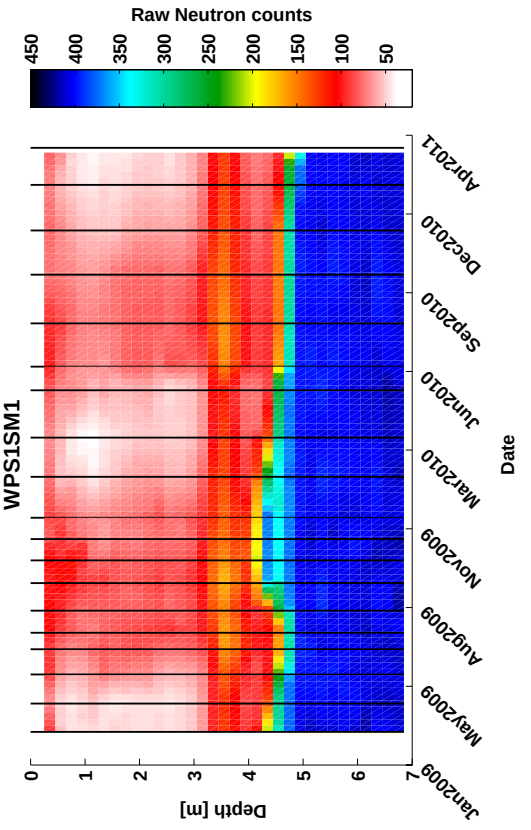

Figure B.150: *WPS1SM1 - Gridded raw time-lapse neutron counts. Colour scaled for saturated zone.*

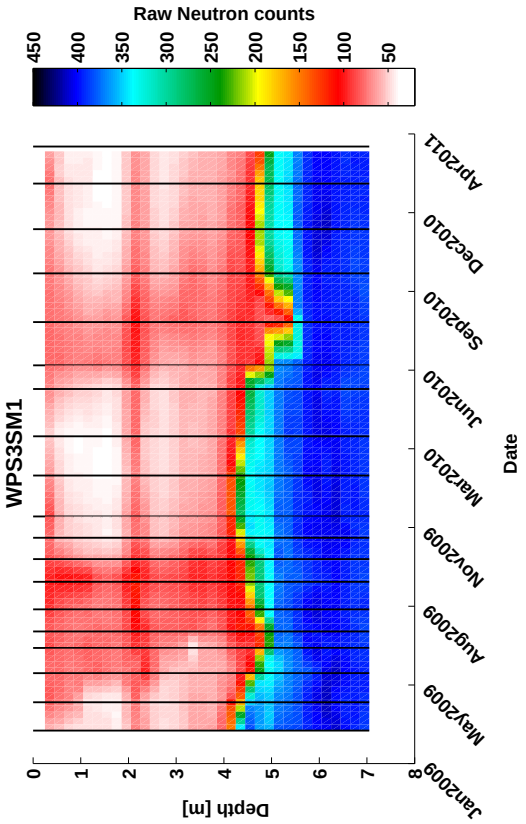

Figure B.153: *WPS3SM1 - Gridded raw time-lapse neutron counts. Colour scaled for saturated zone.*

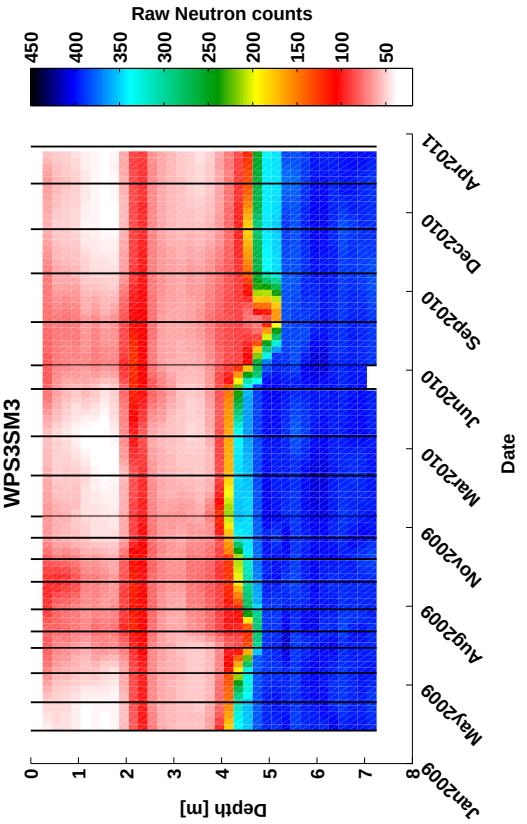

Figure B.155: *WPS3SM3 - Gridded raw time-lapse neutron counts. Colour scaled for saturated zone.*

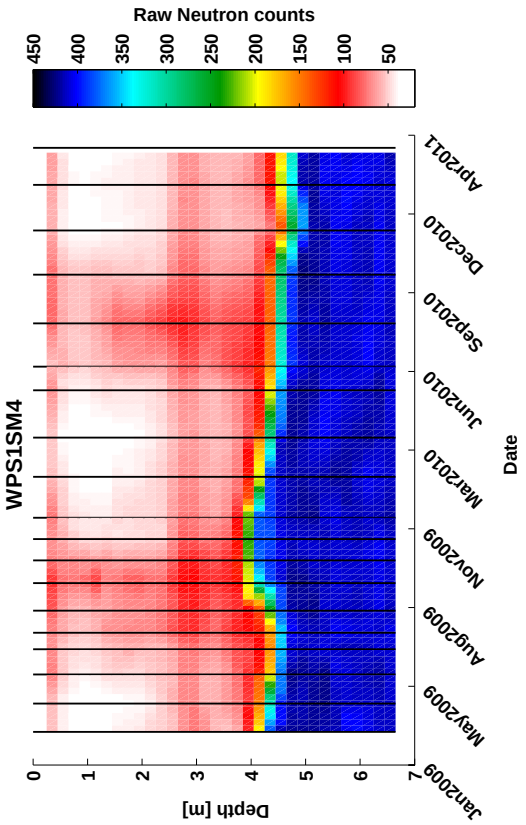

Figure B.152: *WPS1SM4 - Gridded raw time-lapse neutron counts. Colour scaled for saturated zone.*

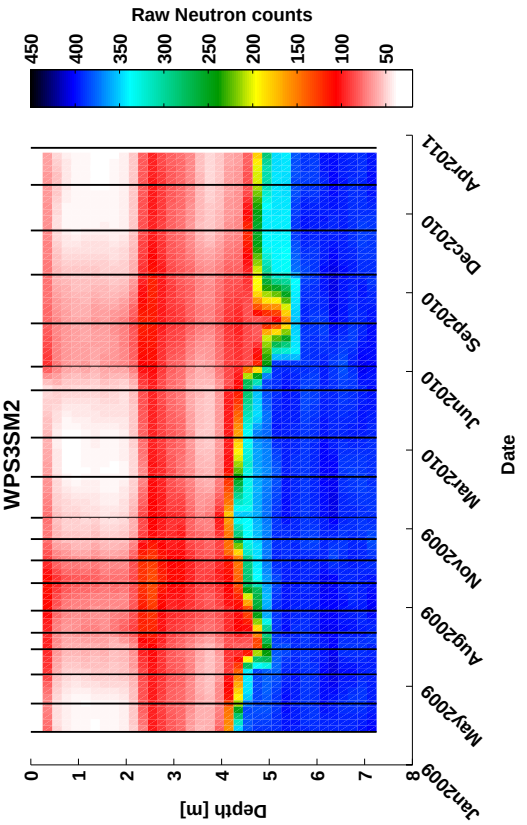

Figure B.154: *WPS3SM2 - Gridded raw time-lapse neutron counts. Colour scaled for saturated zone.*

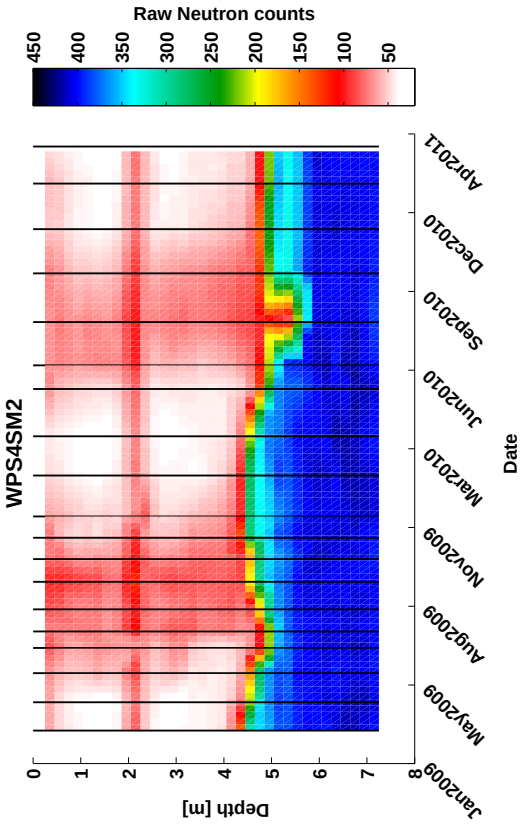

Figure B.157: *WPS4SM2 - Gridded raw time-lapse neutron counts. Colour scaled for saturated zone.*

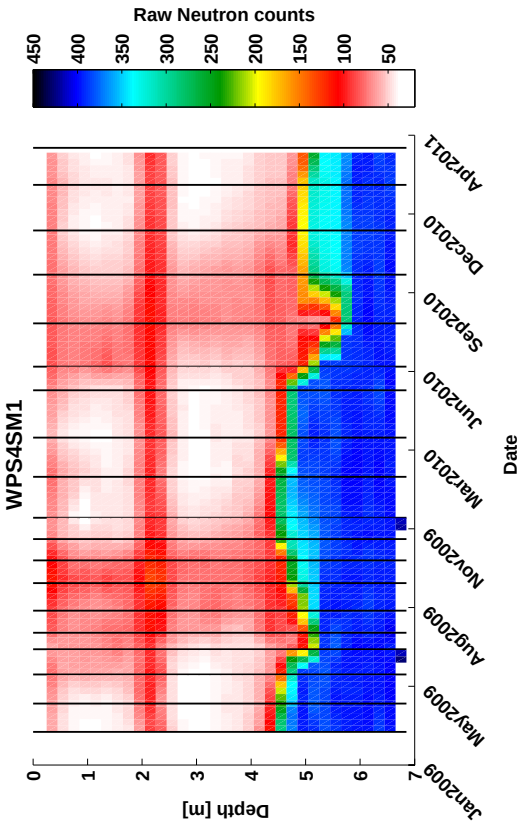

Figure B.156: *WPS4SM1 - Gridded raw time-lapse neutron counts. Colour scaled for saturated zone.*

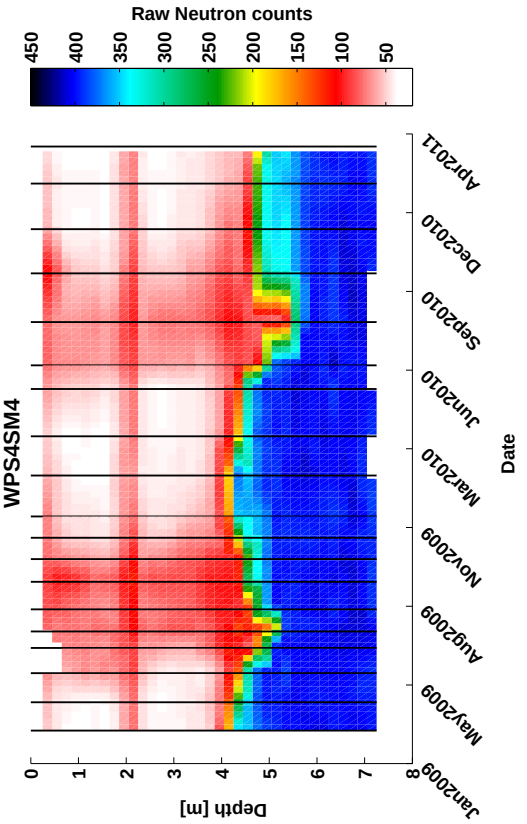

Figure B.159: *WPS4SM4 - Gridded raw time-lapse neutron counts. Colour scaled for saturated zone.*

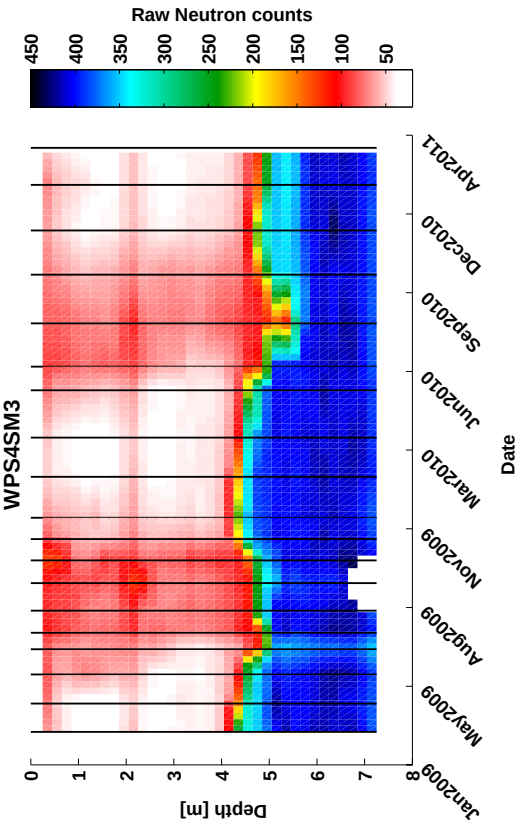

Figure B.158: *WPS4SM3 - Gridded raw time-lapse neutron counts. Colour scaled for saturated zone.*

Appendix C

Copyright consent

Perth, 27.11.2012

To Department of Water
168 St. Georges Terrace, Perth, Western Australia 6000

Dear Dept. of Water representative,

It is my understanding that you/your organisation holds copyrights in the following material:

1. **Davidson, W.A. & Yu, X. (2006), *Perth Regional Aquifer Modelling System (PRAMS) model development: Hydrogeology and groundwater modelling*, Western Australia Department of Water, Hydrogeological record series, report no. HG 20**

2. **C. Xu, M. Canci, M. Martin, M. Donnelly & R Stokes (2008), *Perth regional aquifer modelling system (PRAMS) model development: Application of the vertical flux model*, Department of Water, Western Australia, Hydrogeological record series, report no. HG 27**

I would like to reproduce an extract of this work in a doctoral thesis which I am currently undertaking at Curtin University of Technology in Perth, Western Australia. The subject of my research is hydrogeophysical characterization of groundwater recharge into the Gnangara Mound. I am carrying out this research in my own right and have no association with any commercial organisation or sponsor. The specific material / extract that I would like to use for the purposes of the thesis are

1. **From HG20: Figures 6 (p. 78) and 12 (p.85)**
2. **From HG27: Figures 8 (p. 65) and 30 (p. 79)**

Note that I made minor adjustments to the maps (i.e. move legend elements, removed profiles) which do not alter the maps' information content.
Once completed, the thesis will be made available in hard-copy form in the Curtin Library and in digital form on the Internet via the Australasian Digital Thesis Program. The material will be provided strictly for educational purposes and on a non-commercial basis. Further information on the ADT program can be found at http://adt.caul.edu.au.
I would be most grateful for your consent to the copying and communication of the work as proposed. If you are willing to grant this consent, please complete and sign the attached approval slip and return it to me at the address shown. Full acknowledgement of the ownership of the copyright and the source of the material will be provided with the material. I would be willing to use a specific form of acknowledgement that you may require and to communicate any conditions relating to its use. If you are not the copyright owner of the material in question, I would be grateful for any information you can provide as to who is likely to hold the copyright. I look forward to hearing from you and thank you in advance for your consideration of my request.
Yours sincerely

Elmar Strobach

Elmar Strobach | *PhD Student*
Department of Exploration Geophysics | Western Australian School of Mines
[**Postal Address**: GPO Box U1987, Perth, Western Australia, 6845] [Bld 613, Rm 4H23]
[**Street Address**: ARRC/CSIRO Building, H Block, Level 4, 26 Dick Perry Avenue, Kensington, WA]
Tel | +61 8 9266 3521
Fax | +61 8 9266 3407

Curtin University

Email | elmar.strobach@postgrad.curtin.edu.au
Web | www.geophysics.curtin.edu.au

Our ref: WT3237 Department of Water

Enquiries: Stella Carroll 6364 6475

Mr Elmar Strobach
PhD Student
Department of Exploration Geophysics
ARRC/CSIRO Building
HR Block, Level 4, 26 Dick Perry Avenue
Kensington WA

Dear Mr Strobach

Copyright Permission

Thank you for your email of 28 November 2012, requesting copyright permission for the use of the material/s below for use in your higher degree thesis for the Curtin University of Technology, and to communicate this material via the Australian Digital Thesis Program.

1. **Davidson, W.A. & Yu, X. (2006), *Perth Regional Aquifer Modelling System (PRAMS) model development: Hydrogeology and groundwater modelling*, Western Australia Department of Water, Hydrogeological record series, report no. HG 20**
    a. **Figure 6 (p. 78)**
    b. **Figure 12 (p.85)**

2. **C. Xu, M. Canci, M. Martin, M. Donnelly & R Stokes (2008), *Perth regional aquifer modelling system (PRAMS) model development: Application of the vertical flux model*, Department of Water, Western Australia, Hydrogeological record series, report no. HG 27**
    a. **Figure 8 (p. 65)**
    b. **Figure 30 (p. 79)**

I am pleased to advise that the Department of Water grants permission subject to full acknowledgement of the source in the publication and the department receiving a copy of the publication once it has been released.

Yours sincerely

David Brewster
Manager Corporate Communications

28 November 2012

Perth, 27.11.2012

To CSIRO, Land and Water Division

Dear CSIRO representative,

It is my understanding that you/your organisation holds copyrights in the following material:

Salama, R., Bekele, E.B., Hatton, T., Pollock, D., and Lee-Steere, N. (2002). ***Sustainable yield of groundwater of the Gnangara Mound, Perth, Western Australia*****. Proceedings International Conference on Balancing the Groundwater Budget, 12-17 May, 2002, Darwin. IAH Australia - Northern Territory Branch.**

I would like to reproduce an extract of this work in a doctoral thesis which I am currently undertaking at Curtin University of Technology in Perth, Western Australia. The subject of my research is hydrogeophysical characterization of groundwater recharge into the Gnangara Mound. I am carrying out this research in my own right and have no association with any commercial organisation or sponsor.
The specific material / extract that I would like to use for the purposes of the thesis is **Figure 1 on page 2**. Note that I made minor adjustments to the map (i.e. move legend elements, removed cadastre/logger locations, changed colour) which do not alter the geologic information content of the map.
Once completed, the thesis will be made available in hard-copy form in the Curtin Library and in digital form on the Internet via the Australasian Digital Thesis Program. The material will be provided strictly for educational purposes and on a non-commercial basis. Further information on the ADT program can be found at http://adt.caul.edu.au.
I would be most grateful for your consent to the copying and communication of the work as proposed. If you are willing to grant this consent, please complete and sign the attached approval slip and return it to me at the address shown. Full acknowledgement of the ownership of the copyright and the source of the material will be provided with the material. I would be willing to use a specific form of acknowledgement that you may require and to communicate any conditions relating to its use. If you are not the copyright owner of the material in question, I would be grateful for any information you can provide as to who is likely to hold the copyright. I look forward to hearing from you and thank you in advance for your consideration of my request.
Yours sincerely

Elmar Strobach

Elmar Strobach | *PhD Student*
Department of Exploration Geophysics | Western Australian School of Mines
[**Postal Address**: GPO Box U1987, Perth, Western Australia, 6845] [Bld 613, Rm 4H23]
[**Street Address**: ARRC/CSIRO Building, H Block, Level 4, 26 Dick Perry Avenue, Kensington, WA]
Tel | +61 8 9266 3521
Fax | +61 8 9266 3407

Email | elmar.strobach@postgrad.curtin.edu.au
Web | www.geophysics.curtin.edu.au

PERMISSION TO USE COPYRIGHT MATERIAL AS SPECIFIED BELOW:

Figure 1 (on page 2) of

Salama, R., Bekele, E.B., Hatton, T., Pollock, D., and Lee-Steere, N. (2002). *Sustainable yield of groundwater of the Gnangara Mound, Perth, Western Australia.* Proceedings International Conference on Balancing the Groundwater Budget, 12-17 May, 2002, Darwin. IAH Australia - Northern Territory Branch.

I hereby give permission for Elmar Strobach to include the abovementioned material in his higher degree thesis for the Curtin University of Technology, and to communicate this material via the Australasian Digital Thesis Program. This permission is granted on a non-exclusive basis and for an indefinite period.
I confirm that the authors (CSIRO) are the copyright owners of the specified material.

Permission to use this material is subject to the following conditions: [Delete if not applicable]

Signed: 

Name: Leane Regan

Position: Communications Manager CSIRO Water-Environment

Date: 17 December 2012

Please return signed form to Elmar Strobach

From: Michael Connolly
To: elmar.strobach@postgrad.curtin.edu.au
Subject: permission
Date: Friday, 30 November 2012 2:38:57 AM

We are pleased to grant permission for the use of the material requested for inclusion in your thesis. The following non-exclusive rights are granted to AGU authors:

- All proprietary rights other than copyright (such as patent rights).
- The right to present the material orally.
- The right to reproduce figures, tables, and extracts, appropriately cited.
- The right to make hard paper copies of all or part of the paper for classroom use.
- The right to deny subsequent commercial use of the paper.

Further reproduction or distribution is not permitted beyond that stipulated. The copyright credit line should appear on the first page of the article or book chapter. The following must also be included, "Reproduced by permission of American Geophysical Union." To ensure that credit is given to the original source(s) and that authors receive full credit through appropriate citation to their papers,
we recommend that the full bibliographic reference be cited in the reference list. The standard credit line for journal articles is: "Author(s), title of work, publication title, volume number, issue number, citation number (or page number(s) prior to 2002), year. Copyright [year] American Geophysical Union."

If an article was placed in the public domain, in which case the words "Not subject to U.S. copyright" appear on the bottom of the first page or screen of the article, please substitute "published" for the word "copyright" in the credit line mentioned above.

Michael Connolly
Program Manager, Journals
American Geophysical Union
+1.202.777.7365
MConnolly@agu.org
www.agu.org

AGU galvanizes a community of Earth and space scientists that collaboratively advances and communicates science and its power to ensure a sustainable future.

Appendix D

List of Publications

Some aspects of this thesis have been presented at conferences and published in expanded abstracts or conference papers. The work in section 5 is published in the Journal of Geophysical Research - Solid Earth.

As part of my time at the Department of Exploration Geophysics at Curtin University, I was also involved in other research projects, where I contributed to radar and refraction seismic work and have been listed as co-author on journal publications and technical reports. Those, however, are not directly related to this study, but provided me with experience that influenced this study and are therefore listed here as well.

The concepts, modeling, data acquisition, data analysis and interpretations presented in the following publications are the work of the main author, while the co-authors contribution was general guidance and editorial of the original manuscripts. Except for large-scale 2D GPR data analysed in *Strobach et al.* (2010a) which was acquired by GeoForce Ltd. (now GroundProbe Ltd.), Neutron logging data used in *Strobach et al.* (2011, 2012b) acquired by Kel Baldock from HydroSmart Ltd. for Ray Froend from Edith Cowan University. My contribution in *Jahnert et al.* (2012) and the co-authored technical report was data acquisition, processing and editorial of the manuscript. My contribution in *Yavuz et al.* (2012) was guidance and support in the seismic refraction processing and interpretation.

Conference papers:

Strobach et al. (2010a): Strobach, E., B. Harris, J. Dupuis, A. Kepic, and M. Martin (2010), Gpr for large-scale estimation of groundwater recharge distribution, in *13th International Conference on Ground Penetrating Radar (GPR), Lecce, Italy*, pp. 1–6, IEEE. **(poster presentation)**

Strobach et al. (2012a): Strobach, E., B. D. Harris, J. C. Dupuis, A. W. Kepic, and M. W. Martin (2012), Time-lapse borehole radar measurements in a sandy groundwater system during a winter recharge cycle, in *14th International Conference on Ground Penetrating Radar (GPR), Shanghai, China*, pp. 1–6. **(oral presentation)**

Expanded abstracts:

Strobach et al. (2010b): Strobach, E., B. Harris, J. Dupuis, A. Kepic, and M. Martin (2010), Ground-penetrating radar for delineation of hydraulically significant layers

in the unsaturated zone of the Gnangara Mound, WA, in *21st ASEG Conference Extended Abstracts*, pp. 1–4, CSIRO. **(oral presentation)**

Strobach et al. (2011): Strobach, E., B. D. Harris, J. C. Dupuis, A. W. Kepic, and M. W. Martin (2011), Estimation of water content in partially saturated soil horizons with Ground-Penetrating Radar, in *73rd EAGE Conference and Exhibition, 23-25 May 2011, Vienna*. **(oral presentation)**

Strobach et al. (2012b): Strobach, E., B. D. Harris, J. Christian Dupuis, A. W. Kepic, and M. W. Martin (2012), Cross well radar and vertical radar profiling methods for time lapse monitoring of rainfall infiltration, in *22nd ASEG Conference Extended Abstracts*, pp. 1–4. **(oral presentation)**

Yavuz, S., K. Tertyshnikov, E. Strobach, and M. Urosevic (2012), The Use of Seismic Methods for Imaging Complex Mineral Bodies in Hard Rock Environments, in *Near Surface Geoscience 2012 – 18th European Meeting of Environmental and Engineering Geophysics, Paris, France*.

Journal Publications:

Strobach et al. (2013): Strobach, E., B. D. Harris, J. C. Dupuis, and A. W. Kepic, (2012), Waveguide properties recovered from common offset GPR, *Journal of Geophysical Research - Solid Earth*, **in press**.

Jahnert, R., O. de Paula, L. Collins, E. Strobach, and R. Pevzner (2012), Evolution of a Coquina Barrier in Shark Bay, Australia by GPR Imaging: Architecture of a Holocene Reservoir Analogue, *Sedimentary Geology*, available online.

Technical reports:

Pevzner, R., E. Strobach, and A. W. Kepic, (2010c), Ground penetrating radar (GPR) survey on the southern part of Lot 775 - East Perth, *Report to Perth Police department*, Dept. of Expl. Geophy., Curtin University

Strobach, E. and D. Howman, (2011), Ground penetrating radar (GPR) survey at the Deanery site, Lot 24 in Perth, Western Australia, *Report to Heritage Link Ltd.*, Dept. of Expl. Geophy., Curtin University

List of Tables

List of Figures